

NASA/CR—2012-217656



Experimental Studies of Low-Pressure Turbine Flows and Flow Control

Final Report

Ralph J. Volino

United States Naval Academy, Annapolis, Maryland

Notice for Copyrighted Information

This manuscript has been authored by an employee of the United States Naval Academy under a NASA Interagency Agreement No. C-31011-K with the National Aeronautics and Space Administration. The United States Government has a nonexclusive, irrevocable, worldwide license to prepare derivative works, publish or reproduce this manuscript, and allow others to do so, for United States Government purposes. Any publisher accepting this manuscript for publication acknowledges that the United States Government retains such a license in any published form of this manuscript. All other rights are retained by the copyright owner. Attachments are reprinted by permission.

NASA STI Program . . . in Profile

Since its founding, NASA has been dedicated to the advancement of aeronautics and space science. The NASA Scientific and Technical Information (STI) program plays a key part in helping NASA maintain this important role.

The NASA STI Program operates under the auspices of the Agency Chief Information Officer. It collects, organizes, provides for archiving, and disseminates NASA's STI. The NASA STI program provides access to the NASA Aeronautics and Space Database and its public interface, the NASA Technical Reports Server, thus providing one of the largest collections of aeronautical and space science STI in the world. Results are published in both non-NASA channels and by NASA in the NASA STI Report Series, which includes the following report types:

- **TECHNICAL PUBLICATION.** Reports of completed research or a major significant phase of research that present the results of NASA programs and include extensive data or theoretical analysis. Includes compilations of significant scientific and technical data and information deemed to be of continuing reference value. NASA counterpart of peer-reviewed formal professional papers but has less stringent limitations on manuscript length and extent of graphic presentations.
- **TECHNICAL MEMORANDUM.** Scientific and technical findings that are preliminary or of specialized interest, e.g., quick release reports, working papers, and bibliographies that contain minimal annotation. Does not contain extensive analysis.
- **CONTRACTOR REPORT.** Scientific and technical findings by NASA-sponsored contractors and grantees.
- **CONFERENCE PUBLICATION.** Collected papers from scientific and technical conferences, symposia, seminars, or other meetings sponsored or cosponsored by NASA.
- **SPECIAL PUBLICATION.** Scientific, technical, or historical information from NASA programs, projects, and missions, often concerned with subjects having substantial public interest.
- **TECHNICAL TRANSLATION.** English-language translations of foreign scientific and technical material pertinent to NASA's mission.

Specialized services also include creating custom thesauri, building customized databases, organizing and publishing research results.

For more information about the NASA STI program, see the following:

- Access the NASA STI program home page at <http://www.sti.nasa.gov>
- E-mail your question to help@sti.nasa.gov
- Fax your question to the NASA STI Information Desk at 443-757-5803
- Telephone the NASA STI Information Desk at 443-757-5802
- Write to:
STI Information Desk
NASA Center for AeroSpace Information (CASI)
7115 Standard Drive
Hanover, MD 21076-1320



Experimental Studies of Low-Pressure Turbine Flows and Flow Control

Final Report

Ralph J. Volino
United States Naval Academy, Annapolis, Maryland

Prepared under NASA Interagency Agreement No. C-31011-K

Notice for Copyrighted Information

This manuscript has been authored by an employee of the United States Naval Academy under a NASA Interagency Agreement No. C-31011-K with the National Aeronautics and Space Administration. The United States Government has a nonexclusive, irrevocable, worldwide license to prepare derivative works, publish or reproduce this manuscript, and allow others to do so, for United States Government purposes. Any publisher accepting this manuscript for publication acknowledges that the United States Government retains such a license in any published form of this manuscript. All other rights are retained by the copyright owner. Attachments are reprinted by permission.

National Aeronautics and
Space Administration

Glenn Research Center
Cleveland, Ohio 44135

Acknowledgments

This project was performed under the NASA Glenn Research Center's Low Pressure Turbine (LPT) Flow Physics program. The contract monitor was David E. Ashpis. His support, useful discussions, input, and suggestions are greatly appreciated and contribute to the success of this project.

Trade names and trademarks are used in this report for identification only. Their usage does not constitute an official endorsement, either expressed or implied, by the National Aeronautics and Space Administration.

This work was sponsored by the Fundamental Aeronautics Program at the NASA Glenn Research Center.

Level of Review: This material has been technically reviewed by NASA technical management.

Available from

NASA Center for Aerospace Information
7115 Standard Drive
Hanover, MD 21076-1320

National Technical Information Service
5301 Shawnee Road
Alexandria, VA 22312

Available electronically at <http://www.sti.nasa.gov>

Experimental Studies of Low-Pressure Turbine Flows and Flow Control Final Report

Ralph J. Volino
United States Naval Academy
Annapolis, Maryland 21402

Summary

An experimental study of the suction side boundary layer on an airfoil under simulated low pressure turbine conditions has been completed. Detailed measurements from the boundary layer have been acquired under a wide range of experimental conditions. The data have been saved and analyzed and results have been published. Models describing the flow behavior have been produced. The nature of the boundary layer separation, transition to turbulence, and reattachment has been documented. Methods for controlling the separation, transition and reattachment have been developed, experimentally implemented, studied in detail through boundary layer measurements, and reported through publications. Ten baseline cases without flow control were documented under high and low freestream turbulence conditions at five Reynolds numbers of 25,000, 50,000, 100,000, 200,000 and 300,000 based on passage exit velocity and suction surface wetted length. Boundary layer profiles were acquired at eleven streamwise locations between the leading and trailing edge of the airfoil, documenting the streamwise component of the velocity. Integral quantities such as boundary layer thicknesses and shape factors, as well as skin friction coefficients were computed based on the mean velocity results. Turbulence statistics were computed including the intermittency for the transitional flow. Large amounts of data were acquired at each measurement location in every profile, which allowed the calculation of turbulence spectra at all locations. The mean flow quantities, turbulence statistics and spectra have all been reported in the publications listed below. Addition two-component velocity profile measurements were acquired at the five most downstream measurement locations, where separation, transition, and reattachment occur. Mean flow quantities, turbulence statistics and spectra were again documented for the two component measurements, and included documentation of the turbulent shear stress and its spectra.

Passive flow control was investigated under the same 10 experimental conditions with the same documentation at the five most downstream measurement locations. Passive control was first achieved using two-dimensional bars located at the pressure minimum on the suction side of the airfoil. Cases with three different bar thicknesses were fully documented, for a total of 30 new experimental cases. Cases with three-dimensional passive devices were documented next. The three-dimensional devices were small circular cylinders extending from the airfoil surface. Two different cylinder heights were considered, matching two of the two-dimensional bar heights. The cylinders were located at the same streamwise position as the two-dimensional bars. Many cases with different cylinder separations were documented. Data were acquired at multiple spanwise locations downstream of the three-dimensional devices. Based on the transition behavior and the spectral data of the baseline and passive flow control cases, a transition model and correlation were developed and successfully compared to other experimental cases from the literature. Passive flow control was successful at controlling the separation problem at low Reynolds numbers, with varying degrees of success from case to case and varying levels of impact at higher Reynolds numbers.

Active flow control was achieved using a row of oscillating (synthetic) vortex generator jets located at the pressure minimum on the suction side of the airfoil. One case with low freestream turbulence and a low Reynolds number of 25,000 was studied. All of the data acquisition and documentation noted above were done for this case. Data were acquired at multiple spanwise locations to document the three-dimensional nature of the flow downstream of the jets along the airfoil surface. Time averaged flow

results were presented and phase averaged results were also computed to show the response of the boundary layer to the unsteady jets. The active flow control successfully eliminated the large separation problem for the low Reynolds number case.

Detailed documentation of the experimental conditions, descriptions of the experiments, experimental results and modeling efforts are presented for all the experimental cases in the following publications. Reprints are included in the appendix.

Journal Publications

1. Volino, R.J. "Separated Flow Transition Under Low-Pressure Turbine Airfoil Conditions: Part 1—Mean Flow and Turbulence Statistics," *ASME Journal of Turbomachinery*, Vol. 124, pp. 545-655, 2002.
2. Volino, R.J. "Separated Flow Transition Under Low-Pressure Turbine Airfoil Conditions: Part 2—Turbulence Spectra," *ASME Journal of Turbomachinery*, Vol. 124, pp. 656-664, 2002.
3. Volino, R.J. "Passive Flow Control on Low-Pressure Turbine Airfoils," *ASME Journal of Turbomachinery*, Vol. 125, pp. 754-764, 2003.
4. Volino, R.J. "Separation Control on Low-Pressure Turbine Airfoils Using Synthetic Vortex Generator Jets," *ASME Journal of Turbomachinery*, Vol. 125, pp. 765-777, 2003.
5. Bohl, D.G. and Volino, R.J. "Experiments With Three-Dimensional Passive Flow Control Devices on Low-Pressure Turbine Airfoils," *ASME Journal of Turbomachinery*, Vol. 128, pp. 251-260, 2006.
6. Suzen, Y.B., Huang, P.G., Ashpis, D.E., Volino, R.J., Corke, T.C., Thomas, F.O., Huang, J., Lake, J.P. and King, P.I. "A Computational Fluid Dynamics Study of Transitional Flows in Low-Pressure Turbines Under a Wide Range of Operating Conditions," *ASME Journal of Turbomachinery*, Vol. 129, pp. 527-541, 2007.

Peer Reviewed Conference Papers (fully reviewed by 3 independent reviewers)

1. Volino, R.J. "Separated Flow Transition Under Low-Pressure Turbine Airfoil Conditions: Part 1—Mean Flow and Turbulence Statistics," ASME paper GT-2002-30236. Presented at the 2002 ASME International Gas Turbine Conference, Amsterdam, The Netherlands.
2. Volino, R.J. "Separated Flow Transition Under Low-Pressure Turbine Airfoil Conditions: Part 2—Turbulence Spectra," ASME paper GT-2002-30237. Presented at the 2002 ASME International Gas Turbine Conference, Amsterdam, The Netherlands.
3. Volino, R.J. "Passive Flow Control on Low-Pressure Turbine Airfoils," ASME paper GT2003-38728. Presented at the 2003 ASME International Gas Turbine Conference, Atlanta, GA.
4. Volino, R.J. "Separation Control on Low-Pressure Turbine Airfoils Using Synthetic Vortex Generator Jets," ASME paper GT2003-38729. Presented at the 2003 ASME International Gas Turbine Conference, Atlanta, GA.

5. Volino, R.J. and Bohl, D.G. "Separated Flow Transition Mechanism and Prediction with High and Low Freestream Turbulence under Low Pressure Turbine Conditions," ASME paper GT2004-53360. Presented at the 2004 ASME International Gas Turbine Conference, Vienna, Austria.
6. Bohl, D.G. and Volino, R.J. "Experiments with Three-Dimensional Passive Flow Control Devices on Low-Pressure Turbine Airfoils," ASME paper GT2005-68969. Presented at the 2005 ASME International Gas Turbine Conference, Reno, NV.

Other Conference Papers (peer reviewed)

1. Suzen, Y.B., Huang, P.G., Volino, R.J., Corke, T.C., Thomas, F.O., Huang, J., Lake, J.P., and King, P.I. "A Comprehensive CFD Study of Transitional Flows in Low-Pressure Turbines Under a Wide Range of Operating Conditions," AIAA paper 2003-3591. Presented at the 33rd AIAA Fluid Dynamics Conference, Orlando, FL.
2. Volino, R.J. and Bohl, D.G. "Structure of Oscillating Vortex Generator Jets," Proceedings of the Fourth International Symposium on Turbulence and Shear Flow Phenomena, Vol. 2, pp. 589-594, 2005. Presented at the Fourth International Symposium on Turbulence and Shear Flow Phenomena, Williamsburg, VA.

Other Conference Presentations With Published Abstracts

1. Volino, R.J. "Separation Control Using Synthetic Vortex Generator Jets," Bulletin of the American Physical Society, DFD 2002, Vol. 47, No. 10, pp. 82-83. Presented at the 55th Annual Meeting of the Division of Fluid Dynamics of the American Physical Society, Dallas, TX, 2002. <http://flux.aps.org/meetings/YR02/DFD02/baps/abs/S710004.html> (as of November 21, 2011).
2. Volino, R.J. "Active and Passive Flow Control on Low Pressure Turbine Airfoils," Minnowbrook IV Workshop on Transition and Unsteady Aspects of Turbomachinery Flows, NASA/TM-2004-212913, p. 34. Presented at the Minnowbrook IV Workshop, Blue Mountain Lake, NY, 2003.
3. Volino, R.J. and Bohl, D.G. "Separated Flow Transition Mechanism with Passive Flow Control under Low Pressure Turbine Conditions," Bulletin of the American Physical Society, DFD 2003, Vol. 48, No. 10, pp. 75-76. Presented at the 56th Annual meeting of the Division of Fluid Dynamics of the American Physical Society, East Rutherford, NJ, 2003. <http://flux.aps.org/meetings/YR03/DFD03/baps/abs/S310008.html> (as of November 21, 2011).
4. Volino, R.J. and Bohl, D.G. "Three-Dimensional Flow Structure Resulting from Oscillating Vortex Generator Jets," Bulletin of the American Physical Society, DFD 2004, Vol. 49, No. 9, p. 157. Presented at the 57th Annual Meeting of the Division of Fluid Dynamics of the American Physical Society, Seattle, WA, 2004. <http://flux.aps.org/meetings/YR04/DFD04/baps/abs/S910010.html> (As of November, 21, 2011).

Appendix

Reprints of Papers and Publications

Copyrighted papers are reprinted with permission of the American Society of Mechanical Engineers (ASME) and the American Institute of Aeronautics and Astronautics (AIAA).

Separated Flow Transition Under Simulated Low-Pressure Turbine Airfoil Conditions—Part 1: Mean Flow and Turbulence Statistics

Ralph J. Volino

Mem. ASME,
Department of Mechanical Engineering,
United States Naval Academy,
Annapolis, MD 21402
e-mail: volino@usna.edu

Boundary layer separation, transition and reattachment have been studied experimentally under low-pressure turbine airfoil conditions. Cases with Reynolds numbers (Re) ranging from 25,000 to 300,000 (based on suction surface length and exit velocity) have been considered at low (0.5%) and high (9% inlet) free-stream turbulence levels. Mean and fluctuating velocity and intermittency profiles are presented for streamwise locations all along the airfoil, and turbulent shear stress profiles are provided for the downstream region where separation and transition occur. Higher Re or free-stream turbulence level moves transition upstream. Transition is initiated in the shear layer over the separation bubble and leads to rapid boundary layer reattachment. At the lowest Re , transition did not occur before the trailing edge, and the boundary layer did not reattach. Turbulent shear stress levels can remain low in spite of high free-stream turbulence and high fluctuating streamwise velocity in the shear layer. The beginning of a significant rise in the turbulent shear stress signals the beginning of transition. A slight rise in the turbulent shear stress near the trailing edge was noted even in those cases which did not undergo transition or reattachment. The present results provide detailed documentation of the boundary layer and extend the existing database to lower Re . The present results also serve as a baseline for an investigation of turbulence spectra in Part 2 of the present paper, and for ongoing work involving transition and separation control.

[DOI: 10.1115/1.1506938]

Introduction

Modern low-pressure (LP) turbine airfoils are subject to increasingly stronger pressure gradients as designers impose higher loading in an effort to improve efficiency and lower cost by reducing the number of airfoils in an engine. If the adverse pressure gradient on the suction side of these airfoils becomes strong enough, the boundary layer will separate. Separation bubbles, particularly those which fail to reattach, can result in a significant loss of lift and a subsequent degradation of engine efficiency (e.g., Hourmouziadis [1], Mayle [2], and Sharma et al. [3]). The problem is particularly relevant in aircraft engines. Airfoils optimized to produce maximum power under takeoff conditions may still experience boundary layer separation at cruise conditions, due to the thinner air and lower Reynolds numbers at altitude. A component efficiency drop of 2% may occur between takeoff and cruise conditions in large commercial transport engines, and the difference could be as large as 7% in smaller engines operating at higher altitudes. Component life may also be affected by more than an order of magnitude (Hodson [4]). Because the LP turbine produces the bulk of the net power in many engines, changes in its component efficiency can result in nearly equal changes in overall engine efficiency (Wisler [5]). There are several sources for losses in an engine, including secondary flows, but the suction side boundary layer has been identified as the primary source of losses in the LP turbine (Curtis et al. [6]). Prediction and control of suction side separation, without sacrifice of the benefits of higher loading, is therefore, necessary for improved engine design.

Separation on LP turbine airfoils is complicated by boundary layer transition. Turbulent boundary layers are much more resis-

tant to separation than laminar boundary layers. A substantial fraction of the boundary layer on both sides of a turbine airfoil may be transitional (Mayle [2]), so accurately predicting transition location is crucial for accurate prediction of separation. Transition prediction for turbine airfoils is complex and can depend on a number of factors, including the free-stream turbulence intensity (FSTI), streamwise pressure gradient, airfoil curvature, surface roughness, and the unsteadiness associated with passing wakes from upstream stages. Several transition mechanisms are possible under engine conditions. Mayle [2] classified the modes of transition as “natural transition” involving Tollmien-Schlichting waves; “bypass” transition caused by high free-stream turbulence or other large disturbances; “separated flow” transition of the shear layer over a separation bubble; “periodic-unsteady” transition, which might also be called wake-induced transition; and reverse transition. If transition occurs far enough upstream, it can prevent separation. If transition occurs in the shear layer over a separation bubble, it will tend to induce boundary layer reattachment. The lower the Reynolds number, the farther downstream transition will tend to occur, hence the problems associated with performance at altitude.

Boundary layer transition has been studied extensively, and in recent years several studies have focused on transition in the LP turbine. Halstead et al. [7] present a study from a rotating cascade with multiple stages and FSTI characteristic of engine conditions. The adverse pressure gradients in this study were not strong enough to induce separation, however. Solomon [8] subsequently modified the facility and provides documentation of separation from a more aggressive airfoil. Gier and Ardey [9] provide another example from a rotating facility. Boundary layers and separation bubbles on flat plates subject to adverse pressure gradients have been considered in several studies. Recent work has included the studies of Hatman and Wang [10], Sohn et al. [11], Lou and Hourmouziadis [12], Volino and Hultgren [13] and Yaras [14]. On

Contributed by the International Gas Turbine Institute and presented at the International Gas Turbine and Aeroengine Congress and Exhibition, Amsterdam, The Netherlands, June 3–6, 2002. Manuscript received by the IGTI, January 22, 2002. Paper No. 2002-GT-30236. Review Chair: E. Benvenuti.

airfoils, either in cascade or single-passage cascade-simulators, studies have included Murawski et al. [15], Qiu and Simon [16] and Simon et al. [17]. Cascades with moving wakes, simulating the effect of upstream blade rows, were utilized by Brunner et al. [18], Stadtmüller et al. [19], Howell et al. [20] and Kaszeta et al. [21]. Numerical studies have included the work of Dorney et al. [22], Chernobrovkin and Lakshminarayana [23], Huang and Xiong [24], and Thermann et al. [25]. A few studies have included attempts to control transition and separation. Howell et al. [20] studied modified airfoil shapes, Van Treuren et al. [26] utilized vortex generators, and Lake et al. [27] considered various passive devices including dimples. Bons et al. [28] showed considerable success using both steady and pulsed vortex generator jets. The preceding list of studies, while long, is by no means inclusive. It is merely a sample of recent work, biased toward the most recent studies.

Much has been learned from the work to date, but the nature of separated flow transition is still not completely clear, and existing models are still not as robust as needed for accurate prediction. The present study expands the existing database. The flow through a single-passage cascade-simulator is documented under both high and low FSTI conditions at several different Reynolds numbers. The geometry of the passage corresponds to that of the “Pak-B” airfoil, which is an industry supplied research airfoil that is representative of a modern, aggressive LP turbine design. This geometry was used in several of the studies mentioned above ([15–17,21,23,24,27,28]), and the pressure profile from the suction side of this airfoil was matched in the flat plate study of Volino and Hultgren [13]. Previous work has included documentation at Re (based on suction surface length and exit free-stream velocity) as low as 50,000 (e.g., [13,16,21]). The present work includes the first complete documentation (to the author’s knowledge) of cases with Re as low as 25,000. Also new is documentation of the turbulent shear stress in the boundary layer under both high and low FSTI.

Details of the experimental facility and results of the study follow. The present paper focuses on mean and statistical quantities. Part 2 of this work [29] includes turbulence spectral results, providing evidence of the important transition mechanisms.

Experiments

Experiments were conducted in a low speed wind tunnel, described by Volino et al. [30]. Briefly, air enters through blowers and passes through a series of screens, a honeycomb, two settling chambers, and a three-dimensional contraction before entering the test section. At the exit of the contraction, the mean velocity is uniform to within 1%. The FSTI is $0.5 \pm 0.05\%$. Nearly all of this free-stream “turbulence” is actually streamwise unsteadiness at frequencies below 20 Hz and is not associated with turbulent eddies. The rms intensities of the three components of the unsteadiness are 0.7, 0.2, and 0.2% in the streamwise, pitchwise and spanwise directions, respectively. For low FSTI cases, the test section immediately follows the contraction. For high FSTI, a passive grid is installed at the contraction exit followed by a 1 m long rectangular settling chamber. Details of the grid are available in Volino et al. [30]. At the inlet to the test section the high FSTI mean flow and turbulence are spatially uniform to within 3 and 6%, respectively. The free-stream turbulence is nearly isotropic with rms intensities of 8.8, 8.9, and 8.3% in the streamwise, pitchwise and spanwise directions. The integral length scales of these components are 3, 1.6, and 1.4 cm. The integral scales were computed from the power spectra of each component.

The test section, shown in Fig. 1, consists of the passage between two airfoils. Details are listed in Table 1. Cascade simulators of this type have been used in studies such as Chung and Simon [31], more recently in the present facility by Aunapu et al. [32], and with the PakB geometry by Qiu and Simon [16] and Kaszeta et al. [21]. A large span to chord ratio of 4.3 was chosen to insure two-dimensional flow at the spanwise centerline of the

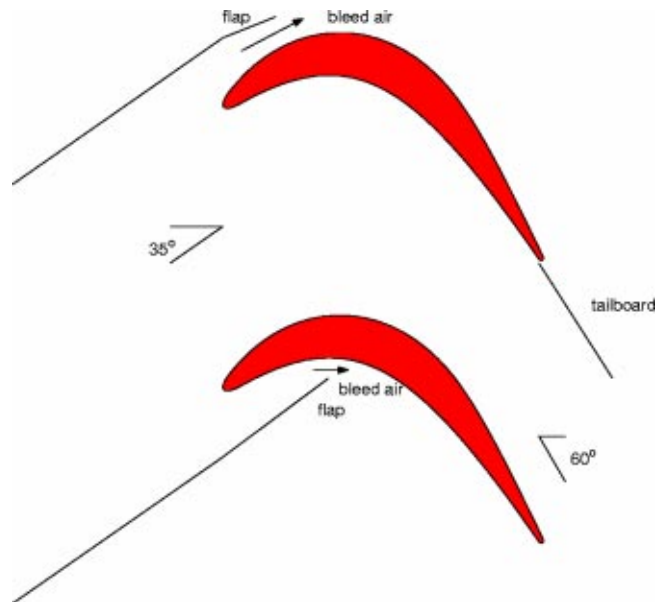


Fig. 1 Schematic of the test section

airfoils, where all measurements were made. Upstream of each airfoil are flaps, which control the amount of bleed air allowed to escape from the passage. These are adjusted to produce the correct leading edge flow and pressure gradient along the airfoils. A tail-board on the pressure side of the passage also aids in setting the pressure gradient.

Single passage test sections have several advantages. For a given wind tunnel with fixed maximum flow rate, the single passage can be considerably larger than a passage in a multi-blade facility. The larger size and simpler geometry can also result in better probe access. Previous studies (e.g., [31,32]) demonstrated that the full flow field, including the three-dimensional secondary flows near the endwalls, in a single passage can be set to match that in a corresponding multi-blade cascade. The present test section also has some advantages over flat plate test sections. First, the airfoil curvature is matched. Second, with an adverse pressure gradient, suction is often needed to prevent separation on the wall opposite a flat test plate (e.g., Volino and Hultgren [13]). A cascade simulator does not require suction due to the favorable pressure gradient on the pressure side of the passage.

Single passages also have disadvantages. It is, of course, impossible to establish periodicity. Stage losses cannot be directly determined since there is flow only on one side of each airfoil and the downstream wake is, therefore, unlike that in a multi-blade facility. This limitation, however, is not prohibitive for the present study. Primary concern is with boundary layer separation and transition, which occur *in the passage*. Although the downstream wake may be different, the flow in the passage does match that of a multi-blade facility.

Ten different cases have been documented including high and low FSTI cases at five Reynolds numbers ($Re=25,000, 50,000, 100,000, 200,000, \text{ and } 300,000$). The Reynolds number range is representative of conditions from cruise to takeoff. The FSTI levels in an engine may vary considerably, but the values in the present work are believed to span the range of most interest. Solomon [8] surveyed several studies that included wake effects and

Table 1 Test section parameters

Axial Chord [mm]	True Chord [mm]	Pitch [mm]	Span [mm]	Suction side, L_s [mm]	Inlet flow angle	Exit flow angle
153.6	170.4	136.0	660.4	228.6	35°	60°

Table 2 Measurement stations locations, local acceleration (inviscid soln.), and measured local free-stream turbulence

Station	s/L_s	ReK	Low FSTI u'/U_∞ [%]	Low FSTI v'/U_∞ [%]	High FSTI u'/U_∞ [%]	High FSTI v'/U_∞ [%]
1	0.111	1.58	0.44		5.2	
2	0.194	1.20	0.39		4.6	
3	0.278	0.86	0.37		4.0	
4	0.361	0.75	0.38		3.5	
5	0.444	0.62	0.39		3.2	
6	0.528	-0.02	0.41		2.8	
7	0.611	-0.81	0.47	0.05	2.9	5.9
8	0.694	-0.95	0.47	0.12	3.0	6.2
9	0.777	-0.58	0.48	0.14	3.4	6.6
10	0.861	-0.53	0.54	0.11	3.8	6.8
11	0.944	-0.18	0.51	0.11	4.0	6.8

found FSTI values ranging from 1 to 5% between wakes and from 3 to 23% within wakes. Wakes can affect transition and separation in the boundary layer in three ways. First, the FSTI rises during a wake passage compared to the between-wake value. Second, a calmed region follows wake induced transition. The calmed flow is nonturbulent, but unlike a steady nonturbulent flow, it can be very resistant to separation. Finally, independent of the FSTI effect, each wake includes a mean velocity deficit, resulting in temporal deceleration and acceleration as the wake passes. Lou and Hourmouziadis [12] separated this temporal effect from the wake turbulence effect, using downstream control to create an oscillating velocity in their test section. In the present study, only steady flow is considered. While the significant effects of temporal acceleration and calming are not present, the high and low FSTI cases of the present study do allow a means for evaluating the effect of wake turbulence level.

Measurements. Pressure surveys were made for each case using a pressure transducer (0–870 Pa range Validyne transducer) and a Scanivalve. Stagnation pressure was measured with a pitot tube upstream of the passage inlet, and eleven pressure taps were located on each airfoil along their spanwise centerlines. Locations of the taps on the suction side are listed in Table 2 along with measured local FSTI components, and the ReK product at these stations based on a nonseparating, inviscid solution. The pressure distribution on the upstream portion of the suction side always closely matched the inviscid solution for flow over the airfoil. This allowed the use of the measured static pressure at the third pressure tap on the suction side, along with the inviscid flow solution for the passage and the upstream stagnation pressure, to determine the nominal passage exit velocity, which was used to normalize the measured pressure distributions. More conventionally the measured inlet velocity and the inlet and exit flow angles are used to compute the exit velocity. Because the velocity at the third tap is 1.9 times that at the passage inlet, and therefore easier to measure, using the third tap velocity reduced the bias uncertainty in the pressure coefficients, particularly at the lower Reynolds numbers. The uncertainty in the suction side pressure coefficients was 7% at the lowest Re , and below 4% in other cases. Most of this uncertainty was due to bias error. Stochastic error was minimized by averaging pressure transducer readings over a 10-s period.

Velocity profiles were measured at eleven streamwise stations along the suction side at the locations given in Table 2. Profiles were measured near but not at the spanwise centerline of the airfoil to insure that the pressure taps did not interfere with the velocity measurements. Profiles were acquired with a hot-wire anemometer (TSI model IFA100) and a single sensor boundary layer probe (TSI model 1218-T1.5). The sensor diameter is 3.8 μm , and the active length is 1.27 mm. At each measurement location, data were acquired for 26 seconds at a 20 kHz sampling

rate (2^{19} samples). All raw data were saved. The high sampling rate provides an essentially continuous signal, which is needed for intermittency and spectral post-processing. The long sampling time results in low uncertainty in both statistical and spectral quantities. Data were acquired at 60 wall normal locations in each profile, extending from the wall to the free-stream, with most points concentrated in the near wall region. The closest point was 0.1 mm from the wall, which corresponds to $y/L_s = 0.0004$ and between 0.01 and 0.2 boundary layer thicknesses. Flow direction in a separation bubble cannot be determined with a single-sensor hotwire, but velocity magnitude can be measured and was found to be essentially zero within the bubbles of the present cases. Determining the direction was not, therefore, considered essential. At locations where the boundary layer was attached, local wall shear stress was computed from the near wall profile using the technique of Volino and Simon [33]. Uncertainties in the mean velocity are 3–5%, except in the very near wall region ($y^+ < 5$) where near-wall corrections (Wills [34]) were applied to the mean velocity. Uncertainties in the momentum and displacement thicknesses computed from the mean profiles are 10%. Uncertainty in the shape factor, H , and the wall shear stress are both 8%.

The uncertainty in the fluctuating streamwise velocity is below 10%, except in the very near wall region, where spatial averaging effects become important in some cases. Ligrani and Bradshaw [35,36] showed that spatial averaging over the length of a hot-wire sensor can result in low apparent u' . Their experiments were done in a fully-turbulent boundary layer with $Re_\theta = 2600$. The spatial averaging effects become important when the sensor length is longer than the width of the smaller near wall streaks in a turbulent boundary layer. Ligrani and Bradshaw [35,36] found that the spatial averaging effects become small when the dimensionless sensor length, $\ell u_\tau/\nu$, is less than about 25. The error also becomes smaller as the sensor is moved away from the wall. This is expected since the average size of the turbulent eddies should increase with distance from the wall. The Ligrani and Bradshaw [35,36] results suggest that when the distance from the wall, y , is larger than the sensor length, ℓ , that spatial averaging errors are under 10% even for large $\ell u_\tau/\nu$. Closer to the wall they showed errors in u' as large as 30% when $\ell u_\tau/\nu = 60$.

In the present study, $\ell u_\tau/\nu$ remains below 25 in all cases with $Re < 200,000$. Spatial averaging is not, therefore, expected to be a problem, even near the wall. For the $Re = 200,000$ cases, $\ell u_\tau/\nu$ is above 25 at Station 11 of the low FSTI case and at Stations 9–11 of the high FSTI case, reaching values as high as 60. Spatial averaging should not be significant for $y > 1$ mm ($y/L_s > 0.004$), but may cause errors as high as 30% closer to the wall. It is not certain that the errors are this large, however. The momentum thickness Reynolds numbers in the present cases are all below 700, which is significantly below the $Re_\theta = 2600$ value of the Ligrani and Bradshaw [35,36] study. This may indicate less developed turbulence in the present study, which could imply fewer small-scale eddies and lower averaging errors. For the $Re = 300,000$ cases, $\ell u_\tau/\nu$ reaches values as high as 90 at Stations 10 and 11 of the low FSTI case and Stations 9–11 of the high FSTI case. As in the $Re = 200,000$ cases, errors should be small when $y > 1$ mm, but may be larger closer to the wall.

A boundary layer cross-wire probe (TSI model 1243-T1.5) was used to measure profiles of the wall normal velocity and turbulent shear stress at Stations 7–11 for each case. The upstream boundary layer was too thin for cross-wire measurements. Data were acquired at 25 locations in each profile, beginning 1 mm from the wall and extending to the free-stream. Sampling rates and times were the same as for the single sensor probe. Uncertainty in the turbulent shear stress is 10%.

Measurements with the cross-wire probe are subject to spatial averaging errors due to the length of the sensors (1.27 mm active length) and the spacing between the two sensors (1 mm). Applying the results of Ligrani and Bradshaw [35,36] and Ligrani et al. [37] to the present cases, spatial averaging may be significant at

locations very near the wall, particularly for the high Reynolds number cases. At locations farther from the wall than 1 mm, however, the errors should become small and within the 10% uncertainty estimate given in the foregoing. Hence, no measurements were made at y locations below 1 mm. Because all measurements were at $y > 1$ mm and a boundary layer type probe was used, probe blockage effects were not expected to be significant.

The intermittency, γ , is the fraction of time the flow is turbulent within the transition region, and was determined at each measurement location using the technique described in Volino et al. [30] with an uncertainty of 10%. Turbulent flow in the boundary layer is defined here as flow which includes a range of large and small scales, turbulence production, and dissipation. Using this definition, a boundary layer may be characterized by significant fluctuations, but still be nonturbulent if these fluctuations are induced by an external source which does not cause near-wall turbulence production. Such is often the case under high FSTI conditions. Free-stream eddies “buffet” the boundary layer, inducing nonturbulent boundary layer fluctuations. Buffeting may occur through pressure fluctuations. Boundary layer fluid is pushed in the wall normal direction across the mean gradient in the streamwise velocity, resulting in significant u' fluctuations. This type of motion was termed “inactive” by Bradshaw [38] since it does not result in momentum transport, in spite of potentially high u' levels. In addition to buffeting, some free-stream eddies may penetrate into the boundary layer and cause some mixing. As described in Volino [39], the eddies which have the greatest effect, whether through buffeting or penetrating the boundary layer, will be the larger, energy containing eddies. The nonturbulent boundary layer subject to these external effects will be characterized by large-amplitude, low-frequency fluctuations. Transition to turbulence is characterized not so much by large increases in u' levels, which may remain essentially constant, but by the appearance of higher frequencies superimposed on the low frequencies. The higher frequencies signal the generation of turbulence in the near wall region. Volino et al. [30] provide examples of an intermittent flow switching in time between disturbed nonturbulent and turbulent states.

The presence or absence of high frequencies in a signal is used to distinguish between turbulent and nonturbulent flow, using the algorithm presented by Volino et al. [30]. The algorithm is similar to others found in the literature. Briefly, the time derivative of a signal is computed and compared to a threshold. Rapid (high-frequency) fluctuations result in high derivatives. When the derivative is larger than the threshold, the flow is declared instantaneously turbulent and the intermittency function is assigned a value of 1. When the derivative is below the threshold, the intermittency is assigned a value of 0. The time average of the function is the intermittency, γ . Volino et al. [30] showed that intermittency can be computed based on u' or $u'v'$ signals with essentially the same result. Results based on u' are presented in this paper.

Results

Pressure Profiles. Pressure coefficients for all ten cases are shown in Fig. 2. At the upstream stations on the suction side, there is good agreement between the data at all Reynolds numbers and the inviscid flow solution. Separation appears to occur at s/L_s of about 0.6 in all cases. These results agree with those of Volino and Hultgren [13], who also observed that the separation location did not depend strongly on the Reynolds number or FSTI. They are in contrast to other studies, such as Qiu and Simon [16], which showed that the separation location depended more strongly on Re. Reattachment depends strongly on both Re and FSTI. With low FSTI (Fig. 2(a)), the boundary layer appears to be separated in all cases at Stations 8 and 9. It reattaches by Station 10 for the Re=200,000 and 300,000 cases, reattaches by Station 11 for the Re=100,000 case, and does not reattach at all for the Re=25,000 and 50,000 cases. Reattachment for the high FSTI cases

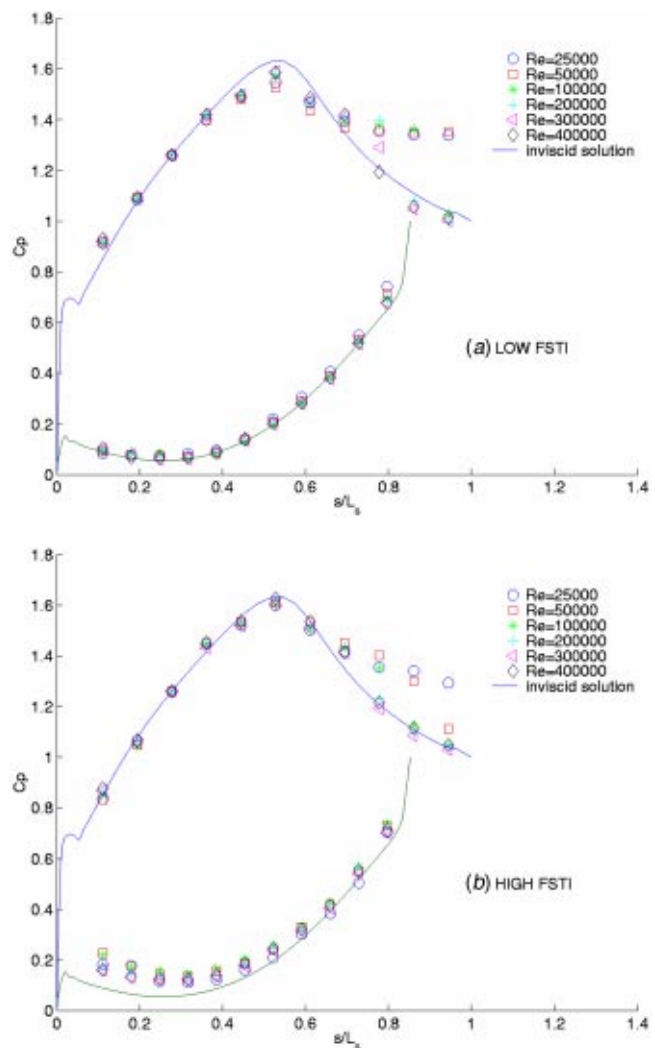


Fig. 2 C_p profiles: (a) low FSTI, (b) high FSTI

(Fig. 2(b)) occurs upstream of the low FSTI locations. The boundary layer appears to be separated in all cases at Station 8, but has already reattached by Station 9 in the Re=200,000 and 300,000 cases. Reattachment has occurred by Station 10 for the Re=100,000 case, and appears to be beginning at Station 11 for the Re=50,000 case. The boundary layer does not appear to reattach when Re=25,000, in spite of the high FSTI. Results for the low FSTI cases are very similar to the flat plate results of Volino and Hultgren [13]. The present high FSTI results appear to show about a 10% larger separation region than the flat plate cases of [13]. The differences are small and of the order of the resolution of the measurement stations. Any differences between the studies are presumably due to differences in the free-stream turbulence. Although the high FSTI in both studies was about 8%, the inlet free-stream turbulence was more anisotropic in Volino and Hultgren [13], and the integral length scales of the free-stream turbulence in [13] were about double those in the present study. The larger length scale presumably caused earlier transition in the Volino and Hultgren [13] study, resulting in a slightly shorter separation bubble. Comparison to the high FSTI cases of Simon et al. [17] shows reattachment about 14% farther upstream in [17] than in the present study. With low FSTI, Simon et al. [17] did not observe reattachment at all when Re=100,000, while it was observed in the present study. For the low FSTI Re=200,000 case, they indicate reattachment about 6% farther upstream than the present study. Although the streamwise pressure gradients were

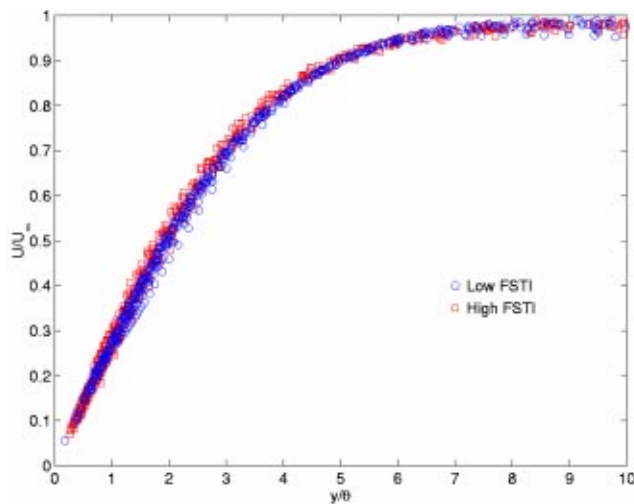


Fig. 3 Mean velocity profiles from Station 1–5, all cases

nominally the same in the present study and Simon et al. [17], small differences in the pressure gradients along with differences in the intensity and length scales of the free-stream turbulence were apparently responsible for the differences in reattachment location.

Upstream Boundary Layer. The local free-stream velocities at Station 1–5 for all 10 cases closely followed the equation

$$\frac{U_\infty}{U_e} = 1.48 \left(\frac{s}{L_s} \right)^{0.214} \quad (1)$$

which corresponds to the free-stream velocity distribution for a Falkner-Skan wedge flow. Figure 3 shows that the 50 mean velocity profiles from all 10 cases at these stations collapse onto the same Falkner-Skan profile. Skin friction coefficients, shown in Fig. 4, which were computed using the near wall profiles, also follow the Falkner-Skan solution. There is no significant difference between the low and high FSTI cases. Agreement with the flat plate data of Volino and Hultgren [13] is good. For the low FSTI cases, it is not surprising that the laminar boundary layer closely follows the expected laminar solution. Under the same high FSTI inlet conditions, however, Volino et al. [30] showed that a non-turbulent boundary layer may be strongly influenced by

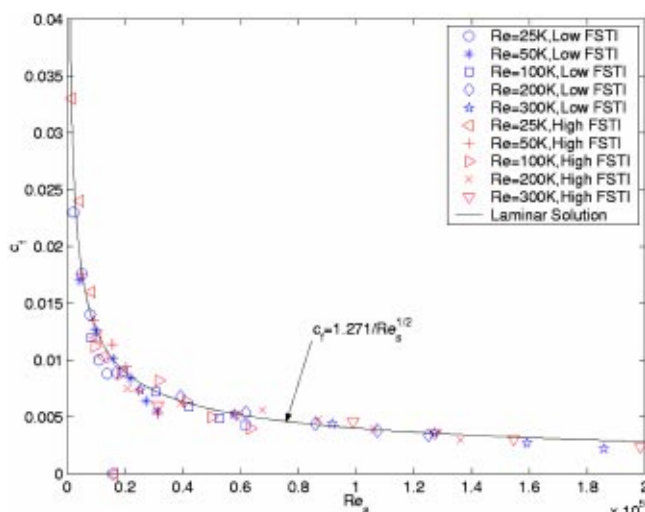


Fig. 4 Skin friction coefficients from Station 1–6, all cases

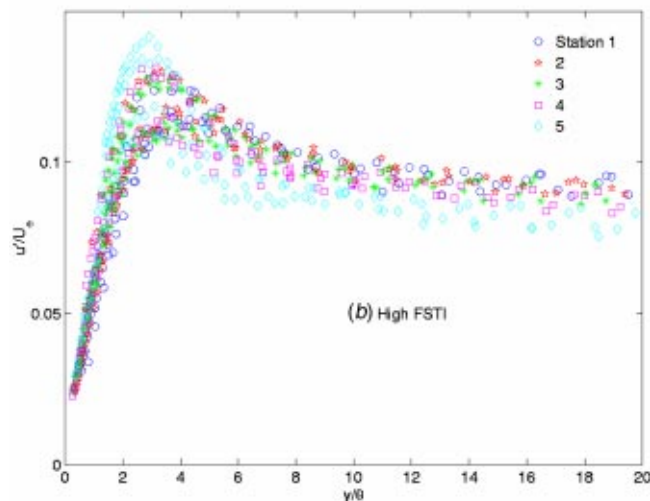
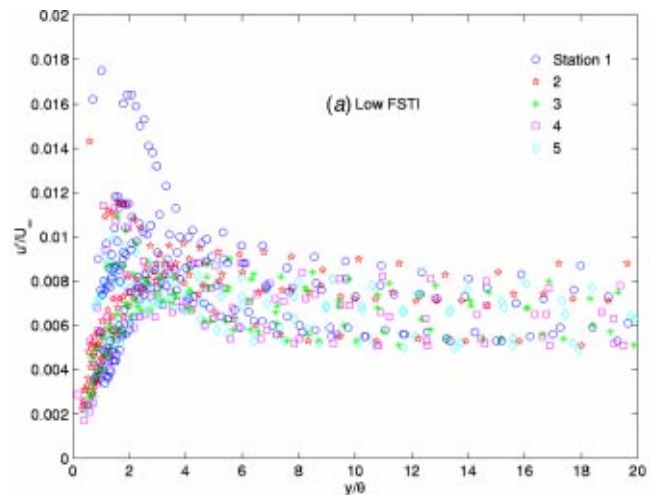


Fig. 5 Boundary layer u' profiles from Stations 1–5—(a) low FSTI cases, (b) high FSTI cases

the free-stream turbulence and exhibit large deviation from laminar behavior. In the present study, the acceleration parameter, K , is in some of the cases over 10 times larger than in the Volino et al. [30] study, and the boundary layer thickness is as little as 1/5 that in [30]. These differences apparently limit the free-stream effect on the upstream boundary layer, resulting in the observed laminar-like behavior.

Figure 5 shows profiles of the rms fluctuating streamwise velocity, u' , for the 50 upstream profiles. The low FSTI u' is mainly streamwise unsteadiness that scales with the local U_∞ . Values are low everywhere, increasing slightly from the free-stream value to a peak at $y/\theta = 3$ and then dropping to zero at the wall. For the high FSTI cases the free-stream u' level does not change significantly within the test section and scales with U_e . Since the boundary layer fluctuations are caused by the free-stream fluctuations, the u' profiles collapse when normalized on U_e . The collapse is not perfect since the free-stream u' does drop somewhat as the eddies are strained in the accelerating flow. Qualitatively the behavior is the same as in the low FSTI cases, with high values in the free-stream rising to a peak at $y/\theta = 3$ and dropping to zero near the wall. The peak in u' has lower magnitude and is farther from the wall than would be expected in a turbulent boundary layer. In all cases the boundary layer is clearly laminar-

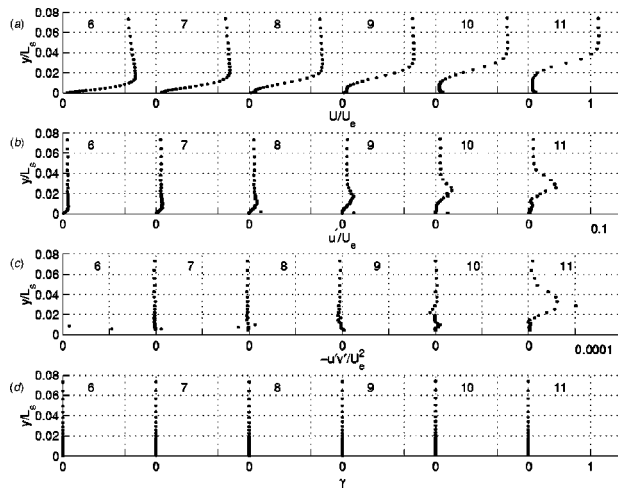


Fig. 6 Station 6–11 profiles for low FSTI, Re=25,000 case—(a) mean velocity, (b) u' , (c) $-u'v'$, (d) intermittency

like in spite of the high u' level. This is shown in both the mean velocity profiles (Fig. 3) and the local skin friction coefficients (Fig. 4) which follow laminar flow solutions.

Low FSTI Transition. Downstream of Station 6, the pressure gradient becomes adverse and separation and transition occur. Figures 6 through 10 show profiles at Stations 6–11 of U , u' , the turbulent shear stress, $-u'v'$, and the intermittency, γ , for the five low FSTI cases. The v' profiles are qualitatively very similar to the $-u'v'$ profiles in all cases and are not shown. In the $Re = 25,000$ case (Fig. 6), the mean velocity profile has just separated at Station 7, and the separation bubble grows continuously larger at the downstream stations. There is no reattachment, but rather a massive separation with a burst bubble at the trailing edge. The intermittency is nearly zero everywhere, indicating that the shear layer remains essentially laminar. Although the flow is laminar, u' is nonzero. The u' peak grows as the flow moves downstream, and its location is concurrent with the inflection point in the mean profile. The $-u'v'$ values remain near zero through Station 10, but then rise at Station 11 with a peak in the shear layer at the same location as the u' peak. The magnitude of this peak is extremely low; the eddy viscosity at the peak is only about 1/30th of the molecular kinematic viscosity. Although not significant in terms of eddy transport, this peak may signify the beginning of transition.

Figure 7 shows the profiles for the $Re = 50,000$ case. Results are very similar to the $Re = 25,000$ case of Fig. 6. The boundary layer does not reattach. The $-u'v'$ profile at Station 11 again exhibits a low level peak. The dimensionless value of this peak is about three times that of the peak in Fig. 6, indicating that the $Re = 50,000$ case may be closer to transitioning.

Results for the $Re = 100,000$ case are shown in Fig. 8. The mean velocity profiles show that the boundary layer is on the verge of separating at Station 7, but is still attached. It has separated by Station 8, and the separation bubble grows through Station 10, although it does not become as thick as in the lower Re cases. At Station 10, the mean velocity near the wall rises slightly above zero, indicating the beginning of reattachment. At Station 11 the boundary layer is clearly reattached. The intermittency is near zero through Station 10, and then suddenly increases to 1 at Station 11, indicating fully turbulent flow as the boundary layer reattaches. The peak in the intermittency is well away from the wall, indicating that transition begins in the shear layer over the separation bubble. The u' profiles exhibit a peak in the shear layer at Stations 8 and 9, similar to the behavior at the lower Re . At Station 10 there is an increase in u' near the wall as reattachment

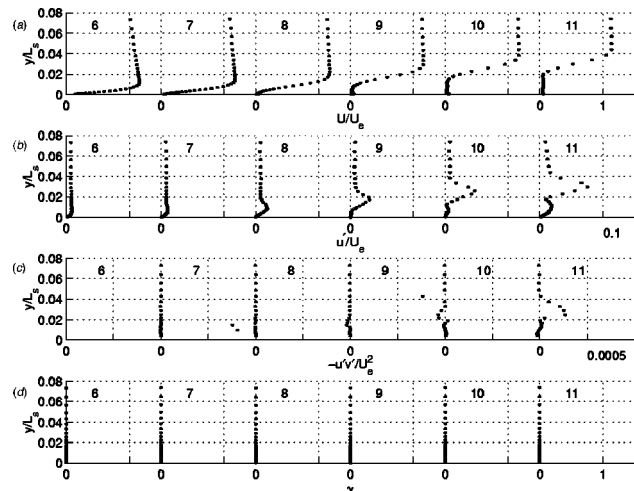


Fig. 7 Station 6–11 profiles for low FSTI, Re=50,000 case—(a) mean velocity, (b) u' , (c) $-u'v'$, (d) intermittency

begins. The turbulent shear stress profile rises above zero at Station 10 with a dimensionless value that is an order of magnitude larger than the peak shown in Fig. 7 for the $Re = 50,000$ case. At Station 11 the magnitude of the peak has increased by another order of magnitude and the boundary layer is clearly turbulent. The peak in $-u'v'$ is well away from the wall, indicating that while the boundary layer is turbulent and reattached, it has not yet recovered to fully developed turbulent conditions.

Figure 9 shows the profiles for the $Re = 200,000$ case. The mean velocity profiles indicate that separation does not occur until near Station 8. There is a clear separation bubble at Station 9, and the boundary layer is reattached by Station 10. By Station 11 the mean profile appears to have recovered to a fully developed turbulent shape. The intermittency jumps from near 0 at Station 9 to 1 at Station 10, indicating a rapid transition and reattachment. The magnitude of u' increases similarly, from a small peak near the inflection point of the mean profile at Station 9 to high values throughout the boundary layer at Station 10. The turbulent shear stress profiles show the same sudden increase between Stations 9 and 10, and the peak is still away from the wall at Station 11, indicating that recovery from separation may not be fully complete.

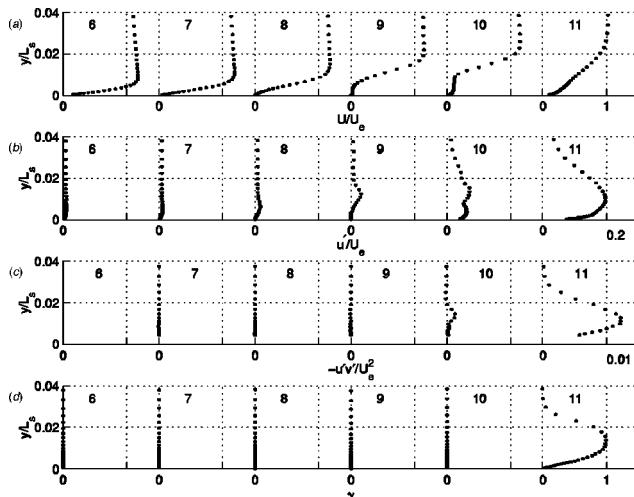


Fig. 8 Station 6–11 profiles for low FSTI, Re=100,000 case—(a) mean velocity, (b) u' , (c) $-u'v'$, (d) intermittency

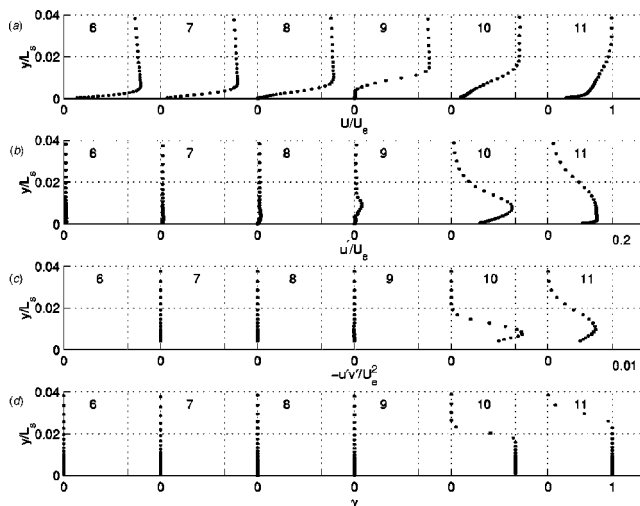


Fig. 9 Station 6–11 profiles for low FSTI, Re=200,000 case—(a) mean velocity, (b) u' , (c) $-u'v'$, (d) intermittency

The Re=300,000 case profiles are shown in Fig. 10. Separation again occurs near Station 8. By Station 9 the separation bubble has clearly grown and the nonzero mean velocities near the wall indicate that the boundary layer is on the verge of reattachment. The u' values increase greatly between Stations 8 and 9. The u' profile has a peak in the shear layer over the separation bubble and a second peak near the wall, which is indicative of reattachment. The intermittency profile at Station 9 shows this same double peak. The boundary layer is reattached and fully turbulent by Station 10. The turbulent shear stress profile rises to a small but discernable nonzero level at Station 9, corresponding to the beginning of reattachment and the rise of the intermittency. By Station 11, $-u'v' = u_\tau^2$ near the wall, which would be expected for a fully developed, attached turbulent boundary layer.

The velocity data of Figs. 6–10 agree with the pressure profiles of Fig. 2(a). The separation locations agree, although the velocity profiles provide better resolution and indicate that separation does move downstream somewhat as Reynolds number increases. The reattachment locations indicated by the pressure profiles correspond to locations where the velocity profiles have clearly reattached. Incipient reattachment is visible in the mean velocity one station upstream of full reattachment in some cases. In all cases

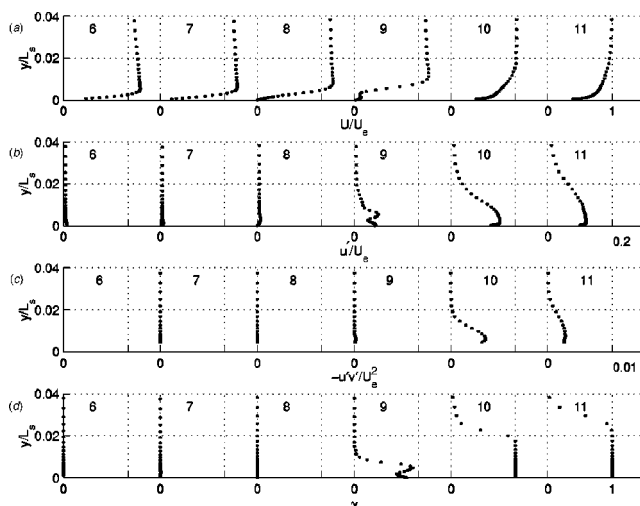


Fig. 10 Station 6–11 profiles for low FSTI, Re=300,000 case—(a) mean velocity, (b) u' , (c) $-u'v'$, (d) intermittency

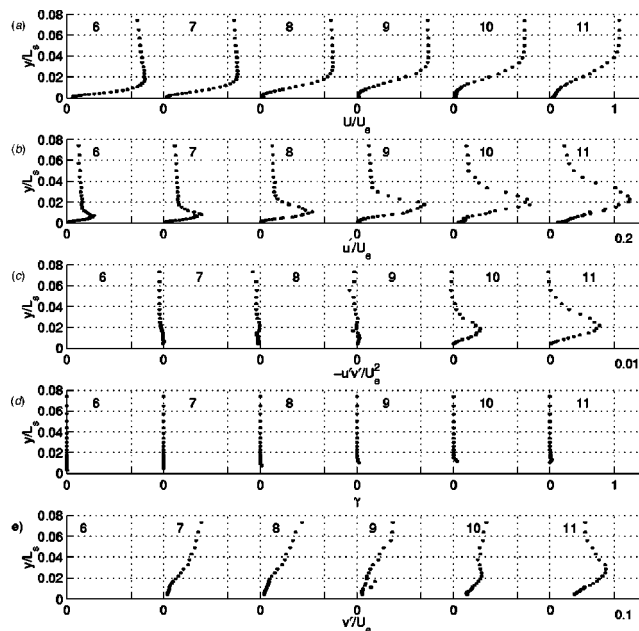


Fig. 11 Station 6–11 profiles for high FSTI, Re=25,000 case—(a) mean velocity, (b) u' , (c) $-u'v'$, (d) intermittency, (e) v'

the magnitude of u' begins to increase in the shear layer after separation. At first this increase in u' occurs without a corresponding increase in $-u'v'$, which remains near zero, and the shear layer remains laminar. As the flow continues downstream, low but nonzero $-u'v'$ values eventually appear in the shear layer, and at the higher Reynolds numbers this is quickly followed by a rapid rise of $-u'v'$, sudden transition to turbulence, and almost immediate reattachment of the boundary layer. At the two lowest Reynolds numbers, the initial rise in $-u'v'$ was detected, but it occurred so far downstream that transition and reattachment never occurred. The present results are consistent with those of Hatman and Wang [10], Lou and Hourmouziadis [12], and Volino and Hultgren [13], who also considered low FSTI separated flow transition. They also reported rapid transition and attributed it to the breakdown of a Kelvin-Helmholtz-type instability of the shear layer. The transition mechanism in the present study will be discussed in more detail in Part 2 [29].

High FSTI Transition. Profiles for the high FSTI cases are shown in Figs. 11–15. For the Re=25,000 case (Fig. 11), the mean velocity profiles show that the boundary layer has separated by Station 6. The boundary layer appears on the verge of reattaching at Stations 10 and 11, but is not clearly reattached. The u' level rises rapidly after separation, with a peak in the shear layer at each station. The free-stream buffets the shear layer, forcing fluid across a large mean velocity gradient, dU/dy , which causes high u' levels. The same effect is present in the attached boundary layer upstream (Fig. 5b), but is damped somewhat by the wall. Free-stream buffeting and high u' do not necessarily imply turbulent transport, and the turbulent shear stress remains low through Station 9. The $-u'v'$ level rises to high levels at Stations 10 and 11, but the peak is in the shear layer and drops to zero at the wall. Perhaps at this very low Reynolds number, even significant transport in the shear layer is insufficient to promote full reattachment of the boundary layer. Turbulent reattachment may be an intermittent phenomenon, related to and much like transition. At the lower Re it may occur over an extended distance. The intermittency indicates that the flow remains nonturbulent, in spite of the high levels of $-u'v'$ at the downstream stations. The intermittency function, as defined above, only declares the flow turbulent when

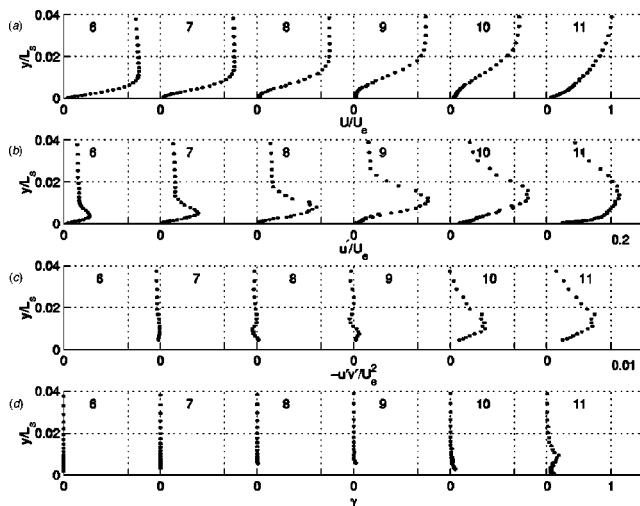


Fig. 12 Station 6–11 profiles for high FSTI, Re=50,000 case—(a) mean velocity, (b) u' , (c) $-u'v'$, (d) intermittency

the velocity fluctuations include a full range of both large and small scales. The apparent mismatch between the $-u'v'$ and γ profiles of Fig. 11 may indicate that the fluctuations which cause the turbulent shear stress initially do not include this range of scales. Turbulent shear stress spectra are presented in Part 2 [29]. Profiles of the wall normal fluctuating velocity, v' , are also shown in Fig. 11. At Stations 7–9, high free-stream values drop to zero at the wall, with no peak corresponding to the peak in u' . The free-stream buffeting effect on v' is damped by the wall, a phenomenon also observed in attached, nonturbulent boundary layers under high FSTI conditions (Volino et al. [30]). A peak emerges in v' in the shear layer at Station 10 and 11, corresponding completely with the rise in $-u'v'$ at these stations. The link between v' and $-u'v'$ was clear at all Re, making it unnecessary to present both v' and $-u'v'$ for the remaining cases.

The Re=50,000 case of Fig. 12 is very similar to the Re=25,000 case. Reattachment is clearer, however, at Station 11, and the intermittency is nonzero at this station. Figure 13 shows the Re=100,000 case. In this case the intermittency indicates that transition has begun by Station 9, which corresponds to an initial rise in $-u'v'$. The mean profile shows that the boundary layer is

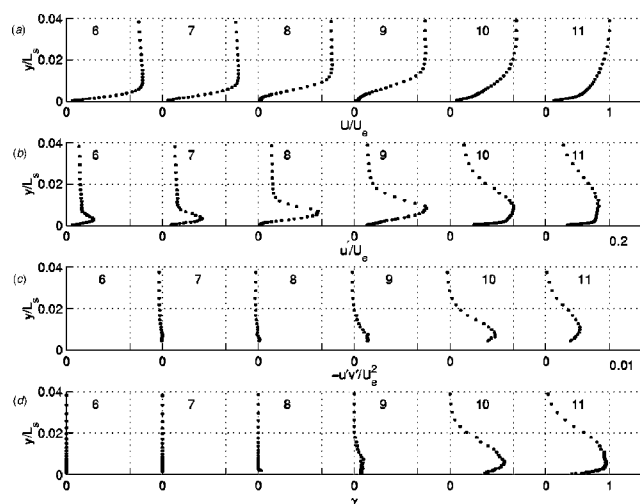


Fig. 13 Station 6–11 profiles for high FSTI, Re=100,000 case—(a) mean velocity, (b) u' , (c) $-u'v'$, (d) intermittency

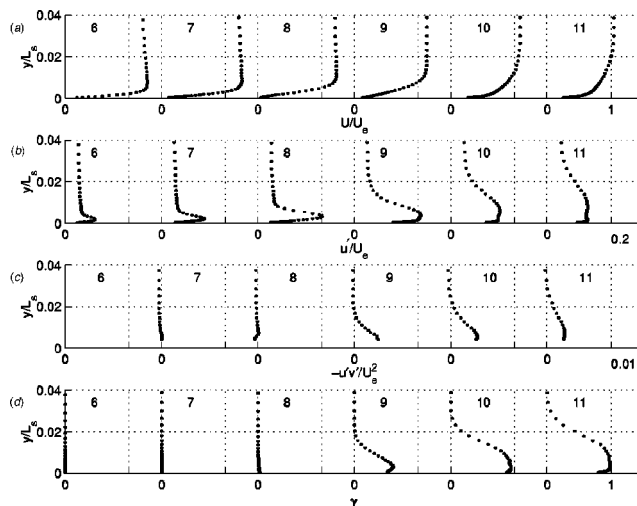


Fig. 14 Station 6–11 profiles for high FSTI, Re=200,000 case—(a) mean velocity, (b) u' , (c) $-u'v'$, (d) intermittency

reattached at the last two stations. The high $-u'v'$ peaks away from the wall indicate that the boundary layer has not fully recovered from the separation at Station 11.

It is not clear that separation occurs in the Re=200,000 case (Fig. 14), but the velocity mean profile at Station 8 has an inflection point and appears to be close to separating. By Station 9 the boundary layer is clearly attached, the intermittency indicates transition is underway, u' is high even near the wall, and $-u'v'$ has risen to a turbulent level. At Station 11, $-u'v'$ reaches a maximum equal to u_τ^2 near the wall, indicating a fully developed attached turbulent flow.

The Re=300,000 results of Fig. 15 are very similar to those at Re=200,000. Transition begins slightly earlier at Re=300,000, with the intermittency greater than zero at Station 8. The thin boundary layer at Re=300,000 results in peaks in $-u'v'$ at Stations 9 and 10 that are too close to the wall to resolve with the cross-wire probe.

In general, transition in the high FSTI cases began upstream of the locations in the corresponding low FSTI cases, and the transition region length was longer with high FSTI. This agrees with the observations of Volino and Hultgren [13], who also observed

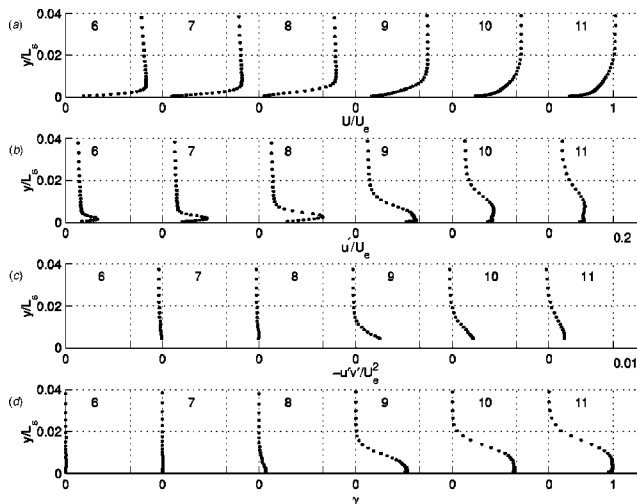


Fig. 15 Station 6–11 profiles for high FSTI, Re=300,000 case—(a) mean velocity, (b) u' , (c) $-u'v'$, (d) intermittency

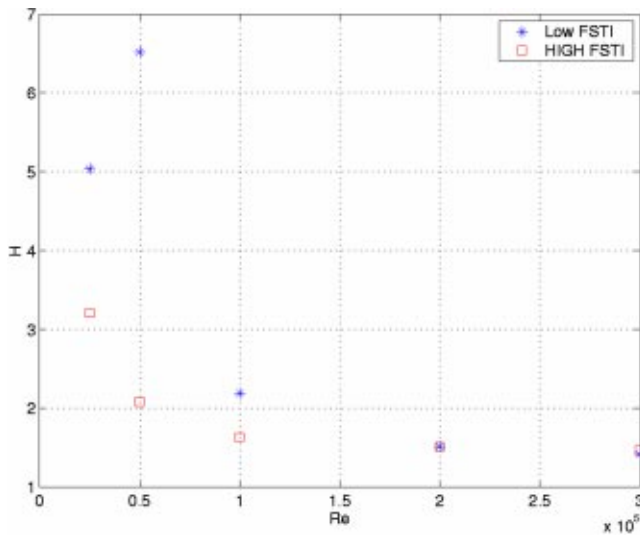


Fig. 16 Shape factor at Station 11

that transition was less abrupt with high FSTI. Boundary layer u' levels are much higher with high FSTI, but the turbulent shear stress magnitude remains low until transition begins and does not appear to depend strongly on FSTI.

Shape Factor and Momentum Thickness. As discussed above, stage losses cannot be determined quantitatively using a single passage test section, but is possible to compute the momentum thickness of the suction side boundary layer at the trailing edge. As explained by Howell et al. [20], this momentum thickness is proportional to the suction side profile loss when the boundary layer shape factor and passage exit angle remain constant. For those cases in which the boundary layer reattaches and recovers to a fully developed turbulent shape, H is approximately equal to 1.4. In these cases the suction side profile loss is likely the dominant loss mechanism (Howell et al. [20]). In those cases in which the boundary layer does not fully reattach, or reattaches near the trailing edge, the shape factor will be very large due to a large displacement thickness. The momentum thickness may be relatively small compared to the displacement thickness in these cases, since the wall shear is essentially zero and θ will not grow significantly in the free-shear layer. Large losses would then be expected in the wake, downstream of the airfoil.

Figure 16 shows the shape factor at Station 11 ($s/L_s=0.94$) as a function of Re . In the $Re=200,000$ and $300,000$ cases, the shape factor is approximately 1.4, indicating that the boundary layer is reattached and that the momentum thickness is a good indicator of overall losses. For the lower Re cases, H is significantly higher, particularly in the low FSTI cases. The lower H in the high FSTI cases indicates that high FSTI helps to keep the separation bubble thinner by promoting more mixing in the shear layer over the bubble and by inducing earlier transition and reattachment. Figure 17 shows the Station 11 momentum thickness as a function of Re . High FSTI helps keep the separation bubble thinner, as shown above in the mean velocity profiles of Figs. 6–15, which tends to result in lower θ and lower losses when the boundary layer reattaches. High FSTI also promotes increased mixing, however, which tends to increase θ . For the $Re=300,000$ cases, Fig. 17 indicates that the second effect is more significant and θ is higher for the high FSTI case. Transition and reattachment occur sufficiently far upstream in the low FSTI case that the effect of the high FSTI in promoting even earlier reattachment is not enough to counter the enhanced mixing effects. This suggests that small, controllable separation bubbles may be acceptable or even desirable in some cases, as proposed by Hourmouziadis [1] for controlled diffusion blading. For the $Re=200,000$ and $100,000$ cases,

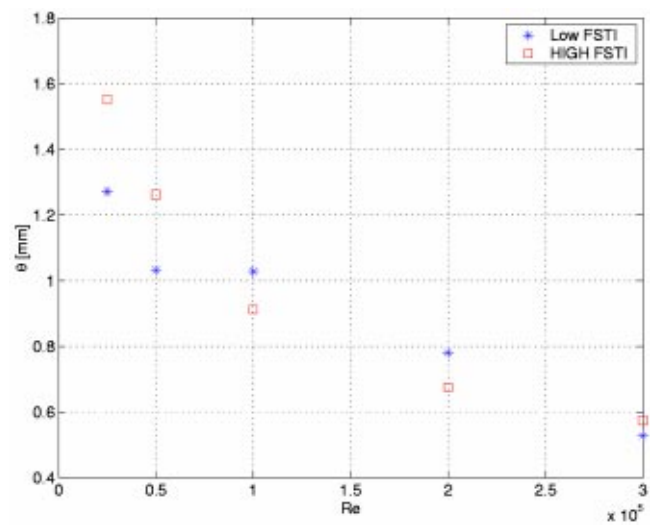


Fig. 17 Momentum thickness at Station 11

the earlier reattachment caused by high FSTI is more significant and θ is lower for the high FSTI cases. This result is consistent with the observation in several studies that unsteady wakes from upstream airfoils result in lower losses. Enhanced mixing in the shear layer explains the higher θ for the high FSTI cases at $Re=25,000$. These momentum thicknesses do not relate directly to losses since the shear layer does not reattach in either of the $Re=25,000$ cases.

Comparison to Correlations. Hatman and Wang [10] discuss three modes of separated flow transition. Based on their criteria, the present cases all fall into their laminar-separation long-bubble category. The data support this; separation occurred before transition. Hatman and Wang [10], Mayle [2] and others suggest that the Thwaites [40] criteria, $Re_\theta^2 K = -0.082$, is a good predictor for laminar separation. A laminar, attached flow solution would put $Re_\theta^2 K = -0.082$ between Stations 6 and 7 in all cases of the present study. The presence of the separation bubble changes the local acceleration, however, which tends to move the location where $Re_\theta^2 K = -0.082$. Volino and Hultgren [13] found the Thwaites criteria to be a good predictor of separation and it appears to work well for the present study as well. Exact prediction of the separation point is not straightforward, however, due to the interdependence of local K values and the separation bubble location.

Prediction of transition and reattachment is more difficult. Hatman and Wang [10] present a transition correlation based on low FSTI data which predicts that transition should not occur in any of the present cases. Clearly, however, transition and reattachment do occur. The $-u'v'$ profiles indicate that transition is imminent even in the low FSTI, low Re cases. Volino and Hultgren [13] drew comparisons to correlations from Mayle [2] and Davis et al. [41] with mixed results. Comparisons to the present data are similarly mixed. The Mayle correlations predict the distance from the separation point to the onset of transition based on Re_θ at the separation location. He presents a correlation for short separation bubble length and a correlation for long bubble length, which is 3.3 times the short bubble length. The Davis et al. [41] correlation also predicts the distance from separation to transition onset, but as a function of the FSTI. Table 3 presents the distance from separation to the start of transition, normalized on the suction surface length, for all cases of the present experiments and as predicted by the Mayle [2] and Davis et al. [41] correlations. The finite spacing between the measurement stations results in uncertainty in Re_θ at separation and in the exact locations of separation and transition, so a range of values is given for each quantity in

Table 3 Distance from separation location to start of transition as a fraction of L_s ; measured values and correlation predictions for each case

FSTI	$Re \times 10^{-3}$	Measured	Mayle [2] short bubble	Mayle [2] long bubble	Davis et al. [41]
Low	25	> 0.41	0.25	0.83	1.54
	50	> 0.33	0.16-0.19	0.53-0.64	0.77
	100	0.17-0.33	0.12-0.14	0.39-0.48	0.38
	200	0-0.17	0.09-0.11	0.31-0.36	0.19
	300	0-0.08	0.07-0.08	0.23-0.28	0.13
High	25	> 0.33	0.27-0.29	0.89-0.98	0.17
	50	0.17-0.33	0.16-0.18	0.53-0.61	0.08
	100	0.08-0.17	0.12-0.14	0.39-0.48	0.04
	200	0-0.08	0.07-0.12	0.25-0.39	0.02
	300	0-0.08	0.06-0.09	0.19-0.31	0.02

the table. The results of the present cases lie between the Mayle long and short bubble correlations to within the resolution of the measurement locations. The Davis et al. correlation tends to predict too long a distance for the low FSTI cases and too short a distance for the high FSTI cases.

Existing correlations appear to give reasonable rough estimates of separated flow transition in some cases, but they are not particularly accurate or robust predictors. The general agreement between the similar cases of the present study, Volino and Hultgren [13], and Simon et al. [17] suggests that prediction of separated flow transition should be possible to some extent. The differences between the results of these studies, noted above, suggest that very accurate prediction of the flow may prove difficult and strongly dependent on small differences in boundary conditions. It is doubtful that a simple, robust correlation can be developed to incorporate all relevant boundary condition effects and provide very accurate predictions. It is also questionable whether the boundary conditions could be specified accurately enough for actual engine conditions. Perhaps they can, with addition research, however, and it may be possible to improve predictions with advanced computational schemes. The difficulty of predicting transition suggests that it may be advantageous to develop flow control schemes to force transition to occur at desired locations rather than try to predict it under existing conditions.

Conclusions

Separated flow transition has been documented for cases with Reynolds numbers ranging from 25,000 to 300,000 at both high and low FSTI. The following conclusions can be drawn from the results.

1 The start of boundary layer reattachment occurs near the start of transition, and both depend strongly on Re and FSTI.

2 High FSTI results in competing effects with regard to losses. It causes enhanced mixing, which tends to promote boundary layer growth and increase losses. At the same time, it promotes earlier transition and reattachment, which reduces boundary layer thickness and losses. At the highest Re, reattachment occurred shortly after separation regardless of FSTI level, and high FSTI resulted in higher losses. At the intermediate Re, high FSTI reduced losses. At the lowest Re, the boundary layer did not reattach even with high FSTI, so losses would be high regardless of FSTI level.

3 The turbulent shear stress level can remain near zero in spite of high FSTI and high u' in the boundary layer. The beginning of a rise in $-u'v'$ signals the beginning of transition. In the lowest Re cases, transition did not occur and the boundary layer did not reattach, but the beginning of a rise in $-u'v'$ was observed near the trailing edge. This hints that it may be possible to induce transition even at very low Re.

4 The present results agree roughly with similar studies from the literature and existing correlations but there are significant differences. Attempts to control transition and force its location may prove more fruitful than prediction of unmodified flow. The present study provides an extensive, detailed baseline data set for ongoing flow control experiments.

Acknowledgments

This work was sponsored by the NASA Glenn Research Center. The grant monitor is Dr. David Ashpis. Additional matching support was provided through a U.S. Naval Academy Recognition Grant. Mr. Dale Boyer of the Technical Support Department at the Naval Academy fabricated the airfoils for the test section.

Nomenclature

- C_f = skin friction coefficient
- $C_p = 2(P_T - P)/\rho U_e^2$, pressure coefficient
- FSTI = free-stream turbulence intensity
- $H = \delta^*/\theta$, shape factor
- $K = (\nu/U_\infty^2)(dU_\infty/ds)$, acceleration parameter
- L_s = suction surface length
- ℓ = hot-wire sensor length
- P = pressure
- P_T = upstream stagnation pressure
- $Re = U_e L_s / \nu$, exit Reynolds number
- $Re_s = U_\infty s / \nu$, local Reynolds number
- Re_θ = momentum thickness Reynolds number
- s = streamwise coordinate, distance from leading edge
- U = mean streamwise velocity
- U_∞ = local free-stream velocity
- U_e = nominal exit free-stream velocity, based on inviscid solution
- u' = rms streamwise fluctuating velocity
- $u_\tau = \sqrt{\tau_w / \rho}$, friction velocity
- $-u'v'$ = time averaged turbulent shear stress
- v' = rms wall normal fluctuating velocity
- y = cross-stream coordinate, distance from wall
- $y^+ = y u_\tau / \nu$, distance from wall in wall coordinates
- δ^* = displacement thickness
- γ = intermittency, fraction of time flow is turbulent
- ν = kinematic viscosity
- ρ = density
- τ_w = wall shear stress
- θ = momentum thickness

References

- [1] Hourmouziadis, J., 1989, "Aerodynamic Design of Low Pressure Turbines," AGARD Lecture Series, 167.
- [2] Mayle, R. E., 1991, "The Role of Laminar-Turbulent Transition in Gas Turbine Engines," ASME J. Turbomach., **113**, pp. 509-537.
- [3] Sharma, O. P., Ni, R. H., and Tanrikut, S., 1994, "Unsteady Flow in Turbines," AGARD Lecture Series 195, Paper No. 5.
- [4] Hodson, H. P., 1991, "Aspects of Unsteady Blade-Surface Boundary Layers and Transition in Axial Turbomachines," *Boundary Layers in Turbomachines*, VKI Lecture Series 1991-2006.
- [5] Wisler, D. C., 1998, "The Technical and Economic Relevance of Understanding Boundary Layer Transition in Gas Turbine Engines," *Minnowbrook II, 1997 Workshop on Boundary Layer Transition in Turbomachines*, J. E. LaGraff and D. E. Ashpis, eds., NASA/CP-1998-206958, pp. 53-64.
- [6] Curtis, E. M., Hodson, H. P., Banieghbal, M. R., Denton, J. D., Howell, R. J., and Harvey, N. W., 1996, "Development of Blade Profiles for Low-Pressure Turbine Applications," ASME Paper 96-GT-358.
- [7] Halstead, D. E., Wisler, D. C., Okiishi, T. H., Walker, G. J., Hodson, H. P., and Shin, H.-W., 1997, "Boundary Layer Development in Axial Compressors and Turbines: Part 3 of 4—LP Turbines," ASME J. Turbomach., **119**, pp. 225-237.
- [8] Solomon, W. J., 2000, "Effects of Turbulence and Solidity on the Boundary Layer Development in a Low Pressure Turbine," ASME Paper 2000-GT-0273.
- [9] Gier, J., and Ardey, S., 2001, "On the Impact of Blade Count Reduction on Aerodynamic Performance and Loss Generation in a Three-Stage LP Turbine," ASME Paper 2001-GT-0197.
- [10] Hatman, A., and Wang, T., 1999, "A Prediction Model for Separated Flow Transition," ASME J. Turbomach., **121**, pp. 594-602.

- [11] Sohn, K. H., DeWitt, K. J., and Shyne, R. J., 2000, "Experimental Investigation of Boundary Layer Behavior in a Simulated Low Pressure Turbine," *ASME J. Fluids Eng.*, **122**, pp. 84–89.
- [12] Lou, W., and Hourmouziadis, J., 2000, "Separation Bubbles Under Steady and Periodic-Unsteady Main Flow Conditions," *ASME J. Turbomach.*, **122**, pp. 634–643.
- [13] Volino, R. J., and Hultgren, L. S., 2001, "Measurements in Separated and Transitional Boundary Layers Under Low-Pressure Turbine Airfoil Conditions," *ASME J. Turbomach.*, **123**, pp. 189–197.
- [14] Yaras, M. I., 2001, "Measurements of the Effects of Pressure-Gradient History on Separation-Bubble Transition," *ASME Paper 2001-GT-0193*.
- [15] Murawski, C. G., Sondergaard, R., Rivir, R. B., Simon, T. W., Vafai, K., and Volino, R. J., 1997, "Experimental Study of the Unsteady Aerodynamics in a Linear Cascade with Low Reynolds Number Low Pressure Turbine Blades," *ASME Paper 97-GT-95*.
- [16] Qiu, S., and Simon, T. W., 1997, "An Experimental Investigation of Transition as Applied to Low Pressure Turbine Suction Surface Flows," *ASME Paper 97-GT-455*.
- [17] Simon, T. W., Qiu, S., and Yuan, K., 2000, "Measurements in a Transitional Boundary Layer Under Low-Pressure Turbine Conditions," *NASA/CR-2000-209957*.
- [18] Brunner, S., Fottner, L., and Schiffer, H.-P., 2000, "Comparison of Two Highly Loaded Low Pressure Turbine Cascades Under the Influence of Wake-Induced Transition," *ASME Paper 2000-GT-268*.
- [19] Stadtmüller, P., Fottner, L., and Fiala, A., 2000, "Experimental and Numerical Investigation of Wake-Induced Transition on a Highly Loaded LP Turbine at Low Reynolds Numbers," *ASME Paper 2000-GT-0269*.
- [20] Howell, R. J., Ramesh, O. N., Hodson, H. P., Harvey, N. W., and Schulte, V., 2001, "High Lift and Aft-Loaded Profiles for Low-Pressure Turbines," *ASME J. Turbomach.*, **123**, pp. 181–188.
- [21] Kaszeta, R. W., Simon, T. W., and Ashpis, D. E., 2001, "Experimental Investigation of Transition to Turbulence as Affected by Passing Wakes," *ASME Paper 2001-GT-195*.
- [22] Dorney, D. J., Ashpis, D. E., Halstead, D. E., and Wisler, D. C., 1999, "Study of Boundary Layer Development in a Two-Stage Low Pressure Turbine," *AIAA Paper 99-0742*; also *NASA TM-1999-208913*.
- [23] Chernobrovkin, A., and Lakshminarayana, B., 1999, "Turbulence Modeling and Computation of Viscous Transitional Flow for Low Pressure Turbines," *ASME J. Fluids Eng.*, **121**, pp. 824–833.
- [24] Huang, P. G., and Xiong, G., 1998, "Transition and Turbulence Modeling of Low Pressure Turbine Flows," *AIAA Paper 98-0339*.
- [25] Thermann, H., Müller, M., and Niehuis, R., 2001, "Numerical Simulation of the Boundary Layer Transition in Turbomachinery Flows," *ASME Paper 2001-GT-0475*.
- [26] VanTreuren, K. W., Simon, T., von Koller, M., Byerley, A. R., Baughn, J. W., and Rivir, R., 2001, "Measurements in a Turbine Cascade Flow Under Ultra Low Reynolds Number Conditions," *ASME Paper 2001-GT-0164*.
- [27] Lake, J. P., King, P. I., and Rivir, R. B., 2000, "Low Reynolds Number Loss Reduction on Turbine Blades With Dimples and V-Grooves," *AIAA Paper 00-738*.
- [28] Bons, J. P., Sondergaard, R., and Rivir, R. B., 2001, "Turbine Separation Control Using Pulsed Vortex Generator Jets," *ASME J. Turbomach.*, **123**, pp. 198–206.
- [29] Volino, R. J., 2002, "Separated Flow Transition under Simulated Low-Pressure Turbine Airfoil Conditions: Part 2—Turbulence Spectra," *ASME J. Turbomach.*, **124**, pp. 656–664.
- [30] Volino, R. J., Schultz, M. P., and Pratt, C. M., 2001, "Conditional Sampling in a Transitional Boundary Layer Under High Free-Stream Turbulence Conditions," *ASME Paper 2001-GT-0192*.
- [31] Chung, J. T., and Simon, T. W., 1990, "Three-Dimensional Flow Near the Blade/Endwall Junction of a Gas Turbine: Visualization in a Large-Scale Cascade Simulator," *ASME Paper 90-WA/HT-4*.
- [32] Aunapu, N. V., Volino, R. J., Flack, K. A., and Stoddard, R. M., 2000, "Secondary Flow Measurements in a Turbine Passage With Endwall Flow Modification," *ASME J. Turbomach.*, **122**, pp. 651–658.
- [33] Volino, R. J., and Simon, T. W., 1997, "Velocity and Temperature Profiles in Turbulent Boundary Layers Experiencing Streamwise Pressure Gradients," *ASME J. Heat Transfer*, **119**, pp. 433–439.
- [34] Wills, J. A. B., 1962, "The Correction of Hot-Wire Readings for Proximity to a Solid Boundary," *J. Fluid Mech.*, **12**, pp. 65–92.
- [35] Ligrani, P. M., and Bradshaw, P., 1987, "Spatial Resolution and Measurement of Turbulence in the Viscous Sublayer Using Subminiature Hot-Wire Probes," *Exp. Fluids*, **5**, pp. 407–417.
- [36] Ligrani, P. M., and Bradshaw, P., 1987, "Subminiature Hot-Wire Sensors: Development and Use," *J. Phys. E*, **20**, pp. 323–332.
- [37] Ligrani, P. M., Westphal, R. V., and Lemos, F. R., 1989, "Fabrication and Testing of Subminiature Multi-Sensor Hot-Wire Probes," *J. Phys. E*, **22**, pp. 262–268.
- [38] Bradshaw, P., 1994, "Turbulence: the Chief Outstanding Difficulty of Our Subject," *Exp. Fluids*, **16**, pp. 203–216.
- [39] Volino, R. J., 2002, "An Investigation of the Scales in Transitional Boundary Layers Under High Free-Stream Turbulence Conditions," *ASME Paper GT-2002-30233*.
- [40] Thwaites, B., 1949, "Approximate Calculations of the Laminar Boundary Layer," *Aeronaut. Q.*, **7**, pp. 245–280.
- [41] Davis, R. L., Carter, J. E., and Reshotko, E., 1985, "Analysis of Transitional Separation Bubbles on Infinite Swept Wings," *AIAA Paper 85-1685*.

Separated Flow Transition Under Simulated Low-Pressure Turbine Airfoil Conditions—Part 2: Turbulence Spectra

Ralph J. Volino

Mem. ASME,
Department of Mechanical Engineering,
United States Naval Academy,
Annapolis, MD 21402
e-mail: volino@usna.edu

Spectral analysis was used to investigate boundary layer separation, transition and reattachment under low-pressure turbine airfoil conditions. Cases with Reynolds numbers ranging from 25,000 to 300,000 (based on suction surface length and exit velocity) have been considered at low (0.5%) and high (9% inlet) free-stream turbulence levels. Spectra of the fluctuating streamwise velocity and the turbulent shear stress are presented. The spectra for the low free-stream turbulence cases are characterized by sharp peaks. The high free-stream turbulence case spectra exhibit more broadband peaks, but these peaks are centered at the same frequencies observed in the corresponding low turbulence cases. The frequencies of the peaks suggest that a Tollmien-Schlichting instability mechanism drives transition, even in the high turbulence cases. The turbulent shear stress spectra proved particularly valuable for detection of the early growth of the instability. The predictable nature of the instability may prove useful for future flow control work.

[DOI: 10.1115/1.1506939]

Introduction

In Part 1 of the present study [1], the significance of boundary layer separation, transition, and reattachment to the flow over modern low-/pressure turbine airfoils was discussed. Measured mean velocity and statistical turbulence quantities were presented for cases with high and low free-stream turbulence intensity (FSTI) and Reynolds numbers (based on suction surface length and exit velocity) ranging from 25,000 to 300,000. The separation point tended to move downstream somewhat as Reynolds number increased. Transition and reattachment locations moved upstream significantly as Re or FSTI were increased.

While the statistical quantities presented in Part 1 [1] provide a quantitative description of what happens under different Re and FSTI conditions, they do not explain the transition mechanism. To better explain the transition process and accurately predict or control it, an understanding of the physics which cause the results observed in Part 1 [1] is needed. The present paper uses spectral analysis to investigate separated flow transition.

Mayle [2] classified the modes of transition as “natural transition,” “bypass” transition; “separated flow” transition of the shear layer over a separation bubble; “periodic-unsteady” transition, which might also be called wake-induced bypass transition; and reverse transition. Under low FSTI, zero streamwise pressure gradient conditions, natural transition is expected. This type of transition has been extensively documented and can be predicted with linear stability analysis. As described by Schlichting [3], when the displacement thickness Reynolds number exceeds a critical value, the boundary layer becomes unstable to small disturbances, which begin to grow as Tollmien-Schlichting (TS) waves. These waves eventually become three dimensional and result in turbulent spots. Under high FSTI, zero pressure gradient conditions, large disturbances can cause a bypass of the linear growth stages of transition, resulting in the sudden appearance of turbulent spots. At intermediate FSTI, elements of both bypass and natural transition may be observed. Sohn and Reshotko [4],

for example, presented data for a 1% FSTI case, showing both spectral peaks at possible TS frequencies and broadband unsteadiness more typical of bypass transition.

In some cases, transition is observed even though linear stability theory predicts that the boundary layer should not develop TS waves. Volino [5], for example, considered a favorable pressure gradient case with high FSTI that clearly underwent transition. The boundary layer thickness remained low in this case due to the acceleration, resulting in Re_{δ^*} below the critical limit for linear instability.

Separated flow transition could potentially include elements of either natural or bypass transition. In separated flow cases the pressure gradient is adverse, resulting in a boundary layer or shear layer that typically is unstable to TS waves. High FSTI, however, might be the dominant factor in a separated shear layer, overwhelming the effect of any TS waves and producing bypass transition. Hughes and Walker [6] list several studies with FSTI below 0.9% in which TS waves were detected in adverse pressure gradient cases. They also note that Halstead et al. [7] did not detect TS waves in the flow through a rotating cascade with more representative, higher FSTI. Solomon and Walker [8], however, provide evidence of TS waves under conditions similar to those of Halstead et al. [7]. Hughes and Walker [6] considered a flow with wakes, in which the FSTI between wakes ranged from less than 1% to about 3%, and the FSTI in the wakes was about 8%. They provide clear evidence of TS waves.

Hatman and Wang [9], Volino and Hultgren [10], and Lou and Hourmouziadis [11] all considered low FSTI, adverse pressure gradient flows and observed transition in the shear layer over separation bubbles. Spectral data in all three studies showed clear evidence of an instability along with harmonics. It was expected that this instability was very similar to the Kelvin-Helmholtz instabilities observed in free shear layers, although the unstable frequencies were somewhat different than expected for free shear layers since the separation bubbles were bounded by the wall on one side. Volino and Hultgren [10] also considered high FSTI cases and observed broadband unsteadiness in the spectra of the streamwise fluctuating velocity, u' . Spikes at discrete frequencies, which were observed in the low FSTI cases, were not present. They stated that transition in the high FSTI cases appeared to be through a bypass mode.

Contributed by the International Gas Turbine Institute and presented at the International Gas Turbine and Aeroengine Congress and Exhibition, Amsterdam, The Netherlands, June 3–6, 2002. Manuscript received by the IGTI, January 22, 2002. Paper No. 2002-GT-30237. Review Chair: E. Benvenuti.

Clearly there is some disagreement regarding the transition mechanism in separated boundary layers, particularly under high FSTI conditions. Some of these differences may stem from physical differences in the boundary conditions between the various studies. The present study addresses the issue through spectral analysis of flows over a range of Reynolds numbers at both high and low FSTI. Included in the analysis are spectra of the turbulent shear stress, which were not considered in previous studies.

Experiments

The experimental facility and the cases considered are described in detail in Part 1 [1]. A low-speed wind tunnel supplies air to a single-passage cascade-simulator with geometry and flow angles matching those for the industry supplied Pak-B airfoil. For the low FSTI cases, the background turbulence level for the wind tunnel is nominally 0.5%, and consists primarily of low frequency unsteadiness. A passive grid is used to generate a high inlet FSTI of 8.7%.

Velocity data were acquired at 11 streamwise measurement stations along the spanwise centerline of the suction side of the passage. Station locations are given in Table 1. At each station, instantaneous streamwise velocity was measured at 60 locations as a single sensor hot-wire probe was traversed from the airfoil surface to the free-stream. The voltage from the hot-wire was offset and amplified by a factor of 10 and low pass filtered at 10 kHz using signal conditioners (TSI model 157). At each location, data were acquired for 26 s at a 20 kHz sampling rate (2^{19} samples). The high sampling rate provides an essentially continuous signal, which is needed for spectral processing. The long sampling time results in low uncertainty in both statistical and spectral quantities. Two component velocity measurements were made at Stations 7–11 with a cross-wire probe. The upstream boundary layer was too thin for cross-wire measurements. Data were acquired at 25 locations in each profile, beginning 1 mm from the wall and extending to the free-stream. Sampling rates and times were the same as with the single sensor probe. Power spectra of u' , the wall normal fluctuating velocity, v' , and the turbulent shear stress, $-u'v'$, were computed for the data from all measurement locations. Uncertainties in the u' , v' and $-u'v'$ spectra are all 10%. Frequencies are resolved from 4.88 to 10 kHz in 4.88 Hz increments using a 4096 point Fast Fourier Transform to compute the spectra. As a check, the spectra were integrated with respect to frequency and found to equal the corresponding time averaged Reynolds stresses.

Data sets were acquired for cases at high and low FSTI with exit Reynolds numbers of 25,000, 50,000, 100,000, 200,000 and 300,000. The upstream boundary layer through Station 6 remained laminar in all of these cases, with the mean velocity following a Falkner-Skan wedge flow solution. Downstream of Station 6 the pressure gradient becomes adverse. Separation occurred between Stations 6 and 8, with the separation point moving downstream as Re increased. Reattachment did not occur in the high or low FSTI, Re=25,000 cases or the low FSTI, Re=50,000 case. In all other cases the boundary layer did reattach, and the reattachment point moved upstream as Re or FSTI was increased. Details are available in Part 1 [1]. The u' level rose in the shear layer in each case after the boundary layer separated, but the turbulent shear stress remained near zero until transition began. Transition began in the shear layer and quickly led to boundary layer reattachment. In the Re=25,000 cases, low but non-zero turbulent shear stress was

observed at the most downstream stations, indicating that although the shear layer was still non-turbulent and separated, it was showing signs of the start of transition.

As discussed in Part 1 [1], the finite length of the hot-wire sensors (1.27 mm) will result in some spatial averaging and could result in attenuation of the measured fluctuating velocity components. Based on the results of Ligrani and Bradshaw [12,13], it was explained in Part 1 that the errors in the rms fluctuating quantities are within the 10% uncertainty estimates in the majority of cases in the present study. Exceptions occur for the Re=200,000 cases at Station 11 of the low FSTI case and Stations 9–11 of the high FSTI case. For the Re=300,000 cases, larger errors are expected for Stations 10–11 of the low FSTI case and Stations 9–11 of the high FSTI case. For these cases, errors may be as large as 30% near the wall, but should be under 10% at y locations greater than 1 mm. As explained by Ligrani et al. [14], measurements with the cross-wire probe are subject to potentially larger errors due to the finite spacing (1 mm) between the two sensors. These errors will be largest near the wall, but become smaller than the 10% uncertainty for y locations above 1 mm. For this reason, cross-wire measurements were only made for $y > 1$ mm.

The spectra in the present paper are presented to show the energy content of the fluctuating quantities as a function of frequency. The average errors in these spectra, therefore, should be the same as those given in the foregoing for the corresponding rms quantities. The errors will not be uniform with respect to frequency across the spectra, however. As explained by Ligrani and Bradshaw [13], spatial averaging effects will be most severe for the smallest scales (highest frequencies) in the flow. Applying the spectral results of Ligrani and Bradshaw [13] to the present study, errors due to spatial averaging at y locations above 1 mm will rise above 10% at frequencies above 150, 300, 600, 1200, and 1800 Hz for the Re=25,000, 50,000, 100,000, 200,000, and 300,000 cases respectively. Below these frequencies the errors should be under 10%. These frequencies are all above the frequencies of the spectral peaks in the results presented below, so the peaks should not be significantly attenuated. For the Re=25,000 and 50,000 cases, all significant energy in the spectra is below the frequencies given above, so there is no significant attenuation of the results at any frequency. For the Re=100,000 case, only the high frequency “tail” of the spectra will be subject to significant error. Magnitudes at these high frequencies may be as much as 30% low. Similarly for the Re=200,000 and 300,000 cases, errors will only rise above 10% at frequencies about twice those of the spectral peaks. Magnitudes at the highest frequencies may be as much as 40% low in these cases.

Frequencies of Interest

Transition in the shear layer over the separation bubble could be initiated by Tollmien-Schlichting waves originating in the boundary layer upstream of separation. Upstream of Station 6, the pressure gradient is favorable and the boundary layer should not develop TS waves at any frequencies. At Station 6 the flow begins to decelerate and immediately becomes unstable. Walker [15] provides the following equation for the frequency of maximum amplification rate for TS waves:

$$2\pi\nu f/U_\infty^2 = 3.2 \text{Re}_{\delta_s}^{-3/2} \quad (1)$$

The TS frequencies predicted by Eq. (1) are listed in Table 2. Values are given for Stations 6 and 7 for the cases in which the boundary layer is still attached at these stations.

Another possible path to transition is breakdown of the shear layer through a Kelvin-Helmholtz-type instability. The frequency of the instability should scale with the velocity change across the shear layer and inversely with the shear layer thickness. Since the velocity in the separation bubble is nearly zero, the velocity difference across the shear layer equals the local free-stream velocity. The shear layer thickness, δ_s , is determined from the mean

Table 1 Measurement stations

Station	1	2	3	4	5	6
s/L_s	0.111	0.194	0.278	0.361	0.444	0.527
Station	7	8	9	10	11	$L_s=228.6$
s/L_s	0.611	0.694	0.778	0.861	0.944	mm

Table 2 Most unstable Tollmien-Schlichting frequencies prior to separation and U_∞/δ_s values in shear layer

FSTI	$Re \times 10^{-3}$	TS freq. [Hz]		U_∞/δ_s [$s^{-1} \times 10^{-3}$]						
		Station		Station						
		6	7	6	7	8	9	10	11	
Low	25	80		1.0	0.8	0.6	0.5	0.4	0.4	
	50	176			2.1	1.5	1.3	1.2	1.0	
	100	443	266			3.9	3.2	3.8		
	200	1175	645			11	8.7			
	300	1554	1134			22	20			
High	25	60		1.1	0.8	0.6	0.4	0.4	0.3	
	50	174		3.1	2.4	1.6	1.1	0.8		
	100	408	272			4.1	3.1			
	200	1138	732			15				
	300	1747	1195			25				

velocity profiles presented in Part 1 [1]. Table 2 lists the quantity U_∞/δ_s for each station where the boundary layer is separated.

Results

Free-Stream Spectra. The u' and v' free-stream spectra are shown in Fig. 1 for each station of the low FSTI, $Re=300,000$ case. Frequency is plotted on a log scale versus frequency times

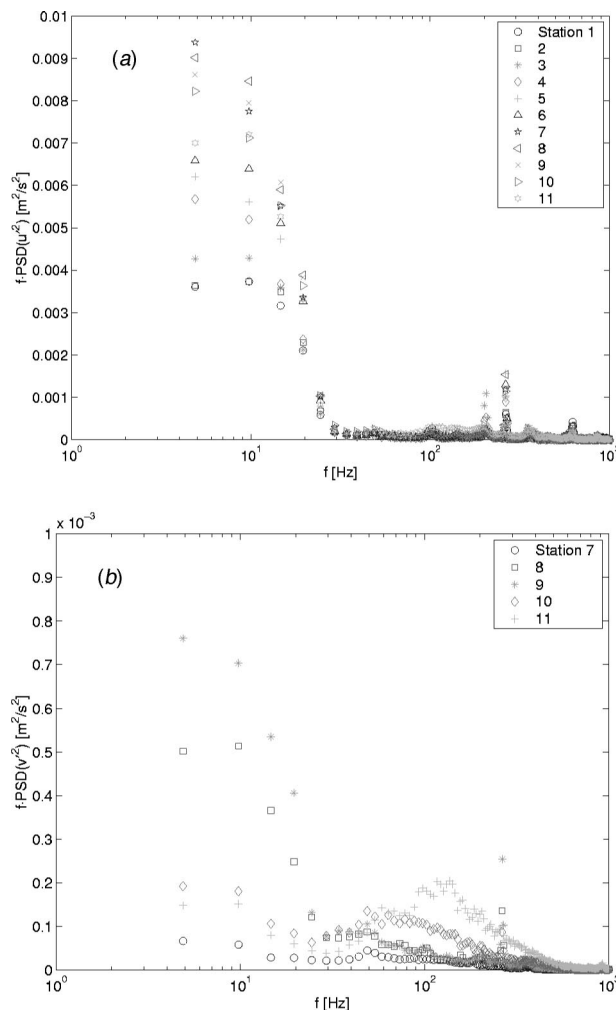


Fig. 1 Free-stream spectra for low FSTI, $Re=300,000$ case—(a) u' , (b) v'

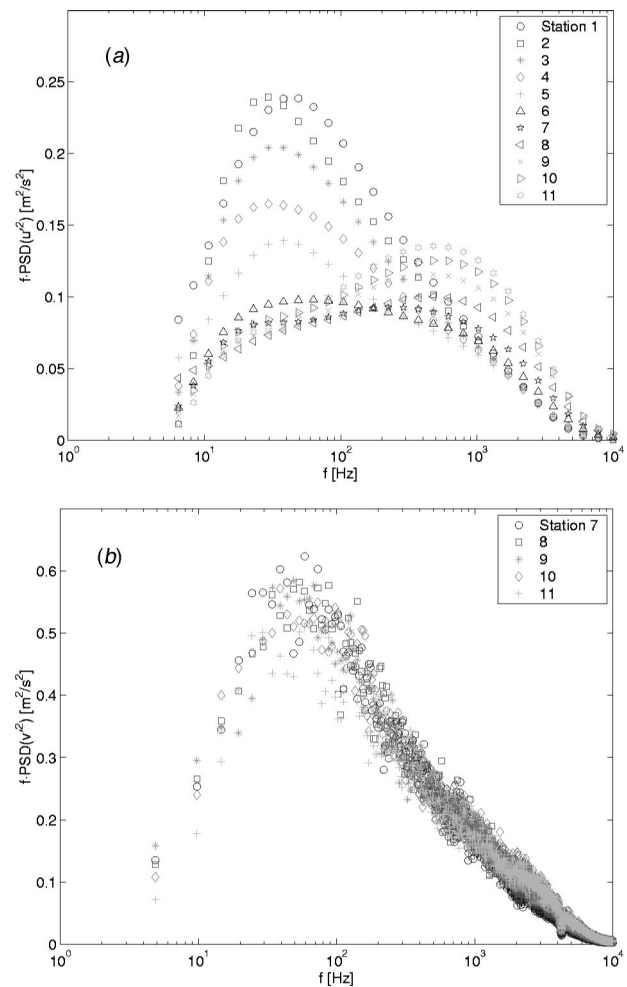


Fig. 2 Free-stream spectra for high FSTI, $Re=300,000$ case—(a) u' , (b) v'

power spectral density on a linear scale. In these coordinates the area under the curve in any frequency band is proportional to the contribution to the quantity of interest in that band. The u' spectra are dominated by low amplitude unsteadiness at frequencies below 20 Hz. The u' spectra for the lower Re cases (not shown) have proportionately lower amplitudes, but the frequency range remains the same. The frequencies associated with turbulent eddies would be expected to scale with the free-stream velocity. Since the frequencies in the present cases remain constant as Re is changed, the unsteadiness in the wind tunnel is most likely not associated with turbulent eddies. The v' spectra show the same low frequencies as u' but at $1/10^{\text{th}}$ the magnitude. A second lower peak is centered at about 100 Hz. This peak is also present with the same magnitude in u' , and is visible in an expanded version of Fig. 1(a). The frequency of this second peak scales with the free-stream velocity and is proportionately lower for the lower Re cases. Its magnitude is very low, and by itself would correspond to an rms turbulence level of about 0.01%. It is likely the residual turbulence remaining after the wind tunnel screens.

The u' and v' free-stream spectra for the high FSTI $Re=300,000$ case are shown in Fig. 2. The magnitude of u' is about 25 times larger than in the low FSTI case of Fig. 1(a). At the upstream stations there is a peak at about 30 Hz. This peak decays due to streamwise straining of the flow as it is accelerated through Station 6. In the adverse pressure gradient region downstream of Station 6, a broadband peak emerges centered at about 700 Hz. In the lower Re cases, the u' spectra is qualitatively the same, but

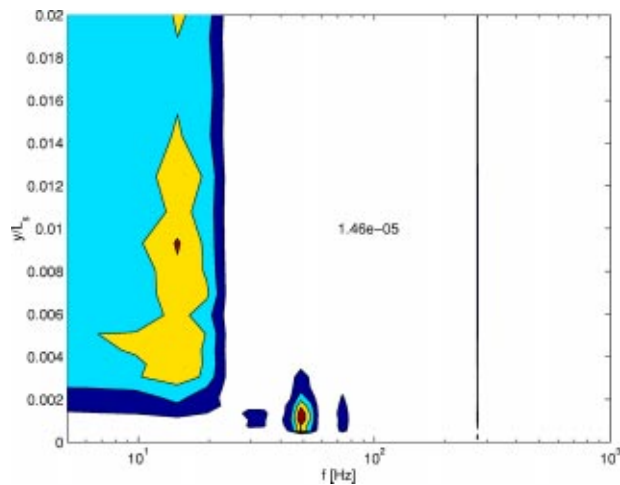


Fig. 3 Contours of $fPSD(u'^2)$, low FSTI, $Re=100,000$, Station 4; outer contour magnitude and contour spacing indicated by numerical value in field of figure

the magnitudes scale with U_∞^2 and the frequencies scale with U_∞ . The v' spectra of Fig. 2(b) all appear similar with a broadband peak centered at 60 Hz. As with u' , the magnitudes and frequencies of the v' spectra in the lower Re cases scale with the free-stream velocity, and appear qualitatively similar to those of Fig. 2(b).

Upstream Boundary Layer. Contours of the boundary layer u' spectra from Station 4 of the low FSTI $Re=100,000$ case are shown in Fig. 3. Frequency in Hz is shown on the horizontal axis on a log scale, and distance from the wall normalized on the suction surface length is on the vertical axis on a linear scale. The frequency is left dimensional since there is no single appropriate normalization for all regions of the flow. The contours in Fig. 3 show the dimensionless magnitude of the spectra as $f \cdot PSD(u'^2)/U_\infty^2$. A slice through the data of Fig. 3 at a fixed distance from the wall would produce a spectrum in the coordinates of Fig. 2, except with dimensionless magnitude. The number (1.46e-05), which appears in the center of the figure, indicates the magnitude of the outermost contour and the contour spacing. Hence, the outermost contour value is 1.46×10^{-5} , the next contour value is 2.92×10^{-5} , the next is 4.38×10^{-6} , etc. The same format is used in all the figures which follow. Figure 3 shows a peak near the wall centered at 50 Hz and unsteadiness below 20 Hz extending from the free-stream to near the wall. The results shown in Fig. 3 are typical of the behavior at Stations 1–6 in all the low FSTI cases. The 50 Hz peak was also visible in the $Re=200,000$ and $300,000$ cases, but not at the two lower Re . This peak did not appear to have any significant effect on the downstream boundary layer.

Figure 4 shows the spectra from Station 4 of the high FSTI $Re=300,000$ case in the coordinates of Fig. 3. The Fig. 4 spectra are typical of the spectra at Stations 1–6 of all the high FSTI cases. There is a near wall peak at 100 Hz, which is 1.7 times the frequency of the free-stream v' frequency peak shown in Fig. 2(b). The distance of the peak from the wall is larger in the lower Re cases, scaling with the boundary layer thickness. The frequency of the peak scales with Re , and is consistently 1.7 times the dominant v' frequency in the free-stream. This indicates that the boundary layer unsteadiness is induced by free-stream buffeting. Volino [5] discusses free-stream buffeting of boundary layers in more detail.

Low FSTI Transition. Upstream of Station 6, the boundary layer unsteadiness is attributable to low amplitude streamwise unsteadiness in the low FSTI cases, and free-stream buffeting in the

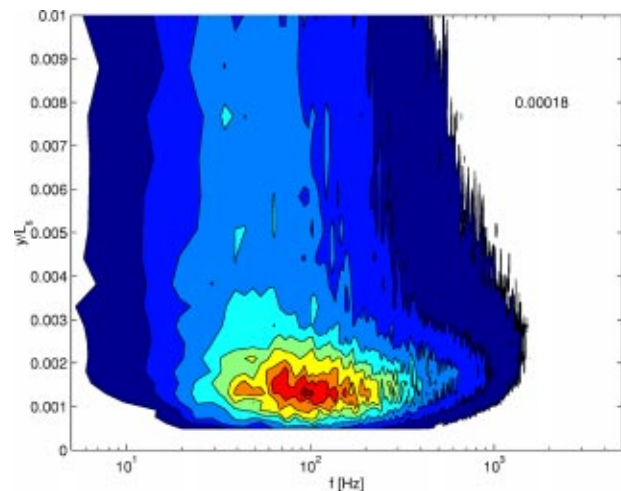


Fig. 4 Contours of $fPSD(u'^2)$, high FSTI, $Re=300,000$, Station 4; outer contour magnitude and contour spacing indicated by numerical value in field of figure

high FSTI cases. Buffeting, as explained in Part 1 [1], refers to the effect of free-stream pressure fluctuations on the boundary layer as fluid is pushed in the wall normal direction across the gradient in the mean streamwise velocity. Downstream of Station 6, the pressure gradient becomes adverse, and the spectra become more interesting. Figure 5 shows the u' spectra contours for Stations 7–11 of all the low FSTI cases. The coordinates of each subplot are the same as those of Fig. 3. In the $Re=25,000$ case (top row of Fig. 5), the contours at Station 7 show the low frequency unsteadiness observed at the upstream stations. Between Stations 7 and 10, the magnitude of the peak increases by an order of magnitude. The peak at each station moves away from the wall. Comparison to the mean velocity profiles presented in Part 1 [1] shows that the location of the peak corresponds, not surprisingly, to the shear layer over the separation bubble. The $Re=50,000$ case (row 2) shows similar behavior through Station 10, but a second peak emerges at about 78 Hz at Station 11. This second peak is indicative of transition.

In the $Re=100,000$ case (row 3 of Fig. 5), a sharp peak appears at Station 10 at 273 Hz. The contour spacing increases by two orders of magnitude between Stations 9 and 10, indicating a similar increase in the magnitude of the peak. The peak is so sharp and so large that it appears as a line in the contour plot. Figure 6 shows this $Re=100,000$, Station 10 data in the same coordinates as Fig. 5, but three dimensionally. The low frequency unsteadiness visible at Station 9 is still present, but since its magnitude is only $1/50^{\text{th}}$ that of the 273 Hz peak, it is barely visible in Fig. 6. The sharp peak in the shear layer is typical of all the low FSTI cases.

In the $Re=200,000$ case (row 4 of Fig. 5), a small peak appears in the shear layer at 698 Hz at Station 9. By Station 10 this peak has increased in size by two orders of magnitude and is becoming more broadband as the boundary layer reattaches and becomes turbulent. Although not clear in Fig. 5, the sharp spectral peak remains in the center of this broadband turbulence and is clear in the format of Fig. 6. Similar behavior is apparent in the $Re=300,000$ case, but the spectral peak and subsequent turbulence are centered at 922 Hz.

Contours of the normalized turbulent shear stress spectra, $f \cdot PSD(-u'v')/U_\infty^2$, for the low FSTI cases are shown in Fig. 7. The format is the same as in Fig. 5. The shear layer is laminar at Stations 7 and 8 in all cases, and the turbulent shear stress is near zero. The $Re=25,000$ case shows a low magnitude, 15 Hz peak at Station 10. The peak was obscured in the u' spectra of Fig. 5 due to the presence of other streamwise unsteadiness at similar frequencies. The magnitude of the 15 Hz shear stress peak increases

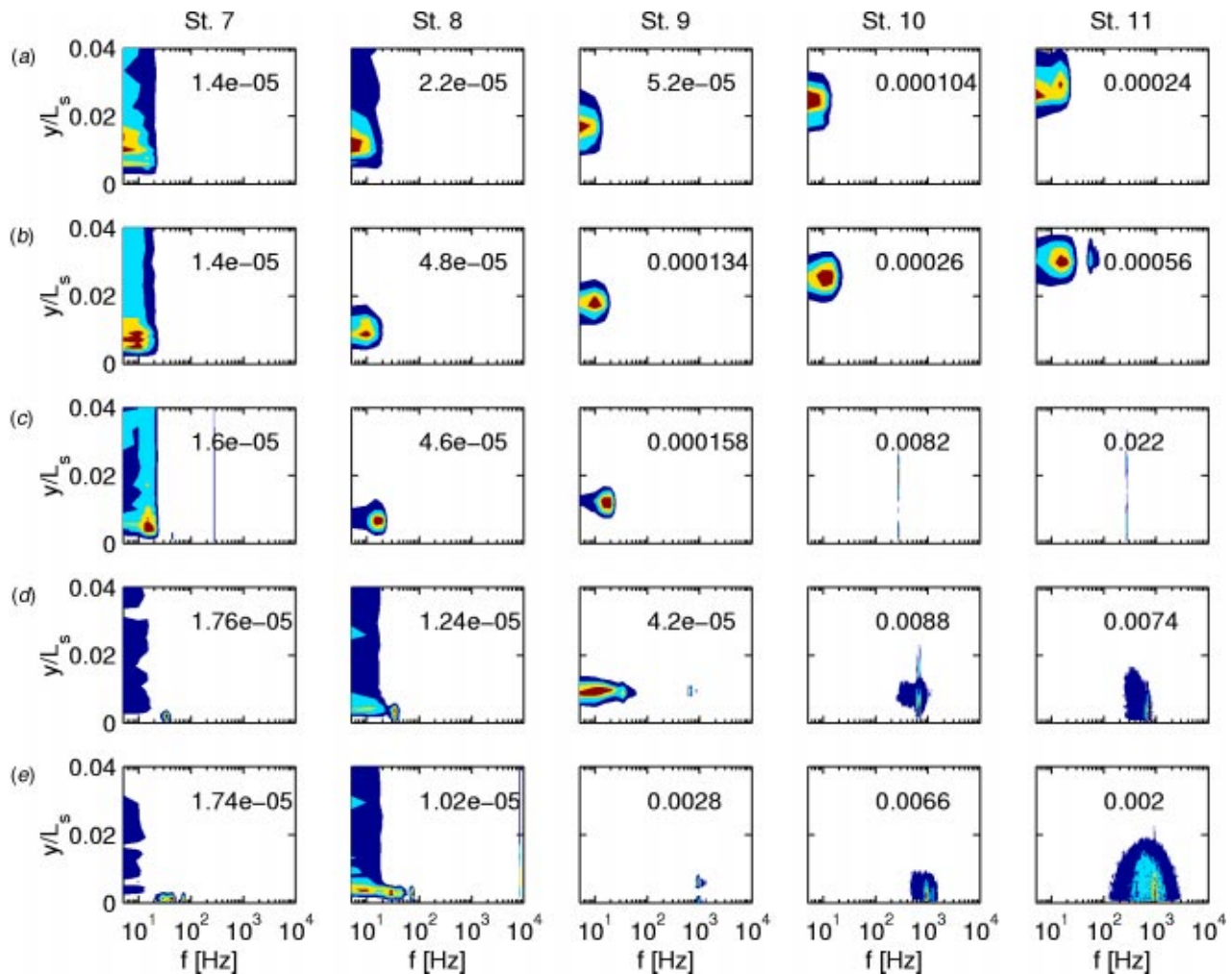


Fig. 5 Contours of $f \cdot \text{PSD}(u'^2)/U_\infty^2$, low FSTI cases; station number indicated above each column; by row—(a) $\text{Re}=25,000$, (b) $\text{Re}=50,000$, (c) $\text{Re}=100,000$, (d) $\text{Re}=200,000$, (e) $\text{Re}=300,000$; outer contour magnitude and contour spacing indicated by numerical value in field of each subplot, 5 contours shown in each subplot

by a factor of 15 between Station 10 and 11, but its amplitude is still quite low. Close inspection of the u' spectra (Fig. 5) at Station 11 shows a double peak, with one peak at 15 Hz. The mean profiles of Part 1 [1] indicate that transition may be imminent, but the shear layer is still laminar at Station 11.

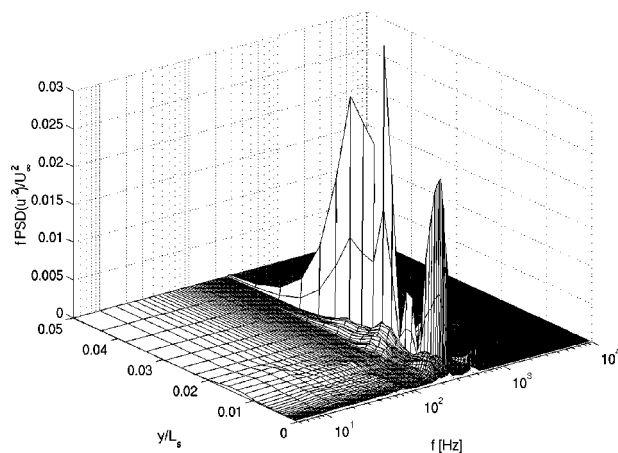


Fig. 6 Spectra of $f \cdot \text{PSD}(u'^2)/U_\infty^2$, low FSTI, $\text{Re}=100,000$, Station 10

The $\text{Re}=50,000$ case shows similar behavior to that at $\text{Re}=25,000$. A turbulent shear stress peak appears at Station 10 and is 37 times larger by Station 11. This peak did not become visible until Station 11 in the u' spectra. Similarly, in the $\text{Re}=100,000$ case a sharp turbulent shear stress peak emerges at Station 9, one station upstream of its appearance in u' . The shear stress peak appears at Station 9 in the $\text{Re}=200,000$ and $300,000$ cases. In all cases, the peak appears at the same frequency in u' and $-u'v'$, but tends to become visible earlier in the $-u'v'$ spectra due to the lower magnitude of the low-frequency “noise” in $-u'v'$.

The frequencies of the spectral peaks are listed for all cases in Table 3. Also indicated in the table are the stations at which these frequencies were determined. The frequencies of the peaks did not change significantly in the streamwise direction. Because the peaks do not appear until after the boundary layer has separated, there is some reason to believe that a Kelvin-Helmholtz-type in-

Table 3 Measured peak frequencies in spectra

FSTI	$\text{Re} \times 10^{-3}$	25	50	100	200	300
Low	Station	10	10	9	9	9
	f [Hz]	15	78	273	698	922
High	Station	9	9	9	9	9
	f [Hz]	20	85	230	600	1100

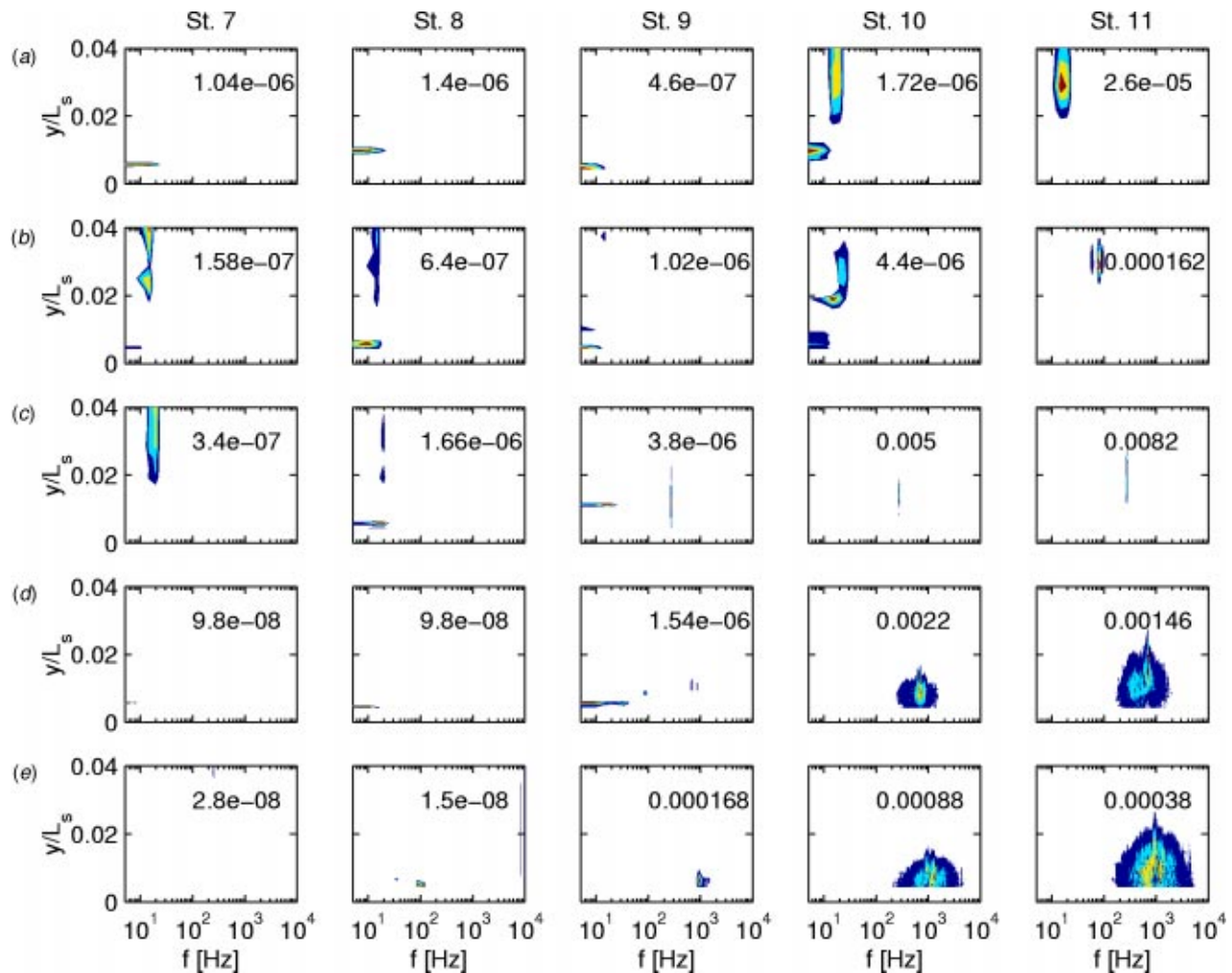


Fig. 7 Contours of $f\text{-PSD}(-u'v')/U_\infty^2$, low FSTI cases; see Fig. 5 caption for further explanation

stability may be involved. For the low FSTI cases, comparison of the spectral peak frequencies to the U_∞/δ_S values in Table 2 shows that the spectral frequencies and U_∞/δ_S values both increase with Re, as expected. The ratio of the measured frequency to U_∞/δ_S is not a constant, however, ranging from about 0.04 to about 0.08. Comparison of the measured frequencies to the TS frequencies of Table 2 shows better correlation. At the three highest Re, the measured frequencies agree with the TS frequencies at Station 7 (the last station before separation) to within 20%. The boundary layer is already separated at Station 7 in the Re = 25,000 and 50,000 cases, so the frequency comparison must be made at Station 6. Agreement with the TS frequencies is not as good in these cases as at the high Re. Hughes and Walker [6] note that since the most unstable TS frequency changes with streamwise position, the frequency observed in the shear layer need not equal the TS value at any single upstream position.

High FSTI Transition. Contours of the u' spectra for the high FSTI cases are shown in Fig. 8. In the Re=25,000 case (top row), there is low frequency unsteadiness at the same frequencies observed upstream (Fig. 4). As in the low FSTI cases, the peak u' location is in the shear layer over the separation bubble. In the Re=50,000 case, the outermost contour at Station 10 extends to higher frequencies than at the upstream stations, and by Station 11 a new peak has emerged at 60 Hz, extending from the shear layer down to the wall. The magnitude of this new peak is about equal to the magnitude of the original, low-frequency peak, which is also still visible. Similar behavior is clear for the Re=100,000

case. Higher frequencies begin to emerge at Station 9, and a large, clear peak centered at 260 Hz is visible at Stations 10 and 11. In the Re=200,000 and 300,000 cases, some signs of higher frequencies are already visible at Station 8, and a double peak is clear at Station 9. At Stations 10 and 11, the higher frequency peak overwhelms the lower frequencies.

Comparing Fig. 8 to Fig. 5, the contour levels in the high FSTI case are about 2 orders of magnitude higher than in the low FSTI case at Stations 7 and 8. This is expected and due to the higher u' caused by free-stream buffeting in the high FSTI case. Farther downstream, however, after the higher frequencies emerge, the contour levels are higher for the low FSTI cases. This is somewhat misleading, as the rms u' levels are actually very similar in the high and low FSTI cases at these stations. The lower contour levels in the high FSTI case result because the u' fluctuations are distributed over a wider frequency band. The spectral peaks of Fig. 8 are much broader than the corresponding peaks of the low FSTI cases shown in Figs. 5–7. Figure 9 shows the u' spectra at Station 10 of the high FSTI, Re=100,000 case. Comparing to Fig. 6, the high FSTI case exhibits much more low frequency activity due to free-stream buffeting, and the peak is clearly broader in frequency than the 273 Hz spike of the low FSTI case.

Figure 10 shows contours of the turbulent shear stress spectra for the high FSTI cases. Values at Stations 7 and 8 are low, in spite of the high FSTI, indicating that much of the u' unsteadiness observed in Fig. 8 does not involve turbulent transport. Distinct, broadband peaks emerge by Station 9 in all cases. As in the low

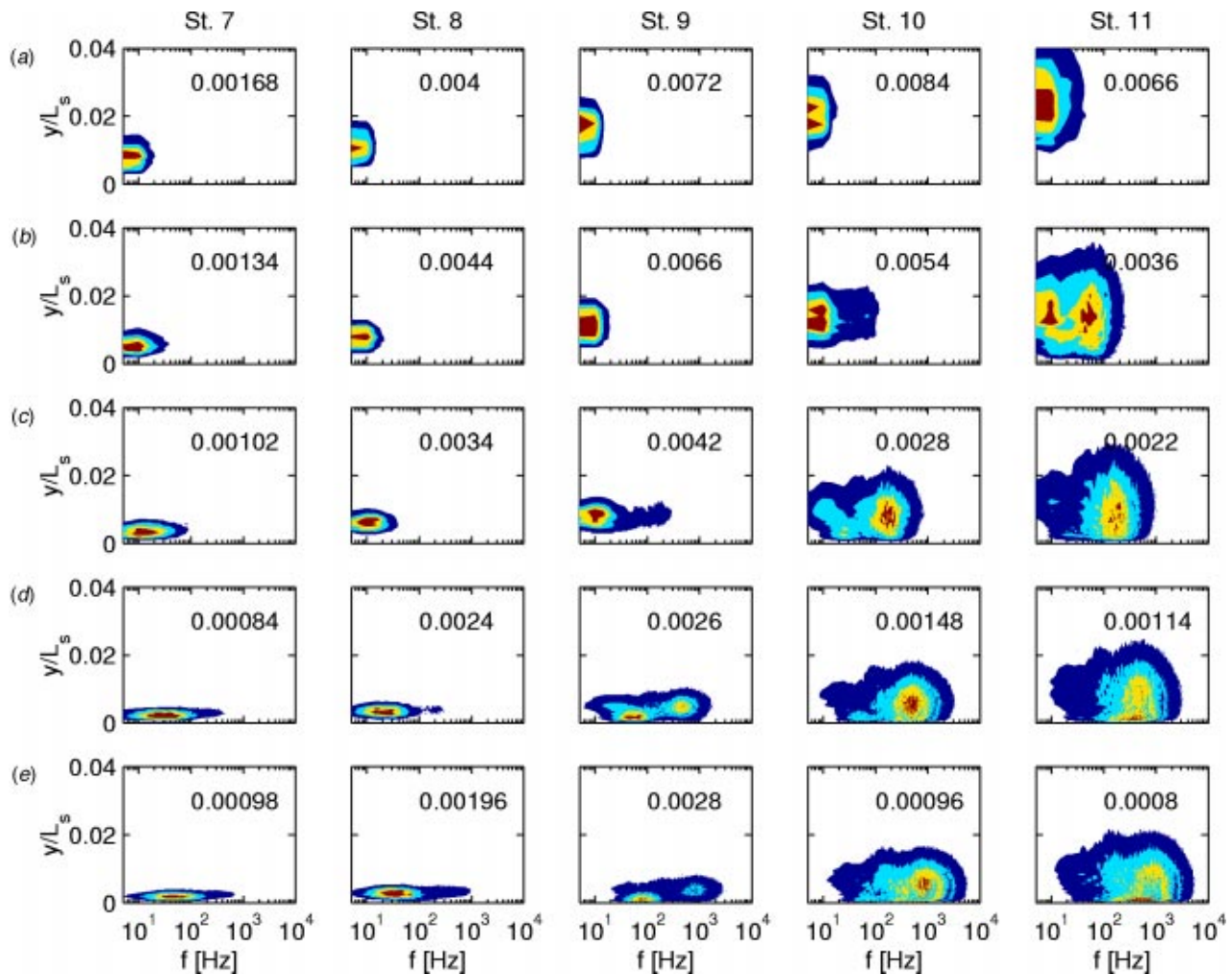


Fig. 8 Contours of $f\text{-PSD}(u'^2)/U_\infty^2$, high FSTI cases; see Fig. 5 caption for further explanation

FSTI cases, these peaks are visible in $-u'v'$ farther upstream than they are in u' . The peak becomes visible in $-u'v'$ soon after it forms, but the u' peak must grow to become larger than the free-stream induced fluctuations before it is discernable.

The broad peaks in the high FSTI cases might suggest that transition occurs through a bypass mode. This was the conclusion

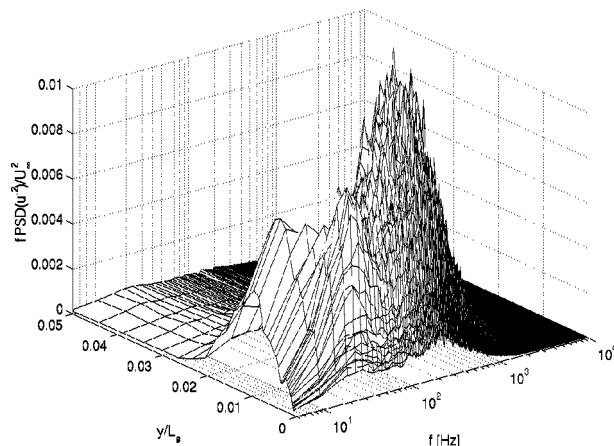


Fig. 9 Spectra of $f\text{-PSD}(u'^2)/U_\infty^2$, high FSTI, $Re=100,000$, Station 10

of Volino and Hultgren [10]. Closer inspection, however, reveals strong similarity to the low FSTI cases. The frequencies of the peaks in the high FSTI cases are listed in Table 3. The broad nature of the high FSTI case peaks, as shown in Fig. 9, result in an uncertainty of about 20% in the frequency values in Table 3. With this uncertainty, the frequency at each Re is essentially the same as in the corresponding low FSTI case. Comparison to the TS frequencies in Table 2 show the same good agreement observed in the low FSTI cases. Close inspection of Fig. 10 reveals that at the four highest Re , the peak in $-u'v'$ begins to appear, with very low magnitude, at Stations 7 and 8. The boundary layer is still thin at these stations, so part of the peak lies closer to the wall than can be measured with the cross-wire probe. The closest measurement to the wall with the cross-wire was at $y=1$ mm, which corresponds to $y/\delta_{99.5}$ between 0.2 and 0.65 at the stations in question. What is visible, however, is at the same frequencies as present downstream. Since the boundary layer is still attached at Station 7, it is doubtful these fluctuations could be induced by a Kelvin-Helmholtz-type instability. Instead, it appears that a TS instability plays a role, even in the high FSTI cases. This agrees with the findings of Hughes and Walker [6], who used instantaneous wall shear measurements to identify wave packets both within and between wakes in an unsteady flow. Although it appears that TS waves play a role in the high FSTI cases, it should be noted that it is also possible that transition occurs through a bypass mode, and

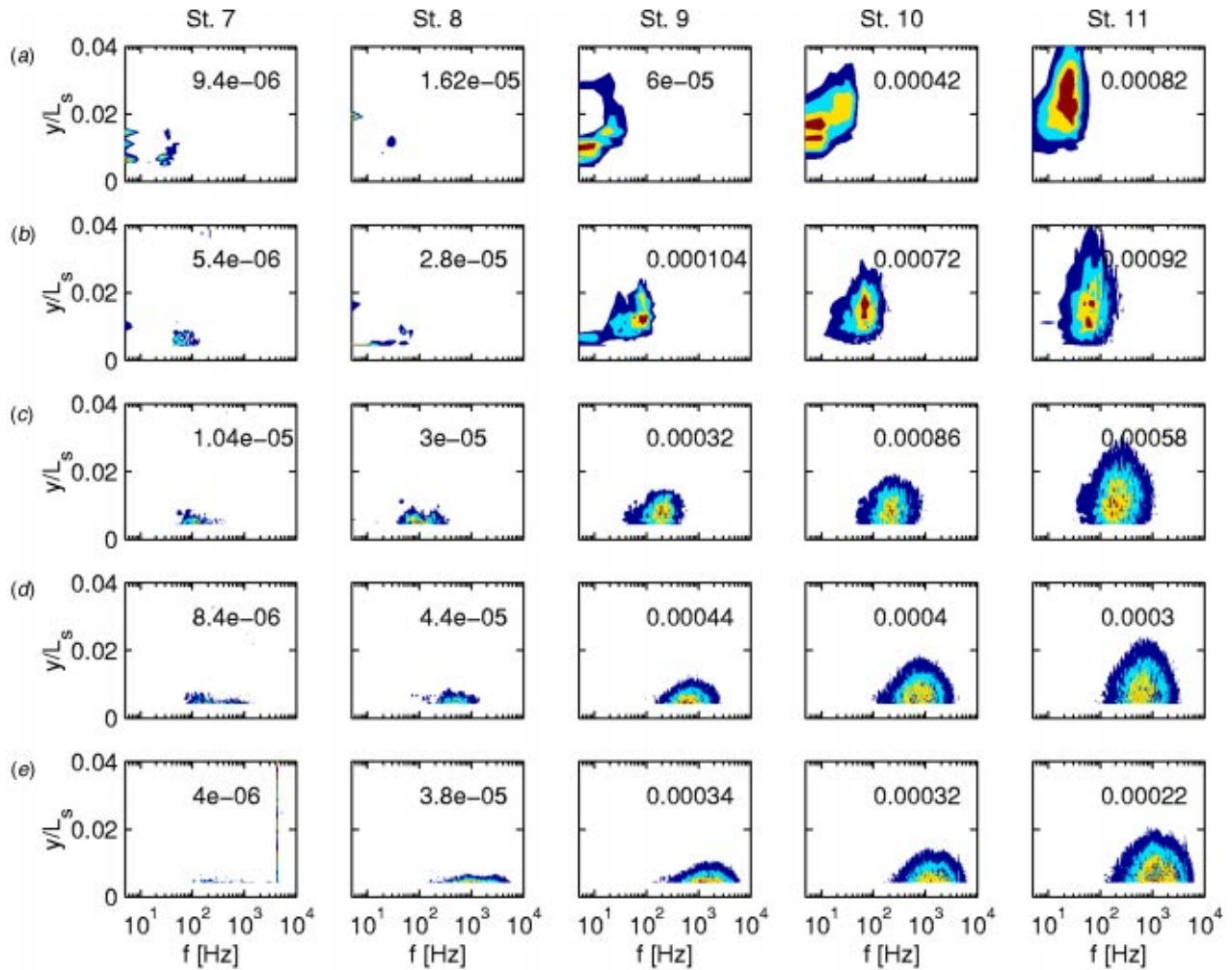


Fig. 10 Contours of $f \cdot \text{PSD}(-u'v')/U_\infty^2$, high FSTI cases; see Fig. 5 caption for further explanation

that the spectral peaks are due not to TS waves, but to the turbulence within turbulent spots. Perhaps both TS and bypass modes play a role, as suggested by Mayle [2].

Conclusions

Turbulence spectra provide valuable insights into the transition mechanism. Clear sharp peaks were observed in the spectra of the low FSTI cases, at frequencies indicating a probable TS instability mechanism for the breakdown of the shear layer over the separation bubble to turbulence. The spectra were more broadband for the high FSTI cases, but the peaks of these spectra occurred at the same frequencies as in the corresponding low FSTI cases, suggesting a possible similar transition mechanism at high and low FSTI. The turbulent shear stress spectra were valuable for detection of instabilities upstream of the location where peaks became discernable in the u' spectra. In the high FSTI cases, low magnitude peaks were detected in $-u'v'$ upstream of separation, further supporting the argument for a TS transition. Larger initial disturbances in the high FSTI cases resulted in detectable $-u'v'$ farther upstream than in the low FSTI cases. Since the adverse pressure gradient boundary layer is unstable to disturbances over a broad range of frequencies and the free-stream turbulence contains a range of scales, broad peaks emerge in the boundary layer spectra of the high FSTI cases. These peaks contrast with the sharp peaks of the low FSTI cases, which result from the growth of small disturbances at the most unstable fre-

quencies. The presence and predictability of the shear layer instability may prove useful in future attempts to induce transition for separation control.

Acknowledgments

This work was sponsored by the NASA Glenn Research Center. The grant monitor is Dr. David Ashpis. Additional matching support was provided through a U.S. Naval Academy Recognition Grant.

Nomenclature

FSTI	= free-stream turbulence intensity
f	= frequency in Hz
L_s	= suction surface length
PSD	= power spectral density of u'^2 or $-u'v'$
Re	= $U_e L_s / \nu$, exit Reynolds number
Re_{δ^*}	= $U_\infty \delta^* / \nu$ displacement thickness Reynolds number
s	= streamwise coordinate, distance from leading edge
U_∞	= local free-stream velocity
U_e	= nominal exit free-stream velocity
u'	= streamwise fluctuating velocity
$-u'v'$	= turbulent shear stress
v'	= wall normal fluctuating velocity
y	= cross-stream coordinate, distance from wall
δ^*	= displacement thickness

δ_s = shear layer thickness
 $\delta_{99.5}$ = 99.5% boundary layer thickness
 ν = kinematic viscosity

References

- [1] Volino, R. J., 2002, "Separated Flow Transition Under Low Pressure Turbine Airfoil Conditions: Part 1 - Mean Flow and Turbulence Statistics," *ASME J. Turbomach.*, **124**, pp. 645–655.
- [2] Mayle, R. E., 1991, "The Role of Laminar-Turbulent Transition in Gas Turbine Engines," *ASME J. Turbomach.*, **116**, pp. 509–537.
- [3] Schlichting, H., 1979, *Boundary Layer Theory*, 7th ed., McGraw Hill, New York, NY.
- [4] Sohn, K. H., and Reshotko, E., 1991, "Experimental Study of Boundary Layer Transition with Elevated Freestream Turbulence on a Heated Flat Plate," NASA CR 187068.
- [5] Volino, R. J., 2002, "An Investigation of the Scales in Transitional Boundary Layers Under High Free-Stream Turbulence Conditions," ASME Paper GT-2002-30233.
- [6] Hughes, J. D., and Walker, G. J., 2001, "Natural Transition Phenomena on an Axial Compressor Blade," *ASME J. Turbomach.*, **123**, pp. 392–401.
- [7] Halstead, D. E., Wisler, D. C., Okiishi, T. H., Walker, G. J., Hodson, H. P., and Shin, H.-W., 1997, "Boundary Layer Development in Axial Compressors and Turbines: Part 3 of 4—LP Turbines," *ASME J. Turbomach.*, **119**, pp. 225–237.
- [8] Solomon, W. J., and Walker, G. J., 1995, "Incidence Effects on Wake-Induced Transition on an Axial Compressor Blade," *Proc. 12th Int. Symposium on Air Breathing Engines*, Melbourne, Australia, pp. 954–964.
- [9] Hatman, A., and Wang, T., 1999, "A Prediction Model for Separated Flow Transition," *ASME J. Turbomach.*, **121**, pp. 594–602.
- [10] Volino, R. J., and Hultgren, L. S., 2001, "Measurements in Separated and Transitional Boundary Layers Under Low-Pressure Turbine Airfoil Conditions," *ASME J. Turbomach.*, **123**, pp. 189–197.
- [11] Lou, W., and Hourmouziadis, J., 2000, "Separation Bubbles Under Steady and Periodic-Unsteady Main Flow Conditions," *ASME J. Turbomach.*, **122**, pp. 634–643.
- [12] Ligrani, P. M., and Bradshaw, P., 1987, "Spatial Resolution and Measurement of Turbulence in the Viscous Sublayer Using Subminiature Hot-Wire Probes," *Exp. Fluids*, **5**, pp. 407–417.
- [13] Ligrani, P. M., and Bradshaw, P., 1987, "Subminiature Hot-Wire Sensors: Development and Use," *J. Phys. E*, **20**, pp. 323–332.
- [14] Ligrani, P. M., Westphal, R. V., and Lemos, F. R., 1989, "Fabrication and Testing of Subminiature Multi-Sensor Hot-Wire Probes," *J. Phys. E*, **22**, pp. 262–268.
- [15] Walker, G. J., 1989, "Transitional Flow on Axial Turbomachine Blading," *AIAA J.*, **27**, pp. 595–602.

Passive Flow Control on Low-Pressure Turbine Airfoils

Ralph J. Volino

Department of Mechanical Engineering,
United State Naval Academy,
Annapolis, MD 21402
e-mail: volino@usna.edu

Two-dimensional rectangular bars have been used in an experimental study to control boundary layer transition and reattachment under low-pressure turbine conditions. Cases with Reynolds numbers (Re) ranging from 25,000 to 300,000 (based on suction surface length and exit velocity) have been considered at low (0.5%) and high (8.5% inlet) free-stream turbulence levels. Three different bars were considered, with heights ranging from 0.2% to 0.7% of suction surface length. Mean and fluctuating velocity and intermittency profiles are presented and compared to results of baseline cases from a previous study. Bar performance depends on the bar height and the location of the bar trailing edge. Bars located near the suction surface velocity maximum are most effective. Large bars trip the boundary layer to turbulent and prevent separation, but create unnecessarily high losses. Somewhat smaller bars had no immediate detectable effect on the boundary layer, but introduced small disturbances that caused transition and reattachment to move upstream from their locations in the corresponding baseline case. The smaller bars were effective under both high and low free-stream turbulence conditions, indicating that the high free-stream turbulence transition is not simply a bypass transition induced by the free stream. Losses appear to be minimized when a small separation bubble is present, so long as reattachment begins far enough upstream for the boundary layer to recover from the separation. Correlations for determining optimal bar height are presented. The bars appear to provide a simple and effective means of passive flow control. Bars that are large enough to induce reattachment at low Re , however, cause higher losses at the highest Re . Some compromise would, therefore, be needed when choosing a bar height for best overall performance. [DOI: 10.1115/1.1626685]

Introduction

Modern low-pressure turbine (LPT) airfoils are subject to increasingly stronger pressure gradients as designers impose higher loading in an effort to improve efficiency and lower cost by reducing the number of airfoils in an engine. If the adverse pressure gradient on the suction side of these airfoils becomes strong enough, the boundary layer will separate. Separation bubbles, particularly those that fail to reattach, can result in a significant loss of lift and a subsequent degradation of engine efficiency (e.g., Hourmouziadis [1], Mayle [2], and Sharma et al. [3]). The problem is particularly relevant in aircraft engines. Airfoils optimized to produce maximum power under takeoff conditions may still experience boundary layer separation at cruise conditions, due to the thinner air and lower Reynolds numbers at altitude. A component efficiency drop of 2% may occur between takeoff and cruise conditions in large commercial transport engines, and the difference could be as large as 7% in smaller engines operating at higher altitudes. Component life may also be affected by more than an order of magnitude (Hodson [4]). Because the LPT produces the bulk of the net power in many engines, changes in its component efficiency can result in nearly equal changes in overall engine efficiency (Wisler [5]). There are several sources for losses in an engine, including secondary flows, but the suction side boundary layer has been identified as the primary source of losses in the LPT (Curtis et al. [6]). Prediction and control of suction side separation, without sacrifice of the benefits of higher loading, are therefore, necessary for improved engine design.

Separation on LPT airfoils is complicated by boundary layer transition. Turbulent boundary layers are much more resistant to separation than laminar boundary layers. If transition occurs far enough upstream, it can prevent separation. If transition occurs in the shear layer over a separation bubble, it will tend to induce

boundary layer reattachment. The lower the Reynolds number, the farther downstream transition will tend to occur and hence the problems associated with performance at altitude.

Separated flow transition has been studied extensively, and in recent years several studies have focused on transition in the LPT. Volino [7] provides a review of much of that work. Separation can be affected through naturally occurring phenomena in an engine and through deliberate attempts at flow control. Several studies have shown that high free-stream turbulence intensity (FSTI) tends to cause the transition to move upstream, resulting in a smaller separation bubble. Reducing the separation bubble size tends to result in thinner boundary layers after reattachment, thereby reducing losses. Moving the transition upstream, however, results in a longer turbulent region on the airfoil, which tends to increase losses. Volino [7] showed that the net result of these competing effects depends on the Reynolds number. High FSTI tends to reduce losses at low Re . At high Re , where separation bubbles are relatively small even with low FSTI, high FSTI results in higher losses. At very low Re , boundary layers may fail to reattach even with high FSTI (e.g., Volino [7] and Van Treuren et al. [8]). Unsteadiness caused by wakes generated upstream of an airfoil has been shown in several studies (e.g., Howell et al. [9]) to reduce the extent of separation bubbles and reduce losses. As with elevated FSTI, wake unsteadiness is most effective at reducing losses at lower Re , where the steady flow separation bubbles are largest. Stadtmüller et al. [10] found that at high Re , losses were higher with wakes than in steady flow.

Existing results suggest that separation bubbles should be kept small, but without producing an unnecessarily long turbulent region. Hourmouziadis [1] discussed "controlled diffusion blading," in which an airfoil is designed so that a small separation bubble is present. The bubble itself is not thick enough to produce high losses, and its presence allows a shorter turbulent region near the trailing edge. This idea is discussed below in conjunction with the present results.

Capitalizing on the beneficial effects of unsteady wakes, Howell et al. [9] and Brunner et al. [11] studied airfoils modified for

Contributed by the International Gas Turbine Institute and presented at the International Gas Turbine and Aeroengine Congress and Exhibition, Atlanta, GA, June 16–19, 2003. Manuscript received by the IGTI Dec. 2002; final revision Mar. 2003. Paper No. 2003-GT-38728. Review Chair: H. R. Simmons.

higher lift. Losses increased with airfoil loading, as adverse pressure gradients became stronger and separation bubbles became larger. With wake passing, however, the magnitude of the loss increase was in some cases relatively small compared to the increase in lift. Aft loaded airfoils tended to have lower losses, since separation and transition occurred closer to the trailing edge, resulting in a shorter turbulent region.

While high FSTI and wakes help to mitigate separated flow problems, they clearly do not solve all problems, as evidenced by the known efficiency drop in modern engines at altitude. Howell et al. [9] indicated that their highly loaded airfoils might be close to a limit, and that higher loading could cause unacceptable separation problems even in the presence of wakes. Looking beyond FSTI and wakes, other types of flow control could prove useful. The literature contains numerous examples of separation control. Most have been applied to external flows over aircraft, but a few studies have considered passive devices added to LPT airfoils. Van Treuren et al. [8] utilized vortex generators on the suction surface of an LPT airfoil. The vortex generators caused reattachment at $Re=50,000$ (all Re in the present paper are based on exit velocity and suction surface length). Losses appeared to be slightly lower with the vortex generators. The vortex generators were not effective at $Re=25,000$, and the boundary layer did not reattach even with 8% FSTI. Van Treuren et al. [8] did not consider higher Re . In another study, Lake et al. [12] used various passive devices including dimples and boundary layer trips in an LPT cascade. They considered cases with Re above 100,000. Murawski and Vafai [13] added extensions to the trailing edges of the airfoils in their cascade. These extensions tended to move the separation location downstream. At low Re , they reduced the length of the separation bubble and reduced losses. At high Re , losses increased. Byerley et al. [14] used “Gurney flaps” to control separation. These devices were trips, near the trailing edge on the pressure side of the airfoils. They helped to keep the boundary layer attached on the suction side, but also increased losses in the cascade. Active separation control has also been employed. Bons et al. [15,16] used steady and pulsed vortex generator jets to successfully control separation under LPT conditions.

The studies listed above indicate that separation control should be possible under LPT conditions. Existing results are, however, limited both in the range of Reynolds numbers considered in each study and in the types of data acquired. More experiments are needed with various types of devices to expand the experimental data base. Detailed measurements will also help in the explanation of the physical mechanisms by which various devices affect the flow.

Passive flow control is considered in the present work. Thin bars of rectangular cross section are placed on the suction surface of an LPT airfoil near the suction surface velocity peak. Experiments were conducted in a single-passage cascade simulator, described in Volino [7]. The geometry of the passage corresponds to that of the “Pak-B” airfoil, which is an industry supplied research airfoil that is representative of a modern, aggressive LPT design. Volino [7] documented cases in the present facility without flow control. These serve as baseline cases for the present study.

Experiments

Experiments were conducted in a low speed wind tunnel, described by Volino et al. [17]. Briefly, air enters through blowers and passes through a honeycomb, a series of screens, two settling

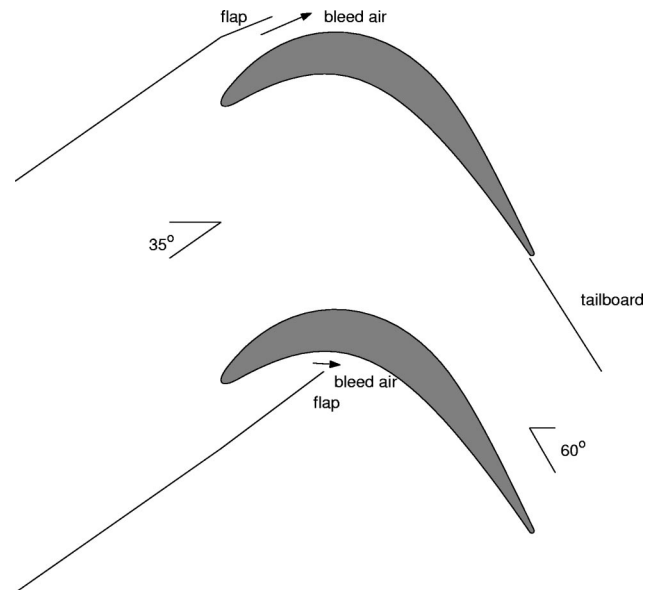


Fig. 1 Schematic of the test section

chambers, and a three-dimensional contraction before entering the test section. At the exit of the contraction, the mean velocity is uniform to within 1%. The FSTI is $0.5\% \pm 0.05\%$. Nearly all of this free-stream “turbulence” is actually streamwise unsteadiness at frequencies below 20 Hz and is not associated with turbulent eddies. The rms intensities of the three components of the unsteadiness are 0.7%, 0.2%, and 0.2% in the streamwise, pitchwise, and spanwise directions, respectively. For low-FSTI cases, the test section immediately follows the contraction. For high FSTI, a passive grid is installed at the contraction exit followed by a 1-m-long rectangular settling chamber. At the inlet to the test section the high-FSTI mean flow and turbulence are spatially uniform to within 3% and 6%, respectively. The free-stream turbulence is nearly isotropic with rms intensities of 8.8%, 8.9%, and 8.3% in the streamwise, pitchwise, and spanwise directions. The integral length scales of these components are 3 cm, 1.6 cm and 1.4 cm. The integral scales were computed from the power spectra of each component.

The test section, shown in Fig. 1, consists of the passage between two airfoils. Details are listed in Table 1 and more information is available in Ref. [7]. A large span-to-chord ratio of 4.3 was chosen to ensure two-dimensional flow at the spanwise centerline of the airfoils, where all measurements were made. Upstream of each airfoil are flaps, which control the amount of bleed air allowed to escape from the passage. The flaps, along with a tailboard on the pressure side of the passage, are adjusted to produce the correct leading edge flow and pressure gradient along the airfoils. The flow in the passage matches that in a multiblade cascade.

Experimental conditions match those of the ten baseline cases of Volino [7], who considered high- and low-FSTI cases at five Reynolds numbers ($Re=25,000$, 50,000, 100,000, 200,000, and 300,000). The Reynolds number range is representative of condi-

Table 1 Test section parameters

Axial chord (mm)	True chord (mm)	Pitch (mm)	Span (mm)	Suction side, L_s (mm)	Inlet flow angle	Exit flow angle
153.6	170.4	136.0	660.4	228.6	35°	60°

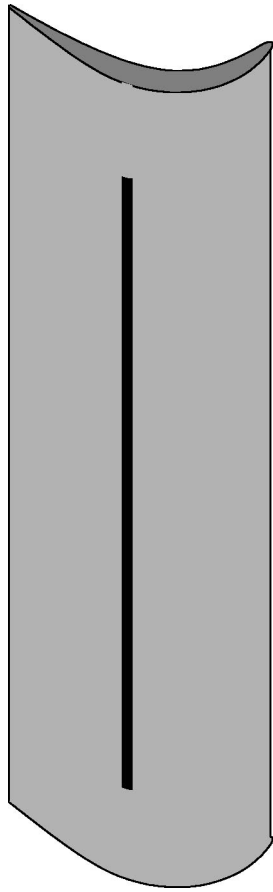


Fig. 2 Scale drawing of suction side airfoil showing location of bar

tions from cruise to takeoff. The FSTI levels in an engine may vary considerably, but the values in the present work are believed to span the range of most interest.

Prior to the detailed experiments of the present study, various devices were used in preliminary attempts at flow control. The devices included trip wires of various diameters, rectangular bars of various widths and thicknesses, and delta wing vortex generators of various heights, spacing, and angles with respect to the flow. All of these devices were tried at several streamwise locations along the suction surface. Documentation included streamwise pressure profiles and velocity profiles acquired near the trailing edge. Large devices of any type eliminated separation (as indicated by the pressure profiles), but caused large increases in

losses (as indicated by large increases in momentum deficit at the trailing edge). As the size of the devices was reduced, it was found that all devices that were just large enough to induce boundary layer reattachment at $Re=25,000$ caused about the same increase in losses at higher Re . This was somewhat unexpected, as it was thought that the delta wings vortex generators might present less blockage, and more effectively promote mixing and inhibit separation than the trips or bars. Reasons for this unexpected finding are discussed with the results below. Since no device appeared to have a clear advantage, rectangular bars were chosen for further study because of their simplicity. The bars were of uniform rectangular cross section and extended along the airfoil span, as shown in Fig. 2. It should be noted that the tests described above were not exhaustive, and do not preclude the possible usefulness of vortex generators or other types of devices.

The results of the preliminary tests with the bars indicated that the streamwise width of a bar and the location of its leading edge were unimportant. The bar height and the location of its trailing edge were critical. Hence, it appeared that the backward-facing step at the trailing edge was most important for flow control. Bars were most effective when the trailing edge was near the location of the suction surface velocity peak. If the trailing edge was much farther downstream, it was located under the separation bubble and was ineffective. If the trailing edge was upstream in the favorable pressure gradient region, the stabilizing effect of the accelerating flow appeared to lessen the bar's effectiveness.

In the present study, rectangular bars were fabricated from multiple layers of vinyl tape. The trailing edge of the bar was located at $s/L_s=0.51$, near the suction surface velocity peak. All bars were 6 mm wide in the streamwise direction. Bar heights of 0.4 mm, 0.8 mm, and 1.6 mm were used. The bar heights were all less than 1% of L_s . They compare to local boundary layer thickness at the bar location of about 3.8 mm, 2.7 mm, 2.0 mm, 1.4 mm, and 1.2 mm in the baseline $Re=25,000$ through 300,000 cases, respectively. For each bar height, all 10 cases of the baseline study were redocumented, for a total of 30 new experimental cases.

Measurements. Pressure surveys were made for each case using a pressure transducer (0–870 Pa range Validyne transducer) and a Scanivalve. Stagnation pressure was measured with a pitot tube upstream of the passage inlet, and 11 pressure taps were located on each airfoil along their spanwise centerlines. Locations of the taps on the suction side are listed in Table 2 along with measured local FSTI components, and the $Re K$ product at these stations based on a nonseparating, inviscid solution. The uncertainty in the suction side pressure coefficients was 7% at the lowest Re , and below 4% in other cases. Most of this uncertainty was due to bias error. Stochastic error was minimized by averaging pressure transducer readings over a 10-s period.

Velocity profiles on the suction surface were measured at streamwise stations corresponding to pressure taps 7–11, as given

Table 2 Measurement stations locations, local acceleration (inviscid solution), and measured local free-stream turbulence

Station	s/L_s	$Re K$	Low FSTI u'/U_∞ (%)	Low FSTI v'/U_∞ (%)	High FSTI u'/U_∞ (%)	High FSTI v'/U_∞ (%)
1	0.111	1.58	0.44		5.2	
2	0.194	1.20	0.39		4.6	
3	0.278	0.86	0.37		4.0	
4	0.361	0.75	0.38		3.5	
5	0.444	0.62	0.39		3.2	
6	0.528	−0.02	0.41		2.8	
7	0.611	−0.81	0.47	0.05	2.9	5.9
8	0.694	−0.95	0.47	0.12	3.0	6.2
9	0.777	−0.58	0.48	0.14	3.4	6.6
10	0.861	−0.53	0.54	0.11	3.8	6.8
11	0.944	−0.18	0.51	0.11	4.0	6.8

in Table 2. These stations are downstream of the bar. Profiles at stations 1–6 are fully documented for the baseline cases in Refs. [7,18], and show that the upstream boundary layer closely follows a laminar solution, even in the high-FSTI cases. Profiles were measured near but not at the spanwise centerline of the airfoil to insure that the pressure taps did not interfere with the velocity measurements. Profiles were acquired with a hot-wire anemometer (AA Lab Systems model AN-1003) and a single-sensor boundary layer probe (TSI model 1218-T1.5). The sensor diameter is $3.8\ \mu\text{m}$, and the active length is $1.27\ \text{mm}$. At each measurement location, data were acquired for 26 s at a 20-kHz sampling rate (2^{19} samples). All raw data were saved. The high sampling rate provides an essentially continuous signal, which is needed for intermittency and spectral postprocessing. The long sampling time results in low uncertainty in both statistical and spectral quantities. Data were acquired at 60 wall normal locations in each profile, extending from the wall to the free stream, with most points concentrated in the near-wall region. The closest point was within $0.1\ \text{mm}$ of the wall, which corresponds to $y/L_s = 0.0004$ and between 0.01 and 0.2 boundary layer thicknesses. Flow direction in a separation bubble cannot be determined with a single-sensor hot-wire, but velocity magnitude can be measured and was found to be essentially zero within the bubbles of the present cases. Determining the direction was not, therefore, considered essential. Uncertainties in the mean velocity are 3–5% except in the very near wall region where near-wall corrections (Wills [19]) were applied to the mean velocity. Uncertainties in the momentum and displacement thicknesses computed from the mean profiles are 10%. Uncertainty in the shape factor, H , is 8%.

The uncertainty in the fluctuating streamwise velocity is below 10%, except in the very-near-wall region, where spatial averaging effects, due to the finite length of the hot-wire sensor, become important in some cases. For the present cases, as explained by Volino [7] based on the work of Ligrani and Bradshaw [20,21], spatial averaging should not be significant for the $Re=25,000$ and $50,000$ cases, even near the wall. For the higher Re cases, spatial averaging should not be significant for $y > 1\ \text{mm}$ ($y/L_s > 0.004$), but may cause errors as high as 30% closer to the wall. It is not certain that the errors are this large, however. The estimates are based on the results of Ligrani and Bradshaw [20,21], who considered a boundary layer with $Re_\theta=2600$. The momentum thickness Reynolds numbers in the present cases are all below 1300. This may indicate less developed turbulence in the present study, which could imply fewer small-scale eddies and lower averaging errors.

The intermittency, γ , is the fraction of time the flow is turbulent within the transition region. It was determined at each measurement location based on the instantaneous streamwise velocity signal, using the technique described by Volino et al. [17]. The uncertainty in γ is 10%. As explained by Volino et al. [17], turbulent flow is defined here to include a range of large- and small-scale eddies, turbulence production, and dissipation. A boundary layer may be characterized by significant u' fluctuations but still be nonturbulent if these fluctuations are induced by an external source that does not also cause near-wall turbulence production. Such is often the case under high-FSTI conditions. Free-stream eddies buffet the boundary layer, inducing nonturbulent boundary layer fluctuations but very little momentum transport. Transition to turbulence is characterized not so much by large increases in u' levels, which may remain essentially constant, but by the appearance of higher frequencies. The higher frequencies signal the generation of turbulence in the near-wall region and are used to distinguish between turbulent and nonturbulent flow. Further discussion is available in Ref. [17].

Results

Velocity and Pressure Profiles. Pressure coefficients for the low-FSTI, $Re=25,000$ cases are shown in Fig. 3. Also shown is the inviscid solution for the present geometry. In all cases there is

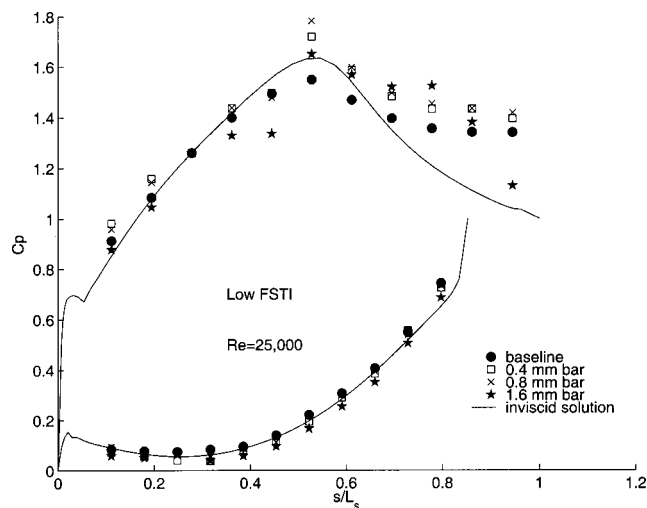


Fig. 3 C_p profiles, low FSTI, $Re=25,000$ cases

good agreement with the inviscid solution on the pressure side. On the suction side, the baseline case shows good agreement with the inviscid solution in the favorable pressure gradient region, but a large separation bubble in the adverse pressure gradient region. Separation is indicated by the nearly constant C_p values, which are well above the inviscid solution. The C_p values remain high to the trailing edge, showing no sign of reattachment. With the 0.4-mm-thick bar, there is an increase in C_p over the baseline value at $s/L_s = 0.53$. The pressure tap at this location is immediately downstream of the bar, and the flow over the tap is probably affected by the close proximity of the bar. The C_p values in this case remain high to the trailing edge, indicating that the boundary layer does not reattach. The same is true for the 0.8-mm bar case. With the 1.6-mm bar, C_p drops below the baseline values near the end of the favorable pressure gradient region. The larger bar is apparently enough of an obstruction to slow the near-wall flow upstream of the bar. Downstream of the 1.6-mm bar, C_p values are high, as in the other cases, but at the most downstream pressure tap C_p drops to near the inviscid solution value, indicating boundary layer reattachment.

The velocity profiles for the low-FSTI, $Re=25,000$ cases are shown in Fig. 4. The top row of the figure shows dimensionless mean velocity profiles at stations 7–11. The baseline case shows a boundary layer near separation at station 7, a small separation bubble at station 8, and an increasingly larger bubble at stations 9–11. The mean profiles of the 0.4-mm and 0.8-mm bar cases are

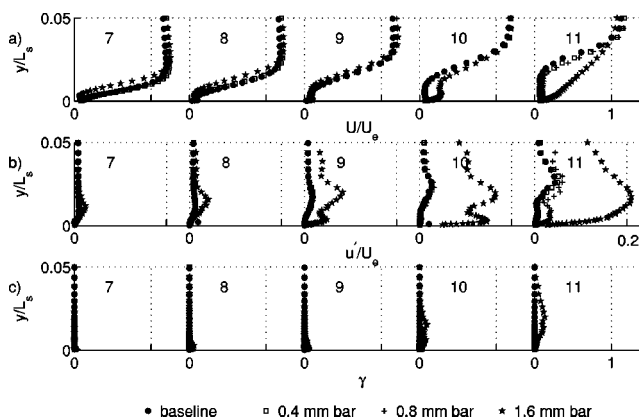


Fig. 4 Station 7–11 profiles, low FSTI, $Re=25,000$ cases: (a) mean velocity, (b) u' , (c) intermittency

virtually indistinguishable from the baseline case. The 1.6-mm bar case shows a clear separation bubble at station 7, suggesting that the boundary layer has separated from the trailing edge of the bar. This bubble continues to grow, and at station 8 the separation bubble is larger with the 1.6-mm bar than in the other cases. At station 9 all cases appear similar. This agreement is really a crossing, as the shear layer in the 1.6-mm bar case is on the verge of reattaching, while the separation bubble is growing in the other cases. At station 10, the near-wall velocity in the 1.6-mm bar case has begun to rise, indicating incipient reattachment. By station 11, the boundary layer has clearly reattached in the 1.6-mm bar case, although the mean profile has not recovered to a fully developed turbulent shape. Dimensionless u' profiles are shown in the second row of Fig. 4. As with the mean profiles, the baseline case and the 0.4-mm and 0.8-mm bar cases are indistinguishable through station 10. All show a small u' peak growing in the shear layer over the separation bubble. As explained by Volino [7,18], this peak is not indicative of transition. It is caused primarily by low-frequency fluctuations that are amplified when they act across the region of high mean velocity gradient in the shear layer. At station 11, there is a slight increase in u' in the 0.8-mm bar case over the baseline case, and the high values extend into the near-wall region. These near-wall fluctuations suggest the beginning of transition and reattachment, but they are not large enough in this case to significantly affect the mean profile. The 1.6-mm bar case shows a larger u' peak than the other cases at stations 7 and 8. The peak is in the shear layer and is similar to the peaks at stations 9 and 10 of the other cases. It does not indicate transition. The peak becomes larger at station 9, and extends into the near-wall region, which is a sign of incipient transition. By station 10 u' is much larger with a clear double peak. This rise in u' corresponds to the beginning of reattachment observed in the mean profile. The third row of Fig. 4 shows the local intermittency. It is zero in all cases through station 9, but begins to rise at stations 10 and 11 of the 1.6-mm bar case. The intermittency peak is in the shear layer, indicating that this is where transition begins. Intermittency only reaches about 13% at station 11. This is consistent with the mean velocity profile, which shows the boundary layer is reattached but not yet a fully developed turbulent profile. As the turbulence is intermittent, it is likely that the boundary layer is only intermittently reattached. The high u' peak at station 11 is also consistent with a transitional boundary layer. As a boundary layer becomes fully turbulent, the dimensionless u' peak will decrease in magnitude to about 0.1, and move close to the wall.

The behavior in the 1.6-mm bar case is interesting. The bar was not large enough to immediately trip the boundary layer to turbulent, but it did move the separation point upstream. This caused the transition to move upstream, and led to at least a partial reattachment by the trailing edge, which did not occur in the other cases. The 0.8-mm bar trip case is also very interesting. The bar in this case was so small that it had no immediate measurable effect on the mean or u' profiles. Well downstream at station 11, however, the effect of this bar became visible in the u' profile. Apparently this bar introduced a very small disturbance in the flow, which was too small to detect at first, but grew as it moved downstream.

The velocity profiles of Fig. 4 and the pressure profiles of Fig. 3 are in good agreement. Both show transition and reattachment at the same locations, and the measured static pressures agree with the local free-stream velocities of Fig. 4. The agreement between the pressure and velocity results was apparent in all cases. For brevity, the pressure profiles are not presented in the cases which follow.

Figure 5 shows the velocity profiles for the high-FSTI, $Re = 25,000$ cases. The format is that same as in Fig. 4. As in the low-FSTI case, the baseline, 0.4-mm trip and 0.8-mm trip cases are nearly indistinguishable at the upstream stations. By station 11, some differences are apparent in the mean profiles for these cases. The separation bubble is less distinct in the cases with the

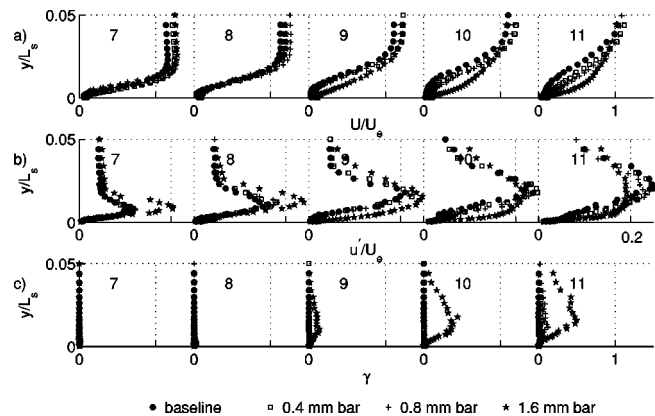


Fig. 5 Station 7—profiles, high FSTI, $Re=25,000$ cases: (a) mean velocity, (b) u' , (c) intermittency

bars, but the boundary layer still does not appear fully reattached. Intermittency rises slightly above zero at station 11 of the 0.8-mm bar case, while remaining essentially at zero with the smaller bar and in the baseline case. The u' profiles show a large peak in the shear layer, which grows in the streamwise direction. As shown in Volino [7], this peak is caused by the action of the high FSTI on the shear layer, and does not indicate significant momentum transport. As in the low-FSTI cases of Fig. 4, the 1.6-mm bar case shows significant differences from the other cases in Fig. 5. The u' peak is significantly higher in this case at stations 7 and 8. At station 9, u' values are higher in the near-wall region, the intermittency rises above zero, and the mean profile appears to be reattached. At stations 10 and 11 the intermittency continues to increase. The mean profile adjusts toward a more turbulent shape between stations 9 and 11. The u' peak decreases somewhat by station 11, but still shows the relatively high values of a transitional boundary layer, rather than the somewhat lower values of a fully turbulent boundary layer. As in the low-FSTI, $Re=25,000$ case, the 1.6-mm bar is not large enough to immediately trip the boundary layer to turbulent, but it causes transition to move upstream and leads to a reattachment that did not occur in the baseline or smaller bar cases.

The velocity profiles of the low-FSTI, $Re=50,000$ case are shown in Fig. 6. The effects of the bars are clear. At station 7, the 1.6-mm bar has caused a relatively large separation bubble compared to the other cases and a small u' peak in the shear layer over this bubble. The smaller bar cases are indistinguishable from the baseline case, with mean profiles only on the verge of separation and u' near zero. By station 8, the 1.6-mm bar case has

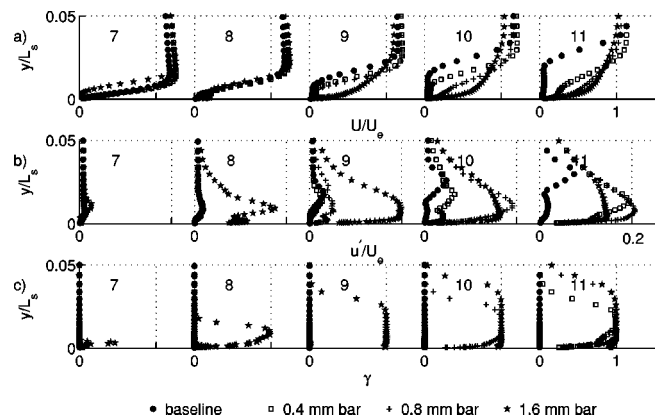


Fig. 6 Station 7–11 profiles, low FSTI, $Re=50,000$ cases: (a) mean velocity, (b) u' , (c) intermittency

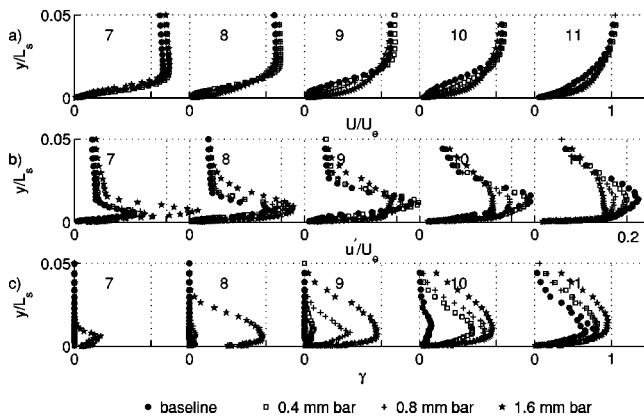


Fig. 7 Station 7–11 profiles, high FSTI, $Re=50,000$ cases: (a) mean velocity, (b) u' , (c) intermittency

undergone a sudden transition, with $\gamma=1$, high u' levels in both the shear layer and near-wall regions, and the beginning of reattachment as indicated by nonzero mean velocity near the wall. The other cases are indistinguishable, exhibiting a small separation bubble and showing no sign of transition or reattachment. At station 9, the boundary layer is clearly reattached in the 1.6-mm bar case, and u' values are beginning to rise in the 0.8-mm bar case. At station 10 the intermittency indicates fully turbulent flow and the boundary layer has reattached in the 0.8-mm bar case. The 0.4-mm bar case is still separated with $\gamma=0$, but u' has begun to rise near the wall. By station 11 the 0.4-mm bar case has become turbulent and the boundary layer has started to reattach. The baseline case remains nonturbulent with a large separation bubble at station 11. As observed in the $Re=25,000$ cases, the 1.6-mm bar is not large enough to immediately trip the boundary layer to turbulent, but it does move separation upstream, which causes transition and reattachment to move significantly upstream. The smaller bars appear to have no immediate effect on the boundary layer, but they must introduce small disturbances that grow in the streamwise direction and have a significant effect in moving the transition and reattachment upstream. The 0.8-mm bar must introduce a larger disturbance than the 0.4-mm bar, since transition and reattachment occur one station farther upstream with the 0.8-mm bar.

Figure 7 shows the high-FSTI, $Re=50,000$ cases. With the larger bars, transition and reattachment move upstream. With the 1.6-mm bar, the intermittency is already nonzero by station 7, and the boundary layer is fully turbulent and attached by station 8. With the 0.8-mm bar, γ rises above zero at station 8 and is near fully turbulent by station 10. The mean profile appears to indicate reattachment by station 9. The intermittency rises above zero in the 0.4-mm bar case at station 9, and continues to rise at stations 10 and 11. The mean profile shows reattachment at station 10. In the baseline case, the intermittency begins to rise at station 10, and the boundary layer is reattached at station 11. At station 11 the mean profiles are indistinguishable in the cases with bars, and fuller than in the baseline case. In all cases, the transition begins upstream of the location in the corresponding low-FSTI case of Fig. 6, but the transition length is longer. Volino and Hultgren [22] also observed that transition begins farther upstream with high-FSTI, but is more abrupt in low-FSTI cases.

Figure 8 shows the low-FSTI, $Re=100,000$ cases. The 1.6-mm bar immediately trips the boundary layer to turbulent and eliminates the separation bubble. The 0.8-mm bar causes a small u' peak above the baseline values at station 7. The intermittency jumps from 0 to 1 between stations 7 and 8, and the separation bubble is effectively eliminated. As in the lower- Re cases, the 0.4-mm bar has no visible effect at station 7, and the mean and u' profiles are indistinguishable from the baseline case. The bound-

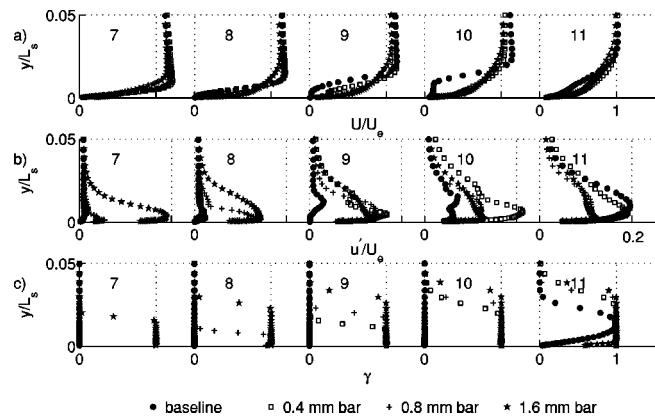


Fig. 8 Station 7–11 profiles, low FSTI, $Re=100,000$ cases: (a) mean velocity, (b) u' , (c) intermittency

ary layer separates, but by station 9 the shear layer has become fully turbulent and begun to reattach. In the baseline case, u' does not begin to show elevated near wall values until station 10, and transition and reattachment occur at station 11. The mean profiles at station 11 show the fullest profile and thinnest boundary layer in the 0.4-mm bar case. The larger bars result in thicker boundary layers. The mean profile in the baseline case has not yet recovered to a fully turbulent shape. As will be discussed below, the thinner attached boundary layer in the 0.4-mm bar case suggests that this case will have lower losses than the other cases.

The high-FSTI, $Re=100,000$ cases are shown in Fig. 9. As in the low-FSTI case, the 1.6-mm bar trips the boundary layer to turbulent and eliminates separation at this Re . The intermittency is nonzero at station 7 of the 0.8-mm bar case, and it continues to rise through station 10, indicating an extended transition zone. Because the transition begins so far upstream, the separation bubble is eliminated and transition occurs in an attached boundary layer. With the 0.4-mm bar, the intermittency indicates that the transition does not begin until station 8, so a small separation bubble forms, as in the baseline case. The boundary layer is reattached by station 9, however, and the transition is nearly complete by station 10. In the baseline case, the transition begins at station 9, and the boundary layer is reattached at station 10. Examining the mean profiles, the 1.6-mm bar causes an immediate thickening of the boundary layer, and the separation bubble in the baseline case also causes a thicker boundary layer. By station 11, the mean profiles for these two cases agree closely. The boundary layers are thinner in the cases with the smaller bars.

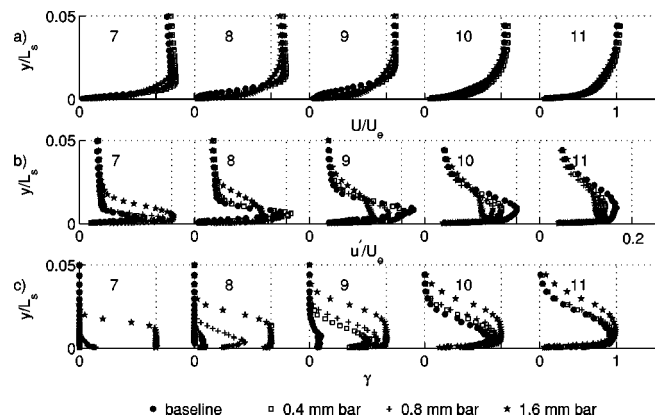


Fig. 9 Station 7–11 profiles, high FSTI, $Re=100,000$ cases: (a) mean velocity, (b) u' , (c) intermittency

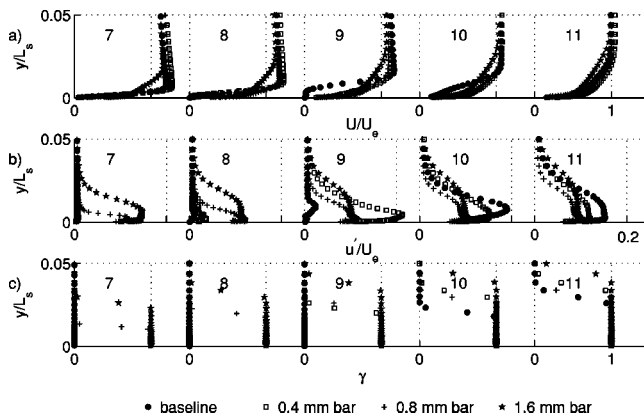


Fig. 10 Station 7–11 profiles, low FSTI, $Re=200,000$ cases: (a) mean velocity, (b) u' , (c) intermittency

In the low-FSTI, $Re=200,000$ cases of Fig. 10, the intermittency profiles show that the 0.8-mm and 1.6-mm bars immediately trip the boundary layer to turbulent and eliminate the separation bubble. The 1.6-mm bar, which is the same thickness as the boundary layer at station 7 of the baseline case, results in a substantially thicker boundary layer than in all of the other cases. The 0.4-mm bar shows a small separation bubble at station 8, but is fully turbulent and reattached by station 9. The baseline case exhibits a clear separation bubble at station 9, and is fully turbulent and reattached by station 10. The mean profiles at station 11 show that the growth of the bubble in the baseline case results in a thicker boundary layer than in the 0.8- and 0.4-mm bar cases.

Figure 11 shows the high-FSTI, $Re=200,000$ cases. As in the low-FSTI cases of Fig. 10, the 0.8- and 1.6-mm bars trip the boundary layer to turbulent. The transition has already started, as indicated by the nonzero intermittency, in the 0.4-mm bar case at station 7. In all of these cases, there is no separation. In the baseline case, γ does not rise above zero until station 9, and there may be a small separation bubble at station 8. At station 11, the mean, u' , and intermittency profiles of the baseline, 0.4-mm, and 0.8-mm bar cases are all in good agreement, while the 1.6-mm bar case exhibits a noticeably thicker boundary layer.

The low FSTI, $Re=300,000$ cases are shown in Fig. 12. As in the $Re=200,000$ cases, the 0.8-mm and 1.6-mm bars trip the boundary layer to turbulent. The 0.4-mm bar appears to have no effect at station 7, where the mean and u' profiles agree with the baseline case and the intermittency is zero. By station 8, however, the boundary layer in the 0.4-mm bar case has become fully turbulent, while in the baseline case it is still laminar and has sepa-

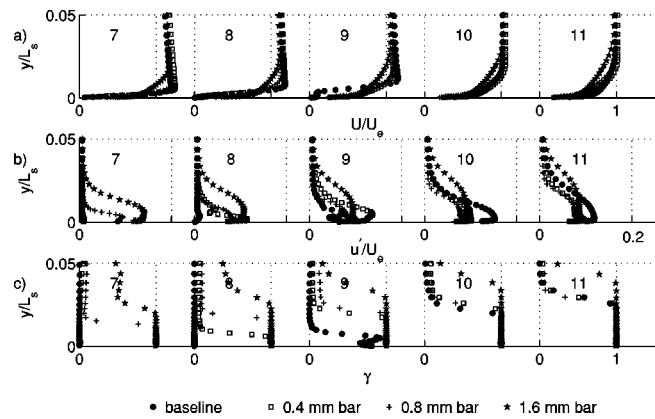


Fig. 12 Station 7–11 profiles, low FSTI, $Re=300,000$ cases: (a) mean velocity, (b) u' , (c) intermittency

rated. By station 9 the shear layer in the baseline case is transitional, and it is fully turbulent and reattached by Station 10. At Station 11 the mean profiles for the four cases are all different, with the 0.4-mm bar and baseline cases having the thinnest boundary layers.

Figure 13 shows the high-FSTI, $Re=300,000$ cases. As in the low-FSTI cases, the 0.8-mm and 1.6-mm bars trip the boundary layer to fully turbulent, and the 0.4-mm bar causes the transition to start by station 7 and finish by station 8. Transition has started at station 8 of the baseline case and is complete near station 10. In all of these cases the transition begins far enough upstream to prevent separation. The mean profiles at all stations show that the boundary layer is thinnest in the baseline case and that the thickness increases with the bar size. With the 0.4-mm and 0.8-mm bars the boundary layer is only slightly thicker than in the baseline case, but it is substantially thicker in the 1.6-mm bar case.

Some consistent trends run through the data from all cases. If a bar is large enough, it will immediately trip the boundary layer to fully turbulent and prevent separation. As Reynolds number increases, the boundary layer thickness decreases as does the thickness of the bar required for tripping. If a bar is small enough, it initially appears to have no effect on the boundary layer. The boundary layer appears to proceed over the bar with no measurable change in the mean velocity or u' from the corresponding baseline case. The bars must, however, introduce some small disturbance into the boundary layer. The boundary layer is unstable against small disturbances in the adverse pressure gradient region, so the small disturbances grow and eventually cause transition. Larger bars must impart larger (albeit sometimes still undetect-

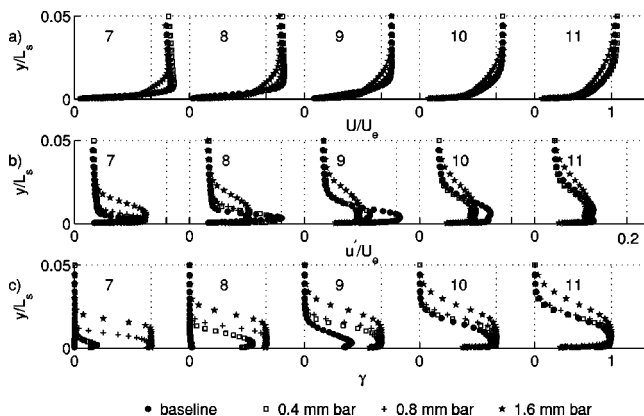


Fig. 11 Station 7–11 profiles, high FSTI, $Re=200,000$ cases: (a) mean velocity, (b) u' , (c) intermittency

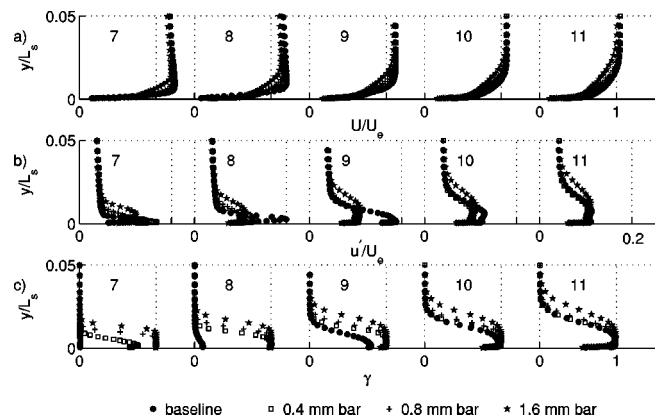


Fig. 13 Station 7–11 profiles, high FSTI, $Re=300,000$ cases: (a) mean velocity, (b) u' , (c) intermittency

able) perturbations than the smaller bars, resulting in transition locations that move upstream as bar size is increased. The optimal bar size depends on the Reynolds number and is discussed further below.

The present results shed some light on the transition mechanism under both high- and low-FSTI conditions. Volino [18] examined spectra of the fluctuating velocity in the boundary layers and shear layers of the baseline cases. He observed sharp peaks in the spectra of the low-FSTI cases at frequencies that matched the most unstable frequencies for Tollmien-Schlichting (TS) waves in the boundary layer just upstream of separation. He therefore concluded that the transition in the shear layer might be through a TS mechanism in these cases. In the high-FSTI cases, Volino [18] observed broadband peaks in the spectra and the relatively long transition regions noted above. Volino and Hultgren [22] made similar observations, and concluded that the high-FSTI separated flow transition was through a bypass mode, very similar to the high-FSTI transition in an attached boundary layer. Volino [18], however, noted that the broadband peaks in the high-FSTI case spectra were centered at the same frequencies as in the low-FSTI cases, suggesting a similar transition mechanism under high- and low-FSTI conditions. He concluded that disturbances that began to grow in the boundary layer prior to separation were causing a TS-type transition in the shear layer over the separation bubble in both the high- and low-FSTI cases. High-FSTI has a strong effect in moving the transition upstream, but the bars in the present cases had an equally strong or stronger effect in both the high- and low-FSTI cases. This confirms that the free-stream turbulence is not solely responsible for bypass transition in the high-FSTI cases.

The magnitude of the disturbances induced by the bars is too small to be quantified based on the mean or u' results presented above. Perhaps more can be learned from boundary layer spectra. Analyses of spectra based on u' fluctuations for the present cases show some interesting but inconclusive results. Volino [18] found that u' spectra are often characterized by low-frequency fluctuations that are induced by the free stream and have no direct effect on transition. In the early stages of transition, these low-frequency fluctuations can hide the very-low-amplitude fluctuations important for transition. Volino [18] found that spectra of the turbulent shear stress are less affected by the low-frequency unsteadiness and can provide a better means for detecting the early stages of transition. Acquisition and analysis of turbulent shear stress data for the cases of the present study may prove useful for explaining and quantifying the transition mechanism.

Shape Factor and Momentum Thickness. The shape factor and momentum thickness are useful parameters for evaluating the state of the boundary layer with respect to separation, transition, and losses. They provide a means for summarizing the information presented in the velocity profiles of Figs. 4–13. In the present cases, the boundary layer has a shape factor H of about 2.4 at the end of the favorable pressure gradient region. This is the expected value for this laminar, accelerated boundary layer. If the boundary layer separates, the displacement thickness grows rapidly, while the momentum thickness remains nearly constant. The result is a very high shape factor. If the boundary layer reattaches, the displacement thickness drops, and the momentum thickness begins to grow. The boundary layer eventually recovers to a fully turbulent shape, with a shape factor of about 1.6 in the present cases.

Stage losses in a multiblade turbine cascade can be determined through measurement of the momentum deficit in the wake downstream of the blade row. With the single-passage facility of the present study, wake measurements are not meaningful, since there is flow on only one side of the airfoils on each side of the passage. If a boundary layer separates and does not fully reattach, or reattaches near the trailing edge, momentum thickness will be relatively low at the trailing edge, and high losses will be generated in the wake downstream of the passage. While the losses in such a case cannot be quantified in the present study, it is safe to assume that they would be unacceptably high, and that there would be an

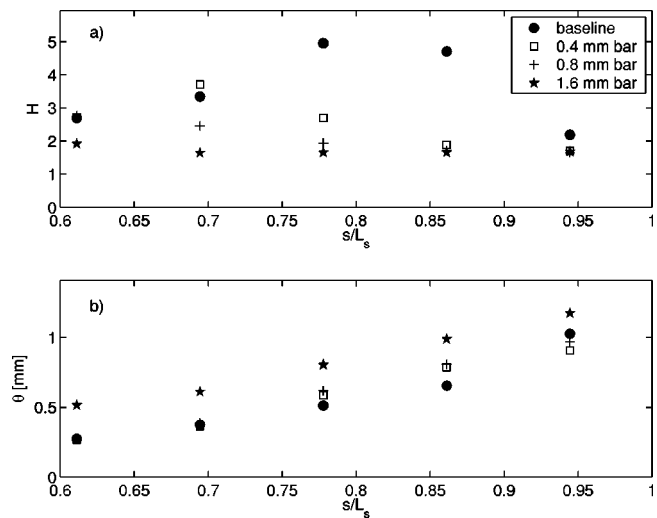


Fig. 14 Shape factor and momentum thickness versus streamwise location, low FSTI, $Re=100,000$: (a) H , (b) θ

unacceptable loss of lift from the airfoils. For those cases in which the boundary layer reattaches and recovers to a fully developed turbulent shape, the suction side profile loss is likely the dominant loss mechanism in the passage (Howell et al. [9]). As explained by Howell et al. [9], for a given shape factor and passage exit angle, the momentum thickness of the suction side boundary layer at the trailing edge is proportional to the suction side profile loss.

Figure 14 provides an example of the development of the shape factor and momentum thickness, using the low-FSTI, $Re=100,000$ cases. In the baseline case, H increases from 2.4 to a high value of about 5 as the boundary layer separates. Reattachment occurs near the trailing edge, and H drops to about 2.2, which is still above the turbulent value of 1.6, indicating that recovery from the separation is not complete. In the 0.4-mm bar case, the boundary layer separates and H reaches a value of 3.7. The boundary layer then reattaches, and H gradually drops to a fully turbulent value by the trailing edge. With the 0.8-mm bar, transition occurs far enough upstream to prevent separation, and H drops continuously from a laminar value to a turbulent value as transition occurs. In the 1.6-mm bar case the boundary layer is tripped to turbulence, and H quickly reaches its turbulent value. The 1.6-mm bar causes an immediate thickening of the boundary layer, and the momentum thickness remains higher than in the other cases at all streamwise locations. The 0.4- and 0.8-mm bars appear to have no immediate effect on θ . When transition and reattachment occur, however, θ begins to rise. When reattachment occurs in the baseline case, it causes θ to increase to a higher value than in the 0.4- and 0.8-mm bar cases. Near the trailing edge θ is lowest in the 0.4-mm bar case. This would presumably be the case with the lowest profile losses. The larger bars force the transition to occur farther upstream than necessary, resulting in a longer turbulent region and higher losses. In the baseline case the separation bubble becomes relatively thick, resulting in a thick boundary layer after reattachment. The 0.4-mm bar case provides a good example of the controlled diffusion described by Hourmouziadis [1]. With the 0.4-mm bar, the separation bubble is relatively thin, and the turbulent region is relatively short, resulting in lower losses.

Figure 15 shows the shape factor and momentum thickness at station 11 ($s/L_s=0.94$), near the trailing edge, for all the low-FSTI cases. In the $Re=25,000$ cases, the shape factor indicates that the boundary layer only reattaches in the 1.6-mm bar case. The shape factor in this case is still above the expected turbulent value, indicating that recovery from the separation is not complete. Comparison of momentum thicknesses is not meaningful at

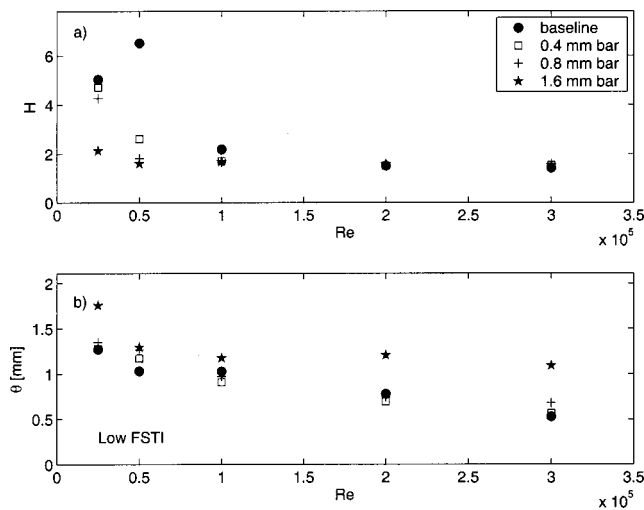


Fig. 15 Station 11 shape factor and momentum thickness versus Re, low-FSTI cases: (a) H , (b) θ

this Re. For the $Re=50,000$ cases, the 0.8- and 1.6-mm bars cause reattachment, while recovery from the separation is only partially complete in the 0.4-mm bar case and the shear layer remains separated in the baseline case. The 0.8- and 1.6-mm bar cases are, therefore, preferable at this Re, and both have about the same momentum thickness at station 11. At $Re=100,000$, already described in Fig. 14, the 0.4-mm bar produces the lowest losses. The 0.4-mm bar case is also best at $Re=200,000$, with slightly lower losses than with the 0.8-mm bar or in the baseline case. At $Re=300,000$, the transition occurs sufficiently far upstream in the baseline case to keep the separation bubble small and produce lower losses than in any of the cases with bars.

The station 11 shape factors and momentum thicknesses for the high-FSTI cases are shown in Fig. 16. As in the low-FSTI cases, only the 1.6-mm bar is large enough to force reattachment at $Re=25,000$, and it does not even quite result in full recovery to a turbulent profile. At $Re=50,000$, the shape factor shows that all of the bars cause reattachment, while the boundary layer in the baseline case has reattached but not fully recovered from the separation. The 0.4- and 0.8-mm bar cases have lower momentum thickness than the 1.6-mm bar case. At the higher Re, reattachment is complete in all cases, and the 1.6-mm bar cases have significantly

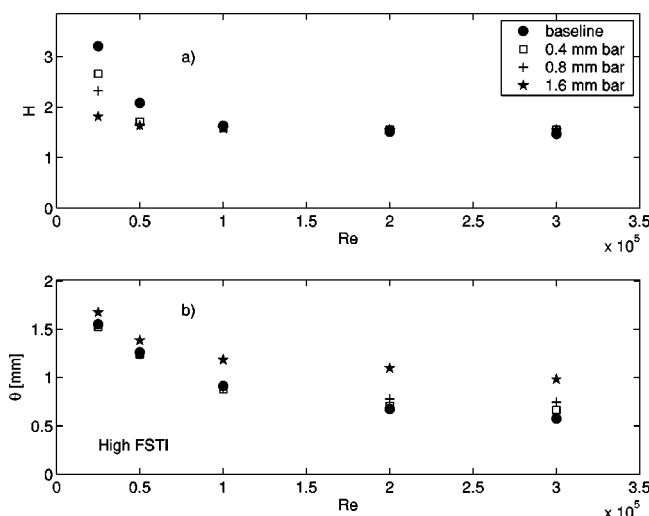


Fig. 16 Station 11 shape factor and momentum thickness versus Re, high-FSTI cases: (a) H , (b) θ

higher losses than the other cases. At $Re=100,000$, the 0.4- and 0.8-mm bar cases and the baseline case all have about the same losses. As Re increases to 200,000 and 300,000, the baseline case emerges as the case with lowest losses, in agreement with the low-FSTI cases of Fig. 15.

The optimal bar height clearly varies with the Reynolds number. As Re increases, the boundary layer becomes thinner and more prone to transition, so a smaller bar is needed. At $Re=25,000$, the 1.6-mm bar is needed, and a larger bar would be desirable to force a more complete reattachment. At $Re=50,000$, the 0.8-mm bar is best, since it is large enough to cause reattachment at low FSTI, but produces lower losses than the thicker bar at high FSTI. At $Re=100,000$ and 200,000, the 0.4-mm bar is best, since it is large enough to force complete reattachment at low FSTI, and results in equal or slightly lower losses than the baseline or 0.8-mm bar cases. At $Re=300,000$, the baseline case is best, although the losses are only slightly lower than those of the 0.4-mm bar case. If a bar is used for passive flow control, a single bar thickness must be chosen for optimal overall performance. The best size will depend on the operating range of the engine. If the operating range is large, a compromise between improved performance at cruise and higher losses at takeoff may be needed.

Correlation of Results. The size of a bar necessary to trip a boundary layer to turbulence can be predicted using the following correlation from Gibbings [23].

$$Re_d = U_d d / \nu > 600, \quad (1)$$

where d is the bar thickness and U_d is the velocity in the untripped boundary layer at $y=d$ at the streamwise location of the bar. Equation (1) predicts that bar thicknesses of 4.7 mm, 2.3 mm, 1.3 mm, 0.68 mm, and 0.50 mm would be needed to immediately trip the boundary layer to turbulent in the $Re=25,000$ through 300,000 cases, respectively. In agreement with this prediction, the results above show that the boundary layer was only tripped in the $Re=200,000$ and 300,000 cases with the 0.8-mm and 1.6-mm bars, and in the $Re=100,000$ cases with the 1.6-mm bar. Since an optimal bar does not immediately trip the boundary layer; it will be thinner than indicated by Eq. (1).

The most effective bars in the present cases appear to be those that cause reattachment to begin between stations 8 and 9, at s/L_s of about 0.74. When reattachment begins by this location, there is sufficient distance downstream for the reattachment and recovery from the separation to be completed before the trailing edge. The beginning of reattachment and the start of transition are related and occur at approximately the same location. There are a few correlations in the literature for prediction of the distance from separation to transition onset. In general they are not very robust, but some give reasonable estimates. Mayle [2] provides the following correlations:

$$Re_{st} = 300 Re_{\theta_s}^{0.7} \quad (\text{short bubble}), \quad (2)$$

$$Re_{st} = 1000 Re_{\theta_s}^{0.7} \quad (\text{long bubble}). \quad (3)$$

Equations (2) and (3) apply to short and long separation bubbles, respectively. Volino [7] found that the present baseline case results lie between the predictions of Eqs. (2) and (3) tending toward the long bubble correlation at low FSTI and about midway between the two correlations at high FSTI. Although they differ by a factor of 3, Eqs. (2) and (3) provide at least a rough estimate of the reattachment location.

The following correlation provides an estimate of the effect of bar height on reattachment location. The equation is based on a curve fit of the present data:

$$(s_t - s_p)_m / (s_t - s_p)_b = [1 + 0.23(d/\theta_p)^{1.56}]^{-1}, \quad (4)$$

where $(s_t - s_p)_b$ is the distance from the suction side velocity maximum ($s/L_s = 0.53$) to the location of the beginning of reattachment in the baseline case, and $(s_t - s_p)_m$ is this distance with a bar in place. The present data along with Eq. (4) are shown in

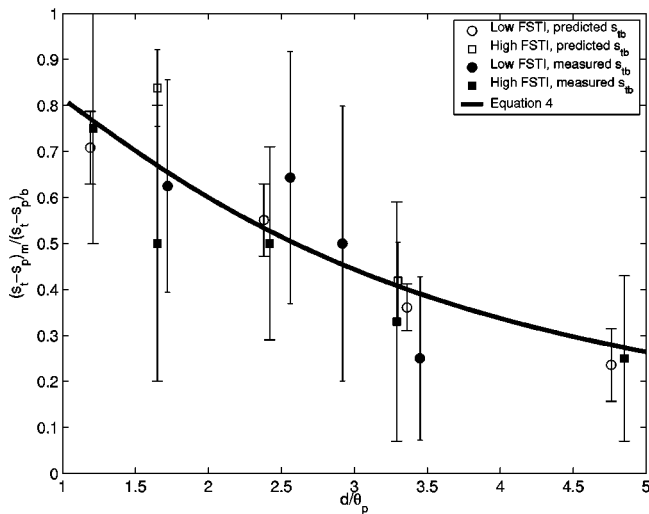


Fig. 17 Correlation of transition and reattachment start location to bar height; bars indicate range of possible values resulting from finite station spacing

Fig. 17. The finite spacing of the streamwise measurement stations results in some uncertainty in the transition start location, as indicated by the error bars in Fig. 17. Volino [7] showed that the boundary layer behavior upstream of the separation is predictable and laminar. To predict reattachment in a case with a bar, the laminar solution could be used to predict the separation location and the momentum thickness before separation. A correlation such as Eqs. (2) or (3) could then be used to estimate the distance to transition and reattachment in the baseline flow. This would give s_{ib} . Equation (4) could then be used to predict s_{tm} for a given bar thickness. Alternatively, the desired s_{tm} could be specified and used with Eq. (4) to predict the optimal bar thickness. Setting $s_{tm} = 169 \text{ mm}$ ($s_{tm}/L_s = 0.74$) and using the measured (when available) or predicted values for s_{ib} and θ_p for the baseline cases, optimal bar heights have been predicted for the present cases and are presented in Table 3.

Discussion. The above correlations are based only on the present data set, so it is doubtful that they are universally applicable. Still, they provide a start in the assessment of passive flow control devices. With more experiments with different airfoils, it may be possible to refine correlations such as Eq. (4), to make them more generally applicable.

Alternative passive devices such as vortex generators or dimples should also be considered. There is no guarantee, however, that these devices will provide improvement over the present bars. Dimples have been used in some applications such as internal blade cooling, to provide enhanced heat transfer with lower pressure drop than boundary layer trips. Dimples enhance heat transfer by promoting turbulence and mixing, which would also tend to promote boundary layer attachment. In the present appli-

cation, however, we do not seek to enhance turbulence or heat transfer, or even to fully eliminate the separation bubble. Since the smaller bars in the present experiments did not increase losses or boundary layer thickness, or have any other immediate measurable effect on the boundary layer, it is not clear that any other device will be superior.

While the present bars have proven effective, it is clear from Table 3 and Figs. 15 and 16 that the optimal bar height varies with Re and FSTI. If applied passively, a single bar height would be selected for the entire operating range of the engine. If the operating range is large, a compromise will be necessary between improved performance at low Re and higher losses at high Re . Passive flow control has the distinct advantage of being relatively simple to implement in practice, but active flow control may provide a means for optimizing performance over a wider range of conditions. Unsteady active control also provides possibilities for further flexibility and improved performance not available with passive devices. Further consideration of active control is presented by Volino [24].

The present cases all involve steady inlet flow. In engine flows, the periodic wakes from upstream airfoils will make the flow unsteady. While steady flow experiments are necessary for building understanding of the flow and flow control devices, experiments should eventually be performed in flows with wakes.

Conclusions

1. Rectangular bars have been successfully employed as flow control devices on the suction side of a low-pressure turbine airfoil. Boundary layer reattachment was forced even in very-low-Reynolds-number cases.
2. Optimal bars are not large enough to immediately trip the boundary layer to turbulent or prevent separation, but rather induce very small disturbances that at first are essentially undetectable, but eventually promote transition in the shear layer at a downstream location.
3. Bars were effective under both high- and low-FSTI conditions, indicating that the high-FSTI transition is not simply a bypass transition induced by the free stream.
4. The optimal location for reattachment results in a relatively short turbulent region, but occurs sufficiently far upstream to prevent a large separation bubble and ensure complete recovery from the separation before the trailing edge. A bar height can be selected to induce reattachment at the desired location.
5. The optimal bar height varies with the Reynolds number and free-stream turbulence level. Bars that were large enough to induce reattachment at the lowest Re produced significantly higher losses at the higher Re . If a wide range of Reynolds numbers are encountered in practice, some compromise between improved performance at low Re and higher losses at high Re will be necessary in the choice of an overall best bar height.

Table 3 Baseline case boundary layer thickness at bar location ($s/L_s = 0.53$), and predicted bar heights for tripping (d_{trip}) and for incipient reattachment (d_{opt}) at $s/L_s = 0.74$ (all values in mm)

$Re \times 10^{-3}$	Low FSTI				High FSTI			
	$\delta_{99,5p}$	θ_p	d_{trip}	d_{opt}	$\delta_{99,5p}$	θ_p	d_{trip}	d_{opt}
25	3.8	0.48	4.7	2.4	3.9	0.48	4.7	1.5
50	2.7	0.34	2.3	1.2	2.8	0.33	2.3	0.6
100	1.9	0.23	1.3	0.4	2.2	0.24	1.3	0.2
200	1.3	0.16	0.7	0.2	1.6	0.16	0.7	0
300	1.2	0.14	0.5	0.1	1.4	0.14	0.5	0

Acknowledgments

This work was sponsored by the NASA Glenn Research Center. The grant monitor is Dr. David Ashpis. Additional matching support was provided through a U.S. Naval Academy Recognition Grant.

Nomenclature

- $C_p = 2(P_T - P)/\rho U_e^2$, pressure coefficient
 d = Bar height
 FSTI = Free-stream turbulence intensity
 $H = \delta^*/\theta$, shape factor
 $K = (\nu/U_\infty^2)(dU_\infty/ds)$, acceleration parameter
 L_s = Suction surface length
 P = Pressure
 P_T = Upstream stagnation pressure
 $Re = U_e L_s/\nu$, exit Reynolds number
 $Re_d = U_d d/\nu$, Reynolds number based on bar height
 $Re_{st} = U_\infty(s_t - s_s)/\nu$, separation to transition distance Reynolds number
 Re_θ = Momentum thickness Reynolds number
 s = Streamwise coordinate, distance from leading edge
 U = Mean streamwise velocity
 U_∞ = Local free-stream velocity
 U_d = Mean velocity at bar height in baseline boundary layer
 U_e = Nominal exit free-stream velocity, based on the inviscid solution
 u' = rms streamwise fluctuating velocity
 y = Cross-stream coordinate, distance from wall
 $\delta_{99.5}$ = 99.5% boundary layer thickness
 δ^* = Displacement thickness
 γ = Intermittency, fraction of time flow is turbulent
 ν = Kinematic viscosity
 ρ = Density
 θ = Momentum thickness

Subscripts

- b = Baseline flow
 m = Modified flow
 p = Suction surface pressure minimum, velocity maximum
 s = Separation location
 t = Transition start location

References

- [1] Hourmouziadis, J., 1989, "Aerodynamic Design of Low Pressure Turbines," AGARD Lecture Series 167.
- [2] Mayle, R. E., 1991, "The Role of Laminar-Turbulent Transition in Gas Turbine Engines," ASME J. Turbomach., **113**, pp. 509–537.
- [3] Sharma, O. P., Ni, R. H., and Tanrikut, S., 1994, "Unsteady Flow in Turbines," AGARD Lecture Series 195, Paper No. 5.
- [4] Hodson, H. P., 1991, "Aspects of Unsteady Blade-Surface Boundary Layers and Transition in Axial Turbomachines," *Boundary Layers in Turbomachines*, VKI Lecture Series 1991-06.
- [5] Wisler, D. C., 1998, "The Technical and Economic Relevance of Understanding Boundary Layer Transition in Gas Turbine Engines," in *Minnowbrook II, 1997 Workshop on Boundary Layer Transition in Turbomachines*, LaGraff, J. E., and Ashpis, D. E., eds., NASA/CP-1998-206958, NASA Glenn Research Center, Cleveland, OH, pp. 53–64.
- [6] Curtis, E. M., Hodson, H. P., Banieghbal, M. R., Denton, J. D., Howell, R. J., and Harvey, N. W., 1997, "Development of Blade Profiles for Low-Pressure Turbine Applications," ASME J. Turbomach., **119**, pp. 531–538.
- [7] Volino, R. J., 2002, "Separated Flow Transition Under Simulated Low-Pressure Turbine Airfoil Conditions: Part 1—Mean Flow and Turbulence Statistics," ASME J. Turbomach., **124**, pp. 645–655.
- [8] Van Treuren, K. W., Simon, T., von Koller, M., Byerley, A. R., Baughn, J. W., and Rivir, R., 2002, "Measurements in a Turbine Cascade Flow Under Ultra Low Reynolds Number Conditions," ASME J. Turbomach., **124**, pp. 100–106.
- [9] Howell, R. J., Ramesh, O. N., Hodson, H. P., Harvey, N. W., and Schulte, V., 2001, "High Lift and Aft-Loaded Profiles for Low-Pressure Turbines," ASME J. Turbomach., **123**, pp. 181–188.
- [10] Stadtmüller, P., Fottner, L., and Fiala, A., 2000, "Experimental and Numerical Investigation of Wake-Induced Transition on a Highly Loaded LP Turbine at Low Reynolds Numbers," ASME paper no. 2000-GT-0269.
- [11] Brunner, S., Fottner, L., and Schiffer, H.-P., 2000, "Comparison of Two Highly Loaded Low Pressure Turbine Cascades Under the Influence of Wake-Induced Transition," ASME paper no. 2000-GT-268.
- [12] Lake, J. P., King, P. I., and Rivir, R. B., 2000, "Low Reynolds Number Loss Reduction on Turbine Blades With Dimples and V-Grooves," AIAA paper no. 00-738.
- [13] Murawski, C. G., and Vafai, K., 1999, "Effect of Variable Axial Chord on a Low-Pressure Turbine Blade," J. Propul. Power, **15**, pp. 667–674.
- [14] Byerley, A. R., Störmer, O., Baughn, J. W., Simon, T. W., Van Treuren, K. W., and List, J., 2002, "Using Gurney Flaps to Control Laminar Separation on Linear Cascade Blades," ASME J. Turbomach., **125**, pp. 114–120.
- [15] Bons, J. P., Sondergaard, R., and Rivir, R. B., 2001, "Turbine Separation Control Using Pulsed Vortex Generator Jets," ASME J. Turbomach., **123**, pp. 198–206.
- [16] Bons, J. P., Sondergaard, R., and Rivir, R. B., 2002, "The Fluid Dynamics of LPT Blade Separation Control Using Pulsed Jets," ASME J. Turbomach., **124**, pp. 77–85.
- [17] Volino, R. J., Schultz, M. P., and Pratt, C. M., 2001, "Conditional Sampling in a Transitional Boundary Layer Under High Free-Stream Turbulence Conditions," ASME J. Fluids Eng., **125**, pp. 28–37.
- [18] Volino, R. J., 2002, "Separated Flow Transition Under Simulated Low-Pressure Turbine Airfoil Conditions: Part 2—Turbulence Spectra," ASME J. Turbomach., **124**, pp. 656–664.
- [19] Wills, J. A. B., 1962, "The Correction of Hot-Wire Readings for Proximity to a Solid Boundary," J. Fluid Mech., **12**, pp. 65–92.
- [20] Ligrani, P. M., and Bradshaw, P., 1987, "Spatial Resolution and Measurement of Turbulence in the Viscous Sublayer Using Subminiature Hot-Wire Probes," Exp. Fluids, **5**, pp. 407–417.
- [21] Ligrani, P. M., and Bradshaw, P., 1987, "Subminiature Hot-Wire Sensors: Development and Use," J. Phys. E, **20**, pp. 323–332.
- [22] Volino, R. J., and Hultgren, L. S., 2001, "Measurements in Separated and Transitional Boundary Layers Under Low-Pressure Turbine Airfoil Conditions," ASME J. Turbomach., **123**, pp. 189–197.
- [23] Gibbings, J. C., 1959, "On Boundary-Layer Transition Wires," Aeronautical Research Council, Current Papers 462.
- [24] Volino, R. J., 2003, "Separation Control on Low-Pressure Turbine Airfoils Using Synthetic Vortex Generator Jets," ASME J. Turbomach., **125**, pp. 765–777.

Separation Control on Low-Pressure Turbine Airfoils Using Synthetic Vortex Generator Jets

Ralph J. Volino

Department of Mechanical Engineering,
United States Naval Academy,
Annapolis, MD 21402
e-mail: volino@usna.edu

Oscillating vortex generator jets have been used to control boundary layer separation from the suction side of a low-pressure turbine airfoil. A low Reynolds number ($Re = 25,000$) case with low free-stream turbulence has been investigated with detailed measurements including profiles of mean and fluctuating velocity and turbulent shear stress. Ensemble averaged profiles are computed for times within the jet pulsing cycle, and integral parameters and local skin friction coefficients are computed from these profiles. The jets are injected into the mainflow at a compound angle through a spanwise row of holes in the suction surface. Preliminary tests showed that the jets were effective over a wide range of frequencies and amplitudes. Detailed tests were conducted with a maximum blowing ratio of 4.7 and a dimensionless oscillation frequency of 0.65. The outward pulse from the jets in each oscillation cycle causes a disturbance to move down the airfoil surface. The leading and trailing edge celerities for the disturbance match those expected for a turbulent spot. The disturbance is followed by a calmed region. Following the calmed region, the boundary layer does separate, but the separation bubble remains very thin. Results are compared to an uncontrolled baseline case in which the boundary layer separated and did not reattach, and a case controlled passively with a rectangular bar on the suction surface. The comparison indicates that losses will be substantially lower with the jets than in the baseline or passively controlled cases. [DOI: 10.1115/1.1626686]

Introduction

Modern low-pressure turbine (LPT) airfoils are subject to increasingly stronger pressure gradients as designers impose higher loading in an effort to improve efficiency and lower cost by reducing the number of airfoils in an engine. If the adverse pressure gradient on the suction side of these airfoils becomes strong enough, the boundary layer will separate. Separation bubbles, particularly those which fail to reattach, can result in a significant loss of lift and a subsequent degradation of engine efficiency (e.g., Hourmouziadis [1], Mayle [2], and Sharma et al. [3]). The problem is particularly relevant in aircraft engines. Airfoils optimized to produce maximum power under takeoff conditions may still experience boundary layer separation at cruise conditions, due to the thinner air and lower Reynolds numbers at altitude. A component efficiency drop of 2% may occur between takeoff and cruise conditions in large commercial transport engines, and the difference could be as large as 7% in smaller engines operating at higher altitudes.

Separation on LPT airfoils is complicated by boundary layer transition, which can prevent separation if it occurs far enough upstream, or induce boundary layer reattachment if it occurs in the shear layer over a separation bubble. At lower Reynolds numbers transition will tend to occur farther downstream, hence the problems associated with performance at altitude.

Separated flow transition has been studied extensively, and in recent years several studies have focused on transition in the LPT. Volino [4] provides a review of much of that work. Separation can be affected through naturally occurring phenomena such as high free-stream turbulence intensity (FSTI) or the unsteadiness caused by wakes generated upstream of an airfoil. Further discussion of

these effects is available in Volino [5]. While high FSTI and wakes help to mitigate separated flow problems, they clearly do not solve all problems, as evidenced by the known efficiency drop in modern engines at altitude. Howell et al. [6], for example, studied airfoils modified for higher lift, noting that their highly loaded airfoils might be close to a limit, and that even higher loading could cause unacceptable separation problems even in the presence of wakes. Looking beyond free-stream turbulence and wakes, other types of separation control could prove useful. Gad-el-Hak [7] provides a recent review. Techniques include boundary layer tripping, vortex generation, suction, and injection of fluid normal to the wall to either increase the boundary layer momentum or promote turbulence.

While the general literature is extensive, only a few studies have considered separation control under LPT conditions. Some have utilized passive techniques. Lake et al. [8] considered dimples and boundary layer trips. Van Treuren et al. [9] considered vortex generators. Volino [5] used rectangular bars to impose disturbances in a boundary layer and move transition upstream. Passive flow control is appealing for its simplicity and the relative ease with which it might be implemented in gas turbine environments. It has its limitations, however. Volino [5] found that passive devices can successfully control separation even at the lowest Reynolds number of interest, but that these devices caused substantial increases in losses at higher Re . This is an important limitation for aircraft engines, where the Re range between takeoff and cruise is large. An active device could be turned off at high Re . Static passive devices are also unable to take advantage of the unsteadiness caused by wake passing. An active device might be timed to turn on and off in response to wake passing events. Unsteady devices might also take advantage of the calmed region following a transient turbulent event.

The literature contains several examples of active separation control. Lee et al. [10] used blowing in supersonic engine inlets to prevent or control separation. Sturm et al. [11] reported on blow-

Contributed by the International Gas Turbine Institute and presented at the International Gas Turbine and Aeroengine Congress and Exhibition, Atlanta, GA, June 16–19, 2003. Manuscript received by the IGTI December 2002; final revision March 2003. Paper No. 2003-GT-38729. Review Chair: H. R. Simmons.

ing in a compressor cascade. Johnston and Nishi [12] used vortex-generator-jets (VGJ's) to control separation in turbulent boundary layers. This method utilizes blowing from "small, skewed, and pitched holes" to create streamwise vortices similar to those created by solid vortex generators. Any jet injected into a flow will tend to produce some turbulence, and the turbulent mixing will tend to bring some high momentum fluid into the near wall region and inhibit separation. Streamwise vortices bring additional high momentum fluid into the near wall region. The most effective VGJ's enter the boundary layer at a relatively shallow pitch angle (typically 30–45°) relative to the wall and a high skew angle (45–90°) relative to the main flow. Compton and Johnston [13] showed that the co-rotating vortices produced by VGJ's are stronger and more effective for separation control than the counter-rotating vortices which form downstream of a normal jet. McManus et al. [14] and Raghunathan et al. [15] used pulsed VGJ's. Sinha and Pal [16] used acoustic excitation to perturb an unsteady separating flow. Jacobson and Reynolds [17] used piezoelectrically driven cantilevers to influence the near wall turbulence structure on a flat plate. They noted that the devices could be used in separation control. Miao et al. [18] used an oscillating fence to promote reattachment downstream of a backward facing step. Sinha et al. [19] used a driven flexible wall transducer to detect pressure fluctuations and then produce near wall vortices upstream of separation. Whitehead et al. [20] used a film transducer to produce airfoil vibrations and reduce separation at high angles of attack. Oscillatory blowing has been used in several studies to control separation on airfoils. Amitay and Glezer [21] provide one recent example. Oscillatory jets are often referred to as "synthetic jets" since they have no net mass flow. They are typically directed normal to a surface, meaning that they probably do not produce such strong streamwise vortices as VGJ's.

Only a few active control studies have been conducted under LPT conditions. Huang et al. [22] and Hultgren and Ashpis [23] employed high voltage electrodes to produce glow discharge plasma in a boundary layer to control separation. Bons et al. [24,25] used steady and pulsed VGJ's to successfully control separation on LPT airfoils. They used the "Pak-B" airfoil, which is an industry supplied research airfoil that is prone to separation problems at low Re. It has been used in numerous studies, as noted by Volino [4]. Bons et al. [24] used spanwise rows of VGJ's at several streamwise locations on the suction surface of the airfoil, and found that a row near the suction surface velocity maximum (pressure minimum) was most effective. The VGJ holes were oriented at 30° to the surface and 90° to the main flow. All holes were oriented in the same direction, to produce co-rotating vortices. Reynolds numbers as low as 60,000 (based on suction surface length and exit velocity) were considered. Bons et al. [25] found that both steady and pulsed jets were effective in controlling separation. The pulsed jets were fully effective even when the dimensionless pulsing frequency F^+ was as low as 0.1, where F^+ is a ratio of the transit time for flow between the VGJ hole and the trailing edge to the time interval between pulses. Ensemble averaged velocity profiles showed a long relaxation or "calmed" period following each jet pulse. During this calm period the boundary layer remained attached long after the turbulence generated by the pulse had moved downstream. Calmed regions have been observed following turbulent spots in transitional boundary layers (e.g., Gostelow et al. [26] and Schulte and Hodson [27]). The mean velocity profiles in the calmed region gradually relax from the turbulent shape associated with the turbulent spot they follow, to a laminar (and in some cases separated) profile shape. The calmed boundary layer is very resistant to separation, much like a turbulent boundary layer, but it is very laminarlike in terms of its fluctuation levels and low losses. The pulsed jets were more effective than continuous jets, even when the pulsed jet duty cycle was as low as 1%. This was believed to indicate that the starting vortex formed at the beginning of each jet pulse was responsible for most of the flow control in the pulsed jet cases.

Synthetic jets hold an advantage over continuous or pulsed jets in that they require no net mass flow. In the LPT environment, this means that no compressor bleed air is required. Use of bleed air for flow control or cooling comes at a cost in efficiency, although the small amount of air required for the pulsed jets of Bons et al. [25] might not be prohibitive if bleed air were already routed to the airfoils for cooling. Synthetic jets would not be useful for a cooled airfoil since ingestion of hot gas into the airfoil would be harmful. For uncooled LPT airfoils, however, the airfoil temperature will match the main flow temperature, and ingestion of hot gas should be acceptable. Routing of bleed air to uncooled airfoils for flow control may present a prohibitive addition of complexity and weight. With synthetic jets this problem could be avoided. In the present study, the oscillating flow of synthetic jets and the compound angle injection of vortex generator jets are combined to produce synthetic VGJ's. This is believed to be the first application of synthetic VGJ's. They are used to control the flow over a Pak-B airfoil. A survey of the literature indicates that the jet locations and angles chosen by Bons et al. [25] were likely optimal, so their geometry has been copied in the present study.

There are many parameters which could be varied in a synthetic jet study, including Reynolds number, FSTI, jet geometry, jet location, jet velocity, jet oscillation frequency, and jet waveform, to name a few. These are all potentially important parameters and should eventually be studied. The scope of the present study is more focused. A single experimental case is completely documented with detailed measurements including time resolved mean and fluctuating velocity and turbulent shear stress throughout the flow field. The goals of the study are to build an understanding of the physics of how synthetic VGJ's control separation and to generate questions for future parametric studies which may lead to optimized flow control for a broad range of flow conditions.

Volino [4,28] studied unmodified flow over the Pak-B airfoil at Reynolds numbers ranging from 25,000 to 300,000 under both high and low FSTI. In nearly all cases the boundary layer separated from the suction side of the airfoil. At all but the lowest Reynolds numbers it reattached before the trailing edge. The most severely separated case was the low FSTI, $Re=25,000$ case. This case has therefore been chosen as the test case for the present application of synthetic VGJ's. The unmodified case from Volino [4] is used as a baseline case for comparison to the new results. Also used for comparison is a case from Volino [5] in which a passive bar was employed to force reattachment. The bar was located at $s/L_s=0.51$, extending along the airfoil span. Its streamwise width was 6.35 mm and its height was 1.6 mm. The suction surface length was 228.6 mm. Bars of various heights were tested. The 1.6-mm bar was the smallest bar to cause reattachment at $Re=25,000$. Volino [5] found that the most effective bars in terms of minimizing losses were not large enough to immediately trip the boundary layer to turbulent. Rather, they induced small disturbances which grew and caused transition and reattachment downstream of a small separation bubble.

Experiment

Experiments were conducted in a low speed wind tunnel, described by Volino et al. [29]. Briefly, air enters through blowers and passes through a honeycomb, a series of screens, two settling chambers, and a three-dimensional contraction before entering the test section. At the exit of the contraction, the mean velocity is uniform to within 1%. The FSTI is $0.5\% \pm 0.05\%$. Nearly all of this free-stream "turbulence" is actually streamwise unsteadiness at frequencies below 20 Hz and is not associated with turbulent eddies. The rms intensities of the three components of the unsteadiness are 0.7%, 0.2%, and 0.2% in the streamwise, pitchwise and spanwise directions, respectively. The test section immediately follows the contraction.

The test section, shown in Fig. 1, consists of the passage between two airfoils. Details are listed in Table 1, and more information is available in Volino [4]. A large span-to-chord ratio of

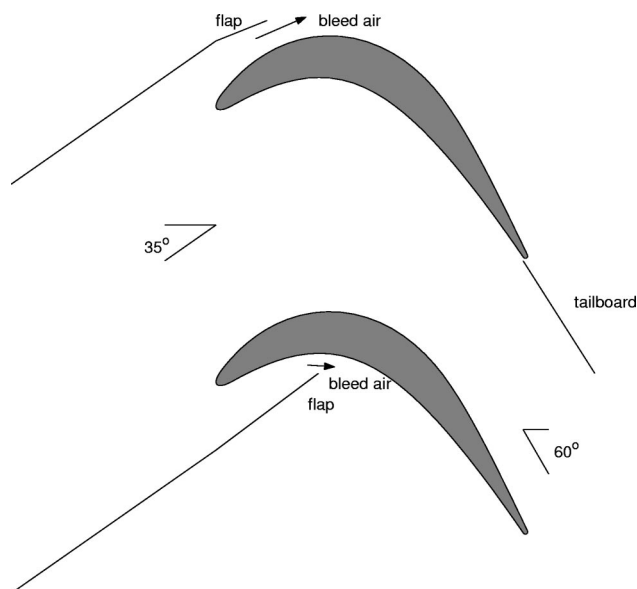


Fig. 1 Schematic of the test section

4.3 was chosen to insure two-dimensional flow at the spanwise centerline of the airfoils, where all measurements were made. Upstream of each airfoil are flaps, which control the amount of bleed air allowed to escape from the passage. The flaps, along with a tailboard on the pressure side of the passage, are adjusted to produce the correct leading edge flow and pressure gradient along the airfoils. The flow in the passage matches that in a multiblade cascade. The single passage configuration allows for a large scale passage and better probe access than possible with a multiblade cascade in the same size wind tunnel. The wake downstream of the passage is not representative of a multiblade facility, however, since there is flow only on one side of each airfoil. Downstream effects that could influence the upstream flow in the passage are also potentially missed. Experimental conditions match those of the low FSTI, $Re=25,000$ baseline case of Volino [4] and the passive bar case of Volino [5].

The synthetic VGJ's were produced from a cavity within the suction side airfoil. The airfoils are machined from high density foam, which has a consistency much like hard wood. The surface of each airfoil was sanded smooth, painted, and sanded again to provide a smooth surface. A 1.27-cm-diameter hole was drilled through the airfoil span at about mid-chord, as shown in Fig. 2, to form a plenum. One end of the plenum is plugged, and the narrow end of a funnel is inserted in the other. A 20.3-cm-diameter loud-speaker (100-W subwoofer) is attached at the wide end of the funnel. The funnel is sealed to the speaker and to the airfoil with silicone RTV to prevent air leakage. The speaker is driven with a 200-W audio amplifier, which is in turn powered with a 12-V dc power supply and driven by a function generator. For the present study the function generator was set to output a sine wave. The amplitude of the signal from the function generator and the gain of the amplifier were adjusted to provide the desired input voltage to the speaker. Holes for the VGJ's were drilled into the suction surface in a spanwise line at $s/L_s=0.514$. The holes are 0.8 mm in diameter (0.35% of L_s) and are spaced 8.5 mm apart (3.7% of

Table 1 Test section parameters

Axial Chord [mm]	True Chord [mm]	Pitch [mm]	Span [mm]	Suction side, L_s [mm]	Inlet flow angle	Exit flow angle
153.6	170.4	136.0	660.4	228.6	35°	60°

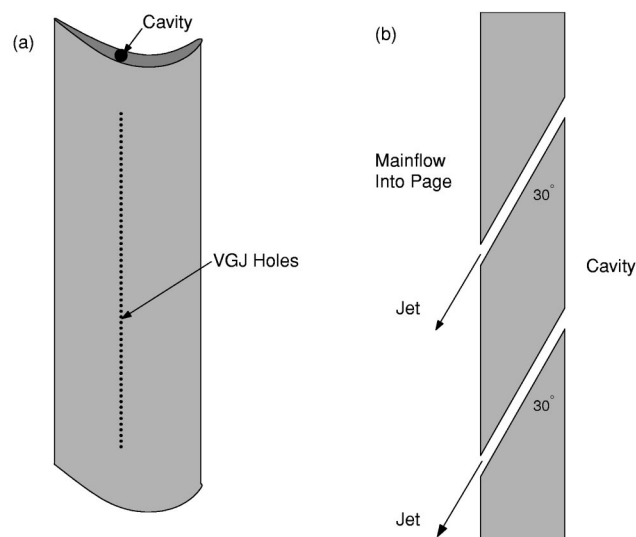


Fig. 2 Drawing of suction side airfoil with cavity and VGJ's: (a) full airfoil, (b) cross section of VGJ holes

L_s). The holes are drilled at a 90° skew angle with respect to the main flow and a 30° pitch with respect to the surface, as shown in Fig. 2. Each hole extends from the suction surface into the cavity in the core of the airfoil. The length to diameter ratio of the holes is 7.5.

Measurements. Pressure surveys were made using a pressure transducer (0–870-Pa range Validyne transducer) and a Scani-valve. Stagnation pressure was measured with a pitot tube upstream of the passage inlet, and eleven pressure taps were located on each airfoil along their spanwise centerlines. Locations of the taps on the suction side are listed in Table 2 along with measured local FSTI components and the acceleration parameter K at these stations based on a nonseparating, inviscid solution. The uncertainty in the suction side pressure coefficients was 7%. Most of this uncertainty was due to bias error. Stochastic error was minimized by averaging pressure transducer readings over a 10-s period.

Velocity profiles on the suction surface were measured at streamwise stations corresponding to pressure taps 7–11, as given in Table 2, and at four additional stations, labeled 7.5, 8.5, 9.5, and 10.5, centered between the pressure taps. All stations are downstream of the VGJ holes. Stations 7, 8, 9, 10, and 11 correspond to stations documented in the baseline case in Volino [4,28]. Profiles at Stations 1–6 are fully documented for the baseline case in Volino [4,28], and show that the upstream boundary layer closely follows a laminar solution. Profiles were measured near but not at the spanwise centerline of the airfoil to insure that the pressure taps did not interfere with the velocity measurements.

Table 2 Measurement station locations, local acceleration (inviscid soln.), and measured local free-stream turbulence

Station	s/L_s	$K \times 10^6$	\bar{u}'/U_∞ [%]	\bar{v}'/U_∞ [%]
1	0.111	6.32	0.44	
2	0.194	4.80	0.39	
3	0.278	3.44	0.37	
4	0.361	3.00	0.38	
5	0.444	2.48	0.39	
6	0.528	−0.08	0.41	
7	0.611	−3.24	0.47	0.05
8	0.694	−3.80	0.47	0.12
9	0.777	−2.32	0.48	0.14
10	0.861	−2.12	0.54	0.11
11	0.944	−0.72	0.51	0.11

Profiles were acquired with a hot-wire anemometer (AA Lab Systems model AN-1003) and a single sensor boundary layer probe (TSI model 1218-T 1.5). The sensor diameter is $3.8\text{ }\mu\text{m}$, and the active length is 1.27 mm . At each measurement location, data were acquired for 26 s at a 20-kHz sampling rate (2^{19} samples). All raw data were saved. The high sampling rate provides an essentially continuous signal, and the long sampling time results in low uncertainty in both statistical and spectral quantities. Data were acquired at 60 wall normal locations in each profile, extending from the wall to the free stream, with most points concentrated in the near wall region. The closest point was within 0.1 mm of the wall, which corresponds to $y/L_s=0.0004$ and about 0.015 boundary layer thicknesses. Flow direction in a separation bubble cannot be determined with a single-sensor hot wire, but velocity magnitude can be measured and was found to be essentially zero within the bubbles of the present cases. Determining the direction was not therefore considered essential. Uncertainty in the mean velocity is 3–5% except in the very near wall region, where near-wall corrections (Wills [30]) were applied to the mean velocity. Uncertainties in the momentum and displacement thicknesses computed from the mean profiles are 10%. Uncertainty in the shape factor H is 8%. Local skin friction coefficients were computed from the near wall mean velocity profiles using the technique of Volino and Simon [31]. This technique accounts for streamwise pressure gradient effects on the mean profile. The uncertainty in C_f is 8%. The uncertainty in the fluctuating streamwise velocity is below 10%. As explained in Volino [4] based on the work of Ligrani and Bradshaw [32], spatial averaging effects due to the finite length of the hot-wire sensor should not be significant in the present case.

Profiles were also acquired using a cross-sensor boundary layer probe (TSI 1243-20). The sensors are $51\text{-}\mu\text{m}$ -diameter hot films with 1.02-mm active lengths. The probe is used to document the instantaneous turbulent shear stress, $-u'v'$. Profiles were acquired at the same stations as with the single-sensor probe. Data were acquired at 25 locations in each profile, extending from 1 mm from the wall to the free stream. Sampling rates and times were the same as for the single-sensor profiles. The vortices induced by the oscillating jets cause significant secondary velocity, particularly at the streamwise stations immediately downstream of the jet holes. The magnitude of these secondary velocity components remains below 20% of the local streamwise velocity, however, so they should not cause significant error in the hot-wire measurements. The uncertainty in $-u'v'$ is 10%.

The VGJ velocities were measured using a hot-film probe (TSI model 1210-10A) with a 0.25-mm active sensor length. The sensor was placed directly over the exit of the jet hole. During outflow from the hole, the jet was expected to blow directly across the sensor, providing an accurate measure of the jet velocity. Uncertainty in the velocity is 5% and results mainly from uncertainty in the position of the sensor, which could lead to a slightly lower velocity reading than the velocity at the jet exit plane. During inflow of the oscillating jet, the flow is expected to behave more like a sink flow than a jet. The measured velocity does not therefore provide an accurate indicator of the velocity inside the hole during inflow. The jet velocity was calibrated against the rms input voltage to the speaker with the main flow in the wind tunnel turned off, and the calibration was used to set the jet velocity in later experiments. The jet velocity is fixed by the frequency and amplitude of the displacement of the speaker diaphragm, which causes a pressurization of the cavity relative to the pressure at the jet exits. The dynamic pressure of the flow through the test section is about 2.4 Pa at the jet location. Since the test section exits to atmosphere, the dynamic pressure results in an average pressure of 2.4-Pa vacuum in the cavity, and a 2.4-Pa pressure difference across the speaker diaphragm. This pressure is much smaller than the pressure experienced by the speaker when driving the jets, and is not expected to influence its motion. If the amplitude of the diaphragm motion is unchanged by the presence of flow in the test

section, the jets should drive approximately the same mass flow through the holes with the wind tunnel on or off. The jet velocity at the exit plane will presumably be affected by the mean flow, however.

The measured maximum jet exit velocity was 9.4 m/s for most of the cases presented below. Given the sensor length and the diameter of the holes, the measured velocity is an average over the middle 30% of the jet. The Reynolds number based on this velocity and the jet diameter is 500. At this Reynolds number, approximately 30 diameters would be needed to establish fully developed laminar flow inside the jet holes. Since the length to diameter ratio is only 7.5 and the jets are unsteady, the jet velocity is not expected to have a fully developed parabolic laminar profile, but rather a more flat profile. Given the averaging due to the sensor size and the expectation of a flat profile, the instantaneous mean velocity of the jet is assumed to approximately equal the measured velocity. Ideally this assumption would be checked with a survey of velocity across the jet exit plane, but the very small jet diameter precludes an accurate survey. The uncertainty in instantaneous mean velocity is, therefore, higher than the 5% uncertainty in the measured velocity. The uncertainty is estimated to be between 10 and 20%.

Data Processing. In addition to conventional time averaging, the velocity data were ensemble averaged relative to the time within each jet oscillation cycle. For this purpose, the speaker input voltage was digitized simultaneously along with the instantaneous velocity data. Data were ensemble averaged at 24 instances within the cycle. At each instance, data were averaged over $1/180$ th of the cycle. For each 26-s data trace, this results in roughly 3000 data points to average for each ensemble. With this many data points to average over a 26-s time record, the ensemble averaged results are well resolved and have uncertainties as low as those given above for the time averaged results. The start of the cycle was arbitrarily chosen as the instant when the speaker input voltage crossed from negative to positive. As will be shown below, this roughly corresponds to the beginning of the jets' outward pulse.

Results

Jet Velocity. Figure 3 shows a typical time trace of the measured jet velocity and the speaker input voltage. The frequency of the input signal was set to a nominal value of 10 Hz (actual value was 10.5 Hz). The maximum and average velocities in each outward pulse were 9.4 and 5.9 m/s , respectively. The jet velocity can be expressed as a blowing ratio B , defined as

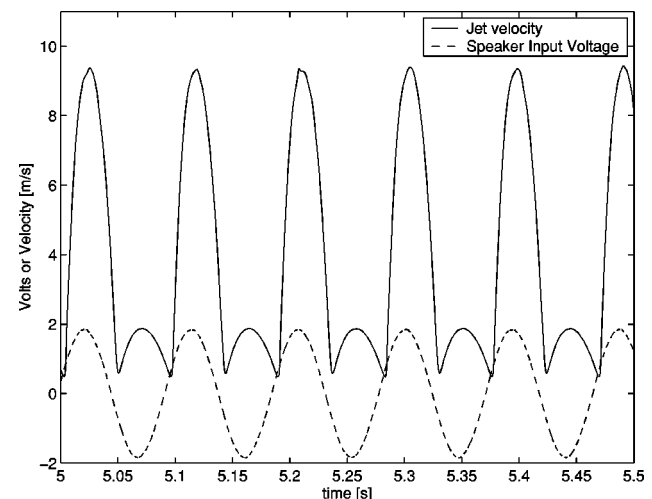


Fig. 3 Time trace of jet velocity and speaker input voltage, $F^+=0.65$

$$B = \rho_{\text{jet}} V_{\text{jet}} / \rho_{\infty} U_{\infty},$$

where $\rho_{\text{jet}} = \rho_{\infty}$ since the jet fluid comes from the boundary layer, and $U_{\infty} (= 2 \text{ m/s})$ is the local free-stream velocity at the jet location. For the present cases $B_{\text{max}} = 4.7$ during each cycle and $B_{\text{ave}} = 3.0$ during the outward pulse. The mass flux of the jets can be compared to the velocity deficit in the boundary layer as

$$M = [\rho_{\text{jet}} V_{\text{jet}} (\pi D_{\text{jet}}^2 / 4) S] / [\rho_{\infty} U_{\infty} \delta^*],$$

where $S = 0.118 \text{ holes/mm}$ is the number of holes per unit span. The displacement thickness, $\delta^* (= 1.08 \text{ mm})$ is the baseline case value at the jet location. This gives $M_{\text{max}} = 0.258$ and $M_{\text{ave}} = 0.162$. This could be interpreted to mean that 16% of the boundary layer in terms of displacement thickness is sucked off during the inflow half of each jet cycle, and then re-injected into the boundary layer during the outward pulse.

The momentum coefficient c_{μ} is defined as the ratio of the jet momentum to the free-stream dynamic pressure. Using the definition of Bons et al. [25],

$$c_{\mu} = [\rho_{\text{jet}} V_{\text{jet}}^2 (\pi D_{\text{jet}}^2 / 4) S] / [\rho_{\infty} U_{\infty}^2 \text{Chord}],$$

where the axial chord is 153.6 mm. The maximum value of c_{μ} in each cycle is 0.0085. The average value of V_{jet}^2 for the outpulse is $44 \text{ m}^2/\text{s}^2$. This gives an average $c_{\mu} = 0.0042$.

Figure 3 shows that the speaker input voltage and the jet velocity are slightly out of phase. The jets lag the input voltage by about 0.006 s, which is a dimensionless lag $\Delta t/T$ of 0.063, where T is the jet oscillation period of 0.095 s. The lag is expected, as the jets respond dynamically to the pressurizing of the cavity in the airfoil by the speaker, and there is no reason to expect the speaker voltage and the jet velocity to be exactly in phase. The finite distance from the speaker to the jet holes (of the order 0.5 m) and the finite speed of sound (340 m/s) will also lead to a time lag of the order 1 ms. The time lag increases with distance from the speaker along the airfoil span. At high jet frequencies, the time lag causes the jets along the span to be significantly out of phase with each other. Measurements, however, show that the jet amplitude along the span is uniform, regardless of the frequency. Variation in phase along the span could lead to difficulty in practice if attempts were made to time the jet pulsing to other cyclic events such as wake passing. It is not an issue in the present study. At the relatively low frequency of 10 Hz, the phase lag was not significant, and the jets were uniform in both phase and amplitude along the span.

Pressure Profiles. Pressure profiles were acquired for several jet amplitudes and jet frequencies. The general finding was that the jets were effective over a broad frequency range, so long as the amplitude was sufficiently high. Figure 4 shows C_p profiles for a range of jet amplitudes, with the jet frequency set to 10.5 Hz ($F^+ = 0.65$). In all cases there is good agreement between the data and an inviscid solution for the Pak-B airfoil on the pressure side and the upstream portion of the suction side. In the adverse pressure gradient region on the suction side, differences are clear. Without the jets the boundary layer separates and does not reattach, as indicated by the region of constant C_p values. With $B_{\text{max}} = 1.9$ the boundary layer still does not reattach, but there is some sign that C_p is starting to drop at the last pressure tap. For the cases with $B_{\text{max}} = 4.7$ and above, the boundary layer does not appear to separate. Significant case to case differences in C_p are present right at the suction peak, but these are likely due to the injection of the jets at this location and their effect on the flow over the adjacent pressure tap. The differences diminish rapidly and are essentially gone by the next downstream measurement station. Bons et al. [24] demonstrated effective flow control with B_{max} as low as 0.4 in their study. The significantly lower Re in the present study may explain the need for stronger jets. Figure 5 shows C_p profiles for several different jet frequencies with B_{max} held approximately constant at about 5. There does not appear to be any clear separated region in any of the cases with jets. The

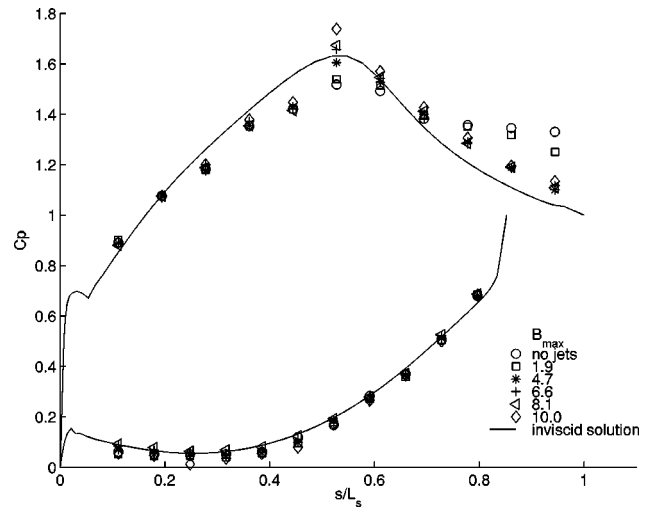
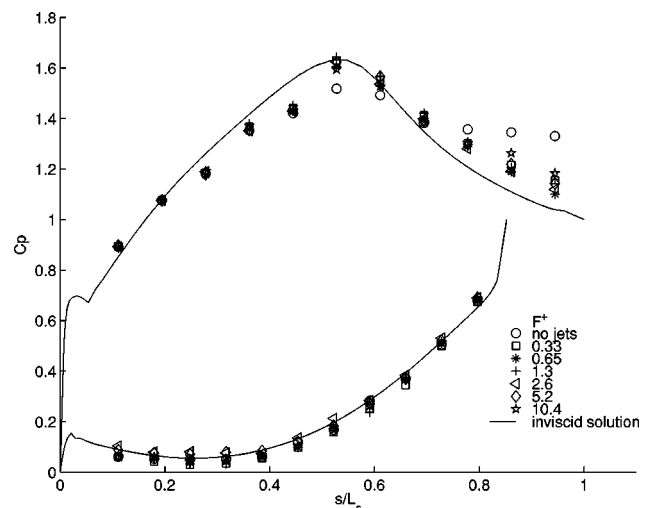


Fig. 4 C_p profiles, $F^+ = 0.65$, various blowing ratios

suction peak is higher in all the cases with jets than in the baseline case. This is an expected result, suggesting that the lift will be higher when the boundary layer is attached. The $F^+ = 0.65$ case appears to agree most closely with the inviscid solution. The broad range of effective frequencies agrees with the results of Bons et al. [25].

The objective of the present study is not to establish the optimal jet conditions for the present case, but to investigate in detail a case in which the jets provide effective flow control. The dimensionless frequency $F^+ = 0.65$ was chosen since it appeared to provide slightly better results than the other cases in Fig. 5, and $B_{\text{max}} = 4.7$ was chosen since it was the lowest effective blowing ratio tested. Figure 6 shows the C_p profile for the chosen case with jets along with the baseline case and the passive bar case of Volino [5].

Velocity Profiles. Figure 7 shows mean velocity \bar{u}' and turbulent shear stress profiles for the present case, the baseline case, and the passive bar case. In the baseline case, the mean profiles show the boundary layer is on the verge of separating at station 7, is clearly separated at station 8, and the separation bubble grows through station 11. In the bar case, the boundary layer separates from the bar. The separation bubble is visible at station 7, and it grows through station 9. At station 10, the near wall velocities



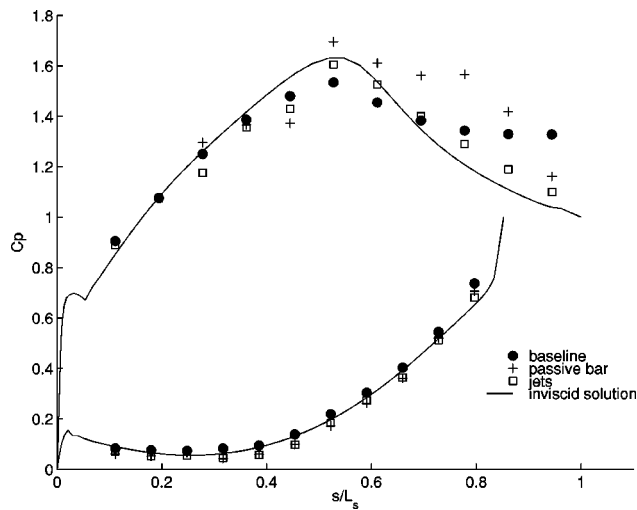


Fig. 6 C_p profiles, comparison of baseline, passive bar, and present jet case with $B_{\max}=4.7$ and $F^+=0.65$

begin to rise, indicating the beginning of reattachment, and the mean profile shows clear reattachment at station 11. With the VGJ's, the behavior is much different. There is no clear separation bubble. The mean profile appears to have an attached, laminarlike shape. The momentum deficit with the jets appears to be significantly lower at station 11 than in the case with the bars, indicating lower losses with the jets.

The \bar{u}' values in the baseline and bar cases are very low at station 7, as expected since the boundary layer is still laminar. A peak appears downstream in the shear layer over the separation bubble. In the bar case, \bar{u}' begins to rise in the near wall region at station 9, signaling imminent reattachment. At stations 10 and 11, \bar{u}' in the bar case rises to the high values typical of a transitional boundary layer. In the jet case, \bar{u}' is high at all stations. At the upstream locations it is much higher than would be expected for a turbulent boundary layer. As will be shown below, however, much of the contribution to \bar{u}' is from 10-Hz unsteadiness associated with the jets and is not turbulence. The turbulent shear stress

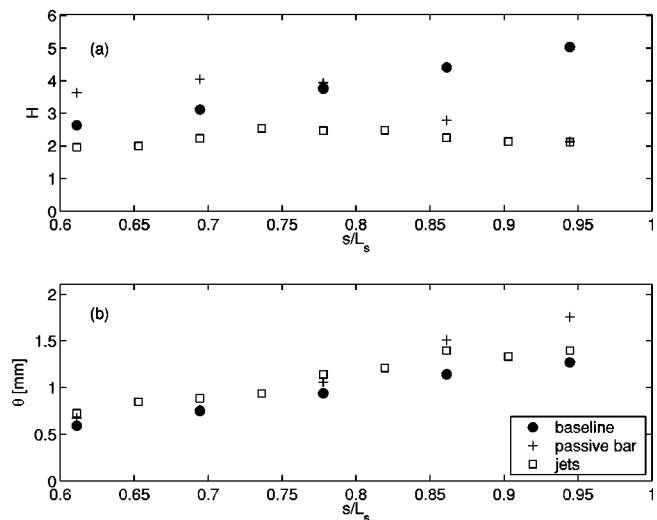


Fig. 8 Time averaged shape factor and momentum thickness versus streamwise location; comparison of baseline, passive bar and present jet cases: (a) H , (b) θ

profiles show considerable momentum transport in the jet case at all stations, which helps to explain how the boundary layer remains attached. Unlike in a turbulent boundary layer, the $-\overline{u'v'}$ peak is well away from the wall. In the baseline case the shear layer does not transition to turbulent, and $-\overline{u'v'}$ remains near zero. In the bar case $-\overline{u'v'}$ profiles were not acquired.

Figure 8 shows shape factor and momentum thickness as computed from the mean profiles of Fig. 7. The shape factor H provides a measure of the state of the boundary layer with respect to separation and transition. The shape factor in the baseline and bar cases rises rapidly after separation, as δ^* increases while θ remains nearly constant. In the baseline case the boundary layer never reattaches. In the bar case, transition and reattachment occur, causing δ^* to fall and θ to rise. The shape factor begins to drop toward a turbulent value of about 1.6, but does not reach this value, indicating that the recovery from the separation is not com-

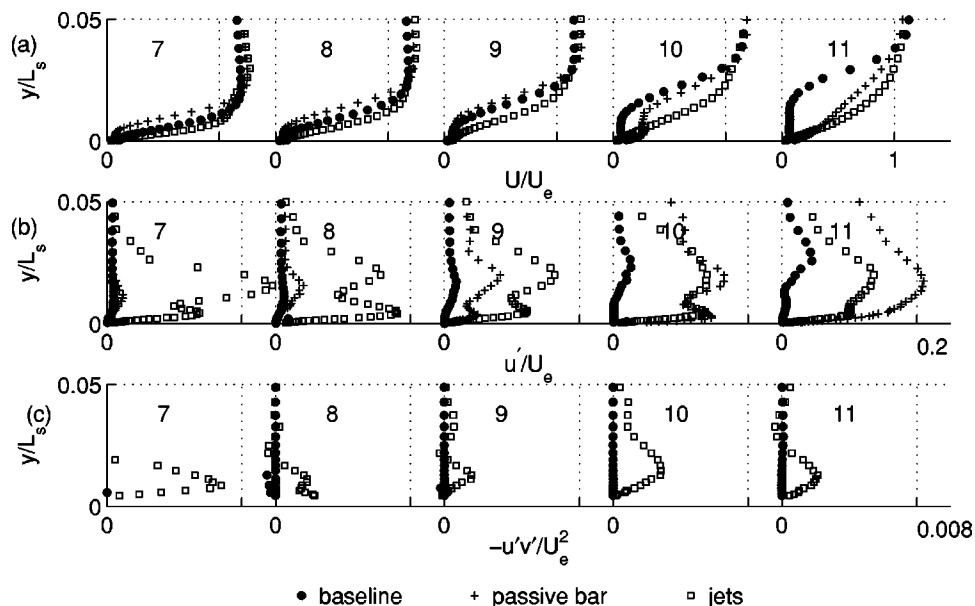


Fig. 7 Station 7–11 dimensionless time averaged profiles; comparison of baseline, passive bar and present jet cases: (a) mean velocity, (b) \bar{u}' , (c) turbulent shear stress

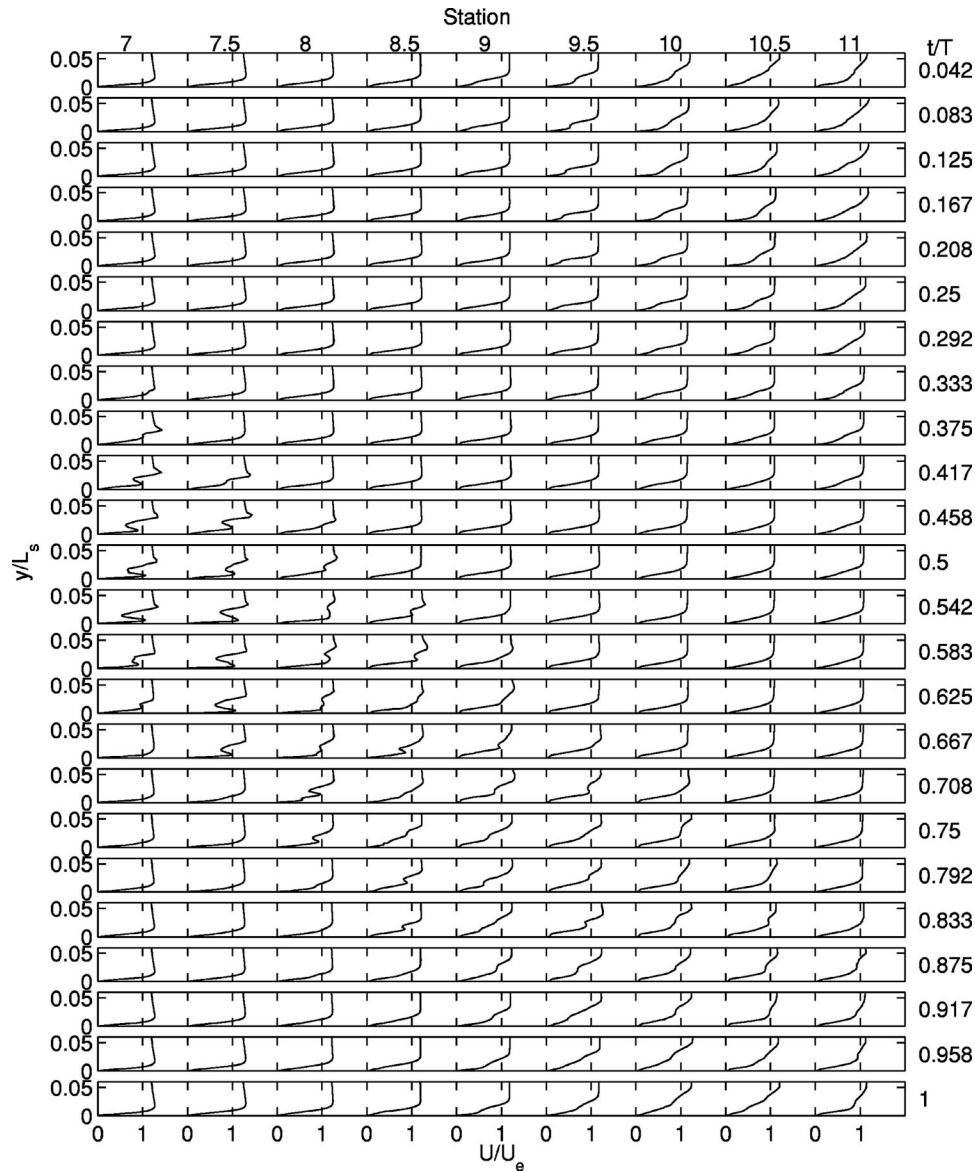


Fig. 9 Ensemble averaged dimensionless mean velocity (\tilde{U}/U_e) profiles

plete. In the jet case, the shape factor remains at a laminar value of about 2. It never rises to a separated flow value, nor does it drop to a turbulent value. The momentum thickness provides a measure of the losses in a boundary layer. If the boundary layer reattaches before the trailing edge, the suction side boundary layer losses will be the dominant losses in an LPT passage (Howell et al. [6]). In the baseline case the boundary layer does not reattach, so although θ remains low, high losses would be expected in the wake downstream of the airfoils. For the bar and jet cases, however, the boundary layer is attached at the trailing edge. Momentum thickness is about 20% higher in the bar case, indicating that the jets are better able to control separation, while causing lower losses.

Ensemble Average Velocity Profiles. The time averaged profiles of Fig. 7 indicate that the jets are effective in controlling the boundary layer, but they do not explain the mechanism by which the jets work. Figure 9 shows ensemble averaged mean velocity profiles. Profiles are shown for nine streamwise stations at 24 time increments within the jet oscillation cycle. Figures 10 and 11 show the corresponding \tilde{u}' and $-\tilde{u}'\tilde{v}'$ profiles. Examining the profiles at station 7, the mean profile initially appears to be lami-

nar and attached, and both the \tilde{u}' and $-\tilde{u}'\tilde{v}'$ values are near zero, indicating again that the flow is laminar. Given the phase lag shown in Fig. 3 between the speaker input and the jets, and the finite convection time between the jet hole and station 7, one would expect that the disturbance created by the jet outpulse should arrive at station 7 at $t/T=0.18$. In fact, however, the disturbance is not seen in the mean profile until $t/T=0.333$. In agreement, the \tilde{u}' and $-\tilde{u}'\tilde{v}'$ values also rise above zero at $t/T=0.333$. This may suggest that the rising jet velocity must reach a sufficiently high amplitude before it can significantly affect the boundary layer. Comparing the observed phase lag and the jet velocity of Fig. 3 suggests that the jet velocity must be about 8 m/s, corresponding to an instantaneous $B=4$, for the jets to be effective. Continuing forward in time at station 7, the jets cause a large disturbance in the mean profiles that continues until $t/T=0.667$. The time $t/T=0.667$ corresponds very closely with the end of the jet outpulse when the phase lag and convection time from the jet holes to station 7 are considered. The large local minima and maxima in the mean velocity profiles indicate the jets are not merely adding turbulence to the boundary layer, but are inducing some flow structure, most likely streamwise vortices.

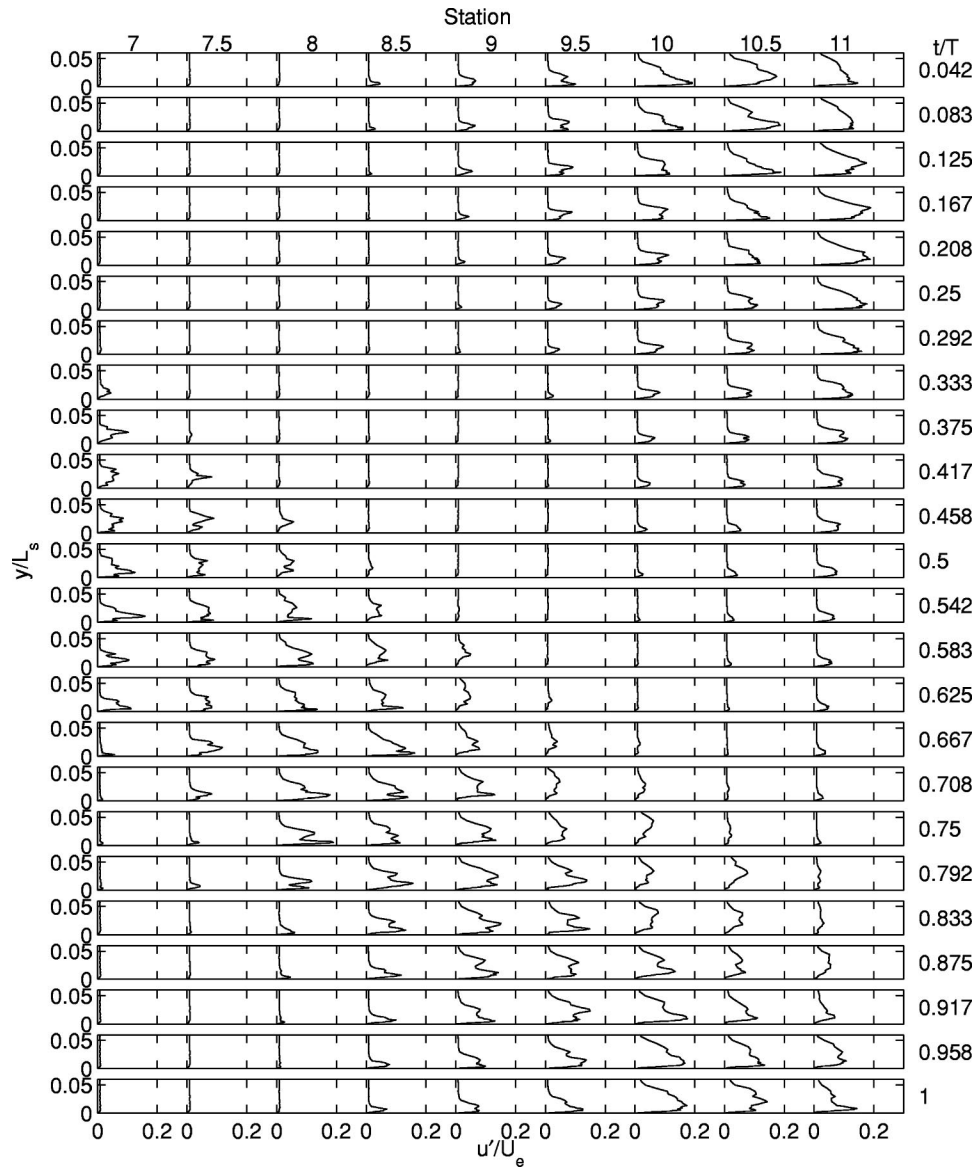


Fig. 10 Ensemble averaged rms value of dimensionless streamwise fluctuating velocity (\tilde{u}'/U_e) profiles

These vortices likely cause spanwise variation in the velocity, particularly at the stations nearest the jets. In the present study, data were only acquired at one spanwise location. Spanwise surveys should be considered in future work. The \tilde{u}' and $-\tilde{u}'\tilde{v}'$ profiles exhibit large peaks in the regions where the mean velocity gradients are highest in Fig. 9. The $-\tilde{u}'\tilde{v}'$ values have the appropriate sign, corresponding to the sign of $d\tilde{U}/dy$ in the mean profiles. It should be noted that the magnitude of \tilde{u}' is smaller in the ensemble averaged profiles of Fig. 10 than in the time averaged profiles of Fig. 7. This indicates that much of the contribution to \tilde{u}' in Fig. 7 is due to 10-Hz oscillations and not to turbulence. After $t/T=0.667$, the mean velocity profile resumes a laminar shape. There is no tendency toward boundary layer separation. The boundary layer did not separate in the baseline case at this station (Fig. 7), but the mean profile in the baseline case did appear closer to separation than in the present case.

Moving to the downstream stations, the leading edge of the disturbance, as observed in the mean profiles and the \tilde{u}' and $-\tilde{u}'\tilde{v}'$ profiles moves to later values of t/T , as expected since the disturbance takes some time to convect downstream. The leading

edge of the disturbance appears to move at about 90% of the local free-stream velocity, which corresponds with the expected leading edge celerity of a turbulent spot (e.g., Gostelow et al. [26], Schulte and Hodson [27]). The trailing edge of the disturbance appears to move at about 45% of the local free-stream velocity, agreeing with the expected trailing edge celerity of a turbulent spot. Because the leading and trailing edge celerities are different, the boundary layer is only disturbed by the jets during approximately 30% of the cycle at station 7, but is disturbed during approximately 70% of the cycle at station 11. The beginning of the disturbance at each station is seen simultaneously in the mean profile and the \tilde{u}' and $-\tilde{u}'\tilde{v}'$ profiles of Figs. 9–11. At the trailing edge of the disturbance, return of the mean velocity profile to a smooth shape corresponds closely with the return of $-\tilde{u}'\tilde{v}'$ to near zero (see, for example, the profiles at station 8 at $t/T=0.833$ or station 10.5 at $t/T=0.417$). The \tilde{u}' profiles, in contrast, take somewhat longer to return to an undisturbed condition. At station 11, for example, there is at least a small near wall \tilde{u}' peak at all times, while the $-\tilde{u}'\tilde{v}'$ values are essentially zero between $t/T=0.625$ and 0.792 .

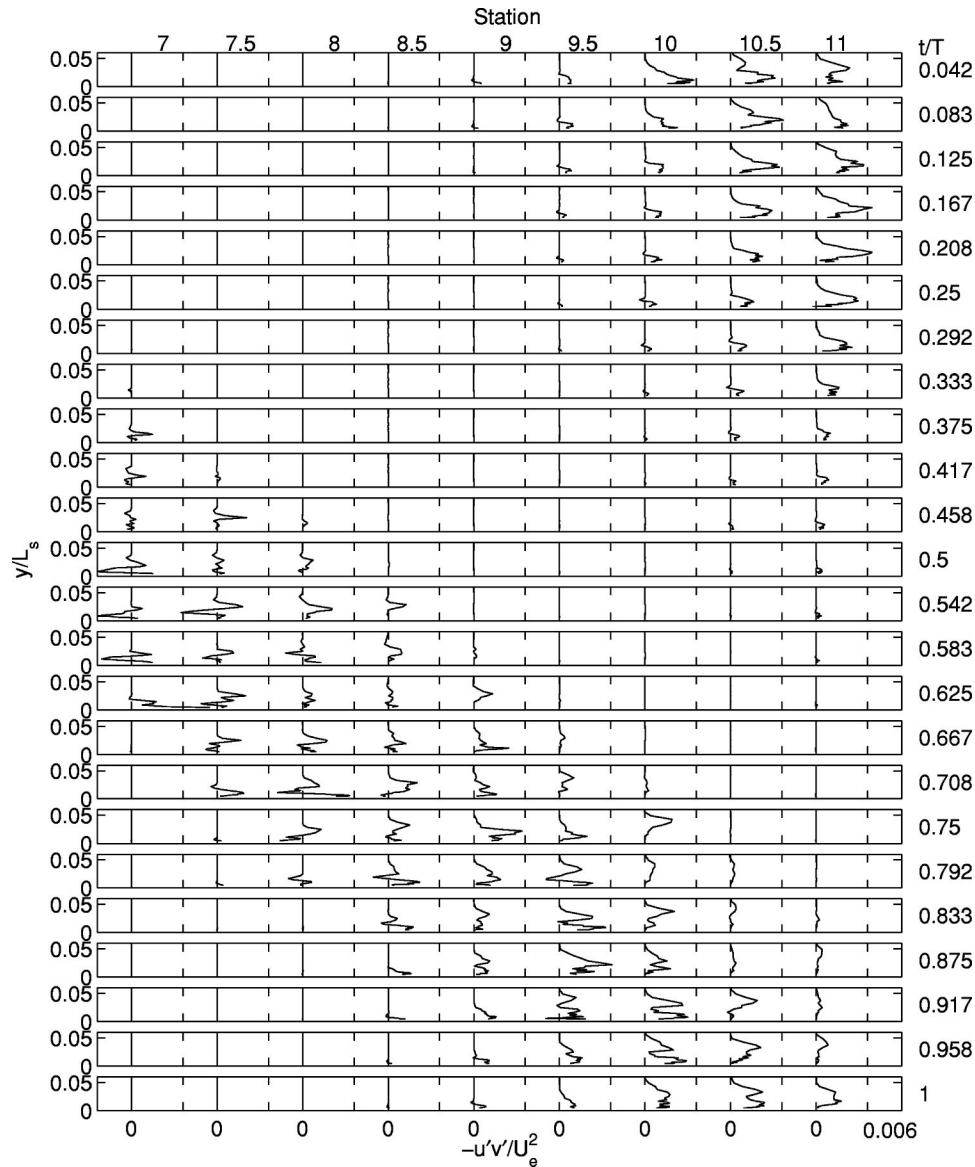


Fig. 11 Ensemble averaged dimensionless turbulent shear stress ($-\tilde{u}'\tilde{v}'/U_e^2$) profiles

The flow structure at the downstream stations appears to be less distinct than at stations 7 and 7.5. Inflection points are still present in the mean profiles, but the local minima and maxima in the mean profiles are less sharp. Still, the mean profile shapes and the multiple peaks in the \tilde{u}' and $-\tilde{u}'\tilde{v}'$ profiles, particularly those far from the wall (see for example the station 10 profiles of Figs. 10 and 11 between $t/T=0.75$ and 0.958) are evidence that the flow structures induced by the jets persist downstream.

After the disturbance caused by the jets passes, the boundary layer eventually separates at locations between stations 8 and 11. At station 8.5, for example, the trailing edge of the disturbance passes at about $t/T=0.9$. By $t/T=0.1$ the near wall profile appears separated. The separation appears to coincide with the return of \tilde{u}' to near zero. The separation appears to persist until about $t/T=0.6$, after the start of the next disturbance event. The reattachment within the disturbance event corresponds to the motion of high \tilde{u}' and $-\tilde{u}'\tilde{v}'$ into the near wall region at $t/T=0.667$. The same sequence of events is visible at downstream stations. At station 10.5, for example, the trailing edge of the disturbance has passed by $t/T=0.4$, but the boundary layer remains attached until about $t/T=0.75$. Reattachment is visible at $t/T=1$, and a near

wall peak emerges at the same time in $-\tilde{u}'\tilde{v}'$. It should be noted that the separation bubble remains thin at all stations, and never begins to approach the thickness observed in the baseline flow of Fig. 7.

The period between the passage of the disturbance and boundary layer separation is believed to indicate a “calmed” region. Calmed regions have been observed in previous studies to follow turbulent spots and wake induced turbulent strips. The duration of the calmed region increases at the downstream stations, since the trailing edge celerity of the calmed region, shown in Fig. 9 to be about 0.3 the local free-stream velocity (in agreement with previous studies of calmed regions), is slower than the trailing edge celerity of the disturbed region. Hence at station 8.5 the calmed region extends for $\Delta t/T$ of about 0.2, while at station 10.5 it extends for $\Delta t/T$ of about 0.4. The presence of the calmed region may help to limit the separation bubble thickness.

Figure 12 shows the ensemble \tilde{u}' data in a different format. Contours of near wall \tilde{u}' at $y=0.095$ mm ($y/L_s=0.0004$) are shown in a time-space plot. The horizontal axis shows the dimensionless streamwise location, and the vertical axis indicates the dimensionless time within the cycle. Two complete cycles are

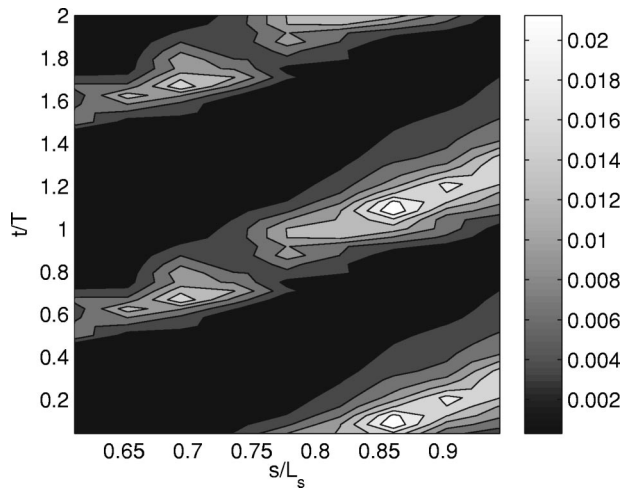


Fig. 12 Time-space plot of ensemble averaged \tilde{u}'/U_e at $y/L_s = 0.0004$

shown to better illustrate the periodicity of the event. The data in the bottom half of the figure is shown again in the top half. In this format, it is clear that the jet outpulse causes a high \tilde{u}' event to appear at $s/L_s = 0.6$ (station 7) and $t/T = 0.6$. This event then proceeds downstream in a widening wedge of turbulence. The lower and upper slopes of the wedge indicate its leading and trailing edge celerities, respectively. Within the wedge, a local \tilde{u}' peak is visible at $s/L_s = 0.7$ (station 8). This peak indicates that the flow structure produced by the jets has penetrated very near the wall. Slightly farther downstream at $s/L_s = 0.75$ (station 8.5) a local minimum is visible in the \tilde{u}' contours. This may indicate that the flow structure induced by the jets has lifted off the wall slightly. The mean profiles of Fig. 9, support this, showing lower near wall mean velocity gradients at station 8.5, which indicates that high speed fluid is not as effectively brought into the near wall region at this station. Farther downstream in Fig. 12, the \tilde{u}' level in the turbulent wedge rises again as a fully turbulent boundary layer begins to develop. Outside of the wedge the \tilde{u}' level is very low, indicating laminar flow.

Figure 13 shows ensemble averaged $-\tilde{u}'\tilde{v}'$ contours at $y/L_s = 0.0128$ in the format of Fig. 12. As in Fig. 12, the wedge of turbulence is clear. Within the wedge momentum transport is high, but outside the wedge the flow appears to be laminar.

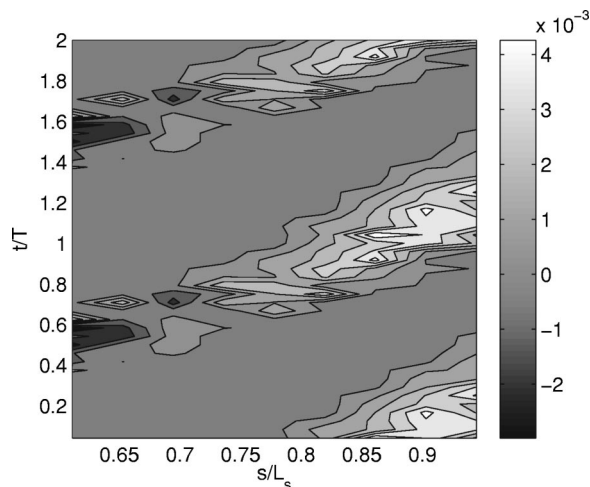


Fig. 13 Time-space plot of ensemble averaged $-\tilde{u}'\tilde{v}'/U_e^2$ at $y/L_s = 0.0128$

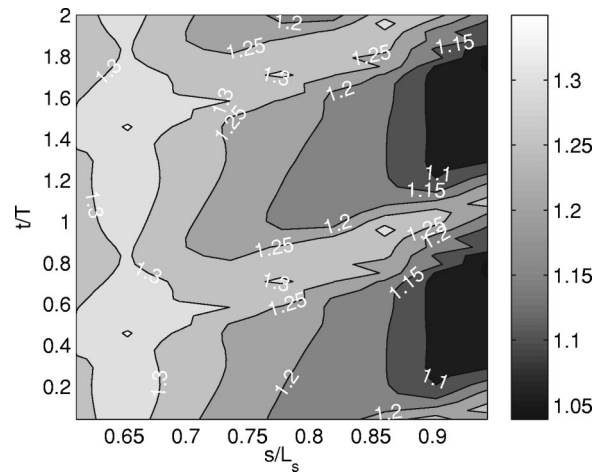


Fig. 14 Time-space plot of ensemble averaged dimensionless free-stream velocity \tilde{U}_∞/U_e

Figure 14 shows a time-space plot of the local ensemble averaged free-stream velocity. The free-stream velocity varies both spatially and temporally. Spatially, the shape of the airfoil passage causes the flow to decelerate. Temporally, when the jets cause a turbulent event to move down the surface, it causes the boundary layer to thicken and accelerates the free-stream. During the laminar and calmed periods the boundary layer is thinner and the free-stream velocity is lower. Figure 15 shows the local Thwaites parameter, λ_θ , as computed from the free-stream velocity data of Fig. 14. In a laminar boundary layer, separation is expected when λ_θ is less than -0.082 . With the exception of the turbulent strip, where the boundary layer is locally accelerated, λ_θ is below -0.082 at most times and locations on the surface, and at some times is below -2 . Hence it is not a surprise that the boundary layer tends to separate when not controlled by turbulence or a calmed region.

Integral Parameters. Local displacement and momentum thickness values can be computed from the ensemble mean velocity profiles of Fig. 9. Momentum thickness is shown in Fig. 16. Both δ^* and θ grow in the streamwise direction and are about twice as large in the turbulent region than in the laminar flow region. The slow growth of the momentum thickness in the non-turbulent flow indicates that losses should be low in this region, as might be expected based on the low \tilde{u}' and $-\tilde{u}'\tilde{v}'$ values of Figs.

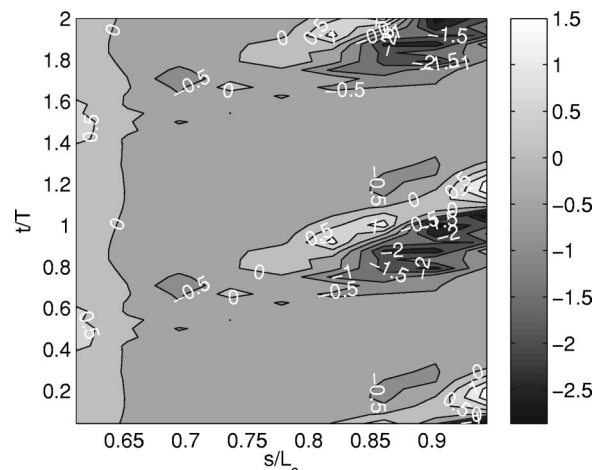


Fig. 15 Time-space plot of ensemble averaged Thwaites acceleration parameter λ_θ

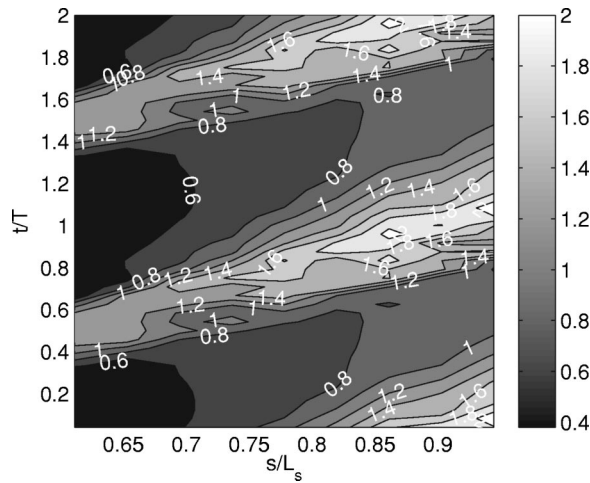


Fig. 16 Time-space plot of ensemble averaged momentum thickness θ in mm

10 and 11. At $s/L_s = 0.6$ (station 7), δ^* and θ in the laminar flow are both roughly 67% of their values in the baseline case of Volino [4]. The lower values in the present case may be due to the suppression of the large separation bubble downstream, which changes the local pressure gradient at station 7. The suction during the inflow portion of the jet cycle could also be an explanation, but δ^* and θ are uniformly low in the laminar flow at station 7. If the suction were causing a thinner boundary layer, one would expect the effect to be stronger during the time of strongest inflow into the jet holes. Figure 17 shows the local shape factor H , computed from the δ^* and θ values. Within the turbulent region, the shape factor remains between 2 and 2.4, which is well above the expected value of 1.6 for a fully turbulent boundary layer subject to the strong adverse pressure gradient of the present case. In the nonturbulent flow, H reaches values as high as 3.4, which is consistent with the observed flow separation.

Skin Friction Coefficient. It is clear from the mean profiles of Fig. 9 that the local wall shear stress varies greatly during the jet oscillation cycle. At the upstream stations at $t/T = 0.6$, for example, the jets bring high speed fluid very close to the wall, producing a very high mean velocity gradient at the wall. At other times at all stations, the boundary layer appears very laminarlike, indicating a relatively low wall shear stress. When the boundary layer is separated the wall shear goes to zero. Figure 18 shows the

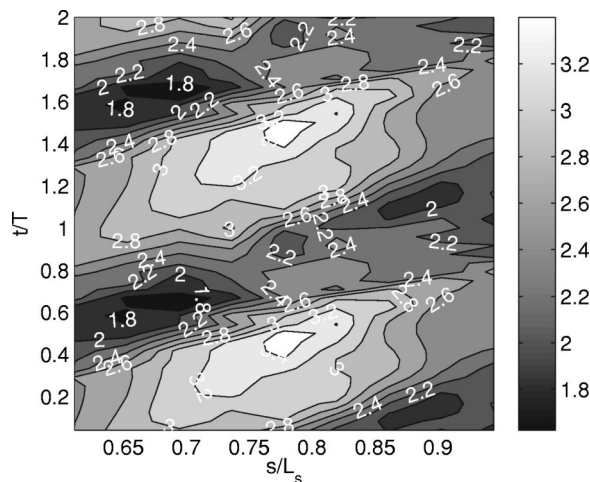


Fig. 17 Time-space plot of ensemble averaged shape factor H

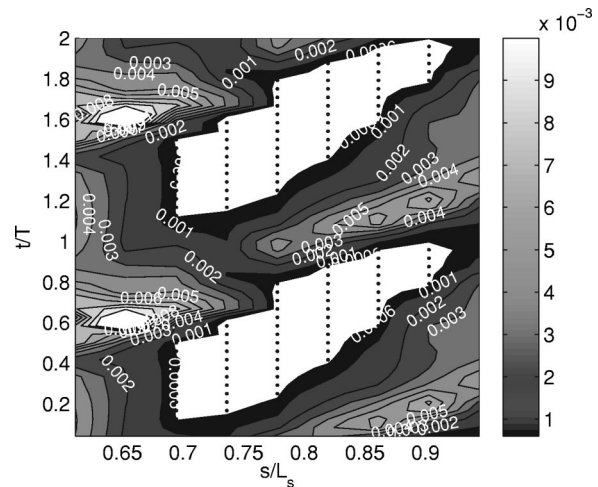


Fig. 18 Time-space plot of ensemble averaged skin friction coefficient C_f ; white areas with dots indicate separated flow

local skin friction coefficients C_f . The white regions with dots indicate where the flow is separated and the local skin friction is essentially zero. At $s/L_s = 0.6$ (station 7) there is a laminar boundary layer with $C_f = 0.005$ between jet outward pulses. The corresponding momentum thickness Reynolds is about 60. The skin friction drops in the streamwise direction and the boundary layer separates at $s/L_s = 0.7$ (station 8). At $t/T = 0.6$ and $s/L_s = 0.6$, the skin friction is much higher, following the jet outpulse. The momentum thickness Reynolds number is as high as 180, and C_f reaches values as high as 0.014. Moving downstream along this turbulent region, C_f rapidly drops to 0.001 at $t/T = 0.8$ and $s/L_s = 0.75$ (station 8.5). The turbulence at this time and position is also low (Fig. 10). As stated above, the vortices produced by the jets appear to quickly bring high speed fluid near the wall, resulting in high skin friction and turbulence, but by $s/L_s = 0.75$ this effect may weaken, resulting in lower C_f and \tilde{u}' . Moving farther downstream to $t/T = 1.1$ and $s/L_s = 0.85$, C_f rises again to as high as 0.007. The corresponding Re_θ is about 200 at this time and location. $C_f = 0.007$ is about what one would expect for a fully turbulent boundary layer with $Re_\theta = 200$, based on the standard correlation $C_f = 0.0256/Re_\theta^{0.25}$ (Schlichting [33]).

Figure 18 clearly shows the calmed region described above. It is the triangular shaped region centered at $t/T = 0.4$ and $s/L_s = 0.9$ that in the figure is bounded below by the strip of high C_f and above by the separated flow region. Comparing Figs. 12, 13, 16, and 18 shows that the calmed region has low skin friction, low momentum thickness, and low turbulence. Losses should therefore be low for the calmed region, as expected.

A comparison of the momentum thickness and skin friction in Figs. 16 and 18 is interesting. The wedge of high θ overlaps both the upper portion of the separated flow region and the strip of high C_f . As shown in the profiles of Figs. 10 and 11, downstream of $s/L_s = 0.75$ (station 8.5), the turbulence and mixing induced by the jet outpulse initially affects the outer part of the boundary layer and does not immediately eliminate the separation bubble. Figure 16 shows that this outer region mixing causes a rise in the momentum thickness. It is only somewhat later and farther downstream that this mixing moves into the near wall region, causing reattachment and high C_f . Kaszeta et al. [34] reported a similar result for flow over the Pak-B airfoil subject to wake passing events. They observed a time lag between the wake arrival and near wall transition.

Kaszeta et al. [34] also observed a relation between the temporal acceleration and deceleration of the flow associated with the wake passing, and its relation to transition and the thickening and thinning of the boundary layer. Similarly, a comparison of Figs.

15, 16, and 18 show the relation between the local acceleration, θ and C_f . The region of overlap between high θ and separated flow corresponds to the region of strong deceleration centered at $s/L_s = 0.9$ and $t/T = 0.85$. One could argue that the deceleration inhibits reattachment in spite of the mixing in the outer part of the boundary layer. At slightly later t/T , the flow is accelerated. Under the combination of acceleration and high $-\tilde{u}'\tilde{v}'$ the boundary layer reattaches.

Open Questions. The first objective of the present study was to assess the effectiveness of synthetic VGJ's on separation control for an LPT airfoil and provide some description of the mechanisms through which the jets work. This has been addressed above. The second objective was to use these results to generate questions for further consideration. These are discussed below.

What is the effect of jet frequency on flow control? In the present case, with $F^+ = 0.65$, the airfoil boundary layer at any given time was approximately half disturbed by the jets and half laminar or calmed. The effects of one jet outpulse are present in the boundary layer at all times. Separation occurred, but the separation bubble was small and did not appear to result in any harmful effects. How thick a separation bubble is tolerable? If F^+ were increased, the duration of each event would be reduced, but more events would be present in the boundary layer at any given time. It is not clear what effect this would have. In other studies with synthetic jets, some have found that F^+ of the order 1, as in the present study, is most effective (e.g., Seifert and Pack [35]). Others, such as Amitay and Glezer [21] report that under some conditions jets with F^+ of the order 10 are more effective. Lowering the jet frequency might be beneficial. Losses appear to be generated primarily in the flow disturbed by the jets, while the flow between these events is laminar or calmed with low losses. Reducing F^+ could presumably result in a smaller fraction of the airfoil covered by disturbed flow at any time. At some point, however, if the jets are too widely spaced, the flow will become uncontrolled at times and revert to the large separation bubble of the baseline case. Based on the trailing edge celerity of the disturbed flow, if F^+ were reduced below 0.45, there would be instances within the jet cycle when no disturbances would be present in the boundary layer. If F^+ were reduced below 0.3, there would be times when neither disturbed or calmed flow would be present. In flow around a single airfoil, Seifert and Pack [35] found that jets with F^+ between 0.5 and 1.5 were most effective at all Re, but that with $F^+ = 0.25$ the jets were ineffective. Bons et al. [25], in contrast, found that their VGJ's were effective at F^+ as low as 0.1. They suggested that the more controlled nature of the LPT flow, where adjacent airfoils provide covered turning, might explain the lower effective F^+ in their study. It should be noted that the Bons et al. [25] experiments were conducted at a Reynolds number of 60,000, where separation effects are not as severe as in the present case with $Re = 25,000$.

What is the effect of jet amplitude on flow control? The pressure profiles of Fig. 4 indicate that the jet amplitude must be sufficiently high for the jets to be effective. It is expected that using a higher amplitude than necessary will result in higher losses, but the extent to which the losses would increase is not known. Volino [5] using passive bars found that cases with a small separation bubble followed by reattachment had lower losses than cases in which the boundary layer was tripped to turbulent to prevent separation. Low amplitude jets could potentially produce a similar effect.

What is the effect of jet wave form? In the present case the speaker was driven with a sine wave input. A square wave with a short duty cycle, as in the study of Bons et al. [25], might be better. By keeping the duty cycle short, the amount of calmed flow relative to disturbed flow could be increased. This might allow a reduction of losses without a sacrifice of separation control.

What is the effect of jet inflow? The outward flow portion of each jet cycle appears to dominate the flow control. It is possible,

however, that the inflow may help reduce the boundary layer thickness in the undisturbed flow periods and help reduce separation effects. A direct comparison of cases at the same Re using synthetic VGJ's and pulsed VGJ's could help answer this question.

What is the effect of jet geometry? The VGJ's are clearly effective. Through the generation of streamwise vortices they appear to provide more mixing than would be produced with normal jets that simply produced turbulence. The relative magnitudes of the effects of turbulence and streamwise vortices in enhancing mixing are uncertain. Might the generation of turbulent spots with a normal jet be sufficient? Which would result in lower losses?

What are the effect of Reynolds number and free-stream turbulence level? The baseline cases of Volino [4] show that at higher Re and higher FSTI the boundary layer is more likely to transition and reattach even without flow control. The generation of calmed attached flow between jet events could still prove beneficial at higher Re, however. There would be a tradeoff between the losses generated by the jets themselves and the reduction in losses the jets might provide by reducing the separation bubble thickness and producing low-loss calmed regions. It might be possible to control the flow at higher Re with significantly lower blowing ratios than in the present case. Natural transition in the undisturbed flow between jet events and its interaction with calmed regions would be an added complication at higher Re not seen in the present study. If the Re were sufficiently high so that separation did not occur in the uncontrolled case, it is unlikely that the jets would provide any benefit. Schulte and Hodson [27] noted that the presence of calmed regions produced by unsteady wake passing could not significantly lower the losses in an already attached boundary layer.

Conclusions

1. Synthetic vortex generator jets proved effective for controlling boundary layer separation on an LPT airfoil at very low Reynolds numbers. The separation bubble was effectively eliminated, and losses were lower than in a similar case with passive flow control.
2. The VGJ's prevent separation by bringing high momentum fluid into the near wall region and by promoting momentum transport through turbulent mixing.
3. The disturbance produced by the VGJ's behaves in many ways like the disturbance associated with a turbulent spot or a wake induced turbulent strip. The leading edge celerity of the disturbance is approximately $0.9U_\infty$, and the trailing edge celerity is about $0.45U_\infty$. A calmed region with a trailing edge celerity of $0.3U_\infty$ follows the disturbance. The calmed region is resistant to separation.
4. The adverse pressure gradient in the present case was strong enough so that the boundary layer did separate after the passage of the calmed flow. The separation bubble remained thin, however. The appearance of a disturbance did not immediately induce reattachment. The disturbance appeared initially in the outer part of the boundary layer. After some lag time the disturbance spread into the near wall region and caused reattachment.
5. While much has been learned regarding the effectiveness and physics of synthetic VGJ's in LPT flows, many questions remain regarding their applicability under different flow conditions and their optimal design. These questions have been discussed.

Acknowledgments

This work was sponsored by the NASA Glenn Research Center. The grant monitor is Dr. David Ashpis. Additional matching support was provided through a U.S. Naval Academy Recognition Grant. Mr. Dale Boyer of the Technical Support Department at the

Naval Academy fabricated the test section and the airfoils. Midshipman Dirk Heron conducted preliminary tests which led into the present study.

Nomenclature

B = blowing ratio
 C_f = skin friction coefficient
 $C_p = 2(P_T - P)/\rho U_\infty^2$, pressure coefficient
 c_μ = momentum coefficient
 D = diameter
 $F^+ = (0.442L_s)/(U_e T)$, dimensionless frequency
 $FSTI$ = free-stream turbulence intensity
 $H = \delta^*/\theta$, shape factor
 $K = (\nu/U_\infty^2)(dU_\infty/ds)$, acceleration parameter
 L_s = suction surface length
 M = jet to boundary layer mass flux ratio
 P = pressure
 P_T = upstream stagnation pressure
 $Re = U_e L_s/\nu$, exit Reynolds number
 Re_θ = momentum thickness Reynolds number
 S = jet holes per unit span
 s = streamwise coordinate, distance from leading edge
 T = jet oscillation period
 t = time
 U = mean streamwise velocity
 U_∞ = local free-stream velocity
 U_e = nominal exit free-stream velocity, based on inviscid solution
 V_{jet} = jet velocity
 \bar{u}' = time averaged rms streamwise fluctuating velocity
 \tilde{u}' = ensemble averaged rms streamwise fluctuating velocity
 $-\bar{u}'v'$ = time averaged turbulent shear stress
 $-\tilde{u}'\tilde{v}'$ = ensemble averaged turbulent shear stress
 y = cross-stream coordinate, distance from wall
 δ^* = displacement thickness
 $\lambda_\theta = Re_\theta^2 K$, Thwaites parameter
 ν = kinematic viscosity
 ρ = density
 θ = momentum thickness

Subscripts

ave = average over jet outpulse
 jet = jet condition
 max = maximum in jet cycle
 ∞ = free stream

References

- [1] Hourmouziadis, J., 1989, "Aerodynamic Design of Low Pressure Turbines," AGARD Lecture Series 167.
- [2] Mayle, R. E., 1991, "The Role of Laminar-Turbulent Transition in Gas Turbine Engines," ASME J. Turbomach., **113**, pp. 509–537.
- [3] Sharma, O. P., Ni, R. H., and Tanrikut, S., 1994, "Unsteady Flow in Turbines," AGARD Lecture Series 195, Paper No. 5.
- [4] Volino, R. J., 2002, "Separated Flow Transition Under Simulated Low-Pressure Turbine Airfoil Conditions: Part 1—Mean Flow and Turbulence Statistics," ASME J. Turbomach., **124**, pp. 645–655.
- [5] Volino, R. J., 2003, "Passive Flow Control on Low-Pressure Turbine Airfoils," ASME J. Turbomach., **125**, pp. 754–764.
- [6] Howell, R. J., Ramesh, O. N., Hodson, H. P., Harvey, N. W., and Schulte, V., 2001, "High Lift and Aft-Loaded Profiles for Low-Pressure Turbines," ASME J. Turbomach., **123**, pp. 181–188.
- [7] Gad-el-Hak, M., 2000, *Flow Control, Passive, Active, and Reactive Flow Management*, Cambridge University Press, Cambridge.

- [8] Lake, J. P., King, P. I., and Rivir, R. B., 2000, "Low Reynolds Number Loss Reduction on Turbine Blades With Dimples and V-Grooves," AIAA Paper 00-738.
- [9] Van Treuren, K. W., Simon, T., von Koller, M., Byerley, A. R., Baughn, J. W., and Rivir, R., 2001, "Measurements in a Turbine Cascade Flow Under Ultra Low Reynolds Number Conditions," ASME J. Turbomach., **124**, pp. 100–106.
- [10] Lee, J., Sloan, M. L., and Paynter, G. C., 1994, "Lag Model for Turbulent Boundary Layers Over Rough Bleed Surfaces," J. Propul. Power, **10**, pp. 562–568.
- [11] Sturm, W., Schuggenpflug, H., and Fottner, L., 1992, "Performance Improvements of Compressor Cascades by Controlling the Profile and Sidewall Boundary Layers," ASME J. Turbomach., **114**, pp. 477–486.
- [12] Johnston, J. P., and Nishi, M., 1990, "Vortex Generator Jets. Means for Flow Separation Control," AIAA J., **28**, pp. 989–994.
- [13] Compton, D. A., and Johnston, J. P., 1992, "Streamwise Vortex Production by Pitched and Skewed Jets in a Turbulent Boundary Layer," AIAA J., **30**, pp. 640–647.
- [14] McManus, K., Legner, H., and Davis, S., 1994, "Pulsed Vortex Generator Jets for Active Control of Flow Separation," AIAA Paper 94-2218.
- [15] Raghunathan, S., Watterson, J., Cooper, R., and Lee, S., 1999, "Short Wide Angle Diffuser With Pulse Jet Control," AIAA Paper 99-0280.
- [16] Sinha, S. K., and Pal, D., 1993, "Optimizing the Use of Acoustic Perturbation to Control Unsteady Boundary Layer Separation," FED (Am. Soc. Mech. Eng.), **157**, pp. 253–263.
- [17] Jacobson, S. A., and Reynolds, W. C., 1998, "Active Control of Streamwise Vortices and Streaks in Boundary Layers," J. Fluid Mech., **360**, pp. 179–211.
- [18] Miao, J. J., Lee, K. C., Chen, M. H., and Chou, J. H., 1991, "Control of Separated Flow by a Two-Dimensional Oscillating Fence," AIAA J., **29**, pp. 1140–1148.
- [19] Sinha, S. K., Pal, D., and Banerjee, D., 1996, "Control of Flow Separation Using the MEMS Approach: Proof of Concept Experiments," DSC (Am. Soc. Mech. Eng.), **59**, pp. 253–263.
- [20] Whitehead, L. A., Graham, D. J., Moore, F. A., Bolleman, B. J., Lake, R., and Dunwoody, A. B., 1996, "Investigation of Boundary Layer Flow Separation Control by Airfoil Surface Vibration," Can. Aeronautics Space J., **42**, pp. 213–219.
- [21] Amitay, M., and Glezer, A., 2002, "Role of Actuation Frequency in Controlled Flow Reattachment Over a Stalled Airfoil," AIAA J., **40**, pp. 209–216.
- [22] Huang, J., Corke, T. C., and Thomas, F. O., 2002, "Separation Control Over Low Pressure Turbine Blades," Bull. Am. Phys. Soc., DFD2002, **47**(10), p. 167.
- [23] Hultgren, L. S., and Ashpis, D. E., 2002, "Glow Discharge Plasma Active Control of Separation at Low Pressure Turbine Conditions," Bull. Am. Phys. Soc., DFD2002, **47**(10), pp. 167–168.
- [24] Bons, J. P., Sondergaard, R., and Rivir, R. B., 2001, "Turbine Separation Control Using Pulsed Vortex Generator Jets," ASME J. Turbomach., **123**, pp. 198–206.
- [25] Bons, J. P., Sondergaard, R., and Rivir, R. B., 2002, "The Fluid Dynamics of LPT Blade Separation Control Using Pulsed Jets," ASME J. Turbomach., **124**, pp. 77–85.
- [26] Gostelow, J. P., Walker, G. J., Solomon, W. J., Hong, G., and Melwani, N., 1997, "Investigation of the Calmed Region Behind a Turbulent Spot," ASME J. Turbomach., **119**, pp. 802–809.
- [27] Schulte, V., and Hodson, H. P., 1998, "Prediction of the Becalmed Region for LP Turbine Profile Design," ASME J. Turbomach., **120**, pp. 839–846.
- [28] Volino, R. J., 2002, "Separated Flow Transition Under Simulated Low-Pressure Turbine Airfoil Conditions: Part 2—Turbulence Spectra," ASME J. Turbomach., **124**, pp. 656–664.
- [29] Volino, R. J., Schultz, M. P., and Pratt, C. M., 2001, "Conditional Sampling in a Transitional Boundary Layer Under High Free-Stream Turbulence Conditions," ASME J. Fluids Eng., **125**, pp. 28–37.
- [30] Wills, J. A. B., 1962, "The Correction of Hot-Wire Readings for Proximity to a Solid Boundary," J. Fluid Mech., **12**, pp. 65–92.
- [31] Volino, R. J., and Simon, T. W., 1997, "Velocity and Temperature Profiles in Turbulent Boundary Layers Experiencing Streamwise Pressure Gradients," ASME J. Heat Transfer, **119**, pp. 433–439.
- [32] Ligrani, P. M., and Bradshaw, P., 1987, "Spatial Resolution and Measurement of Turbulence in the Viscous Sublayer Using Subminiature Hot-Wire Probes," Exp. Fluids, **5**, pp. 407–417.
- [33] Schlichting, H., 1979, *Boundary Layer Theory*, 7th ed. McGraw-Hill, New York.
- [34] Kaszeta, R. W., Simon, T. W., and Ashpis, D. E., 2001, "Experimental Investigation of Transition to Turbulence as Affected by Passing Wakes," ASME Paper 2001-GT-195.
- [35] Seifert, A., and Pack, L. G., 1999, "Oscillatory Control of Separation at High Reynolds Numbers," AIAA J., **37**, pp. 1062–1071.

Experiments With Three-Dimensional Passive Flow Control Devices on Low-Pressure Turbine Airfoils

Douglas G. Bohl

Ralph J. Volino

e-mail: volino@usna.edu

Department of Mechanical Engineering,
United States Naval Academy,
Annapolis, MD 21402

The effectiveness of three-dimensional passive devices for flow control on low pressure turbine airfoils was investigated experimentally. A row of small cylinders was placed at the pressure minimum on the suction side of a typical airfoil. Cases with Reynolds numbers ranging from 25,000 to 300,000 (based on suction surface length and exit velocity) were considered under low freestream turbulence conditions. Streamwise pressure profiles and velocity profiles near the trailing edge were documented. Without flow control a separation bubble was present, and at the lower Reynolds numbers the bubble did not close. Cylinders with two different heights and a wide range of spanwise spacings were considered. Reattachment moved upstream as the cylinder height was increased or the spacing was decreased. If the spanwise spacing was sufficiently small, the flow at the trailing edge was essentially uniform across the span. The cylinder size and spacing could be optimized to minimize losses at a given Reynolds number, but cylinders optimized for low Reynolds number conditions caused increased losses at high Reynolds numbers. The effectiveness of two-dimensional bars had been studied previously under the same flow conditions. The cylinders were not as effective for maintaining low losses over a range of Reynolds numbers as the bars. [DOI: 10.1115/1.2137743]

Introduction

Boundary layer separation is a known problem on some modern low-pressure turbine (LPT) airfoils, due to the strong adverse pressure gradients created when designers impose higher loading in an effort to improve efficiency and lower cost by reducing airfoil count in engines. Separation bubbles, particularly those which fail to close, can result in a significant loss of lift and a subsequent degradation of engine efficiency (e.g., Hourmouziadis [1], Mayle [2], and Sharma et al. [3]). The problem is particularly relevant in aircraft engines. Airfoils optimized to produce maximum power under takeoff conditions may still experience boundary layer separation at cruise conditions, due to the lower density and therefore lower Reynolds numbers at altitude. A component efficiency drop of 2% may occur between takeoff and cruise conditions in large commercial transport engines, and the difference could be as large as 7% in smaller engines operating at higher altitudes [4,5]. Prediction and control of suction side separation, without sacrifice of the benefits of higher loading, is therefore, crucial for improved engine design.

Separation on airfoils is complicated by boundary layer transition. Separated flow transition in the LPT has been the focus of several recent studies. Volino [6] provides a review and describes as follows the transition process on the suction side of a typical LPT airfoil. The strong acceleration on the leading section of the airfoil keeps the boundary layer thin and laminar, even in the presence of elevated freestream turbulence. In most cases Volino [6] observed that the boundary layer separated just downstream of the suction peak. If transition then occurred in the shear layer over the separation bubble, it caused the boundary layer to reattach.

A few recent studies have focused on control of transition and reattachment in the LPT. Some have used active devices. Huang et

al. [7] and Hultgren and Ashpis [8] employed high voltage electrodes to produce glow discharge plasma in a boundary layer to control separation. Bons et al. [4] used steady and pulsed vortex generator jets. Volino [9] used oscillating vortex generator jets with no net mass flow. Sieverding et al. [10] used adjustable devices built into the suction surface.

While active flow control provides a means for adjusting to changing flow conditions and in some cases the benefits of calmed regions [4,9], passive flow control holds the advantage of simplicity. Van Treuren et al. [11], Lake et al. [12], Murawski and Vafai [13], Byerley et al. [14], Volino [15], Sieverding [10], Vera et al. [16], and Zhang and Hodson [17] used various passive devices under LPT conditions to control separation and in many cases reduce losses. Most employed a relatively simple modification, such as a small trip wire or bar (essentially roughness), on the suction surface of an airfoil.

Successful flow control results in a thin, attached boundary layer at the trailing edge of an airfoil, thereby reducing losses. The consensus of the studies listed above is that a device on the suction surface should be placed at or slightly downstream of the pressure minimum. This is a logical result, since the effects of a device farther upstream would be damped by the favorable pressure gradient, and a device too far downstream would lie under the separation bubble and be ineffective. Volino [15] used rectangular bars and found that the optimal bars were not large enough to immediately trip the boundary layer to turbulent, but instead allowed a small separation bubble to form. The bars introduced small disturbances that grew and caused transition and reattachment to move upstream of their location in the uncontrolled case, as explained in Volino and Bohl [18]. The optimal bar height depended on the flow conditions. As Re or freestream turbulence is lowered, the separation bubble becomes larger, so a larger bar is needed to produce enough of a disturbance to move transition sufficiently far upstream. A flow control device producing too small a disturbance will allow a larger separation bubble than desired, resulting in a thicker boundary layer downstream of reattachment and higher losses. Similarly, too large a disturbance will

Contributed by the International Gas Turbine Institute (IGTI) of ASME for publication in the JOURNAL OF TURBOMACHINERY. Manuscript received October 1, 2004; final manuscript received December 1, 2004. IGTI Review Chair: K. C. Hall. Paper presented at the ASME Turbo Expo 2005: Land, Sea and Air, Reno, NV, June 6–9, 2005, Paper No. GT2005-68969.

move transition farther upstream than necessary, resulting in a longer turbulent region and higher losses. Volino [15], Sieverding et al. [10], and Zhang and Hodson [17] all found that under steady flow conditions, devices optimized for low Re tend to increase losses at high Re . Devices optimized for high Re can be too small to be effective at low Re . Unsteady wakes from upstream airfoils promote transition and reattachment, and Zhang and Hodson [17] found that in unsteady flow optimal control was achieved using smaller devices than in comparable steady flow cases. This made it possible in unsteady flow to reduce losses with a single device over a wider range of Re .

Passive flow control devices of various geometries have been tested, but it is still uncertain if any particular device is superior. In preliminary testing, Volino [15] considered trip wires, rectangular bars, and delta wing vortex generators. All produced similar results. Sieverding et al. [10] found that straight trip wires were somewhat better than rows of spherical roughness elements, but only a limited number of cases were tested. Lake et al. [12] found dimples superior to other devices, presumably because the dimples produced less blockage than devices that protruded into the flow. Again, however, the number of cases considered was limited, and more recent evidence [15,17] suggests that optimal devices should be quite small and produce minimal blockage even if they do extend into the flow. Zhang and Hodson [17] noted differences in transition location with straight and “wavy” trip wires and rectangular bars. The sharp backward facing step on a bar, for example, produced an earlier transition than a round trip wire of the same height. Still, this does not preclude that a bar and a slightly larger wire could produce comparable results.

It is still possible that some devices might prove better for reducing losses than others. Reynolds number can vary by an order of magnitude during engine operation given the change in ambient pressure between takeoff and cruise. Since passive devices by definition cannot be adjusted as conditions change, it is highly desirable to use devices that reduce losses over as large a Reynolds number range as possible. Given the potential payoff of a more efficient engine, it is worthwhile to further consider passive flow control devices of different geometries.

A row of small vertical cylinders is considered in the present study. The cylinders are located at the pressure minimum on the suction surface and the spacing between cylinders is varied. The geometry was chosen in the hope that in comparison to two-dimensional bars or trips wires of the same height, isolated elements might produce a stronger disturbance due to the three-dimensional nature of the flow around them, while presenting less blockage due to the gaps between elements. The net result would presumably be successful separation control with lower losses. Experimental conditions match the low freestream turbulence cases of Volino [15]. Details of the experimental conditions and the results are presented below.

Experiments

Experiments were conducted in a low speed wind tunnel, described by Volino et al. [19]. Briefly, air enters through blowers and passes through a honeycomb, a series of screens, two settling chambers, and a three-dimensional contraction before entering the test section. At the exit of the contraction, the mean velocity is uniform to within 1%. The freestream turbulence intensity is $0.5\% \pm 0.05\%$. Nearly all of this freestream “turbulence” is actually streamwise unsteadiness at frequencies below 20 Hz and is not associated with turbulent eddies. The root-mean-square intensities of the three components of the unsteadiness are 0.7%, 0.2%, and 0.2% in the streamwise, pitchwise, and spanwise directions, respectively.

The test section, shown in Fig. 1, follows the contraction and consists of the passage between two airfoils. Details are listed in Table 1 and more information is available in Volino [6]. A large span to chord ratio of 4.3 was chosen to insure two-dimensional flow at the spanwise centerline of the airfoils, where all measure-

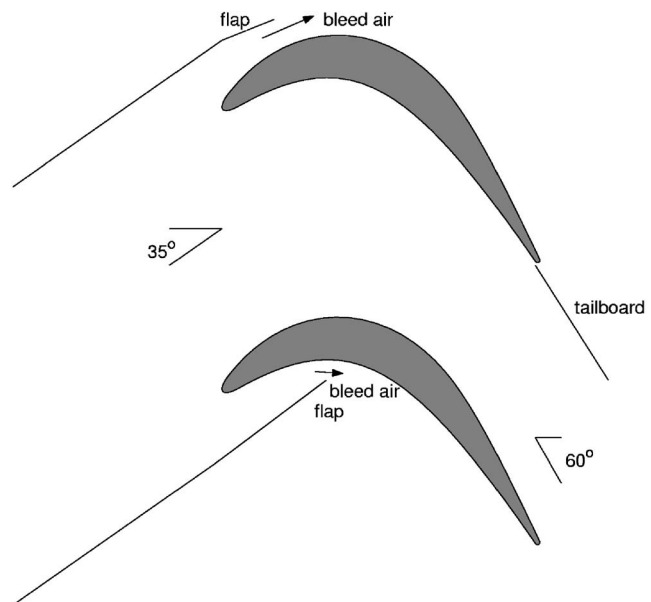


Fig. 1 Schematic of the test section

ments were made. Upstream of each airfoil are flaps, which control the amount of bleed air allowed to escape from the passage. The flaps, along with a tailboard on the pressure side of the passage, are adjusted to produce the correct leading edge flow and pressure gradient along the airfoils. The flow in the passage matches that in a multiblade cascade. The geometry of the passage corresponds to that of the Pak-B airfoil, which is an industry supplied research airfoil that is representative of a modern LPT design. It has been used in several studies, as noted in Volino [6].

Experimental conditions match the smooth airfoil baseline cases of Volino [6], who considered five Reynolds numbers ($Re = 25,000, 50,000, 100,000, 200,000,$ and $300,000$). Reynolds numbers are based on the exit velocity from the passage and the suction surface length, L_s . Comparison data from cases with passive-bar flow control are from Volino [15]. The bars were of uniform rectangular cross section and extended along the airfoil, as shown in Fig. 2. The trailing edge of the bar was located at $s/L_s = 0.51$, near the suction surface velocity peak. All bars were 6 mm wide in the streamwise direction. Bar heights of 0.4, 0.8, and 1.6 mm were used. The bar heights were all less than 1% of L_s . They compare to local boundary layer thickness at the bar location of about 3.8, 2.7, 2.0, 1.4, and 1.2 mm in the base line $Re = 25,000$ – $300,000$ cases, respectively.

A row of small vertical cylinders is used in the present experimental cases. The cylinders are $D = 6$ mm in diameter with one end affixed to the suction surface and the other extending into the flow. The cylinders are located in a line at the suction peak, in the same location as the bars described above, as shown in Fig. 2. Cylinder heights of 0.4 and 1.6 mm were considered, matching the smaller and larger bar heights of Volino [15]. Center to center cylinder spacings ranging from a pitch, P , of $1D$ (i.e., the cylinders were touching) to $30D$ were considered.

Measurements. Pressure surveys were made for each case using a pressure transducer (0–870 Pa range Validyne transducer) and a Scanivalve. Stagnation pressure was measured with a pitot tube upstream of the passage inlet, and 11 pressure taps were located on each airfoil along their spanwise centerlines. The uncertainty in C_p is 7% at $Re = 25,000$, and 4% in other cases. Most of this uncertainty is due to bias error. Stochastic error was minimized by averaging pressure transducer readings over a 10 s period. The flow control cylinders were moved in the spanwise di-

Table 1 Test section parameters

Axial chord (mm)	True chord (mm)	Pitch (mm)	Span (mm)	Suction side, L_s (mm)	Inlet flow angle	Exit flow angle	$\frac{U_e}{U_{inlet}}$
153.6	170.4	136.0	660.4	228.6	35 deg	60 deg	1.64

rection allowing documentation with the pressure taps directly downstream of the center of one cylinder and with the taps mid-way between the centers of two adjacent cylinders.

Profiles of the streamwise velocity component in the suction side boundary layer were measured for the $Re=50,000$ and $300,000$ cases near the trailing edge at $s/L_s=0.944$. Profiles were measured at several spanwise locations relative to the position of the upstream cylinders. Data were acquired with a hot-wire anemometer (AA Lab Systems model AN-1003) and a single sensor boundary layer probe (TSI model 1218-T1.5). The sensor diameter is $3.8 \mu m$, and the active length is 1.27 mm . At each measurement location, data were acquired for 26 s at a 20 kHz sampling rate (2^{19} samples). Data were acquired at 60 wall normal locations in each profile, extending from the wall to the freestream, with most points concentrated in the near wall region. The closest point was within 0.1 mm of the wall, which corresponds to $y/L_s=0.0004$ and between 0.02 and 0.04 boundary layer thicknesses. Uncertainties in the mean velocity are $3\text{--}5\%$ except in the very near wall region where near-wall corrections (Wills [20]) were applied to the mean velocity. Uncertainties in the momentum and displacement thicknesses computed from the mean profiles are 10% . Uncertainty in the shape factor, H , is 8% . The uncertainty in the fluctuating streamwise velocity is below 10% , except in the very near wall region ($y < 1 \text{ mm}$, $y/L_s < 0.004$) of

the $Re=300,000$ cases, where spatial averaging effects, due to the finite length of the hot-wire sensor, may become important. This is discussed in Volino [6].

Results

Pressure Profiles. Suction side pressure profiles for the cases with larger (1.6 mm high) cylinders are shown in Figs. 3–5. Also shown in each figure are the corresponding baseline results from Volino [6], the 1.6-mm -thick bar case results from Volino [15], and an inviscid solution for flow through the passage. Figure 3 shows results at $Re=25,000$ with various cylinder spacings and the pressure taps directly downstream of one cylinder. The data agree with the inviscid solution in the favorable pressure gradient region. The near wall flow slows as it approaches a cylinder or bar, causing a drop in the measured C_p below the inviscid solution at the fifth pressure tap. If the boundary layer separates and does not reattach, there is a drop in the suction peak, as indicated by low C_p values. In addition to this effect, if the blockage caused by a bar or cylinder is sufficiently high, the streamlines immediately downstream will be displaced as they flow over the sixth pressure tap, which may cause the measured local C_p to either rise or fall relative to the inviscid solution, depending on the geometry of a particular case. For controlling separation, cylinders with spacing of $P=2D$ or more are ineffective at $Re=25,000$. There is a plateau in C_p in the adverse pressure gradient region extending to the trailing edge, indicating a separation bubble that does not reattach. The $P=1D$ (touching) cylinders and the solid bar result in a large separation bubble which appears to be starting to reattach by the trailing edge, as indicated by the drop in C_p back toward the inviscid value at the last pressure tap. Figure 4 shows the results at $Re=50,000$ with the pressure taps directly downstream of one cylinder ($z/P=0$, Fig. 4(a)) and with the taps downstream of the midpoint between adjacent cylinders ($z/P=0.5$, Fig. 4(b)). In the base line case, the boundary layer does not reattach.

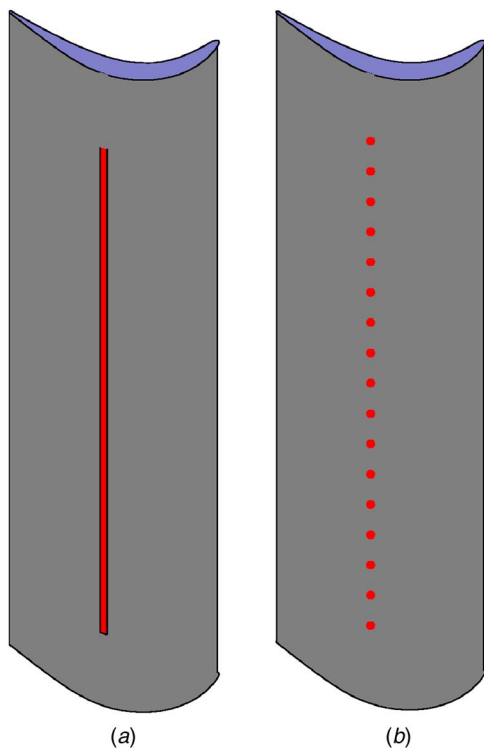


Fig. 2 Scale drawing of suction side airfoil showing location of (a) bar, or (b) cylinders

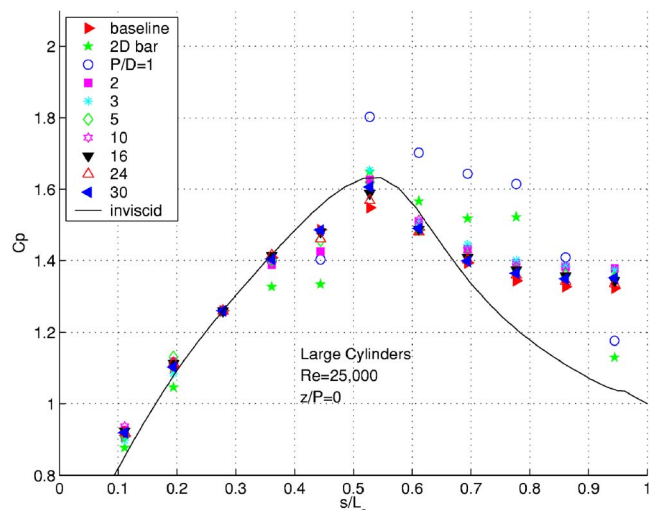


Fig. 3 Pressure profiles, large cylinders, $Re=25,000$, $z/P=0$

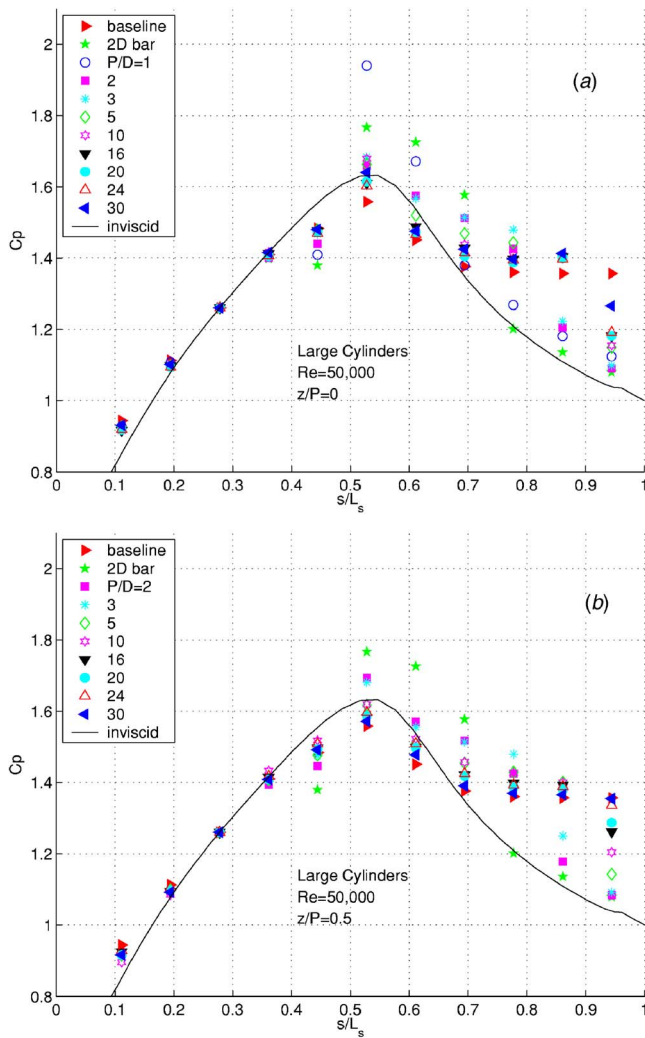


Fig. 4 Pressure profiles, large cylinders, $Re=50,000$, (a) $z/P=0$, (b) $z/P=0.5$

With $P=1D$ or the solid bar, reattachment moves upstream to $s/L_s=0.78$. With $P=2D$ reattachment occurs at $s/L_s=0.86$. With $P>2D$ the effect of the cylinders is not observed until the last pressure tap, but even with $P=30D$ there is some effect on C_p at $s/L_s=0.94$ and $z/P=0$. As the spacing increases, the C_p values increase from the inviscid solution toward the baseline case value. At $z/P=0.5$ and $s/L_s=0.94$, C_p is affected for spacings up to $20D$, although not as strongly as it is at $z/P=0$. For $P=24D$ and $30D$, the cylinders are too far apart to affect C_p at $z/P=0.5$. The results at $Re=100,000$ are shown in Fig. 5. In the base line case, there is a clear separation bubble, and it reattaches near the trailing edge. With $P\leq 3D$, the separation is essentially eliminated. With $P=5D$ there is a separation, but reattachment by $s/L_s=0.78$. For $P\leq 5D$, the C_p values are nearly uniform across the span. For $10D\leq P\leq 30D$, the boundary layer appears to be at least starting to reattach by $s/L_s=0.86$, with the effect on C_p greater at $z/P=0$. Results for the $Re=200,000$ cases (not shown) are similar to those described above. The boundary layer separates in the base line case and reattaches by $s/L_s=0.86$. Cylinders with $P\leq 16D$ effectively suppress the separation across the span. For $P>16D$, the boundary layer is attached at $s/L_s=0.78$ and $z/P=0$, but is still separated at $z/P=0.5$. At $Re=300,000$ there is only a small separation bubble in the base line case, and it reattaches by $s/L_s=0.78$. Cylinders with spacing up to $30D$ appear to suppress this small bubble across the span.

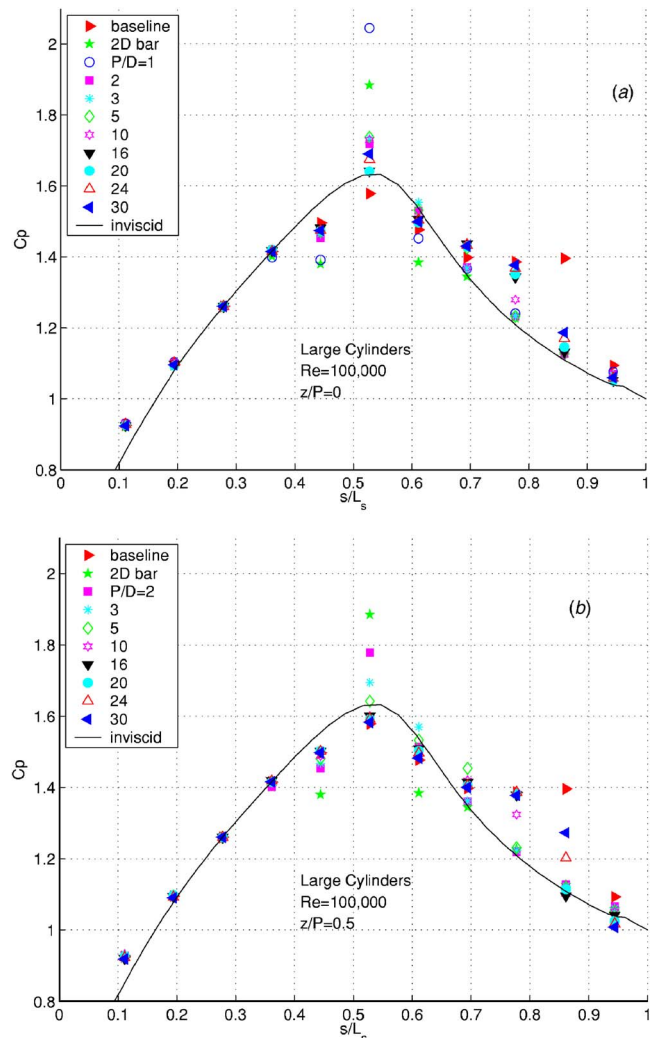


Fig. 5 Pressure profiles, large cylinders, $Re=100,000$, (a) $z/P=0$, (b) $z/P=0.5$

Comparing the results at $z/P=0$ and $z/P=0.5$, the spanwise influence of each cylinder can be estimated. If the region affected by the cylinder is assumed to spread linearly in the spanwise direction as the flow convects downstream, the half angle for the spreading is between roughly 30 and 40 deg. Changes in C_p at $z/P=0.5$ could be due to local turbulence arising from the cylinder induced disturbances. It is also possible, however, that these changes in C_p are due to changes in the mean flow resulting from the cylinder induced changes at $z/P=0$.

The smaller (0.4 mm high) cylinders and bar are ineffective at $Re=25,000$ and $50,000$. The boundary layer separates and does not reattach. At $Re=100,000$, as shown in Fig. 6, the cylinders cause the first indication of reattachment to move upstream from near the trailing edge to $s/L_s=0.78$ or 0.86 . Cylinder spacings up to $10D$ were considered, and the C_p values decrease from the base line case values toward the inviscid solution as P is decreased. No significant spanwise variation in C_p was observed. The results at $z/P=0.5$ are essentially the same as those shown in Fig. 6 for $z/P=0$. Results for the $Re=200,000$ cases are shown in Fig. 7. The results are very similar to those of the $Re=100,000$ cases, but with reattachment shifted about $0.08L_s$ upstream. When $Re=300,000$ the base line separation bubble is small, and cylinders effectively eliminate it for all value of P .

The presumably more complex three-dimensional flow around isolated ($P>1D$) cylinders did not produce disturbances better

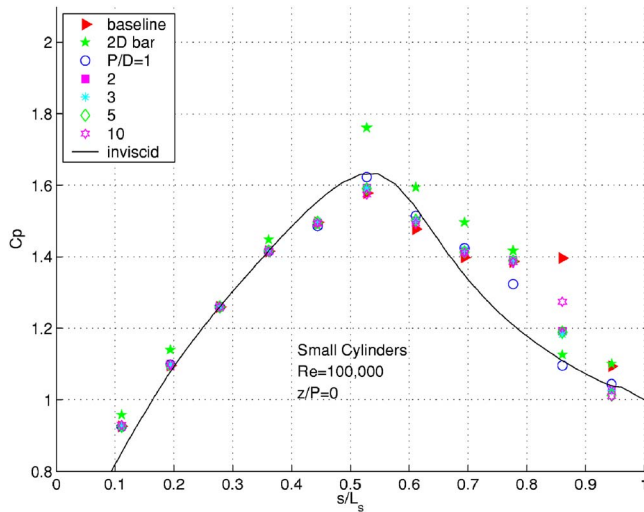


Fig. 6 Pressure profiles, small cylinders, $Re=100,000$, $z/P=0$

able to control separation than the touching ($P=1D$) cylinders or two-dimensional bars. In fact, the opposite was observed. The pressure profiles show that as the spacing between cylinders increases, their ability to promote reattachment decreases. This is not simply due to the finite spanwise influence of each cylinder, as very little spanwise variation was observed for cases with $P < 10D$. Whether increasing the spacing results in reduced flow blockage and losses will be considered next as the velocity profile results are considered.

Velocity Profiles. Mean and fluctuating streamwise velocity profiles for the large cylinder $Re=50,000$ cases at $z/P=0$ are shown in Fig. 8. Data were acquired near the trailing edge ($s/L_s = 0.94$). The base line case shows a thick separation bubble in the mean profile and a small peak in u' in the shear layer over the bubble. The two-dimensional bar case exhibits a fully attached turbulent mean profile shape and a typical turbulent u' profile with a near wall peak. For the cases with cylinder spacing up to $P=5D$, the mean profiles appear attached and turbulent, but the trend is toward a less full profile as P increases. This trend continues for the cases with $P \geq 20D$, with the mean profiles in these cases appearing only partially reattached. The peaks in the u' profiles increase in magnitude and move farther from the wall as the cylinder spacing is increased. High peaks away from the wall

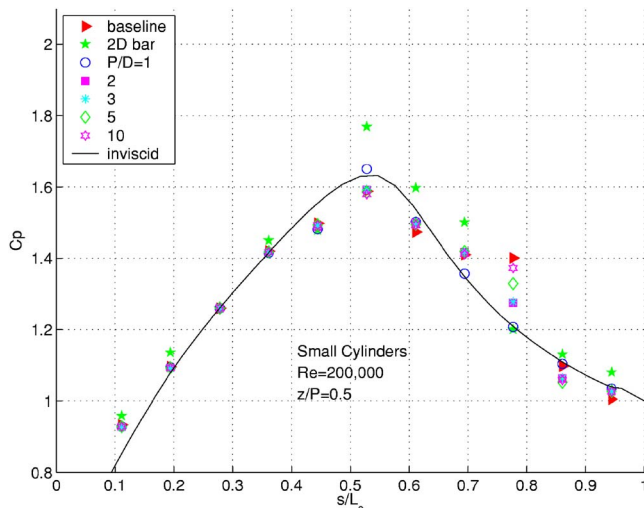


Fig. 7 Pressure profiles, small cylinders, $Re=200,000$, $z/P=0$

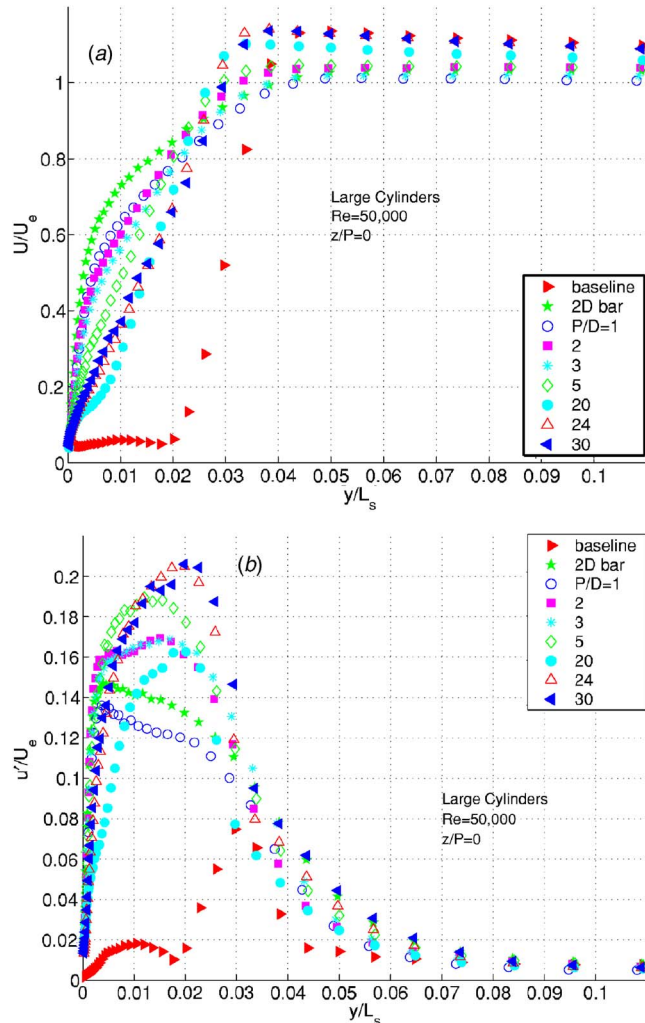


Fig. 8 Trailing edge velocity profiles, large cylinders, $Re=50,000$, $z/P=0$, (a) U/U_e , (b) u'/U_e

are typical of transitioning and reattaching boundary layers. Transition begins in the shear layer over the separation bubble, so u' should be high at this location. The high u' peaks result from the switching between intermittently attached-turbulent-like and separated-laminar-like states. Figure 9 shows the profiles at $z/P=0.5$. For $P \leq 5D$, the profiles appear essentially the same as those at $z/P=0$. For $P \geq 20D$ the mean profiles show a separation bubble, somewhat thinner than that of the base line case, and u' profiles with only a small peak in the shear layer over the separation bubble. Figure 10 shows the velocity profiles at several spanwise positions for the $P=30D$ case. The progression from attached flow at $z/P=0$ to separated flow at $z/P=0.5$ is clear. The profiles at $z/P=0.13$ and 0.20 are on the edge of the attached flow region with u' peaks between the high peaks at low z/P and the small shear layer peaks at higher z/P . The influence of the cylinders to a spanwise position between $z/P=0.13$ and 0.20 suggests a half angle for the spread of the cylinder influence of about 20° . The velocity profile data of Figs. 8–10 are consistent with the conclusions drawn from the corresponding pressure coefficient data of Fig. 4.

The information concerning separation in the mean profiles can be presented in terms of the shape factor, H . The shape factor rises to about 4 when a laminar boundary layer separates, and reaches higher values as a separation bubble thickens. This is due to an increase in the displacement thickness while the momentum thickness remains nearly constant. If the boundary layer reattaches, the

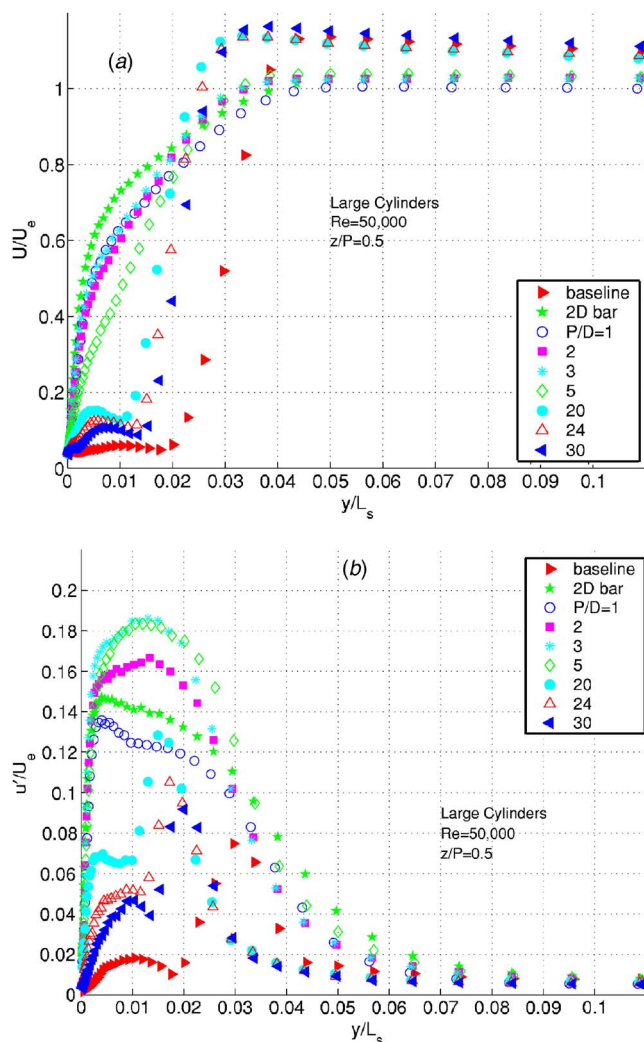


Fig. 9 Trailing edge velocity profiles, large cylinders, $Re=50,000$, $z/P=0.5$, (a) U/U_e , (b) u'/U_e

displacement thickness drops and the momentum thickness begins to rise. The shape factor reaches a turbulent value of about 1.4 after recovering from the separation. Figure 11 shows H as a function of z/P for the $Re=50,000$ cases with the larger cylinders. In the base line case, $H=6.5$, indicating a thick separation bubble. With the two-dimensional bar, $H=1.6$, indicating that the boundary layer has reattached and is nearing fully developed turbulent conditions. With cylinder spacing up to $P=5D$, H is spanwise uniform. With $P=5D$, H is about 2.3, indicating that the boundary layer has reattached but is not fully recovered from the separation. For $P \geq 20D$, $H \approx 3$ at $z/P=0$, indicating the boundary layer has just begun to reattach at this location. For $P \geq 20D$ and higher z/P , H is between 4 and 5.5 indicating the boundary layer is still separated. These values are still below the base line value of 6.5, however, indicating that even the widely spaced cylinders are effective in keeping this separation bubble thinner.

Velocity profiles for the $Re=300,000$ cases with the larger bar and cylinders are shown in Figs. 12–14. Figure 12 shows the profiles at $z/P=0$. The mean profiles show that the boundary layer is attached in all cases. The u' peaks are near the wall, as expected for attached turbulent boundary layers. The base line case has the highest u' peak, indicating that it is the case with the least developed turbulence. The bar and cylinders move transition upstream, resulting in a more developed turbulent boundary layer by the trailing edge. Both the mean and u' profiles collapse for the cases with $P \geq 20D$. This suggests that the cylinders are far enough

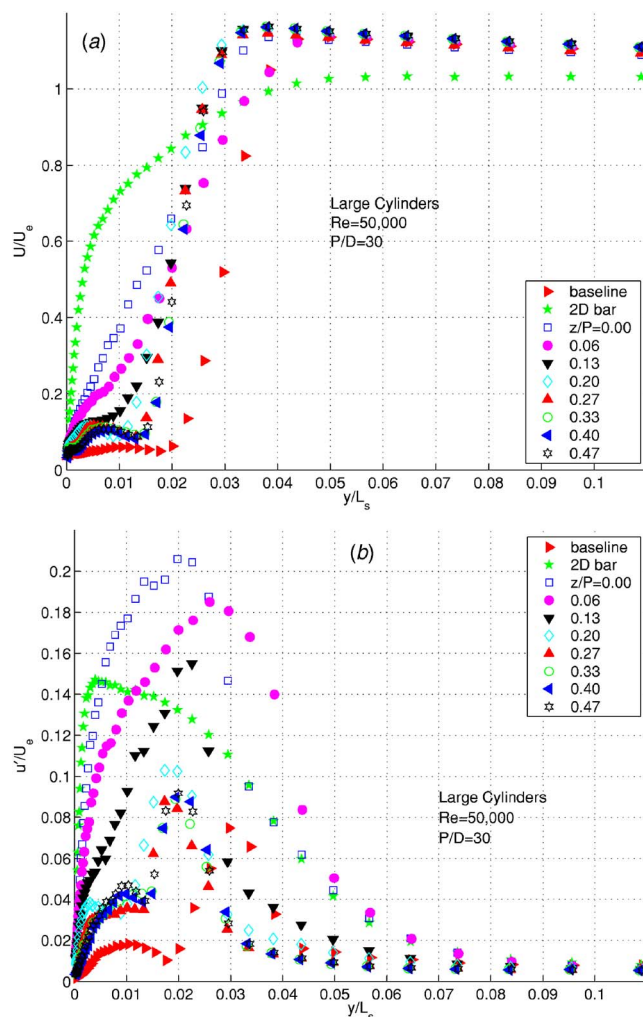


Fig. 10 Trailing edge velocity profiles, large cylinders, $Re=50,000$, $P/D=30$, (a) U/U_e , (b) u'/U_e

apart in these cases so that they act as if isolated from each other. Both the mean and u' profiles show that the boundary layer becomes thicker as the cylinder spacing is decreased. The $P=1D$ case has a second u' peak away from the wall that is not present

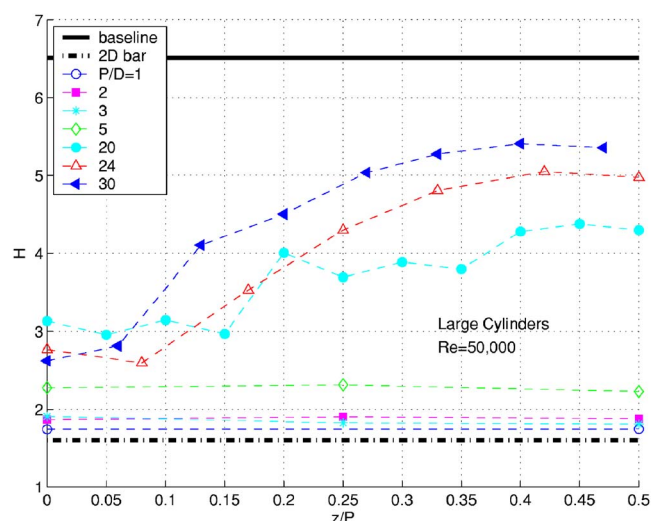


Fig. 11 Shape factor, H , at trailing edge, large cylinders, $Re=50,000$

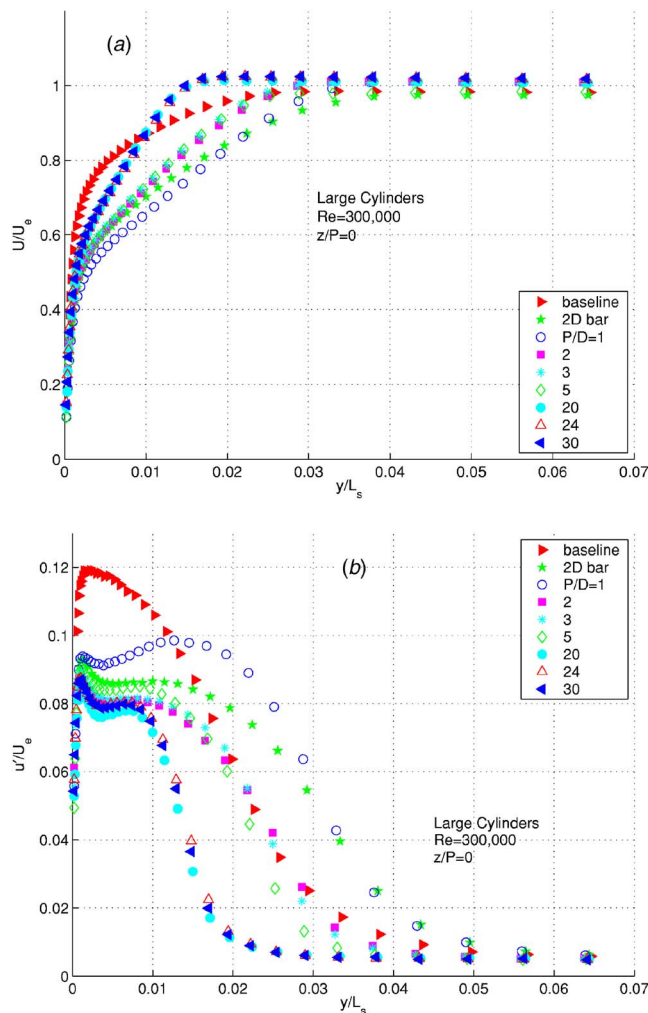


Fig. 12 Trailing edge velocity profiles, large cylinders, $Re=300,000$, $z/P=0$, (a) U/U_e , (b) u'/U_e

in the two-dimensional bar case. The touching cylinders appear to generate more turbulence than the bar. Figure 13 shows the profiles at $z/P=0.5$. The profiles for the $P=24D$ and $30D$ cases are very similar to the baseline results, again suggesting that with large enough spacing the cylinders are effectively isolated from each other and cannot directly influence the flow across the entire span. As P is reduced, the boundary layer becomes thicker, and u' assumes a more turbulent like shape. Figure 14 shows the profiles at several spanwise positions for the $P=30D$ case. The cylinders appear to influence the boundary layer u' nearly uniformly from $z/P=0$ to $z/P=20$. For $z/P>27$, the cylinders have little influence and the profiles are very similar to the base line case profiles. The spanwise extent of the cylinder influence spreads at a half angle of about 20 deg for a strong effect on the boundary layer and about 30 deg for some effect.

Figure 15 shows the shape factor at $s/L_s=0.94$ for the profiles of the $Re=300,000$ cases with the larger cylinders. The boundary layer is attached, so the shape factor is between 1.4 and 1.7 in all cases. Figure 16 shows the momentum thickness for these cases. The momentum thickness is related to losses in the boundary layer, and in cases with equal shape factor and exit flow angle, the momentum thickness is directly proportional to profile losses (Howell et al. [21]). In the $Re=50,000$ cases, the large variation in H (Fig. 11) precludes a comparison of losses based on θ , but with the smaller range of H at $Re=300,000$ (Fig. 15) the comparison is appropriate. Figure 16 shows that the cylinders cause a rise in momentum thickness above the base line case value and

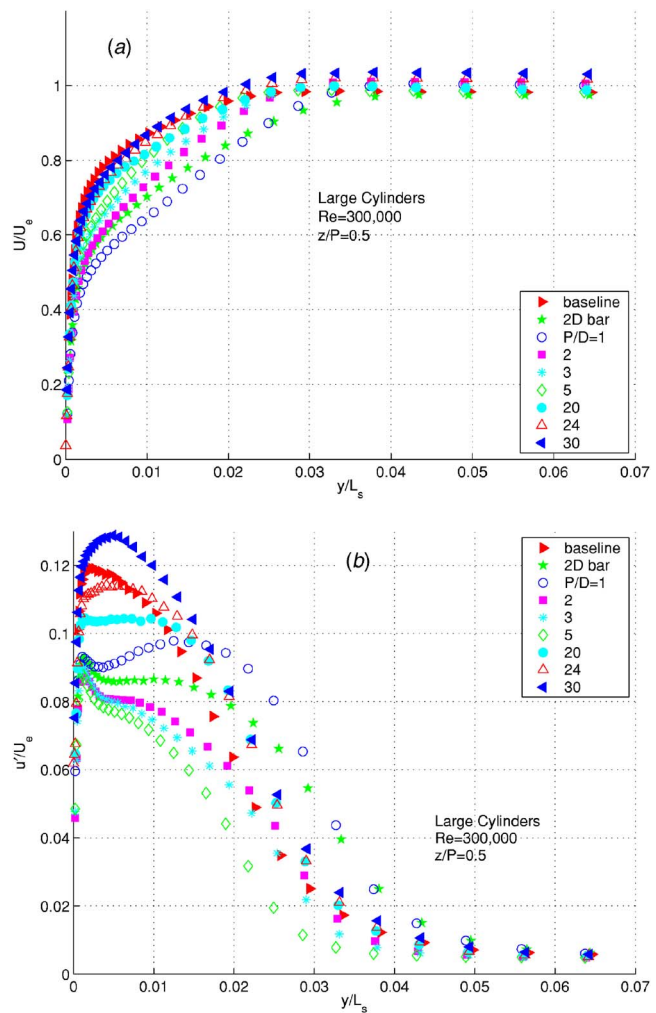


Fig. 13 Trailing edge velocity profiles, large cylinders, $Re=300,000$, $z/P=0.5$, (a) U/U_e , (b) u'/U_e

that the effect increases as cylinder spacing is decreased. Since the separation bubble is small even in the base line case, the cylinders and bars add an unnecessary disturbance and increase losses. The more widely spaced cylinders cause less blockage and create less of a disturbance, therefore the losses are lower.

Velocity profiles for the $Re=50,000$ cases with the smaller bar and cylinders are shown in Fig. 17. Cylinder spacings up to $P=5D$ were considered. No variation was observed between the results from different spanwise locations, so only the results from $z/P=0$ are shown. The boundary layer did not reattach for cases with $P\geq 2D$, although the separation bubble was slightly thinner and there was a slight increase in the u' peak compared to the base line case. With $P=1D$ the boundary layer appears to be on the verge of reattachment, and with the two-dimensional bar the boundary layer has just begun to reattach. The smaller cylinders are inadequate for control of the boundary layer at this Reynolds number, as previously indicated by the pressure profiles.

The effect of the smaller cylinders on the velocity profiles at $Re=300,000$ are shown in Fig. 18. No spanwise variation was observed, so only results from $z/P=0$ are shown. The mean profile for the $P/D=1$ case is noticeably different than those for the other cases, including the two-dimensional (2D) bar case. As was noted above, the touching cylinders apparently generate more turbulence than the 2D bar, resulting in a thicker boundary layer. As was the case with the larger cylinders (Fig. 12), the smaller cylinders cause a drop in the u' peak from the base line case value, indicating that the cases with cylinders are closer to fully devel-

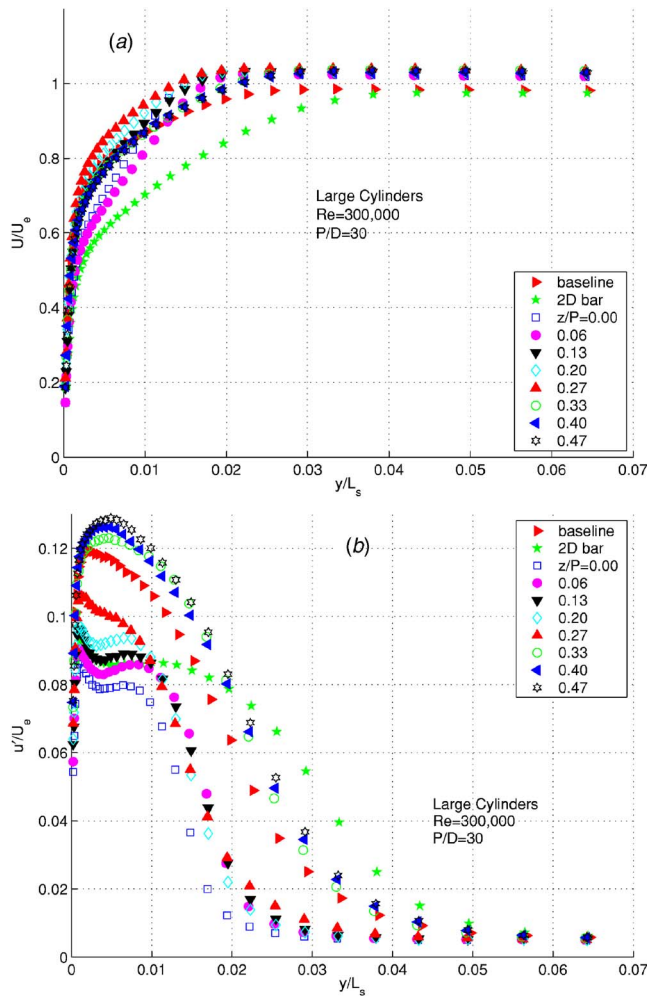


Fig. 14 Trailing edge velocity profiles, large cylinders, $Re=300,000$, $P/D=30$, (a) U/U_e , (b) u'/U_e

oped turbulent behavior. Shape factors are shown in Fig. 19 as a function of spanwise position. There is little variation between cases, as expected since the separation bubble is small and the boundary layer has fully reattached in all cases. The momentum thickness is shown in Fig. 20. All of the cases with cylinders have

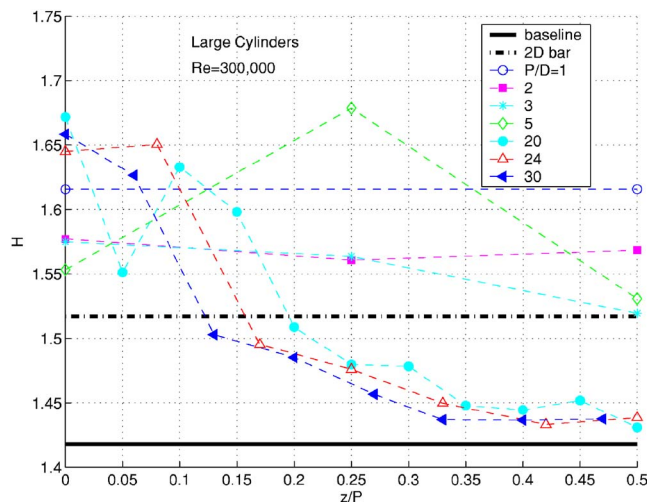


Fig. 15 Shape factor, H , at trailing edge, large cylinders, $Re=300,000$

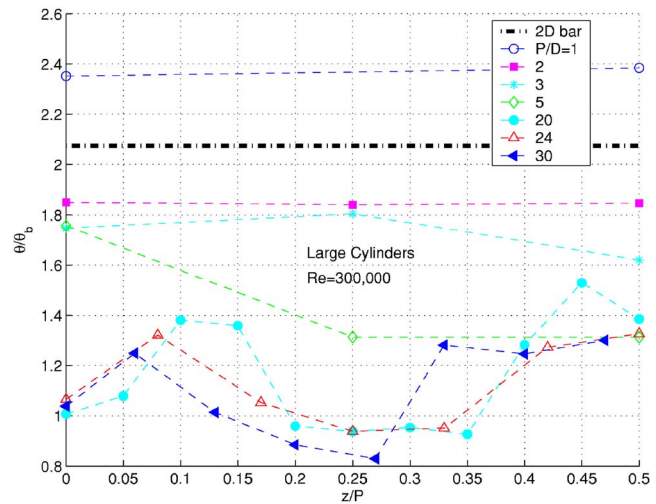


Fig. 16 Momentum thickness at trailing edge, large cylinders, $Re=300,000$

higher momentum thickness than the base line case. The case with $P=1D$ has the highest values, again indicating that the touching cylinders generate higher losses than the two-dimensional bars or more widely spaced cylinders.

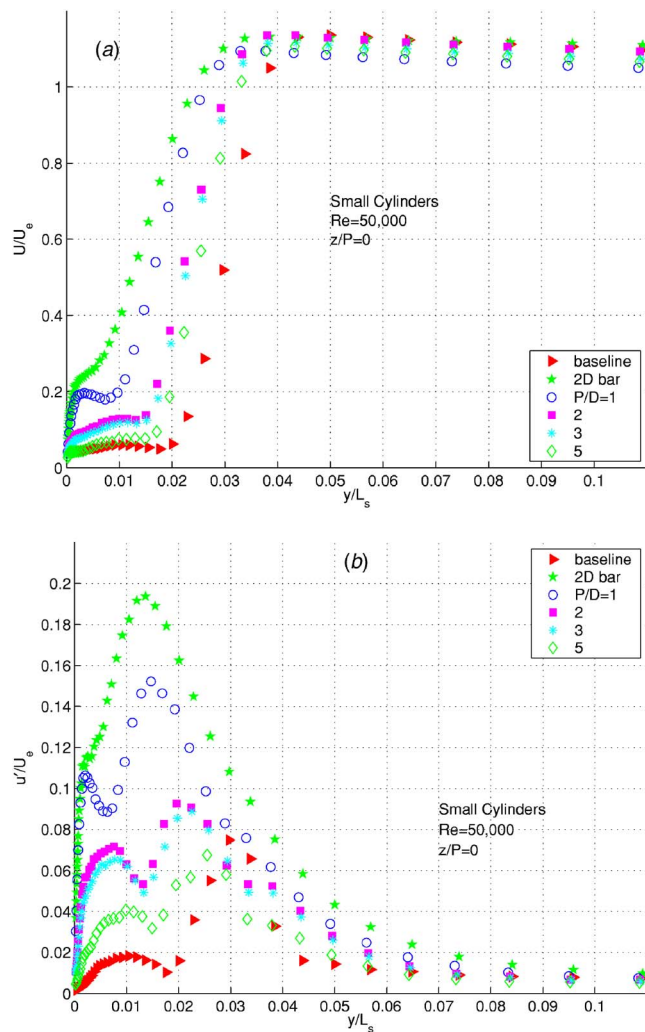


Fig. 17 Trailing edge velocity profiles, small cylinders, $Re=50,000$, $z/P=0$, (a) U/U_e , (b) u'/U_e

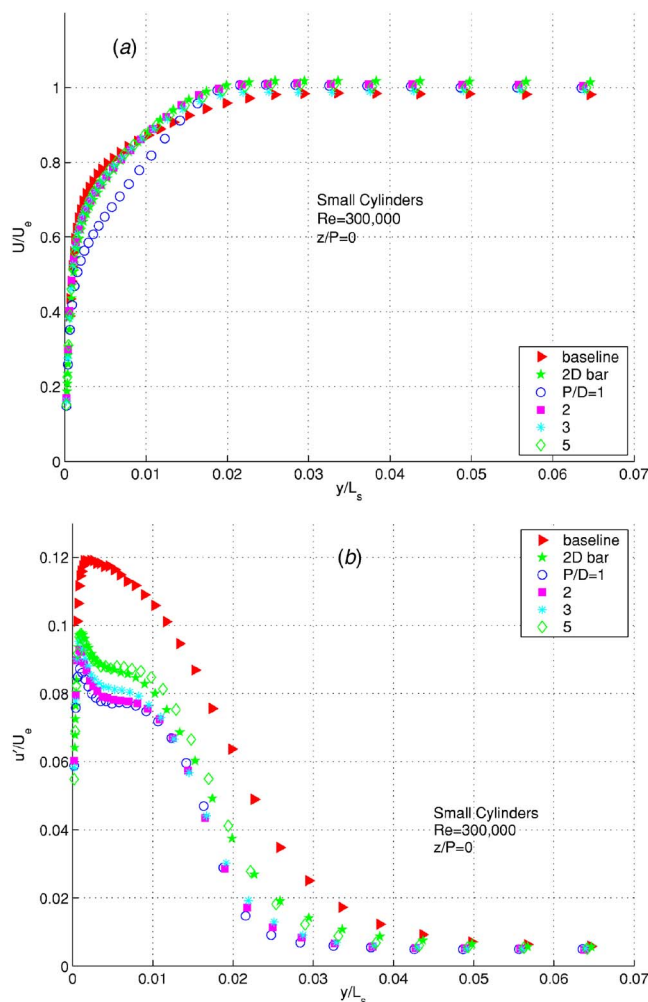


Fig. 18 Trailing edge velocity profiles, small cylinders, $Re=300,000$, $z/P=0$, (a) U/U_e , (b) u'/U_e

Discussion

The results presented above suggest that the half angle for the spreading of the disturbances from the cylinders is about 30 deg. This is a rough estimate due to the finite spacing between pressure tap locations and the finite number of cylinder spacings investi-

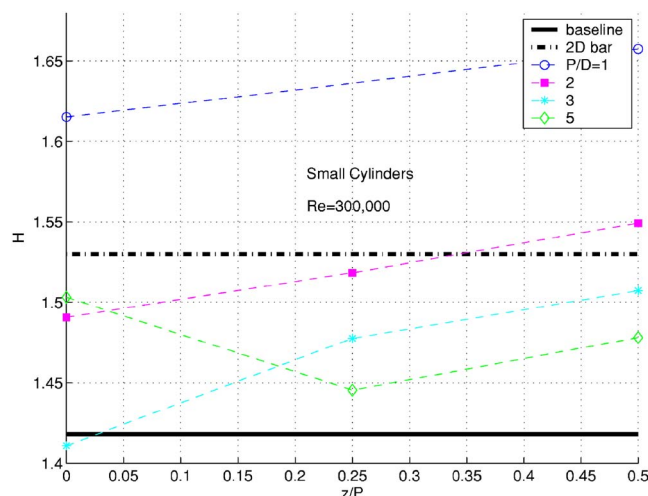


Fig. 19 Shape factor, H , at trailing edge, small cylinders, $Re=300,000$

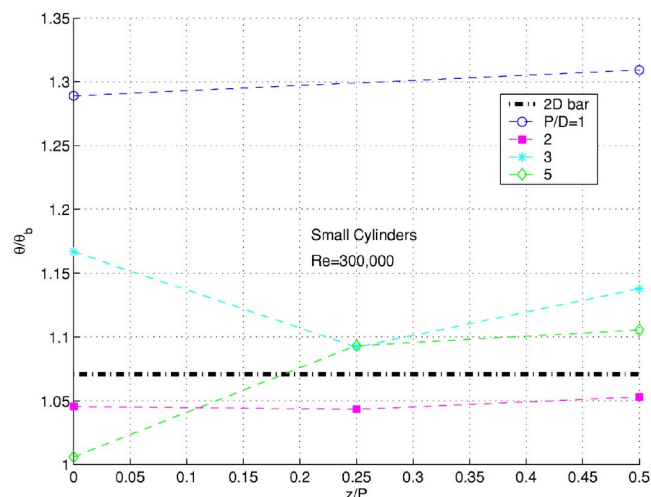


Fig. 20 Momentum thickness at trailing edge, small cylinders, $Re=300,000$

gated, but the half angle roughly agrees with the spreading angle for turbulent spots in an adverse pressure gradient, as given by D'Ovidio et al. [22]. This angle suggests that a cylinder spacing of between $P/D=5$ and $P/D=10$ is necessary to insure flow control across the span. The velocity profiles showed good spanwise uniformity for $P/D < 10$.

The optimal spacing for spanwise disturbances was investigated in an analytical study by Tumin and Ashpis [23]. They considered disturbances in both favorable and adverse pressure gradient flows, including the favorable pressure gradient found in the upstream region of the present test section. Although these results do not apply directly to the adverse pressure gradient region of the present study, they can be extrapolated to the present conditions. They suggest an optimal spacing for maximum disturbance growth in the $Re=50,000$ cases of $P/L_s \approx 0.03$. For the $Re=300,000$ cases, the optimal spacing would be $P/L_s \approx 0.012$. With the present cylinder diameter of 6 mm, these spacings correspond to $P/D=1$ and $P/D=0.4$, respectively, and could not be achieved unless the cylinders were touching. Consistent with this, the present results show that the disturbance created by the cylinders decreases as the spacing increases. To better test the Tumin and Ashpis [23] results, however, smaller diameter, separated cylinders with the recommended spacing should be considered.

The results at $Re=50,000$ show that the larger cylinders with the closest spacing are needed to effectively control separation. At $Re=300,000$, the separation bubble is small in the base line case, and cylinders or bars cause transition to move upstream, increasing losses. Hence, the thinnest, most widely spaced (which in the limit means nonexistent) devices are optimal. The cylinders which are best at $Re=50,000$ cause significantly higher losses at $Re=300,000$. This is the same result found by Volino [15] using two-dimensional bars, and agrees with other findings in the literature, as noted above. So long as the cylinders are close enough to provide spanwise uniformity, it appears that varying the cylinder (or bar) thickness and varying the cylinder spacing are both effective for controlling the transition location and moving it to an optimal location for minimizing losses.

The present results can address the question of whether separated cylinders provide an advantage over a two-dimensional bar. A case with a two-dimensional bar that is capable of controlling separation while keeping losses to a minimum at a low Reynolds number should be compared to a case with cylinders that are thicker than this optimal bar but produce the same reattachment and low losses. Cases with these same geometries should then be compared at a high Reynolds number to see which results in lower high-Re losses. The thin bar in the present study results in mar-

ginally reattached flow at $Re=50,000$. The larger cylinders result in spanwise uniform reattachment at $Re=50,000$ when $P/D=5$. The momentum thicknesses at $s/L_s=0.94$ for these two cases are within 8% of each other. At $Re=300,000$ the thin bar results in a momentum thickness 7% above the base line case value, while the thick, $P/D=5$ cylinders result in a spanwise averaged momentum thickness that is 46% above the baseline value. Clearly the thin two-dimensional bar is superior to the thicker cylinders. This comparison is not completely adequate, however, since the thin bar only causes marginal reattachment at $Re=50,000$, while the thick cylinders result in a somewhat more complete reattachment. Volino [15] also considered an intermediate bar with thickness twice that of the thin bar considered above. At $Re=50,000$ the intermediate bar induced complete reattachment with $H=1.8$ and $\theta/\theta_b=1.23$. These results are very close to those obtained with the large cylinders spaced at $P/D=3$. At $Re=300,000$ the intermediate bar resulted in $H=1.59$ and $\theta/\theta_b=1.29$. The thick, $P/D=3$ spaced cylinders resulted in an approximately equal shape factor, but $\theta/\theta_b=1.72$. With this better comparison, it is still clear that a thin bar is superior to larger cylinders.

The present results support the conclusions of Sieverding [10] and Zhang and Hodson [17] who found that two-dimensional bars or trips are as good or better than three-dimensional devices for controlling separation. The present results cannot be considered absolutely conclusive, however, since only a single geometry was considered under a limited number of conditions. The number of possible geometries and spacings for three dimensional devices is infinite, so it will never be possible to prove conclusively through experiments that two-dimensional devices are always better. Further study of devices such as the dimples considered by Lake et al. [12] would be useful. The effects of high freestream turbulence and unsteady wakes should also be considered. Perhaps thinner, smaller diameter cylinders with spacings closer to those extrapolated from Tumin and Ashpis [23] could provide better separation control with lower losses. This is merely speculation. What can be said is that the present results add to the evidence that simple two-dimensional bars are preferable.

Conclusions

A row of small cylinders located at the suction peak on a LPT airfoil were effective for separation control. The reattachment of the boundary layer moves upstream as the cylinder height is increased or the cylinder spacing is decreased. The half angle of the spreading of the disturbance created by the cylinders was of the order 30 deg. This is roughly the same as the expected spreading angle for a turbulent spot under the same adverse pressure gradient conditions. Based on this angle, the maximum allowable spacing for spanwise uniform separation control can be determined. By varying the cylinder height and spacing, an optimal reattachment location can be achieved for minimum losses at a given Reynolds number. Cylinders optimized for low Reynolds numbers resulted in higher losses at high Reynolds numbers. The present results add to the evidence that three-dimensional passive flow control devices are not as effective as two-dimensional bars for minimizing losses over a range of Reynolds numbers.

Acknowledgment

This work was sponsored by the NASA Glenn Research Center. The grant monitor was Dr. David Ashpis. The first author received matching support from the Office of Naval Research.

Nomenclature

$C_p = 2(p_T - p)/\rho U_e^2$, pressure coefficient
 D = cylinder diameter
 H = shape factor, δ^*/θ
 L_s = suction surface length

P = center to center spacing of cylinders
 p = pressure
 p_T = upstream stagnation pressure
 $Re = U_e L_s / \nu$, exit Reynolds number
 s = streamwise coordinate, distance from leading edge
 U_e = nominal exit freestream velocity, based on inviscid solution
 u = mean streamwise velocity
 u' = rms streamwise fluctuating velocity
 y = cross-stream coordinate, distance from wall
 z = spanwise coordinate
 δ^* = displacement thickness
 ν = kinematic viscosity
 ρ = density
 θ = momentum thickness
 θ_b = momentum thickness in base line case

References

- [1] Hourmouziadis, J., 1989, "Aerodynamic Design of Low Pressure Turbines," AGARD Lecture Series 167.
- [2] Mayle, R. E., 1991, "The Role of Laminar-Turbulent Transition in Gas Turbine Engines," ASME J. Turbomach., **113**, pp. 509–537.
- [3] Sharma, O. P., Ni, R. H., and Tanrikut, S., 1994, "Unsteady Flow in Turbines," AGARD Lecture Series 195, Paper No. 5.
- [4] Bons, J. P., Sondergaard, R., and Rivir, R. B., 2001, "Turbine Separation Control Using Pulsed Vortex Generator Jets," ASME J. Turbomach., **123**, pp. 198–206.
- [5] Volino, R. J., and Hultgren, L. S., 2001, "Measurements in Separated and Transitional Boundary Layers Under Low-Pressure Turbine Airfoil Conditions," ASME J. Turbomach., **123**, pp. 189–197.
- [6] Volino, R. J., 2002, "Separated Flow Transition Under Simulated Low-Pressure Turbine Airfoil Conditions: Part 1—Mean Flow and Turbulence Statistics," ASME J. Turbomach., **124**, pp. 645–655.
- [7] Huang, J., Corke, T., and Thomas, F., 2003, "Plasma Actuators for Separation Control on Low Pressure Turbine Blades," AIAA Paper No. 2003-1027.
- [8] Hultgren, L. S., and Ashpis, D. E., 2003, "Demonstration of Separation Delay With Glow Discharge Plasma Actuators," AIAA Paper No. 2003-1025.
- [9] Volino, R. J., 2003, "Separation Control on Low-Pressure Turbine Airfoils Using Synthetic Vortex Generator Jets," ASME J. Turbomach., **125**, pp. 765–777.
- [10] Sieverding, C. H., Bagnera, C., Boege, A. C., Antòn, J. A. C., and Luère, V., 2004, "Investigation of the Effectiveness of Various Types of Boundary Layer Transition Elements of Low Reynolds Number Turbine Bladings," ASME Paper No. GT2004-54103.
- [11] Van Treuren, K. W., Simon, T., von Koller, M., Byerley, A. R., Baughn, J. W., and Rivir, R., 2002, "Measurements in a Turbine Cascade Flow Under Ultra Low Reynolds Number Conditions," ASME J. Turbomach., **124**, pp. 100–106.
- [12] Lake, J. P., King, P. I., and Rivir, R. B., 2000, "Low Reynolds Number Loss Reduction on Turbine Blades With Dimples and V-Grooves," AIAA Paper No. 00-738.
- [13] Murawski, C. G., and Vafai, K., 1999, "Effect of Variable Axial Chord on a Low-Pressure Turbine Blade," J. Propul. Power, **15**, pp. 667–674.
- [14] Byerley, A. R., Störmer, O., Baughn, J. W., Simon, T. W., VanTreuren, K. W., and List, J., 2002, "Using Gurney Flaps to Control Laminar Separation on Linear Cascade Blades," ASME J. Turbomach., **125**, pp. 114–120.
- [15] Volino, R. J., 2003, "Passive Flow Control on Low-Pressure Turbine Airfoils," ASME J. Turbomach., **125**, pp. 754–764.
- [16] Vera, M., Hodson, H. P., and Vazquez, R., 2004, "The Effects of a Trip Wire and Unsteadiness on a High Speed Highly Loaded Low-Pressure Turbine Blade," ASME Paper No. GT2004-53822.
- [17] Zhang, X. F., and Hodson, H., 2004, "Combined Effects of Surface Trips and Unsteady Wakes on the Boundary Layer Development of an Ultra-High-Lift LP Turbine Blade," ASME J. Turbomach., **127**, pp. 479–488.
- [18] Volino, R. J., and Bohl, D. G., 2003, "Separated Flow Transition Mechanisms and Prediction With High and Low Freestream Turbulence Under Low Pressure Turbine Conditions," ASME Paper No. GT2004-63360.
- [19] Volino, R. J., Schultz, M. P., and Pratt, C. M., 2001, "Conditional Sampling in a Transitional Boundary Layer Under High Free-Stream Turbulence Conditions," ASME J. Fluids Eng., **125**, pp. 28–37.
- [20] Wills, J. A. B., 1962, "The Correction of Hot-Wire Readings for Proximity to a Solid Boundary," J. Fluid Mech., **12**, pp. 65–92.
- [21] Howell, R. J., Ramesh, O. N., Hodson, H. P., Harvey, N. W., and Schulte, V., 2001, "High Lift and Aft-Loaded Profiles for Low-Pressure Turbines," ASME J. Turbomach., **123**, pp. 181–188.
- [22] D'Ovidio, A., Harkins, J. A., and Gostelow, J. P., 2001, "Turbulent Spots in Strong Adverse Pressure Gradients: Part 2—Spot Propagation and Spreading Rates," ASME Paper No. 2001-GT-0406.
- [23] Tumin, A., and Ashpis, D. E., 2003, "Optimal Disturbances in Boundary Layers Subject to Streamwise Pressure Gradients," AIAA J., **41**, pp. 2297–2300.

Y. B. Suzen

Assistant Professor
Department of Mechanical Engineering and
Applied Mechanics,
North Dakota State University,
Fargo, ND 58105

P. G. Huang

Professor and Chair
Mechanical and Materials Engineering
Department,
Wright State University,
Dayton, OH 45435

D. E. Ashpis

Aerospace Engineer
Mem. ASME
NASA Glenn Research Center at Lewis Field,
Cleveland, OH 44135

R. J. Volino

Associate Professor
Mem. ASME
Department of Mechanical Engineering,
United States Naval Academy,
Annapolis, MD 21402-5042

T. C. Corke

Clark Chair Professor
Fellow ASME

F. O. Thomas

Professor
Mem. ASME

J. Huang

Graduate Assistant

Department of Aerospace and Mechanical
Engineering,
Center for Flow Physics and Control,
University of Notre Dame,
Notre Dame, IN 46556

J. P. Lake

Special Projects Flight Commander,
586th FLTS/DON,
Holloman AFB, NM 88330

P. I. King

Professor
Mem. ASME
Department of Aeronautics and Astronautics,
Air Force Institute of Technology,
Wright-Patterson AFB, OH 45433

A Computational Fluid Dynamics Study of Transitional Flows in Low-Pressure Turbines Under a Wide Range of Operating Conditions

A transport equation for the intermittency factor is employed to predict the transitional flows in low-pressure turbines. The intermittent behavior of the transitional flows is taken into account and incorporated into computations by modifying the eddy viscosity, μ_t , with the intermittency factor, γ . Turbulent quantities are predicted by using Menter's two-equation turbulence model (SST). The intermittency factor is obtained from a transport equation model which can produce both the experimentally observed streamwise variation of intermittency and a realistic profile in the cross stream direction. The model had been previously validated against low-pressure turbine experiments with success. In this paper, the model is applied to predictions of three sets of recent low-pressure turbine experiments on the Pack B blade to further validate its predicting capabilities under various flow conditions. Comparisons of computational results with experimental data are provided. Overall, good agreement between the experimental data and computational results is obtained. The new model has been shown to have the capability of accurately predicting transitional flows under a wide range of low-pressure turbine conditions.
[DOI: 10.1115/1.2218888]

1 Introduction

The process of transition from laminar to turbulent flow is a major unsolved problem in fluid dynamics and aerodynamics. One

area where the transition process plays an important role and is even more complicated due to the diverse flow conditions encountered is the low-pressure turbine applications. Transitional flows in these applications are affected by several factors such as varying pressure gradients, wide range of Reynolds number and freestream turbulence variations, flow separation, and unsteady wake-boundary layer interactions. Accurate simulation and prediction of transitional flows under these diverse conditions is key

Contributed by the Turbomachinery Division of ASME for publication in the JOURNAL OF TURBOMACHINERY. Manuscript received February 14, 2004; final manuscript received February 13, 2006. Review conducted by R. L. Davis.

to design of more efficient jet engines.

In low-pressure turbine applications, flow over the blades is mostly turbulent at the high Reynolds number conditions encountered at takeoff and the efficiency is at its design maximum. However, at lower Reynolds number conditions which correspond to high altitudes and cruise speeds the boundary layers on the airfoil surface have a tendency to remain laminar; hence, the flow may separate on the suction surface of the turbine blades before it becomes turbulent. This laminar separation causes unpredicted losses, substantial drops in efficiency, and increase in fuel consumption [1–3].

In order to calculate the losses and heat transfer on various components of gas turbine engines, and to be able to improve component efficiencies and reduce losses through better designs, accurate prediction of development of transitional boundary layers is essential [1].

One approach proven to be successful for modeling transitional flows is to incorporate the concept of intermittency into computations. This can be done by multiplying the eddy viscosity obtained from a turbulence model, μ_t , used in the diffusive parts of the mean flow equations, by the intermittency factor, γ (Simon and Stephens [4]). This method can be easily incorporated into any Reynolds averaged Navier-Stokes solver. In this approach, the intermittency factor, γ , can be obtained from an empirical relation such as the correlation of Dhawan and Narasimha [5], or it can be obtained from a transport model.

Dhawan and Narasimha [5] correlated the experimental data and proposed a generalized intermittency distribution function across flow transition. Gostelow et al. [6] extended this correlation to flows with pressure gradients under the effects of a range of freestream turbulence intensities. Solomon et al. [7], following the work of Chen and Thyson [8], developed an improved method to predict transitional flows involving changes in pressure gradients. These empirical methods led to development of transport equations for intermittency.

Steelant and Dick [9] proposed a transport equation for intermittency, in which the source term of the equation is developed such that the γ distribution of Dhawan and Narasimha [5] across the transition region can be reproduced. Steelant and Dick used their model, coupled with two sets of conditioned Navier-Stokes equations, to predict transitional flows with zero, favorable, and adverse pressure gradients. However, since their technique involved the solution of two sets of strongly coupled equations, the method is not compatible with existing computational fluid dynamics (CFD) codes, in which only one set of Navier-Stokes equations is involved. Moreover, the model was designed to provide a realistic streamwise γ behavior but with no consideration of the variation of γ in the cross-stream direction.

Cho and Chung [10] developed a k - ϵ - γ turbulence model for free shear flows. Their turbulence model explicitly incorporates the intermittency effect into the conventional k - ϵ model equations by introducing an additional transport equation for γ . They applied this model to compute a plane jet, a round jet, a plane far wake, and a plane mixing layer with good agreement. Although this method was not designed to reproduce flow transition, it provided a realistic profile of γ in the cross-stream direction.

Suzen and Huang [11] developed an intermittency transport equation combining the best properties of Steelant and Dick's model and Cho and Chung's model. The model reproduces the streamwise intermittency distribution of Dhawan and Narasimha [5] and also produces a realistic variation of intermittency in the cross-stream direction. This model has been validated against European Research Community On Flow Turbulence And Combustion (ERCOTAC) benchmark T3-series experiments reported by Savill [12,13], low-pressure turbine experiments of Simon et al. [14], and separated and transitional boundary layer experiments of Hultgren and Volino [15] with success [11,16–21].

In this paper we concentrate on prediction of three recent low-pressure turbine experiments on the Pratt and Whitney's Pack B

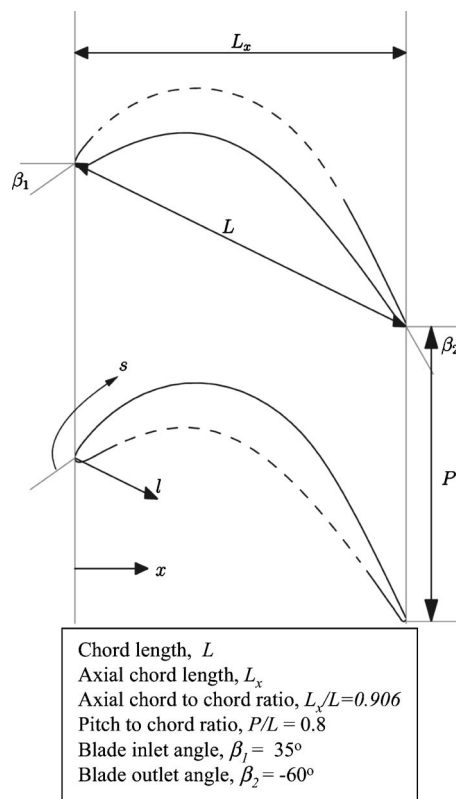


Fig. 1 P&W Pack B blade cascade details

blade under low Reynolds number conditions using the transport model for intermittency. Due to the fact that the Pack B blade is very sensitive to changes of flow conditions, it is an ideal test blade for validating the transition/turbulence models. The three sets of experiments considered are conducted by Lake et al. [3,22], Huang et al. [23], and Volino [24] at three independent facilities. These experiments provide an extensive database for investigating transitional flows under low-pressure turbine conditions and are employed as benchmark cases for further testing of the predicting capabilities of the current intermittency model. A summary of the experiments are given in the next section. In Sec. 3, the intermittency transport model is presented and implementation of the model and the empirical correlations employed for the onset of transition are described. In Sec. 4, the predictions of the new intermittency model are compared against the experimental data. Conclusions are provided in Sec. 5.

2 Low-Pressure Turbine Experiments

In this paper, we concentrate on computation of three sets of low-pressure turbine experiments using the intermittency transport model. These experiments are conducted by Lake et al. [3,22], Huang et al. [23], and Volino [24]. In these experiments Pratt and Whitney's Pack B blade is used; the details of the blade are shown in Fig. 1. Overall, these experiments cover a Reynolds number range from 10,000 to 172,000 and the freestream turbulence intensity ranges from 0.08% to 4%. The cases and data used for comparison in this paper are summarized in Table 1. In the following sections details of these experimental efforts are given.

2.1 Pack B Blade Cascade Experiments of Lake et al. [3,22]. Lake et al. [3,22] conducted experiments on the Pack B blade in order to identify methods for reducing separation losses on low-pressure turbine blades under low Reynolds number conditions. In the experiments, they investigated flows at low Reynolds numbers of 43,000, 86,000, and 172,000 based on inlet

Table 1 Details of the experiments used for comparison with computations

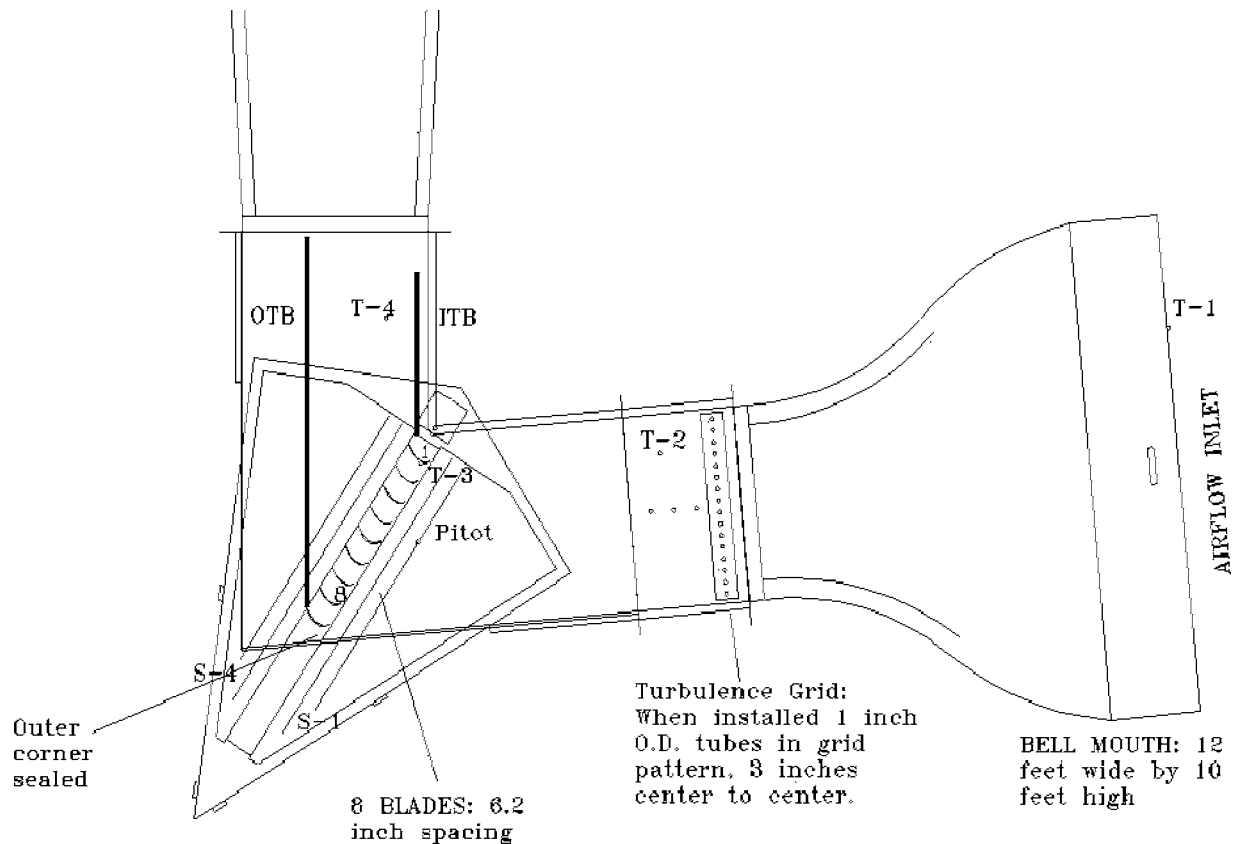
Source	Test Section	C_x (m)	Re ($U_{in} C_x / \nu$)	FSTI (%)	Data used for Comparison
Lake et al. [3,22]	P&W Pack B cascade	0.1778	86,000 172,000	1 & 4 1 & 4	C_p distribution C_p distribution
Huang et al. [23]	P&W Pack B cascade	0.1595	10,000 25,000 50,000 75,000 100,000	0.08 0.08 0.08, 1.6, 2.85 0.08, 1.6, 2.85 0.08, 1.6, 2.85	C_p distribution C_p distribution C_p distribution, velocity profiles ^a C_p distribution, velocity profiles ^a C_p distribution, velocity profiles ^a
Volino [24]	P&W Pack B single passage	0.1537	10,291 20,581 41,162 82,324	0.5 0.5 0.5 0.5	C_p distribution, velocity profiles C_p distribution, velocity profiles C_p distribution, velocity profiles C_p distribution, velocity profiles

^aVelocity profiles are available for FSTI=0.08% and 2.85% from experiments.

velocity and axial chord and freestream turbulence intensities (FSTI) of 1% and 4%. These conditions are similar to those encountered at high-altitude, low-speed flight of reconnaissance unmanned aerial vehicles used by USAF.

In Lake's experiments, surface pressure coefficients, boundary layer velocity, and turbulence profiles, total pressure loss data were obtained at FSTI=1% and FSTI=4%. The test setup shown in Fig. 2 included eight blades with axial chord of 0.1778 m

(7 in.), and blade spacing of 0.1575 m (6.2 in.). The blades were numbered 1 through 8 starting from the inside bend. Boundary layer measurements were taken on blade 5 and surface pressures were measured around blades 4 and 6. In this paper, the Pack B blade experiments with Reynolds numbers of 86,000 and 172,000 and freestream turbulence intensities of 1% and 4% are computed and comparison of pressure distributions between experiments and computations are performed.

**Fig. 2 Experimental setup used by Lake et al. [3,22]**

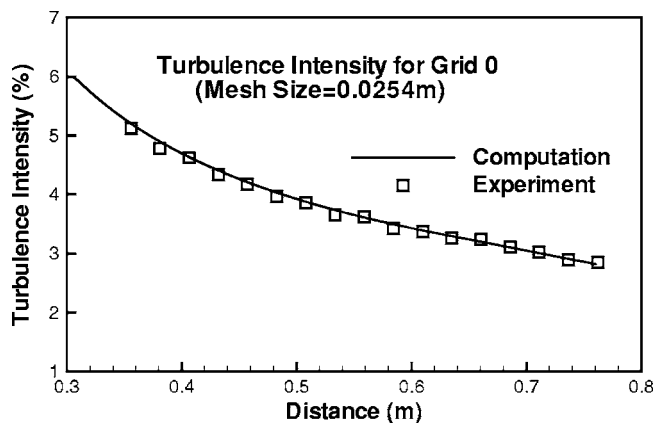


Fig. 3 Comparison of computed and experimental decay of turbulence for experiments of Huang et al. [23], with grid 0

2.2 Pack B Blade Cascade Experiments of Huang et al. [23]. Huang et al. [23] conducted experiments on Pack B blade cascade for a range of Reynolds numbers and turbulence intensities. The Reynolds numbers range from 10,000 to 100,000 based on inlet velocity and axial chord as listed in Table 1. In their experiments the blades had an axial chord length of 0.1595 m (6.28 in.). The freestream turbulence intensity in the tunnel was measured as 0.08%. In order to increase the turbulence intensity, two grids with different mesh sizes were used. One of the grids had the mesh size of 0.0254 m (denoted as grid 0) and the other had 0.008 m (denoted as grid 3). The decay of turbulence after the grids was measured using crosswire and they are shown in Figs. 3 and 4 along with the computed results for grid 0 and grid 3, respectively. The grids were movable in the tunnel so that the turbulence level of the flow that reaches the blades could be controlled by moving the grid that is, by increasing or decreasing the distance between the grid and the blade. Experiments were performed for Reynolds numbers 50,000, 75,000, and 100,000, with grids placed 0.762 m (30 in.) away from the blade leading edge, corresponding to turbulence intensities of 2.85% and 1.6% at the leading edge for grid 0 and grid 3, respectively. For $Re = 100,000$, grid 0 is placed at 0.5588 m (22 in.) and 0.3556 m (14 in.), corresponding to turbulence intensities of 3.62% and 5.2%, respectively. Pressure coefficient data are available for all cases and detailed boundary layer measurements are available for $Re = 50,000$, 75,000, and 100,000 with $FSTI = 0.08\%$ and 2.85% cases. The cases and data used for comparisons in this paper are listed in Table 1.

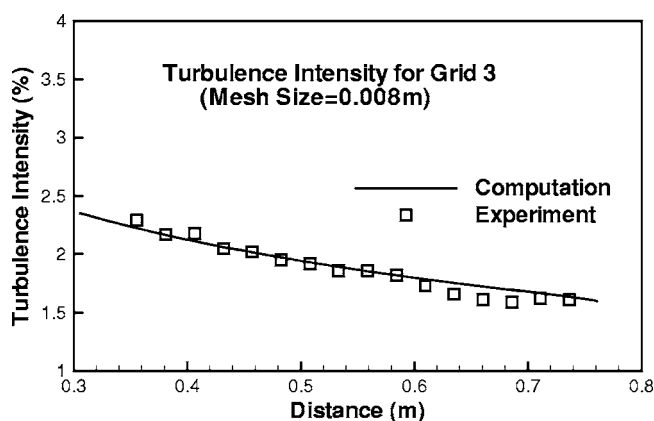


Fig. 4 Comparison of computed and experimental decay of turbulence for experiments of Huang et al. [23], with grid 3

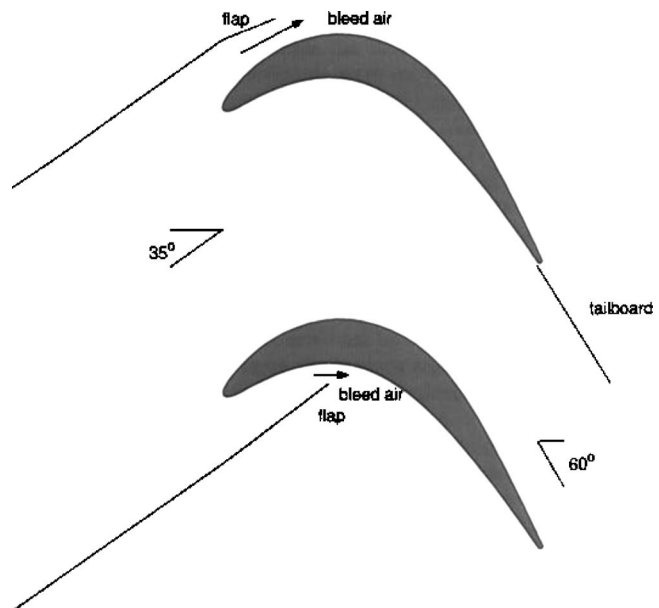


Fig. 5 Schematic of the test section for experiments of Volino [24]

2.3 Pack B Experiments of Volino [24]. Volino [24] investigated the boundary layer separation, transition, and reattachment under low-pressure turbine airfoil conditions. The experiments included five different Reynolds numbers ranging between 10,291 and 123,492 and freestream turbulence intensities of 0.5% and 9%. The test section consisted of a single passage between two Pack B blades as shown in Fig. 5. The axial chord length of the blades was 0.1537 m (6.05 in.). There are flaps located upstream of each blade to control the amount of bleed air allowed to escape from the passage. These flaps were adjusted by matching measured pressure distribution for a high Reynolds number with the inviscid pressure distribution on the blade. In addition to the upstream bleed flaps, a tailboard on the pressure side was used to set the pressure gradient. The compiled data include pressure surveys, mean and fluctuating velocity profiles, intermittency profiles, and turbulent shear stress profiles. It was observed that the effect of high Reynolds number or high freestream turbulence level was to move transition upstream. Transition started in the shear layer over the separation bubble and led to rapid boundary layer reattachment. At the lowest Re case, transition did not take place before the trailing edge and the boundary layer did not reattach. The beginning of transition corresponded to the beginning of a significant rise in the turbulent shear stress. These experimental results provide detailed documentation of the boundary layer and extend the existing database to lower Reynolds numbers. The cases used for comparisons with computations in this paper are listed in Table 1 along with the type of data used for comparisons.

3 Intermittency Transport Model

In this section, the transport model for intermittency is presented. The model combines the transport equation models of Steelant and Dick [9] and Cho and Chung [10]. Details of the development and implementation of the transport model are given in Suzen and Huang [11,16,17], and in Suzen et al. [18].

The model equation is given by

$$\begin{aligned}
& \frac{\partial \rho \gamma}{\partial t} + \frac{\partial \rho u_j \gamma}{\partial x_j} \\
& = (1 - \gamma) \left[\frac{(1 - F) 2 C_0 \rho \sqrt{u_k u_k} f(s) f'(s)}{k} + F \left(\frac{C_1 \gamma}{k} \tau_{ij} \frac{\partial u_i}{\partial x_j} - C_2 \gamma \rho \frac{k^{3/2}}{\varepsilon} \frac{u_i}{(u_k u_k)^{1/2}} \frac{\partial u_i}{\partial x_j} \frac{\partial \gamma}{\partial x_j} \right) \right] \\
& + C_3 \rho \frac{k^2}{\varepsilon} \frac{\partial \gamma}{\partial x_j} \frac{\partial \gamma}{\partial x_j} \\
& + \frac{\partial}{\partial x_j} \left(((1 - \gamma) \gamma \sigma_{\gamma i} \mu + (1 - \gamma) \sigma_{\gamma i} \mu_t) \frac{\partial \gamma}{\partial x_j} \right) \quad (1)
\end{aligned}$$

The distributed breakdown function, $f(s)$ has the form

$$f(s) = \frac{as'^4 + bs'^3 + cs'^2 + ds' + e}{gs'^3 + h} \quad (2)$$

where $s' = s - s_t$, and s is the distance along the streamline coordinate, and s_t is the transition location. The coefficients are

$$\begin{aligned}
a &= 50 \sqrt{\frac{n\sigma}{U}} \quad b = -0.4906 \\
c &= 0.204 \left(\frac{n\sigma}{U} \right)^{-0.5} \quad d = 0.0 \quad e = 0.04444 \left(\frac{n\sigma}{U} \right)^{-1.5} \\
h &= 10e \quad g = 50 \quad (3)
\end{aligned}$$

The shear stresses are defined as

$$\tau_{ij} = \mu_t \left[\frac{\partial u_i}{\partial x_j} + \frac{\partial u_j}{\partial x_i} - \frac{2}{3} \frac{\partial u_k}{\partial x_k} \delta_{ij} \right] - \frac{2}{3} \rho k \delta_{ij} \quad (4)$$

The blending function F is constructed using a nondimensional parameter $k/W\nu$, where k is the turbulent kinetic energy and W is the magnitude of the vorticity. The blending function has the form

$$F = \tanh^4 \left[\frac{k/W\nu}{200(1 - \gamma^{0.1})^{0.3}} \right] \quad (5)$$

The model constants used in Eq. (1) are

$$\begin{aligned}
\sigma_{\gamma i} &= \sigma_{\gamma i} = 1.0 \quad C_0 = 1.0 \quad C_1 = 1.6 \\
C_2 &= 0.16 \quad C_3 = 0.15
\end{aligned}$$

The intermittency is incorporated into the computations simply by multiplying the eddy viscosity obtained from a turbulence model, μ_t , by the intermittency factor, γ . Simon and Stephens [4] showed that, by combining the two sets of conditioned Navier-Stokes equations and making the assumption that the Reynolds stresses in the nonturbulent part are negligible, the intermittency can be incorporated into the computations by using the eddy viscosity, μ_t^* which is obtained by multiplying the eddy viscosity from a turbulence model, μ_t , with the intermittency factor, γ . That is

$$\mu_t^* = \gamma \mu_t \quad (6)$$

is used in the mean flow equations. It must be noted that γ does not appear in the generation term of the turbulent kinetic energy equations.

Computations of the experiments are performed using a recently developed multiblock Navier-Stokes solver, called GHOST. The code was developed at the University of Kentucky, by Huang, and is a pressure-based code based on the SIMPLE algorithm with second-order accuracy in both time and space. Advection terms are approximated by a QUICK scheme and central differencing is used for the viscous terms. The "Rhie and Chow" momentum interpolation method [25] is employed to avoid checkerboard oscillations usually associated with the nonstaggered grid arrangement. This code is capable of handling complex geometries, moving, and overset grids and includes multiprocessor computation capability using message passing interface (MPI). Since multiple

processors are used during the computations, it is more efficient to divide the computational domain into several smaller pieces with very fine grids and distribute the zones to processors with the consideration of load balancing. This code has been used extensively in a recent turbulence model validation effort (Hsu et al. [26]) and computations of unsteady wake/blade interaction (Suzen and Huang [27]) conducted at the University of Kentucky.

The multiblock grid systems used in the computations are obtained by conducting a series of grid refinement studies in order to ensure that the details of the flow field are captured accurately and the results are grid independent. All grid systems have first y^+ less than 0.5 near solid walls.

In using this intermittency approach, the turbulence model selected to obtain μ_t must produce fully turbulent features before transition location in order to allow the intermittency to have full control of the transitional behavior. Menter's [28] SST model satisfies this requirement. It produces almost fully turbulent flow in the leading edge of the boundary layer and therefore is used as a baseline model to compute μ_t and other turbulent quantities in the computations [18].

The value of $n\sigma$ used in evaluating the constants given by Eq. (3) is provided by the following correlation for zero-pressure gradient flows [18]

$$\hat{n}\sigma = (nv^2/U^3)\sigma = 1.8 \times 10^{-11} Tu^{7/4} \quad (7)$$

When flows are subject to pressure gradients, the following correlation is used

$$\frac{\hat{n}\sigma}{(\hat{n}\sigma)_{ZPG}} = \begin{cases} M^{[1 - \exp(0.75 \times 10^6 K_t Tu^{-0.7})]}, & K_t < 0 \\ 10^{-3227 K_t^{0.5985}}, & K_t > 0 \end{cases} \quad (8)$$

with M defined as

$$M = (850 Tu^{-3} - 100 Tu^{-0.5} + 120)$$

where $(\hat{n}\sigma)_{ZPG}$ is the value for flow at zero pressure gradient and can be obtained from Eq. (7), and $K_t = (\nu/U_t^2)(dU/dx)_t$ is the flow acceleration parameter. The favorable pressure gradient part of the above correlation (for $K_t > 0$) is from Steelant and Dick [9]. The portion of the correlation for adverse pressure gradient flows for $K_t < 0$ is formulated using the transition data of Gostelow et al. [6] and Simon et al. [14] (Suzen et al. [18]).

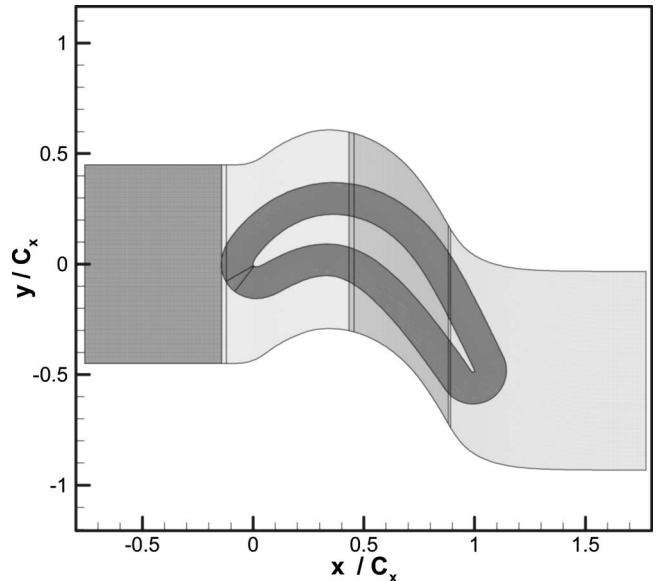


Fig. 6 Multiblock grid used for computations of experiments of Lake et al. [3,22] and FSTI=0.08% experiments of Huang et al. [23]

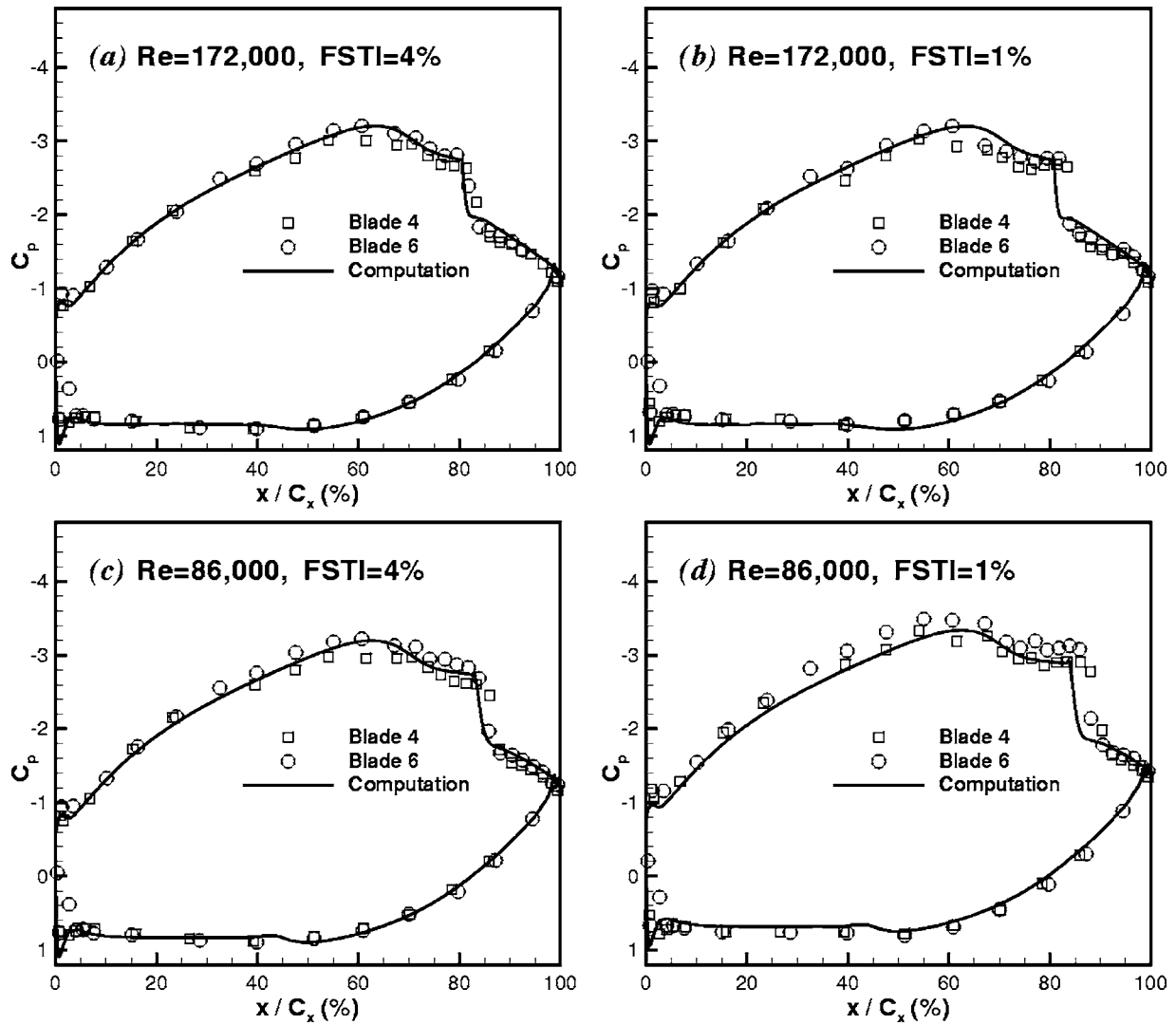


Fig. 7 Comparison of computed pressure coefficient with experiments of Lake et al. [3,22]

The current approach uses the intermittency transport model to obtain the intermittency distribution for the transitional flows, while the onset of transition is defined by correlations.

The onset of attached flow transition is determined by the following correlation in terms of turbulence intensity, Tu , and the acceleration parameter, K_t ,

$$Re_{\theta_t} = (120 + 150Tu^{-2/3})\coth[4(0.3 - K_t \times 10^5)] \quad (9)$$

where K_t was chosen as the maximum absolute value of that parameter in the downstream deceleration region [18]. This correlation maintains the good features of Abu-Ghannam and Shaw [29] correlation in the adverse pressure gradient region, and in addition reflects the fact that the flow becomes less likely to have transition when subject to favorable pressure gradients by rapidly rising as K_t becomes positive.

In order to determine the onset of separated flow transition Re_{st} is expressed in terms of the turbulence intensity (Tu) and the momentum thickness Reynolds number at the point of separation (Re_{θ_s}) in the form [19]

$$Re_{st} = 874Re_{\theta_s}^{0.71} \exp[-0.4Tu] \quad (10)$$

This correlation provides a better representation of the experimental data than Davis et al. [30] correlation and is used to predict onset of separated flow transition in the present computations.

4 Results and Discussion

4.1 Simulations of Experiments of Lake et al. [3,22]. The intermittency model is applied to predict the Pack B blade experiments of Lake et al. [3,22]. In the computations, flows at Reynolds numbers of 86,000 and 172,000 based on inlet velocity and axial chord with freestream intensities of 1% and 4% were investigated.

The computations were performed using the grid system shown in Fig. 6 consisting of five zones obtained as a result of a grid refinement study. In the grid refinement study computations were performed on a series of successively finer grids and the variations in the results were observed. The grid shown in Fig. 6 was chosen to be adequate for obtaining grid-independent solutions for all cases. The four zones on which the blade grid is superposed each have 125×225 grid points and the O-type grid around the blade has 401×101 points with first y^+ less than 0.5.

The comparisons of computed and experimental pressure coefficient distributions are shown in Figs. 7(a)–7(d). In these figures, the experimental distributions correspond to the measurements made on test blades 4 and 6.

The computed results compare well with the experiments for high turbulence intensity, $FSTI=4\%$, cases shown in Figs. 7(a) and 7(c). However, for $FSTI=1\%$ cases shown in Figs. 7(b) and

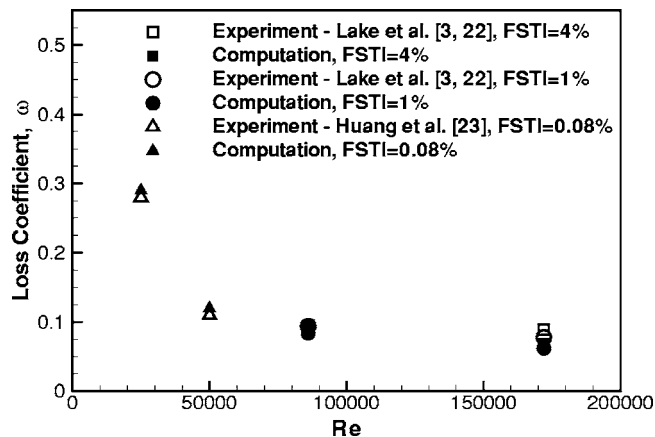


Fig. 8 Comparison of computed total pressure loss coefficients with experiments of Lake et al. [3,22] and Huang et al. [23]

7(d), the extent of the separation bubbles is underpredicted in the computations. For example, for $Re=86,000$, $FSTI=1\%$, shown in Fig. 7(d), the flow reattaches earlier in computations than it does in the experiment, as can be observed from the difference in the pressure coefficient distributions between $x/C_x=80$ to 85%.

The comparison of computed total pressure loss coefficients with experiments is shown in Fig. 8. For the $Re=86,000$ case, the computed loss coefficient is in good agreement with the experiments for both $FSTI$ levels. However, for the $Re=172,000$ case the computations underpredicted the loss coefficient compared to experiments for both $FSTI=1\%$ and $FSTI=4\%$. From Fig. 8 it is evident that the cascade losses decrease as the Reynolds number increases. This reduction in cascade losses with increasing Reynolds number is due to the decrease in size of the separated flow region on the suction side of the blades.

The onset of separation locations, reattachment locations, and onset of transition locations on the suction surface are summarized in Table 2 for these cases, along with the corresponding values from experiments. In the experiments, the onset of transition locations and the reattachment locations are not reported. The experimental onset of separation and reattachment points are extracted from the experimental pressure coefficient data. The onset of separation is taken to be the axial location where the plateau in the pressure coefficient distribution of the suction side begins, and the reattachment point is taken to be the axial location after the sharp change in C_p following the plateau. This procedure may lead to an error of approximately $\pm 1.5\%$ of axial chord in the estimated onset locations.

The onset of separation, reattachment, and onset of transition locations are plotted against Reynolds number in Figs. 9(a) and 9(b) for $FSTI=4\%$ and 1% , respectively. The uncertainty in the estimated experimental values is indicated by error bars in the figures. For the high turbulence intensity case, computation predicts onset of separation and reattachment slightly upstream of the experiment. For the low $FSTI$ case shown in Fig. 9(b), the separation zone is predicted smaller than the experiments. The onset of transition is predicted over the separated flow region in the shear

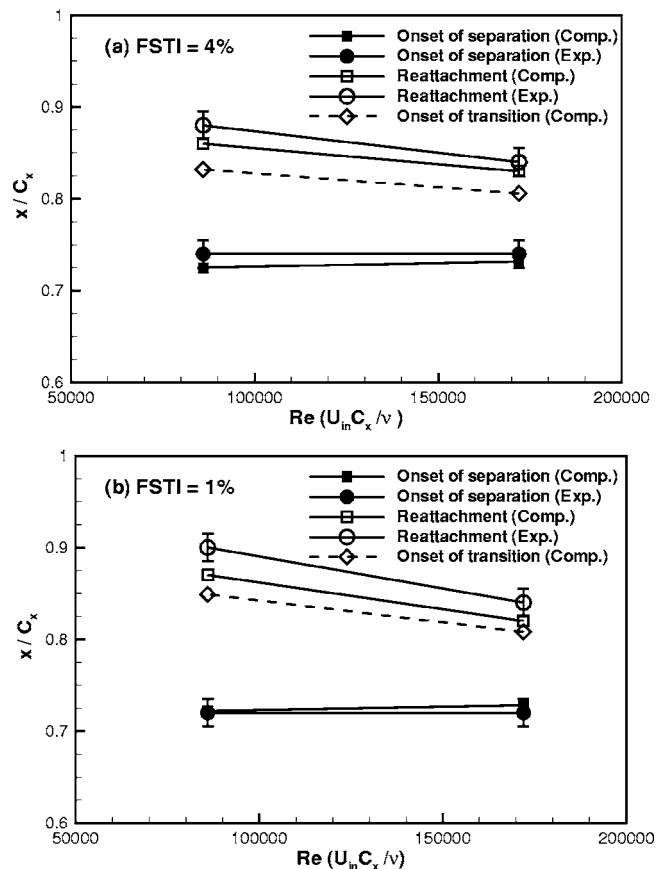


Fig. 9 Comparison of separation, reattachment, and transition locations for experiments of Lake et al. [3,22]

layer. From comparison of these figures it is evident that, with decreasing freestream turbulence intensity, the separation zone becomes larger, and for a given $FSTI$ condition, the separated flow region gets smaller with increasing Reynolds number.

4.2 Simulations of Experiments of Huang et al. [23]. In this set of experiments, first the cases with no grid in tunnel corresponding to $FSTI=0.08\%$ are computed. In these computations, the same grid system used for the computations of experiments of Lake et al. [3,22] shown in Fig. 6 is used.

The comparisons of the computed and the experimental pressure coefficients are shown in Figs. 10(a)–10(e) for $Re=100,000$, 75,000, 50,000, 25,000, and 10,000 based on inlet velocity and axial chord. The agreement between the experiments and computations is very good for all cases.

The computed total pressure loss coefficients are compared to the available data for $Re=25,000$ and 50,000 in Fig. 8. The loss coefficients predicted in the computations are 2% to 3% higher compared to the experiments for both Reynolds numbers.

The onset of separation, transition, and reattachment locations are tabulated in Table 3 for all cases and plotted against Reynolds number in Figs. 11(a)–11(c) for $FSTI=0.08\%$, 1.6%, and 2.85%,

Table 2 Separation, reattachment, and transition locations for cases of Lake et al. [3,22]

Re ($U_{in} C_x / \nu$)	FSTI (%)	x_s / C_x (Computation)	x_r / C_x (Experiment)	x_p / C_x (Computation)	x_r / C_x (Experiment)	x_{tr} / C_x (Computation)
172,000	4	0.732	0.74	0.83	0.84	0.806
86,000	4	0.725	0.74	0.86	0.88	0.832
172,000	1	0.728	0.72	0.82	0.84	0.808
86,000	1	0.722	0.72	0.87	0.90	0.849

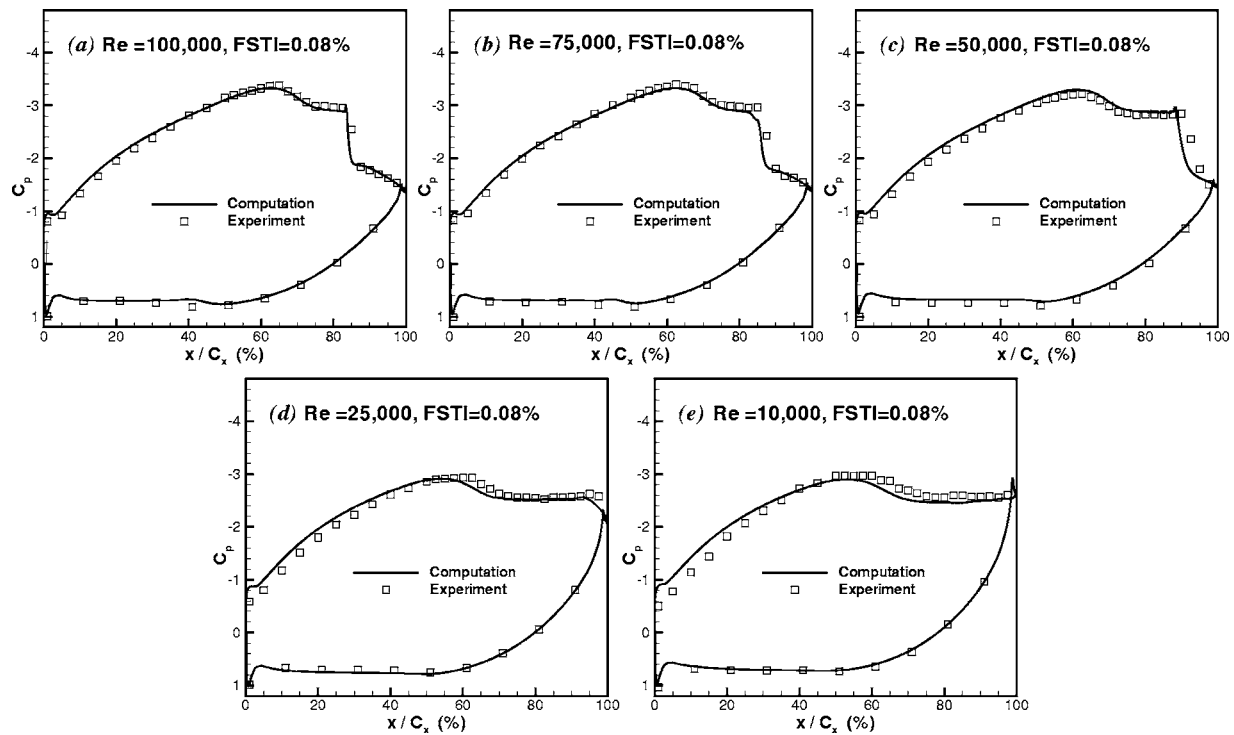


Fig. 10 Comparison of computed pressure coefficients with experiments of Huang et al. [23] for FSTI=0.08% cases

respectively.

Computed velocity profiles at seven axial stations along the suction surface of the blade are compared to the experiments for $Re=100,000$, $75,000$, and $50,000$ in Figs. 12–14, respectively.

For the $Re=100,000$ case, the computed velocity profiles compare very well with the experiment as shown in Figs. 12(a)–12(g). At the first three measurement stations, flow is laminar and attached as shown in Figs. 12(a)–12(c). Flow separation takes place at $x/C_x=0.725$ and the separated flow region is visible in Figs. 12(d) and 12(e), corresponding to axial locations of $x/C_x=0.75$ and 0.80 . The flow transition and reattachment takes place around $x/C_x=0.84$ in the computation. Reattachment location is earlier than the experiment which takes place at $x/C_x=0.875$. In Fig. 12(f) corresponding to axial station of $x/C_x=0.85$ the computed flow field has already attached, although the experimental profile indicates a very small separation zone close to wall. At $x/C_x=0.9$ the flow is completely attached as shown in Fig. 12(g).

When the Reynolds number is reduced to $75,000$, the size of the separation bubble increases as can be observed from the comparison of the velocity profiles shown in Figs. 13(a)–13(g). At this Reynolds number the flow separates around $x/C_x \approx 0.72$ and reattaches around $x/C_x \approx 0.87$. The transition onset location is pre-

dicted at $x/C_x=0.854$. The size of the separation bubble is larger than the $Re=100,000$ case from comparison of Figs. 13(d)–13(f) and 12(d)–12(f).

Next, the Reynolds number is reduced to $50,000$ and the comparison of computed and experimental velocity profiles is shown in Figs. 14(a)–14(g). For this case the separation bubble is much larger from the previous cases and extends until $x/C_x \approx 0.975$ in the experiment and $x/C_x \approx 0.93$ in the computations, as can be seen in Figs. 14(d)–14(g). Computations predicted the transition onset location at $x/C_x=0.89$. In the computations, the onset of separation is predicted well in agreement with experiment; however, the reattachment point is earlier, making the size of the separation bubble smaller when compared to experiment. This is evident from the comparison of velocity profiles at the last two stations shown in Figs. 14(f) and 14(g).

The onset of separation and reattachment points for $FSTI=0.08\%$ cases is predicted upstream of the experiments as shown in Fig. 11(a).

Next, the high FSTI cases are computed using the six zone multiblock grid system shown in Fig. 15. The computational domain is extended upstream of the blade in order to specify the correct turbulence intensity at the inlet and to match the decay of

Table 3 Separation, reattachment, and transition locations for cases of Huang et al. [23]

Re ($U_{in}C_x/\nu$)	FSTI (%)	x_s/C_x (Computation)	x_s/C_x (Experiment)	x_r/C_x (Computation)	x_r/C_x (Experiment)	x_{tr}/C_x (Computation)
10,000	0.08	0.661	0.725
25,000	0.08	0.656	0.725	0.980	...	0.936
50,000	0.08	0.714	0.725	0.925	0.975	0.890
75,000	0.08	0.718	0.725	0.860	0.870	0.854
100,000	0.08	0.725	0.725	0.840	0.875	0.840
50,000	1.6	0.722	0.728	0.900	0.900	0.854
75,000	1.6	0.728	0.730	0.867	0.875	0.834
100,000	1.6	0.732	0.730	0.860	0.877	0.821
50,000	2.85	0.728	0.722	0.887	0.900	0.837
75,000	2.85	0.732	0.729	0.840	0.870	0.816
100,000	2.85	0.735	0.734	0.842	0.850	0.806

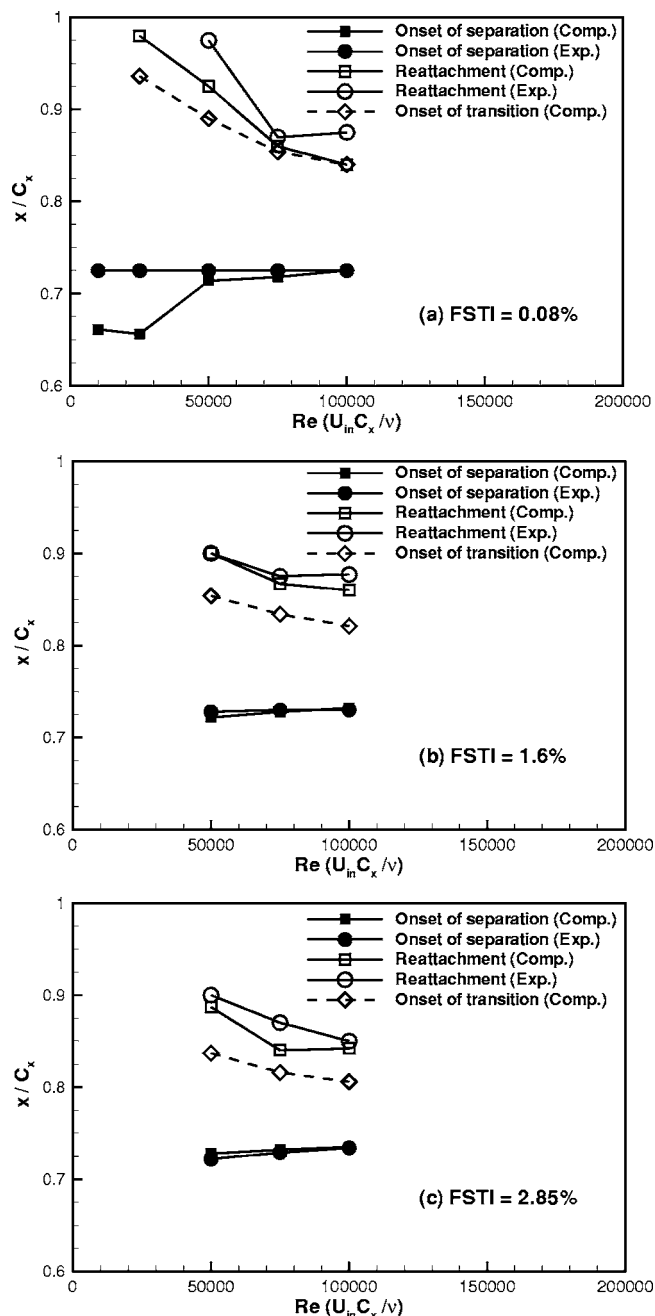


Fig. 11 Comparison of separation, reattachment, and transition locations for experiments of Huang et al. [23]

turbulence that reaches the blade. The matched computed and experimental turbulence decays are shown in Figs. 3 and 4 for grid 0 and grid 3, respectively. The cases considered have the grids placed 0.762 m (30 in) upstream of the blade, corresponding to turbulence intensities of 2.85% and 1.6% for grid 0 and grid 3, respectively.

The comparison of the computed and the experimental pressure coefficient distributions for $Re=50,000$, $75,000$, and $100,000$ for FSTI=2.85% cases is shown in Fig. 16. The agreement is very good between computations and experiments.

Comparisons of computed velocity profiles with the experiments for $Re=100,000$ are given in Figs. 17(a)–17(g). In this case, the flow separates around $x/C_x \approx 0.74$ and reattaches at $x/C_x \approx 0.85$. The onset of transition is predicted at $x/C_x = 0.806$.

The computed size and extent of the separation bubble is in good agreement with the experiment as tabulated in Table 3 and as can be seen in Figs. 11(c) and 16(d)–16(f).

For the lower Reynolds number of 75,000, computed velocity profiles are compared with the experiments in Figs. 18(a)–18(g). The agreement between experiment and computation is good prior to the reattachment as shown in Figs. 18(a)–18(e). There is a discrepancy in the reattachment region. The flow separation takes place around $x/C_x \approx 0.73$ and reattaches at $x/C_x \approx 0.87$ according to the experiment, whereas computation predicts reattachment earlier at around $x/C_x \approx 0.84$ with the onset of transition predicted at $x/C_x = 0.816$. The difference in reattachment points is evident in the comparison of the computed and experimental velocity profiles shown in Fig. 18(f). At this station the experimental profile indicates separated flow and the computed profile shows an already attached flow.

The next case considered has the same FSTI=2.85% but with Reynolds number being reduced to 50,000. The comparison of velocity profiles is shown in Figs. 19(a)–19(g). The computations agree well with the experiment, and the size and extent of the separation bubble are well predicted as can be seen from Fig. 11(c). The onset of separation is around $x/C_x \approx 0.72$ and the flow reattaches around $x/C_x \approx 0.9$, with transition onset at $x/C_x = 0.837$.

In Fig. 20, computed and experimental pressure coefficient distributions for grid 3 case which correspond to FSTI=1.6% are compared for $Re=50,000$, $75,000$, and $100,000$. Again, very good agreement between computations and experiments is obtained. The onset of separation and reattachment locations shown in Fig. 11(b) compares well with the experiments.

Overall, Figs. 11(a)–11(c) indicate that, as FSTI increases, the separated flow region decreases, and at a given FSTI, increasing Reynolds number has the same effect on the separated flow region.

4.3 Simulations of Pack B Experiments of Volino [24]. In computation of experiments of Volino [24] the flow field is modeled with the 31-zone multiblock grid shown in Fig. 21 obtained as a result of a series of grid refinement studies. The bleed flaps below the lower blade and above the upper blade are defined by fitting third-order polynomials through the available points obtained from experimental setup; these curves are used as the flap shapes in generating the computational grid. Initial computations indicated that the shape of the bleed flaps and the orientation of the tailboard behind the upper blade greatly affect the computed results, especially the onset of separation and reattachment points on the lower blade's suction surface. In order to select the most accurate orientation for the tailboard and the shape of the bleed flaps, several test computations were performed for the case with $Re=41,162$ and FSTI=0.5% using different tailboard orientations and bleed flap shapes. In these computations the main goal was to match the experimental velocity profiles in the laminar flow part and to capture the correct onset point of separation. Once an acceptable geometry is obtained, the final bleed flap shapes and tailboard orientation are used for computation of all other Reynolds number cases.

Computed pressure coefficient distributions are compared to experiments in Figs. 22(a)–22(d) for $Re=82,324$, $41,162$, $20,581$, and $10,291$, and the separation onset, reattachment, and transition onset information is summarized in Table 4. The C_p comparison for $Re=82,324$ shown in Fig. 22(a) indicates that the computation predicts early reattachment of the flow; in the recovery region following reattachment the pressure coefficient distribution is overpredicted.

The computed pressure coefficient distributions for the lower Reynolds number cases shown in Figs. 22(c) and 22(d) compare well with experiments. For the $Re=41,162$ case shown in Fig. 22(b), the onset of separation and reattachment locations matches the experiment as given in Table 4; however, in the recovery re-

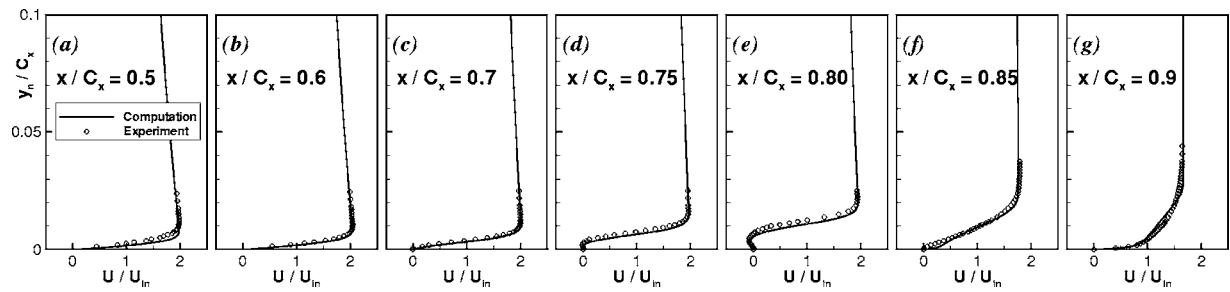


Fig. 12 Comparison of computed velocity profiles with experiments of Huang et al. [23], $Re=100,000$, $FSTI=0.08\%$ case

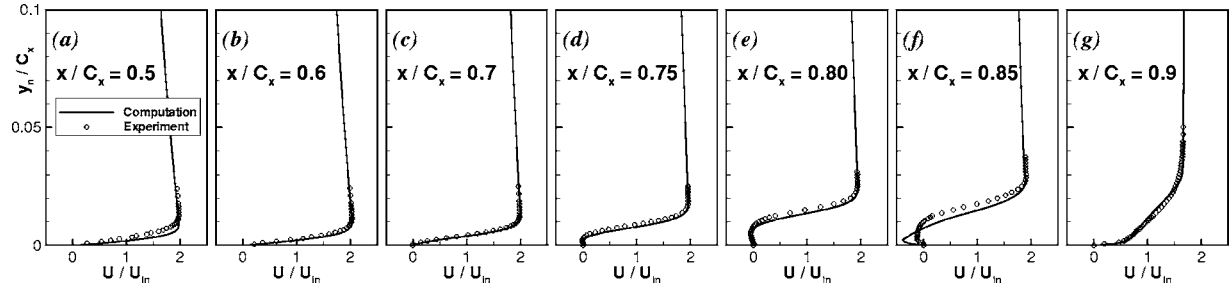


Fig. 13 Comparison of computed velocity profiles with experiments of Huang et al. [23], $Re=75,000$, $FSTI=0.08\%$ case

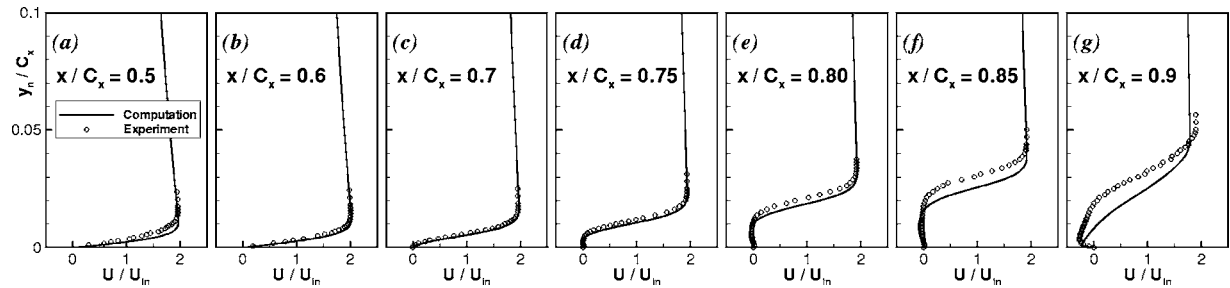


Fig. 14 Comparison of computed velocity profiles with experiments of Huang et al. [23], $Re=50,000$, $FSTI=0.08\%$ case

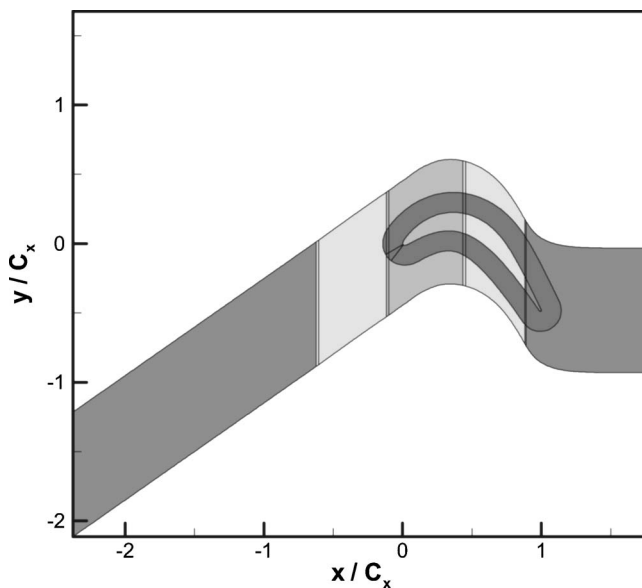


Fig. 15 Grid used for computation of experiments of Huang et al. [23] with $FSTI=1.6\%$ and 2.85%

gion the pressure coefficient distribution is overpredicted.

Computed velocity profiles are compared to experiment at 11 stations along the suction surface of the blade in Figs. 23(a)–23(k) for $Re=82,324$ and $FSTI=0.5\%$. The results compare well with the experiment up to $x/C_x=0.732$ shown in Figs. 23(a)–23(g). After this station flow separation takes place. Separation onset and reattachment are slightly earlier in the computations compared to experiment as given in Table 4. This also can be observed from the velocity profiles at stations $x/C_x=0.798$ to 0.912 shown in Figs. 23(h)–23(j). Overall computations compare well with the experimental measurements.

Next the Reynolds number is reduced to $41,162$ and the computed and experimental velocity profiles are compared in Figs. 24(a)–24(k). The computed profiles agree well with experiments except at $x/C_x=0.912$ shown in Fig. 24(j). At this station the computation indicates a smaller separated flow region close to reattachment in contrast to the experiment. However, the flow reattaches around $x/C_x=0.95$ both in computation and experiment, and in the next measurement station the agreement is well.

The next case considered has a Reynolds number of $20,581$. Computed velocity profiles are shown along with the experimental data at 11 axial stations in Figs. 25(a)–25(k). In this case flow separates around $x/C_x \approx 0.76$ and does not reattach in experiment; however, computations indicated reattachment at $x/C_x \approx 0.98$. This discrepancy is evident from the comparison of velocity pro-

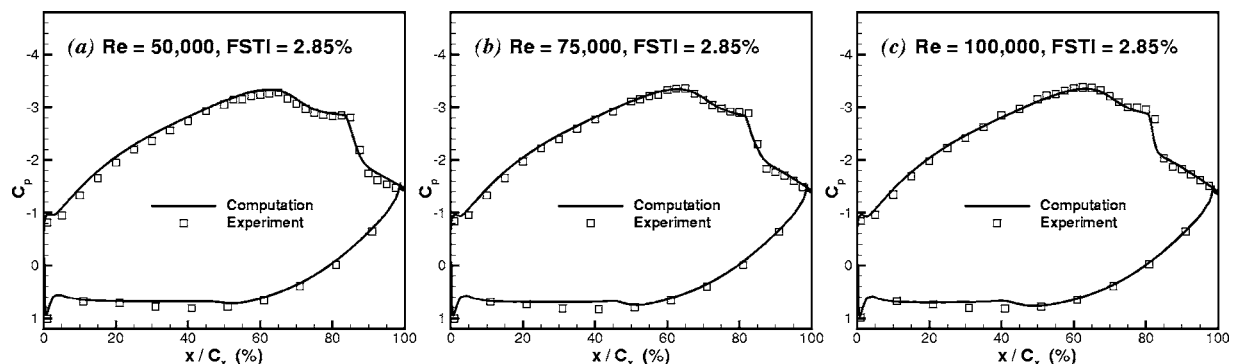


Fig. 16 Comparison of computed pressure coefficients with experiments of Huang et al. [23] for FSTI=2.85% cases

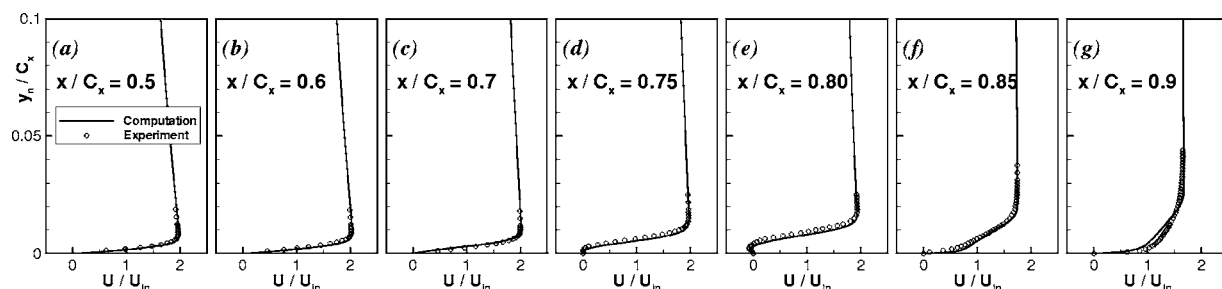


Fig. 17 Comparison of computed velocity profiles with experiments of Huang et al. [23], $Re=100,000$, FSTI=2.85% case

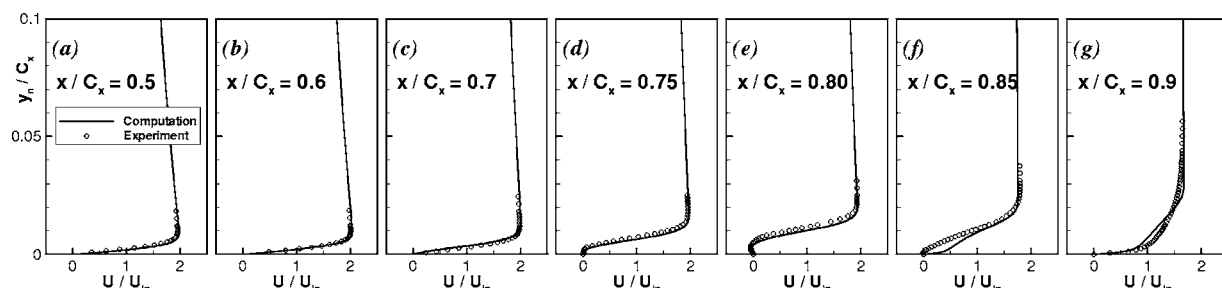


Fig. 18 Comparison of computed velocity profiles with experiments of Huang et al. [23], $Re=75,000$, FSTI=2.85% case

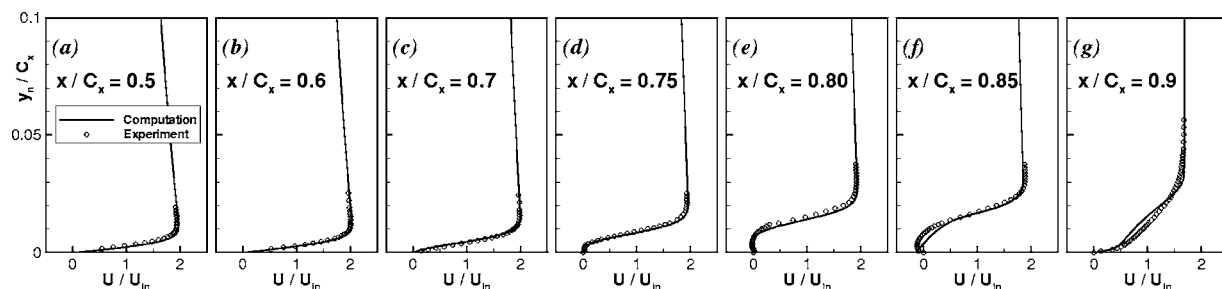


Fig. 19 Comparison of computed velocity profiles with experiments of Huang et al. [23], $Re=50,000$, FSTI=2.85% case

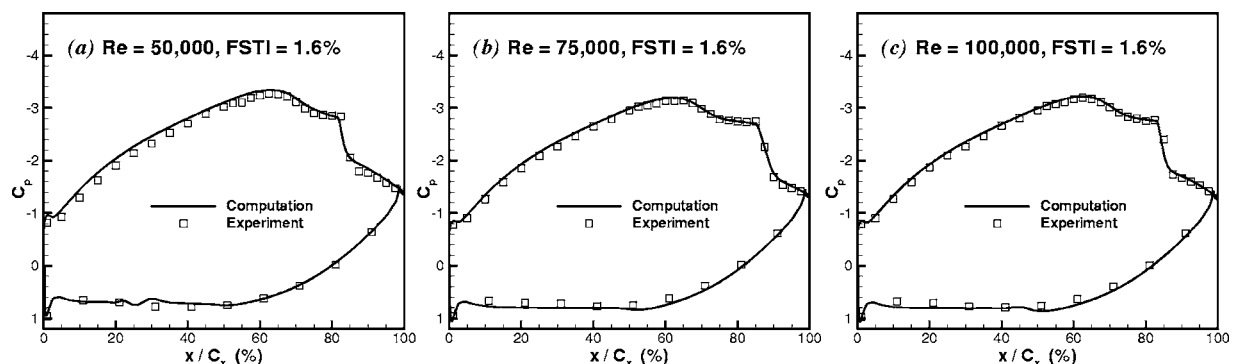


Fig. 20 Comparison of computed pressure coefficients with experiments of Huang et al. [23] for FSTI=1.6% cases

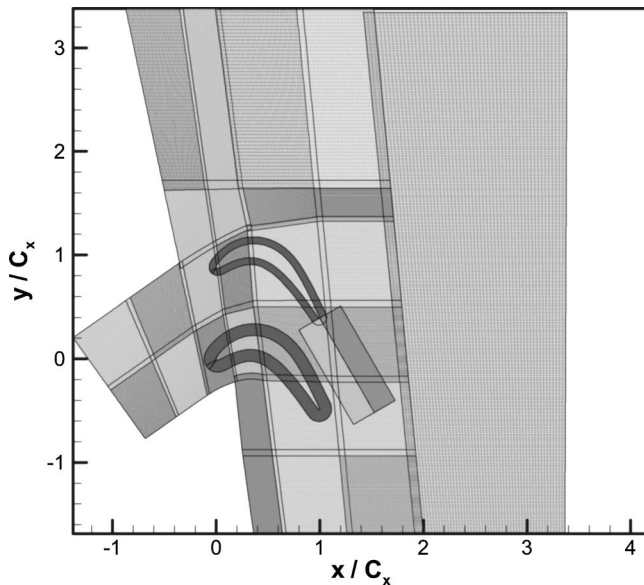


Fig. 21 Thirty-one zone multiblock grid used for computation of experiments of Volino [24]

files at the last two measurement stations shown in Figs. 25(j) and 25(k). The computation indicates a smaller separated region in these stations and finally reattaches very close to the trailing edge. Onset of transition was predicted at $x/C_x=0.978$.

The final case in this set of experiments is the one with $Re = 10,291$. The computed velocity profiles compare very well with the experimental data as shown in Figs. 26(a)–26(k). In this case the flow separates around $x/C_x \approx 0.76$ and does not reattach. The flow is completely laminar; transition was not predicted on the blade.

5 Concluding Remarks

A transport equation for the intermittency factor is employed to predict three sets of recent low-pressure turbine experiments on the Pack B blade. The intermittent behavior of the transitional flows is taken into account by modifying the eddy viscosity with the intermittency factor. Comparisons of the computed and experimental data are made and overall good agreement with the experimental data is obtained. The predicting capabilities of the current intermittency approach and the intermittency transport model in prediction of transitional flows under a wide range of low-pressure turbine conditions is demonstrated.

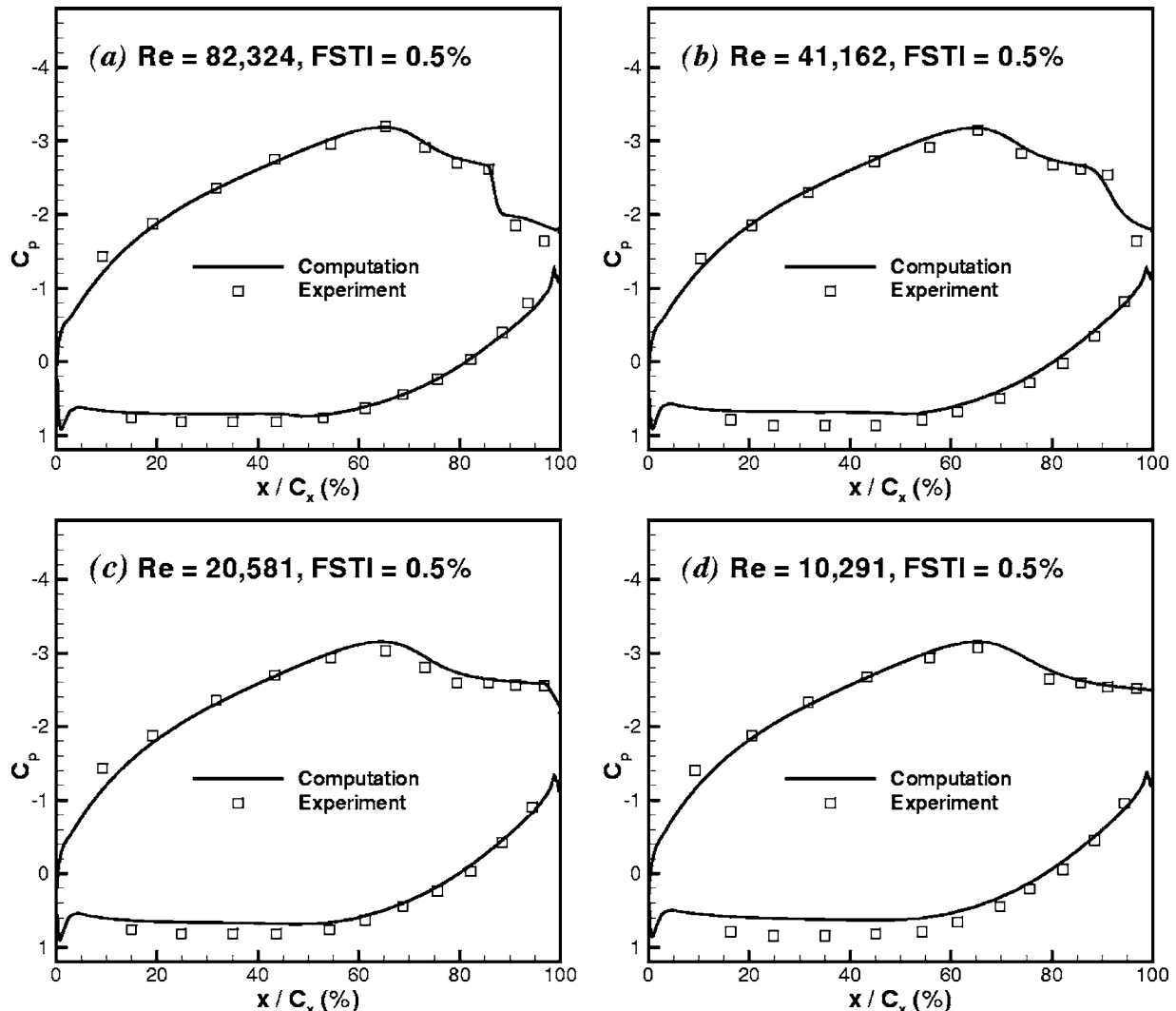


Fig. 22 Comparison of computed pressure coefficient distributions with experiments of Volino [24], FSTI=0.5%

Table 4 Separation, reattachment, and transition locations for cases of Volino [24]

Re ($U_{in}C_x/\nu$)	FSTI (%)	x_s/C_x (Computation)	x_s/C_x (Experiment)	x_r/C_x (Computation)	x_r/C_x (Experiment)	x_{tr}/C_x (Computation)
10,291	0.5	0.760	0.750
20,581	0.5	0.765	0.760	0.980	...	0.978
41,162	0.5	0.760	0.770	0.950	0.950	0.840
82,324	0.5	0.757	0.767	0.890	0.900	0.857

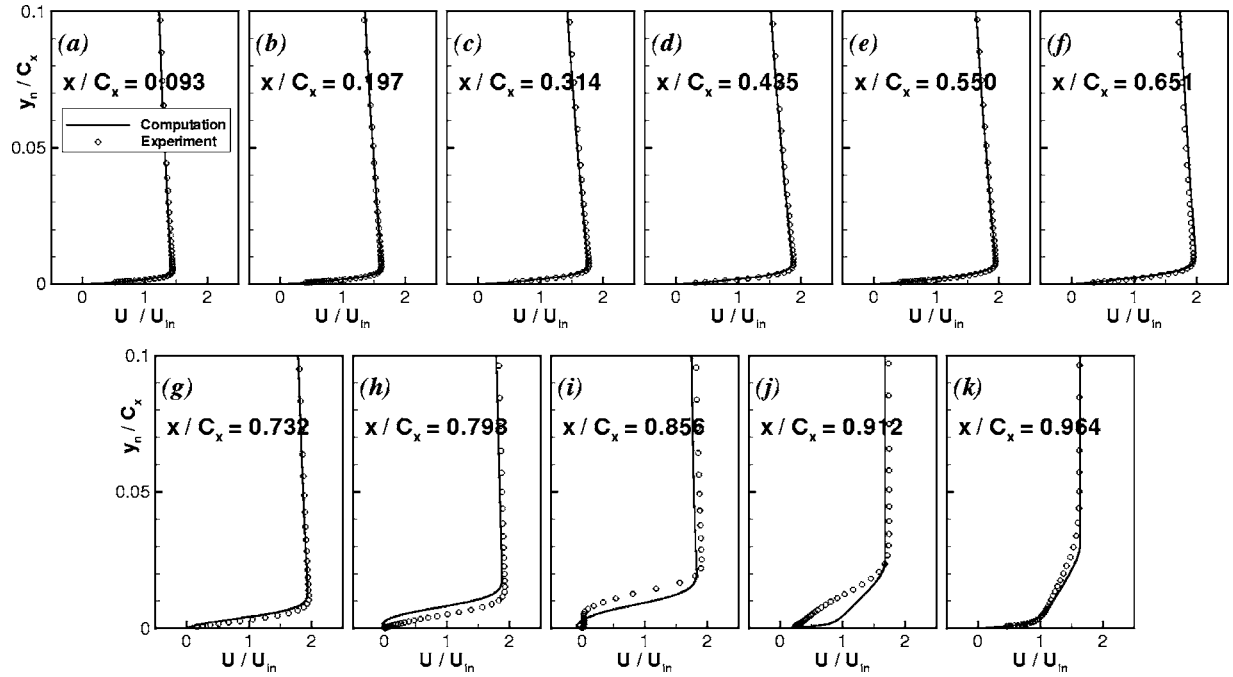


Fig. 23 Comparison of computed velocity profiles with experiments of Volino [24], Re=82,324, FSTI=0.5%

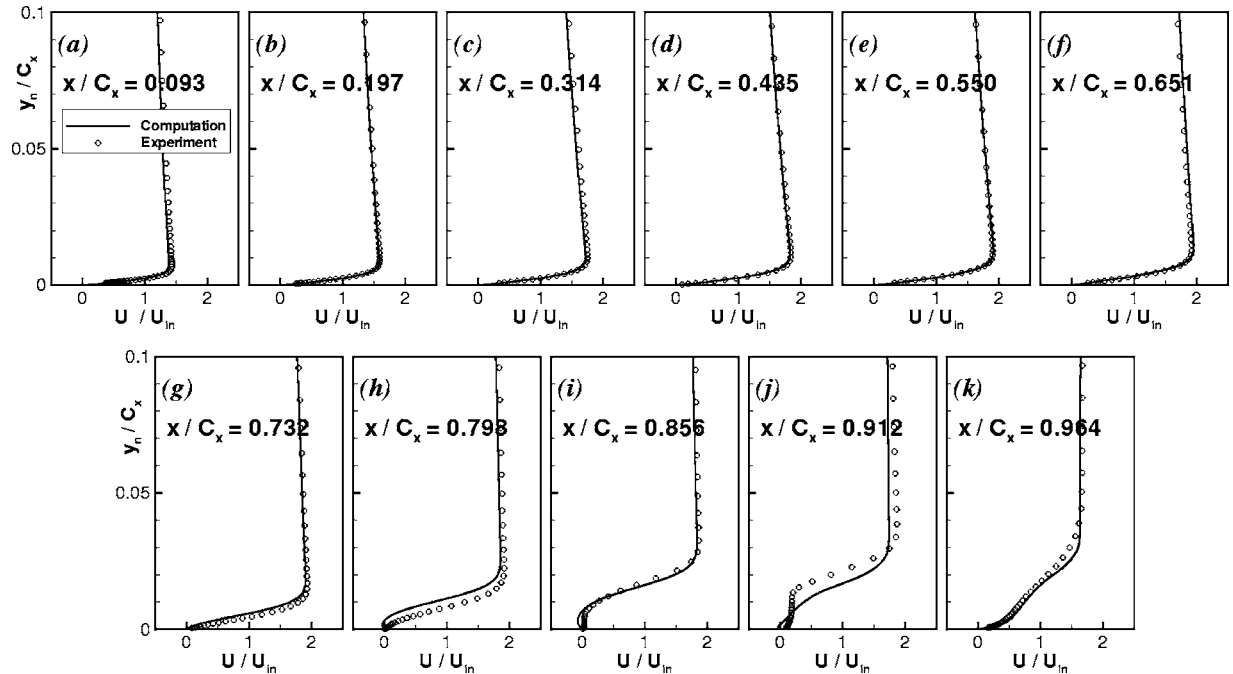


Fig. 24 Comparison of computed velocity profiles with experiments of Volino [24], Re=41,162, FSTI=0.5%

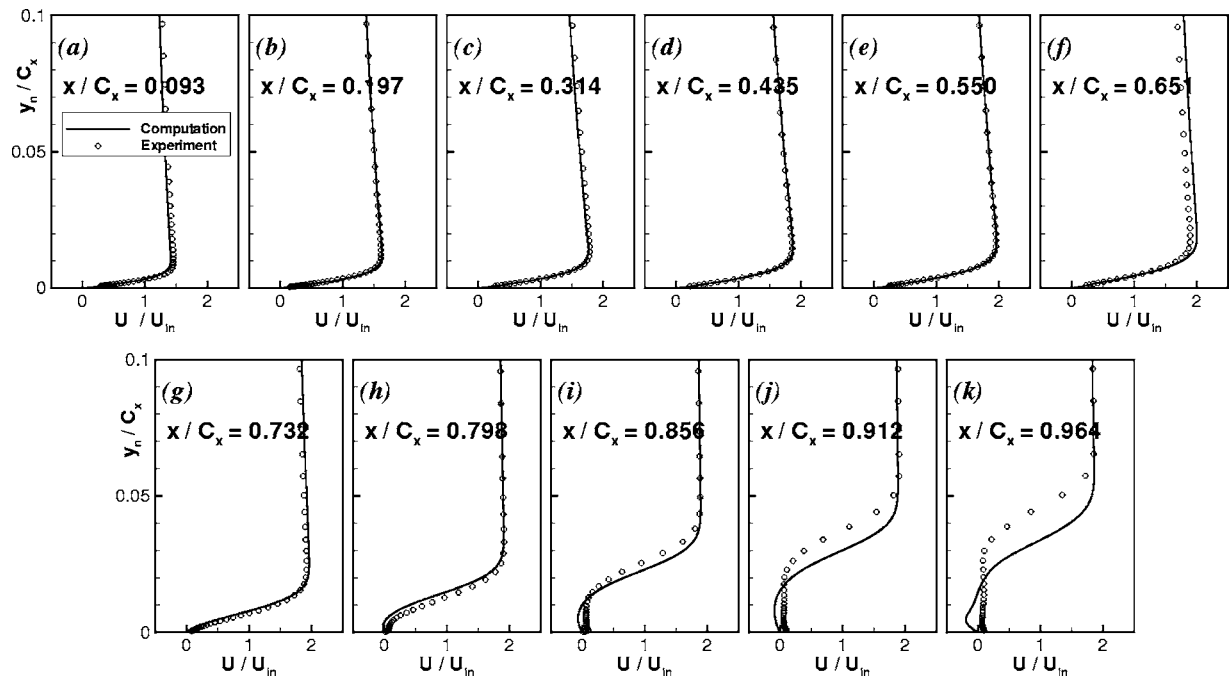


Fig. 25 Comparison of computed velocity profiles with experiments of Volino [24], $Re=20,581$, $FSTI=0.5\%$

Acknowledgment

This work is supported by NASA Glenn Research Center under Cooperative Agreement NCC3-590 and followed by NCC3-1040. The project is part of the Low Pressure Turbine Flow Physics Program of NASA-Glenn.

The experimental efforts at University of Notre Dame are supported by Cooperative Agreement NCC3-935 and Cooperative Agreement NCC3-775 and the research at U.S. Naval Academy is supported by Contract C-31011-K. This paper was originally published as AIAA Paper 2003-3591.

Nomenclature

- C_p = pressure coefficient, $2(P - P_\infty)/(\rho_\infty U_{in}^2)$
- C_x = axial chord
- $FSTI$ = freestream turbulence intensity (%)
- K_t = flow acceleration parameter $(\nu/U_e^2)(dU_e/ds)$
- k = turbulent kinetic energy
- L_x = axial chord
- N = nondimensional spot breakdown rate parameter, $n\sigma\theta_i^3/\nu$

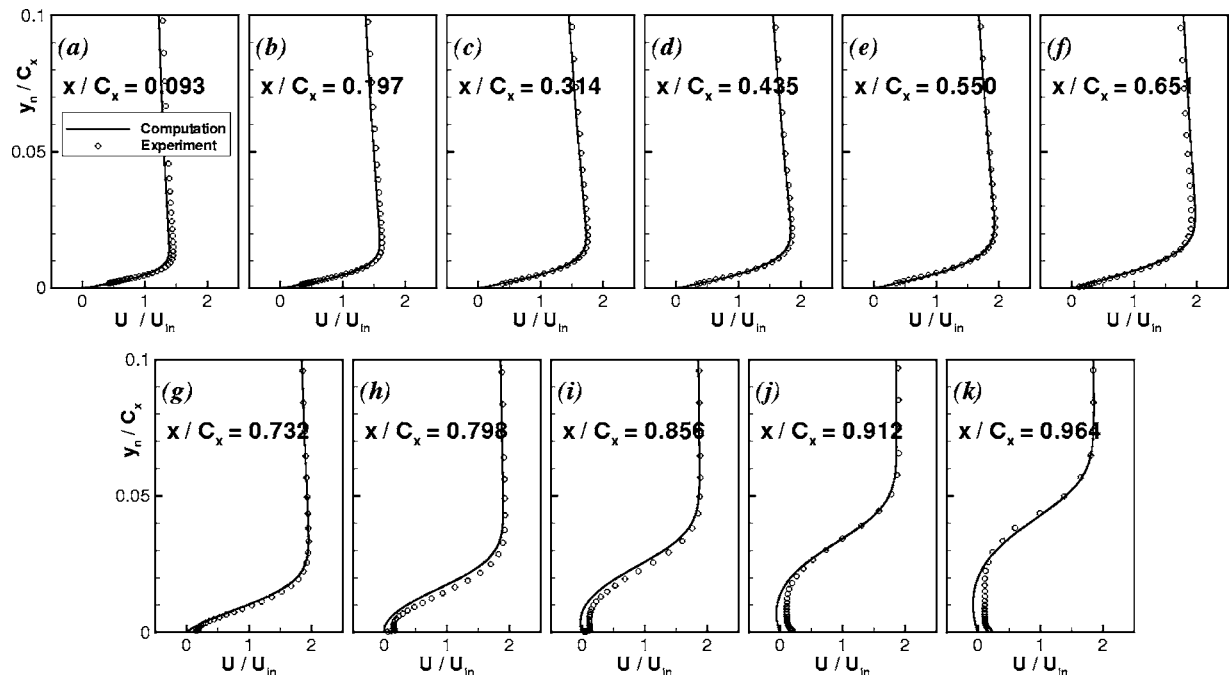


Fig. 26 Comparison of computed velocity profiles with experiments of Volino [24], $Re=10,291$, $FSTI=0.5\%$

n = spot generation rate
 P = static pressure
 P_{total} = total pressure
 Re = Reynolds number
 $\text{Re}_{st} = (s_t - s_s)U_e/\nu$
 $\text{Re}_{\theta} = \theta U_e/\nu$
 s = streamwise distance along suction surface
 Tu = turbulence intensity (%), u'/U
 U = boundary layer streamwise velocity
 U_e = local freestream velocity
 U_{in} = inlet freestream velocity
 u_τ = friction velocity
 W = magnitude of vorticity
 y_n = distance normal to the wall
 $y^+ = y_n u_\tau / \nu$
 γ = intermittency factor
 θ = momentum thickness
 λ_θ = pressure gradient parameter $(\theta^2/\nu)(dU/ds)$
 μ = molecular viscosity
 μ_t = eddy viscosity
 $\nu = \mu/\rho$
 $\nu_t = \mu_t/\rho$
 ω = total pressure loss coefficient,
 $2(P_{\text{total inlet}} - P_{\text{total exit}})/(\rho_\infty U_\infty^2)$
 ρ = density
 σ = spot propagation parameter

Subscripts

e = freestream
 s = onset of separation
 t = onset of transition

References

- [1] Mayle, R. E., 1991, "The Role of Laminar-Turbulent Transition in Gas Turbine Engines," *ASME J. Turbomach.*, **113**, pp. 509–537.
- [2] Rivir, R. B., 1996, "Transition on Turbine Blades and Cascades at Low Reynolds Numbers," AIAA Paper No. 96-2079.
- [3] Lake, J. P., King, P. I., and Rivir, R. B., 2000, "Low Reynolds Number Loss Reduction on Turbine Blades With Dimples and V-Grooves," AIAA Paper No. 00-0738.
- [4] Simon, F. F., and Stephens, C. A., 1991, "Modeling of the Heat Transfer in Bypass Transitional Boundary-Layer Flows," NASA Technical Paper No. 3170.
- [5] Dhawan, S., and Narasimha, R., 1958, "Some Properties of Boundary Layer During the Transition from Laminar to Turbulent Flow Motion," *J. Fluid Mech.*, **3**, pp. 418–436.
- [6] Gostelow, J. P., Blunden, A. R., and Walker, G. J., 1994, "Effects of Free-Stream Turbulence and Adverse Pressure Gradients on Boundary Layer Transition," *ASME J. Turbomach.*, **116**, pp. 392–404.
- [7] Solomon, W. J., Walker, G. J., and Gostelow, J. P., 1995, "Transition Length Prediction for Flows With Rapidly Changing Pressure Gradients," *ASME Paper No. 95-GT-241*.
- [8] Chen, K. K., and Thyson, N. A., 1971, "Extension of Emmons' Spot Theory to Flows on Blunt Bodies," *AIAA J.*, **9**(5), pp. 821–825.
- [9] Steelant, J., and Dick, E., 1996, "Modelling of Bypass Transition With Conditioned Navier-Stokes Equations Coupled to an Intermittency Transport Equation," *Int. J. Numer. Methods Fluids*, **23**, pp. 193–220.
- [10] Cho, J. R., and Chung, M. K., 1992, "A $k-\epsilon-\gamma$ Equation Turbulence Model," *J. Fluid Mech.*, **237**, pp. 301–322.
- [11] Suzen, Y. B., and Huang, P. G., 1999, "Modelling of Flow Transition Using an Intermittency Transport Equation," NASA Contractor Report, NASA-CR-1999-209313, Cleveland, OH.
- [12] Savill, A. M., 1993, "Some Recent Progress in The Turbulence Modeling of By-pass Transition," in *Near-Wall Turbulent Flows*, R. M. C. So, C. G. Speziale, and B. E. Launder, eds., Elsevier Science Publishers B.V., Amsterdam, pp. 829–848.
- [13] Savill, A. M., 1993, "Further Progress in The Turbulence Modeling of By-pass Transition," *Engineering Turbulence Modeling and Experiments 2*, W. Rodi and F. Martelli, eds., Elsevier Science Publishers B.V., Amsterdam, pp. 583–592.
- [14] Simon, T. W., Qiu, S., and Yuan, K., 2000, "Measurements in a Transitional Boundary Layer Under Low-Pressure Turbine Airfoil Conditions," NASA Contractor Report, NASA-CR-2000-209957, Cleveland, OH.
- [15] Hultgren, L. S., and Volino, R. J., 2000, "Separated and Transitional Boundary Layers Under Low-Pressure Turbine Airfoil Conditions," in preparation.
- [16] Suzen, Y. B., and Huang, P. G., 2000, "Modeling of Flow Transition Using an Intermittency Transport Equation," AIAA Paper AIAA-2000-0287.
- [17] Suzen, Y. B., and Huang, P. G., 2000, "Modeling of Flow Transition Using an Intermittency Transport Equation," *ASME J. Fluids Eng.*, **122**, pp. 273–284.
- [18] Suzen, Y. B., Xiong, G., and Huang, P. G., 2000, "Predictions of Transitional Flows in Low-Pressure Turbines Using an Intermittency Transport Equation," AIAA Paper AIAA-2000-2654.
- [19] Suzen, Y. B., Huang, P. G., Hultgren, L. S., and Ashpis, D. E., 2001, "Predictions of Separated and Transitional Boundary Layers Under Low-Pressure Turbine Airfoil Conditions Using an Intermittency Transport Equation," AIAA Paper AIAA-2001-0446.
- [20] Suzen, Y. B., Huang, P. G., Hultgren, L. S., and Ashpis, D. E., 2003, "Predictions of Separated and Transitional Boundary Layers Under Low-Pressure Turbine Airfoil Conditions Using an Intermittency Transport Equation," *ASME J. Turbomach.*, **125**(3), pp. 455–464.
- [21] Suzen, Y. B., Xiong, G., and Huang, P. G., 2002, "Predictions of Transitional Flows in Low-Pressure Turbines Using an Intermittency Transport Equation," *AIAA J.*, **40**(2), pp. 254–266.
- [22] Lake, J. P., King, P. I., and Rivir, R. B., 1999, "Reduction of Separation Losses on a Turbine Blade With Low Reynolds Number," AIAA Paper AIAA-99-0242.
- [23] Huang, J., Corke, T. C., and Thomas, F. O., 2003, "Plasma Actuators for Separation Control of Low Pressure Turbine Blades," AIAA Paper AIAA-2003-1027.
- [24] Volino, R. J., 2002, "Separated Flow Transition Under Simulated Low-Pressure Turbine Airfoil Conditions: Part 1-Mean Flow and Turbulence Statistics," *ASME Paper ASME-GT-30236*.
- [25] Rhie, C. M., and Chow, W. L., 1983, "Numerical Study of the Turbulent Flow Past an Airfoil With Trailing Edge Separation," *AIAA J.*, **21**, pp. 1525–1532.
- [26] Hsu, M. C., Vogiatzis, K., and Huang, P. G., 2003, "Validation and Implementation of Advanced Turbulence Models in Swirling and Separated Flows," AIAA Paper AIAA 2003-0766.
- [27] Suzen, Y. B., and Huang, P. G., 2005, "Numerical Simulation of Unsteady Wake/Blade Interactions in Low-Pressure Turbine Flows Using an Intermittency Transport Equation," *ASME J. Turbomach.*, **127**(3), pp. 431–444.
- [28] Menter, F. R., 1994, "Two-Equation Eddy-Viscosity Turbulence Models for Engineering Applications," *AIAA J.*, **32**(8), pp. 1598–1605.
- [29] Abu-Ghannam, B. J., and Shaw, R., 1980, "Natural Transition of Boundary Layers—The Effects of Turbulence, Pressure Gradient, and Flow History," *J. Mech. Eng. Sci.*, **22**(5), pp. 213–228.
- [30] Davis, R. L., Carter, J. E., and Reshotko, E., 1987, "Analysis of Transitional Separation Bubbles on Infinite Swept Wings," *AIAA J.*, **25**(3), pp. 421–428.

GT-2002-30236

SEPARATED FLOW TRANSITION UNDER SIMULATED LOW-PRESSURE TURBINE AIRFOIL CONDITIONS: PART 1 – MEAN FLOW AND TURBULENCE STATISTICS

Ralph J. Volino

Department of Mechanical Engineering
 United States Naval Academy
 Annapolis, Maryland 21402
 Email: volino@usna.edu

ABSTRACT

Boundary layer separation, transition and reattachment have been studied experimentally under low-pressure turbine airfoil conditions. Cases with Reynolds numbers (Re) ranging from 25,000 to 300,000 (based on suction surface length and exit velocity) have been considered at low (0.5%) and high (9% inlet) free-stream turbulence levels. Mean and fluctuating velocity and intermittency profiles are presented for streamwise locations all along the airfoil, and turbulent shear stress profiles are provided for the downstream region where separation and transition occur. Higher Re or free-stream turbulence level moves transition upstream. Transition is initiated in the shear layer over the separation bubble and leads to rapid boundary layer reattachment. At the lowest Re , transition did not occur before the trailing edge, and the boundary layer did not reattach. Turbulent shear stress levels can remain low in spite of high free-stream turbulence and high fluctuating streamwise velocity in the shear layer. The beginning of a significant rise in the turbulent shear stress signals the beginning of transition. A slight rise in the turbulent shear stress near the trailing edge was noted even in those cases which did not undergo transition or reattachment. The present results provide detailed documentation of the boundary layer and extend the existing database to lower Re . The present results also serve as a baseline for an investigation of turbulence spectra in Part 2 of the present paper, and for ongoing work involving transition and separation control.

NOMENCLATURE

C_f	skin friction coefficient
C_p	$2(P_T - P)/\rho U_e^2$, pressure coefficient
$FSTI$	free-stream turbulence intensity
H	δ^*/θ , shape factor
K	$(v/U_\infty^2)(dU_\infty/dx)$, acceleration parameter
L_s	suction surface length
ℓ	hot-wire sensor length
P	pressure
P_T	upstream stagnation pressure
Re	$U_e L_s / \nu$, exit Reynolds number

Re_s	$U_\infty s / \nu$, local Reynolds number
Re_θ	momentum thickness Reynolds number
s	streamwise coordinate, distance from leading edge
U	mean streamwise velocity
U_∞	local free-stream velocity
U_e	nominal exit free-stream velocity, based on inviscid solution
u'	rms streamwise fluctuating velocity
u_τ	$\sqrt{\tau_w / \rho}$, friction velocity
$-u'v'$	time averaged turbulent shear stress
v'	rms wall normal fluctuating velocity
y	cross-stream coordinate, distance from wall
y^+	yu_τ / ν , distance from wall in wall coordinates
δ^*	displacement thickness
γ	intermittency, fraction of time flow is turbulent
ν	kinematic viscosity
ρ	density
τ_w	wall shear stress
θ	momentum thickness

INTRODUCTION

Modern low-pressure (LP) turbine airfoils are subject to increasingly stronger pressure gradients as designers impose higher loading in an effort to improve efficiency and lower cost by reducing the number of airfoils in an engine. If the adverse pressure gradient on the suction side of these airfoils becomes strong enough, the boundary layer will separate. Separation bubbles, particularly those which fail to reattach, can result in a significant loss of lift and a subsequent degradation of engine efficiency (e.g. Hourmouziadis [1], Mayle [2], and Sharma et al. [3]). The problem is particularly relevant in aircraft engines. Airfoils optimized to produce maximum power under takeoff conditions may still experience boundary layer separation at cruise conditions, due to the thinner air and lower Reynolds numbers at altitude. A component efficiency drop of 2 percent may occur between takeoff and cruise conditions in large commercial transport engines, and the difference could be as large as 7 percent in smaller engines operating at higher altitudes. Component life may also be

affected by more than an order of magnitude (Hodson [4]). Because the LP turbine produces the bulk of the net power in many engines, changes in its component efficiency can result in nearly equal changes in overall engine efficiency (Wisler [5]). There are several sources for losses in an engine, including secondary flows, but the suction side boundary layer has been identified as the primary source of losses in the LP turbine (Curtis et al. [6]). Prediction and control of suction side separation, without sacrifice of the benefits of higher loading, is therefore, necessary for improved engine design.

Separation on LP turbine airfoils is complicated by boundary layer transition. Turbulent boundary layers are much more resistant to separation than laminar boundary layers. A substantial fraction of the boundary layer on both sides of a turbine airfoil may be transitional (Mayle [2]), so accurately predicting transition location is crucial for accurate prediction of separation. Transition prediction for turbine airfoils is complex and can depend on a number of factors, including the free-stream turbulence intensity ($FSTI$), streamwise pressure gradient, airfoil curvature, surface roughness, and the unsteadiness associated with passing wakes from upstream stages. Several transition mechanisms are possible under engine conditions. Mayle [2] classified the modes of transition as “natural transition” involving Tollmien-Schlichting waves; “bypass” transition caused by high free-stream turbulence or other large disturbances; “separated flow” transition of the shear layer over a separation bubble; “periodic-unsteady” transition, which might also be called wake-induced transition; and reverse transition. If transition occurs far enough upstream, it can prevent separation. If transition occurs in the shear layer over a separation bubble, it will tend to induce boundary layer reattachment. The lower the Reynolds number, the farther downstream transition will tend to occur, hence the problems associated with performance at altitude.

Boundary layer transition has been studied extensively, and in recent years several studies have focused on transition in the LP turbine. Halstead et al. [7] present a study from a rotating cascade with multiple stages and $FSTI$ characteristic of engine conditions. The adverse pressure gradients in this study were not strong enough to induce separation, however. Solomon [8] subsequently modified the facility and provides documentation of separation from a more aggressive airfoil. Gier and Ardey [9] provide another example from a rotating facility. Boundary layers and separation bubbles on flat plates subject to adverse pressure gradients have been considered in several studies. Recent work has included the studies of Hatman and Wang [10], Sohn et al. [11], Lou and Hourmouziadis [12], Volino and Hultgren [13] and Yaras [14]. On airfoils, either in cascade or single-passage cascade-simulators, studies have included Murawski et al. [15], Qiu and Simon [16] and Simon et al. [17]. Cascades with moving wakes, simulating the effect of upstream blade rows, were utilized by Brunner et al. [18], Stadtmüller et al. [19], Howell et al. [20] and Kaszeta et al. [21]. Numerical studies have included the work of Dorney et al. [22], Chernomovkin and Lakshminarayana [23], Huang and Xiong [24], and Thermann et al. [25]. A few studies have included attempts to control transition and separation. Howell et al. [20] studied modified airfoil shapes, Van Treuren et al. [26] utilized vortex generators, and Lake et al. [27] considered various passive devices including dimples. Bons et al. [28] showed considerable success using both steady and pulsed vortex generator jets. The preceding list of studies, while long, is by no means inclusive. It is merely a sample of recent work, biased toward the most recent studies.

Much has been learned from the work to date, but the nature of separated flow transition is still not completely clear, and existing models are still not as robust as needed for accurate prediction. The present study expands the existing database. The flow through a

single-passage cascade-simulator is documented under both high and low $FSTI$ conditions at several different Reynolds numbers. The geometry of the passage corresponds to that of the “Pak-B” airfoil, which is an industry supplied research airfoil that is representative of a modern, aggressive LP turbine design. This geometry was used in several of the studies mentioned above ([15, 16, 17, 21, 22, 23, 27, 28]), and the pressure profile from the suction side of this airfoil was matched in the flat plate study of Volino and Hultgren [13]. Previous work has included documentation at Re (based on suction surface length and exit free-stream velocity) as low as 50,000 (e.g. [13, 16, 21]). The present work includes the first complete documentation (to the author’s knowledge) of cases with Re as low as 25,000. Also new is documentation of the turbulent shear stress in the boundary layer under both high and low $FSTI$.

Details of the experimental facility and results of the study follow. The present paper focuses on mean and statistical quantities. Part 2 of this work [29] includes turbulence spectral results, providing evidence of the important transition mechanisms.

EXPERIMENTS

Experiments were conducted in a low speed wind tunnel, described by Volino et al. [30]. Briefly, air enters through blowers and passes through a series of screens, a honeycomb, two settling chambers, and a three-dimensional contraction before entering the test section. At the exit of the contraction, the mean velocity is uniform to within 1%. The $FSTI$ is $0.5\% \pm 0.05\%$. Nearly all of this free-stream “turbulence” is actually streamwise unsteadiness at frequencies below 20 Hz and is not associated with turbulent eddies. The rms intensities of the three components of the unsteadiness are 0.7%, 0.2% and 0.2% in the streamwise, pitchwise and spanwise directions, respectively. For low $FSTI$ cases, the test section immediately follows the contraction. For high $FSTI$, a passive grid is installed at the contraction exit followed by a 1 m long rectangular settling chamber. Details of the grid are available in Volino et al. [30]. At the inlet to the test section the high $FSTI$ mean flow and turbulence are spatially uniform to within 3% and 6% respectively. The free-stream turbulence is nearly isotropic with rms intensities of 8.8%, 8.9% and 8.3% in the streamwise, pitchwise and spanwise directions. The integral length scales of these components are 3 cm, 1.6 cm and 1.4 cm. The integral scales were computed from the power spectra of each component.

The test section, shown in Fig. 1, consists of the passage between two airfoils. Details are listed in Table 1. Cascade simulators of this type have been used in studies such as Chung and Simon [31], more recently in the present facility by Aunapu et al. [32], and with the Pak-B geometry by Qiu and Simon [16] and Kaszeta et al. [21]. A large span to chord ratio of 4.3 was chosen to insure two-dimensional flow at the spanwise centerline of the airfoils, where all measurements were made. Upstream of each airfoil are flaps, which control the amount of bleed air allowed to escape from the passage. These are adjusted to produce the correct leading edge flow and pressure gradient along the airfoils. A tailboard on the pressure side of the passage also aids in setting the pressure gradient.

Single passage test sections have several advantages. For a given wind tunnel with fixed maximum flow rate, the single passage can be considerably larger than a passage in a multi-blade facility. The larger size and simpler geometry can also result in better probe access. Previous studies (e.g. [31, 32]) demonstrated that the full flow field, including the three-dimensional secondary flows near the endwalls, in a single passage can be set to match that in a corresponding multi-blade cascade. The present test section also has some advantages over flat plate test sections. First, the airfoil curvature is matched. Second, with an adverse pressure gradient, suction is often needed to prevent

Table 1: Test section parameters

Axial Chord [mm]	True Chord [mm]	Pitch [mm]	Span [mm]	Suction side, L_s [mm]	Inlet flow angle	Exit flow angle
153.6	170.4	136.0	660.4	228.6	35°	60°

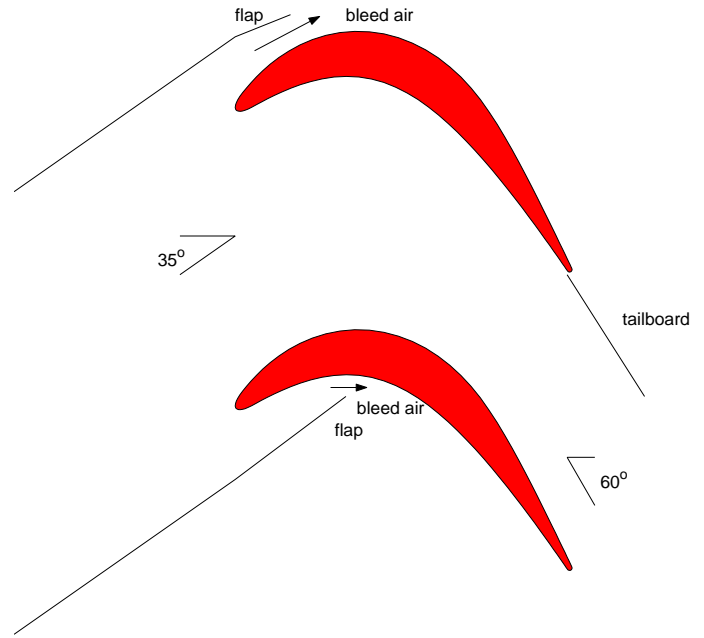
separation on the wall opposite a flat test plate (e.g. Volino and Hultgren [13]). A cascade simulator does not require suction due to the favorable pressure gradient on the pressure side of the passage.

Single passages also have disadvantages. It is, of course, impossible to establish periodicity. Stage losses cannot be directly determined since there is flow only on one side of each airfoil and the downstream wake is, therefore, unlike that in a multi-blade facility. This limitation, however, is not prohibitive for the present study. Primary concern is with boundary layer separation and transition, which occur *in the passage*. Although the downstream wake may be different, the flow in the passage does match that of a multi-blade facility.

Ten different cases have been documented including high and low *FSTI* cases at five Reynolds numbers ($Re=25,000, 50,000, 100,000, 200,000, \text{ and } 300,000$). The Reynolds number range is representative of conditions from cruise to takeoff. The *FSTI* levels in an engine may vary considerably, but the values in the present work are believed to span the range of most interest. Solomon [8] surveyed several studies that included wake effects and found *FSTI* values ranging from 1 to 5% between wakes and from 3 to 23% within wakes. Wakes can affect transition and separation in the boundary layer in three ways. First, the *FSTI* rises during a wake passage compared to the between-wake value. Second, a calmed region follows wake induced transition. The calmed flow is non-turbulent, but unlike a steady non-turbulent flow, it can be very resistant to separation. Finally, independent of the *FSTI* effect, each wake includes a mean velocity deficit, resulting in temporal deceleration and acceleration as the wake passes. Lou and Hourmouziadis [12] separated this temporal effect from the wake turbulence effect, using downstream control to create an oscillating velocity in their test section. In the present study, only steady flow is considered. While the significant effects of temporal acceleration and calming are not present, the high and low *FSTI* cases of the present study do allow a means for evaluating the effect of wake turbulence level.

Measurements

Pressure surveys were made for each case using a pressure transducer (0-870 Pa range Validyne transducer) and a Scanivalve. Stagnation pressure was measured with a pitot tube upstream of the passage inlet, and eleven pressure taps were located on each airfoil along their spanwise centerlines. Locations of the taps on the suction side are listed in Table 2 along with measured local *FSTI* components, and the ReK product at these stations based on a non-separating, inviscid solution. The pressure distribution on the upstream portion of the suction side always closely matched the inviscid solution for flow over the airfoil. This allowed the use of the measured static pressure at the third pressure tap on the suction side, along with the inviscid flow solution for the passage and the upstream stagnation pressure, to determine the nominal passage exit velocity, which was used to normalize the measured pressure distributions. More conventionally the measured inlet velocity and the inlet and exit flow angles are used to compute the exit velocity. Because the velocity at the third tap is 1.9 times that at the passage inlet, and therefore easier to measure, using the third tap velocity reduced the bias uncertainty in the pressure coefficients, particularly at the lower Reynolds numbers. The uncertainty in the suction side pressure coefficients was 7% at the lowest Re , and below 4% in other cases. Most of this uncertainty was

**Fig. 1: Schematic of the test section**

due to bias error. Stochastic error was minimized by averaging pressure transducer readings over a 10 second period.

Velocity profiles were measured at eleven streamwise stations along the suction side at the locations given in Table 2. Profiles were measured near but not at the spanwise centerline of the airfoil to insure that the pressure taps did not interfere with the velocity measurements. Profiles were acquired with a hot-wire anemometer (TSI model IFA100) and a single sensor boundary layer probe (TSI model 1218-T1.5). The sensor diameter is 3.8 μm , and the active length is 1.27 mm. At each measurement location, data were acquired for 26 seconds at a 20 kHz sampling rate (2^{19} samples). All raw data were saved. The high sampling rate provides an essentially continuous signal, which is needed for intermittency and spectral post-processing. The long sampling time results in low uncertainty in both statistical and spectral quantities. Data were acquired at 60 wall normal locations in each profile, extending from the wall to the free-stream, with most points concentrated in the near wall region. The closest point was 0.1 mm from the wall, which corresponds to $y/L_s=0.0004$ and between 0.01 and 0.2 boundary layer thicknesses. Flow direction in a separation bubble cannot be determined with a single-sensor hot-wire, but velocity magnitude can be measured and was found to be essentially zero within the bubbles of the present cases. Determining the direction was not, therefore, considered essential. At locations where the boundary layer was attached, local wall shear stress was computed from the near wall profile using the technique of Volino and Simon [33]. Uncertainties in the mean velocity are 3-5% except in the very near wall region ($y^+ < 5$) where near-wall corrections (Wills [34]) were applied to the mean velocity. Uncertainties in the momentum and displacement thicknesses computed from the mean profiles are 10%. Uncertainty in the shape factor, H , and the wall shear stress are both 8%.

The uncertainty in the fluctuating streamwise velocity is below 10%, except in the very near wall region, where spatial averaging effects become important in some cases. Ligrani and Bradshaw [35, 36] showed that spatial averaging over the length of a hot-wire sensor can result in low apparent u' . Their experiments were done in a fully-

Table 2: Measurement stations locations, local acceleration (inviscid soln.), and measured local free-stream turbulence

Station	s/L_s	$ReK \times 10^3$	Low $FSTI$ u'/U_∞ [%]	Low $FSTI$ v'/U_∞ [%]	High $FSTI$ u'/U_∞ [%]	High $FSTI$ v'/U_∞ [%]
1	0.111	209.3	0.44		5.2	
2	0.194	121.4	0.39		4.6	
3	0.278	77.6	0.37		4.0	
4	0.361	58.2	0.38		3.5	
5	0.444	37.2	0.39		3.2	
6	0.528	-0.2	0.41		2.8	
7	0.611	-60.6	0.47	0.05	2.9	5.9
8	0.694	-71.7	0.47	0.12	3.0	6.2
9	0.777	-57.3	0.48	0.14	3.4	6.6
10	0.861	-48.7	0.54	0.11	3.8	6.8
11	0.944	-17.5	0.51	0.11	4.0	6.8

turbulent boundary layer with $Re_\theta=2600$. The spatial averaging effects become important when the sensor length is longer than the width of the smaller near wall streaks in a turbulent boundary layer. Ligrani and Bradshaw [35, 36] found that the spatial averaging effects become small when the dimensionless sensor length, $\ell u_\tau / \nu$, is less than about 25. The error also becomes smaller as the sensor is moved away from the wall. This is expected since the average size of the turbulent eddies should increase with distance from the wall. The Ligrani and Bradshaw [35, 36] results suggest that when the distance from the wall, y , is larger than the sensor length, ℓ , that spatial averaging errors are under 10% even for large $\ell u_\tau / \nu$. Closer to the wall they showed errors in u' as large as 30% when $\ell u_\tau / \nu = 60$.

In the present study, $\ell u_\tau / \nu$ remains below 25 in all cases with $Re < 200,000$. Spatial averaging is not, therefore, expected to be a problem, even near the wall. For the $Re=200,000$ cases, $\ell u_\tau / \nu$ is above 25 at Station 11 of the low $FSTI$ case and at Stations 9-11 of the high $FSTI$ case, reaching values as high as 60. Spatial averaging should not be significant for $y > 1$ mm ($y/L_s > 0.004$), but may cause errors as high as 30% closer to the wall. It is not certain that the errors are this large, however. The momentum thickness Reynolds numbers in the present cases are all below 700, which is significantly below the $Re_\theta=2600$ value of the Ligrani and Bradshaw [35, 36] study. This may indicate less developed turbulence in the present study, which could imply fewer small scale eddies and lower averaging errors. For the $Re=300,000$ cases, $\ell u_\tau / \nu$ reaches values as high as 90 at Stations 10 and 11 of the low $FSTI$ case and Stations 9-11 of the high $FSTI$ case. As in the $Re=200,000$ cases, errors should be small when $y > 1$ mm, but may be larger closer to the wall.

A boundary layer cross-wire probe (TSI model 1243-T1.5) was used to measure profiles of the wall normal velocity and turbulent shear stress at Stations 7-11 for each case. The upstream boundary layer was too thin for cross-wire measurements. Data were acquired at 25 locations in each profile, beginning 1 mm from the wall and extending to the free-stream. Sampling rates and times were the same as for the single sensor probe. Uncertainty in the turbulent shear stress is 10%.

Measurements with the cross-wire probe are subject to spatial averaging errors due to the length of the sensors (1.27 mm active length) and the spacing between the two sensors (1 mm). Applying the results of Ligrani and Bradshaw [35, 36] and Ligrani et al. [37] to the present cases, spatial averaging may be significant at locations very near the wall, particularly for the high Reynolds number cases.

At locations farther from the wall than 1 mm, however, the errors should become small and within the 10% uncertainty estimate given above. Hence, no measurements were made at y locations below 1 mm. Because all measurements were at $y > 1$ mm and a boundary layer type probe was used, probe blockage effects were not expected to be significant.

The intermittency, γ , is the fraction of time the flow is turbulent within the transition region, and was determined at each measurement location using the technique described in Volino et al. [30] with an uncertainty of 10%. Turbulent flow in the boundary layer is defined here as flow which includes a range of large and small scales, turbulence production, and dissipation. Using this definition, a boundary layer may be characterized by significant fluctuations but still be non-turbulent if these fluctuations are induced by an external source which does not cause near wall turbulence production. Such is often the case under high $FSTI$ conditions. Free-stream eddies "buffet" the boundary layer, inducing non-turbulent boundary layer fluctuations. Buffeting may occur through pressure fluctuations. Boundary layer fluid is pushed in the wall normal direction across the mean gradient in the streamwise velocity, resulting in significant u' fluctuations. This type of motion was termed "inactive" by Bradshaw [38] since it does not result in momentum transport, in spite of potentially high u' levels. In addition to buffeting, some free-stream eddies may penetrate into the boundary layer and cause some mixing. As described in Volino [39], the eddies which have the greatest effect, whether through buffeting or penetrating the boundary layer, will be the larger, energy containing eddies. The non-turbulent boundary layer subject to these external effects will be characterized by large amplitude, low frequency fluctuations. Transition to turbulence is characterized not so much by large increases in u' levels, which may remain essentially constant, but by the appearance of higher frequencies superimposed on the low frequencies. The higher frequencies signal the generation of turbulence in the near wall region. Volino et al. [30] provide examples of an intermittent flow switching in time between disturbed non-turbulent and turbulent states.

The presence or absence of high frequencies in a signal is used to distinguish between turbulent and non-turbulent flow, using the algorithm presented by Volino et al. [30]. The algorithm is similar to others found in the literature. Briefly, the time derivative of a signal is computed and compared to a threshold. Rapid (high frequency) fluctuations result in high derivatives. When the derivative is larger than the threshold, the flow is declared instantaneously turbulent and the intermittency function is assigned a value of 1. When the derivative is below the threshold, the intermittency is assigned a value of 0. The time average of the function is the intermittency, γ . Volino et al. [30] showed that intermittency can be computed based on u' or $u'v'$ signals with essentially the same result. Results based on u' are presented in this paper.

RESULTS

Pressure Profiles

Pressure coefficients for all ten cases are shown in Fig. 2. At the upstream stations on the suction side, there is good agreement between the data at all Reynolds numbers and the inviscid flow solution. Separation appears to occur at s/L_s of about 0.6 in all cases. These results agree with those of Volino and Hultgren [13], who also observed that the separation location did not depend strongly on the Reynolds number or $FSTI$. They are in contrast to other studies, such as Qiu and Simon [16], which showed that the separation location depended more strongly on Re . Reattachment depends strongly on

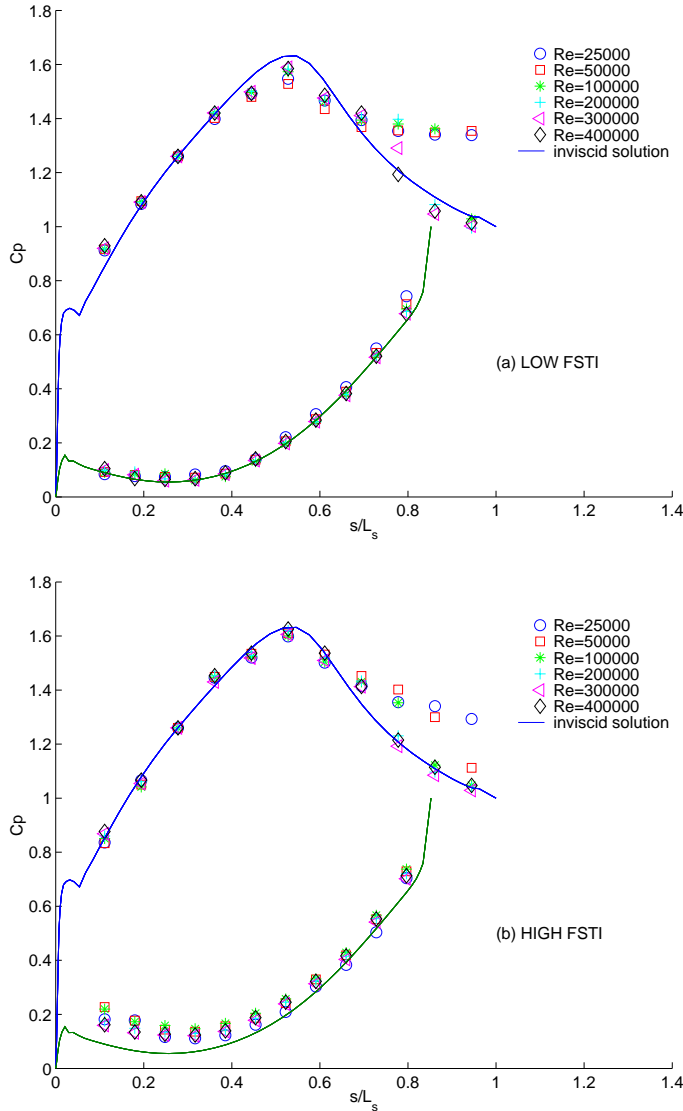


Fig. 2: C_p profiles: (a) low $FSTI$, (b) high $FSTI$

both Re and $FSTI$. With low $FSTI$ (Fig. 2a), the boundary layer appears to be separated in all cases at Stations 8 and 9. It reattaches by Station 10 for the $Re=200,000$ and $300,000$ cases, reattaches by Station 11 for the $Re=100,000$ case, and does not reattach at all for the $Re=25,000$ and $50,000$ cases. Reattachment for the high $FSTI$ cases (Fig. 2b) occurs upstream of the low $FSTI$ locations. The boundary layer appears to be separated in all cases at Station 8, but has already reattached by Station 9 in the $Re=200,000$ and $300,000$ cases. Reattachment has occurred by Station 10 for the $Re=100,000$ case, and appears to be beginning at Station 11 for the $Re=50,000$ case. The boundary layer does not appear to reattach when $Re=25,000$, in spite of the high $FSTI$. Results for the low $FSTI$ cases are very similar to the flat plate results of Volino and Hultgren [13]. The present high $FSTI$ results appear to show about a 10% larger separation region than the flat plate cases of [13]. The differences are small and of the order of the resolution of the measurement stations. Any differences between the studies are presumably due to differences in the free-stream turbulence. Although the high $FSTI$ in both studies was about 8%, the inlet free-stream turbulence was more anisotropic in Volino

and Hultgren [13], and the integral length scales of the free-stream turbulence in [13] were about double those in the present study. The larger length scale presumably caused earlier transition in the Volino and Hultgren [13] study, resulting in a slightly shorter separation bubble. Comparison to the high $FSTI$ cases of Simon et al. [17] shows reattachment about 14% farther upstream in [17] than in the present study. With low $FSTI$, Simon et al. [17] did not observe reattachment at all when $Re=100,000$, while it was observed in the present study. For the low $FSTI$ $Re=200,000$ case, they indicate reattachment about 6% farther upstream than the present study. Although the streamwise pressure gradients were nominally the same in the present study and Simon et al. [17], small differences in the pressure gradients along with differences in the intensity and length scales of the free-stream turbulence were apparently responsible for the differences in reattachment location.

Upstream Boundary Layer

The local free-stream velocities at Station 1-5 for all 10 cases closely followed the equation

$$\frac{U_\infty}{U_e} = 1.48 \left(\frac{s}{L_s} \right)^{0.214} \quad (1)$$

which corresponds to the free-stream velocity distribution for a Falkner-Skan wedge flow. Figure 3 shows that the 50 mean velocity profiles from all 10 cases at these stations collapse onto the same Falkner-Skan profile. Skin friction coefficients, shown in Fig. 4, which were computed using the near wall profiles, also follow the Falkner-Skan solution. There is no significant difference between the low and high $FSTI$ cases. Agreement with the flat plate data of Volino and Hultgren [13] is good. For the low $FSTI$ cases, it is not surprising that the laminar boundary layer closely follows the expected laminar solution. Under the same high $FSTI$ inlet conditions, however, Volino et al. [30] showed that a non-turbulent boundary layer may be strongly influenced by the free-stream turbulence and exhibit large deviation from laminar behavior. In the present study, the acceleration parameter, K , is in some of the cases over 10 times larger than in the Volino et al. [30] study, and the boundary layer thickness is as little as 1/5 that in [30]. These differences apparently limit the free-stream effect on the upstream boundary layer, resulting in the observed laminar-like behavior.

Fig. 5 shows profiles of the rms fluctuating streamwise velocity, u' , for the 50 upstream profiles. The low $FSTI$ u' is mainly streamwise unsteadiness that scales with the local U_∞ . Values are low everywhere, increasing slightly from the free-stream value to a peak at $y/\theta=3$ and then dropping to zero at the wall. For the high $FSTI$ cases the free-stream u' level does not change significantly within the test section and scales with U_e . Since the boundary layer fluctuations are caused by the free-stream fluctuations, the u' profiles collapse when normalized on U_e . The collapse is not perfect since the free-stream u' does drop somewhat as the eddies are strained in the accelerating flow. Qualitatively the behavior is the same as in the low $FSTI$ cases, with high values in the free-stream rising to a peak at $y/\theta=3$ and dropping to zero near the wall. The peak in u' has lower magnitude and is farther from the wall than would be expected in a turbulent boundary layer. In all cases the boundary layer is clearly laminar-like in spite of the high u' level. This is shown in both the mean velocity profiles (Fig. 3) and the local skin friction coefficients (Fig. 4) which follow laminar flow solutions.

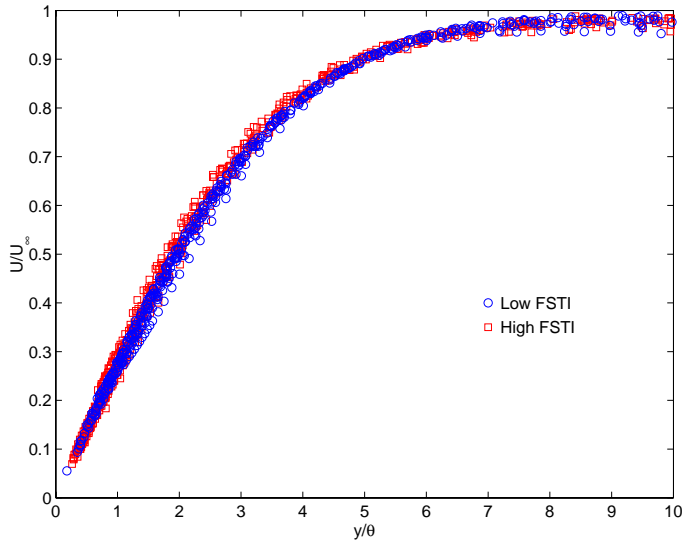


Fig. 3: Mean velocity profiles from Station 1-5, all cases

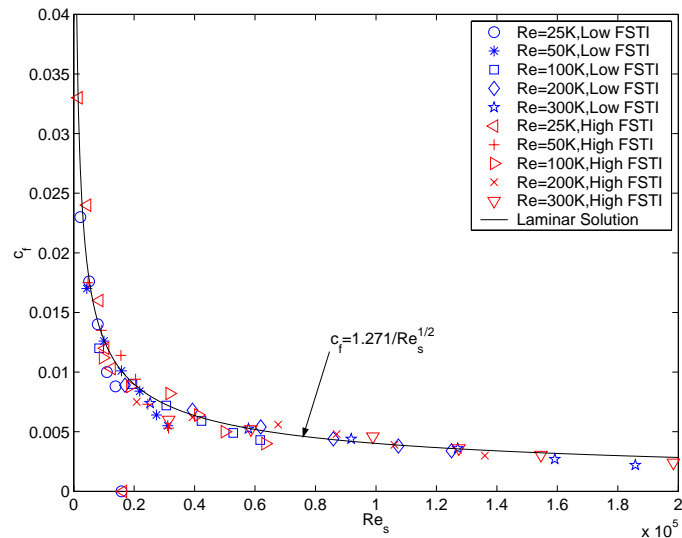


Fig. 4: Skin friction coefficients from Station 1-6, all cases

Low FSTI Transition

Downstream of Station 6, the pressure gradient becomes adverse and separation and transition occur. Figures 6 through 10 show profiles at Stations 6-11 of U , u' , the turbulent shear stress, $-u'v'$, and the intermittency, γ , for the five low *FSTI* cases. The v' profiles are qualitatively very similar to the $-u'v'$ profiles in all cases and are not shown. In the $Re=25,000$ case (Fig. 6), the mean velocity profile has just separated at Station 7, and the separation bubble grows continuously larger at the downstream stations. There is no reattachment, but rather a massive separation with a burst bubble at the trailing edge. The intermittency is nearly zero everywhere, indicating that the shear layer remains essentially laminar. Although the flow is laminar, u' is non-zero. The u' peak grows as the flow moves downstream, and its location is concurrent with the inflection point in the mean profile. The $-u'v'$ values remain near zero through Station 10, but then rise at Station 11 with a peak in the shear layer at the same

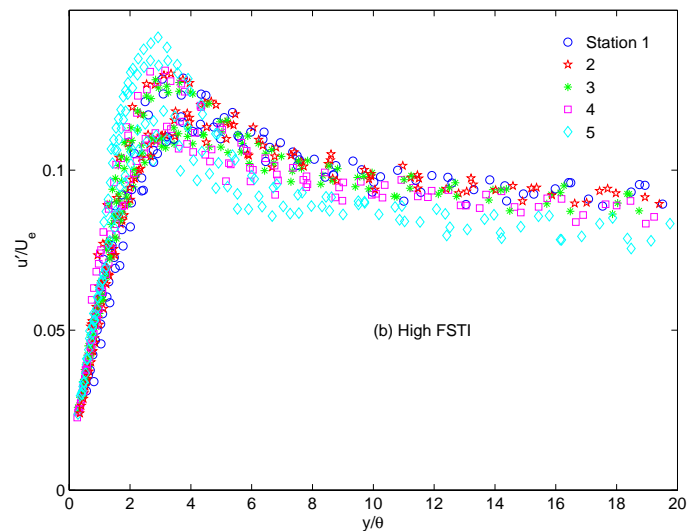
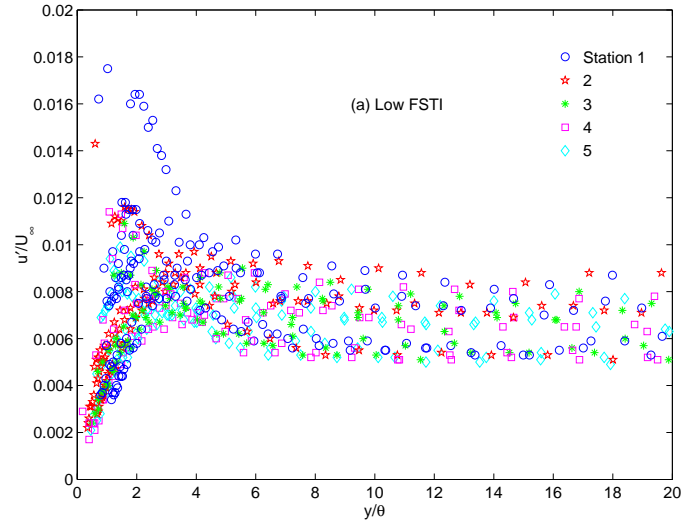


Fig. 5: Boundary layer u' profiles from Stations 1-5; (a) low FSTI cases, (b) high FSTI cases

location as the u' peak. The magnitude of this peak is extremely low; the eddy viscosity at the peak is only about $1/30^{\text{th}}$ of the molecular kinematic viscosity. Although not significant in terms of eddy transport, this peak may signify the beginning of transition.

Figure 7 shows the profiles for the $Re=50,000$ case. Results are very similar to the $Re=25,000$ case of Fig. 6. The boundary layer does not reattach. The $-u'v'$ profile at Station 11 again exhibits a low level peak. The dimensionless value of this peak is about three times that of the peak in Fig. 6, indicating that the $Re=50,000$ case may be closer to transitioning.

Results for the $Re=100,000$ case are shown in Fig. 8. The mean velocity profiles show that the boundary layer is on the verge of separating at Station 7, but is still attached. It has separated by Station 8, and the separation bubble grows through Station 10, although it does not become as thick as in the lower Re cases. At Station 10, the mean velocity near the wall rises slightly above zero, indicating the beginning of reattachment. At Station 11 the boundary layer is clearly reattached. The intermittency is near zero through Station 10, and then

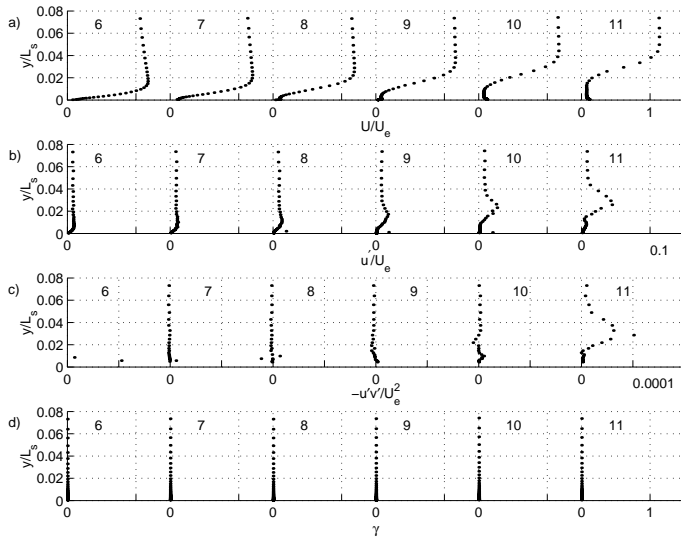


Fig. 6: Station 6-11 profiles for low FSTI, $Re=25,000$ case:
(a) mean velocity, (b) u' , (c) $-u'v'$, (d) intermittency

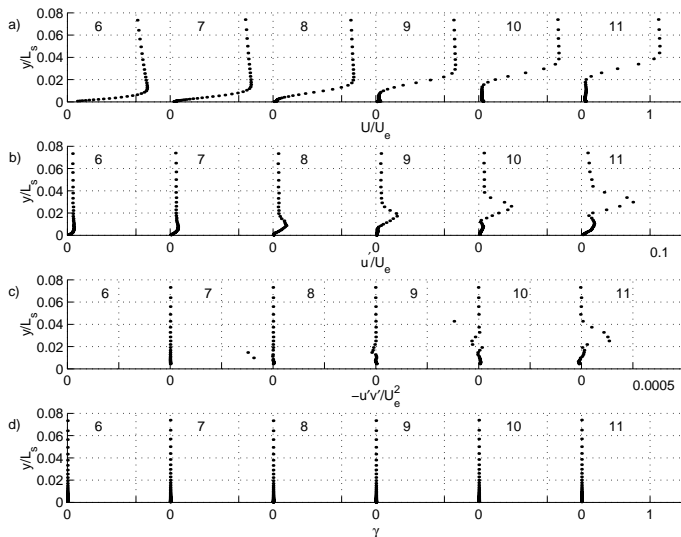


Fig. 7: Station 6-11 profiles for low FSTI, $Re=50,000$ case:
(a) mean velocity, (b) u' , (c) $-u'v'$, (d) intermittency

suddenly increases to 1 at Station 11, indicating fully-turbulent flow as the boundary layer reattaches. The peak in the intermittency is well away from the wall, indicating that transition begins in the shear layer over the separation bubble. The u' profiles exhibit a peak in the shear layer at Stations 8 and 9, similar to the behavior at the lower Re . At Station 10 there is an increase in u' near the wall as reattachment begins. The turbulent shear stress profile rises above zero at Station 10 with a dimensionless value that is an order of magnitude larger than the peak shown in Fig. 7 for the $Re=50,000$ case. At Station 11 the magnitude of the peak has increased by another order of magnitude and the boundary layer is clearly turbulent. The peak in $-u'v'$ is well away from the wall, indicating that while the boundary layer is turbulent and reattached, it has not yet recovered to fully-developed turbulent conditions.

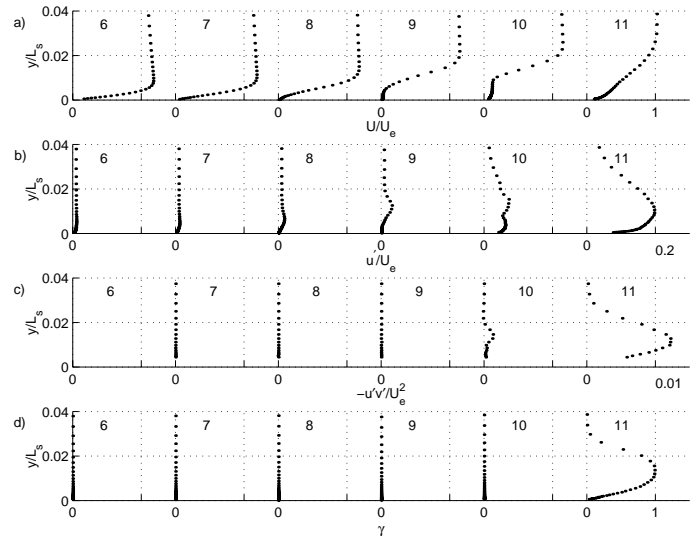


Fig. 8: Station 6-11 profiles for low FSTI, $Re=100,000$ case:
(a) mean velocity, (b) u' , (c) $-u'v'$, (d) intermittency

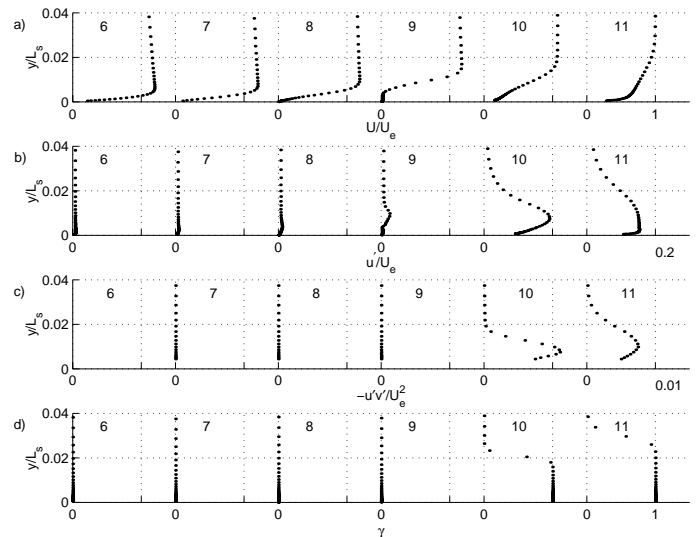


Fig. 9: Station 6-11 profiles for low FSTI, $Re=200,000$ case:
(a) mean velocity, (b) u' , (c) $-u'v'$, (d) intermittency

Figure 9 shows the profiles for the $Re=200,000$ case. The mean velocity profiles indicate that separation does not occur until near Station 8. There is a clear separation bubble at Station 9, and the boundary layer is reattached by Station 10. By Station 11 the mean profile appears to have recovered to a fully-developed turbulent shape. The intermittency jumps from near 0 at Station 9 to 1 at Station 10, indicating a rapid transition and reattachment. The magnitude of u' increases similarly, from a small peak near the inflection point of the mean profile at Station 9 to high values throughout the boundary layer at Station 10. The turbulent shear stress profiles show the same sudden increase between Stations 9 and 10, and the peak is still away from the wall at Station 11, indicating that recovery from separation may not be fully complete.

The $Re=300,000$ case profiles are shown in Fig. 10. Separation again occurs near Station 8. By Station 9 the separation bubble has

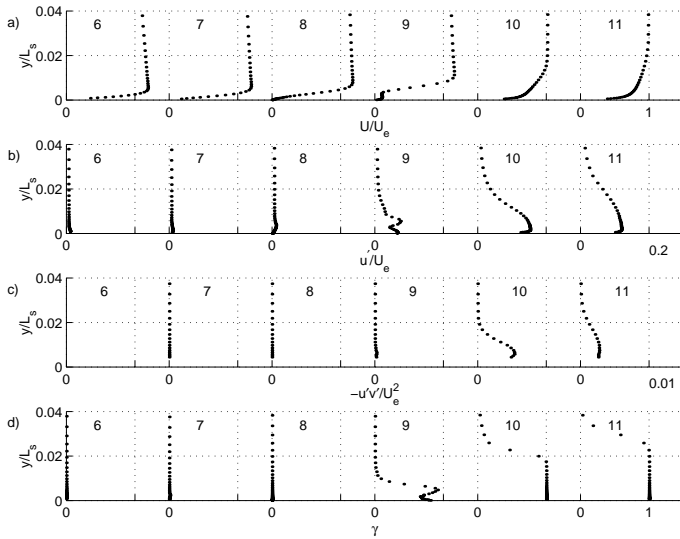


Fig. 10: Station 6-11 profiles for low FSTI, $Re=300,000$ case: (a) mean velocity, (b) u' , (c) $-u'v'$, (d) intermittency

clearly grown and the non-zero mean velocities near the wall indicate that the boundary layer is on the verge of reattachment. The u' values increase greatly between Stations 8 and 9. The u' profile has a peak in the shear layer over the separation bubble and a second peak near the wall, which is indicative of reattachment. The intermittency profile at Station 9 shows this same double peak. The boundary layer is reattached and fully turbulent by Station 10. The turbulent shear stress profile rises to a small but discernable non-zero level at Station 9, corresponding to the beginning of reattachment and the rise of the intermittency. By Station 11, $-u'v' = u_\tau^2$ near the wall, which would be expected for a fully-developed, attached turbulent boundary layer.

The velocity data of Figs. 6-10 agree with the pressure profiles of Fig. 2a. The separation locations agree, although the velocity profiles provide better resolution and indicate that separation does move downstream somewhat as Reynolds number increases. The reattachment locations indicated by the pressure profiles correspond to locations where the velocity profiles have clearly reattached. Incipient reattachment is visible in the mean velocity one station upstream of full reattachment in some cases. In all cases the magnitude of u' begins to increase in the shear layer after separation. At first this increase in u' occurs without a corresponding increase in $-u'v'$, which remains near zero, and the shear layer remains laminar. As the flow continues downstream, low but nonzero $-u'v'$ values eventually appear in the shear layer, and at the higher Reynolds numbers this is quickly followed by a rapid rise of $-u'v'$, sudden transition to turbulence, and almost immediate reattachment of the boundary layer. At the two lowest Reynolds numbers, the initial rise in $-u'v'$ was detected, but it occurred so far downstream that transition and reattachment never occurred. The present results are consistent with those of Hatman and Wang [10], Lou and Hourmouziadis [12] and Volino and Hultgren [13], who also considered low *FSTI* separated flow transition. They also reported rapid transition and attributed it to the breakdown of a Kelvin-Helmholtz type instability of the shear layer. The transition mechanism in the present study will be discussed in more detail in Part 2 [29].

High FSTI Transition

Profiles for the high *FSTI* cases are shown in Figs. 11-15. For the $Re=25,000$ case (Fig. 11), the mean velocity profiles show that the boundary layer has separated by Station 6. The boundary layer appears on the verge of reattaching at Stations 10 and 11, but is not clearly reattached. The u' level rises rapidly after separation, with a peak in the shear layer at each station. The free-stream buffets the shear layer, forcing fluid across a large mean velocity gradient, dU/dy , which causes high u' levels. The same effect is present in the attached boundary layer upstream (Fig. 5b), but is damped somewhat by the wall. Free-stream buffeting and high u' do not necessarily imply turbulent transport, and the turbulent shear stress remains low through Station 9. The $-u'v'$ level rises to high levels at Stations 10 and 11, but the peak is in the shear layer and drops to zero at the wall. Perhaps at this very low Reynolds number, even significant transport in the shear layer is insufficient to promote full reattachment of the boundary layer. Turbulent reattachment may be an intermittent phenomenon, related to and much like transition. At the lower Re it may occur over an extended distance. The intermittency indicates that the flow remains non-turbulent, in spite of the high levels of $-u'v'$ at the downstream stations. The intermittency function, as defined above, only declares the flow turbulent when the velocity fluctuations include a full range of both large and small scales. The apparent mismatch between the $-u'v'$ and γ profiles of Fig. 11 may indicate that the fluctuations which cause the turbulent shear stress initially do not include this range of scales. Turbulent shear stress spectra are presented in Part 2 [29]. Profiles of the wall normal fluctuating velocity, v' , are also shown in Fig. 11. At Stations 7-9, high free-stream values drop to zero at the wall, with no peak corresponding to the peak in u' . The free-stream buffeting effect on v' is damped by the wall, a phenomenon also observed in attached, non-turbulent boundary layers under high *FSTI* conditions (Volino et al. [30]). A peak emerges in v' in the shear layer at Station 10 and 11, corresponding completely with the rise in $-u'v'$ at these stations. The link between v' and $-u'v'$ was clear at all Re , making it unnecessary to present both v' and $-u'v'$ for the remaining cases.

The $Re=50,000$ case of Fig. 12 is very similar to the $Re=25,000$ case. Reattachment is clearer, however, at Station 11, and the intermittency is non-zero at this station. Fig. 13 shows the $Re=100,000$ case. In this case the intermittency indicates that transition has begun by Station 9, which corresponds to an initial rise in $-u'v'$. The mean profile shows that the boundary layer is reattached at the last two stations. The high $-u'v'$ peaks away from the wall indicate that the boundary layer has not fully recovered from the separation at Station 11.

It is not clear that separation occurs in the $Re=200,000$ case (Fig. 14), but the velocity mean profile at Station 8 has an inflection point and appears to be close to separating. By Station 9 the boundary layer is clearly attached, the intermittency indicates transition is underway, u' is high even near the wall, and $-u'v'$ has risen to a turbulent level. At Station 11, $-u'v'$ reaches a maximum equal to u_τ^2 near the wall, indicating a fully-developed attached turbulent flow.

The $Re=300,000$ results of Fig. 15 are very similar to those at $Re=200,000$. Transition begins slightly earlier at $Re=300,000$, with the intermittency greater than zero at Station 8. The thin boundary layer at $Re=300,000$ results in peaks in $-u'v'$ at Stations 9 and 10 that are too close to the wall to resolve with the cross-wire probe.

In general, transition in the high *FSTI* cases began upstream of the locations in the corresponding low *FSTI* cases, and the transition

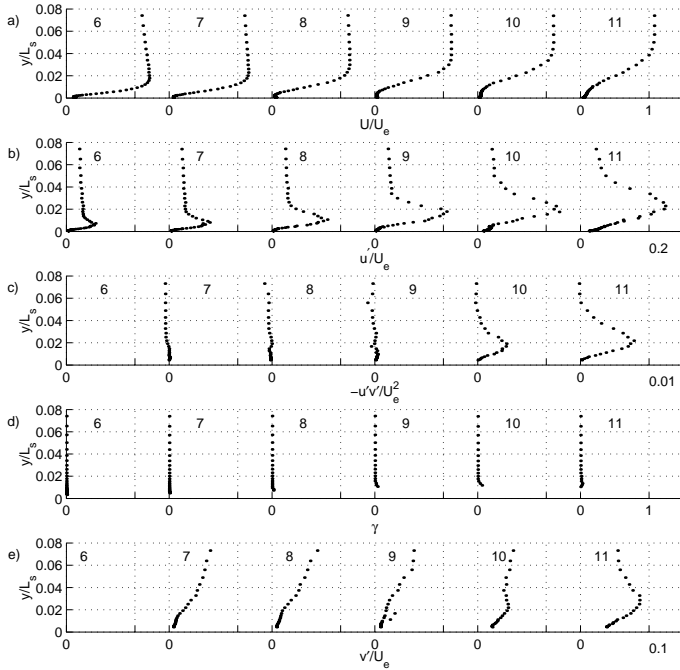


Fig. 11: Station 6-11 profiles for high FSTI, Re=25,000 case: (a) mean velocity, (b) u' , (c) $-u'v'$, (d) intermittency, (e) v'

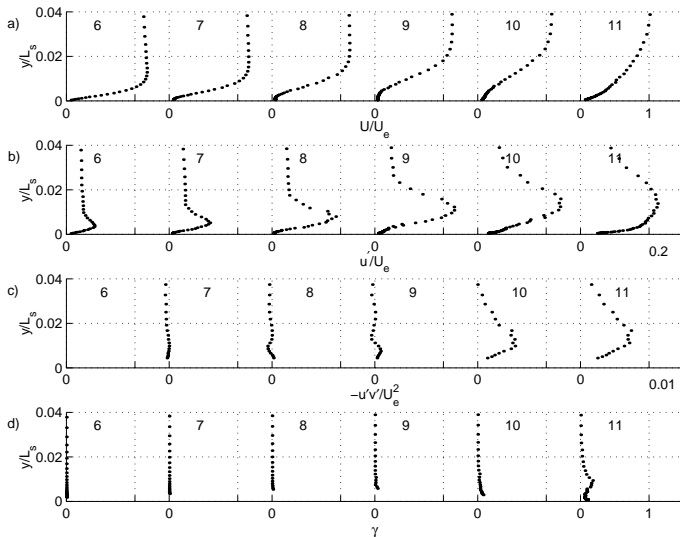


Fig. 12: Station 6-11 profiles for high FSTI, Re=50,000 case: (a) mean velocity, (b) u' , (c) $-u'v'$, (d) intermittency

region length was longer with high *FSTI*. This agrees with the observations of Volino and Hultgren [13], who also observed that transition was less abrupt with high *FSTI*. Boundary layer u' levels are much higher with high *FSTI*, but the turbulent shear stress magnitude remains low until transition begins and does not appear to depend strongly on *FSTI*.

Shape Factor and Momentum Thickness

As discussed above, stage losses cannot be determined quantitatively using a single passage test section, but is possible to

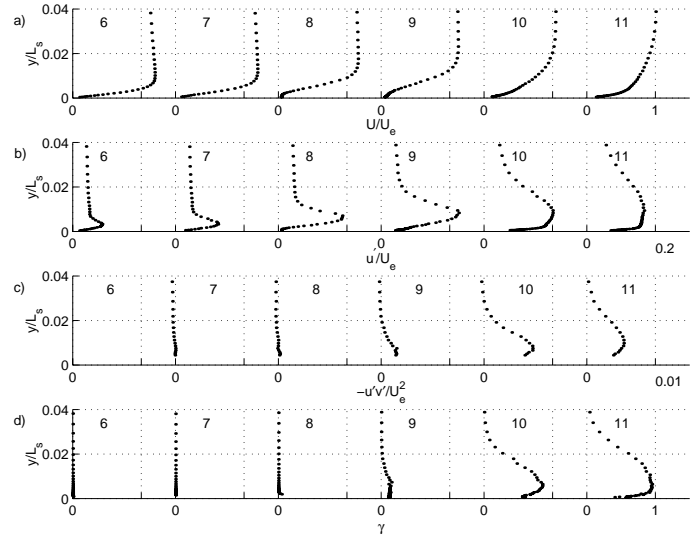


Fig. 13: Station 6-11 profiles for high FSTI, Re=100,000 case: (a) mean velocity, (b) u' , (c) $-u'v'$, (d) intermittency

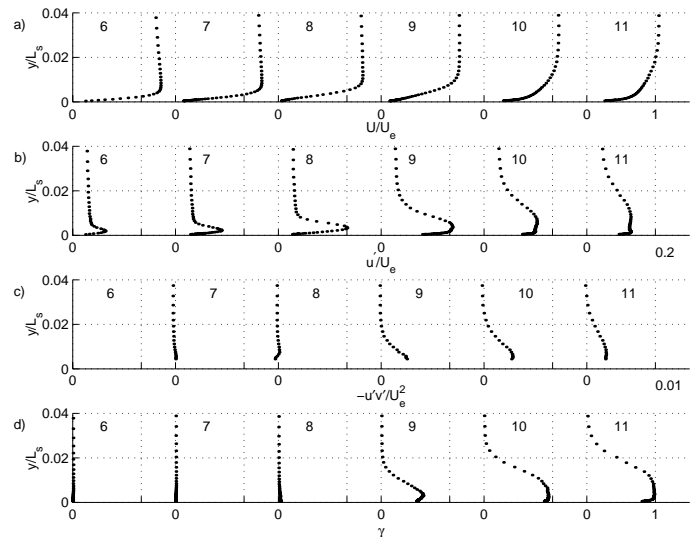


Fig. 14: Station 6-11 profiles for high FSTI, Re=200,000 case: (a) mean velocity, (b) u' , (c) $-u'v'$, (d) intermittency

compute the momentum thickness of the suction side boundary layer at the trailing edge. As explained by Howell et al. [20], this momentum thickness is proportional to the suction side profile loss when the boundary layer shape factor and passage exit angle remain constant. For those cases in which the boundary layer reattaches and recovers to a fully developed turbulent shape, H is approximately equal to 1.4. In these cases the suction side profile loss is likely the dominant loss mechanism (Howell et al. [20]). In those cases in which the boundary layer does not fully reattach, or reattaches near the trailing edge, the shape factor will be very large due to a large displacement thickness. The momentum thickness may be relatively small compared to the displacement thickness in these cases, since the wall shear is essentially zero and θ will not grow significantly in the free-shear layer. Large losses would then be expected in the wake, downstream of the airfoil.

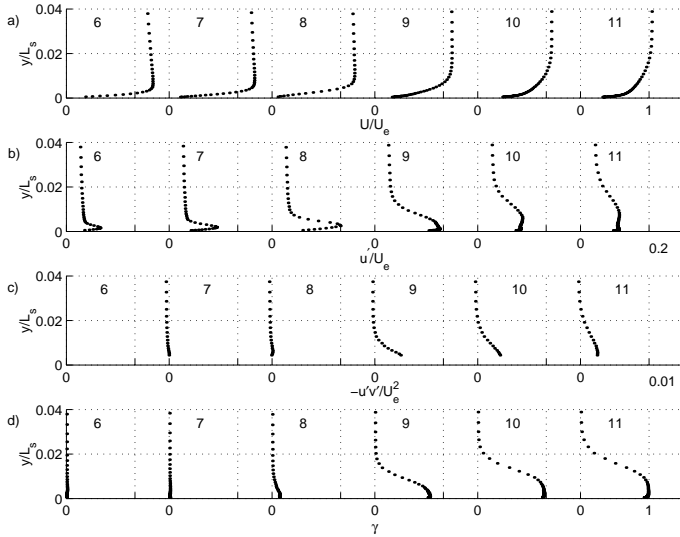


Fig. 15: Station 6-11 profiles for high FSTI, $Re=300,000$ case: (a) mean velocity, (b) u' , (c) $-u'v'$, (d) intermittency

Fig. 16 shows the shape factor at Station 11 ($s/L_s=0.94$) as a function of Re . In the $Re=200,000$ and $300,000$ cases, the shape factor is approximately 1.4, indicating that the boundary layer is reattached and that the momentum thickness is a good indicator of overall losses. For the lower Re cases, H is significantly higher, particularly in the low $FSTI$ cases. The lower H in the high $FSTI$ cases indicates that high $FSTI$ helps to keep the separation bubble thinner by promoting more mixing in the shear layer over the bubble and by inducing earlier transition and reattachment. Fig. 17 shows the Station 11 momentum thickness as a function of Re . High $FSTI$ helps keep the separation bubble thinner, as shown above in the mean velocity profiles of Figs. 6-15, which tends to result in lower θ and lower losses when the boundary layer reattaches. High $FSTI$ also promotes increased mixing, however, which tends to increase θ . For the $Re=300,000$ cases, Fig. 17 indicates that the second effect is more significant and θ is higher for the high $FSTI$ case. Transition and reattachment occur sufficiently far upstream in the low $FSTI$ case that the effect of the high $FSTI$ in promoting even earlier reattachment is not enough to counter the enhanced mixing effects. This suggests that small, controllable separation bubbles may be acceptable or even desirable in some cases, as proposed by Hourmouziadis [1] for controlled diffusion blading. For the $Re=200,000$ and $Re=100,000$ cases, the earlier reattachment caused by high $FSTI$ is more significant and θ is lower for the high $FSTI$ cases. This result is consistent with the observation in several studies that unsteady wakes from upstream airfoils result in lower losses. Enhanced mixing in the shear layer explains the higher θ for the high $FSTI$ cases at $Re=25,000$. These momentum thicknesses do not relate directly to losses since the shear layer does not reattach in either of the $Re=25,000$ cases.

Comparison to Correlations

Hatman and Wang [10] discuss three modes of separated flow transition. Based on their criteria, the present cases all fall into their laminar-separation long-bubble category. The data support this; separation occurred before transition. Hatman and Wang [10], Mayle [2] and others suggest that the Thwaites [40] criteria, $Re_\theta^2 K = -0.082$, is a good predictor for laminar separation. A laminar, attached flow solution would put $Re_\theta^2 K = -0.082$ between Stations 6 and 7 in all cases

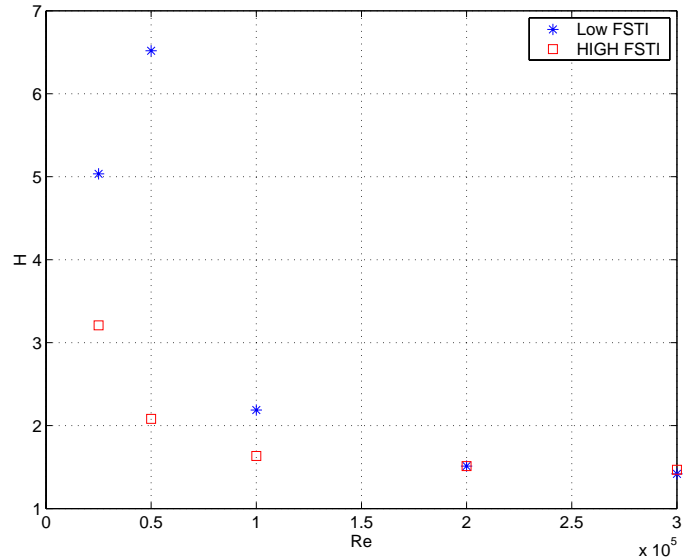


Fig. 16: Shape factor at Station 11

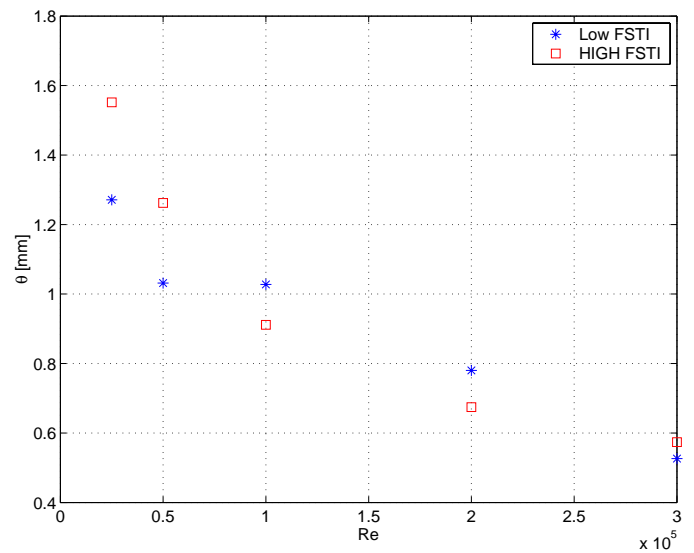


Fig. 17: Momentum thickness at Station 11

of the present study. The presence of the separation bubble changes the local acceleration, however, which tends to move the location where $Re_\theta^2 K = -0.082$. Volino and Hultgren [13] found the Thwaites criteria to be a good predictor of separation and it appears to work well for the present study as well. Exact prediction of the separation point is not straightforward, however, due to the interdependence of local K values and the separation bubble location.

Prediction of transition and reattachment is more difficult. Hatman and Wang [10] present a transition correlation based on low $FSTI$ data which predicts that transition should not occur in any of the present cases. Clearly, however, transition and reattachment do occur. The $-u'v'$ profiles indicate that transition is imminent even in the low $FSTI$, low Re cases. Volino and Hultgren [13] drew comparisons to correlations from Mayle [2] and Davis et al. [41] with mixed results.

Table 3: Distance from separation location to start of transition as a fraction of L_s ; measured values and correlation predictions for each case

$FSTI$	$Re \times 10^{-3}$	Measured	Mayle [2] short bubble	Mayle [2] long bubble	Davis et al. [41]
Low	25	> 0.41	0.25	0.83	1.54
	50	> 0.33	0.16-0.19	0.53-0.64	0.77
	100	0.17-0.33	0.12-0.14	0.39-0.48	0.38
	200	0-0.17	0.09-0.11	0.31-0.36	0.19
	300	0-0.08	0.07-0.08	0.23-0.28	0.13
High	25	> 0.33	0.27-0.29	0.89-0.98	0.17
	50	0.17-0.33	0.16-0.18	0.53-0.61	0.08
	100	0.08-0.17	0.12-0.14	0.39-0.48	0.04
	200	0-0.08	0.07-0.12	0.25-0.39	0.02
	300	0-0.08	0.06-0.09	0.19-0.31	0.02

Comparisons to the present data are similarly mixed. The Mayle correlations predict the distance from the separation point to the onset of transition based on Re_θ at the separation location. He presents a correlation for short separation bubble length and a correlation for long bubble length, which is 3.3 times the short bubble length. The Davis et al [41] correlation also predicts the distance from separation to transition onset, but as a function of the $FSTI$. Table 3 presents the distance from separation to the start of transition, normalized on the suction surface length, for all cases of the present experiments and as predicted by the Mayle [2] and Davis et al. [41] correlations. The finite spacing between the measurement stations results in uncertainty in Re_θ at separation and in the exact locations of separation and transition, so a range of values is given for each quantity in the table. The results of the present cases lie between the Mayle long and short bubble correlations to within the resolution of the measurement locations. The Davis et al. correlation tends to predict too long a distance for the low $FSTI$ cases and too short a distance for the high $FSTI$ cases.

Existing correlations appear to give reasonable rough estimates of separated flow transition in some cases, but they are not particularly accurate or robust predictors. The general agreement between the similar cases of the present study, Volino and Hultgren [13], and Simon et al. [17] suggests that prediction of separated flow transition should be possible to some extent. The differences between the results of these studies, noted above, suggest that very accurate prediction of the flow may prove difficult and strongly dependent on small differences in boundary conditions. It is doubtful that a simple, robust correlation can be developed to incorporate all relevant boundary condition effects and provide very accurate predictions. It is also questionable whether the boundary conditions could be specified accurately enough for actual engine conditions. Perhaps they can, with addition research, however, and it may be possible to improve predictions with advanced computational schemes. The difficulty of predicting transition suggests that it may be advantageous to develop flow control schemes to force transition to occur at desired locations rather than try to predict it under existing conditions.

CONCLUSIONS

Separated flow transition has been documented for cases with Reynolds numbers ranging from 25,000 to 300,000 at both high and low $FSTI$. The following conclusions can be drawn from the results.

1. The start of boundary layer reattachment occurs near the start of transition, and both depend strongly on Re and $FSTI$.

2. High $FSTI$ results in competing effects with regard to losses. It causes enhanced mixing, which tends to promote boundary layer growth and increase losses. At the same time, it promotes earlier transition and reattachment, which reduces boundary layer thickness and losses. At the highest Re , reattachment occurred shortly after separation regardless of $FSTI$ level, and high $FSTI$ resulted in higher losses. At the intermediate Re , high $FSTI$ reduced losses. At the lowest Re , the boundary layer did not reattach even with high $FSTI$, so losses would be high regardless of $FSTI$ level.
3. The turbulent shear stress level can remain near zero in spite of high $FSTI$ and high u' in the boundary layer. The beginning of a rise in $-u'v'$ signals the beginning of transition. In the lowest Re cases, transition did not occur and the boundary layer did not reattach, but the beginning of a rise in $-u'v'$ was observed near the trailing edge. This hints that it may be possible to induce transition even at very low Re .
4. The present results agree roughly with similar studies from the literature and existing correlations but there are significant differences. Attempts to control transition and force its location may prove more fruitful than prediction of unmodified flow. The present study provides an extensive, detailed baseline data set for ongoing flow control experiments.

ACKNOWLEDGEMENTS

This work was sponsored by the NASA Glenn Research Center. The grant monitor is Dr. David Ashpis. Additional matching support was provided through a U.S. Naval Academy Recognition Grant. Mr. Dale Boyer of the Technical Support Department at the Naval Academy fabricated the airfoils for the test section.

REFERENCES

- [1] Hourmouziadis, J., 1989, "Aerodynamic Design of Low Pressure Turbines," AGARD Lecture Series 167.
- [2] Mayle, R.E., 1991, "The Role of Laminar-Turbulent Transition in Gas Turbine Engines," *ASME Journal of Turbomachinery*, **116**, pp. 509-537.
- [3] Sharma, O.P., Ni, R.H., and Tanrikut, S., 1994, "Unsteady Flow in Turbines," AGARD Lecture Series 195, Paper No. 5.
- [4] Hodson, H.P., 1991, "Aspects of Unsteady Blade-Surface Boundary Layers and Transition in Axial Turbomachines," *Boundary Layers in Turbomachines*, VKI Lecture Series 1991-06.
- [5] Wisler, D.C., 1998, "The Technical and Economic Relevance of Understanding Boundary Layer Transition in Gas Turbine Engines," *Minnowbrook II, 1997 Workshop on Boundary Layer Transition in Turbomachines*, LaGraff, J.E., and Ashpis, D.E., eds., NASA/CP-1998-206958, pp. 53-64.
- [6] Curtis, E.M., Hodson, H.P., Banieghbal, M.R., Denton, J.D., Howell, R.J., and Harvey, N.W., 1996, "Development of Blade Profiles for Low-Pressure Turbine Applications," ASME Paper 96-GT-358.
- [7] Halstead, D.E., Wisler, D.C., Okiishi, T.H., Walker, G.J., Hodson, H.P., and Shin, H.-W., 1997, "Boundary Layer Development in Axial Compressors and Turbines: Part 3 of 4 – LP Turbines," *ASME Journal of Turbomachinery*, **119**, pp. 225-237.
- [8] Solomon, W.J., 2000, "Effects of Turbulence and Solidity on the Boundary Layer Development in a Low Pressure Turbine," ASME Paper 2000-GT-0273.

- [9] Gier, J., and Ardey, S., 2001, "On the Impact of Blade Count Reduction on Aerodynamic Performance and Loss Generation in a Three-Stage LP Turbine," ASME Paper 2001-GT-0197.
- [10] Hatman, A., and Wang, T., 1999, "A Prediction Model for Separated Flow Transition," ASME *Journal of Turbomachinery*, **121**, pp. 594-602.
- [11] Sohn, K.H., DeWitt, K.J., and Shyne, R.J., 2000, Experimental Investigation of Boundary Layer Behavior in a Simulated Low Pressure Turbine," ASME *Journal of Fluids Engineering*, **122**, pp. 84-89.
- [12] Lou, W., and Hourmouziadis, J., 2000, "Separation Bubbles Under Steady and Periodic-Unsteady Main Flow Conditions," ASME *Journal of Turbomachinery*, **122**, pp. 634-643.
- [13] Volino, R.J., and Hultgren, L.S., 2001, "Measurements in Separated and Transitional Boundary Layers Under Low-Pressure Turbine Airfoil Conditions," ASME *Journal of Turbomachinery*, **123**, pp. 189-197.
- [14] Yaras, M.I., 2001, "Measurements of the Effects of Pressure-Gradient History on Separation-Bubble Transition," ASME Paper 2001-GT-0193.
- [15] Murawski, C.G., Sondergaard, R., Rivir, R.B., Simon, T.W., Vafai, K., and Volino, R.J., 1997, "Experimental Study of the Unsteady Aerodynamics in a Linear Cascade with Low Reynolds Number Low Pressure Turbine Blades," ASME Paper 97-GT-95.
- [16] Qiu, S., and Simon, T.W., 1997, "An Experimental Investigation of Transition as Applied to Low Pressure Turbine Suction Surface Flows," ASME Paper 97-GT-455.
- [17] Simon, T.W., Qiu, S., and Yuan, K., 2000, "Measurements in a Transitional Boundary Layer Under Low-Pressure Turbine Conditions," NASA/CR-2000-209957.
- [18] Brunner, S., Fottner, L., and Schiffer, H.-P., 2000, "Comparison of Two Highly Loaded Low Pressure Turbine Cascades Under the Influence of Wake-Induced Transition," ASME Paper 2000-GT-268.
- [19] Stadtmüller, P., Fottner, L., and Fiala, A., 2000, "Experimental and Numerical Investigation of Wake-Induced Transition on a Highly Loaded LP Turbine at Low Reynolds Numbers," ASME Paper 2000-GT-0269.
- [20] Howell, R.J., Ramesh, O.N., Hodson, H.P., Harvey, N.W., and Schulte, V., 2001, "High Lift and Aft-Loaded Profiles for Low-Pressure Turbines," ASME *Journal of Turbomachinery*, **123**, pp. 181-188.
- [21] Kaszeta, R.W., Simon, T.W., and Ashpis, D.E., 2001, "Experimental Investigation of Transition to Turbulence as Affected by Passing Wakes," ASME Paper 2001-GT-195.
- [22] Dorney, D.J., Ashpis, D.E., Halstead, D.E., and Wisler, D.C., 1999, "Study of Boundary Layer Development in a Two-Stage Low Pressure Turbine," AIAA Paper 99-0742; also NASA TM-1999-208913.
- [23] Chernobrovkin, A., and Lakshminarayana, B., 1999, "Turbulence Modeling and Computation of Viscous Transitional Flow for Low Pressure Turbines," *Proc. 4th International Symposium on Engineering Turbulence Modeling and Measurements*, Corsica, France.
- [24] Huang, P.G., and Xiong, G., 1998, "Transition and Turbulence Modeling of Low Pressure Turbine Flows," AIAA Paper 98-0039.
- [25] Thermann, H., Müller, M., and Niehuis, R., 2001, "Numerical Simulation of the Boundary Layer Transition in Turbomachinery Flows," ASME Paper 2001-GT-0475.
- [26] VanTreuren, K.W., Simon, T., von Koller, M., Byerley, A.R., Baughn, J.W., and Rivir, R., 2001, "Measurements in a Turbine Cascade Flow Under Ultra Low Reynolds Number Conditions," ASME Paper 2001-GT-0164.
- [27] Lake, J.P., King, P.I., and Rivir, R.B., 2000, "Low Reynolds Number Loss Reduction on Turbine Blades With Dimples and V-Grooves," AIAA Paper 00-738.
- [28] Bons, J.P., Sondergaard, R., and Rivir, R.B., 2001, "Turbine Separation Control Using Pulsed Vortex Generator Jets," ASME *Journal of Turbomachinery*, **123**, pp. 198-206.
- [29] Volino, R.J., 2002, "Separated Flow Transition under Simulated Low-Pressure Turbine Airfoil Conditions: Part 2 - Turbulence Spectra," ASME Paper GT-2002-30237.
- [30] Volino, R.J., Schultz, M.P., and Pratt, C.M., 2001, "Conditional Sampling in a Transitional Boundary Layer Under High Free-Stream Turbulence Conditions," ASME Paper 2001-GT-0192.
- [31] Chung, J.T., and Simon, T.W., 1990, "Three-Dimensional Flow Near the Blade/Endwall Junction of a Gas Turbine: Visualization in a Large-Scale Cascade Simulator," ASME Paper 90-WA/HT-4.
- [32] Aunapu, N.V., Volino, R.J., Flack, K.A., and Stoddard, R.M., 2000, "Secondary Flow Measurements in a Turbine Passage With Endwall Flow Modification," ASME *Journal of Turbomachinery*, **122**, pp. 651-658.
- [33] Volino, R.J., and Simon, T.W., 1997, "Velocity and Temperature Profiles in Turbulent Boundary Layers Experiencing Streamwise Pressure Gradients," ASME *Journal of Heat Transfer*, **119**, pp. 433-439.
- [34] Wills, J.A.B., 1962, "The Correction of Hot-Wire Readings for Proximity to a Solid Boundary," *Journal of Fluid Mechanics*, **12**, pp. 65-92.
- [35] Ligrani, P.M., and Bradshaw, P., 1987, "Spatial Resolution and Measurement of Turbulence in the Viscous Sublayer Using Subminiature Hot-Wire Probes," *Experiments in Fluids*, **5**, pp. 407-417.
- [36] Ligrani, P.M., and Bradshaw, P., 1987, "Subminiature Hot-Wire Sensors: Development and Use," *Journal of Physics E: Scientific Instruments*, **20**, pp. 323-332.
- [37] Ligrani, P.M., Westphal, R.V., and Lemos, F.R., 1989, "Fabrication and Testing of Subminiature Multi-Sensor Hot-Wire Probes," *Journal of Physics E: Scientific Instruments*, **22**, pp. 262-268.
- [38] Bradshaw, P., 1994, "Turbulence: the Chief Outstanding Difficulty of Our Subject," *Experiments in Fluids*, **16**, pp. 203-216.
- [39] Volino, R.J., 2002, "An Investigation of the Scales in Transitional Boundary Layers Under High Free-Stream Turbulence Conditions," ASME Paper GT-2002-30233.
- [40] Thwaites, B., 1949, "Approximate Calculations of the Laminar Boundary Layer," *Aeronautical Quarterly*, **7**, pp. 245-280.
- [41] Davis, R.L., Carter, J.E., and Reshotko, E., 1985, "Analysis of Transitional Separation Bubbles on Infinite Swept Wings," AIAA Paper 85-1685.

GT-2002-30237

SEPARATED FLOW TRANSITION UNDER SIMULATED LOW-PRESSURE TURBINE AIRFOIL CONDITIONS: PART 2 – TURBULENCE SPECTRA

Ralph J. Volino

Department of Mechanical Engineering
United States Naval Academy
Annapolis, Maryland 21402
Email: volino@usna.edu

ABSTRACT

Spectral analysis was used to investigate boundary layer separation, transition and reattachment under low-pressure turbine airfoil conditions. Cases with Reynolds numbers ranging from 25,000 to 300,000 (based on suction surface length and exit velocity) have been considered at low (0.5%) and high (9% inlet) free-stream turbulence levels. Spectra of the fluctuating streamwise velocity and the turbulent shear stress are presented. The spectra for the low free-stream turbulence cases are characterized by sharp peaks. The high free-stream turbulence case spectra exhibit more broadband peaks, but these peaks are centered at the same frequencies observed in the corresponding low turbulence cases. The frequencies of the peaks suggest that a Tollmien-Schlichting instability mechanism drives transition, even in the high turbulence cases. The turbulent shear stress spectra proved particularly valuable for detection of the early growth of the instability. The predictable nature of the instability may prove useful for future flow control work.

NOMENCLATURE

$FSTI$	free-stream turbulence intensity
f	frequency in Hz
L_s	suction surface length
PSD	power spectral density of u'^2 or $-u'v'$
Re	$U_e L_s / \nu$, exit Reynolds number
Re_{δ^*}	$U_\infty \delta^* / \nu$ displacement thickness Reynolds number
s	streamwise coordinate, distance from leading edge
U_∞	local free-stream velocity
U_e	nominal exit free-stream velocity
u'	streamwise fluctuating velocity
$-u'v'$	turbulent shear stress
v'	wall normal fluctuating velocity
y	cross-stream coordinate, distance from wall
δ^*	displacement thickness
δ_s	shear layer thickness
$\delta_{99.5}$	99.5% boundary layer thickness
ν	kinematic viscosity

INTRODUCTION

In Part 1 of the present study [1], the significance of boundary layer separation, transition, and reattachment to the flow over modern low-pressure turbine airfoils was discussed. Measured mean velocity and statistical turbulence quantities were presented for cases with high and low free-stream turbulence intensity ($FSTI$) and Reynolds numbers (based on suction surface length and exit velocity) ranging from 25,000 to 300,000. The separation point tended to move downstream somewhat as Reynolds number increased. Transition and reattachment locations moved upstream significantly as Re or $FSTI$ were increased.

While the statistical quantities presented in Part 1 [1] provide a quantitative description of what happens under different Re and $FSTI$ conditions, they do not explain the transition mechanism. To better explain the transition process and accurately predict or control it, an understanding of the physics which cause the results observed in Part 1 [1] is needed. The present paper uses spectral analysis to investigate separated flow transition.

Mayle [2] classified the modes of transition as “natural transition,” “bypass” transition; “separated flow” transition of the shear layer over a separation bubble; “periodic-unsteady” transition, which might also be called wake-induced bypass transition; and reverse transition. Under low $FSTI$, zero streamwise pressure gradient conditions, natural transition is expected. This type of transition has been extensively documented and can be predicted with linear stability analysis. As described by Schlichting [3], when the displacement thickness Reynolds number exceeds a critical value, the boundary layer becomes unstable to small disturbances, which begin to grow as Tollmien-Schlichting (TS) waves. These waves eventually become three dimensional and result in turbulent spots. Under high $FSTI$, zero pressure gradient conditions, large disturbances can cause a bypass of the linear growth stages of transition, resulting in the sudden appearance of turbulent spots. At intermediate $FSTI$, elements of both bypass and natural transition may be observed. Sohn and Reshotko [4], for example, presented data for a 1% $FSTI$ case, showing both spectral peaks at possible TS frequencies and broadband unsteadiness more typical of bypass transition.

In some cases, transition is observed even though linear stability theory predicts that the boundary layer should not develop TS waves.

Volino [5], for example, considered a favorable pressure gradient case with high $FSTI$ that clearly underwent transition. The boundary layer thickness remained low in this case due to the acceleration, resulting in Re_{δ^*} below the critical limit for linear instability.

Separated flow transition could potentially include elements of either natural or bypass transition. In separated flow cases the pressure gradient is adverse, resulting in a boundary layer or shear layer that typically is unstable to TS waves. High $FSTI$, however, might be the dominant factor in a separated shear layer, overwhelming the effect of any TS waves and producing bypass transition. Hughes and Walker [6] list several studies with $FSTI$ below 0.9% in which TS waves were detected in adverse pressure gradient cases. They also note that Halstead et al. [7] did not detect TS waves in the flow through a rotating cascade with more representative, higher $FSTI$. Solomon and Walker [8], however, provide evidence of TS waves under conditions similar to those of Halstead et al. [7]. Hughes and Walker [6] considered a flow with wakes, in which the $FSTI$ between wakes ranged from less than 1% to about 3%, and the $FSTI$ in the wakes was about 8%. They provide clear evidence of TS waves.

Hatman and Wang [9], Volino and Hultgren [10], and Lou and Hourmouziadis [11] all considered low $FSTI$, adverse pressure gradient flows and observed transition in the shear layer over separation bubbles. Spectral data in all three studies showed clear evidence of an instability along with harmonics. It was expected that this instability was very similar to the Kelvin-Helmholtz instabilities observed in free shear layers, although the unstable frequencies were somewhat different than expected for free shear layers since the separation bubbles were bounded by the wall on one side. Volino and Hultgren [10] also considered high $FSTI$ cases and observed broadband unsteadiness in the spectra of the streamwise fluctuating velocity, u' . Spikes at discrete frequencies, which were observed in the low $FSTI$ cases, were not present. They stated that transition in the high $FSTI$ cases appeared to be through a bypass mode.

Clearly there is some disagreement regarding the transition mechanism in separated boundary layers, particularly under high $FSTI$ conditions. Some of these differences may stem from physical differences in the boundary conditions between the various studies. The present study addresses the issue through spectral analysis of flows over a range of Reynolds numbers at both high and low $FSTI$. Included in the analysis are spectra of the turbulent shear stress, which were not considered in previous studies.

EXPERIMENTS

The experimental facility and the cases considered are described in detail in Part 1 [1]. A low speed wind tunnel supplies air to a single-passage cascade-simulator with geometry and flow angles matching those for the industry supplied Pak-B airfoil. For the low $FSTI$ cases, the background turbulence level for the wind tunnel is nominally 0.5%, and consists primarily of low frequency unsteadiness. A passive grid is used to generate a high inlet $FSTI$ of 8.7%.

Velocity data were acquired at 11 streamwise measurement stations along the spanwise centerline of the suction side of the passage. Station locations are given in Table 1. At each station, instantaneous streamwise velocity was measured at 60 locations as a single sensor hot-wire probe was traversed from the airfoil surface to the free-stream. The voltage from the hot-wire was offset and amplified by a factor of 10 and low pass filtered at 10 kHz using signal conditioners (TSI model 157). At each location, data were acquired for 26 seconds at a 20 kHz sampling rate (2^{19} samples). The high sampling rate provides an essentially continuous signal, which is needed for spectral processing. The long sampling time results in low uncertainty in both statistical and spectral quantities. Two component velocity

Table 1: Measurement Stations

Station	1	2	3	4	5	6
s/L_s	0.111	0.194	0.278	0.361	0.444	0.527
Station	7	8	9	10	11	$L_s=228.6$ mm
s/L_s	0.611	0.694	0.778	0.861	0.944	

measurements were made at Stations 7-11 with a cross-wire probe. The upstream boundary layer was too thin for cross-wire measurements. Data were acquired at 25 locations in each profile, beginning 1 mm from the wall and extending to the free-stream. Sampling rates and times were the same as with the single sensor probe. Power spectra of u' , the wall normal fluctuating velocity, v' , and the turbulent shear stress, $-u'v'$, were computed for the data from all measurement locations. Uncertainties in the u' , v' and $-u'v'$ spectra are all 10%. Frequencies are resolved from 4.88 Hz to 10 kHz in 4.88 Hz increments using a 4096 point Fast Fourier Transform to compute the spectra. As a check, the spectra were integrated with respect to frequency and found to equal the corresponding time averaged Reynolds stresses.

Data sets were acquired for cases at high and low $FSTI$ with exit Reynolds numbers of 25,000, 50,000, 100,000, 200,000 and 300,000. The upstream boundary layer through Station 6 remained laminar in all of these cases, with the mean velocity following a Falkner-Skan wedge flow solution. Downstream of Station 6 the pressure gradient becomes adverse. Separation occurred between Stations 6 and 8, with the separation point moving downstream as Re increased. Reattachment did not occur in the high or low $FSTI$, $Re=25,000$ cases or the low $FSTI$, $Re=50,000$ case. In all other cases the boundary layer did reattach, and the reattachment point moved upstream as Re or $FSTI$ was increased. Details are available in Part 1 [1]. The u' level rose in the shear layer in each case after the boundary layer separated, but the turbulent shear stress remained near zero until transition began. Transition began in the shear layer and quickly led to boundary layer reattachment. In the $Re=25,000$ cases, low but non-zero turbulent shear stress was observed at the most downstream stations, indicating that although the shear layer was still non-turbulent and separated, it was showing signs of the start of transition.

As discussed in Part 1 [1], the finite length of the hot-wire sensors (1.27 mm) will result in some spatial averaging and could result in attenuation of the measured fluctuating velocity components. Based on the results of Ligrani and Bradshaw [12, 13], it was explained in Part 1 that the errors in the rms fluctuating quantities are within the 10% uncertainty estimates in the majority of cases in the present study. Exceptions occur for the $Re=200,000$ cases at Station 11 of the low $FSTI$ case and Stations 9-11 of the high $FSTI$ case. For the $Re=300,000$ cases, larger errors are expected for Stations 10-11 of the low $FSTI$ case and Stations 9-11 of the high $FSTI$ case. For these cases, errors may be as large as 30% near the wall, but should be under 10% at y locations greater than 1 mm. As explained by Ligrani et al. [14], measurements with the cross-wire probe are subject to potentially larger errors due to the finite spacing (1 mm) between the two sensors. These errors will be largest near the wall, but become smaller than the 10% uncertainty for y locations above 1 mm. For this reason, cross wire measurements were only made for $y>1$ mm.

The spectra in the present paper are presented to show the energy content of the fluctuating quantities as a function of frequency. The average errors in these spectra, therefore, should be the same as those given above for the corresponding rms quantities. The errors will not be uniform with respect to frequency across the spectra, however. As explained by Ligrani and Bradshaw [13], spatial averaging effects will be most severe for the smallest scales (highest frequencies) in the

flow. Applying the spectral results of Ligrani and Bradshaw [13] to the present study, errors due to spatial averaging at y locations above 1 mm will rise above 10% at frequencies above 150, 300, 600, 1200 and 1800 Hz for the $Re=25,000, 50,000, 100,000, 200,000$, and $300,000$ cases respectively. Below these frequencies the errors should be under 10%. These frequencies are all above the frequencies of the spectral peaks in the results presented below, so the peaks should not be significantly attenuated. For the $Re=25,000$ and $50,000$ cases, all significant energy in the spectra is below the frequencies given above, so there is no significant attenuation of the results at any frequency. For the $Re=100,000$ case, only the high frequency “tail” of the spectra will be subject to significant error. Magnitudes at these high frequencies may be as much as 30% low. Similarly for the $Re=200,000$ and $300,000$ cases, errors will only rise above 10% at frequencies about twice those of the spectral peaks. Magnitudes at the highest frequencies may be as much as 40% low in these cases.

FREQUENCIES OF INTEREST

Transition in the shear layer over the separation bubble could be initiated by Tollmien-Schlichting waves originating in the boundary layer upstream of separation. Upstream of Station 6, the pressure gradient is favorable and the boundary layer should not develop TS waves at any frequencies. At Station 6 the flow begins to decelerate and immediately becomes unstable. Walker [15] provides the following equation for the frequency of maximum amplification rate for TS waves.

$$2\pi\nu f / U_\infty^2 = 3.2 Re_{\delta_s}^{-3/2} \quad (1)$$

The TS frequencies predicted by Eq. (1) are listed in Table 2. Values are given for Stations 6 and 7 for the cases in which the boundary layer is still attached at these stations.

Another possible path to transition is breakdown of the shear layer through a Kelvin-Helmholtz type instability. The frequency of the instability should scale with the velocity change across the shear layer and inversely with the shear layer thickness. Since the velocity in the separation bubble is nearly zero, the velocity difference across the shear layer equals the local free-stream velocity. The shear layer thickness, δ_s , is determined from the mean velocity profiles presented in Part 1 [1]. Table 2 lists the quantity U_∞ / δ_s for each station where the boundary layer is separated.

RESULTS

Free-Stream Spectra

The u' and v' free-stream spectra are shown in Fig. 1 for each station of the low $FSTI$, $Re=300,000$ case. Frequency is plotted on a log scale versus frequency times power spectral density on a linear scale. In these coordinates the area under the curve in any frequency band is proportional to the contribution to the quantity of interest in that band. The u' spectra are dominated by low amplitude unsteadiness at frequencies below 20 Hz. The u' spectra for the lower Re cases (not shown) have proportionately lower amplitudes, but the frequency range remains the same. The frequencies associated with turbulent eddies would be expected to scale with the free-stream velocity. Since the frequencies in the present cases remain constant as Re is changed, the unsteadiness in the wind tunnel is most likely not associated with turbulent eddies. The v' spectra show the same low frequencies as u' but at $1/10^{\text{th}}$ the magnitude. A second lower peak is centered at about 100 Hz. This peak is also present with the same magnitude in u' , and is visible in an expanded version of Fig. 1a. The

Table 2: Most unstable Tollmien-Schlichting frequencies prior to separation and U_∞ / δ_s values in shear layer

$FSTI$	$Re \times 10^{-3}$	TS freq. [Hz]		$U_\infty / \delta_s [s^{-1} \times 10^{-3}]$						
		Station		Station						
		6	7	6	7	8	9	10	11	
Low	25	80		1.0	0.8	0.6	0.5	0.4	0.4	
	50	176			2.1	1.5	1.3	1.2	1.0	
	100	443	266			3.9	3.2	3.8		
	200	1175	645			11	8.7			
	300	1554	1134			22	20			
High	25	60		1.1	0.8	0.6	0.4	0.4	0.3	
	50	174		3.1	2.4	1.6	1.1	0.8		
	100	408	272			4.1	3.1			
	200	1138	732			15				
	300	1747	1195			25				

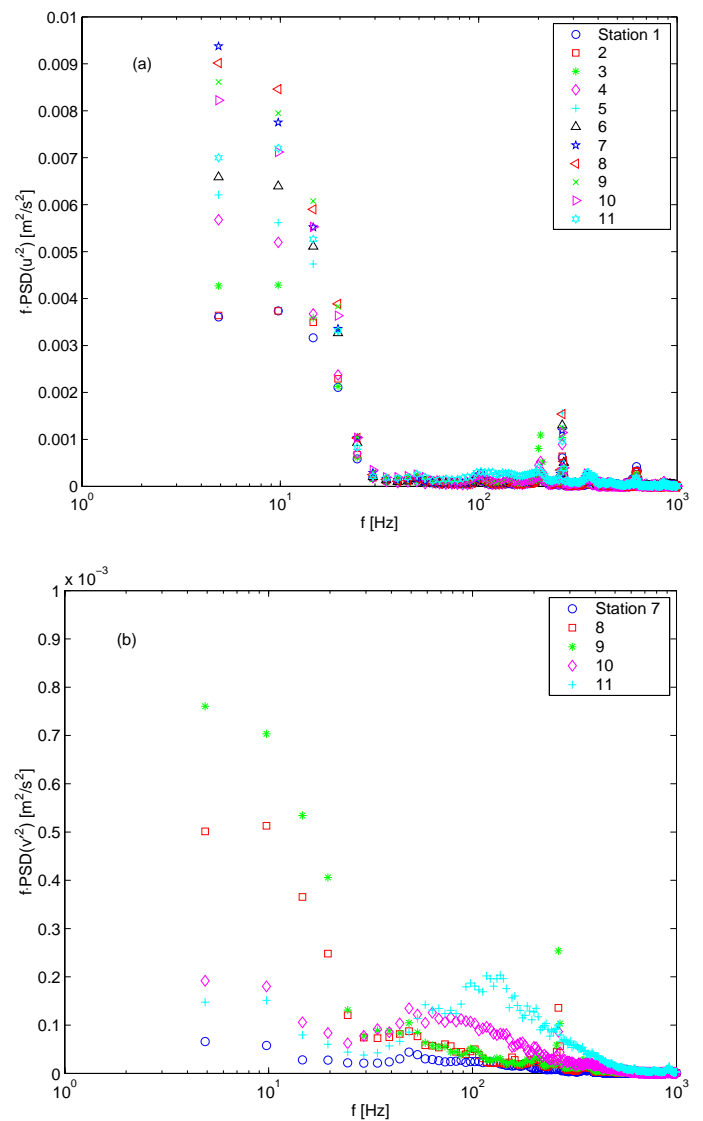


Fig. 1: Free-stream spectra for low $FSTI$, $Re=300,000$ case; (a) u' , (b) v'

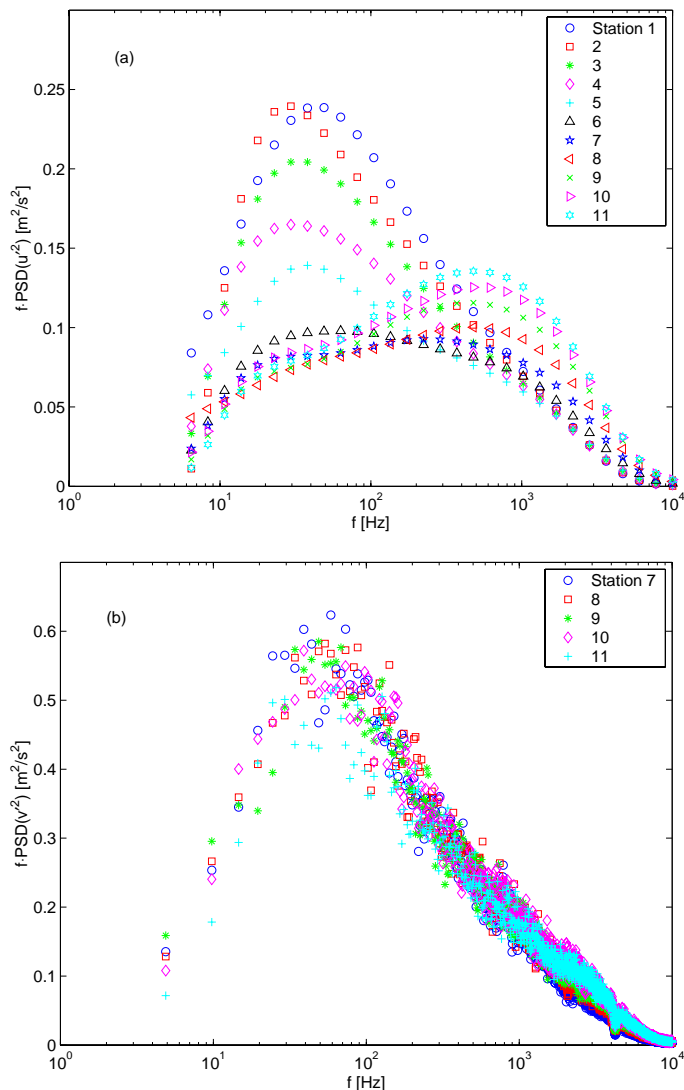


Fig. 2: Free-stream spectra for high FSTI, Re=300,000 case; (a) u' , (b) v'

frequency of this second peak scales with the free-stream velocity and is proportionately lower for the lower Re cases. Its magnitude is very low, and by itself would correspond to an rms turbulence level of about 0.01%. It is likely the residual turbulence remaining after the wind tunnel screens.

The u' and v' free-stream spectra for the high $FSTI$ $Re=300,000$ case are shown in Fig. 2. The magnitude of u' is about 25 times larger than in the low $FSTI$ case of Fig. 1a. At the upstream stations there is a peak at about 30 Hz. This peak decays due to streamwise straining of the flow as it is accelerated through Station 6. In the adverse pressure gradient region downstream of Station 6, a broadband peak emerges centered at about 700 Hz. In the lower Re cases, the u' spectra is qualitatively the same, but the magnitudes scale with U_∞^2 and the frequencies scale with U_∞ . The v' spectra of Fig. 2b all appear similar with a broadband peak centered at 60 Hz. As with u' , the magnitudes and frequencies of the v' spectra in the lower Re cases scale with the free-stream velocity, and appear qualitatively similar to those of Fig. 2b.

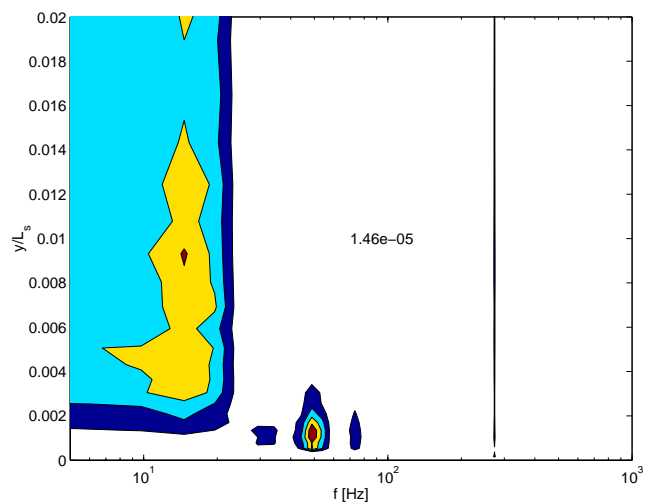


Fig. 3: Contours of $fPSD(u'^2)$, Low FSTI, Re=100,000, Station 4; outer contour magnitude and contour spacing indicated by numerical value in field of figure

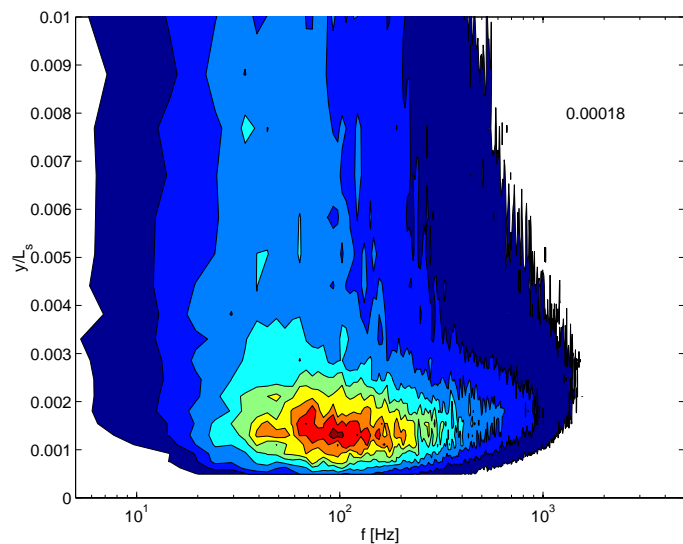


Fig. 4: Contours of $fPSD(u'^2)$, High FSTI, Re=300,000, Station 4; outer contour magnitude and contour spacing indicated by numerical value in field of figure

Upstream Boundary Layer

Contours of the boundary layer u' spectra from Station 4 of the low $FSTI$, $Re=100,000$ case are shown in Fig. 3. Frequency in Hz is shown on the horizontal axis on a log scale, and distance from the wall normalized on the suction surface length is on the vertical axis on a linear scale. The frequency is left dimensional since there is no single appropriate normalization for all regions of the flow. The contours in Fig. 3 show the dimensionless magnitude of the spectra as $f \cdot PSD(u'^2)/U_\infty^2$. A slice through the data of Fig. 3 at a fixed distance from the wall would produce a spectrum in the coordinates of Fig. 2, except with dimensionless magnitude. The number (1.46e-05),

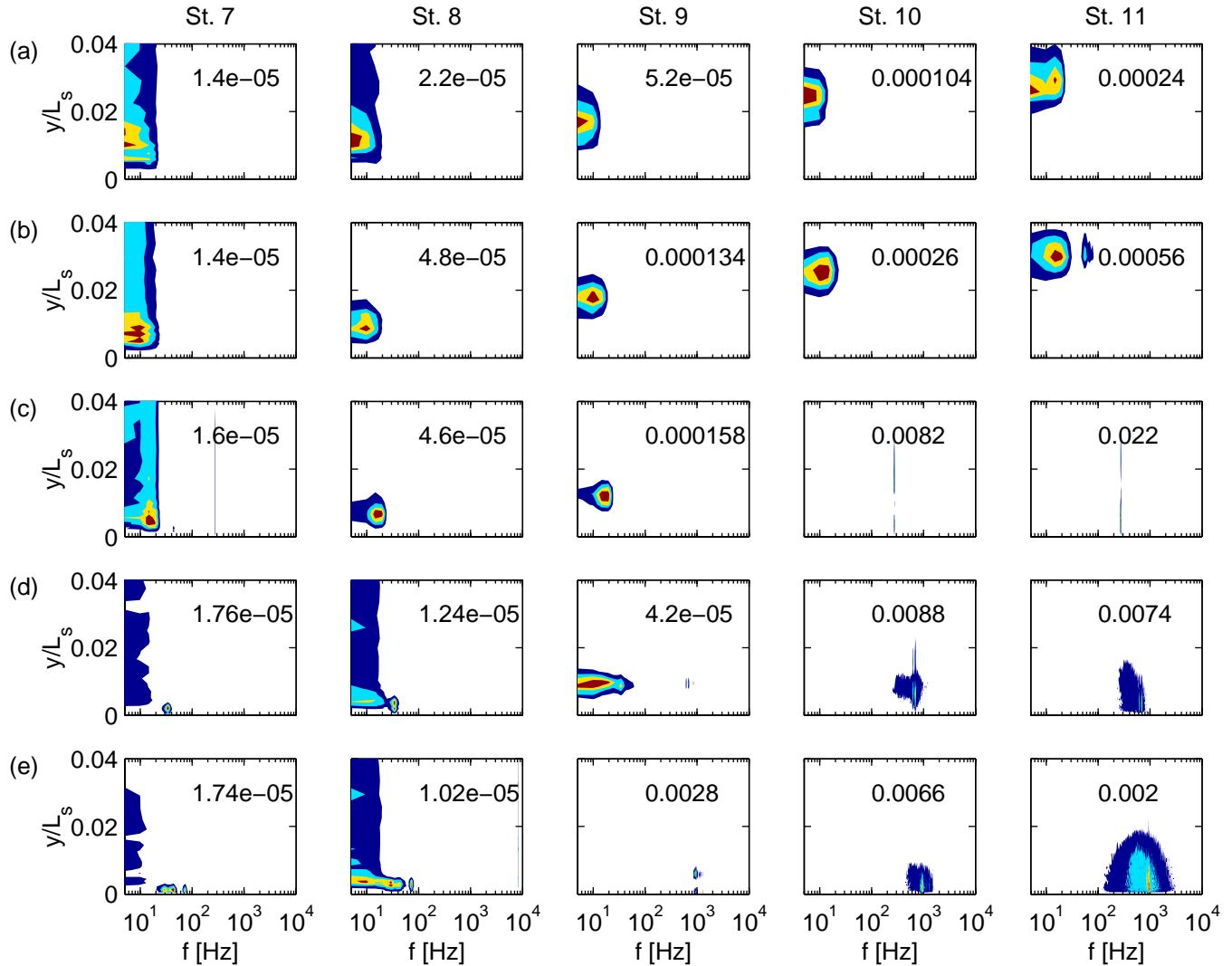


Fig. 5: Contours of $f \cdot \text{PSD}(u'^2) / U_\infty^2$, Low FSTI cases; Station number indicated above each column; by row (a) $Re=25,000$, (b) $Re=50,000$, (c) $Re=100,000$, (d) $Re=200,000$, (e) $Re=300,000$; outer contour magnitude and contour spacing indicated by numerical value in field of each subplot, 5 contours shown in each subplot

which appears in the center of the figure, indicates the magnitude of the outermost contour and the contour spacing. Hence, the outermost contour value is 1.46×10^{-5} , the next contour value is 2.92×10^{-5} , the next is 4.38×10^{-6} , etc. The same format is used in all the figures which follow. Figure 3 shows a peak near the wall centered at 50 Hz and unsteadiness below 20 Hz extending from the free-stream to near the wall. The results shown in Fig. 3 are typical of the behavior at Stations 1-6 in all the low *FSTI* cases. The 50 Hz peak was also visible in the $Re=200,000$ and $300,000$ cases, but not at the two lower *Re*. This peak did not appear to have any significant effect on the downstream boundary layer.

Figure 4 shows the spectra from Station 4 of the high *FSTI*, $Re=300,000$ case in the coordinates of Fig. 3. The Fig. 4 spectra are typical of the spectra at Stations 1-6 of all the high *FSTI* cases. There is a near wall peak at 100 Hz, which is 1.7 times the frequency of the free-stream v' frequency peak shown in Fig. 2b. The distance of the peak from the wall is larger in the lower *Re* cases, scaling with the

boundary layer thickness. The frequency of the peak scales with *Re*, and is consistently 1.7 times the dominant v' frequency in the free-stream. This indicates that the boundary layer unsteadiness is induced by free-stream buffeting. Volino [5] discusses free-stream buffeting of boundary layers in more detail.

Low FSTI Transition

Upstream of Station 6, the boundary layer unsteadiness is attributable to low amplitude streamwise unsteadiness in the low *FSTI* cases, and free-stream buffeting in the high *FSTI* cases. Buffeting, as explained in Part 1 [1], refers to the effect of free-stream pressure fluctuations on the boundary layer as fluid is pushed in the wall normal direction across the gradient in the mean streamwise velocity. Downstream of Station 6, the pressure gradient becomes adverse, and the spectra become more interesting. Figure 5 shows the u' spectra contours for Stations 7-11 of all the low *FSTI* cases. The coordinates of each subplot are the same as those of Fig. 3. In the $Re=25,000$ case

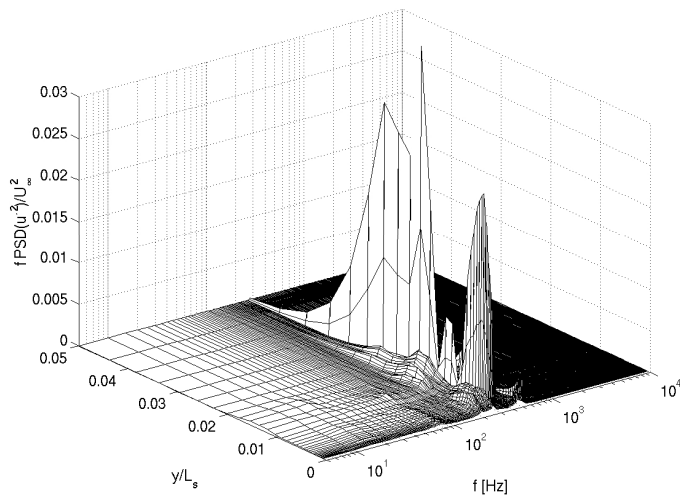


Fig. 6: Spectra of $f \cdot \text{PSD}(u'^2)/U_\infty^2$, Low FSTI, $Re=100,000$, Station 10

(top row of Fig. 5), the contours at Station 7 show the low frequency unsteadiness observed at the upstream stations. Between Stations 7 and 10, the magnitude of the peak increases by an order of magnitude. The peak at each station moves away from the wall. Comparison to the mean velocity profiles presented in Part 1 [1] shows that the location of the peak corresponds, not surprisingly, to the shear layer over the separation bubble. The $Re=50,000$ case (row 2) shows similar behavior through Station 10, but a second peak emerges at about 78 Hz at Station 11. This second peak is indicative of transition.

In the $Re=100,000$ case (row 3 of Fig. 5), a sharp peak appears at Station 10 at 273 Hz. The contour spacing increases by two orders of magnitude between Stations 9 and 10, indicating a similar increase in the magnitude of the peak. The peak is so sharp and so large that it appears as a line in the contour plot. Figure 6 shows this $Re=100,000$, Station 10 data in the same coordinates as Fig. 5, but three dimensionally. The low frequency unsteadiness visible at Station 9 is still present, but since its magnitude is only $1/50^{\text{th}}$ that of the 273 Hz peak, it is barely visible in Fig. 6. The sharp peak in the shear layer is typical of all the low FSTI cases.

In the $Re=200,000$ case (row 4 of Fig. 5), a small peak appears in the shear layer at 698 Hz at Station 9. By Station 10 this peak has increased in size by two orders of magnitude and is becoming more broadband as the boundary layer reattaches and becomes turbulent. Although not clear in Fig. 5, the sharp spectral peak remains in the center of this broadband turbulence and is clear in the format of Fig. 6. Similar behavior is apparent in the $Re=300,000$ case, but the spectral peak and subsequent turbulence are centered at 922 Hz.

Contours of the normalized turbulent shear stress spectra, $f \cdot \text{PSD}(-u'v')/U_\infty^2$, for the low FSTI cases are shown in Fig. 7. The format is the same as in Fig. 5. The shear layer is laminar at Stations 7 and 8 in all cases, and the turbulent shear stress is near zero. The $Re=25,000$ case shows a low magnitude, 15 Hz peak at Station 10. The peak was obscured in the u' spectra of Fig. 5 due to the presence of other streamwise unsteadiness at similar frequencies. The magnitude of the 15 Hz shear stress peak increases by a factor of 15 between Station 10 and 11, but its amplitude is still quite low. Close inspection of the u' spectra (Fig. 5) at Station 11 shows a double peak, with one peak at 15 Hz. The mean profiles of Part 1 [1] indicate that

Table 3: Measured peak frequencies in spectra

FSTI	$Re \times 10^{-3}$	25	50	100	200	300
Low	Station	10	10	9	9	9
	f [Hz]	15	78	273	698	922
High	Station	9	9	9	9	9
	f [Hz]	20	85	230	600	1100

transition may be imminent, but the shear layer is still laminar at Station 11.

The $Re=50,000$ case shows similar behavior to that at $Re=25,000$. A turbulent shear stress peak appears at Station 10 and is 37 times larger by Station 11. This peak did not become visible until Station 11 in the u' spectra. Similarly, in the $Re=100,000$ case a sharp turbulent shear stress peak emerges at Station 9, one station upstream of its appearance in u' . The shear stress peak appears at Station 9 in the $Re=200,000$ and $300,000$ cases. In all cases, the peak appears at the same frequency in u' and $-u'v'$, but tends to become visible earlier in the $-u'v'$ spectra due to the lower magnitude of the low-frequency “noise” in $-u'v'$.

The frequencies of the spectral peaks are listed for all cases in Table 3. Also indicated in the table are the stations at which these frequencies were determined. The frequencies of the peaks did not change significantly in the streamwise direction. Because the peaks do not appear until after the boundary layer has separated, there is some reason to believe that a Kelvin-Helmholtz type instability may be involved. For the low FSTI cases, comparison of the spectral peak frequencies to the U_∞/δ_s values in Table 2 shows that the spectral frequencies and U_∞/δ_s values both increase with Re , as expected.

The ratio of the measured frequency to U_∞/δ_s is not a constant, however, ranging from about 0.04 to about 0.08. Comparison of the measured frequencies to the TS frequencies of Table 2 shows better correlation. At the three highest Re , the measured frequencies agree with the TS frequencies at Station 7 (the last station before separation) to within 20%. The boundary layer is already separated at Station 7 in the $Re=25,000$ and $50,000$ cases, so the frequency comparison must be made at Station 6. Agreement with the TS frequencies is not as good in these cases as at the high Re . Hughes and Walker [6] note that since the most unstable TS frequency changes with streamwise position, the frequency observed in the shear layer need not equal the TS value at any single upstream position.

High FSTI Transition

Contours of the u' spectra for the high FSTI cases are shown in Fig. 8. In the $Re=25,000$ case (top row), there is low frequency unsteadiness at the same frequencies observed upstream (Fig. 4). As in the low FSTI cases, the peak u' location is in the shear layer over the separation bubble. In the $Re=50,000$ case, the outermost contour at Station 10 extends to higher frequencies than at the upstream stations, and by Station 11 a new peak has emerged at 60 Hz, extending from the shear layer down to the wall. The magnitude of this new peak is about equal to the magnitude of the original, low frequency peak, which is also still visible. Similar behavior is clear for the $Re=100,000$ case. Higher frequencies begin to emerge at Station 9, and a large, clear peak centered at 260 Hz is visible at Stations 10 and 11. In the $Re=200,000$ and $300,000$ cases, some signs of higher frequencies are already visible at Station 8, and a double peak is clear at Station 9. At Stations 10 and 11, the higher frequency peak overwhelms the lower frequencies.

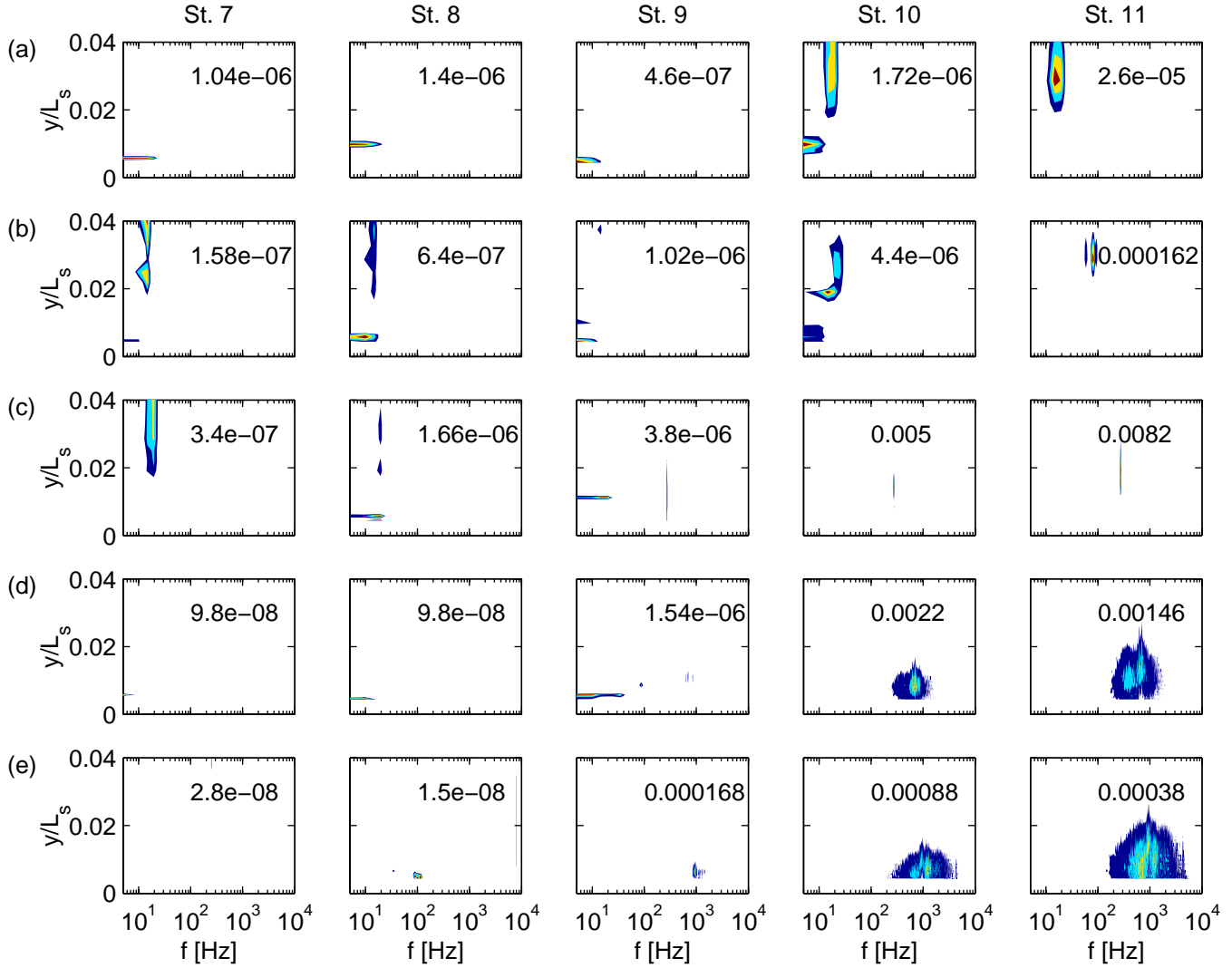


Fig. 7: Contours of $f \cdot \text{PSD}(-u'v')/U_\infty^2$, Low FSTI cases; see Fig. 5 caption for further explanation

Comparing Fig. 8 to Fig. 5, the contour levels in the high *FSTI* case are about 2 orders of magnitude higher than in the low *FSTI* case at Stations 7 and 8. This is expected and due to the higher u' caused by free-stream buffeting in the high *FSTI* case. Farther downstream, however, after the higher frequencies emerge, the contour levels are higher for the low *FSTI* cases. This is somewhat misleading, as the rms u' levels are actually very similar in the high and low *FSTI* cases at these stations. The lower contour levels in the high *FSTI* case result because the u' fluctuations are distributed over a wider frequency band. The spectral peaks of Fig. 8 are much broader than the corresponding peaks of the low *FSTI* cases shown in Figs. 5-7. Figure 9 shows the u' spectra at Station 10 of the high *FSTI*, $Re=100,000$ case. Comparing to Fig. 6, the high *FSTI* case exhibits much more low frequency activity due to free-stream buffeting, and the peak is clearly broader in frequency than the 273 Hz spike of the low *FSTI* case.

Figure 10 shows contours of the turbulent shear stress spectra for the high *FSTI* cases. Values at Station 7 and 8 are low, in spite of the high *FSTI*, indicating that much of the u' unsteadiness observed in

Fig. 8 does not involve turbulent transport. Distinct, broadband peaks emerge by Station 9 in all cases. As in the low *FSTI* cases, these peaks are visible in $-u'v'$ farther upstream than they are in u' . The peak becomes visible in $-u'v'$ soon after it forms, but the u' peak must grow to become larger than the free-stream induced fluctuations before it is discernable.

The broad peaks in the high *FSTI* cases might suggest that transition occurs through a bypass mode. This was the conclusion of Volino and Hultgren [10]. Closer inspection, however, reveals strong similarity to the low *FSTI* cases. The frequencies of the peaks in the high *FSTI* cases are listed in Table 3. The broad nature of the high *FSTI* case peaks, as shown in Fig. 9, result in an uncertainty of about 20% in the frequency values in Table 3. With this uncertainty, the frequency at each Re is essentially the same as in the corresponding low *FSTI* case. Comparison to the TS frequencies in Table 2 show the same good agreement observed in the low *FSTI* cases. Close inspection of Fig. 10 reveals that at the four highest Re , the peak in $-u'v'$ begins to appear, with very low magnitude, at Stations 7 and 8. The boundary layer is still thin at these stations, so part of the peak lies closer to the wall

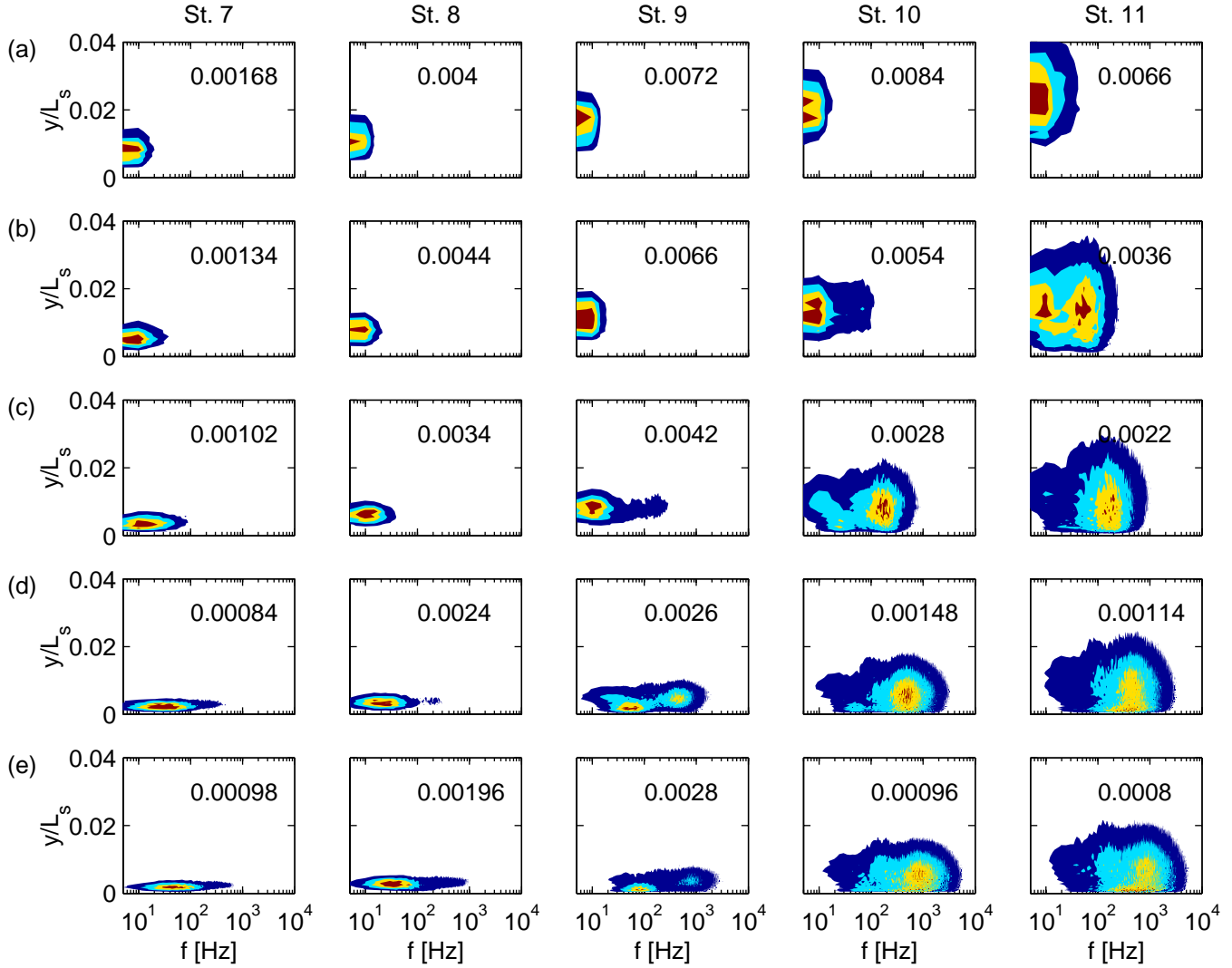


Fig. 8: Contours of $f \cdot \text{PSD}(u^2)/U_\infty^2$, High FSTI cases; see Fig. 5 caption for further explanation

than can be measured with the cross-wire probe. The closest measurement to the wall with the cross-wire was at $y=1$ mm, which corresponds to $y/\delta_{99.5}$ between 0.2 and 0.65 at the stations in question. What is visible, however, is at the same frequencies as present downstream. Since the boundary layer is still attached at Station 7, it is doubtful these fluctuations could be induced by a Kelvin-Helmholtz type instability. Instead, it appears that a TS instability plays a role, even in the high *FSTI* cases. This agrees with the findings of Hughes and Walker [6], who used instantaneous wall shear measurements to identify wave packets both within and between wakes in an unsteady flow. Although it appears that TS waves play a role in the high *FSTI* cases, it should be noted that it is also possible that transition occurs through a bypass mode, and that the spectral peaks are due not to TS waves but to the turbulence within turbulent spots. Perhaps both TS and bypass modes play a role, as suggested by Mayle [2].

CONCLUSIONS

Turbulence spectra provide valuable insights into the transition mechanism. Clear sharp peaks were observed in the spectra of the low *FSTI* cases, at frequencies indicating a probable TS instability

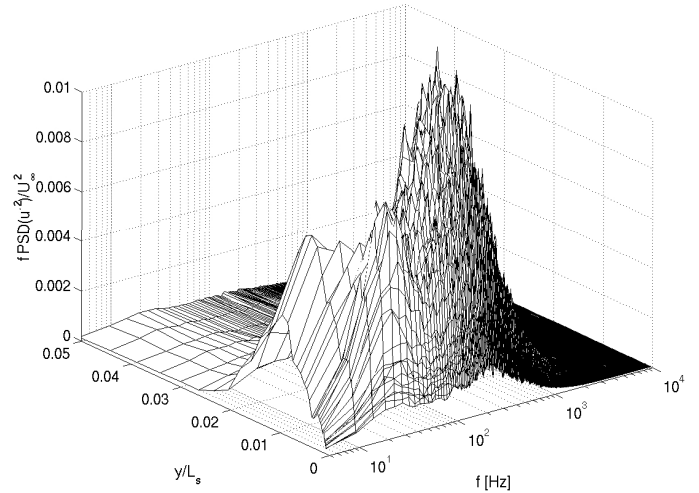


Fig. 9: Spectra of $f \cdot \text{PSD}(u^2)/U_\infty^2$, High FSTI, $Re=100,000$, Station 10

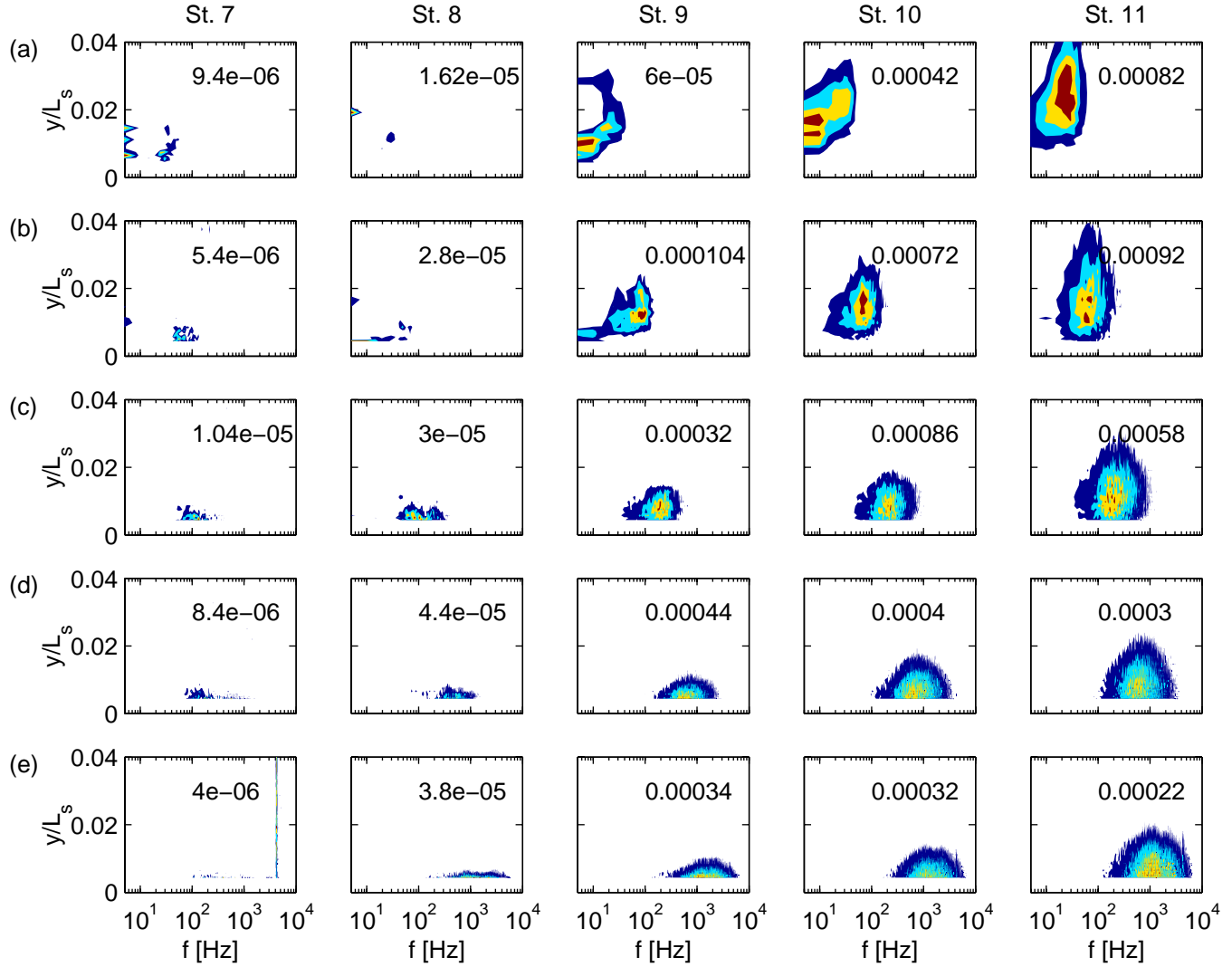


Fig. 10: Contours of $f \cdot \text{PSD}(-u'v')/U_\infty^2$, High FSTI cases; see Fig. 5 caption for further explanation

mechanism for the breakdown of the shear layer over the separation bubble to turbulence. The spectra were more broadband for the high *FSTI* cases, but the peaks of these spectra occurred at the same frequencies as in the corresponding low *FSTI* cases, suggesting a possible similar transition mechanism at high and low *FSTI*. The turbulent shear stress spectra were valuable for detection of instabilities upstream of the location where peaks became discernable in the u' spectra. In the high *FSTI* cases, low magnitude peaks were detected in $-u'v'$ upstream of separation, further supporting the argument for a TS transition. Larger initial disturbances in the high *FSTI* cases resulted in detectable $-u'v'$ farther upstream than in the low *FSTI* cases. Since the adverse pressure gradient boundary layer is unstable to disturbances over a broad range of frequencies and the free-stream turbulence contains a range of scales, broad peaks emerge in the boundary layer spectra of the high *FSTI* cases. These peaks contrast with the sharp peaks of the low *FSTI* cases, which result from the growth of small disturbances at the most unstable frequencies. The presence and predictability of the shear layer instability may prove useful in future attempts to induce transition for separation control.

ACKNOWLEDGEMENTS

This work was sponsored by the NASA Glenn Research Center. The grant monitor is Dr. David Ashpis. Additional matching support was provided through a U.S. Naval Academy Recognition Grant.

REFERENCES

- [1] Volino, R.J., 2002, "Separated Flow Transition Under Low-Pressure Turbine Airfoil Conditions: Part 1 – Mean Flow and Turbulence Statistics," ASME Paper GT-2002-30236.
- [2] Mayle, R.E., 1991, "The Role of Laminar-Turbulent Transition in Gas Turbine Engines," ASME *Journal of Turbomachinery*, **116**, pp. 509-537.
- [3] Schlichting, H., 1979, *Boundary Layer Theory*, 7th ed., McGraw-Hill, New York.
- [4] Sohn, K.H., and Reshotko, E., 1991, "Experimental Study of Boundary Layer Transition with Elevated Freestream Turbulence on a Heated Flat Plate," NASA CR 187068.

- [5] Volino, R.J., 2002, "An Investigation of the Scales in Transitional Boundary Layers Under High Free-Stream Turbulence Conditions," ASME Paper GT-2002-30233.
- [6] Hughes, J.D. and Walker, G.J., 2001, "Natural Transition Phenomena on an Axial Compressor Blade," *ASME Journal of Turbomachinery*, **123**, pp. 392-401.
- [7] Halstead, D.E., Wisler, D.C., Okiishi, T.H., Walker, G.J., Hodson, H.P., and Shin, H.-W., 1997, "Boundary Layer Development in Axial Compressors and Turbines: Part 3 of 4 – LP Turbines," *ASME Journal of Turbomachinery*, **119**, pp. 225-237.
- [8] Solomon, W.J., and Walker, G.J., 1995, "Incidence Effects on Wake-Induced Transition on an Axial Compressor Blade," *Proc. 12th International Symposium on Air Breathing Engines*, Melbourne, Australia, pp. 954-964.
- [9] Hatman, A., and Wang, T., 1999, "A Prediction Model for Separated Flow Transition," *ASME Journal of Turbomachinery*, **121**, pp. 594-602.
- [10] Volino, R.J., and Hultgren, L.S., 2001, "Measurements in Separated and Transitional Boundary Layers Under Low-Pressure Turbine Airfoil Conditions," *ASME Journal of Turbomachinery*, **123**, pp. 189-197.
- [11] Lou, W., and Hourmouziadis, J., 2000, "Separation Bubbles Under Steady and Periodic-Unsteady Main Flow Conditions," *ASME Journal of Turbomachinery*, **122**, pp. 634-643.
- [12] Ligrani, P.M., and Bradshaw, P., 1987, "Spatial Resolution and Measurement of Turbulence in the Viscous Sublayer Using Subminiature Hot-Wire Probes," *Experiments in Fluids*, **5**, pp. 407-417.
- [13] Ligrani, P.M., and Bradshaw, P., 1987, "Subminiature Hot-Wire Sensors: Development and Use," *Journal of Physics E: Scientific Instruments*, **20**, pp. 323-332.
- [14] Ligrani, P.M., Westphal, R.V., and Lemos, F.R., 1989, "Fabrication and Testing of Subminiature Multi-Sensor Hot-Wire Probes," *Journal of Physics E: Scientific Instruments*, **22**, pp. 262-268.
- [15] Walker, G.J., 1989, "Transitional Flow on Axial Turbomachine Blading," *AIAA Journal*, **27**, pp. 595-602.

GT2003-38728

PASSIVE FLOW CONTROL ON LOW-PRESSURE TURBINE AIRFOILS

Ralph J. Volino

Department of Mechanical Engineering
 United States Naval Academy
 Annapolis, Maryland 21402
 Email: volino@usna.edu

ABSTRACT

Two-dimensional rectangular bars have been used in an experimental study to control boundary layer transition and reattachment under low-pressure turbine conditions. Cases with Reynolds numbers (Re) ranging from 25,000 to 300,000 (based on suction surface length and exit velocity) have been considered at low (0.5%) and high (8.5% inlet) free-stream turbulence levels. Three different bars were considered, with heights ranging from 0.2% to 0.7% of suction surface length. Mean and fluctuating velocity and intermittency profiles are presented and compared to results of baseline cases from a previous study. Bar performance depends on the bar height and the location of the bar trailing edge. Bars located near the suction surface velocity maximum are most effective. Large bars trip the boundary layer to turbulent and prevent separation, but create unnecessarily high losses. Somewhat smaller bars had no immediate detectable effect on the boundary layer, but introduced small disturbances which caused transition and reattachment to move upstream from their locations in the corresponding baseline case. The smaller bars were effective under both high and low free-stream turbulence conditions, indicating that the high free-stream turbulence transition is not simply a bypass transition induced by the free-stream. Losses appear to be minimized when a small separation bubble is present, so long as reattachment begins far enough upstream for the boundary layer to recover from the separation. Correlations for determining optimal bar height are presented. The bars appear to provide a simple and effective means of passive flow control. Bars which are large enough to induce reattachment at low Re , however, cause higher losses at the highest Re . Some compromise would, therefore, be needed when choosing a bar height for best overall performance.

NOMENCLATURE

C_p $2(P_T - P)/\rho U_e^2$, pressure coefficient
 d bar height
 $FSTI$ free-stream turbulence intensity
 H δ^*/θ , shape factor
 K $(v/U_\infty)(dU_\infty/ds)$, acceleration parameter

L_s suction surface length
 P pressure
 P_T upstream stagnation pressure
 Re $U_e L_s / \nu$, exit Reynolds number
 Re_d $U_d d / \nu$, Reynolds number based on bar height
 Re_{st} $U_\infty (s_T - s_s) / \nu$, separation to transition distance Reynolds number
 Re_θ momentum thickness Reynolds number
 s streamwise coordinate, distance from leading edge
 U mean streamwise velocity
 U_∞ local free-stream velocity
 U_d mean velocity at bar height in baseline boundary layer
 U_e nominal exit free-stream velocity, based on inviscid solution
 u' rms streamwise fluctuating velocity
 y cross-stream coordinate, distance from wall
 $\delta_{99.5}$ 99.5% boundary layer thickness
 δ^* displacement thickness
 γ intermittency, fraction of time flow is turbulent
 ν kinematic viscosity
 ρ density
 θ momentum thickness

Subscripts

b baseline flow
 m modified flow
 p suction surface pressure minimum, velocity maximum
 s separation location
 t transition start location

INTRODUCTION

Modern low-pressure turbine (LPT) airfoils are subject to increasingly stronger pressure gradients as designers impose higher loading in an effort to improve efficiency and lower cost by reducing the number of airfoils in an engine. If the adverse pressure gradient on the suction side of these airfoils becomes strong enough, the boundary layer will separate. Separation bubbles, particularly those which fail to reattach, can result in a significant loss of lift and a subsequent degradation of engine efficiency (e.g. Hourmouziadis [1], Mayle [2],

and Sharma et al. [3]). The problem is particularly relevant in aircraft engines. Airfoils optimized to produce maximum power under takeoff conditions may still experience boundary layer separation at cruise conditions, due to the thinner air and lower Reynolds numbers at altitude. A component efficiency drop of 2% may occur between takeoff and cruise conditions in large commercial transport engines, and the difference could be as large as 7% in smaller engines operating at higher altitudes. Component life may also be affected by more than an order of magnitude (Hodson [4]). Because the LPT produces the bulk of the net power in many engines, changes in its component efficiency can result in nearly equal changes in overall engine efficiency (Wisler [5]). There are several sources for losses in an engine, including secondary flows, but the suction side boundary layer has been identified as the primary source of losses in the LPT (Curtis et al. [6]). Prediction and control of suction side separation, without sacrifice of the benefits of higher loading, is therefore, necessary for improved engine design.

Separation on LPT airfoils is complicated by boundary layer transition. Turbulent boundary layers are much more resistant to separation than laminar boundary layers. If transition occurs far enough upstream, it can prevent separation. If transition occurs in the shear layer over a separation bubble, it will tend to induce boundary layer reattachment. The lower the Reynolds number, the farther downstream transition will tend to occur, hence the problems associated with performance at altitude.

Separated flow transition has been studied extensively, and in recent years several studies have focused on transition in the LPT. Volino [7] provides a review of much of that work. Separation can be affected through naturally occurring phenomena in an engine and through deliberate attempts at flow control. Several studies have shown that high free-stream turbulence intensity (*FSTI*) tends to cause transition to move upstream, resulting in a smaller separation bubble. Reducing the separation bubble size tends to result in thinner boundary layers after reattachment, thereby reducing losses. Moving transition upstream, however, results in a longer turbulent region on the airfoil, which tends to increase losses. Volino [7] showed that the net result of these competing effects depends on the Reynolds number. High *FSTI* tends to reduce losses at low *Re*. At high *Re*, where separation bubbles are relatively small even with low *FSTI*, high *FSTI* results in higher losses. At very low *Re*, boundary layers may fail to reattach even with high *FSTI* (e.g. Volino [7] and Van Treuren et al. [8]). Unsteadiness caused by wakes generated upstream of an airfoil has been shown in several studies (e.g. Howell et al. [9]) to reduce the extent of separation bubbles and reduce losses. As with elevated *FSTI*, wake unsteadiness is most effective at reducing losses at lower *Re*, where the steady flow separation bubbles are largest. Stadtmüller et al. [10] found that at high *Re*, losses were higher with wakes than in steady flow.

Existing results suggest that separation bubbles should be kept small, but without producing an unnecessarily long turbulent region. Hourmouziadis [1] discussed “controlled diffusion blading,” in which an airfoil is designed so that a small separation bubble is present. The bubble itself is not thick enough to produce high losses, and its presence allows a shorter turbulent region near the trailing edge. This idea is discussed below in conjunction with the present results.

Capitalizing on the beneficial effects of unsteady wakes, Howell et al. [9] and Brunner et al. [11] studied airfoils modified for higher lift. Losses increased with airfoil loading, as adverse pressure gradients became stronger and separation bubbles became larger. With wake passing, however, the magnitude of the loss increase was in some cases relatively small compared to the increase in lift. Aft loaded airfoils tended to have lower losses, since separation and transition

occurred closer to the trailing edge, resulting in a shorter turbulent region.

While high *FSTI* and wakes help to mitigate separated flow problems, they clearly do not solve all problems, as evidenced by the known efficiency drop in modern engines at altitude. Howell et al. [9] indicated that their highly loaded airfoils might be close to a limit, and that higher loading could cause unacceptable separation problems even in the presence of wakes. Looking beyond *FSTI* and wakes, other types of flow control could prove useful. The literature contains numerous examples of separation control. Most have been applied to external flows over aircraft, but a few studies have considered passive devices added to LPT airfoils. Van Treuren et al. [8] utilized vortex generators on the suction surface of an LPT airfoil. The vortex generators caused reattachment at $Re=50,000$ (all *Re* in the present paper are based on exit velocity and suction surface length). Losses appeared to be slightly lower with the vortex generators. The vortex generators were not effective at $Re=25,000$, and the boundary layer did not reattach even with 8% *FSTI*. Van Treuren et al. [8] did not consider higher *Re*. In another study, Lake et al. [12] used various passive devices including dimples and boundary layer trips in an LPT cascade. They considered cases with *Re* above 100,000. Murawski and Vafai [13] added extensions to the trailing edges of the airfoils in their cascade. These extensions tended to move the separation location downstream. At low *Re*, they reduced the length of the separation bubble and reduced losses. At high *Re*, losses increased. Byerley et al. [14] used “Gurney flaps” to control separation. These devices were trips, near the trailing edge on the pressure side of the airfoils. They helped to keep the boundary layer attached on the suction side, but also increased losses in the cascade. Active separation control has also been employed. Bons et al. [15, 16] used steady and pulsed vortex generator jets to successfully control separation under LPT conditions.

The studies listed above indicate that separation control should be possible under LPT conditions. Existing results are, however, limited both in the range of Reynolds numbers considered in each study and in the types of data acquired. More experiments are needed with various types of devices to expand the experimental data base. Detailed measurements will also help in the explanation of the physical mechanisms by which various devices affect the flow.

Passive flow control is considered in the present work. Thin bars of rectangular cross section are placed on the suction surface of an LPT airfoil near the suction surface velocity peak. Experiments were conducted in a single-passage cascade-simulator, described in Volino [7]. The geometry of the passage corresponds to that of the “Pak-B” airfoil, which is an industry supplied research airfoil that is representative of a modern, aggressive LPT design. Volino [7] documented cases in the present facility without flow control. These serve as baseline cases for the present study.

EXPERIMENTS

Experiments were conducted in a low speed wind tunnel, described by Volino et al. [17]. Briefly, air enters through blowers and passes through a honeycomb, a series of screens, two settling chambers, and a three-dimensional contraction before entering the test section. At the exit of the contraction, the mean velocity is uniform to within 1%. The *FSTI* is $0.5\% \pm 0.05\%$. Nearly all of this free-stream “turbulence” is actually streamwise unsteadiness at frequencies below 20 Hz and is not associated with turbulent eddies. The rms intensities of the three components of the unsteadiness are 0.7%, 0.2% and 0.2% in the streamwise, pitchwise and spanwise directions, respectively. For low *FSTI* cases, the test section immediately follows the contraction. For high *FSTI*, a passive grid is installed at the contraction exit followed

by a 1 m long rectangular settling chamber. At the inlet to the test section the high *FSTI* mean flow and turbulence are spatially uniform to within 3% and 6% respectively. The free-stream turbulence is nearly isotropic with rms intensities of 8.8%, 8.9% and 8.3% in the streamwise, pitchwise and spanwise directions. The integral length scales of these components are 3 cm, 1.6 cm and 1.4 cm. The integral scales were computed from the power spectra of each component.

The test section, shown in Fig. 1, consists of the passage between two airfoils. Details are listed in Table 1 and more information is available in Volino [7]. A large span to chord ratio of 4.3 was chosen to insure two-dimensional flow at the spanwise centerline of the airfoils, where all measurements were made. Upstream of each airfoil are flaps, which control the amount of bleed air allowed to escape from the passage. The flaps, along with a tailboard on the pressure side of the passage, are adjusted to produce the correct leading edge flow and pressure gradient along the airfoils. The flow in the passage matches that in a multi-blade cascade.

Experimental conditions match those of the ten baseline cases of Volino [7], who considered high and low *FSTI* cases at five Reynolds numbers ($Re=25,000$, 50,000, 100,000, 200,000, and 300,000). The Reynolds number range is representative of conditions from cruise to takeoff. The *FSTI* levels in an engine may vary considerably, but the values in the present work are believed to span the range of most interest.

Prior to the detailed experiments of the present study, various devices were used in preliminary attempts at flow control. The devices included trip wires of various diameters, rectangular bars of various widths and thicknesses, and delta wing vortex generators of various heights, spacing, and angles with respect to the flow. All of these devices were tried at several streamwise locations along the suction surface. Documentation included streamwise pressure profiles and velocity profiles acquired near the trailing edge. Large devices of any type eliminated separation (as indicated by the pressure profiles), but caused large increases in losses (as indicated by large increases in momentum deficit at the trailing edge). As the size of the devices was reduced, it was found that all devices which were just large enough to induce boundary layer reattachment at $Re=25,000$ caused about the same increase in losses at higher Re . This was somewhat unexpected, as it was thought that the delta wings vortex generators might present less blockage, and more effectively promote mixing and inhibit separation than the trips or bars. Reasons for this unexpected finding are discussed with the results below. Since no device appeared to have a clear advantage, rectangular bars were chosen for further study because of their simplicity. The bars were of uniform rectangular cross section and extended along the airfoil span, as shown in Fig. 2. It should be noted that the tests described above were not exhaustive, and do not preclude the possible usefulness of vortex generators or other types of devices.

The results of the preliminary tests with the bars indicated that the streamwise width of a bar and the location of its leading edge were unimportant. The bar height and the location of its trailing edge were critical. Hence, it appeared that the backward facing step at the trailing edge was most important for flow control. Bars were most effective when the trailing edge was near the location of the suction surface velocity peak. If the trailing edge was much farther downstream, it was located under the separation bubble and was ineffective. If the trailing edge was upstream in the favorable pressure gradient region, the stabilizing effect of the accelerating flow appeared to lessen the bar's effectiveness.

In the present study, rectangular bars were fabricated from multiple layers of vinyl tape. The trailing edge of the bar was located at $s/L_s=0.51$, near the suction surface velocity peak. All bars were 6 mm

Table 1: Test section parameters

Axial Chord [mm]	True Chord [mm]	Pitch [mm]	Span [mm]	Suction side, L_s [mm]	Inlet flow angle	Exit flow angle
153.6	170.4	136.0	660.4	228.6	35°	60°

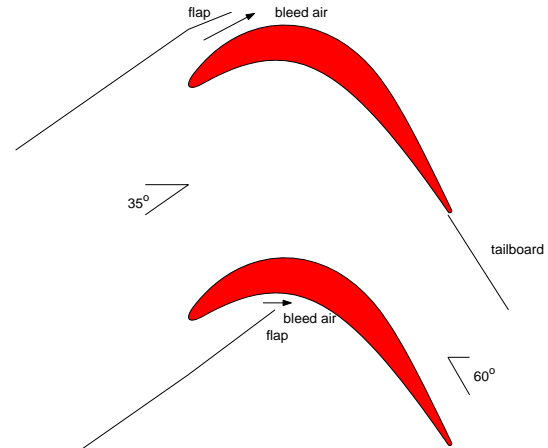


Fig. 1 Schematic of the test section

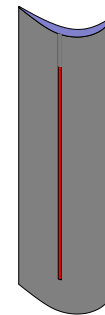


Fig. 2 Scale drawing of suction side airfoil showing location of bar

wide in the streamwise direction. Bar heights of 0.4 mm, 0.8 mm and 1.6 mm were used. The bar heights were all less than 1% of L_s . They compare to local boundary layer thickness at the bar location of about 3.8 mm, 2.7 mm, 2.0 mm, 1.4 mm and 1.2 mm in the baseline $Re=25,000$ through 300,000 cases respectively. For each bar height, all 10 cases of the baseline study were re-documented, for a total of 30 new experimental cases.

Measurements

Pressure surveys were made for each case using a pressure transducer (0-870 Pa range Validyne transducer) and a Scanivalve. Stagnation pressure was measured with a pitot tube upstream of the passage inlet, and eleven pressure taps were located on each airfoil along their spanwise centerlines. Locations of the taps on the suction side are listed in Table 2 along with measured local *FSTI* components, and the ReK product at these stations based on a non-separating, inviscid solution. The uncertainty in the suction side pressure coefficients was 7% at the lowest Re , and below 4% in other cases. Most of this uncertainty was due to bias error. Stochastic error was minimized by averaging pressure transducer readings over a 10 second period.

Table 2: Measurement stations locations, local acceleration (inviscid soln.), and measured local free-stream turbulence

Station	s/L_s	ReK	Low $FSTI$ u'/U_∞ [%]	Low $FSTI$ v'/U_∞ [%]	High $FSTI$ u'/U_∞ [%]	High $FSTI$ v'/U_∞ [%]
1	0.111	1.58	0.44		5.2	
2	0.194	1.20	0.39		4.6	
3	0.278	0.86	0.37		4.0	
4	0.361	0.75	0.38		3.5	
5	0.444	0.62	0.39		3.2	
6	0.528	-0.02	0.41		2.8	
7	0.611	-0.81	0.47	0.05	2.9	5.9
8	0.694	-0.95	0.47	0.12	3.0	6.2
9	0.777	-0.58	0.48	0.14	3.4	6.6
10	0.861	-0.53	0.54	0.11	3.8	6.8
11	0.944	-0.18	0.51	0.11	4.0	6.8

Velocity profiles on the suction surface were measured at streamwise stations corresponding to pressure taps 7-11, as given in Table 2. These stations are downstream of the bar. Profiles at Stations 1-6 are fully documented for the baseline cases in Volino [7, 18], and show that the upstream boundary layer closely follows a laminar solution, even in the high $FSTI$ cases. Profiles were measured near but not at the spanwise centerline of the airfoil to insure that the pressure taps did not interfere with the velocity measurements. Profiles were acquired with a hot-wire anemometer (AA Lab Systems model AN-1003) and a single sensor boundary layer probe (TSI model 1218-T1.5). The sensor diameter is 3.8 μm , and the active length is 1.27 mm. At each measurement location, data were acquired for 26 seconds at a 20 kHz sampling rate (2^{19} samples). All raw data were saved. The high sampling rate provides an essentially continuous signal, which is needed for intermittency and spectral post-processing. The long sampling time results in low uncertainty in both statistical and spectral quantities. Data were acquired at 60 wall normal locations in each profile, extending from the wall to the free-stream, with most points concentrated in the near wall region. The closest point was within 0.1 mm of the wall, which corresponds to $y/L_s=0.0004$ and between 0.01 and 0.2 boundary layer thicknesses. Flow direction in a separation bubble cannot be determined with a single-sensor hot-wire, but velocity magnitude can be measured and was found to be essentially zero within the bubbles of the present cases. Determining the direction was not, therefore, considered essential. Uncertainties in the mean velocity are 3-5% except in the very near wall region where near-wall corrections (Wills [19]) were applied to the mean velocity. Uncertainties in the momentum and displacement thicknesses computed from the mean profiles are 10%. Uncertainty in the shape factor, H , is 8%.

The uncertainty in the fluctuating streamwise velocity is below 10%, except in the very near wall region, where spatial averaging effects, due to the finite length of the hot-wire sensor, become important in some cases. For the present cases, as explained in Volino [7] based on the work of Ligrani and Bradshaw [20, 21], spatial averaging should not be significant for the $Re=25,000$ and 50,000 cases, even near the wall. For the higher Re cases, spatial averaging should not be significant for $y>1$ mm ($y/L_s>0.004$), but may cause errors as high as 30% closer to the wall. It is not certain that the errors are this large, however. The estimates are based on the results of Ligrani and Bradshaw [20, 21], who considered a boundary layer with $Re_\theta=2600$. The momentum thickness Reynolds numbers in the present cases are all below 1300. This may indicate less developed turbulence

in the present study, which could imply fewer small scale eddies and lower averaging errors.

The intermittency, γ , is the fraction of time the flow is turbulent within the transition region. It was determined at each measurement location based on the instantaneous streamwise velocity signal, using the technique described in Volino et al. [17]. The uncertainty in γ is 10%. As explained in Volino [17], turbulent flow is defined here to include a range of large and small scale eddies, turbulence production, and dissipation. A boundary layer may be characterized by significant u' fluctuations but still be non-turbulent if these fluctuations are induced by an external source that does not also cause near wall turbulence production. Such is often the case under high $FSTI$ conditions. Free-stream eddies buffet the boundary layer, inducing non-turbulent boundary layer fluctuations but very little momentum transport. Transition to turbulence is characterized not so much by large increases in u' levels, which may remain essentially constant, but by the appearance of higher frequencies. The higher frequencies signal the generation of turbulence in the near wall region and are used to distinguish between turbulent and non-turbulent flow. Further discussion is available in Volino [17].

RESULTS

Velocity and Pressure Profiles

Pressure coefficients for the low $FSTI$, $Re=25,000$ cases are shown in Fig. 3. Also shown is the inviscid solution for the present geometry. In all cases there is good agreement with the inviscid solution on the pressure side. On the suction side, the baseline case shows good agreement with the inviscid solution in the favorable pressure gradient region, but a large separation bubble in the adverse pressure gradient region. Separation is indicated by the nearly constant C_p values, which are well above the inviscid solution. The C_p values remain high to the trailing edge, showing no sign of reattachment. With the 0.4 mm thick bar, there is an increase in C_p over the baseline value at $s/L_s=0.53$. The pressure tap at this location is immediately downstream of the bar, and the flow over the tap is probably affected by the close proximity of the bar. The C_p values in this case remain high to the trailing edge, indicating that the boundary layer does not reattach. The same is true for the 0.8 mm bar case. With the 1.6 mm bar, C_p drops below the baseline values near the end of the favorable pressure gradient region. The larger bar is apparently enough of an obstruction to slow the near wall flow upstream of the bar. Downstream of the 1.6 mm bar, C_p values are high, as in the other cases, but at the most downstream pressure tap C_p drops to near the inviscid solution value, indicating boundary layer reattachment.

The velocity profiles for the low $FSTI$, $Re=25,000$ cases are shown in Fig. 4. The top row of the figure shows dimensionless mean velocity profiles at Stations 7-11. The baseline case shows a boundary layer near separation at Station 7, a small separation bubble at Station 8, and an increasingly larger bubble at Stations 9-11. The mean profiles of the 0.4 mm and 0.8 mm bar cases are virtually indistinguishable from the baseline case. The 1.6 mm bar case shows a clear separation bubble at Station 7, suggesting that the boundary layer has separated from the trailing edge of the bar. This bubble continues to grow, and at Station 8 the separation bubble is larger with the 1.6 mm bar than in the other cases. At Station 9 all cases appear similar. This agreement is really a crossing, as the shear layer in the 1.6 mm bar case is on the verge of reattaching, while the separation bubble is growing in the other cases. At Station 10, the near wall velocity in the 1.6 mm bar case has begun to rise, indicating incipient reattachment. By Station 11, the boundary layer has clearly reattached in the 1.6 mm bar case, although the mean profile has not recovered to

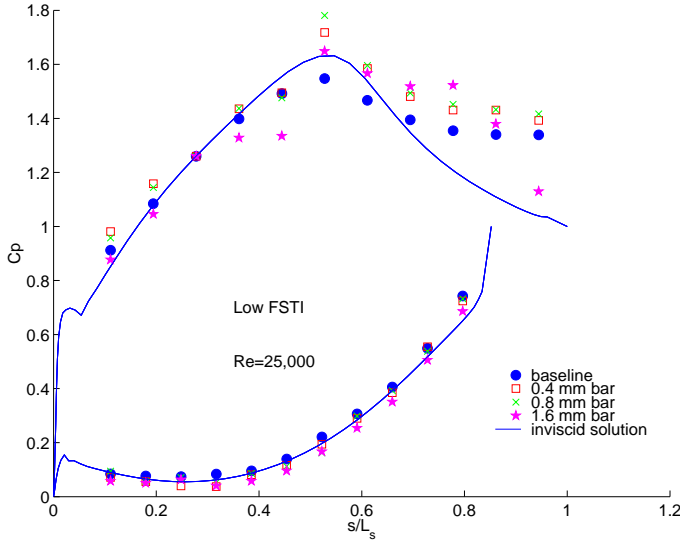


Fig. 3 Cp profiles, Low FSTI, Re=25,000 cases

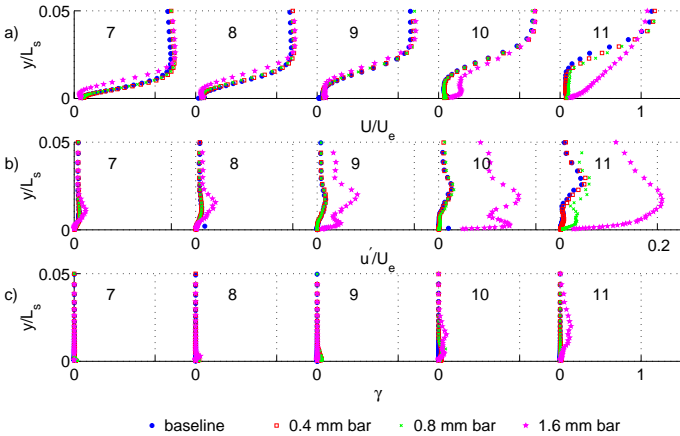


Fig. 4 Station 7-11 profiles, high FSTI, Re=25,000 cases: (a) mean velocity, (b) u' , (c) intermittency

a fully-developed turbulent shape. Dimensionless u' profiles are shown in the second row of Fig. 4. As with the mean profiles, the baseline case and the 0.4 mm and 0.8 mm bar cases are indistinguishable through Station 10. All show a small u' peak growing in the shear layer over the separation bubble. As explained in Volino [7, 18], this peak is not indicative of transition. It is caused primarily by low frequency fluctuations which are amplified when they act across the region of high mean velocity gradient in the shear layer. At Station 11, there is a slight increase in u' in the 0.8 mm bar case over the baseline case, and the high values extend into the near wall region. These near wall fluctuations suggest the beginning of transition and reattachment, but they are not large enough in this case to significantly affect the mean profile. The 1.6 mm bar case shows a larger u' peak than the other cases at Stations 7 and 8. The peak is in the shear layer and is similar to the peaks at Stations 9 and 10 of the other cases. It does not indicate transition. The peak becomes larger at Station 9, and extends into the near wall region, which is a sign of incipient transition. By Station 10 u' is much larger with a clear

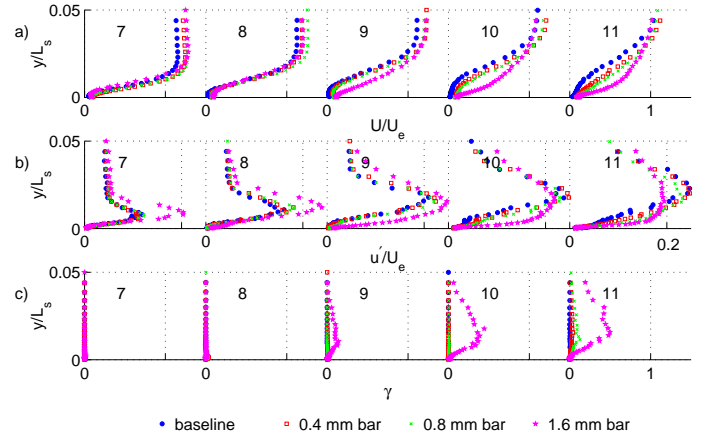


Fig. 5 Station 7-11 profiles, high FSTI, Re=25,000 cases: (a) mean velocity, (b) u' , (c) intermittency

double peak. This rise in u' corresponds to the beginning of reattachment observed in the mean profile. The third row of Fig. 4 shows the local intermittency. It is zero in all cases through Station 9, but begins to rise at Stations 10 and 11 of the 1.6 mm bar case. The intermittency peak is in the shear layer, indicating that this is where transition begins. Intermittency only reaches about 13% at Station 11. This is consistent with the mean velocity profile, which shows the boundary layer is reattached but not yet a fully-developed turbulent profile. As the turbulence is intermittent, it is likely that the boundary layer is only intermittently reattached. The high u' peak at Station 11 is also consistent with a transitional boundary layer. As a boundary layer becomes fully turbulent, the dimensionless u' peak will decrease in magnitude to about 0.1, and move close to the wall.

The behavior in the 1.6 mm bar case is interesting. The bar was not large enough to immediately trip the boundary layer to turbulent, but it did move the separation point upstream. This caused transition to move upstream, and led to at least a partial reattachment by the trailing edge, which did not occur in the other cases. The 0.8 mm bar trip case is also very interesting. The bar in this case was so small that it had no immediate measurable effect on the mean or u' profiles. Well downstream at Station 11, however, the effect of this bar became visible in the u' profile. Apparently this bar introduced a very small disturbance in the flow, which was too small to detect at first, but grew as it moved downstream.

The velocity profiles of Fig. 4 and the pressure profiles of Fig. 3 are in good agreement. Both show transition and reattachment at the same locations, and the measured static pressures agree with the local free-stream velocities of Fig. 4. The agreement between the pressure and velocity results was apparent in all cases. For brevity, the pressure profiles are not presented in the cases which follow.

Figure 5 shows the velocity profiles for the high *FSTI*, *Re*=25,000 cases. The format is that same as in Fig. 4. As in the low *FSTI* case, the baseline, 0.4 mm trip and 0.8 mm trip cases are nearly indistinguishable at the upstream stations. By Station 11, some differences are apparent in the mean profiles for these cases. The separation bubble is less distinct in the cases with the bars, but the boundary layer still does not appear fully reattached. Intermittency rises slightly above zero at Station 11 of the 0.8 mm bar case, while remaining essentially at zero with the smaller bar and in the baseline case. The u' profiles show a large peak in the shear layer which grows in the streamwise direction. As shown in Volino [7], this peak

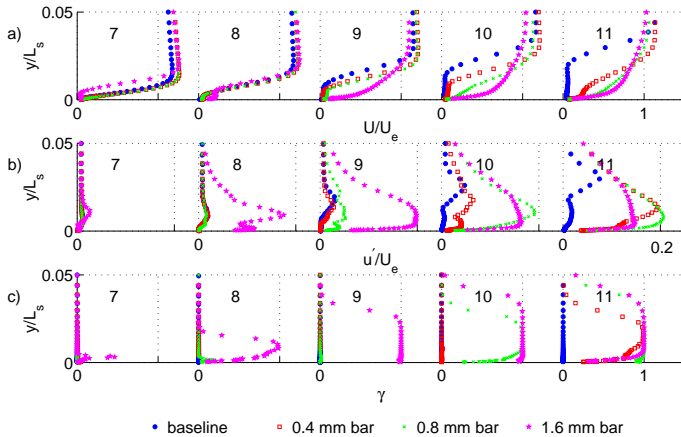


Fig. 6 Station 7-11 profiles, low FSTI, $Re=50,000$ cases: (a) mean velocity, (b) u' , (c) intermittency

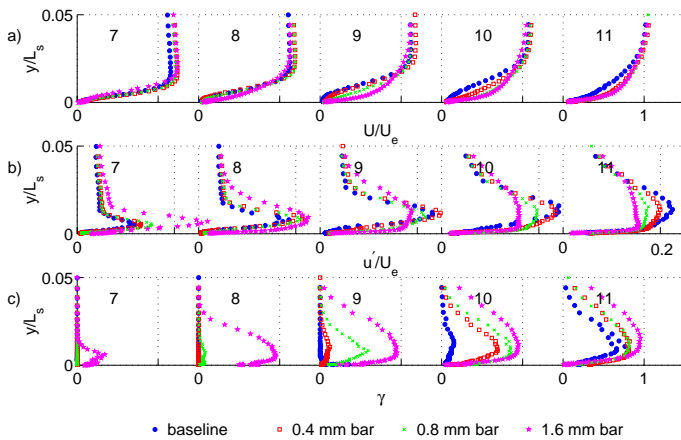


Fig. 7 Station 7-11 profiles, high FSTI, $Re=50,000$ cases: (a) mean velocity, (b) u' , (c) intermittency

is caused by the action of the high $FSTI$ on the shear layer, and does not indicate significant momentum transport. As in the low $FSTI$ cases of Fig. 4, the 1.6 mm bar case shows significant differences from the other cases in Fig. 5. The u' peak is significantly higher in this case at Stations 7 and 8. At Station 9, u' values are higher in the near wall region, the intermittency rises above zero, and the mean profile appears to be reattached. At Stations 10 and 11 the intermittency continues to increase. The mean profile adjusts toward a more turbulent shape between Stations 9 and 11. The u' peak decreases somewhat by Station 11, but still shows the relatively high values of a transitional boundary layer, rather than the somewhat lower values of a fully-turbulent boundary layer. As in the low $FSTI$, $Re=25,000$ case, the 1.6 mm bar is not large enough to immediately trip the boundary layer to turbulent, but it causes transition to move upstream and leads to a reattachment that did not occur in the baseline or smaller bar cases.

The velocity profiles of the low $FSTI$, $Re=50,000$ case are shown in Fig. 6. The effects of the bars are clear. At Station 7, the 1.6 mm bar has caused a relatively large separation bubble compared to the other cases and a small u' peak in the shear layer over this bubble. The smaller bar cases are indistinguishable from the baseline case, with

mean profiles only on the verge of separation and u' near zero. By Station 8, the 1.6 mm bar case has undergone a sudden transition, with $\gamma=1$, high u' levels in both the shear layer and near wall regions, and the beginning of reattachment as indicated by non-zero mean velocity near the wall. The other cases are indistinguishable, exhibiting a small separation bubble and showing no sign of transition or reattachment. At Station 9, the boundary layer is clearly reattached in the 1.6 mm bar case, and u' values are beginning to rise in the 0.8 mm bar case. At Station 10 the intermittency indicates fully-turbulent flow and the boundary layer has reattached in the 0.8 mm bar case. The 0.4 mm bar case is still separated with $\gamma=0$, but u' has begun to rise near the wall. By Station 11 the 0.4 mm bar case has become turbulent and the boundary layer has started to reattach. The baseline case remains non-turbulent with a large separation bubble at Station 11. As observed in the $Re=25,000$ cases, the 1.6 mm bar is not large enough to immediately trip the boundary layer to turbulent, but it does move separation upstream, which causes transition and reattachment to move significantly upstream. The smaller bars appear to have no immediate effect on the boundary layer, but they must introduce small disturbances that grow in the streamwise direction and have a significant effect in moving transition and reattachment upstream. The 0.8 mm bar must introduce a larger disturbance than the 0.4 mm bar, since transition and reattachment occur one station farther upstream with the 0.8 mm bar.

Figure 7 shows the high $FSTI$, $Re=50,000$ cases. With the larger bars, transition and reattachment move upstream. With the 1.6 mm bar, the intermittency is already non-zero by Station 7, and the boundary layer is fully turbulent and attached by Station 8. With the 0.8 mm bar, γ rises above zero at Station 8 and is near fully turbulent by Station 10. The mean profile appears to indicate reattachment by Station 9. The intermittency rises above zero in the 0.4 mm bar case at Station 9, and continues to rise at Stations 10 and 11. The mean profile shows reattachment at Station 10. In the baseline case, the intermittency begins to rise at Station 10, and the boundary layer is reattached at Station 11. At Station 11 the mean profiles are indistinguishable in the cases with bars, and fuller than in the baseline case. In all cases, transition begins upstream of the location in the corresponding low $FSTI$ case of Fig. 6, but the transition length is longer. Volino and Hultgren [22] also observed that transition begins farther upstream with high $FSTI$, but is more abrupt in low $FSTI$ cases.

Figure 8 shows the low $FSTI$, $Re=100,000$ cases. The 1.6 mm bar immediately trips the boundary layer to turbulent and eliminates the separation bubble. The 0.8 mm bar causes a small u' peak above the baseline values at Station 7. The intermittency jumps from 0 to 1 between Stations 7 and 8, and the separation bubble is effectively eliminated. As in the lower Re cases, the 0.4 mm bar has no visible effect at Station 7, and the mean and u' profiles are indistinguishable from the baseline case. The boundary layer separates, but by Station 9 the shear layer has become fully turbulent and begun to reattach. In the baseline case, u' does not begin to show elevated near wall values until Station 10, and transition and reattachment occur at Station 11. The mean profiles at Station 11 show the fullest profile and thinnest boundary layer in the 0.4 mm bar case. The larger bars result in thicker boundary layers. The mean profile in the baseline case has not yet recovered to a fully turbulent shape. As will be discussed below, the thinner attached boundary layer in the 0.4 mm bar case suggests that this case will have lower losses than the other cases.

The high $FSTI$, $Re=100,000$ cases are shown in Fig. 9. As in the low $FSTI$ case, the 1.6 mm bar trips the boundary layer to turbulent and eliminates separation at this Re . The intermittency is non-zero at Station 7 of the 0.8 mm bar case, and it continues to rise through

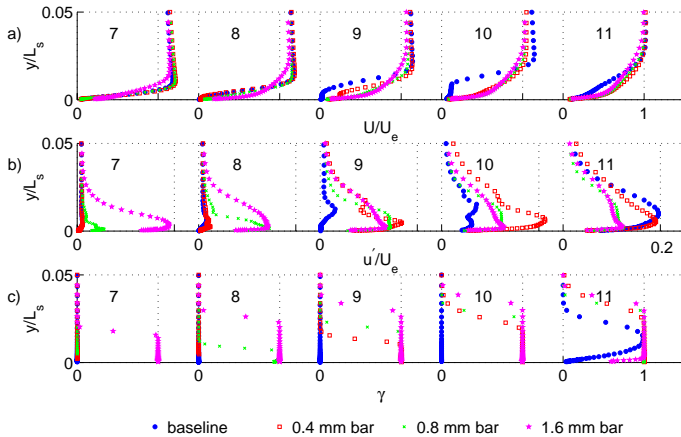


Fig. 8 Station 7-11 profiles, low FSTI, $Re=100,000$ cases: (a) mean velocity, (b) u' , (c) intermittency

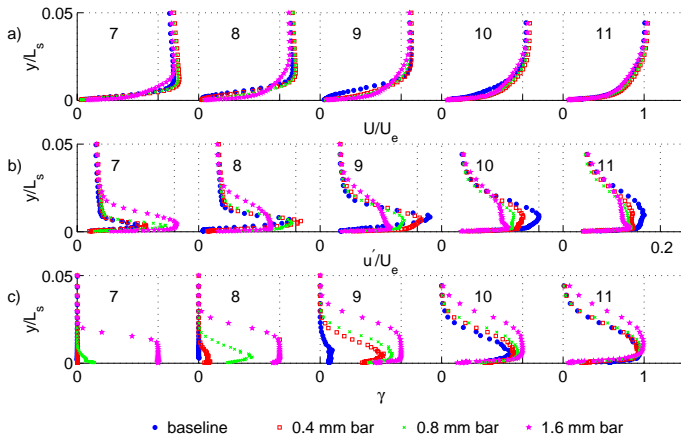


Fig. 9 Station 7-11 profiles, high FSTI, $Re=100,000$ cases: (a) mean velocity, (b) u' , (c) intermittency

Station 10, indicating an extended transition zone. Because transition begins so far upstream, the separation bubble is eliminated and transition occurs in an attached boundary layer. With the 0.4 mm bar, the intermittency indicates that transition does not begin until Station 8, so a small separation bubble forms, as in the baseline case. The boundary layer is reattached by Station 9, however, and transition is nearly complete by Station 10. In the baseline case, transition begins at Station 9, and the boundary layer is reattached at Station 10. Examining the mean profiles, the 1.6 mm bar causes an immediate thickening of the boundary layer, and the separation bubble in the baseline case also causes a thicker boundary layer. By Station 11, the mean profiles for these two cases agree closely. The boundary layers are thinner in the cases with the smaller bars.

In the low $FSTI$, $Re=200,000$ cases of Fig. 10, the intermittency profiles show that the 0.8 mm and 1.6 mm bars immediately trip the boundary layer to turbulent and eliminate the separation bubble. The 1.6 mm bar, which is the same thickness as the boundary layer at Station 7 of the baseline case, results in a substantially thicker boundary layer than in all of the other cases. The 0.4 mm bar case shows a small separation bubble at Station 8, but is fully turbulent and reattached by Station 9. The baseline case exhibits a clear separation bubble at Station 9, and is fully turbulent and reattached by Station 10.

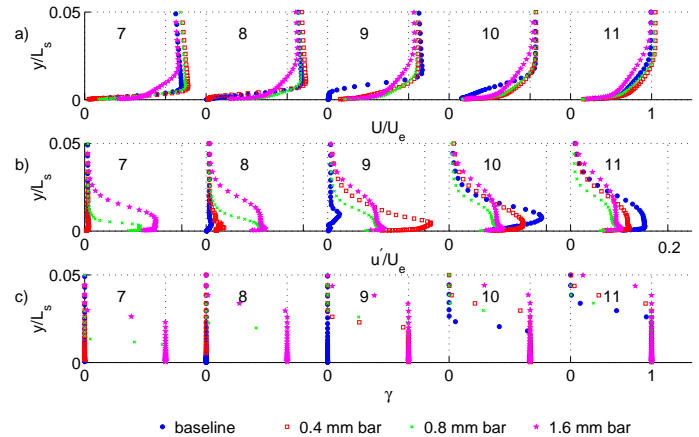


Fig. 10 Station 7-11 profiles, low FSTI, $Re=200,000$ cases: (a) mean velocity, (b) u' , (c) intermittency

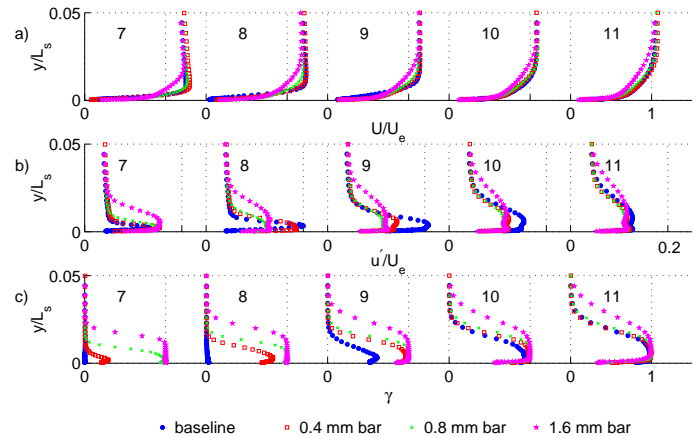


Fig. 11 Station 7-11 profiles, high FSTI, $Re=200,000$ cases: (a) mean velocity, (b) u' , (c) intermittency

The mean profiles at Station 11 show that the growth of the bubble in the baseline case results in a thicker boundary layer than in the 0.8 and 0.4 mm bar cases.

Figure 11 shows the high $FSTI$, $Re=200,000$ cases. As in the low $FSTI$ cases of Fig. 10, the 0.8 and 1.6 mm bars trip the boundary layer to turbulent. Transition has already started, as indicated by the non-zero intermittency, in the 0.4 mm bar case at Station 7. In all of these cases, there is no separation. In the baseline case, γ does not rise above zero until Station 9, and there may be a small separation bubble at Station 8. At Station 11, the mean, u' and intermittency profiles of the baseline, 0.4 mm and 0.8 mm bar cases are all in good agreement, while the 1.6 mm bar case exhibits a noticeably thicker boundary layer.

The low $FSTI$, $Re=300,000$ cases are shown in Fig. 12. As in the $Re=200,000$ cases, the 0.8 mm and 1.6 mm bars trip the boundary layer to turbulent. The 0.4 mm bar appears to have no effect at Station 7, where the mean and u' profiles agree with the baseline case and the intermittency is zero. By Station 8, however, the boundary layer in the 0.4 mm bar case has become fully turbulent, while in the baseline case it is still laminar and has separated. By Station 9 the shear layer in the baseline case is transitional, and it is fully turbulent and reattached by Station 10. At Station 11 the mean profiles for the four cases are all

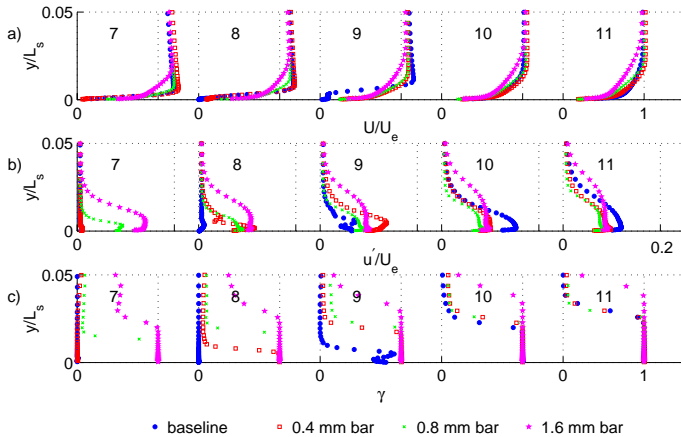


Fig. 12 Station 7-11 profiles, low FSTI, $Re=300,000$ cases:
(a) mean velocity, (b) u' , (c) intermittency

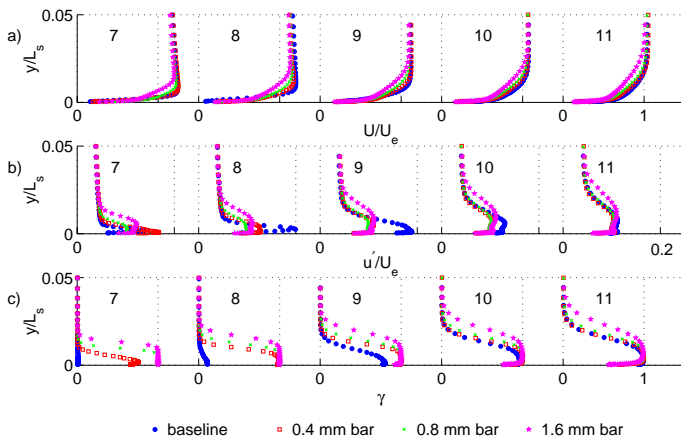


Fig. 13 Station 7-11 profiles, high FSTI, $Re=300,000$ cases:
(a) mean velocity, (b) u' , (c) intermittency

different, with the 0.4 mm bar and baseline cases having the thinnest boundary layers.

Figure 13 shows the high *FSTI*, $Re=300,000$ cases. As in the low *FSTI* cases, the 0.8 mm and 1.6 mm bars trip the boundary layer to fully turbulent, and the 0.4 mm bar causes transition to start by Station 7 and finish by Station 8. Transition has started at Station 8 of the baseline case and is complete near Station 10. In all of these cases transition begins far enough upstream to prevent separation. The mean profiles at all stations show that the boundary layer is thinnest in the baseline case and that the thickness increases with the bar size. With the 0.4 mm and 0.8 mm bars the boundary layer is only slightly thicker than in the baseline case, but it is substantially thicker in the 1.6 mm bar case.

Some consistent trends run through the data from all cases. If a bar is large enough, it will immediately trip the boundary layer to fully turbulent and prevent separation. As Reynolds number increases, the boundary layer thickness decreases as does the thickness of the bar required for tripping. If a bar is small enough, it initially appears to have no effect on the boundary layer. The boundary layer appears to proceed over the bar with no measurable change in the mean velocity or u' from the corresponding baseline case. The bars must, however, introduce some small disturbance into the boundary layer. The

boundary layer is unstable to small disturbances in the adverse pressure gradient region, so the small disturbances grow and eventually cause transition. Larger bars must impart larger (albeit sometimes still undetectable) perturbations than the smaller bars, resulting in transition locations that move upstream as bar size is increased. The optimal bar size depends on the Reynolds number and is discussed further below.

The present results shed some light on the transition mechanism under both high and low *FSTI* conditions. Volino [18] examined spectra of the fluctuating velocity in the boundary layers and shear layers of the baseline cases. He observed sharp peaks in the spectra of the low *FSTI* cases at frequencies that matched the most unstable frequencies for Tollmien-Schlichting (TS) waves in the boundary layer just upstream of separation. He therefore concluded that transition in the shear layer might be through a TS mechanism in these cases. In the high *FSTI* cases, Volino [18] observed broadband peaks in the spectra, and the relatively long transition regions noted above. Volino and Hultgren [22] made similar observation, and concluded that the high *FSTI* separated flow transition was through a bypass mode, very similar to high *FSTI* transition in an attached boundary layer. Volino [18], however, noted that the broadband peaks in the high *FSTI* case spectra were centered at the same frequencies as in the low *FSTI* cases, suggesting a similar transition mechanism under high and low *FSTI* conditions. He concluded that disturbances which began to grow in the boundary layer prior to separation were causing a TS type transition in the shear layer over the separation bubble in both the high and low *FSTI* cases. High *FSTI* has a strong effect in moving transition upstream, but the bars in the present cases had an equally strong or stronger effect in both the high and low *FSTI* cases. This confirms that the free-stream turbulence is not solely responsible for bypass transition in the high *FSTI* cases.

The magnitude of the disturbances induced by the bars is too small to be quantified based on the mean or u' results presented above. Perhaps more can be learned from boundary layer spectra. Analysis of spectra based on u' fluctuations for the present cases show some interesting but inconclusive results. Volino [18] found that u' spectra are often characterized by low frequency fluctuations that are induced by the free-stream and have no direct effect on transition. In the early stages of transition, these low frequency fluctuations can hide the very low amplitude fluctuations important for transition. Volino [18] found that spectra of the turbulent shear stress are less affected by the low frequency unsteadiness and can provide a better means for detecting the early stages of transition. Acquisition and analysis of turbulent shear stress data for the cases of the present study may prove useful for explaining and quantifying the transition mechanism.

Shape Factor and Momentum Thickness

The shape factor and momentum thickness are useful parameters for evaluating the state of the boundary layer with respect to separation, transition and losses. They provide a means for summarizing the information presented in the velocity profiles of Figs. 4 through 13. In the present cases, the boundary layer has a shape factor, H , of about 2.4 at the end of the favorable pressure gradient region. This is the expected value for this laminar, accelerated boundary layer. If the boundary layer separates, the displacement thickness grows rapidly, while the momentum thickness remains nearly constant. The result is a very high shape factor. If the boundary layer reattaches, the displacement thickness drops, and the momentum thickness begins to grow. The boundary layer eventually recovers to a fully turbulent shape, with a shape factor of about 1.6 in the present cases.

Stage losses in a multi-blade turbine cascade can be determined through measurement of the momentum deficit in the wake

downstream of the blade row. With the single-pass facility of the present study, wake measurements are not meaningful, since there is flow on only one side of the airfoils on each side of the passage. If a boundary layer separates and does not fully reattach, or reattaches near the trailing edge, momentum thickness will be relatively low at the trailing edge, and high losses will be generated in the wake downstream of the passage. While the losses in such a case cannot be quantified in the present study, it is safe to assume that they would be unacceptably high, and that there would be an unacceptable loss of lift from the airfoils. For those cases in which the boundary layer reattaches and recovers to a fully developed turbulent shape, the suction side profile loss is likely the dominant loss mechanism in the passage (Howell et al. [9]). As explained by Howell et al. [9], for a given shape factor and passage exit angle, the momentum thickness of the suction side boundary layer at the trailing edge is proportional to the suction side profile loss.

Figure 14 provides an example of the development of the shape factor and momentum thickness, using the low *FSTI*, $Re=100,000$ cases. In the baseline case, H increases from 2.4 to a high value of about 5 as the boundary layer separates. Reattachment occurs near the trailing edge, and H drops to about 2.2, which is still above the turbulent value of 1.6, indicating that recovery from the separation is not complete. In the 0.4 mm bar case, the boundary layer separates and H reaches a value of 3.7. The boundary layer then reattaches, and H gradually drops to a fully turbulent value by the trailing edge. With the 0.8 mm bar, transition occurs far enough upstream to prevent separation, and H drops continuously from a laminar value to a turbulent value as transition occurs. In the 1.6 mm bar case the boundary layer is tripped to turbulence, and H quickly reaches its turbulent value. The 1.6 mm bar causes an immediate thickening of the boundary layer, and the momentum thickness remains higher than in the other cases at all streamwise locations. The 0.4 and 0.8 mm bars appear to have no immediate effect on θ . When transition and reattachment occur, however, θ begins to rise. When reattachment occurs in the baseline case, it causes θ to increase to a higher value than in the 0.4 and 0.8 mm bar cases. Near the trailing edge θ is lowest in the 0.4 mm bar case. This would presumably be the case with the lowest profile losses. The larger bars force transition to occur farther upstream than necessary, resulting in a longer turbulent region and higher losses. In the baseline case the separation bubble becomes relatively thick, resulting in a thick boundary layer after reattachment. The 0.4 mm bar case provides a good example of the controlled diffusion described by Hourmouziadis [1]. With the 0.4 mm bar, the separation bubble is relatively thin, and the turbulent region is relatively short, resulting in lower losses.

Figure 15 shows the shape factor and momentum thickness at Station 11 ($s/L_s=0.94$), near the trailing edge, for all the low *FSTI* cases. In the $Re=25,000$ cases, the shape factor indicates that the boundary layer only reattaches in the 1.6 mm bar case. The shape factor in this case is still above the expected turbulent value, indicating that recovery from the separation is not complete. Comparison of momentum thicknesses is not meaningful at this Re . For the $Re=50,000$ cases, the 0.8 and 1.6 mm bars cause reattachment, while recovery from the separation is only partially complete in the 0.4 mm bar case and the shear layer remains separated in the baseline case. The 0.8 and 1.6 mm bar cases are, therefore, preferable at this Re , and both have about the same momentum thickness at Station 11. At $Re=100,000$, already described in Fig. 14, the 0.4 mm bar produces the lowest losses. The 0.4 mm bar case is also best at $Re=200,000$, with slightly lower losses than with the 0.8 mm bar or in the baseline case. At $Re=300,000$, transition occurs sufficiently far upstream in the

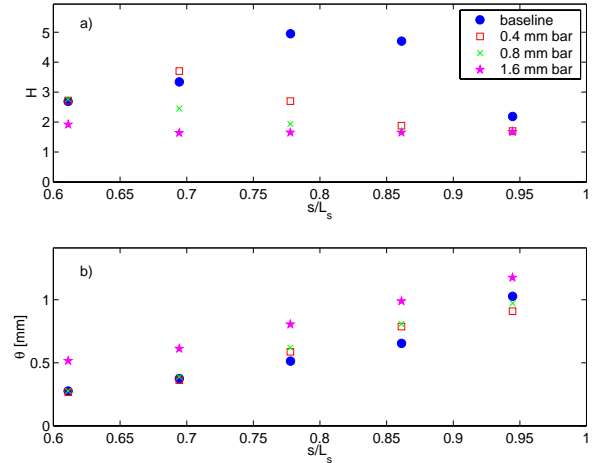


Fig. 14 Shape factor and momentum thickness versus streamwise location, low *FSTI*, $Re=100,000$: (a) H , (b) θ

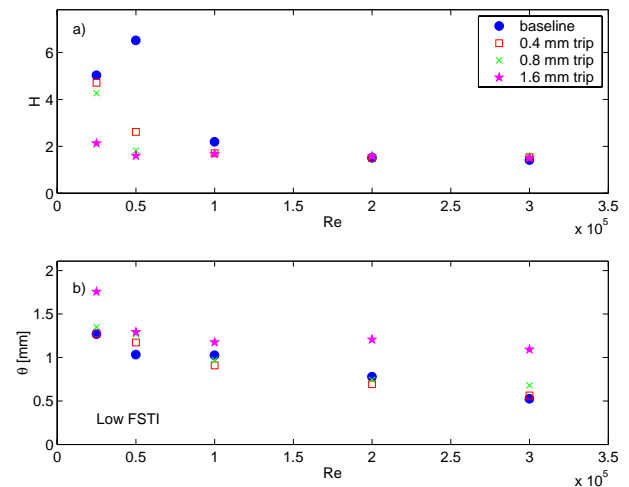


Fig. 15 Station 11 shape factor and momentum thickness vs Re , low *FSTI* cases: (a) H , (b) θ

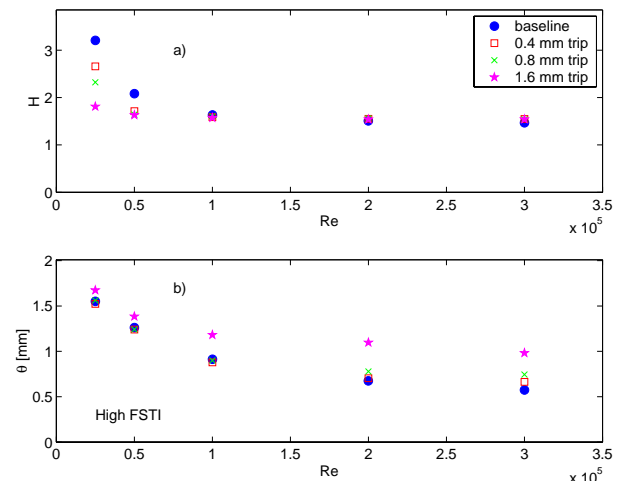


Fig. 16 Station 11 shape factor and momentum thickness versus Re , high *FSTI* cases: (a) H , (b) θ

baseline case to keep the separation bubble small and produce lower losses than in any of the cases with bars.

The Station 11 shape factors and momentum thicknesses for the high *FSTI* cases are shown in Fig. 16. As in the low *FSTI* cases, only the 1.6 mm bar is large enough to force reattachment at $Re=25,000$, and even it does not quite result in full recovery to a turbulent profile. At $Re=50,000$, the shape factor shows that all of the bars cause reattachment, while the boundary layer in the baseline case has reattached but not fully recovered from the separation. The 0.4 and 0.8 mm bar cases have lower momentum thickness than the 1.6 mm bar case. At the higher Re , reattachment is complete in all cases, and the 1.6 mm bar cases have significantly higher losses than the other cases. At $Re=100,000$, the 0.4 and 0.8 mm bar cases and the baseline case all have about the same losses. As Re increases to 200,000 and 300,000, the baseline case emerges as the case with lowest losses, in agreement with the low *FSTI* cases of Fig. 15.

The optimal bar height clearly varies with the Reynolds number. As Re increases, the boundary layer becomes thinner and more prone to transition, so a smaller bar is needed. At $Re=25,000$, the 1.6 mm bar is needed, and a larger bar would be desirable to force a more complete reattachment. At $Re=50,000$, the 0.8 mm bar is best, since it is large enough to cause reattachment at low *FSTI*, but produces lower losses than the thicker bar at high *FSTI*. At $Re=100,000$ and 200,000, the 0.4 mm bar is best, since it is large enough to force complete reattachment at low *FSTI*, and results in equal or slightly lower losses than the baseline or 0.8 mm bar cases. At $Re=300,000$, the baseline case is best, although the losses are only slightly lower than those of the 0.4 mm bar case. If a bar is used for passive flow control, a single bar thickness must be chosen for optimal overall performance. The best size will depend on the operating range of the engine. If the operating range is large, a compromise between improved performance at cruise and higher losses at takeoff may be needed.

Correlation of Results

The size of a bar necessary to trip a boundary layer to turbulence can be predicted using the following correlation from Gibbings [23].

$$Re_d = U_d d / \nu > 600 \quad (1)$$

where d is the bar thickness and U_d is the velocity in the untripped boundary layer at $y=d$ at the streamwise location of the bar. Equation 1 predicts that bar thicknesses of 4.7 mm, 2.3 mm, 1.3 mm, 0.68 mm, and 0.50 mm would be needed to immediately trip the boundary layer to turbulent in the $Re=25,000$ through 300,000 cases respectively. In agreement with this prediction, the results above show that the boundary layer was only tripped in the $Re=200,000$ and 300,000 cases with the 0.8 mm and 1.6 mm bars, and in the $Re=100,000$ cases with the 1.6 mm bar. Since an optimal bar does not immediately trip the boundary layer, it will be thinner than indicated by Eqn. 1.

The most effective bars in the present cases appear to be those which cause reattachment to begin between Stations 8 and 9, at s/L_s of about 0.74. When reattachment begins by this location, there is sufficient distance downstream for the reattachment and recovery from the separation to be completed before the trailing edge. The beginning of reattachment and the start of transition are related and occur at approximately the same location. There are a few correlations in the literature for prediction of the distance from separation to transition onset. In general they are not very robust, but some give reasonable estimates. Mayle [2] provides the following correlations.

$$Re_{st} = 300 Re_{\theta_s}^{0.7} \quad (\text{short bubble}) \quad (2)$$

$$Re_{st} = 1000 Re_{\theta_s}^{0.7} \quad (\text{long bubble}) \quad (3)$$

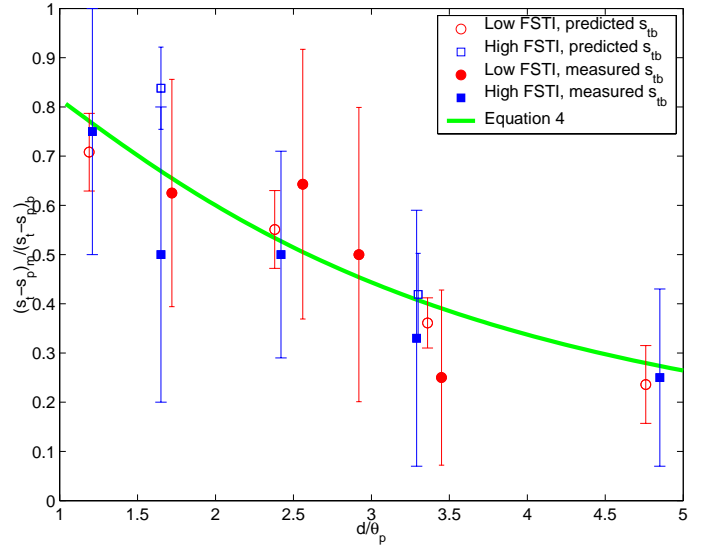


Fig. 17 Correlation of transition and reattachment start location to bar height, bars indicate range of possible values resulting from finite station spacing

Eqns. 2 and 3 apply to short and long separation bubbles respectively. Volino [7] found that the present baseline case results lie between the predictions of Eqns. 2 and 3, tending toward the long bubble correlation at low *FSTI* and about midway between the two correlations at high *FSTI*. Although they differ by a factor of 3, Eqns. 2 and 3 provide at least a rough estimate of the reattachment location.

The following correlation provides an estimate of the effect of bar height on reattachment location. The equation is based on a curve fit of the present data.

$$(s_r - s_p)_m / (s_r - s_p)_b = (1 + 0.23(d/\theta_p)^{1.56})^{-1} \quad (4)$$

where $(s_r - s_p)_b$ is the distance from the suction side velocity maximum ($s/L_s=0.53$) to the location of the beginning of reattachment in the baseline case, and $(s_r - s_p)_m$ is this distance with a bar in place. The present data along with Eqn. 4 are shown in Fig. 17. The finite spacing of the streamwise measurement stations results in some uncertainty in the transition start location, as indicated by the error bars in Fig. 17. Volino [7] showed that the boundary layer behavior upstream of separation is predictable and laminar. To predict reattachment in a case with a bar, the laminar solution could be used to predict the separation location and the momentum thickness before separation. A correlation such as Eqn. 2 or 3 could then be used to estimate the distance to transition and reattachment in the baseline flow. This would give s_{tb} . Equation 4 could then be used to predict s_{tm} for a given bar thickness. Alternatively, the desired s_{tm} could be specified and used with Eqn. 4 to predict the optimal bar thickness. Setting $s_{tm}=169$ mm ($s_{tm}/L_s=0.74$) and using the measured (when available) or predicted values for s_{tb} and θ_p for the baseline cases, optimal bar heights have been predicted for the present cases and are presented in Table 3.

Discussion

The above correlations are based only on the present data set, so it is doubtful that they are universally applicable. Still, they provide a start in the assessment of passive flow control devices. With more experiments with different airfoils, it may be possible to refine correlations such as Eqn. 4, to make them more generally applicable.

Table 3: Baseline case boundary layer thickness at bar location ($s/L_s=0.53$), and predicted bar heights for tripping (d_{trip}) and for incipient reattachment (d_{opt}) at $s/L_s=0.74$ (all values in mm)

Re $\times 10^{-3}$	Low <i>FSTI</i>				High <i>FSTI</i>			
	$\delta_{99.5p}$	θ_p	d_{trip}	d_{opt}	$\delta_{99.5p}$	θ_p	d_{trip}	d_{opt}
25	3.8	0.48	4.7	2.4	3.9	0.48	4.7	1.5
50	2.7	0.34	2.3	1.2	2.8	0.33	2.3	0.6
100	1.9	0.23	1.3	0.4	2.2	0.24	1.3	0.2
200	1.3	0.16	0.7	0.2	1.6	0.16	0.7	0
300	1.2	0.14	0.5	0.1	1.4	0.14	0.5	0

Alternative passive devices such as vortex generators or dimples should also be considered. There is no guarantee, however, that these devices will provide improvement over the present bars. Dimples have been used in some applications such as internal blade cooling, to provide enhanced heat transfer with lower pressure drop than boundary layer trips. Dimples enhance heat transfer by promoting turbulence and mixing, which would also tend to promote boundary layer attachment. In the present application, however, we do not seek to enhance turbulence or heat transfer, or even to fully eliminate the separation bubble. Since the smaller bars in the present experiments did not increase losses or boundary layer thickness, or have any other immediate measurable effect on the boundary layer, it is not clear that any other device will be superior.

While the present bars have proven effective, it is clear from Table 3 and Figs. 15 and 16 that the optimal bar height varies with Re and *FSTI*. If applied passively, a single bar height would be selected for the entire operating range of the engine. If the operating range is large, a compromise will be necessary between improved performance at low Re and higher losses at high Re . Passive flow control has the distinct advantage of being relatively simple to implement in practice, but active flow control may provide a means for optimizing performance over a wider range of conditions. Unsteady active control also provides possibilities for further flexibility and improved performance not available with passive devices. Further consideration of active control is presented in Volino [24].

The present cases all involve steady inlet flow. In engine flows, the periodic wakes from upstream airfoils will make the flow unsteady. While steady flow experiments are necessary for building understanding of the flow and flow control devices, experiments should eventually be performed in flows with wakes.

CONCLUSIONS

1. Rectangular bars have been successfully employed as flow control devices on the suction side of a low pressure turbine airfoil. Boundary layer reattachment was forced even in very low Reynolds number cases.
2. Optimal bars are not large enough to immediately trip the boundary layer to turbulent or prevent separation, but rather induce very small disturbances which at first are essentially undetectable, but eventually promote transition in the shear layer at a downstream location.
3. Bars were effective under both high and low *FSTI* conditions, indicating that the high *FSTI* transition is not simply a bypass transition induced by the free-stream.
4. The optimal location for reattachment results in a relatively short turbulent region, but occurs sufficiently far upstream to prevent a large separation bubble and insure complete recovery from the separation before the trailing edge. A bar height can be selected to induce reattachment at the desired location.

5. The optimal bar height varies with the Reynolds number and free-stream turbulence level. Bars that were large enough to induce reattachment at the lowest Re produced significantly higher losses at the higher Re . If a wide range of Reynolds numbers are encountered in practice, some compromise between improved performance at low Re and higher losses at high Re will be necessary in the choice of an overall best bar height.

ACKNOWLEDGEMENTS

This work was sponsored by the NASA Glenn Research Center. The grant monitor is Dr. David Ashpis. Additional matching support was provided through a U.S. Naval Academy Recognition Grant.

REFERENCES

- [1] Hourmouziadis, J., 1989, "Aerodynamic Design of Low Pressure Turbines," AGARD Lecture Series 167.
- [2] Mayle, R.E., 1991, "The Role of Laminar-Turbulent Transition in Gas Turbine Engines," *ASME Journal of Turbomachinery*, **113**, pp. 509-537.
- [3] Sharma, O.P., Ni, R.H., and Tanrikut, S., 1994, "Unsteady Flow in Turbines," AGARD Lecture Series 195, Paper No. 5.
- [4] Hodson, H.P., 1991, "Aspects of Unsteady Blade-Surface Boundary Layers and Transition in Axial Turbomachines," *Boundary Layers in Turbomachines*, VKI Lecture Series 1991-06.
- [5] Wisler, D.C., 1998, "The Technical and Economic Relevance of Understanding Boundary Layer Transition in Gas Turbine Engines," *Minnowbrook II, 1997 Workshop on Boundary Layer Transition in Turbomachines*, LaGraff, J.E., and Ashpis, D.E., eds., NASA/CP-1998-206958, pp. 53-64.
- [6] Curtis, E.M., Hodson, H.P., Banieghbal, M.R., Denton, J.D., Howell, R.J., and Harvey, N.W., 1997, "Development of Blade Profiles for Low-Pressure Turbine Applications," *ASME Journal of Turbomachinery*, **119**, pp. 531-538.
- [7] Volino, R.J., 2002, "Separated Flow Transition Under Simulated Low-Pressure Turbine Airfoil Conditions: Part 1 – Mean Flow and Turbulence Statistics," *ASME Journal of Turbomachinery*, **124**, pp. 645-655.
- [8] Van Treuren, K.W., Simon, T., von Koller, M., Byerley, A.R., Baughn, J.W., and Rivir, R., 2002, "Measurements in a Turbine Cascade Flow Under Ultra Low Reynolds Number Conditions," *ASME Journal of Turbomachinery*, **124**, pp. 100-106.
- [9] Howell, R.J., Ramesh, O.N., Hodson, H.P., Harvey, N.W., and Schulte, V., 2001, "High Lift and Aft-Loaded Profiles for Low-Pressure Turbines," *ASME Journal of Turbomachinery*, **123**, pp. 181-188.
- [10] Stadtmüller, P., Fottner, L., and Fiala, A., 2000, "Experimental and Numerical Investigation of Wake-Induced Transition on a Highly Loaded LP Turbine at Low Reynolds Numbers," *ASME Paper 2000-GT-0269*.
- [11] Brunner, S., Fottner, L., and Schiffer, H.-P., 2000, "Comparison of Two Highly Loaded Low Pressure Turbine Cascades Under the Influence of Wake-Induced Transition," *ASME Paper 2000-GT-268*.
- [12] Lake, J.P., King, P.I., and Rivir, R.B., 2000, "Low Reynolds Number Loss Reduction on Turbine Blades With Dimples and V-Grooves," *AIAA Paper 00-738*.
- [13] Murawski, C.G., and Vafai, K., 1999, "Effect of Variable Axial Chord on a Low-Pressure Turbine Blade," *Journal of Propulsion and Power*, **15**, pp. 667-674.
- [14] Byerley, A.R., Störmer, O., Baughn, J.W., Simon, T.W., VanTreuren, K.W., and List, J., 2002, "Using Gurney Flaps to

Control Laminar Separation on Linear Cascade Blades,” ASME Paper GT-2002-30662.

- [15] Bons, J.P., Sondergaard, R., and Rivir, R.B., 2001, “Turbine Separation Control Using Pulsed Vortex Generator Jets,” ASME *Journal of Turbomachinery*, **123**, pp. 198-206.
- [16] Bons, J.P., Sondergaard, R., and Rivir, R.B., 2002, “The Fluid Dynamics of LPT Blade Separation Control Using Pulsed Jets,” ASME *Journal of Turbomachinery*, **124**, pp. 77-85.
- [17] Volino, R.J., Schultz, M.P., and Pratt, C.M., 2001, “Conditional Sampling in a Transitional Boundary Layer Under High Free-Stream Turbulence Conditions,” ASME Paper 2001-GT-0192. To appear in the ASME *Journal of Fluids Engineering*, **125**.
- [18] Volino, R.J., 2002, “Separated Flow Transition under Simulated Low-Pressure Turbine Airfoil Conditions: Part 2 - Turbulence Spectra,” ASME *Journal of Turbomachinery*, **124**, pp. 656-664.
- [19] Wills, J.A.B., 1962, “The Correction of Hot-Wire Readings for Proximity to a Solid Boundary,” *Journal of Fluid Mechanics*, **12**, pp. 65-92.
- [20] Ligrani, P.M., and Bradshaw, P., 1987, “Spatial Resolution and Measurement of Turbulence in the Viscous Sublayer Using Subminiature Hot-Wire Probes,” *Experiments in Fluids*, **5**, pp. 407-417.
- [21] Ligrani, P.M., and Bradshaw, P., 1987, “Subminiature Hot-Wire Sensors: Development and Use,” *Journal of Physics E: Scientific Instruments*, **20**, pp. 323-332.
- [22] Volino, R.J., and Hultgren, L.S., 2001, “Measurements in Separated and Transitional Boundary Layers Under Low-Pressure Turbine Airfoil Conditions,” ASME *Journal of Turbomachinery*, **123**, pp. 189-197.
- [23] Gibbings, J.C., 1959, “On Boundary-Layer Transition Wires,” Aeronautical Research Council, Current Papers 462.
- [24] Volino, R.J., 2003, “Separation Control on Low-Pressure Turbine Airfoils Using Synthetic Vortex Generator Jets,” ASME Paper GT2003-38729.

GT2003-38729

SEPARATION CONTROL ON LOW-PRESSURE TURBINE AIRFOILS USING
SYNTHETIC VORTEX GENERATOR JETS

Ralph J. Volino

Department of Mechanical Engineering
United States Naval Academy
Annapolis, Maryland 21402
Email: volino@usna.edu

ABSTRACT

Oscillating vortex generator jets have been used to control boundary layer separation from the suction side of a low-pressure turbine airfoil. A low Reynolds number ($Re=25,000$) case with low free-stream turbulence has been investigated with detailed measurements including profiles of mean and fluctuating velocity and turbulent shear stress. Ensemble averaged profiles are computed for times within the jet pulsing cycle, and integral parameters and local skin friction coefficients are computed from these profiles. The jets are injected into the mainflow at a compound angle through a spanwise row of holes in the suction surface. Preliminary tests showed that the jets were effective over a wide range of frequencies and amplitudes. Detailed tests were conducted with a maximum blowing ratio of 4.7 and a dimensionless oscillation frequency of 0.65. The outward pulse from the jets in each oscillation cycle causes a disturbance to move down the airfoil surface. The leading and trailing edge celerities for the disturbance match those expected for a turbulent spot. The disturbance is followed by a calmed region. Following the calmed region, the boundary layer does separate, but the separation bubble remains very thin. Results are compared to an uncontrolled baseline case in which the boundary layer separated and did not reattach, and a case controlled passively with a rectangular bar on the suction surface. The comparison indicates that losses will be substantially lower with the jets than in the baseline or passively controlled cases.

NOMENCLATURE

B	blowing ratio
C_f	skin friction coefficient
C_p	$2(P_T - P)/\rho U_e^2$, pressure coefficient
c_μ	momentum coefficient
D	diameter
F^+	$(0.442L_s)/(U_e T)$, dimensionless frequency
$FSTI$	free-stream turbulence intensity
H	δ^*/θ , shape factor
K	$(v/U_\infty^2)(dU_\infty/ds)$, acceleration parameter
L_s	suction surface length

M	jet to boundary layer mass flux ratio
P	pressure
P_T	upstream stagnation pressure
Re	$U_e L_s / \nu$, exit Reynolds number
Re_θ	momentum thickness Reynolds number
S	jet holes per unit span
s	streamwise coordinate, distance from leading edge
T	jet oscillation period
t	time
U	mean streamwise velocity
U_∞	local free-stream velocity
U_e	nominal exit free-stream velocity, based on inviscid solution
V_{jet}	jet velocity
\bar{u}	time averaged rms streamwise fluctuating velocity
\tilde{u}	ensemble averaged rms streamwise fluctuating velocity
$-\overline{u'v'}$	time averaged turbulent shear stress
$-\tilde{u'v'}$	ensemble averaged turbulent shear stress
y	cross-stream coordinate, distance from wall
δ^*	displacement thickness
λ_θ	$Re_\theta^2 K$, Thwaites parameter
ν	kinematic viscosity
ρ	density
θ	momentum thickness

Subscripts

<i>ave</i>	average over jet outpulse
<i>jet</i>	jet condition
<i>max</i>	maximum in jet cycle
∞	free-stream

INTRODUCTION

Modern low-pressure turbine (LPT) airfoils are subject to increasingly stronger pressure gradients as designers impose higher loading in an effort to improve efficiency and lower cost by reducing the number of airfoils in an engine. If the adverse pressure gradient on the suction side of these airfoils becomes strong enough, the boundary

layer will separate. Separation bubbles, particularly those which fail to reattach, can result in a significant loss of lift and a subsequent degradation of engine efficiency (e.g. Hourmouziadis [1], Mayle [2], and Sharma et al. [3]). The problem is particularly relevant in aircraft engines. Airfoils optimized to produce maximum power under takeoff conditions may still experience boundary layer separation at cruise conditions, due to the thinner air and lower Reynolds numbers at altitude. A component efficiency drop of 2% may occur between takeoff and cruise conditions in large commercial transport engines, and the difference could be as large as 7% in smaller engines operating at higher altitudes.

Separation on LPT airfoils is complicated by boundary layer transition, which can prevent separation if it occurs far enough upstream, or induce boundary layer reattachment if it occurs in the shear layer over a separation bubble. At lower Reynolds numbers transition will tend to occur farther downstream, hence the problems associated with performance at altitude.

Separated flow transition has been studied extensively, and in recent years several studies have focused on transition in the LPT. Volino [4] provides a review of much of that work. Separation can be affected through naturally occurring phenomena such as high free-stream turbulence intensity (*FSTI*) or the unsteadiness caused by wakes generated upstream of an airfoil. Further discussion of these effects is available in Volino [5]. While high *FSTI* and wakes help to mitigate separated flow problems, they clearly do not solve all problems, as evidenced by the known efficiency drop in modern engines at altitude. Howell et al. [6], for example, studied airfoils modified for higher lift, noting that their highly loaded airfoils might be close to a limit, and that even higher loading could cause unacceptable separation problems even in the presence of wakes. Looking beyond free-stream turbulence and wakes, other types of separation control could prove useful. Gad-el-Hak [7] provides a recent review. Techniques include boundary layer tripping, vortex generation, suction, and injection of fluid normal to the wall to either increase the boundary layer momentum or promote turbulence.

While the general literature is extensive, only a few studies have considered separation control under LPT conditions. Some have utilized passive techniques. Lake et al. [8] considered dimples and boundary layer trips. Van Treuren et al [9] considered vortex generators. Volino [5] used rectangular bars to impose disturbances in a boundary layer and move transition upstream. Passive flow control is appealing for its simplicity and the relative ease with which it might be implemented in gas turbine environments. It has its limitations, however. Volino [5] found that passive devices can successfully control separation even at the lowest Reynolds number of interest, but that these devices caused substantial increases in losses at higher *Re*. This is an important limitation for aircraft engines, where the *Re* range between takeoff and cruise is large. An active device could be turned off at high *Re*. Static passive devices are also unable to take advantage of the unsteadiness caused by wake passing. An active device might be timed to turn on and off in response to wake passing events. Unsteady devices might also take advantage of the calmed region following a transient turbulent event.

The literature contains several examples of active separation control. Lee et al. [10] used blowing in supersonic engine inlets to prevent or control separation. Sturm et al. [11] reported on blowing in a compressor cascade. Johnston and Nishi [12] used vortex-generator-jets (VGJs) to control separation in turbulent boundary layers. This method utilizes blowing from “small, skewed, and pitched holes” to create streamwise vortices similar to those created by solid vortex generators. Any jet injected into a flow will tend to produce some turbulence, and the turbulent mixing will tend to bring some high

momentum fluid into the near wall region and inhibit separation. Streamwise vortices bring additional high momentum fluid into the near wall region. The most effective VGJs enter the boundary layer at a relatively shallow pitch angle (typically 30 to 45 degrees) relative to the wall and a high skew angle (45 to 90 degrees) relative to the main flow. Compton and Johnston [13] showed that the co-rotating vortices produced by VGJs are stronger and more effective for separation control than the counter-rotating vortices which form downstream of a normal jet. McManus et al. [14] and Raghunathan et al. [15] used pulsed VGJs. Sinha and Pal [16] used acoustic excitation to perturb an unsteady separating flow. Jacobson and Reynolds [17] used piezoelectrically driven cantilevers to influence the near wall turbulence structure on a flat plate. They noted that the devices could be used in separation control. Miao et al. [18] used an oscillating fence to promote reattachment downstream of a backward facing step. Sinha et al. [19] used a driven flexible wall transducer to detect pressure fluctuations and then produce near wall vortices upstream of separation. Whitehead et al. [20] used a film transducer to produce airfoil vibrations and reduce separation at high angles of attack. Oscillatory blowing has been used in several studies to control separation on airfoils. Amitay and Glezer [21] provide one recent example. Oscillatory jets are often referred to as “synthetic jets” since they have no net mass flow. They are typically directed normal to a surface, meaning that they probably do not produce such strong streamwise vortices as VGJs.

Only a few active control studies have been conducted under LPT conditions. Huang et al. [22] and Hultgren and Ashpis [23] employed high voltage electrodes to produce glow discharge plasma in a boundary layer to control separation. Bons et al. [24, 25] used steady and pulsed VGJs to successfully control separation on LPT airfoils. They used the “Pak-B” airfoil, which is an industry supplied research airfoil that is prone to separation problems at low *Re*. It has been used in numerous studies, as noted by Volino [4]. Bons et al. [24] used spanwise rows of VGJs at several streamwise locations on the suction surface of the airfoil, and found that a row near the suction surface velocity maximum (pressure minimum) was most effective. The VGJ holes were oriented at 30 degrees to the surface and 90 degrees to the main flow. All holes were oriented in the same direction, to produce co-rotating vortices. Reynolds numbers as low as 60,000 (based on suction surface length and exit velocity) were considered. Bons et al. [25] found that both steady and pulsed jets were effective in controlling separation. The pulsed jets were fully effective even when the dimensionless pulsing frequency, F^+ , was as low as 0.1, where F^+ is a ratio of the transit time for flow between the VGJ hole and the trailing edge to the time interval between pulses. Ensemble averaged velocity profiles showed a long relaxation or “calmed” period following each jet pulse. During this calm period the boundary layer remained attached long after the turbulence generated by the pulse had moved downstream. Calmed regions have been observed following turbulent spots in transitional boundary layers (e.g. Gostelow et al. [26] and Schulte and Hodson [27]). The mean velocity profiles in the calmed region gradually relax from the turbulent shape associated with the turbulent spot they follow, to a laminar (and in some cases separated) profile shape. The calmed boundary layer is very resistant to separation, much like a turbulent boundary layer, but it is very laminar-like in terms of its fluctuation levels and low losses. The pulsed jets were more effective than continuous jets, even when the pulsed jet duty cycle was as low as 1%. This was believed to indicate that the starting vortex formed at the beginning of each jet pulse was responsible for most of the flow control in the pulsed jet cases.

Synthetic jets hold an advantage over continuous or pulsed jets in that they require no net mass flow. In the LPT environment, this

means that no compressor bleed air is required. Use of bleed air for flow control or cooling comes at a cost in efficiency, although the small amount of air required for the pulsed jets of Bons et al. [25] might not be prohibitive if bleed air were already routed to the airfoils for cooling. Synthetic jets would not be useful for a cooled airfoil since ingestion of hot gas into the airfoil would be harmful. For uncooled LPT airfoils, however, the airfoil temperature will match the main flow temperature, and ingestion of hot gas should be acceptable. Routing of bleed air to uncooled airfoils for flow control may present a prohibitive addition of complexity and weight. With synthetic jets this problem could be avoided. In the present study, the oscillating flow of synthetic jets and the compound angle injection of vortex generator jets are combined to produce synthetic VGJs. This is believed to be the first application of synthetic VGJs. They are used to control the flow over a Pak-B airfoil. A survey of the literature indicates that the jet locations and angles chosen by Bons et al. [25] were likely optimal, so their geometry has been copied in the present study.

There are many parameters which could be varied in a synthetic jet study, including Reynolds number, $FSTI$, jet geometry, jet location, jet velocity, jet oscillation frequency, and jet waveform, to name a few. These are all potentially important parameters and should eventually be studied. The scope of the present study is more focused. A single experimental case is completely documented with detailed measurements including time resolved mean and fluctuating velocity and turbulent shear stress throughout the flow field. The goals of the study are to build an understanding of the physics of how synthetic VGJs control separation and to generate questions for future parametric studies which may lead to optimized flow control for a broad range of flow conditions.

Volino [4, 28] studied unmodified flow over the Pak-B airfoil at Reynolds numbers ranging from 25,000 to 300,000 under both high and low $FSTI$. In nearly all cases the boundary layer separated from the suction side of the airfoil. At all but the lowest Reynolds numbers it reattached before the trailing edge. The most severely separated case was the low $FSTI$, $Re=25,000$ case. This case has, therefore, been chosen as the test case for the present application of synthetic VGJs. The unmodified case from Volino [4] is used as a baseline case for comparison to the new results. Also used for comparison is a case from Volino [5] in which a passive bar was employed to force reattachment. The bar was located at $s/L_s=0.51$, extending along the airfoil span. Its streamwise width was 6.35 mm and its height was 1.6 mm. The suction surface length was 228.6 mm. Bars of various heights were tested. The 1.6 mm bar was the smallest bar to cause reattachment at $Re=25,000$. Volino [5] found that the most effective bars in terms of minimizing losses were not large enough to immediately trip the boundary layer to turbulent. Rather, they induced small disturbances which grew and caused transition and reattachment downstream of a small separation bubble.

EXPERIMENTS

Experiments were conducted in a low speed wind tunnel, described by Volino et al. [29]. Briefly, air enters through blowers and passes through a honeycomb, a series of screens, two settling chambers, and a three-dimensional contraction before entering the test section. At the exit of the contraction, the mean velocity is uniform to within 1%. The $FSTI$ is $0.5\% \pm 0.05\%$. Nearly all of this free-stream "turbulence" is actually streamwise unsteadiness at frequencies below 20 Hz and is not associated with turbulent eddies. The rms intensities of the three components of the unsteadiness are 0.7%, 0.2% and 0.2% in the streamwise, pitchwise and spanwise directions, respectively. The test section immediately follows the contraction.

The test section, shown in Fig. 1, consists of the passage between two airfoils. Details are listed in Table 1, and more information is available in Volino [4]. A large span-to-chord ratio of 4.3 was chosen to insure two-dimensional flow at the spanwise centerline of the airfoils, where all measurements were made. Upstream of each airfoil are flaps, which control the amount of bleed air allowed to escape from the passage. The flaps, along with a tailboard on the pressure side of the passage, are adjusted to produce the correct leading edge flow and pressure gradient along the airfoils. The flow in the passage matches that in a multi-blade cascade. The single passage configuration allows for a large scale passage and better probe access than possible with a multi-blade cascade in the same size wind tunnel. The wake downstream of the passage is not representative of a multi-blade facility, however, since there is flow only on one side of each airfoil. Downstream effects that could influence the upstream flow in the passage are also potentially missed. Experimental conditions match those of the low $FSTI$, $Re=25,000$ baseline case of Volino [4] and the passive bar case of Volino [5].

The synthetic VGJs were produced from a cavity within the suction side airfoil. The airfoils are machined from high density foam, which has a consistency much like hard wood. The surface of each airfoil was sanded smooth, painted, and sanded again to provide a smooth surface. A 1.27 cm diameter hole was drilled through the airfoil span at about mid-chord, as shown in Fig. 2, to form a plenum. One end of the plenum is plugged, and the narrow end of a funnel is inserted in the other. A 20.3 cm diameter loudspeaker (100W subwoofer) is attached at the wide end of the funnel. The funnel is sealed to the speaker and to the airfoil with silicone RTV to prevent air leakage. The speaker is driven with a 200W audio amplifier, which is in turn powered with a 12V DC power supply and driven by a function generator. For the present study the function generator was set to output a sine wave. The amplitude of the signal from the function generator and the gain of the amplifier were adjusted to provide the desired input voltage to the speaker. Holes for the VGJs were drilled into the suction surface in a spanwise line at $s/L_s=0.514$. The holes are 0.8 mm in diameter (0.35% of L_s) and are spaced 8.5 mm apart (3.7% of L_s). The holes are drilled at a 90 degree skew angle with respect to the main flow and a 30 degree pitch with respect to the surface, as shown in Fig. 2. Each hole extends from the suction surface into the cavity in the core of the airfoil. The length to diameter ratio of the holes is 7.5.

Measurements

Pressure surveys were made using a pressure transducer (0-870 Pa range Validyne transducer) and a Scanivalve. Stagnation pressure was measured with a pitot tube upstream of the passage inlet, and eleven pressure taps were located on each airfoil along their spanwise centerlines. Locations of the taps on the suction side are listed in Table 2 along with measured local $FSTI$ components and the acceleration parameter, K , at these stations based on a non-separating, inviscid solution. The uncertainty in the suction side pressure coefficients was 7%. Most of this uncertainty was due to bias error. Stochastic error was minimized by averaging pressure transducer readings over a 10 second period.

Velocity profiles on the suction surface were measured at streamwise stations corresponding to pressure taps 7-11, as given in Table 2, and at four additional stations, labeled 7.5, 8.5, 9.5 and 10.5, centered between the pressure taps. All stations are downstream of the VGJ holes. Stations 7, 8, 9, 10 and 11 correspond to stations documented in the baseline case in Volino [4, 28]. Profiles at Stations 1-6 are fully documented for the baseline case in Volino [4, 28], and show that the upstream boundary layer closely follows a laminar solution. Profiles were measured near but not at the spanwise

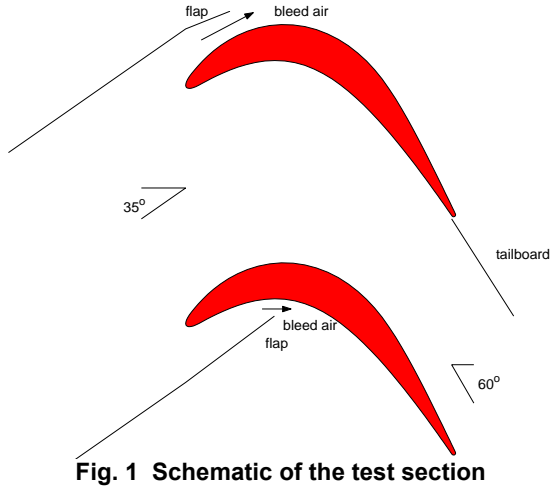


Fig. 1 Schematic of the test section

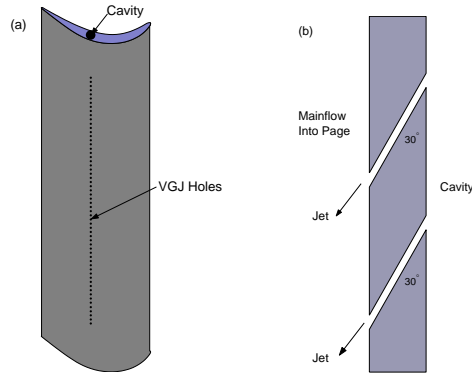


Fig. 2 Drawing of suction side airfoil with cavity and VGJs: (a) full airfoil, (b) cross section of VGJ holes

centerline of the airfoil to insure that the pressure taps did not interfere with the velocity measurements. Profiles were acquired with a hot-wire anemometer (AA Lab Systems model AN-1003) and a single sensor boundary layer probe (TSI model 1218-T1.5). The sensor diameter is 3.8 μm , and the active length is 1.27 mm. At each measurement location, data were acquired for 26 seconds at a 20 kHz sampling rate (2^{19} samples). All raw data were saved. The high sampling rate provides an essentially continuous signal, and the long sampling time results in low uncertainty in both statistical and spectral quantities. Data were acquired at 60 wall normal locations in each profile, extending from the wall to the free-stream, with most points concentrated in the near wall region. The closest point was within 0.1 mm of the wall, which corresponds to $y/L_s=0.0004$ and about 0.015 boundary layer thicknesses. Flow direction in a separation bubble cannot be determined with a single-sensor hot-wire, but velocity magnitude can be measured and was found to be essentially zero within the bubbles of the present cases. Determining the direction was not, therefore, considered essential. Uncertainty in the mean velocity is 3-5% except in the very near wall region, where near-wall corrections (Wills [30]) were applied to the mean velocity. Uncertainties in the momentum and displacement thicknesses computed from the mean profiles are 10%. Uncertainty in the shape factor, H , is 8%. Local skin friction coefficients were computed from the near wall mean velocity profiles using the technique of Volino and Simon [31]. This technique accounts for streamwise pressure gradient effects on the mean profile. The uncertainty in C_f is 8%. The uncertainty in the fluctuating streamwise velocity is below 10%. As

Table 1: Test section parameters

Axial Chord [mm]	True Chord [mm]	Pitch [mm]	Span [mm]	Suction side, L_s [mm]	Inlet flow angle	Exit flow angle
153.6	170.4	136.0	660.4	228.6	35°	60°

Table 2: Measurement station locations, local acceleration (inviscid soln.), and measured local free-stream turbulence

Station	s/L_s	$K \times 10^6$	\bar{u}'/U_∞ [%]	\bar{v}'/U_∞ [%]
1	0.111	6.32	0.44	
2	0.194	4.80	0.39	
3	0.278	3.44	0.37	
4	0.361	3.00	0.38	
5	0.444	2.48	0.39	
6	0.528	-0.08	0.41	
7	0.611	-3.24	0.47	0.05
8	0.694	-3.80	0.47	0.12
9	0.777	-2.32	0.48	0.14
10	0.861	-2.12	0.54	0.11
11	0.944	-0.72	0.51	0.11

explained in Volino [4] based on the work of Ligrani and Bradshaw [32], spatial averaging effects due to the finite length of the hot-wire sensor should not be significant in the present case.

Profiles were also acquired using a cross-sensor boundary layer probe (TSI 1243-20). The sensors are 51 μm diameter hot films with 1.02 mm active lengths. The probe is used to document the instantaneous turbulent shear stress, $-\bar{u}'v'$. Profiles were acquired at the same stations as with the single-sensor probe. Data were acquired at 25 locations in each profile, extending from 1 mm from the wall to the free-stream. Sampling rates and times were the same as for the single-sensor profiles. The vortices induced by the oscillating jets cause significant secondary velocity, particularly at the streamwise stations immediately downstream of the jet holes. The magnitude of these secondary velocity components remains below 20% of the local streamwise velocity, however, so they should not cause significant error in the hot-wire measurements. The uncertainty in $-\bar{u}'v'$ is 10%.

The VGJ velocities were measured using a hot-film probe (TSI model 1210-10A) with a 0.25 mm active sensor length. The sensor was placed directly over the exit of the jet hole. During outflow from the hole, the jet was expected to blow directly across the sensor, providing an accurate measure of the jet velocity. Uncertainty in the velocity is 5% and results mainly from uncertainty in the position of the sensor, which could lead to a slightly lower velocity reading than the velocity at the jet exit plane. During inflow of the oscillating jet, the flow is expected to behave more like a sink flow than a jet. The measured velocity does not, therefore, provide an accurate indicator of the velocity inside the hole during inflow. The jet velocity was calibrated against the rms input voltage to the speaker with the main flow in the wind tunnel turned off, and the calibration was used to set the jet velocity in later experiments. The jet velocity is fixed by the frequency and amplitude of the displacement of the speaker diaphragm, which causes a pressurization of the cavity relative to the pressure at the jet exits. The dynamic pressure of the flow through the test section is about 2.4 Pa at the jet location. Since the test section exits to atmosphere, the dynamic pressure results in an average pressure of 2.4 Pa vacuum in the cavity, and a 2.4 Pa pressure difference across the speaker diaphragm. This pressure is much smaller than the pressure experienced by the speaker when driving the jets, and is not expected to influence its motion. If the amplitude of the diaphragm motion is unchanged by the presence of flow in the test

section, the jets should drive approximately the same mass flow through the holes with the wind tunnel on or off. The jet velocity at the exit plane will presumably be affected by the mean flow, however.

The measured maximum jet exit velocity was 9.4 m/s for most of the cases presented below. Given the sensor length and the diameter of the holes, the measured velocity is an average over the middle 30% of the jet. The Reynolds number based on this velocity and the jet diameter is 500. At this Reynolds number, approximately 30 diameters would be needed to establish fully developed laminar flow inside the jet holes. Since the length to diameter ratio is only 7.5 and the jets are unsteady, the jet velocity is not expected to have a fully developed parabolic laminar profile, but rather a more flat profile. Given the averaging due to the sensor size and the expectation of a flat profile, the instantaneous mean velocity of the jet is assumed to approximately equal the measured velocity. Ideally this assumption would be checked with a survey of velocity across the jet exit plane, but the very small jet diameter precludes an accurate survey. The uncertainty in instantaneous mean velocity is, therefore, higher than the 5% uncertainty in the measured velocity. The uncertainty is estimated to be between 10 and 20%.

Data Processing

In addition to conventional time averaging, the velocity data were ensemble averaged relative to the time within each jet oscillation cycle. For this purpose, the speaker input voltage was digitized simultaneously along with the instantaneous velocity data. Data were ensemble averaged at 24 instances within the cycle. At each instance, data were averaged over 1/180th of the cycle. For each 26 second data trace, this results in roughly 3000 data points to average for each ensemble. With this many data points to average over a 26 second time record, the ensemble averaged results are well resolved and have uncertainties as low as those given above for the time averaged results. The start of the cycle was arbitrarily chosen as the instant when the speaker input voltage crossed from negative to positive. As will be shown below, this roughly corresponds to the beginning of the jets' outward pulse.

RESULTS

Jet Velocity

Figure 3 shows a typical time trace of the measured jet velocity and the speaker input voltage. The frequency of the input signal was set to a nominal value of 10 Hz (actual value was 10.5 Hz). The maximum and average velocities in each outward pulse were 9.4 m/s and 5.9 m/s respectively. The jet velocity can be expressed as a blowing ratio, B , defined as

$$B = \rho_{jet} V_{jet} / \rho_{\infty} U_{\infty}$$

where $\rho_{jet} = \rho_{\infty}$ since the jet fluid comes from the boundary layer, and U_{∞} (≈ 2 m/s) is the local free-stream velocity at the jet location. For the present cases $B_{max} = 4.7$ during each cycle and $B_{ave} = 3.0$ during the outward pulse. The mass flux of the jets can be compared to the velocity deficit in the boundary layer as

$$M = [\rho_{jet} V_{jet} (\pi D_{jet}^2 / 4) S] / [\rho_{\infty} U_{\infty} \delta^*]$$

where $S = 0.118$ holes/mm is the number of holes per unit span. The displacement thickness, δ^* ($= 1.08$ mm) is the baseline case value at the jet location. This gives $M_{max} = 0.258$ and $M_{ave} = 0.162$. This could be interpreted to mean that 16% of the boundary layer in terms of displacement thickness is sucked off during the inflow half of each jet

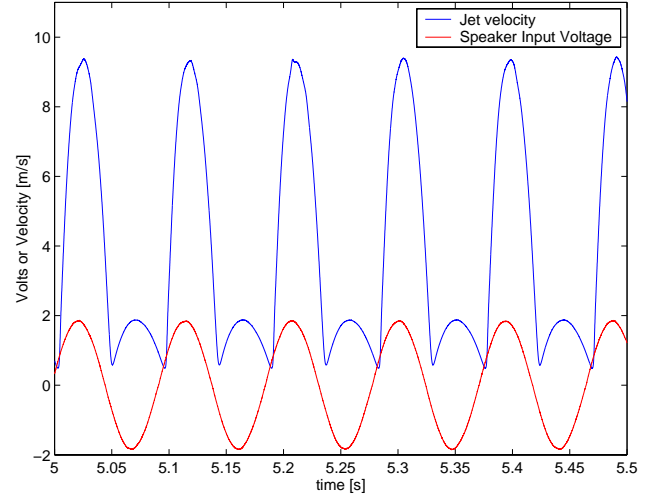


Fig. 3 Time trace of jet velocity and speaker input voltage, $F^+ = 0.65$

cycle, and then re-injected into the boundary layer during the outward pulse.

The momentum coefficient, c_{μ} , is defined as the ratio of the jet momentum to the free-stream dynamic pressure. Using the definition of Bons et al. [25],

$$c_{\mu} = [\rho_{jet} V_{jet}^2 (\pi D_{jet}^2 / 4) S] / [\rho_{\infty} U_{\infty}^2 Chord]$$

where the axial chord is 153.6 mm. The maximum value of c_{μ} in each cycle is 0.0085. The average value of V_{jet}^2 for the outpulse is 44 m²/s². This gives an average $c_{\mu} = 0.0042$.

Figure 3 shows that the speaker input voltage and the jet velocity are slightly out of phase. The jets lag the input voltage by about 0.006 s, which is a dimensionless lag $\Delta t/T$ of 0.063, where T is the jet oscillation period of 0.095 s. The lag is expected, as the jets respond dynamically to the pressurizing of the cavity in the airfoil by the speaker, and there is no reason to expect the speaker voltage and the jet velocity to be exactly in phase. The finite distance from the speaker to the jet holes (of the order 0.5 m) and the finite speed of sound (340 m/s) will also lead to a time lag of the order 1 ms. The time lag increases with distance from the speaker along the airfoil span. At high jet frequencies, the time lag causes the jets along the span to be significantly out of phase with each other. Measurements, however, show that the jet amplitude along the span is uniform, regardless of the frequency. Variation in phase along the span could lead to difficulty in practice if attempts were made to time the jet pulsing to other cyclic events such as wake passing. It is not an issue in the present study. At the relatively low frequency of 10 Hz, the phase lag was not significant, and the jets were uniform in both phase and amplitude along the span.

Pressure Profiles

Pressure profiles were acquired for several jet amplitudes and jet frequencies. The general finding was that the jets were effective over a broad frequency range, so long as the amplitude was sufficiently high. Figure 4 shows C_p profiles for a range of jet amplitudes, with the jet frequency set to 10.5 Hz ($F^+ = 0.65$). In all cases there is good agreement between the data and an inviscid solution for the Pak-B airfoil on the pressure side and the upstream portion of the suction side. In the adverse pressure gradient region on the suction side, differences are clear. Without the jets the boundary layer separates

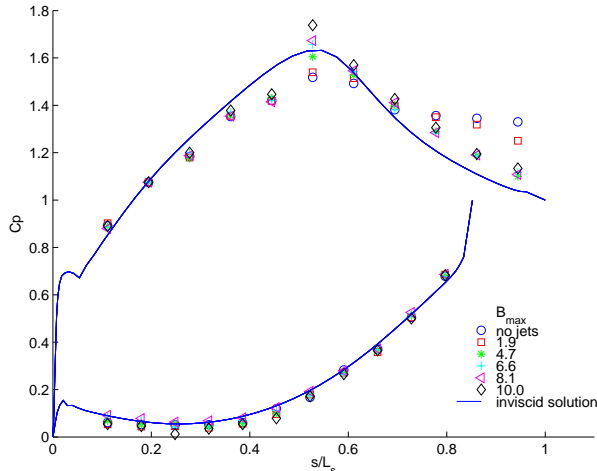


Fig. 4 C_p profiles, $F^+=0.65$, various blowing ratios

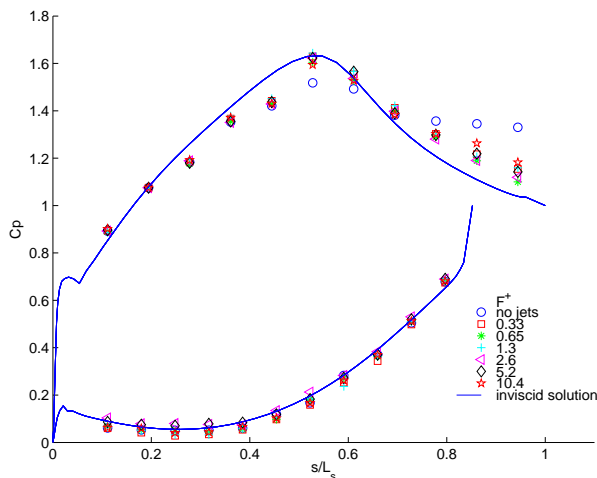


Fig. 5 C_p profiles, $B_{max} \approx 5$, various F^+

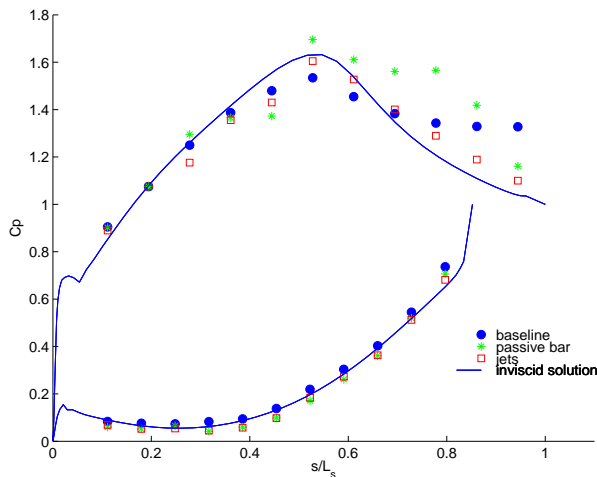


Fig. 6 C_p profiles, comparison of baseline, passive bar, and present jet case with $B_{max}=4.7$ and $F^+=0.65$

and does not reattach, as indicated by the region of constant C_p values. With $B_{max}=1.9$ the boundary layer still does not reattach, but there is some sign that C_p is starting to drop at the last pressure tap. For the cases with $B_{max}=4.7$ and above, the boundary layer does not appear to separate. Significant case to case differences in C_p are present right at the suction peak, but these are likely due to the injection of the jets at this location and their effect on the flow over the adjacent pressure tap. The differences diminish rapidly and are essentially gone by the next downstream measurement station. Bons et al. [24] demonstrated effective flow control with B_{max} as low as 0.4 in their study. The significantly lower Re in the present study may explain the need for stronger jets. Figure 5 shows C_p profiles for several different jet frequencies with B_{max} held approximately constant at about 5. There does not appear to be any clear separated region in any of the cases with jets. The suction peak is higher in all the cases with jets than in the baseline case. This is an expected result, suggesting that the lift will be higher when the boundary layer is attached. The $F^+=0.65$ case appears to agree most closely with the inviscid solution. The broad range of effective frequencies agrees with the results of Bons et al. [25].

The objective of the present study is not to establish the optimal jet conditions for the present case, but to investigate in detail a case in which the jets provide effective flow control. The dimensionless frequency $F^+=0.65$ was chosen since it appeared to provide slightly better results than the other cases in Fig. 5, and $B_{max}=4.7$ was chosen since it was the lowest effective blowing ratio tested. Figure 6 shows the C_p profile for the chosen case with jets along with the baseline case and the passive bar case of Volino [5].

Velocity Profiles

Figure 7 shows mean velocity, \bar{u} and turbulent shear stress profiles for the present case, the baseline case, and the passive bar case. In the baseline case, the mean profiles show the boundary layer is on the verge of separating at Station 7, is clearly separated at Station 8, and the separation bubble grows through Station 11. In the bar case, the boundary layer separates from the bar. The separation bubble is visible at Station 7, and it grows through Station 9. At Station 10, the near wall velocities begin to rise, indicating the beginning of reattachment, and the mean profile shows clear reattachment at Station 11. With the VGJs, the behavior is much different. There is no clear separation bubble. The mean profile appears to have an attached, laminar-like shape. The momentum deficit with the jets appears to be significantly lower at Station 11 than in the case with the bars, indicating lower losses with the jets.

The \bar{u} values in the baseline and bar cases are very low at Station 7, as expected since the boundary layer is still laminar. A peak appears downstream in the shear layer over the separation bubble. In the bar case, \bar{u} begins to rise in the near wall region at Station 9, signaling imminent reattachment. At Stations 10 and 11, \bar{u} in the bar case rises to the high values typical of a transitional boundary layer. In the jet case, \bar{u} is high at all stations. At the upstream locations it is much higher than would be expected for a turbulent boundary layer. As will be shown below, however, much of the contribution to \bar{u} is from 10 Hz unsteadiness associated with the jets and is not turbulence. The turbulent shear stress profiles show considerable momentum transport in the jet case at all stations, which helps to explain how the boundary layer remains attached. Unlike in a turbulent boundary layer, the $-\overline{u'v'}$ peak is well away from the wall. In the baseline case the shear layer does not transition to turbulent, and $-\overline{u'v'}$ remains near zero. In the bar case $-\overline{u'v'}$ profiles were not acquired.

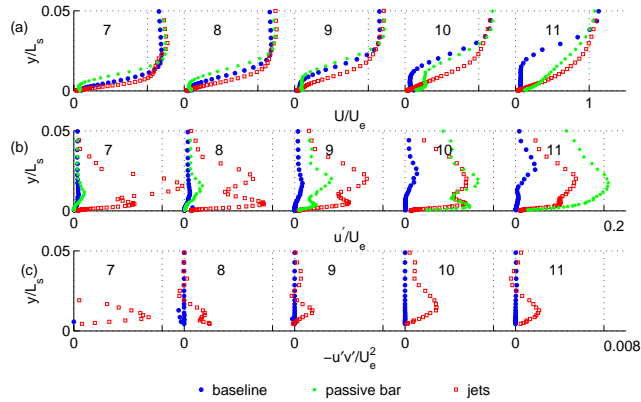


Fig. 7 Station 7-11 dimensionless time averaged profiles; comparison of baseline, passive bar and present jet cases: (a) mean velocity, (b) \bar{u}' , (c) turbulent shear stress

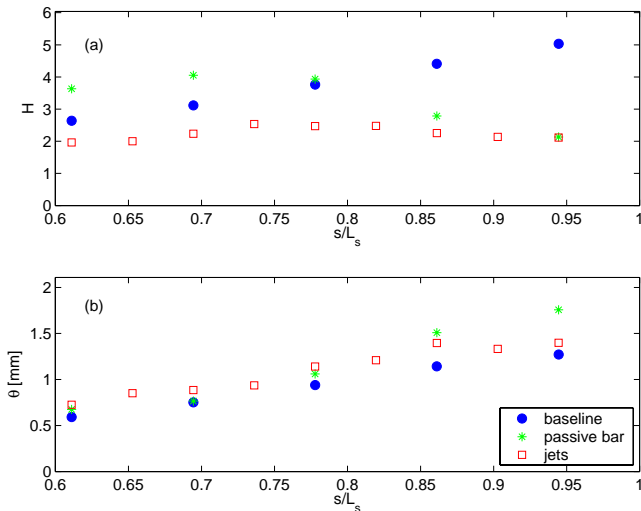


Fig. 8 Time averaged shape factor and momentum thickness versus streamwise location; comparison of baseline, passive bar and present jet cases: (a) H , (b) θ

Figure 8 shows shape factor and momentum thickness as computed from the mean profiles of Fig. 7. The shape factor, H , provides a measure of the state of the boundary layer with respect to separation and transition. The shape factor in the baseline and bar cases rises rapidly after separation, as δ^* increases while θ remains nearly constant. In the baseline case the boundary layer never reattaches. In the bar case, transition and reattachment occur, causing δ^* to fall and θ to rise. The shape factor begins to drop toward a turbulent value of about 1.6, but does not reach this value, indicating that the recovery from the separation is not complete. In the jet case, the shape factor remains at a laminar value of about 2. It never rises to a separated flow value, nor does it drop to a turbulent value. The momentum thickness provides a measure of the losses in a boundary layer. If the boundary layer reattaches before the trailing edge, the suction side boundary layer losses will be the dominant losses in an LPT passage (Howell et al. [6]). In the baseline case the boundary layer does not reattach, so although θ remains low, high losses would be expected in the wake downstream of the airfoils. For the bar and jet cases, however, the boundary layer is attached at the trailing edge. Momentum thickness is about 20% higher in the bar case, indicating

that the jets are better able to control separation, while causing lower losses.

Ensemble Averaged Velocity Profiles

The time averaged profiles of Fig. 7 indicate that the jets are effective in controlling the boundary layer, but they do not explain the mechanism by which the jets work. Figure 9 shows ensemble averaged mean velocity profiles. Profiles are shown for nine streamwise stations at 24 time increments within the jet oscillation cycle. Figures 10 and 11 show the corresponding \bar{u}' and $-\bar{u}'\bar{v}'$ profiles. Examining the profiles at Station 7, the mean profile initially appears to be laminar and attached, and both the \bar{u}' and $-\bar{u}'\bar{v}'$ values are near zero, indicating again that the flow is laminar. Given the phase lag shown in Fig. 3 between the speaker input and the jets, and the finite convection time between the jet hole and Station 7, one would expect that the disturbance created by the jet outpulse should arrive at Station 7 at $t/T=0.18$. In fact, however, the disturbance is not seen in the mean profile until $t/T=0.333$. In agreement, the \bar{u}' and $-\bar{u}'\bar{v}'$ values also rise above zero at $t/T=0.333$. This may suggest that the rising jet velocity must reach a sufficiently high amplitude before it can significantly affect the boundary layer. Comparing the observed phase lag and the jet velocity of Fig. 3 suggests that the jet velocity must be about 8 m/s, corresponding to an instantaneous $B=4$, for the jets to be effective. Continuing forward in time at Station 7, the jets cause a large disturbance in the mean profiles that continues until $t/T=0.667$. The time $t/T=0.667$ corresponds very closely with the end of the jet outpulse when the phase lag and convection time from the jet holes to Station 7 are considered. The large local minima and maxima in the mean velocity profiles indicate the jets are not merely adding turbulence to the boundary layer, but are inducing some flow structure, most likely streamwise vortices. These vortices likely cause spanwise variation in the velocity, particularly at the stations nearest the jets. In the present study, data were only acquired at one spanwise location. Spanwise surveys should be considered in future work. The \bar{u}' and $-\bar{u}'\bar{v}'$ profiles exhibit large peaks in the regions where the mean velocity gradients are highest in Fig. 9. The $-\bar{u}'\bar{v}'$ values have the appropriate sign, corresponding to the sign of $d\bar{U}/dy$ in the mean profiles. It should be noted that the magnitude of \bar{u}' is smaller in the ensemble averaged profiles of Fig. 10 than in the time averaged profiles of Fig. 7. This indicates that much of the contribution to \bar{u}' in Fig. 7 is due to 10 Hz oscillations and not to turbulence. After $t/T=0.667$, the mean velocity profile resumes a laminar shape. There is no tendency toward boundary layer separation. The boundary layer did not separate in the baseline case at this station (Fig. 7), but the mean profile in the baseline case did appear closer to separation than in the present case.

Moving to the downstream stations, the leading edge of the disturbance, as observed in the mean profiles and the \bar{u}' and $-\bar{u}'\bar{v}'$ profiles moves to later values of t/T , as expected since the disturbance takes some time to convect downstream. The leading edge of the disturbance appears to move at about 90% of the local free-stream velocity, which corresponds with the expected leading edge celerity of a turbulent spot (e.g. Gostelow et al. [26], Schulte and Hodson [27]). The trailing edge of the disturbance appears to move at about 45% of the local free-stream velocity, agreeing with the expected trailing edge celerity of a turbulent spot. Because the leading and trailing edge celerities are different, the boundary layer is only disturbed by the jets during approximately 30% of the cycle at Station 7, but is disturbed during approximately 70% of the cycle at Station 11. The beginning of the disturbance at each station is seen simultaneously in the mean

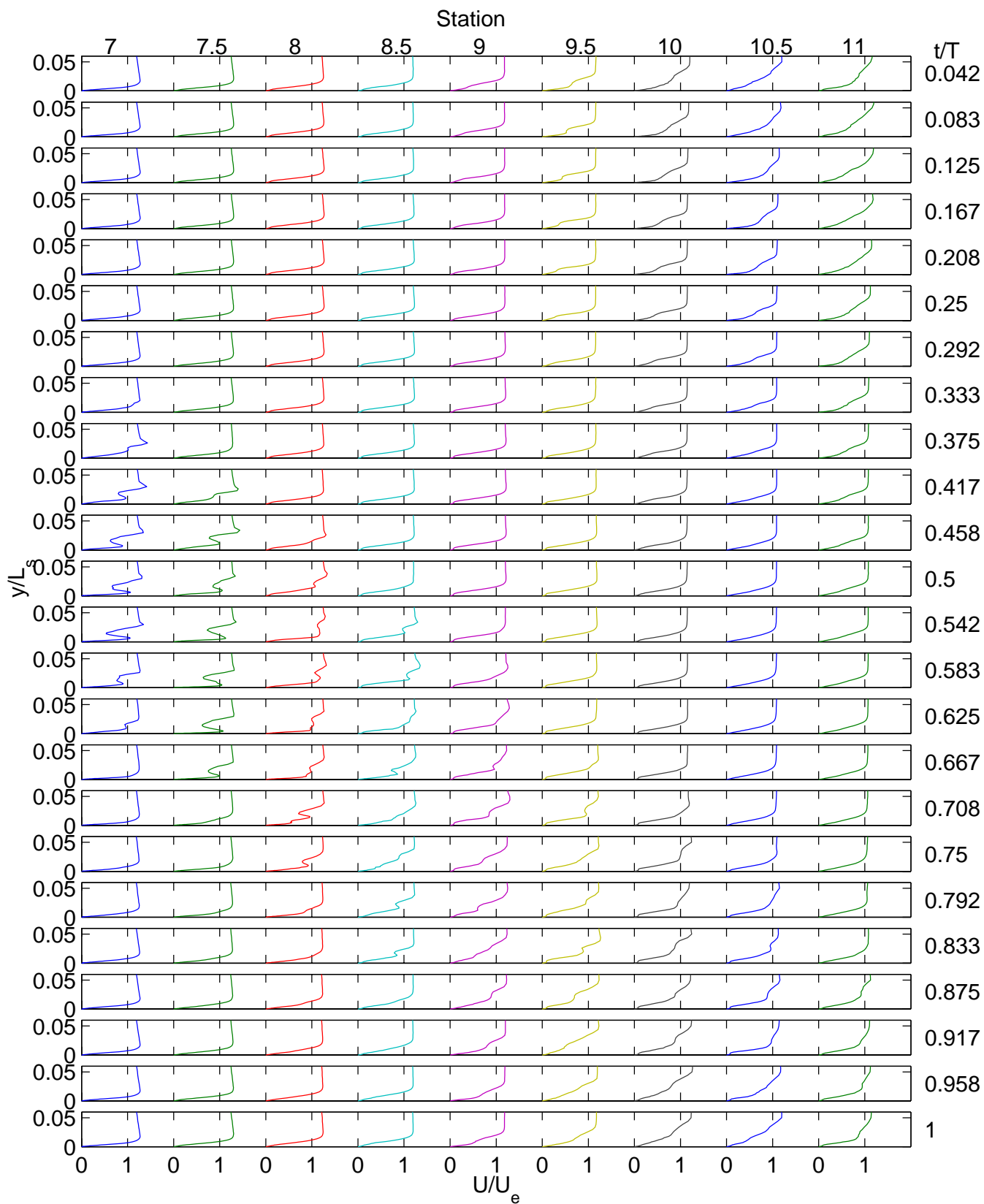


Fig. 9 Ensemble averaged dimensionless mean velocity (\tilde{U}/U_e) profiles

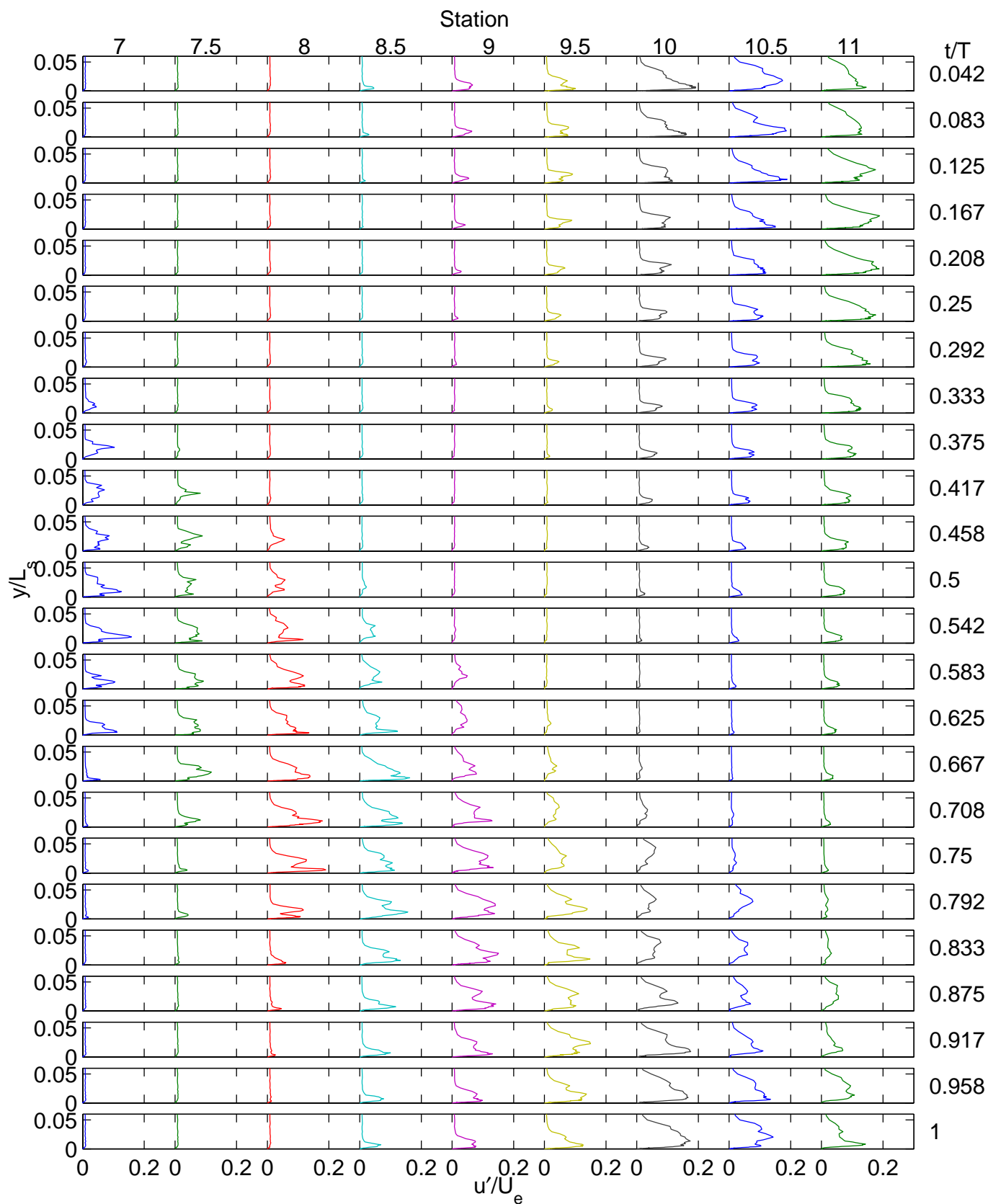


Fig. 10 Ensemble averaged rms value of dimensionless streamwise fluctuating velocity (\tilde{u}'/U_e) profiles

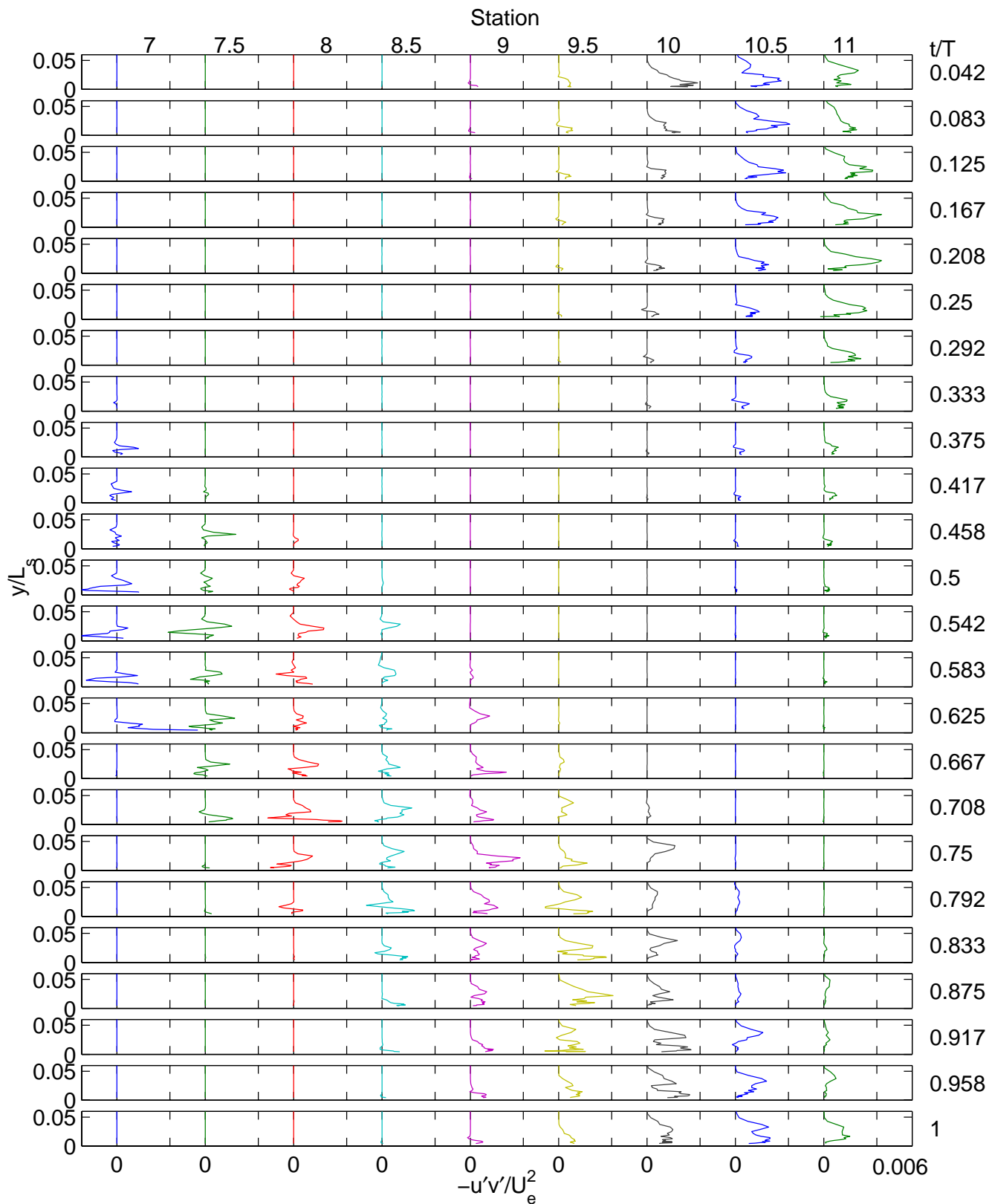


Fig. 11 Ensemble averaged dimensionless turbulent shear stress ($-\tilde{u}\tilde{v}/U_e^2$) profiles

profile and the \tilde{u}' and $-\tilde{u}'\tilde{v}'$ profiles of Figs. 9-11. At the trailing edge of the disturbance, return of the mean velocity profile to a smooth shape corresponds closely with the return of $-\tilde{u}'\tilde{v}'$ to near zero (see for example the profiles at Station 8 at $t/T=0.833$ or Station 10.5 at $t/T=0.417$). The \tilde{u}' profiles, in contrast, take somewhat longer to return to an undisturbed condition. At Station 11, for example, there is at least a small near wall \tilde{u}' peak at all times, while the $-\tilde{u}'\tilde{v}'$ values are essentially zero between $t/T=0.625$ and 0.792 .

The flow structure at the downstream stations appears to be less distinct than at Stations 7 and 7.5. Inflection points are still present in the mean profiles, but the local minima and maxima in the mean profiles are less sharp. Still, the mean profile shapes and the multiple peaks in the \tilde{u}' and $-\tilde{u}'\tilde{v}'$ profiles, particularly those far from the wall (see for example the Station 10 profiles of Figs. 10 and 11 between $t/T=0.75$ and 0.958) are evidence that the flow structures induced by the jets persist downstream.

After the disturbance caused by the jets passes, the boundary layer eventually separates at locations between Stations 8 and 11. At Station 8.5, for example, the trailing edge of the disturbance passes at about $t/T=0.9$. By $t/T=0.1$ the near wall profile appears separated. The separation appears to coincide with the return of \tilde{u}' to near zero. The separation appears to persist until about $t/T=0.6$, after the start of the next disturbance event. The reattachment within the disturbance event corresponds to the motion of high \tilde{u}' and $-\tilde{u}'\tilde{v}'$ into the near wall region at $t/T=0.667$. The same sequence of events is visible at downstream stations. At Station 10.5, for example, the trailing edge of the disturbance has passed by $t/T=0.4$, but the boundary layer remains attached until about $t/T=0.75$. Reattachment is visible at $t/T=1$, and a near wall peak emerges at the same time in $-\tilde{u}'\tilde{v}'$. It should be noted that the separation bubble remains thin at all stations, and never begins to approach the thickness observed in the baseline flow of Fig. 7.

The period between the passage of the disturbance and boundary layer separation is believed to be a "calmed" region. Calmed regions have been observed in previous studies to follow turbulent spots and wake induced turbulent strips. The duration of the calmed region increases at the downstream stations, since the trailing edge celerity of the calmed region, shown in Fig. 9 to be about 0.3 the local free-stream velocity (in agreement with previous studies of calmed regions), is slower than the trailing edge celerity of the disturbed region. Hence at Station 8.5 the calmed region extends for $\Delta t/T$ of about 0.2, while at Station 10.5 it extends for $\Delta t/T$ of about 0.4. The presence of the calmed region may help to limit the separation bubble thickness.

Figure 12 shows the ensemble \tilde{u}' data in a different format. Contours of near wall \tilde{u}' at $y=0.095$ mm ($y/L_s=0.0004$) are shown in a time-space plot. The horizontal axis shows the dimensionless streamwise location, and the vertical axis indicates the dimensionless time within the cycle. Two complete cycles are shown to better illustrate the periodicity of the event. The data in the bottom half of the figure is shown again in the top half. In this format, it is clear that the jet outpulse causes a high \tilde{u}' event to appear at $s/L_s=0.6$ (Station 7) and $t/T=0.6$. This event then proceeds downstream in a widening wedge of turbulence. The lower and upper slopes of the wedge indicate its leading and trailing edge celerities, respectively. Within the wedge, a local \tilde{u}' peak is visible at $s/L_s=0.7$ (Station 8). This peak indicates that the flow structure produced by the jets has penetrated very near the wall. Slightly farther downstream at $s/L_s=0.75$ (Station 8.5) a local minimum is visible in the \tilde{u}' contours. This may indicate that the flow structure induced by the jets has lifted off the wall slightly. The mean profiles of Fig. 9, support this, showing lower near

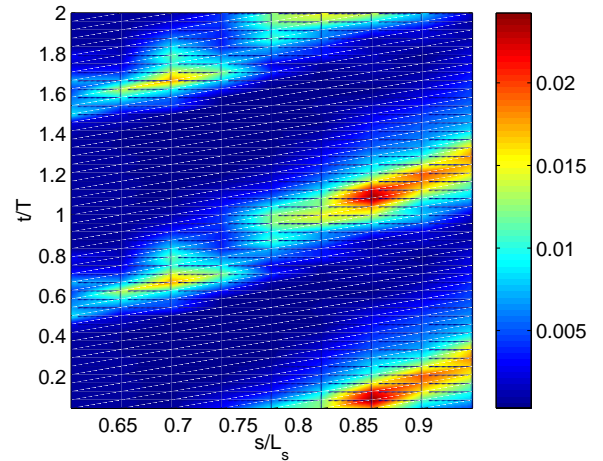


Fig. 12 Time-space plot of ensemble averaged \tilde{u}'/U_e at $y/L_s=0.0004$

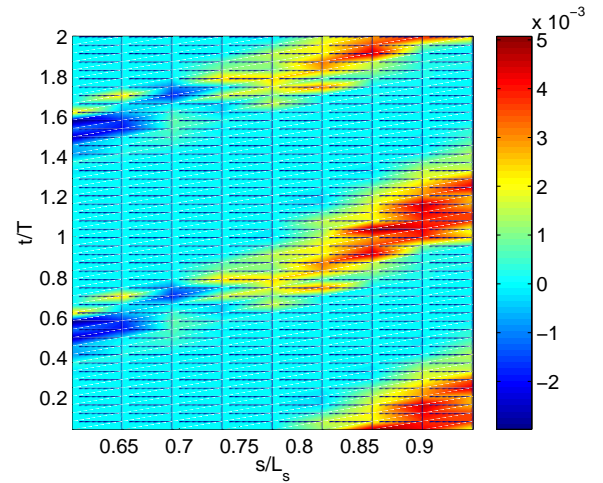


Fig. 13 Time-space plot of ensemble averaged $-\tilde{u}'\tilde{v}'/U_e^2$ at $y/L_s=0.0128$

wall mean velocity gradients at Station 8.5, which indicates that high speed fluid is not as effectively brought into the near wall region at this station. Farther downstream in Fig. 12, the \tilde{u}' level in the turbulent wedge rises again as a fully turbulent boundary layer begins to develop. Outside of the wedge the \tilde{u}' level is very low, indicating laminar flow.

Figure 13 shows ensemble averaged $-\tilde{u}'\tilde{v}'$ contours at $y/L_s=0.0128$ in the format of Fig. 12. As in Fig. 12, the wedge of turbulence is clear. Within the wedge momentum transport is high, but outside the wedge the flow appears to be laminar.

Figure 14 shows a time-space plot of the local ensemble averaged free-stream velocity. The free-stream velocity varies both spatially and temporally. Spatially, the shape of the airfoil passage causes the flow to decelerate. Temporally, when the jets cause a turbulent event to move down the surface, it causes the boundary layer to thicken and accelerates the free-stream. During the laminar and calmed periods the boundary layer is thinner and the free-stream velocity is lower. Figure 15 shows the local Thwaites parameter, λ_θ , as computed from the free-stream velocity data of Fig. 14. In a laminar boundary layer,

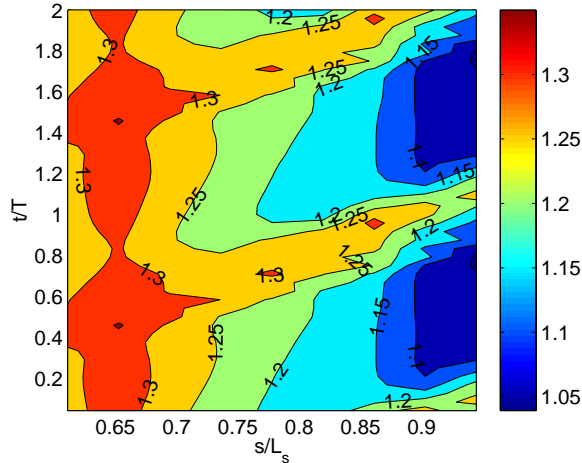


Fig. 14 Time-space plot of ensemble averaged dimensionless free-stream velocity \tilde{U}_∞ / U_e

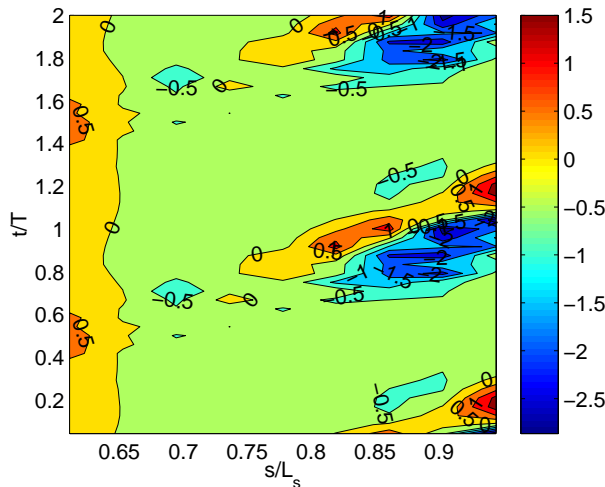


Fig. 15 Time-space plot of ensemble averaged Thwaites acceleration parameter, λ_θ

separation is expected when λ_θ is less than -0.082 . With the exception of the turbulent strip, where the boundary layer is locally accelerated, λ_θ is below -0.082 at most times and locations on the surface, and at some times is below -2 . Hence it is not a surprise that the boundary layer tends to separate when not controlled by turbulence or a calmed region.

Integral Parameters

Local displacement and momentum thickness values can be computed from the ensemble mean velocity profiles of Fig. 9. Momentum thickness is shown in Fig. 16. Both δ^* and θ grow in the streamwise direction and are about twice as large in the turbulent region than in the laminar flow region. The slow growth of the momentum thickness in the non-turbulent flow indicates that losses should be low in this region, as might be expected based on the low \tilde{u}' and $-\tilde{u}'\tilde{v}'$ values of Figs. 10-11. At $s/L_s=0.6$ (Station 7) δ^* and θ in the laminar flow are both roughly 67% of their values in the baseline case of Volino [4]. The lower values in the present case may be due to the suppression of the large separation bubble downstream, which changes the local pressure gradient at Station 7. The suction during

the inflow portion of the jet cycle could also be an explanation, but δ^* and θ are uniformly low in the laminar flow at Station 7. If the suction were causing a thinner boundary layer, one would expect the effect to be stronger during the time of strongest inflow into the jet holes. Figure 17 shows the local shape factor H , computed from the δ^* and θ values. Within the turbulent region, the shape factor remains between 2 and 2.4, which is well above the expected value of 1.6 for a fully-turbulent boundary layer subject to the strong adverse pressure gradient of the present case. In the non-turbulent flow, H reaches values as high as 3.4, which is consistent with the observed flow separation.

Skin Friction Coefficient

It is clear from the mean profiles of Fig. 9 that the local wall shear stress varies greatly during the jet oscillation cycle. At the upstream stations at $t/T=0.6$, for example, the jets bring high speed fluid very close to the wall, producing a very high mean velocity gradient at the wall. At other times at all stations, the boundary layer appears very laminar-like, indicating a relatively low wall shear stress. When the boundary layer is separated the wall shear goes to zero. Figure 18 shows the local skin friction coefficients, C_f . The white regions indicate where the flow is separated and the local skin friction is essentially zero. At $s/L_s=0.6$ (Station 7) there is a laminar boundary layer with $C_f=0.005$ between jet outward pulses. The corresponding momentum thickness Reynolds is about 60. The skin friction drops in the streamwise direction and the boundary layer separates at $s/L_s=0.7$ (Station 8). At $t/T=0.6$ and $s/L_s=0.6$, the skin friction is much higher, following the jet outpulse. The momentum thickness Reynolds number is as high as 180, and C_f reaches values as high as 0.014. Moving downstream along this turbulent region, C_f rapidly drops to 0.001 at $t/T=0.8$ and $s/L_s=0.75$ (Station 8.5). The turbulence at this time and position is also low (Fig. 10). As stated above, the vortices produced by the jets appear to quickly bring high speed fluid near the wall, resulting in high skin friction and turbulence, but by $s/L_s=0.75$ this effect may weaken, resulting in lower C_f and \tilde{u}' . Moving farther downstream to $t/T=1.1$ and $s/L_s=0.85$, C_f rises again to as high as 0.007. The corresponding Re_θ is about 200 at this time and location. $C_f=0.007$ is about what one would expect for a fully turbulent boundary layer with $Re_\theta=200$, based on the standard correlation $C_f=0.0256/Re_\theta^{0.25}$ (Schlichting [33]).

Figure 18 clearly shows the calmed region described above. It is the triangular shaped region centered at $t/T=0.4$ and $s/L_s=0.9$ that in the figure is bounded below by the strip of high C_f and above by the separated flow region. Comparing Figs. 12, 13, 16 and 18 shows that the calmed region has low skin friction, low momentum thickness and low turbulence. Losses should, therefore, be low for the calmed region, as expected.

A comparison of the momentum thickness and skin friction in Figs. 16 and 18 is interesting. The wedge of high θ overlaps both the upper portion of the separated flow region and the strip of high C_f . As shown in the profiles of Figs. 10 and 11, downstream of $s/L_s=0.75$ (Station 8.5), the turbulence and mixing induced by the jet outpulse initially affects the outer part of the boundary layer and does not immediately eliminate the separation bubble. Figure 16 shows that this outer region mixing causes a rise in the momentum thickness. It is only somewhat later and farther downstream that this mixing moves into the near wall region, causing reattachment and high C_f . Kaszeta et al. [34] reported a similar result for flow over the Pak-B airfoil subject to wake passing events. They observed a time lag between the wake arrival and near wall transition.

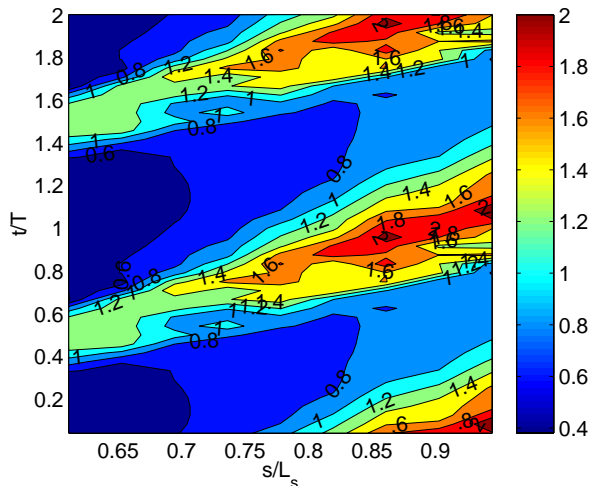


Fig. 16 Time-space plot of ensemble averaged momentum thickness, θ , in mm

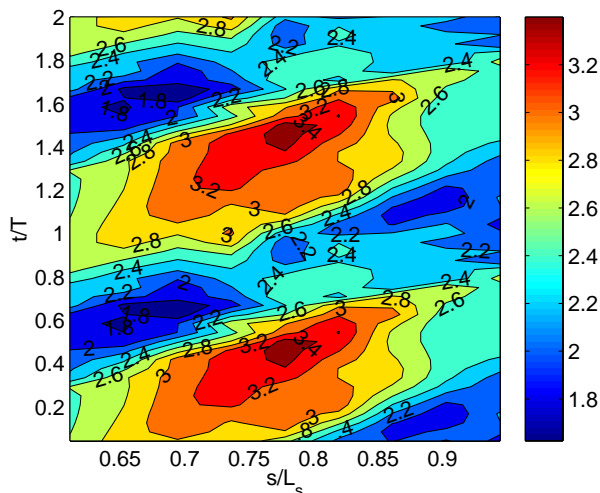


Fig. 17 Time-space plot of ensemble averaged shape factor, H

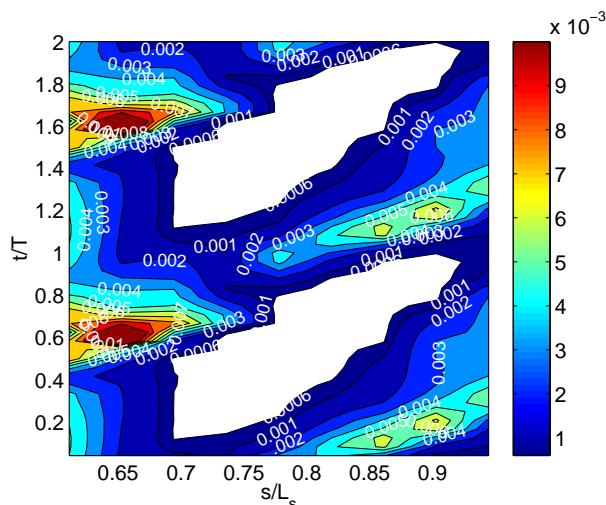


Fig. 18 Time-space plot of ensemble averaged skin friction coefficient, C_f ; white areas indicate separated flow

Kaszeta et al. [34] also observed a relation between the temporal acceleration and deceleration of the flow associated with the wake passing, and its relation to transition and the thickening and thinning of the boundary layer. Similarly, a comparison of Figs. 15, 16 and 18 show the relation between the local acceleration, θ and C_f . The region of overlap between high θ and separated flow corresponds to the region of strong deceleration centered at $s/L_s=0.9$ and $t/T=0.85$. One could argue that the deceleration inhibits reattachment in spite of the mixing in the outer part of the boundary layer. At slightly later t/T , the flow is accelerated. Under the combination of acceleration and higher $-\overline{u'v'}$ the boundary layer reattaches.

Open Questions

The first objective of the present study was to assess the effectiveness of synthetic VGJs on separation control for an LPT airfoil and provide some description of the mechanisms through which the jets work. This has been addressed above. The second objective was to use these results to generate questions for further consideration. These are discussed below.

What is the effect of jet frequency on flow control? In the present case, with $F^+=0.65$, the airfoil boundary layer at any given time was approximately half disturbed by the jets and half laminar or calmed. The effects of one jet outpulse are present in the boundary layer at all times. Separation occurred, but the separation bubble was small and did not appear to result in any harmful effects. How thick a separation bubble is tolerable? If F^+ were increased, the duration of each event would be reduced, but more events would be present in the boundary layer at any given time. It is not clear what effect this would have. In other studies with synthetic jets, some have found that F^+ of the order 1, as in the present study, is most effective (e.g. Seifert and Pack [35]). Others, such as Amitay and Glezer [21] report that under some conditions jets with F^+ of the order 10 are more effective. Lowering the jet frequency might be beneficial. Losses appear to be generated primarily in the flow disturbed by the jets, while the flow between these events is laminar or calmed with low losses. Reducing F^+ could presumably result in a smaller fraction of the airfoil covered by disturbed flow at any time. At some point, however, if the jets are too widely spaced, the flow will become uncontrolled at times and revert to the large separation bubble of the baseline case. Based on the trailing edge celerity of the disturbed flow, if F^+ were reduced below 0.45, there would be instances within the jet cycle when no disturbances would be present in the boundary layer. If F^+ were reduced below 0.3, there would be times when neither disturbed or calmed flow would be present. In flow around a single airfoil, Seifert and Pack [35] found that jets with F^+ between 0.5 and 1.5 were most effective at all Re , but that with $F^+=0.25$ the jets were ineffective. Bons et al. [25], in contrast, found that their VGJ's were effective at F^+ as low as 0.1. They suggested that the more controlled nature of the LPT flow, where adjacent airfoils provide covered turning, might explain the lower effective F^+ in their study. It should be noted that the Bons et al. [25] experiments were conducted at a Reynolds number of 60,000, where separation effects are not as severe as in the present case with $Re=25,000$.

What is the effect of jet amplitude on flow control? The pressure profiles of Fig. 4 indicate that the jet amplitude must be sufficiently high for the jets to be effective. It is expected that using a higher amplitude than necessary will result in higher losses, but the extent to which the losses would increase is not known. Volino [5] using passive bars found that cases with a small separation bubble followed by reattachment had lower losses than cases in which the boundary layer was tripped to turbulent to prevent separation. Low amplitude jets could potentially produce a similar effect.

What is the effect of jet waveform? In the present case the speaker was driven with a sine wave input. A square wave with a short duty cycle, as in the study of Bons et al. [25], might be better. By keeping the duty cycle short, the amount of calmed flow relative to disturbed flow could be increased. This might allow a reduction of losses without a sacrifice of separation control.

What is the effect of jet inflow? The outward flow portion of each jet cycle appears to dominate the flow control. It is possible, however, that the inflow may help reduce the boundary layer thickness in the undisturbed flow periods and help reduce separation effects. A direct comparison of cases at the same Re using synthetic VGJs and pulsed VGJs could help answer this question.

What is the effect of jet geometry? The VGJs are clearly effective. Through the generation of streamwise vortices they appear to provide more mixing than would be produced with normal jets that simply produced turbulence. The relative magnitudes of the effects of turbulence and streamwise vortices in enhancing mixing are uncertain. Might the generation of turbulent spots with a normal jet be sufficient? Which would result in lower losses?

What are the effect of Reynolds number and free-stream turbulence level? The baseline cases of Volino [4] show that at higher Re and higher $FSTI$ the boundary layer is more likely to transition and reattach even without flow control. The generation of calmed attached flow between jet events could still prove beneficial at higher Re , however. There would be a tradeoff between the losses generated by the jets themselves and the reduction in losses the jets might provide by reducing the separation bubble thickness and producing low-loss calmed regions. It might be possible to control the flow at higher Re with significantly lower blowing ratios than in the present case. Natural transition in the undisturbed flow between jet events and its interaction with calmed regions would be an added complication at higher Re not seen in the present study. If the Re were sufficiently high so that separation did not occur in the uncontrolled case, it is unlikely that the jets would provide any benefit. Schulte and Hodson [27] noted that the presence of calmed regions produced by unsteady wake passing could not significantly lower the losses in an already attached boundary layer.

CONCLUSIONS

1. Synthetic vortex generator jets proved effective for controlling boundary layer separation on an LPT airfoil at very low Reynolds numbers. The separation bubble was effectively eliminated, and losses were lower than in a similar case with passive flow control.
2. The VGJs prevent separation by bringing high momentum fluid into the near wall region and by promoting momentum transport through turbulent mixing.
3. The disturbance produced by the VGJs behaves in many ways like the disturbance associated with a turbulent spot or a wake induced turbulent strip. The leading edge celerity of the disturbance is approximately $0.9U_\infty$, and the trailing edge celerity is about $0.45U_\infty$. A calmed region with a trailing edge celerity of $0.3U_\infty$ follows the disturbance. The calmed region is resistant to separation.
4. The adverse pressure gradient in the present case was strong enough so that the boundary layer did separated after the passage of the calmed flow. The separation bubble remained thin, however. The appearance of a disturbance did not immediately induce reattachment. The disturbance appeared initially in the outer part of the boundary layer. After some lag time the disturbance spread into the near wall region and caused reattachment.
5. While much has been learned regarding the effectiveness and physics of synthetic VGJs in LPT flows, many questions remain

regarding their applicability under different flow conditions and their optimal design. These questions have been discussed.

ACKNOWLEDGEMENTS

This work was sponsored by the NASA Glenn Research Center. The grant monitor is Dr. David Ashpis. Additional matching support was provided through a U.S. Naval Academy Recognition Grant. Mr. Dale Boyer of the Technical Support Department at the Naval Academy fabricated the test section and the airfoils. Midshipman Dirk Heron conducted preliminary tests which led into the present study.

REFERENCES

- [1] Hourmouziadis, J., 1989, "Aerodynamic Design of Low Pressure Turbines," AGARD Lecture Series 167.
- [2] Mayle, R.E., 1991, "The Role of Laminar-Turbulent Transition in Gas Turbine Engines," *ASME Journal of Turbomachinery*, **113**, pp. 509-537.
- [3] Sharma, O.P., Ni, R.H., and Tanrikut, S., 1994, "Unsteady Flow in Turbines," AGARD Lecture Series 195, Paper No. 5.
- [4] Volino, R.J., 2002, "Separated Flow Transition Under Simulated Low-Pressure Turbine Airfoil Conditions: Part 1 – Mean Flow and Turbulence Statistics," *ASME Journal of Turbomachinery*, **124**, pp. 645-655.
- [5] Volino, R.J., 2003, "Passive Flow Control on Low-Pressure Turbine Airfoils," ASME Paper GT2003-38728.
- [6] Howell, R.J., Ramesh, O.N., Hodson, H.P., Harvey, N.W., and Schulte, V., 2001, "High Lift and Aft-Loaded Profiles for Low-Pressure Turbines," *ASME Journal of Turbomachinery*, **123**, pp. 181-188.
- [7] Gad-el-Hak, M., 2000, *Flow Control, Passive, Active, and Reactive Flow Management*, Cambridge University Press, Cambridge.
- [8] Lake, J.P., King, P.I., and Rivir, R.B., 2000, "Low Reynolds Number Loss Reduction on Turbine Blades With Dimples and V-Grooves," AIAA Paper 00-738.
- [9] Van Treuren, K.W., Simon, T., von Koller, M., Byerley, A.R., Baughn, J.W., and Rivir, R., 2001, "Measurements in a Turbine Cascade Flow Under Ultra Low Reynolds Number Conditions," *ASME Journal of Turbomachinery*, **124**, pp. 100-106.
- [10] Lee, J., Sloan, M.L., and Paynter, G.C., 1994, "Lag Model for Turbulent Boundary Layers Over Rough Bleed Surfaces," *Journal of Propulsion and Power*, **10**, pp. 562-568.
- [11] Sturm, W., Scheugenpflug, H., and Fottner, L., 1992, Performance Improvements of Compressor Cascades by Controlling the Profile and Sidewall Boundary Layers," *ASME Journal of Turbomachinery*, **114**, pp. 477-486.
- [12] Johnston, J.P., and Nishi, M., 1990, "Vortex Generator Jets. Means for Flow Separation Control," *AIAA Journal*, **28**, pp. 989-994.
- [13] Compton, D.A., and Johnston, J.P., 1992, "Streamwise Vortex Production by Pitched and Skewed Jets in a Turbulent Boundary Layer," *AIAA Journal*, **30**, pp. 640-647.
- [14] McManus, K., Legner, H., and Davis, S., 1994, "Pulsed Vortex Generator Jets for Active Control of Flow Separation," AIAA Paper 94-2218.
- [15] Raghunathan, S., Watterson, J., Cooper, R., and Lee, S., 1999, "Short Wide Angle Diffuser with Pulse Jet Control," AIAA Paper 99-0280.
- [16] Sinha, S.K., and Pal, D., 1993, "Optimizing the Use of Acoustic Perturbation to Control Unsteady Boundary Layer Separation," *ASME FED*, **157**, pp. 253-263.

- [17] Jacobson, S.A., and Reynolds, W.C., 1998, "Active Control of Streamwise Vortices and Streaks in Boundary Layers," *Journal of Fluid Mechanics*, **360**, pp. 179-211.
- [18] Miao, J.J., Lee, K.C., Chen, M.H., and Chou, J.H., 1991, "Control of Separated Flow by a Two-Dimensional Oscillating Fence," *AIAA Journal*, **29**, pp. 1140-1148.
- [19] Sinha, S.K., Pal, D., and Banerjee, D., 1996, Control of Flow Separation Using the EMEMS Approach: Proof of Concept Experiments," *ASME DSC*, **59**, pp. 253-263.
- [20] Whitehead, L.A., Graham, D.J., Moore, F.A., Bolleman, B.J., Lake, R., and Dunwoody, A.B., 1996, "Investigation of Boundary Layer Flow Separation Control by Airfoil Surface Vibration," *Canadian Aeronautics and Space Journal*, **42**, pp. 213-219.
- [21] Amitay, M., and Glezer, A., 2002, "Role of Actuation Frequency in Controlled Flow Reattachment over a Stalled Airfoil," *AIAA Journal*, **40**, pp. 209-216.
- [22] Huang, J., Corke, T.C., and Thomas, F.O., 2002, "Separation Control over Low Pressure Turbine Blades," *Bulletin of the American Physical Society*, **47**, No. 10, p. 167.
- [23] Hultgren, L.S., and Ashpis, D.E., 2002, "Glow Discharge Plasma Active Control of Separation at Low Pressure Turbine Conditions," *Bulletin of the American Physical Society*, **47**, No. 10, p. 167-168.
- [24] Bons, J.P., Sondergaard, R., and Rivir, R.B., 2001, "Turbine Separation Control Using Pulsed Vortex Generator Jets," *ASME Journal of Turbomachinery*, **123**, pp. 198-206.
- [25] Bons, J.P., Sondergaard, R., and Rivir, R.B., 2002, "The Fluid Dynamics of LPT Blade Separation Control Using Pulsed Jets," *ASME Journal of Turbomachinery*, **124**, pp. 77-85.
- [26] Gostelow, J.P., Walker, G.J., Solomon, W.J., Hong, G., and Melwani, N., 1997, "Investigation of the Calmed Region Behind a Turbulent Spot," *ASME Journal of Turbomachinery*, **119**, pp. 802-809.
- [27] Schulte, V., and Hodson, H.P., 1998, "Prediction of the Becalmed Region for LP Turbine Profile Design," *ASME Journal of Turbomachinery*, **120**, pp. 839-846.
- [28] Volino, R.J., 2002, "Separated Flow Transition under Simulated Low-Pressure Turbine Airfoil Conditions: Part 2 - Turbulence Spectra," *ASME Journal of Turbomachinery*, **124**, pp. 656-664.
- [29] Volino, R.J., Schultz, M.P., and Pratt, C.M., 2001, "Conditional Sampling in a Transitional Boundary Layer Under High Free-Stream Turbulence Conditions," *ASME Journal of Fluids Engineering*, **125**, pp. 28-37.
- [30] Wills, J.A.B., 1962, "The Correction of Hot-Wire Readings for Proximity to a Solid Boundary," *Journal of Fluid Mechanics*, **12**, pp. 65-92.
- [31] Volino, R.J., and Simon, T.W., 1997, "Velocity and Temperature Profiles in Turbulent Boundary Layers Experiencing Streamwise Pressure Gradients," *ASME Journal of Heat Transfer*, **119**, pp. 433-439.
- [32] Ligrani, P.M., and Bradshaw, P., 1987, "Spatial Resolution and Measurement of Turbulence in the Viscous Sublayer Using Subminiature Hot-Wire Probes," *Experiments in Fluids*, **5**, pp. 407-417.
- [33] Schlichting, H., 1979, *Boundary Layer Theory*, 7th ed. McGraw-Hill, New York.
- [34] Kaszeta, R.W., Simon, T.W., and Ashpis, D.E., 2001, "Experimental Investigation of Transition to Turbulence as Affected by Passing Wakes," *ASME Paper 2001-GT-195*.
- [35] Seifert, A., and Pack, L.G., 1999, "Oscillatory Control of Separation at High Reynolds Numbers," *AIAA Journal*, **37**, pp. 1062-1071.

GT2004-53360

SEPARATED FLOW TRANSITION MECHANISM AND PREDICTION WITH HIGH AND LOW FREESTREAM TURBULENCE UNDER LOW PRESSURE TURBINE CONDITIONS

Ralph J. Volino and Douglas G. Bohl

Department of Mechanical Engineering

United States Naval Academy

Annapolis, Maryland 21402

Email: volino@usna.edu

ABSTRACT

A correlation for separated flow transition has been developed for boundary layers subject to initial acceleration followed by an unfavorable pressure gradient. The correlation is based on the measured growth of small disturbances in the pre-transitional boundary layer. These disturbances were identified and quantified through spectral analysis of the wall normal component of velocity. Cases typical of low pressure turbine airfoil conditions, with Reynolds numbers (Re) ranging from 25,000 to 300,000 (based on suction surface length and exit velocity) were considered at low (0.5%) and high (8.7% inlet) freestream turbulence levels. In some cases, two-dimensional rectangular bars were placed at the beginning of the adverse pressure gradient region as passive flow control devices. The dimensionless magnitude of the initial disturbance which begins to grow at the suction peak depends on the freestream turbulence level and the size of any bar applied to the surface. The growth rate depends on the Reynolds number. When the pre-transitional disturbances grow to a sufficient magnitude, transition begins. The new correlation is based on the physics observed in the turbulence spectra, but allows transition prediction using only the Reynolds number, freestream turbulence level and bar height. The correlation has been checked against experimental data from the literature, and allows transition location prediction to within the uncertainty of the experimental measurements. The correlation represents an improvement over previous correlations which accounted for Reynolds number or freestream turbulence effects, but not both.

NOMENCLATURE

C_p	$2(P_T - P) / \rho U_e^2$, pressure coefficient
d	bar height
FSTI	freestream turbulence intensity, based on rms u' , v' , or combined u' and v' , and normalized using U_∞ [%]
K	$(v/U_\infty^2)(dU_\infty/ds)$, acceleration parameter
L_s	suction surface length
P	pressure
P_T	upstream stagnation pressure

Re	$U_e L_s / \nu$, exit Reynolds number
Re_{pt}	$U_p(s_T - s_p) / \nu$, suction peak to transition Reynolds number
Re_{st}	$U_s(s_T - s_s) / \nu$, separation to transition Reynolds number
Re_θ	momentum thickness Reynolds number
s	streamwise coordinate, distance from leading edge
U	freestream velocity
U_∞	local freestream velocity
U_e	nominal exit freestream velocity, based on inviscid solution
u	mean streamwise velocity
u'	streamwise fluctuating velocity
v'	wall normal fluctuating velocity
$-u'v'$	time averaged turbulent shear stress
y	cross-stream coordinate, distance from wall
γ	intermittency, fraction of time flow is turbulent
ν	kinematic viscosity
ρ	density
θ	momentum thickness

Subscripts

b	baseline flow
m	modified flow
p	suction surface pressure minimum, velocity maximum
s	separation location
t	transition start location

INTRODUCTION

Boundary layer separation is a known problem on some modern low-pressure turbine (LPT) airfoils, due to the strong adverse pressure gradients created when designers impose higher loading in an effort to improve efficiency and lower cost by reducing airfoil count in engines. Separation bubbles, particularly those which fail to reattach, can result in a significant loss of lift and a subsequent degradation of engine efficiency (e.g. Hourmouziadis [1], Mayle [2], and Sharma et al. [3]). The problem is particularly relevant in aircraft engines. Airfoils optimized to produce maximum power under takeoff conditions may still experience boundary layer separation at cruise conditions, due to

the lower density and therefore lower Reynolds numbers at altitude. A component efficiency drop of 2% may occur between takeoff and cruise conditions in large commercial transport engines, and the difference could be as large as 7% in smaller engines operating at higher altitudes [4, 5]. Prediction and control of suction side separation, without sacrifice of the benefits of higher loading, is therefore, crucial for improved engine design.

Separation on airfoils is complicated by boundary layer transition. Separated flow transition in the LPT has been the focus of several recent studies. Volino [6] provides a review and describes as follows the transition process on the suction side of a typical LPT airfoil. The strong acceleration on the leading section of the airfoil keeps the boundary layer thin and laminar, even in the presence of elevated freestream turbulence. The favorable pressure gradient keeps the boundary layer stable to small disturbances, but immediately downstream of the suction peak, the boundary layer becomes unstable. In most cases Volino [6] observed that the boundary layer separated just downstream of the suction peak. Transition then occurred in the shear layer over the separation bubble and caused the boundary layer to reattach. The transition location moved upstream as the freestream turbulence intensity (FSTI) or Reynolds number was increased. At the highest FSTI and Re , transition occurred far enough upstream to prevent separation. At the lowest Re , transition did not occur in the shear layer and the boundary layer did not reattach.

Separated flow transition under low FSTI conditions appears to occur through instabilities which lead to the growth of small disturbances. Hence it is a natural transition, as opposed to a bypass transition. The shear layer is subject to both global and convective instability, so breakdowns due to Kelvin-Helmholtz (KH) or Tollmien-Schlichting (TS) type disturbances are possible. One or the other may be dominant in particular cases. Hatman and Wang [7] and Lou and Hourmouziadis [8] suspected KH type instabilities in their experiments. Volino [9] documented turbulence spectra in pre-transitional shear layers and found that the frequencies of the spectral peaks closely matched the most unstable frequencies expected for TS waves in the boundary layer just upstream of separation. Under high FSTI conditions, Volino and Hultgren [5] found that the shear layer spectra were more broad banded and did not exhibit the sharp peaks observed in low FSTI cases. They concluded that transition was through a bypass mode induced by the freestream disturbance. Under favorable pressure gradients, transition under high FSTI can occur even when stability analysis indicates that the boundary layer is stable to small disturbances, clearly indicating a bypass mechanism. Recent evidence, however, suggests that with adverse pressure gradients, natural transition is important even with high FSTI. Hughes and Walker [10] used wavelet analysis to document TS frequencies in an adverse pressure gradient boundary layer. These TS waves were clear even in the presence of passing wakes, which raised the FSTI to about 8%. Volino [9] noted that although his spectral peaks were more broad banded with high FSTI, they were centered at the same frequencies as the sharp peaks in otherwise similar low FSTI cases, and could be observed to grow from initially very low magnitudes in the pre-transition region.

Volino [11] provides further evidence of the importance of natural transition in a study of passive flow control using rectangular bars on the suction surface of an LPT airfoil. The bars were thin, ranging from about 0.1 to 1 boundary layer thickness in height, and were placed at the beginning of the adverse pressure gradient region. The thickest bars tripped the boundary layer to turbulent and prevented separation. Thinner bars appeared to have no immediate effect, and both the mean velocity and rms turbulence quantities just downstream of the bars were indistinguishable from those in baseline cases without bars.

Farther downstream, however, transition and reattachment occurred sooner in the cases with bars than in the unmodified flow, with transition moving upstream as bar height increased. The bars appeared to impart a small disturbance that was too small to detect at first, but that grew until it eventually induced transition. This suggests a natural transition mechanism. The same behavior was observed under both low and high FSTI, indicating that although high FSTI does help to promote transition, it is not purely a freestream induced bypass transition.

Studies such as those noted above provide important clues about separated flow transition, but the transition mechanism is still not fully understood. The rate at which disturbances grow has not been quantified or related in a direct way to the prediction of transition. Existing correlations, such as those of Roberts [12], Davis et al. [13], Mayle [2], and Hatman and Wang [7], provide reasonable estimates of transition start location, but they do not always agree with each other and are not always as accurate or robust as desired. Improved computational models and correlations are desired, and incorporation of the physics from recent observations may help.

The objective of the present study is to quantify the growth of disturbances in separated boundary layers under a range of conditions that are representative of LPT airfoil suction side flows, and to use this information to develop a correlation for transition prediction. Data from the studies of Volino [6, 9, 11] along with new experimental data will be used. After a correlation is developed, it will be compared to other data sets from the literature.

EXPERIMENTS

Experiments were conducted in a low speed wind tunnel, described by Volino et al. [14]. Briefly, air enters through blowers and passes through a honeycomb, a series of screens, two settling chambers, and a three-dimensional contraction before entering the test section. At the exit of the contraction, the mean velocity is uniform to within 1%. The FSTI is $0.5\% \pm 0.05\%$. Nearly all of this freestream "turbulence" is actually streamwise unsteadiness at frequencies below 20 Hz and is not associated with turbulent eddies. The rms intensities of the three components of the unsteadiness are 0.7%, 0.2% and 0.2% in the streamwise, pitchwise and spanwise directions, respectively. For low FSTI cases, the test section immediately follows the contraction. For high FSTI, a passive grid is installed at the contraction exit followed by a 1 m long rectangular settling chamber. At the inlet to the test section (10 cm upstream of the plane containing the leading edges of the airfoils) the high FSTI mean flow and turbulence are spatially uniform to within 3% and 6% respectively ($FSTI = 8.7\% \pm 0.5\%$). The freestream turbulence is nearly isotropic with rms intensities of 8.8%, 8.9% and 8.3% in the streamwise, pitchwise and spanwise directions. The integral length scales of these components are 3 cm, 1.6 cm and 1.4 cm. The integral scales were computed from the power spectra of each component.

The test section, shown in Fig. 1, consists of the passage between two airfoils. Details are listed in Table 1 and more information is available in Volino [6]. A large span to chord ratio of 4.3 was chosen to insure two-dimensional flow at the spanwise centerline of the airfoils, where all measurements were made. Upstream of each airfoil are flaps, which control the amount of bleed air allowed to escape from the passage. The flaps, along with a tailboard on the pressure side of the passage, are adjusted to produce the correct leading edge flow and pressure gradient along the airfoils. The flow in the passage matches that in a multi-blade cascade. The geometry of the passage corresponds to that of the Pak-B airfoil, which is an industry supplied research airfoil that is representative of a modern LPT design. It has been used in several studies, as noted in Volino [6].

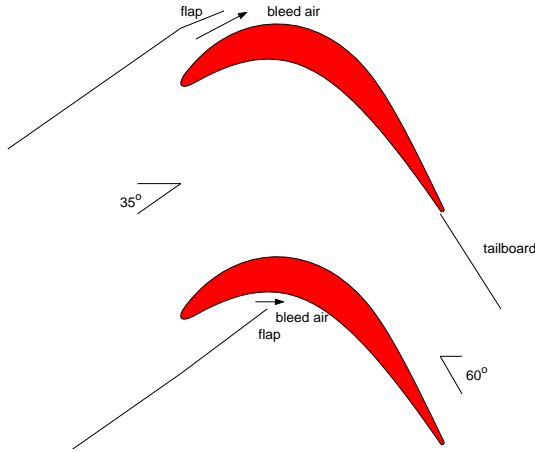


Fig. 1 Schematic of the test section

Data representing 40 experimental conditions are used. Baseline data are from Volino [6, 9], who considered high and low FSTI cases at five Reynolds numbers ($Re=25,000$, $50,000$, $100,000$, $200,000$, and $300,000$). Reynolds numbers are based on the exit velocity from the passage and the suction surface length, L_s . The Reynolds number range is representative of conditions from cruise to takeoff. The FSTI levels in an engine may vary considerably, but the values in the present work are believed to span the range of most interest. Data from cases with passive-bar flow control are from Volino [11]. The bars were of uniform rectangular cross section and extended along the airfoil, as shown in Fig. 2. The trailing edge of the bar was located at $s/L_s=0.51$, near the suction surface velocity peak. All bars were 6 mm wide in the streamwise direction. Bar heights of 0.4 mm, 0.8 mm and 1.6 mm were used. The bar heights were all less than 1% of L_s . They compare to local boundary layer thickness at the bar location of about 3.8 mm, 2.7 mm, 2.0 mm, 1.4 mm and 1.2 mm in the baseline $Re=25,000$ through $300,000$ cases respectively. For each bar height, all 10 cases of the baseline study were re-documented, for a total of 30 new experimental cases.

Measurements

Pressure surveys were made for each case using pressure taps located along the spanwise centerline of each airfoil. Locations of the taps on the suction side are listed in Table 2 along with measured local FSTI components, and U_∞/U_e and the ReK product at these stations based on a non-separating, inviscid solution. The uncertainty in C_p is 7% at $Re=25,000$, and 4% in other cases. Further details of these measurements and their uncertainties are available in Volino [6, 11].

Profiles of the streamwise velocity component in the suction side boundary layer were measured for all cases at streamwise stations corresponding to pressure taps 7-11, as given in Table 2. These stations are in the adverse pressure gradient region. Profiles at Stations 1-6 were fully documented for the baseline cases, and show that the upstream boundary layer closely follows a laminar solution, even in the high FSTI cases. Further details of these measurements are available in Volino [6, 11].

The intermittency, γ , is the fraction of time the flow is turbulent within the transition region. It was determined at each measurement location based on the instantaneous streamwise velocity signal, using the technique described in Volino et al. [14]. Turbulent flow is defined here to include a range of large and small scale eddies, turbulence production, and dissipation. A boundary layer may be characterized by significant u' fluctuations but still be non-turbulent if

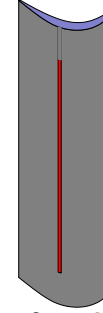


Fig. 2 Scale drawing of suction side airfoil showing location of bar

Table 1: Test section parameters

Axial Chord [mm]	True Chord [mm]	Pitch [mm]	Span [mm]	Suction side, L_s [mm]	Inlet flow angle	Exit flow angle	$\frac{U_e}{U_{inlet}}$
153.6	170.4	136.0	660.4	228.6	35°	60°	1.64

Table 2: Measurement stations locations, local acceleration (inviscid soln.), and measured local freestream turbulence

Station	s/L_s	$\frac{U_\infty}{U_e}$ in- viscid	ReK in- viscid	Low FSTI $\frac{\sqrt{u'^2}}{U_\infty}$ [%]	Low FSTI $\frac{\sqrt{v'^2}}{U_\infty}$ [%]	High FSTI $\frac{\sqrt{u'^2}}{U_\infty}$ [%]	High FSTI $\frac{\sqrt{v'^2}}{U_\infty}$ [%]
1	0.111	0.923	1.58	0.44		5.2	
2	0.194	1.007	1.20	0.39		4.6	
3	0.278	1.123	0.86	0.37		4.0	
4	0.361	1.190	0.75	0.38		3.5	
5	0.444	1.247	0.62	0.39		3.2	
6	0.528	1.277	-0.02	0.41		2.8	
7	0.611	1.240	-0.81	0.47	0.05	2.9	5.9
8	0.694	1.161	-0.95	0.47	0.12	3.0	6.2
9	0.777	1.100	-0.58	0.48	0.14	3.4	6.6
10	0.861	1.053	-0.53	0.54	0.11	3.8	6.8
11	0.944	1.020	-0.18	0.51	0.11	4.0	6.8

these fluctuations are induced by an external source that does not also cause near wall turbulence production. Such is often the case under high FSTI conditions. Freestream eddies buffet the boundary layer, inducing non-turbulent boundary layer fluctuations but very little momentum transport. Transition to turbulence is characterized not so much by large increases in u' levels, which may remain essentially constant, but by the appearance of higher frequencies. The higher frequencies signal the generation of turbulence in the near wall region and are used to distinguish between turbulent and non-turbulent flow.

The measurements of most significance for the present study are profiles of the wall normal fluctuating velocity, v' . One objective of the present study is to track the growth of small disturbances in the pre-transitional flow. Volino [9] found that small disturbances at particular frequencies can be masked by the broadband unsteadiness in a non-turbulent boundary layer, particularly under high FSTI conditions. The broadband unsteadiness tends to be much higher in u' than in v' , making disturbances in v' easier to detect. Wall normal velocity was measured for the baseline cases by Volino [6]. New data were acquired in the present study for the passive bar cases. A hot wire anemometer (AA Lab Systems model AN-1003) and a

boundary layer cross-wire probe (TSI model 1243-T1.5) were used to measure profiles of the wall normal velocity and turbulent shear stress at Stations 7-11 for each case. Profiles were measured near but not at the spanwise centerline of the airfoil to insure that the pressure taps did not interfere with the velocity measurements. At each measurement location, data were acquired for 26 seconds at a 20 kHz sampling rate (2^{19} samples). All raw data were saved. The high sampling rate provides an essentially continuous signal, which is needed for intermittency and spectral post-processing. Data were acquired at 25 locations in each profile, beginning 1 mm from the wall and extending to the freestream. Just upstream of separation, $y=1$ mm is equivalent to $y^+ \approx 10$ when $Re=25,000$ and $y^+ \approx 60$ when $Re=300,000$.

Uncertainties in v'^2 and the turbulent shear stress, $-u'v'$, are 10%.

Power spectra of v' were computed for the data from all measurement locations. Frequencies are resolved from 4.88 Hz to 10 kHz in 4.88 Hz increments using a 4096 point Fast Fourier Transform to compute the spectra. As a check, the spectra were integrated with respect to frequency and found to equal the corresponding time averaged Reynolds stresses. The average uncertainties in the spectra are 10%. Measurements with the cross-wire probe are subject to spatial averaging errors due to the length of the sensors (1.27 mm active length) and the spacing between the two sensors (1 mm). Ligrani and Bradshaw [15] and Ligrani et al. [16] investigated spatial averaging. Their results, when applied to the present cases, indicate that spatial averaging should not result in significant error in average quantities at locations farther from the wall than 1 mm. As explained by Ligrani and Bradshaw [15], however, spatial averaging effects will not be uniform across the frequency spectrum, and will be most severe for the smallest scales (highest frequencies) in the flow. Applying the spectral results of Ligrani and Bradshaw [15] to the present study, errors due to spatial averaging will rise above 10% at frequencies above 150, 300, 600, 1200 and 1800 Hz for the $Re=25,000$, 50,000, 100,000, 200,000, and 300,000 cases respectively. Below these frequencies the errors should be under 10%. These frequencies are all above the frequencies of the spectral peaks in the results presented below, so the peaks should not be significantly attenuated.

RESULTS

Velocity and Pressure Profiles

Examples of the pressure and velocity profiles for the various cases are shown in Figs. 3-6. Figure 3 shows pressure profiles for the low FSTI, $Re=50,000$ cases. On the pressure side of the airfoil, the data from all cases agree with the inviscid solution for flow through the passage. This is expected since the boundary layer on most of the pressure side is subject to a favorable pressure gradient, and is attached. Agreement with the inviscid solution is also good on the upstream portion of the suction side. In the baseline case, the data dips below the inviscid solution at the suction peak (indicating a loss of lift), and then exhibits a plateau of nearly constant value in the adverse pressure gradient region. This plateau indicates that the boundary layer is separated and does not reattach. The behavior is essentially the same with the 0.4 mm thick bar, indicating that this bar is too small to induce transition and reattachment before the trailing edge. With the 0.8 mm thick bar there is still a large separation bubble, but the pressure coefficient drops toward the inviscid solution at the last measurement location. This indicates reattachment just before the trailing edge. With the largest bar, there is still a separation, but the reattachment moves farther upstream.

Figure 4 shows the velocity profiles for the cases presented in Fig. 3. The top row shows the mean velocity at Stations 7-11. At Station 7, the baseline, 0.4 mm and 0.8 mm bar cases are virtually

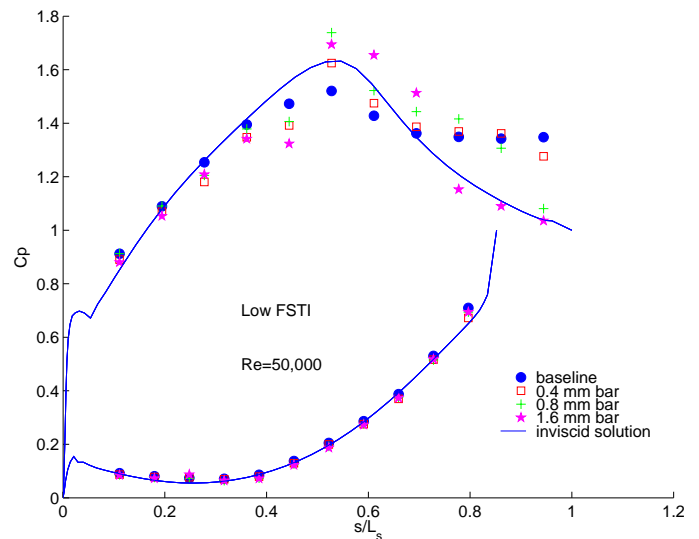


Fig. 3 C_p profiles, low FSTI, $Re=50,000$ cases

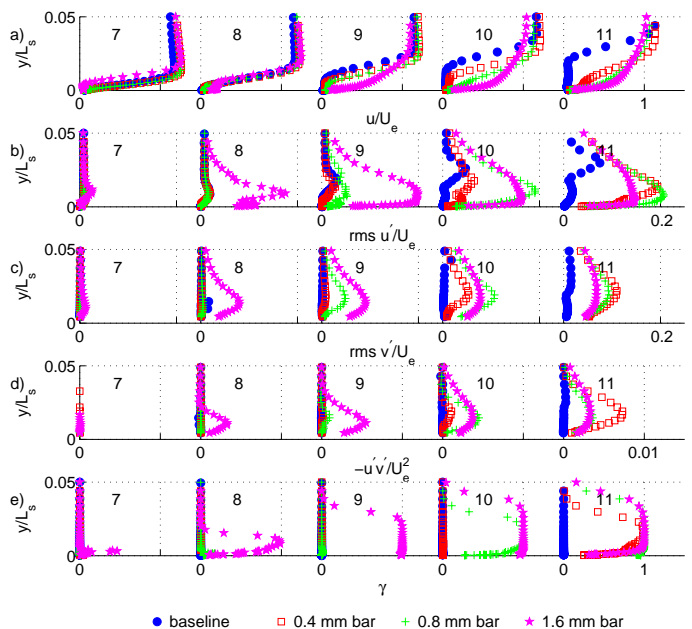


Fig. 4 Station 7-11 profiles, low FSTI, $Re=50,000$ cases: (a) mean velocity, (b) rms u'/U_e , (c) rms v'/U_e , (d) $-u'v'/U_e^2$, (e) intermittency

indistinguishable, while the 1.6 mm bar case shows a separation bubble. The rms streamwise velocity, u' , is very low at Station 7, with the exception of a small peak in the shear layer for the 1.6 mm bar case. The same is true for rms v' . The turbulent shear stress is essentially zero for all cases. The intermittency is also near zero, indicating laminar flow in all cases. At Station 8, the baseline and smaller bar cases are still essentially indistinguishable. The boundary layers have separated in these cases and there is a small peak in u' in the shear layer, but v' , the turbulent shear stress and the intermittency all remain near zero. With the largest bar, the boundary layer has undergone transition and reattached. At Station 9, a small disturbance appears in the turbulence quantities of the 0.8 mm bar case, but the

intermittency remains low. The baseline and 0.4 mm bar cases remain indistinguishable, with a peak in u' in the shear layer, but v' and $-u'v'$ values near zero. By Station 10, the boundary layer is turbulent in the 0.8 mm bar case, and has reattached. In the 0.4 mm bar case, the intermittency is still zero, but u' has begun to rise in the near wall region, and v' and $-u'v'$ have risen as well. This indicates the beginning of transition, and the boundary layer is turbulent and reattached in the 0.4 mm bar case by Station 11. In the baseline case, the shear layer does not transition or reattach before the trailing edge.

Several conclusions can be drawn from the information in Figs. 3 and 4. The reattachment locations observed in the mean velocity profiles agree with the locations in the pressure profiles. The beginning of reattachment coincides closely with the beginning of transition (rise of γ above zero). The rise in u' in the shear layer does not indicate turbulence in the sense defined above, but only streamwise unsteadiness. This is evidenced by the near zero values of v' and $-u'v'$ corresponding to the u' peaks. High u' does not necessarily imply significant momentum transport, and it is momentum transport which characterizes turbulent mixing and promotes reattachment of the boundary layer. The v' and $-u'v'$ values begin to rise simultaneously, signaling the beginning of transition. None of the bars were large enough to immediately trip the boundary layer to turbulent at this Reynolds number, and the smaller bars appeared to have no immediate effect on the profiles. The smaller bars must have imparted a small disturbance in the flow, however, because the transition location moved upstream from its location in the baseline case.

Figures 5 and 6 show pressure and velocity profiles for the high FSTI, $Re=50,000$ cases. The beginning of transition and reattachment in each case are between one and two stations farther upstream than in the corresponding low FSTI cases of Figs. 3 and 4. The u' peaks are much higher than in the low FSTI cases, as is the freestream v' . The near wall v' and $-u'v'$, however, remain low until transition starts, in agreement with the low FSTI cases. As in the low FSTI cases, high u' does not necessarily imply significant turbulent mixing. The effect of the bars in the low and high FSTI cases is similar. The smaller bars appear to have no immediate effect on the profiles, but they must impart a small disturbance which grows and causes transition to move upstream of its location in the baseline case. Hence, the high FSTI does promote transition, but it is not a pure bypass induced only by the freestream. Similar effects can be seen at other Reynolds numbers, as documented in Volino [11].

Volino [11] correlated the reattachment location as a function of bar height as

$$(s_r s_p)_m / (s_r s_p)_b = (1 + 0.23(d/\theta_p)^{1.56})^{-1} \quad (1)$$

where d is the bar height, θ_p is the baseline flow momentum thickness at the suction peak (which corresponds to the bar location), the subscripts p and t indicate suction peak and transition start, and the subscripts b and m denote baseline and modified cases. Equation (1) is based on a single study. More experiments with similar bars under different flow conditions are needed to test its general applicability.

Turbulence Spectra

Although the small disturbances which eventually lead to transition are difficult to detect in the velocity profiles of Figs. 4 and 6, they can be seen in the turbulence spectra. The u' , v' and $-u'v'$ spectra have been inspected, and disturbances are most consistently clear in the v' spectra. Figure 7 shows the v' spectra for baseline low FSTI cases at

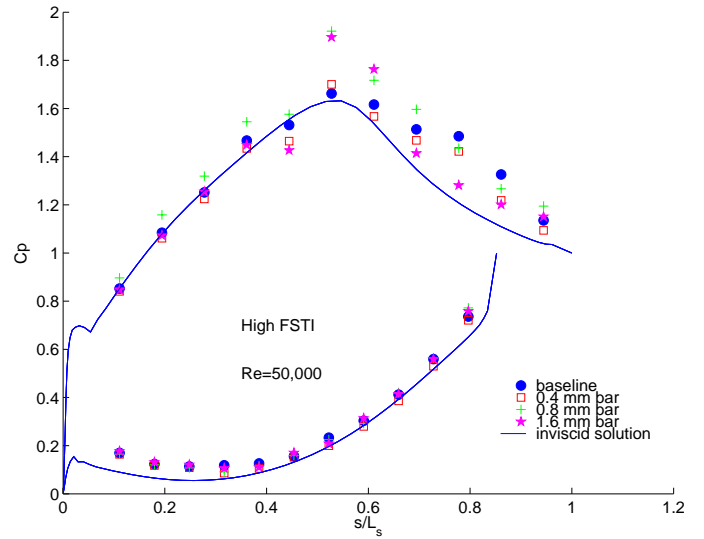


Fig. 5 C_p profiles, high FSTI, $Re=50,000$ cases

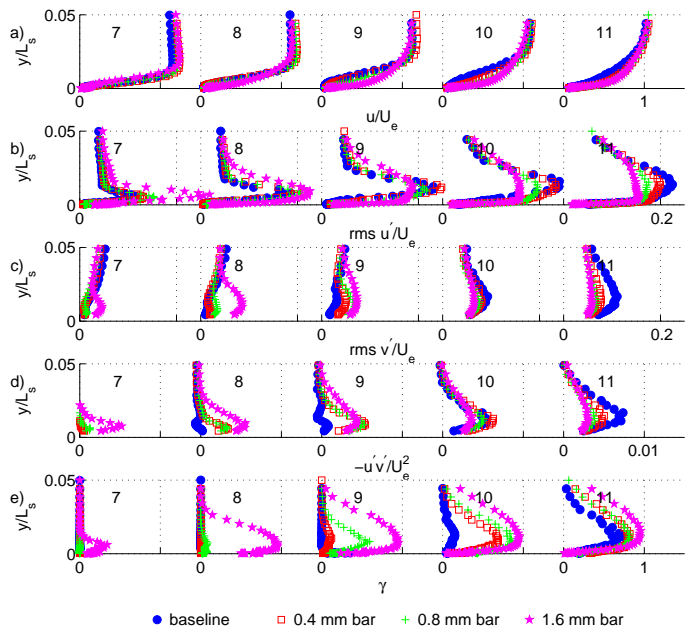


Fig. 6 Station 7-11 profiles, high FSTI, $Re=50,000$ cases: (a) mean velocity, (b) rms u'/U_e , (c) rms v'/U_e , (d) $-u'v'/U_e^2$, (e) intermittency

Re of 50,000 and 200,000. Data at each station are from the y location corresponding to the highest spectral peak. At $Re=50,000$, there are no clear peaks in the spectra at Stations 7-9, indicating that any important disturbances which may be present are as small as the very low background unsteadiness in the flow. By Station 10, a clear peak emerges, centered at about 80 Hz, along with some hints of a higher harmonic. By Station 11 this peak has grown by over 2 orders of magnitude. Note that although the peak grows by 4 orders of magnitude between Stations 9 and 11, the absolute value is still very low. The rms v' profile of Fig. 4 is still near zero for this case at Station 11, and the shear layer remains laminar and separated. Hence, the spectra provide a means of tracking small pre-transitional

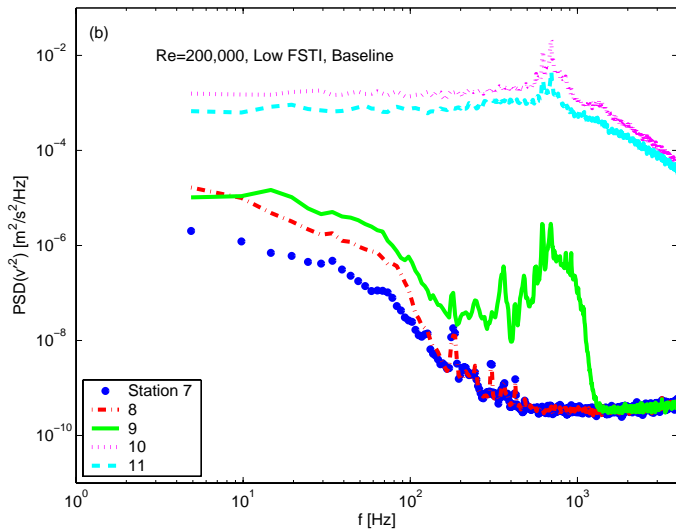
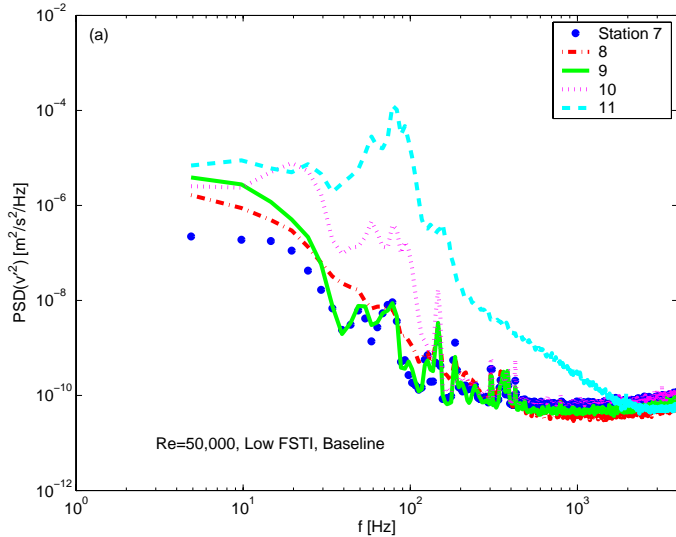


Fig. 7 Low FSTI, baseline case, boundary layer spectra:
(a) $Re=50,000$, (b) $Re=200,000$

disturbances before they become apparent in the turbulence statistics. Figure 7b shows similar behavior at $Re=200,000$. A peak centered at about 600 Hz emerges at Station 9, more than three orders of magnitude larger than the background unsteadiness. It is still too small, however, to have a significant effect on the rms v' profile. A significant rise in the v' profile does not occur until Station 10, after transition has occurred. Transition is clearly visible in the spectra as a rise in energy of several orders of magnitude at all frequencies. This is a reminder that turbulence is broad banded, with a full range of scales, in contrast to the more narrow band disturbances which lead to transition. Similar results are found at all Reynolds numbers. The frequency of the peak in each cases matches the most unstable frequency for TS waves just before separation, as explained in Volino [9] using an analysis from Walker [17].

Figure 8 shows the effect of the bars on the spectra at Station 8 of the $Re=50,000$ cases. The bars result in peaks at the same frequency as in the baseline case. The 0.4 mm and 0.8 mm thick bars cause a rise in the peaks of two and four orders of magnitude respectively above the baseline value. The absolute values of these peaks are still quite

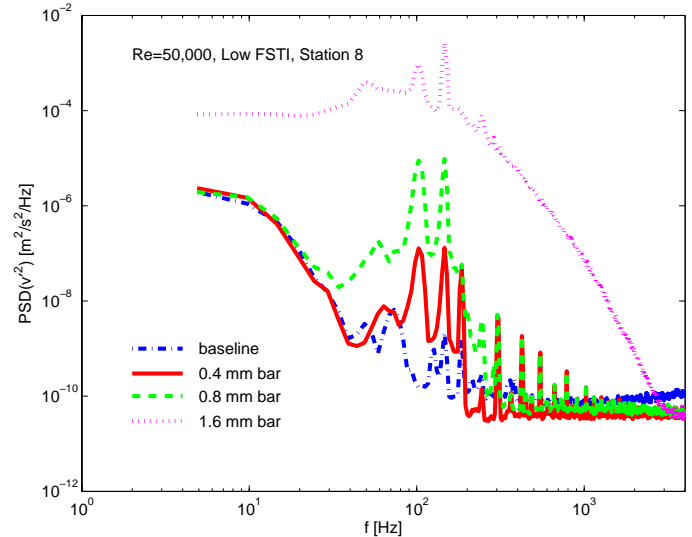


Fig. 8 Low FSTI, Station 8, boundary layer spectra

small, however, in comparison to the turbulent values present in the 1.6 mm bar case.

Growth of Spectral Peaks

To quantify the growth of disturbances such as those shown in Figs. 7 and 8, the data from the y location corresponding to the largest spectral peak at each station were selected, and the energy of the spectral peak was computed by integrating each spectrum over frequencies from 0.8 to 1.2 times the peak frequency of interest. So, for example, at $Re=100,000$, the peak frequency was centered at about 273 Hz, so the spectra were integrated from 220 Hz to 327 Hz. These energies were then normalized using the exit velocity from the passage, U_e , and plotted versus the dimensionless distance from the suction peak $(s-s_p)/L_s$. The distance from the suction peak was chosen because it is at the suction peak that the boundary layer becomes unstable and disturbances should start to grow. Figure 9 shows the resulting plot in log-linear coordinates for all of the low FSTI cases. At first glance, Fig. 9 may appear to be just a random jumble of data points, but on closer inspection, some patterns emerge. In each experimental case, the data have an upward slope, showing the growth of energy in the streamwise direction. The slopes appear to be greater at the higher Reynolds numbers. At any given Re , the cases with thicker bars have higher magnitude data, but the slopes appear to be about the same. The data from individual cases do lie along perfectly straight lines, and the trends noted above might not be noticed in an examination of one case by itself. When all the data are examined together, as in Fig. 9, the trends emerge. It should also be noted that the goal is to extract enough quantitative information from the data to develop a correlation for transition prediction. The exact steps in the data processing (e.g. the frequency range chosen for integration of the spectra) and the scatter of the data in intermediate steps, as apparent in Fig. 9, are not critical.

Figure 10 shows the data from Fig. 9 for the low FSTI baseline cases. There appears to be a background disturbance or “noise” level with a dimensionless magnitude of about $10^{-8.5}$. When the disturbances of interest become large enough, they rise above the noise. Comparison to the mean velocity profile data (e.g. Fig. 4) indicates that when the disturbances reach a magnitude of about $10^{-3.83}$, transition begins. The lines in Fig. 10 are based on fits to all 40 data sets. The slopes are assumed to depend on the Reynolds number as

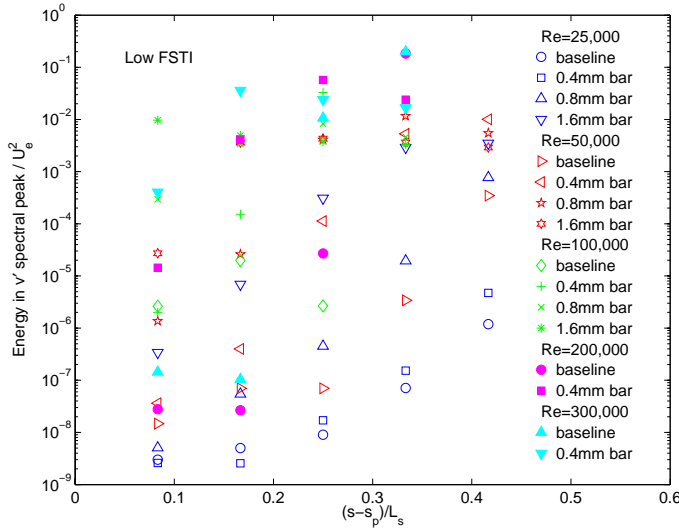


Fig. 9 Normalized v' spectral peak energy vs streamwise location for all low FSTI cases

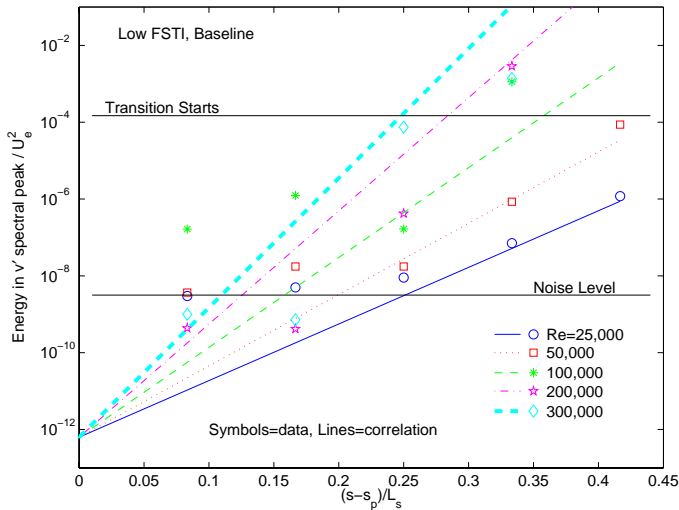


Fig. 10 Normalized v' spectral peak energy vs streamwise location for baseline low FSTI cases

$$\log_{10}[(\text{energy in } v' \text{ spectral peak})/U_e^2]/[(s-s_p)/L_s] = 0.504Re^{1/3} \quad (2)$$

When the data for the baseline cases are extrapolated back to $(s-s_p)=0$, they all appear to begin at a common origin with magnitude $10^{-12.2}$. This magnitude is presumed to be proportional to the size of the initial disturbances which begin to grow at the suction peak. Since all of the experiments were done in the same facility, it is reasonable to believe that the dimensionless initial disturbance may be the same in all cases.

Figure 11 shows the data from Fig. 9 for the low FSTI, $Re=50,000$ cases. The correlation lines all have the same slope, as given by Eq. (2). The intercepts at $(s-s_p)=0$ depend on the bar height as

$$\text{Low FSTI intercept} = 10^{[3.83-12.2]/[1+0.23(d/\theta_p)^{.56}]-3.83} \quad (3)$$

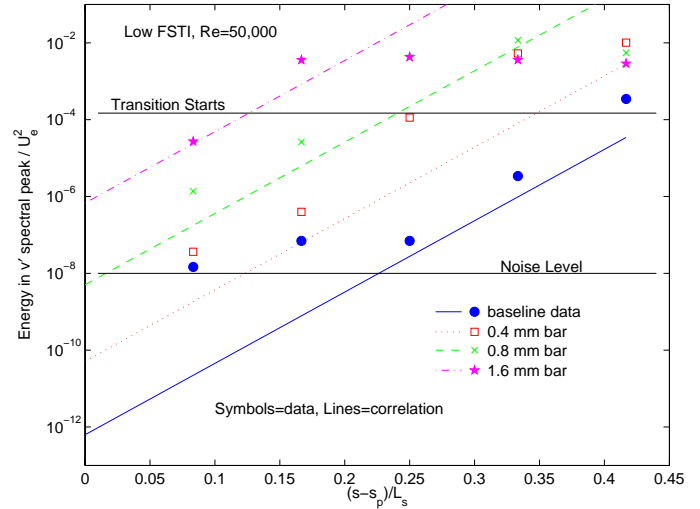


Fig. 11 Normalized v' spectral peak energy vs streamwise location for low FSTI, $Re=50,000$ cases

Equation (3) utilizes the baseline origin and transition magnitude of Fig. 10, and the form of Eq. (1), which relates the transition location in cases with bars to the location in the corresponding baseline case.

Figure 12 shows the data for the high FSTI baseline cases in the format of Fig. 10. The background disturbance or “noise” level is higher than in the low FSTI cases. Since the range through which the disturbances grow between the noise and transition is smaller than in the low FSTI cases, it is doubtful that trends concerning the growth rate could have been extracted from the high FSTI data alone. When the slopes of Eq. (2) are applied to the high FSTI data, however, the fit is not implausible; suggesting that the growth rate of the disturbances depends mainly on the Reynolds number and not the FSTI. As in the low FSTI cases, the correlation lines for the baseline cases appear to extrapolate to a common origin, suggesting that the dimensionless initial disturbance caused by the high FSTI is the same for all cases. The high FSTI raises this initial disturbance level from $10^{-12.2}$ in the low FSTI cases to $10^{-8.9}$ for the high FSTI cases. Figure 13 shows data for the high FSTI $Re=25,000$ cases. The slope of the correlation lines is given by Eq. (2). The intercepts at $(s-s_p)=0$ are based on the baseline value of Fig. 12 and the form of Eq. (3) as

$$\text{High FSTI intercept} = 10^{[3.83-8.9]/[1+0.23(d/\theta_p)^{.56}]-3.83} \quad (4)$$

The ratio of the intercept values for the high and low FSTI cases is $10^{-8.9}/10^{-12.2}=1995$. The intercept value is related to the size of the initial disturbance in the boundary layer, which is believed to be strongly influenced by the freestream turbulence, particularly the wall normal component. The v' component of the FSTI at the suction peak is estimated to be 0.1% and 4.5% for the low and high FSTI cases respectively, based on the inlet FSTI and the acceleration of the flow between the inlet and the suction peak. The ratio of the v' component of the freestream turbulence energy between the high and low FSTI cases, $(4.5\%/0.1\%)^2=2025$, is roughly equivalent to the ratio of the intercepts. The rough agreement may be fortuitous, but suggests the following formula for the intercept as a function of bar thickness, v' component FSTI, and boundary layer thickness at the suction peak.

$$\text{Intercept} = 10^{[3.83-12.2+2+\log_{10}(\text{FSTI}^2)]/[1+0.23(d/\theta_p)^{.56}]-3.83} \quad (5)$$

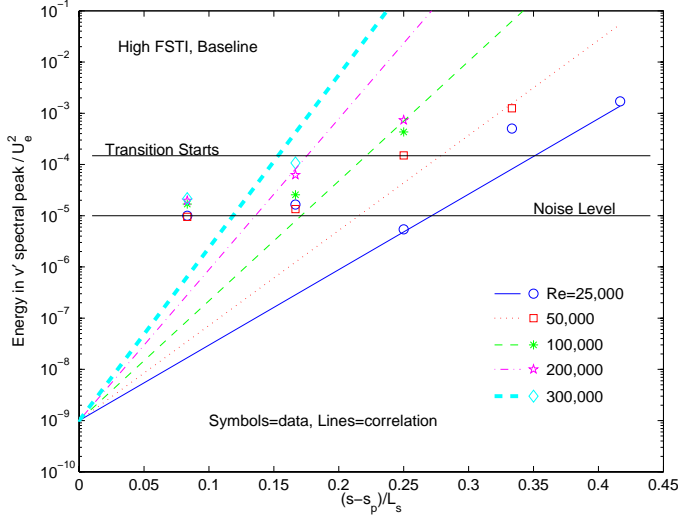


Fig. 12 Normalized v' spectral peak energy vs streamwise location for baseline high FSTI cases

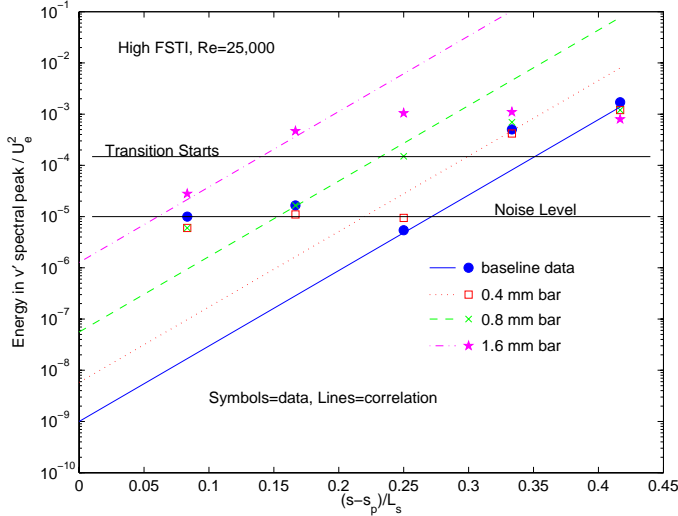


Fig. 13 Normalized v' spectral peak energy vs streamwise location for high FSTI, $Re=25,000$ cases

Simplifying Eq. (5) and combining with Eq. (2), the magnitude of the energy at any location is given as

$$\text{Magnitude} = 10^{[-6.37 + \log_{10}(FSTI^2)] / [1 + 0.23(d/\theta_p)^{1.56}] - 3.83 + 0.042(s-s_p)/L_s} \cdot Re^{1/3} \quad (6)$$

Transition Correlations

To find the transition start location, the magnitude in Eq. (6) is set to $10^{-3.83}$, and solved for the transition location as

$$(s_t - s_p)/L_s = \frac{1.98(6.37 - \log_{10}(FSTI^2))}{1 + 0.23(d/\theta_p)^{1.56}} Re^{-1/3} \quad (7)$$

Utilizing $U_p/U_e=1.277$ from the inviscid C_p profile, Eq. (7) can be expressed in terms of a Reynolds number as

$$Re_{pt} = \frac{2.53(6.37 - \log_{10}(FSTI^2))}{1 + 0.23(d/\theta_p)^{1.56}} Re^{2/3} \quad (8)$$

where Re_{pt} is a Reynolds number based on the local freestream velocity at the suction peak and the distance from the suction peak to the start of transition. To potentially make Eq. (8) more generally applicable, it can be expressed in terms of the local values at the suction peak. For the present cases,

$$Re_{\theta_p} = 0.393 Re^{1/2} \quad (9)$$

This results in

$$Re_{pt} = \frac{8.80(6.37 - \log_{10}(FSTI^2))}{1 + 0.23(d/\theta_p)^{1.56}} Re_{\theta_p}^{4/3} \quad (10)$$

Although Eqs. (7), (8), and (10) were developed based on the turbulence spectra and a particular series of choices in processing the spectral data, the final correlations are only dependent on Reynolds number, FSTI and dimensionless bar height. It should, therefore, be possible to predict transition location without knowledge of the turbulence spectra.

Comparison of Correlations to Experimental Data

Figure 14 compares the transition locations of the present experimental cases to Eq. (7). The error bars on the data indicate the uncertainty in the transition start location resulting from the finite spacing of the measurement stations. The agreement between the correlations and the data is not surprising, given that the correlations are based on these experimental data. Still, given the scatter apparent in Figs. 9-13, the good agreement in nearly all cases is reassuring.

Data from the baseline cases is compared to the present correlation and other correlations from the literature in Fig. 15. Mayle [2] presents the following correlations for short and long separation bubbles.

$$Re_{st} = 300 Re_{\theta_s}^{0.7} \quad \text{short bubble} \quad (11)$$

$$Re_{st} = 1000 Re_{\theta_s}^{0.7} \quad \text{long bubble} \quad (12)$$

where Re_{st} is a Reynolds number based on the freestream velocity at separation and the distance from separation to transition start. The correlation of Davis et al. [13] is

$$Re_{st} = 25000 \log_{10}[\coth(0.1732 FSTI)] \quad (13)$$

The FSTI levels used with Eq. (13) for Fig. 15 are suction peak values based on both u' and v' (0.3% and 3.74% for the low and high FSTI cases). Hatman and Wang [7] identify several transition modes and present correlations for each of them. Their laminar separation mode transition correlation can be cast in terms of Re_{st} as

$$Re_{st} = 0.0816 Re_s + 26805 \quad (14)$$

where $Re_s = U_s s_p / \nu$. Separation occurred at approximately the same location in all of the baseline cases of the present study, and

$$(s_s - s_p)/L_s = 0.0833 \quad (15)$$

$$U_s/U_p = 0.971 \quad (16)$$

$$Re_{\theta_s} = 0.481 Re^{1/2} \quad (17)$$

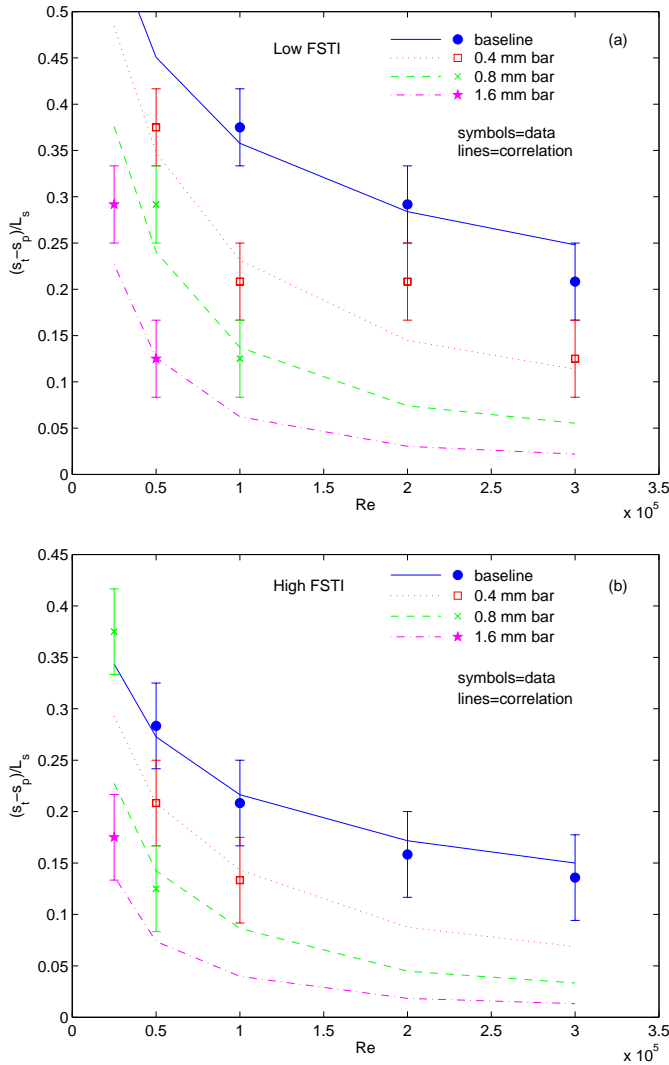


Fig. 14 Comparison of suction peak to transition start distance for experimental data and correlation: (a) low FSTI, (b) high FSTI

Using Eqs. (15)-(17), Eqs. (11)-(14) are cast in the coordinates of Eq. (8) and shown in Fig. 15. The present correlations agree with the data somewhat better than the other correlations, but all give reasonable predictions. The Hatman and Wang [7] correlation is based on low FSTI data, so it is not surprising that it only agrees with the low FSTI data of the present study. The Mayle [2] correlations do not take the FSTI into account explicitly. The long bubble correlation is intended for separation bubbles which do not close and therefore alter the pressure distribution along most of the airfoil surface. The short bubble correlation is intended for cases in which the boundary layer reattaches and the pressure distribution is only significantly altered in the vicinity of the bubble. To the extent that separation bubbles tend to be longer under low FSTI conditions, the Mayle [2] correlations can capture FSTI effects indirectly in some cases. The respective agreement of the long and short bubble correlations with the low and high FSTI data of the present study, however, may be somewhat fortuitous. The Davis et al. [13] correlation includes the effect of FSTI, but does not directly include the effect of Reynolds number. The present correlation appears to be the only one to explicitly include both effects.

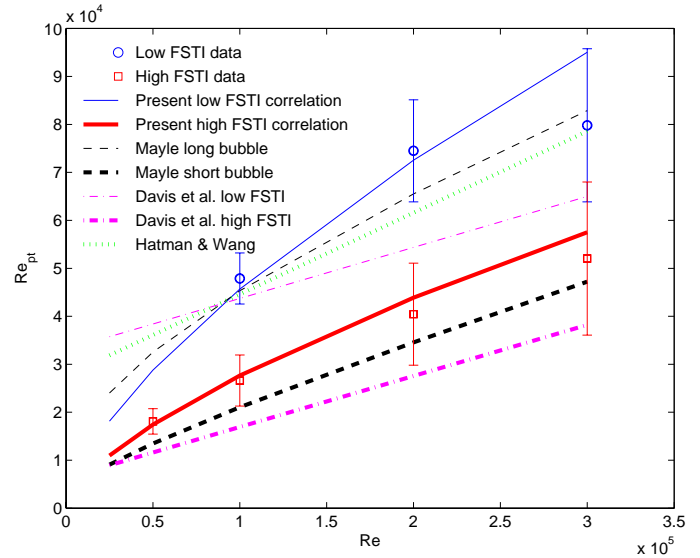


Fig. 15 Comparison of suction peak to transition start Re for baseline data and various correlations

Comparison to Data from Literature

The present correlation is based on the data of the present study. To better test it, data are used from other studies in the literature. The cases chosen for comparison all included flow over flat plates subject to a favorable pressure gradient followed by an adverse pressure gradient, with separation occurring shortly downstream of the suction peak. Cases which did not include these features did not have a single streamwise position which could be identified as the location where small disturbances would begin to grow, or they included elements of attached flow transition which the present correlation was not intended to predict. This limiting to a particular class of flows is not unduly restrictive on the utility of the present correlation, as it includes the flows of most interest for LPT boundary layers. Cases were selected in which FSTI, Re_{ts} , Re_{tp} , Re_{st} , and Re_{pt} were either presented or could be extracted from the available data. The studies include those of Lou and Hourmouziadis [8], who include data for four steady flow cases; 18 cases from Yaras [18]; three cases designated TL10, C and D from Howell [19]; and six cases from Volino and Hultgren [5], who considered a flat plate flow subject to the same pressure gradient as the cases of the present study. The results from these studies and comparisons to correlations are presented in Figs. 16-19. Equations (10)-(14) are used for the predictions.

The FSTI levels used in the comparisons were measured or extrapolated to values at the suction peak. Extrapolations were done, when necessary, using measured upstream FSTI values and the measured U_∞ distributions. The present correlation was developed using FSTI levels based on v' , but in many studies, only the u' component is measured. As shown in Table 2, the u' and v' components can be different. In the absence of a turbulence generating grid, the v' component tends to be lower than the u' unsteadiness. For the cases of the present study and of Volino and Hultgren [5], results are presented based on an overall FSTI which includes the measured u' and v' components, and based on an FSTI which includes only the v' component. For the Yaras [18], Lou and Hourmouziadis [8], and Howell [19] cases, only u' FSTI are available. Results are presented based on these u' FSTI, and also using assumed levels of v' FSTI. For the low FSTI cases of Refs. [8],

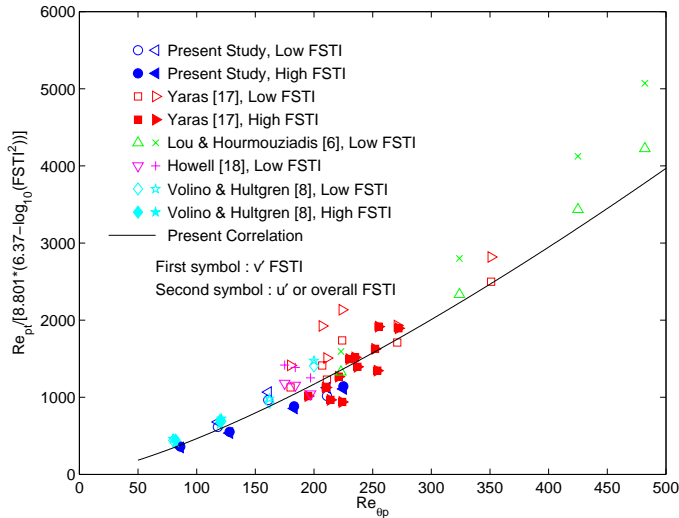


Fig. 16 Comparison of experimental data from various studies to present correlation

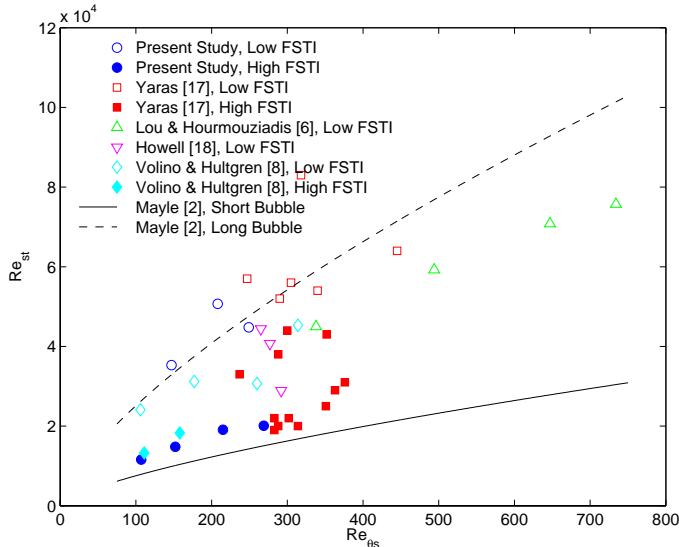


Fig. 17 Comparison of experimental data from various studies to correlations from Mayle [2]

[18], and [19], v' FSTI of 0.1% was assumed. This assumption presumes similar behavior to the present study, in which streamwise unsteadiness results in rms u' of about 0.5% in the freestream, while v' is significantly lower at 0.1%. For the higher FSTI cases of Yaras [18], the freestream turbulence was assumed isotropic, so the u' and v' FSTI were assumed equal. It should be noted that results based on assumed v' levels for Refs. [8], [18], and [19] are presented only to demonstrate the potential differences that may exist between u' and v' based results, and to show the possibility of better prediction if results are based on v' FSTI. Results based on assumed v' FSTI are not used for assessment of correlations. Evaluation of the accuracy of correlations should be based on comparison to the u' FSTI results for Refs. [8], [18], and [19], since the u' FSTI were actually measured.

Figure 16 compares the data from all cases to the present correlation, Eq. (10). The open symbols in Figs. 16-19 represent cases

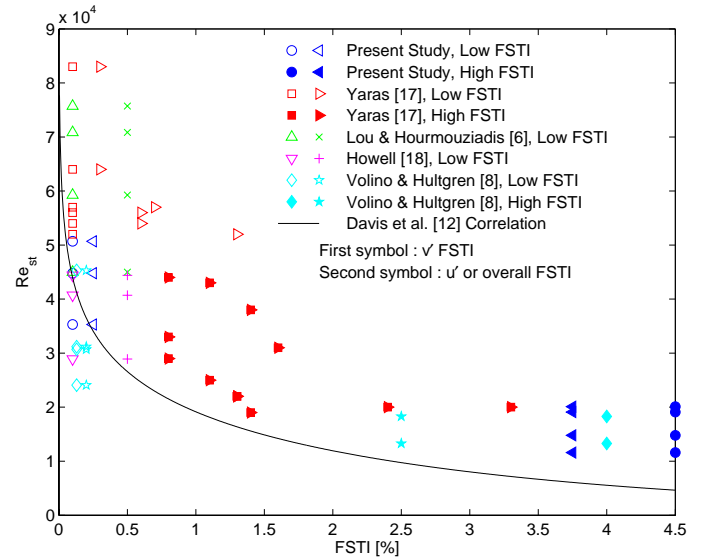


Fig. 18 Comparison of experimental data from various studies to correlation from Davis et al. [13]

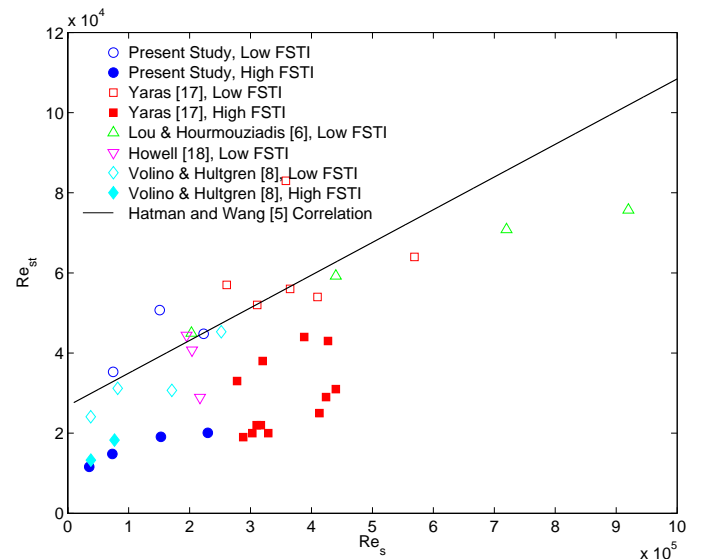


Fig. 19 Comparison of experimental data from various studies to correlation from Hatman and Wang [7]

with low FSTI (no turbulence grid), and the solid symbols are for higher FSTI cases. Agreement between the data and present correlation is good in all cases, and extends to Reynolds numbers over twice those of the present study. The agreement is better when the FSTI is based on v' . In terms of predicting the transition start location, the agreement between the correlation and data is generally within the experimental uncertainty resulting from the finite streamwise measurement station spacing.

Figure 17 compares the data from all cases to the long and short bubble correlations of Mayle [2] (Eq. 11-12). The trend of the data and correlations with Reynolds number agree, and the two correlation lines tend to bracket the data. If the long and short bubble correlations are used for the low and high FSTI cases, respectively, they are able to predict the transition start location about as accurately as the present

correlation in many cases. There are, however, cases in which the data fall midway between the long and short bubble correlations.

Figure 18 compares the data to the Davis et al. [13] correlation (Eq. 13). The correlation under predicts the distance from separation to transition in most cases. It tends to do best at the higher Reynolds numbers, and misses the Reynolds number dependence shown in Figs. 16 and 17.

Figure 19 compares the data to the Hatman and Wang [7] correlation (Eq. 14). Agreement between the data and correlation is good in the low FSTI cases, and prediction of the transition start location is as good as with the present correlation. With higher FSTI, however, the Hatman and Wang [7] correlation over predicts the distance from separation to transition.

CONCLUSIONS

1. A correlation for separated flow transition has been developed based on the measured growth of small disturbances in the separated shear layer. The correlation has been demonstrated effective over a range of Reynolds numbers and freestream turbulence levels through comparison to data from several studies from the literature.
2. Disturbances appear to begin growing at the beginning of the adverse pressure gradient region, where the boundary layer becomes unstable. The size of the initial disturbance at this location depends on the freestream turbulence level and the height of any obstruction placed on the surface. In dimensionless form, the size of the disturbance does not appear to depend on the Reynolds number.
3. The growth rate of the disturbances depends on the Reynolds number, and appears independent of the FSTI or size of the initial disturbance.
4. The transition location depends both on Reynolds number and FSTI. The present correlation represents a physics based improvement over previous correlations that did not account for both of these effects.
5. The wall normal component of the freestream turbulence is preferred for the correlation, and results in better predictions than the u' based FSTI. Measurement of freestream v' should be included in future experimental studies.

ACKNOWLEDGEMENTS

This work was sponsored by the NASA Glenn Research Center. The grant monitor is Dr. David Ashpis. Additional matching support was provided through a U.S. Naval Academy Recognition Grant. The second author received matching support from the Office of Naval Research as a postdoctoral fellow. Tabulated experimental results for Ref. [18] were provided by Stephen Roberts of Carleton University.

REFERENCES

- [1] Hourmouziadis, J., 1989, "Aerodynamic Design of Low Pressure Turbines," AGARD Lecture Series 167.
- [2] Mayle, R.E., 1991, "The Role of Laminar-Turbulent Transition in Gas Turbine Engines," *ASME Journal of Turbomachinery*, **113**, pp. 509-537.
- [3] Sharma, O.P., Ni, R.H., and Tanrikut, S., 1994, "Unsteady Flow in Turbines," AGARD Lecture Series 195, Paper No. 5.
- [4] Bons, J.P., Sondergaard, R., and Rivir, R.B., 2001, "Turbine Separation Control Using Pulsed Vortex Generator Jets," *ASME Journal of Turbomachinery*, **123**, pp. 198-206.
- [5] Volino, R.J., and Hultgren, L.S., 2001, "Measurements in Separated and Transitional Boundary Layers Under Low-Pressure Turbine Airfoil Conditions," *ASME Journal of Turbomachinery*, **123**, pp. 189-197.
- [6] Volino, R.J., 2002, "Separated Flow Transition Under Simulated Low-Pressure Turbine Airfoil Conditions: Part 1 – Mean Flow and Turbulence Statistics," *ASME Journal of Turbomachinery*, **124**, pp. 645-655.
- [7] Hatman, A., and Wang, T., 1999, "A Prediction Model for Separated Flow Transition," *ASME Journal of Turbomachinery*, **121**, pp. 594-602.
- [8] Lou, W., and Hourmouziadis, J., 2000, "Separation Bubbles Under Steady and Periodic-Unsteady Main Flow Conditions," *ASME Journal of Turbomachinery*, **122**, pp. 634-643.
- [9] Volino, R.J., 2002, "Separated Flow Transition under Simulated Low-Pressure Turbine Airfoil Conditions: Part 2 - Turbulence Spectra," *ASME Journal of Turbomachinery*, **124**, pp. 656-664.
- [10] Hughes, J.D. and Walker, G.J., 2001, "Natural Transition Phenomena on an Axial Compressor Blade," *ASME Journal of Turbomachinery*, **123**, pp. 392-401.
- [11] Volino, R.J., 2003, "Passive Flow Control on Low-Pressure Turbine Airfoils," *ASME Journal of Turbomachinery*, **125**, pp. 754-764.
- [12] Roberts, W.B., 1980, "Calculation of Laminar Separation Bubbles and Their Effect on Airfoil Performance," *AIAA Journal*, **18**, pp. 25-31.
- [13] Davis, R.L., Carter, J.E., and Reshotko, E., 1985, "Analysis of Transitional Separation Bubbles on Infinite Swept Wings," AIAA Paper 85-1685.
- [14] Volino, R.J., Schultz, M.P., and Pratt, C.M., 2001, "Conditional Sampling in a Transitional Boundary Layer Under High Free-Stream Turbulence Conditions," *ASME Journal of Fluids Engineering*, **125**, pp. 28-37.
- [15] Ligrani, P.M., and Bradshaw, P., 1987, "Spatial Resolution and Measurement of Turbulence in the Viscous Sublayer Using Subminiature Hot-Wire Probes," *Experiments in Fluids*, **5**, pp. 407-417.
- [16] Ligrani, P.M., Westphal, R.V., and Lemos, F.R., 1989, "Fabrication and Testing of Subminiature Multi-Sensor Hot-Wire Probes," *Journal of Physics E: Scientific Instruments*, **22**, pp. 262-268.
- [17] Walker, G.J., 1989, "Transitional Flow on Axial Turbomachine Blading," *AIAA Journal*, **27**, pp. 595-602.
- [18] Yaras, M.I., 2002, "Measurement of the Effects of Freestream Turbulence on Separation-Bubble Transition," ASME Paper GT-2002-30232.
- [19] Howell, R.J., 1999, "Wake – Separation Bubble Interactions in Low Reynolds Number Turbomachinery," Ph.D. Thesis, Whittle Laboratory, Cambridge University.

GT2005-68969

EXPERIMENTS WITH THREE DIMENSIONAL PASSIVE FLOW CONTROL DEVICES ON LOW-PRESSURE TURBINE AIRFOILS

Douglas G. Bohl and Ralph J. Volino
Department of Mechanical Engineering
United States Naval Academy
Annapolis, Maryland 21402
Email: volino@usna.edu

ABSTRACT

The effectiveness of three dimensional passive devices for flow control on low pressure turbine airfoils was investigated experimentally. A row of small cylinders was placed at the pressure minimum on the suction side of a typical airfoil. Cases with Reynolds numbers ranging from 25,000 to 300,000 (based on suction surface length and exit velocity) were considered under low freestream turbulence conditions. Streamwise pressure profiles and velocity profiles near the trailing edge were documented. Without flow control a separation bubble was present, and at the lower Reynolds numbers the bubble did not close. Cylinders with two different heights and a wide range of spanwise spacings were considered. Reattachment moved upstream as the cylinder height was increased or the spacing was decreased. If the spanwise spacing was sufficiently small, the flow at the trailing edge was essentially uniform across the span. The cylinder size and spacing could be optimized to minimize losses at a given Reynolds number, but cylinders optimized for low Reynolds number conditions caused increased losses at high Reynolds numbers. The effectiveness of two-dimensional bars had been studied previously under the same flow conditions. The cylinders were not as effective for maintaining low losses over a range of Reynolds numbers as the bars.

NOMENCLATURE

C_p	$2(p_T - p)/\rho U_e^2$, pressure coefficient
D	cylinder diameter
H	shape factor, δ^*/θ
L_s	suction surface length
P	center to center spacing of cylinders
p	pressure
p_T	upstream stagnation pressure
Re	$U_e L_s / \nu$, exit Reynolds number
s	streamwise coordinate, distance from leading edge
U_e	nominal exit freestream velocity, based on inviscid solution
u	mean streamwise velocity
u'	rms streamwise fluctuating velocity
y	cross-stream coordinate, distance from wall

z	spanwise coordinate
δ^*	displacement thickness
ν	kinematic viscosity
ρ	density
θ	momentum thickness
θ_b	momentum thickness in baseline case

INTRODUCTION

Boundary layer separation is a known problem on some modern low-pressure turbine (LPT) airfoils, due to the strong adverse pressure gradients created when designers impose higher loading in an effort to improve efficiency and lower cost by reducing airfoil count in engines. Separation bubbles, particularly those which fail to close, can result in a significant loss of lift and a subsequent degradation of engine efficiency (e.g. Hourmouziadis [1], Mayle [2], and Sharma et al. [3]). The problem is particularly relevant in aircraft engines. Airfoils optimized to produce maximum power under takeoff conditions may still experience boundary layer separation at cruise conditions, due to the lower density and therefore lower Reynolds numbers at altitude. A component efficiency drop of 2% may occur between takeoff and cruise conditions in large commercial transport engines, and the difference could be as large as 7% in smaller engines operating at higher altitudes [4, 5]. Prediction and control of suction side separation, without sacrifice of the benefits of higher loading, is therefore, crucial for improved engine design.

Separation on airfoils is complicated by boundary layer transition. Separated flow transition in the LPT has been the focus of several recent studies. Volino [6] provides a review and describes as follows the transition process on the suction side of a typical LPT airfoil. The strong acceleration on the leading section of the airfoil keeps the boundary layer thin and laminar, even in the presence of elevated freestream turbulence. In most cases Volino [6] observed that the boundary layer separated just downstream of the suction peak. If transition then occurred in the shear layer over the separation bubble, it caused the boundary layer to reattach.

A few recent studies have focused on control of transition and reattachment in the LPT. Some have used active devices. Huang et al.

[7] and Hultgren and Ashpis [8] employed high voltage electrodes to produce glow discharge plasma in a boundary layer to control separation. Bons et al. [4] used steady and pulsed vortex generator jets. Volino [9] used oscillating vortex generator jets with no net mass flow. Sieverding et al. [10] used adjustable devices built into the suction surface.

While active flow control provides a means for adjusting to changing flow conditions and in some cases the benefits of calmed regions [4, 9], passive flow control holds the advantage of simplicity. Van Treuren et al. [11], Lake et al. [12], Murawski and Vafai [13], Byerley et al. [14], Volino [15], Sieverding [10], Vera et al. [16], and Zhang and Hodson [17] used various passive devices under LPT conditions to control separation and in many cases reduce losses. Most employed a relatively simple modification, such as a small trip wire or bar (essentially roughness), on the suction surface of an airfoil.

Successful flow control results in a thin, attached boundary layer at the trailing edge of an airfoil, thereby reducing losses. The consensus of the studies listed above is that a device on the suction surface should be placed at or slightly downstream of the pressure minimum. This is a logical result, since the effects of a device farther upstream would be damped by the favorable pressure gradient, and a device too far downstream would lie under the separation bubble and be ineffective. Volino [15] used rectangular bars and found that the optimal bars were not large enough to immediately trip the boundary layer to turbulent, but instead allowed a small separation bubble to form. The bars introduced small disturbances that grew and caused transition and reattachment to move upstream of their location in the uncontrolled case, as explained in Volino and Bohl [18]. The optimal bar height depended on the flow conditions. As Re or freestream turbulence is lowered, the separation bubble becomes larger, so a larger bar is needed to produce enough of a disturbance to move transition sufficiently far upstream. A flow control device producing too small a disturbance will allow a larger separation bubble than desired, resulting in a thicker boundary layer downstream of reattachment and higher losses. Similarly, too large a disturbance will move transition farther upstream than necessary, resulting in a longer turbulent region and higher losses. Volino [15], Sieverding et al. [10], and Zhang and Hodson [17] all found that under steady flow conditions, devices optimized for low Re tend to increase losses at high Re . Devices optimized for high Re can be too small to be effective at low Re . Unsteady wakes from upstream airfoils promote transition and reattachment, and Zhang and Hodson [17] found that in unsteady flow optimal control was achieved using smaller devices than in comparable steady flow cases. This made it possible in unsteady flow to reduce losses with a single device over a wider range of Re .

Passive flow control devices of various geometries have been tested, but it is still uncertain if any particular device is superior. In preliminary testing, Volino [15] considered trip wires, rectangular bars, and delta wing vortex generators. All produced similar results. Sieverding et al. [10] found that straight trip wires were somewhat better than rows of spherical roughness elements, but only a limited number of cases were tested. Lake et al. [12] found dimples superior to other devices, presumably because the dimples produced less blockage than devices that protruded into the flow. Again, however, the number of cases considered was limited, and more recent evidence [15, 17] suggests that optimal devices should be quite small and produce minimal blockage even if they do extend into the flow. Zhang and Hodson [17] noted differences in transition location with straight and “wavy” trip wires and rectangular bars. The sharp backward facing step on a bar, for example, produced an earlier transition than a round trip wire of the same height. Still, this does not preclude that a bar and a slightly larger wire could produce comparable results.

It is still possible that some devices might prove better for reducing losses than others. Reynolds number can vary by an order of magnitude during engine operation given the change in ambient pressure between takeoff and cruise. Since passive devices by definition cannot be adjusted as conditions change, it is highly desirable to use devices that reduce losses over as large a Reynolds number range as possible. Given the potential payoff of a more efficient engine, it is worthwhile to further consider passive flow control devices of different geometries.

A row of small vertical cylinders is considered in the present study. The cylinders are located at the pressure minimum on the suction surface and the spacing between cylinders is varied. The geometry was chosen in the hope that in comparison to 2-dimensional bars or trips wires of the same height, isolated elements might produce a stronger disturbance due to the 3-dimensional nature of the flow around them, while presenting less blockage due to the gaps between elements. The net result would presumably be successful separation control with lower losses. Experimental conditions match the low freestream turbulence cases of Volino [15]. Details of the experimental conditions and the results are presented below.

EXPERIMENTS

Experiments were conducted in a low speed wind tunnel, described by Volino et al. [19]. Briefly, air enters through blowers and passes through a honeycomb, a series of screens, two settling chambers, and a three-dimensional contraction before entering the test section. At the exit of the contraction, the mean velocity is uniform to within 1%. The freestream turbulence intensity is $0.5\% \pm 0.05\%$. Nearly all of this freestream “turbulence” is actually streamwise unsteadiness at frequencies below 20 Hz and is not associated with turbulent eddies. The rms intensities of the three components of the unsteadiness are 0.7%, 0.2% and 0.2% in the streamwise, pitchwise and spanwise directions, respectively.

The test section, shown in Fig. 1, follows the contraction and consists of the passage between two airfoils. Details are listed in Table 1 and more information is available in Volino [6]. A large span to chord ratio of 4.3 was chosen to insure two-dimensional flow at the spanwise centerline of the airfoils, where all measurements were made. Upstream of each airfoil are flaps, which control the amount of bleed air allowed to escape from the passage. The flaps, along with a tailboard on the pressure side of the passage, are adjusted to produce the correct leading edge flow and pressure gradient along the airfoils. The flow in the passage matches that in a multi-blade cascade. The geometry of the passage corresponds to that of the Pak-B airfoil, which is an industry supplied research airfoil that is representative of a modern LPT design. It has been used in several studies, as noted in Volino [6].

Experimental conditions match the smooth airfoil baseline cases of Volino [6], who considered five Reynolds numbers ($Re=25,000$, $50,000$, $100,000$, $200,000$, and $300,000$). Reynolds numbers are based on the exit velocity from the passage and the suction surface length, L_s . Comparison data from cases with passive-bar flow control are from Volino [15]. The bars were of uniform rectangular cross section and extended along the airfoil, as shown in Fig. 2. The trailing edge of the bar was located at $s/L_s=0.51$, near the suction surface velocity peak. All bars were 6 mm wide in the streamwise direction. Bar heights of 0.4 mm, 0.8 mm and 1.6 mm were used. The bar heights were all less than 1% of L_s . They compare to local boundary layer thickness at the bar location of about 3.8 mm, 2.7 mm, 2.0 mm, 1.4 mm and 1.2 mm in the baseline $Re=25,000$ through $300,000$ cases respectively.

A row of small vertical cylinders is used in the present experimental cases. The cylinders are $D=6$ mm in diameter with one end affixed to

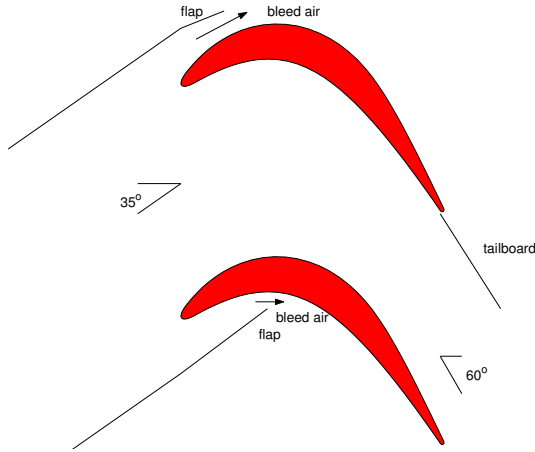


Fig. 1 Schematic of the test section

the suction surface and the other extending into the flow. The cylinders are located in a line at the suction peak, in the same location as the bars described above, as shown in Fig. 2. Cylinder heights of 0.4 mm and 1.6 mm were considered, matching the smaller and larger bar heights of Volino [15]. Center to center cylinder spacings ranging from a pitch, P , of $1D$ (i.e. the cylinders were touching) to $30D$ were considered.

Measurements

Pressure surveys were made for each case using a pressure transducer (0-870 Pa range Validyne transducer) and a Scanivalve. Stagnation pressure was measured with a pitot tube upstream of the passage inlet, and eleven pressure taps were located on each airfoil along their spanwise centerlines. The uncertainty in C_p is 7% at $Re=25,000$, and 4% in other cases. Most of this uncertainty is due to bias error. Stochastic error was minimized by averaging pressure transducer readings over a 10 second period. The flow control cylinders were moved in the spanwise direction allowing documentation with the pressure taps directly downstream of the center of one cylinder and with the taps midway between the centers of two adjacent cylinders.

Profiles of the streamwise velocity component in the suction side boundary layer were measured for the $Re=50,000$ and $300,000$ cases near the trailing edge at $s/L_s=0.944$. Profiles were measured at several spanwise locations relative to the position of the upstream cylinders. Data were acquired with a hot-wire anemometer (AA Lab Systems model AN-1003) and a single sensor boundary layer probe (TSI model 1218-T1.5). The sensor diameter is $3.8 \mu\text{m}$, and the active length is 1.27 mm . At each measurement location, data were acquired for 26 seconds at a 20 kHz sampling rate (2^{19} samples). Data were acquired at 60 wall normal locations in each profile, extending from the wall to the free-stream, with most points concentrated in the near wall region. The closest point was within 0.1 mm of the wall, which corresponds to $y/L_s=0.0004$ and between 0.02 and 0.04 boundary layer thicknesses. Uncertainties in the mean velocity are 3-5% except in the very near wall region where near-wall corrections (Wills [20]) were applied to the mean velocity. Uncertainties in the momentum and displacement thicknesses computed from the mean profiles are 10%. Uncertainty in the shape factor, H , is 8%. The uncertainty in the fluctuating streamwise velocity is below 10%, except in the very near wall region ($y < 1 \text{ mm}$, $y/L_s < 0.004$) of the $Re=300,000$ cases, where spatial averaging effects, due to the finite length of the hot-wire sensor, may become important. This is discussed in Volino [6].

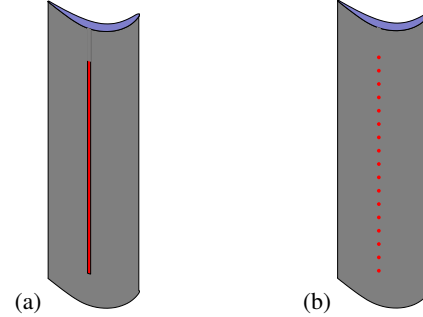


Fig. 2 Scale drawing of suction side airfoil showing location of a) bar, or b) cylinders

Table 1: Test section parameters

Axial Chord [mm]	True Chord [mm]	Pitch [mm]	Span [mm]	Suction side, L_s [mm]	Inlet flow angle	Exit flow angle	$\frac{U_e}{U_{inlet}}$
153.6	170.4	136.0	660.4	228.6	35°	60°	1.64

RESULTS

Pressure Profiles

Suction side pressure profiles for the cases with larger (1.6 mm high) cylinders are shown in Figs. 3-5. Also shown in each figure are the corresponding baseline results from Volino [6], the 1.6 mm thick bar case results from Volino [15], and an inviscid solution for flow through the passage. Figure 3 shows results at $Re=25,000$ with various cylinder spacings and the pressure taps directly downstream of one cylinder. The data agree with the inviscid solution in the favorable pressure gradient region. The near wall flow slows as it approaches a cylinder or bar, causing a drop in the measured C_p below the inviscid solution at the fifth pressure tap. If the boundary layer separates and does not reattach, there is a drop in the suction peak, as indicated by low C_p values. In addition to this effect, if the blockage caused by a bar or cylinder is sufficiently high, the streamlines immediately downstream will be displaced as they flow over the sixth pressure tap, which may cause the measured local C_p to either rise or fall relative to the inviscid solution, depending on the geometry of a particular case. For controlling separation, cylinders with spacing of $P=2D$ or more are ineffective at $Re=25,000$. There is a plateau in C_p in the adverse pressure gradient region extending to the trailing edge, indicating a separation bubble that does not reattach. The $P=1D$ (touching) cylinders and the solid bar result in a large separation bubble which appears to be starting to reattach by the trailing edge, as indicated by the drop in C_p back toward the inviscid value at the last pressure tap. Figure 4 show the results at $Re=50,000$ with the pressure taps directly downstream of one cylinder ($z/P=0$, Fig. 4a) and with the taps downstream of the midpoint between adjacent cylinders ($z/P=0.5$, Fig. 4b). In the baseline case, the boundary layer does not reattach. With $P=1D$ or the solid bar, reattachment moves upstream to $s/L_s=0.78$. With $P=2D$ reattachment occurs at $s/L_s=0.86$. With $P>2D$ the effect of the cylinders is not observed until the last pressure tap, but even with $P=30D$ there is some effect on C_p at $s/L_s=0.94$ and $z/P=0$. As the spacing increases, the C_p values increase from the inviscid solution toward the baseline case value. At $z/P=0.5$ and $s/L_s=0.94$, C_p is affected for spacings up to $20D$, although not as strongly as it is at $z/P=0$. For $P=24D$ and $30D$, the cylinders are too far apart to affect C_p at $z/P=0.5$. The results at $Re=100,000$ are shown in Fig. 5. In the baseline case, there is a clear separation bubble, and it reattaches near

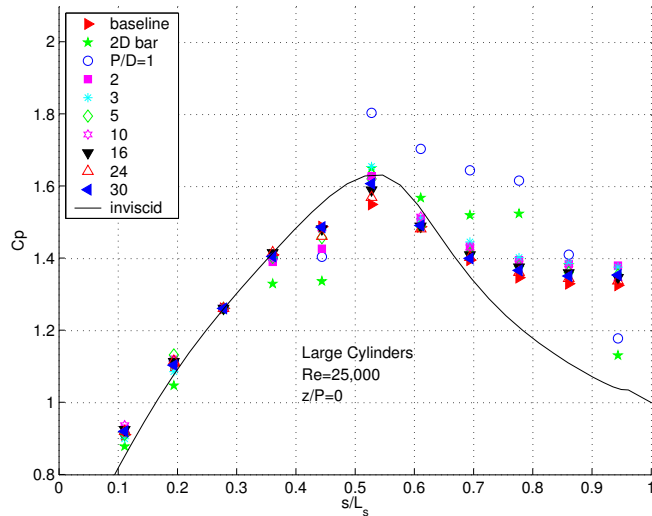


Fig. 3 Pressure profiles, large cylinders, $Re=25,000$, $z/P=0$

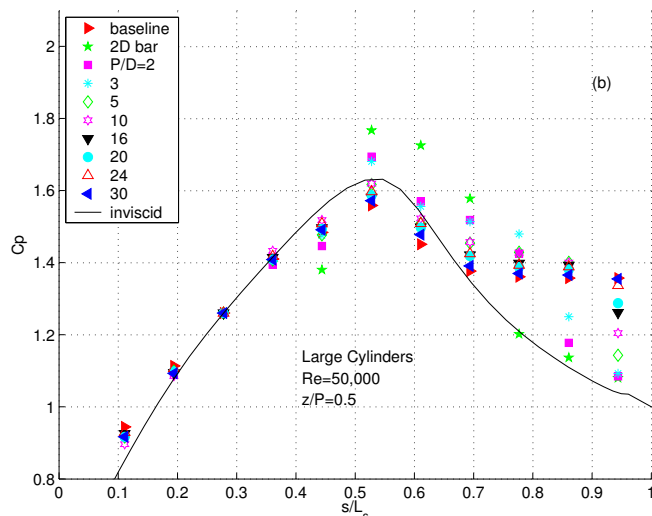
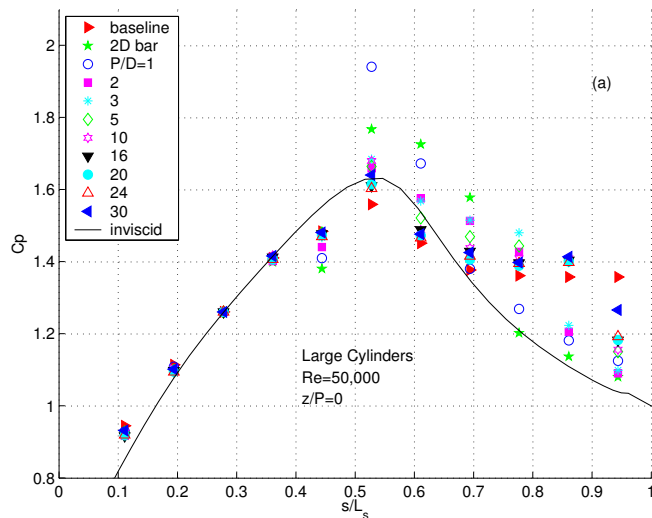


Fig. 4 Pressure profiles, large cylinders, $Re=50,000$, a) $z/P=0$, b) $z/P=0.5$

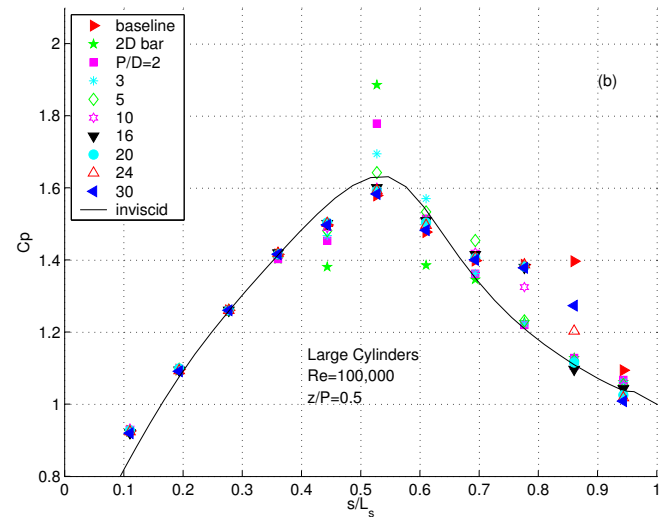
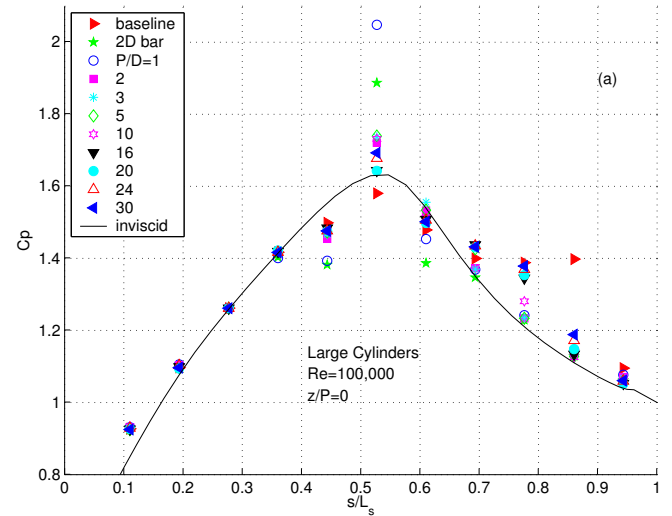


Fig. 5 Pressure profiles, large cylinders, $Re=100,000$, a) $z/P=0$, b) $z/P=0.5$

the trailing edge. With $P \leq 3D$, the separation is essentially eliminated. With $P=5D$ there is a separation, but reattachment by $s/L_s=0.78$. For $P \leq 5D$, the C_p values are nearly uniform across the span. For $10D \leq P \leq 30D$, the boundary layer appears to be at least starting to reattach by $s/L_s=0.86$, with the effect on C_p greater at $z/P=0$. Results for the $Re=200,000$ cases (not shown) are similar to those described above. The boundary layer separates in the baseline case and reattaches by $s/L_s=0.86$. Cylinders with $P \leq 16D$ effectively suppress the separation across the span. For $P > 16D$, the boundary layer is attached at $s/L_s=0.78$ and $z/P=0$, but is still separated at $z/P=0.5$. At $Re=300,000$ there is only a small separation bubble in the baseline case, and it reattaches by $s/L_s=0.78$. Cylinders with spacing up to $30D$ appear to suppress this small bubble across the span.

Comparing the results at $z/P=0$ and $z/P=0.5$, the spanwise influence of each cylinder can be estimated. If the region affected by the cylinder is assumed to spread linearly in the spanwise direction as the flow convects downstream, the half angle for the spreading is between roughly 30 and 40 degrees. Changes in C_p at $z/P=0.5$ could be due to local turbulence arising from the cylinder induced disturbances. It is

also possible, however, that these changes in C_p are due to changes in the mean flow resulting from the cylinder induced changes at $z/P=0$.

The smaller (0.4 mm high) cylinders and bar are ineffective at $Re=25,000$ and $50,000$. The boundary layer separates and does not reattach. At $Re=100,000$, as shown in Fig. 6, the cylinders cause the first indication of reattachment to move upstream from near the trailing edge to $s/L_s=0.78$ or 0.86 . Cylinder spacings up to $10D$ were considered, and the C_p values decrease from the baseline case values toward the inviscid solution as P is decreased. No significant spanwise variation in C_p was observed. The results at $z/P=0.5$ are essentially the same as those shown in Fig. 6 for $z/P=0$. Results for the $Re=200,000$ cases are shown in Fig. 7. The results are very similar to those of the $Re=100,000$ cases, but with reattachment shifted about $0.08L_s$ upstream. When $Re=300,000$ the baseline separation bubble is small, and cylinders effectively eliminate it for all value of P .

The presumably more complex 3-dimensional flow around isolated ($P>1D$) cylinders did not produce disturbances better able to control separation than the touching ($P=1D$) cylinders or two-dimensional bars. In fact, the opposite was observed. The pressure profiles show that as the spacing between cylinders increases, their ability to promote reattachment decreases. This is not simply due to the finite spanwise influence of each cylinder, as very little spanwise variation was observed for cases with $P<10D$. Whether increasing the spacing results in reduced flow blockage and losses will be considered next as the velocity profile results are considered.

Velocity Profiles

Mean and fluctuating streamwise velocity profiles for the large cylinder $Re=50,000$ cases at $z/P=0$ are shown in Fig. 8. Data were acquired near the trailing edge ($s/L_s=0.94$). The baseline case shows a thick separation bubble in the mean profile and a small peak in u' in the shear layer over the bubble. The 2-dimensional bar case exhibits a fully attached turbulent mean profile shape and a typical turbulent u' profile with a near wall peak. For the cases with cylinder spacing up to $P=5D$, the mean profiles appear attached and turbulent, but the trend is toward a less full profile as P increases. This trend continues for the cases with $P\geq 20D$, with the mean profiles in these cases appearing only partially reattached. The peaks in the u' profiles increase in magnitude and move farther from the wall as the cylinder spacing is increased. High peaks away from the wall are typical of transitioning and reattaching boundary layers. Transition begins in the shear layer over the separation bubble, so u' should be high at this location. The high u' peaks result from the switching between intermittently attached-turbulent-like and separated-laminar-like states. Figure 9 shows the profiles at $z/P=0.5$. For $P\leq 5D$, the profiles appear essentially the same as those at $z/P=0$. For $P\geq 20D$ the mean profiles show a separation bubble, somewhat thinner than that of the baseline case, and u' profiles with only a small peak in the shear layer over the separation bubble. Figure 10 shows the velocity profiles at several spanwise positions for the $P=30D$ case. The progression from attached flow at $z/P=0$ to separated flow at $z/P=0.5$ is clear. The profiles at $z/P=0.13$ and 0.20 are on the edge of the attached flow region with u' peaks between the high peaks at low z/P and the small shear layer peaks at higher z/P . The influence of the cylinders to a spanwise position between $z/P=0.13$ and 0.20 suggests a half angle for the spread of the cylinder influence of about 20 degrees. The velocity profile data of Figs. 8-10 are consistent with the conclusions drawn from the corresponding pressure coefficient data of Fig. 4.

The information concerning separation in the mean profiles can be presented in terms of the shape factor, H . The shape factor rises to about 4 when a laminar boundary layer separates, and reaches higher values as a separation bubble thickens. This is due to an increase in

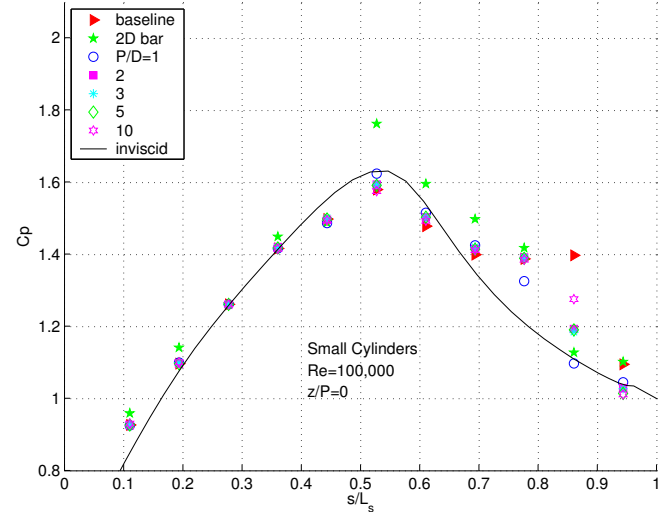


Fig. 6 Pressure profiles, small cylinders, $Re=100,000$, $z/P=0$

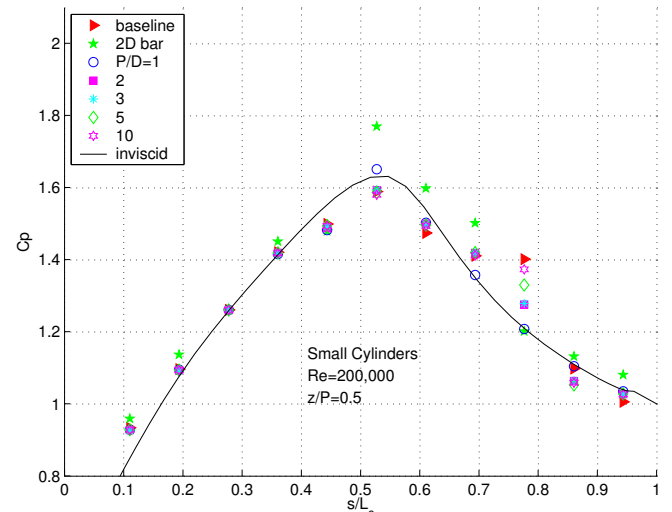


Fig. 7 Pressure profiles, small cylinders, $Re=200,000$, $z/P=0$

the displacement thickness while the momentum thickness remains nearly constant. If the boundary layer reattaches, the displacement thickness drops and the momentum thickness begins to rise. The shape factor reaches a turbulent value of about 1.4 after recovering from the separation. Figure 11 shows H as a function of z/P for the $Re=50,000$ cases with the larger cylinders. In the baseline case, $H=6.5$, indicating a thick separation bubble. With the two-dimensional bar, $H=1.6$, indicating that the boundary layer has reattached and is nearing fully developed turbulent conditions. With cylinder spacing up to $P=5D$, H is spanwise uniform. With $P=5D$, H is about 2.3, indicating that the boundary layer has reattached but is not fully recovered from the separation. For $P\geq 20D$, $H\approx 3$ at $z/P=0$, indicating the boundary layer has just begun to reattach at this location. For $P\geq 20D$ and higher z/P , H is between 4 and 5.5 indicating the boundary layer is still separated. These values are still below the baseline value of 6.5, however, indicating that even the widely spaced cylinders are effective in keeping the separation bubble thinner.

Velocity profiles for the $Re=300,000$ cases with the larger bar and cylinders are shown in Figs. 12-14. Figure 12 shows the profiles at $z/P=0$. The mean profiles show that the boundary layer is attached in

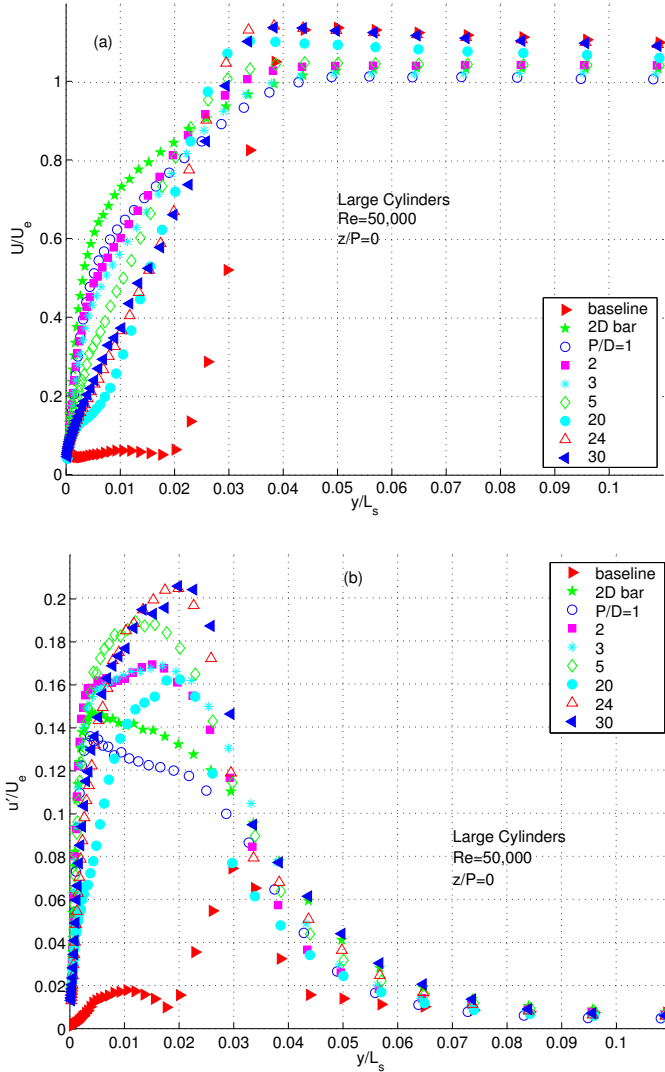


Fig. 8 Trailing edge velocity profiles, large cylinders, $Re=50,000$, $z/P=0$, a) U/U_e , b) u'/U_e

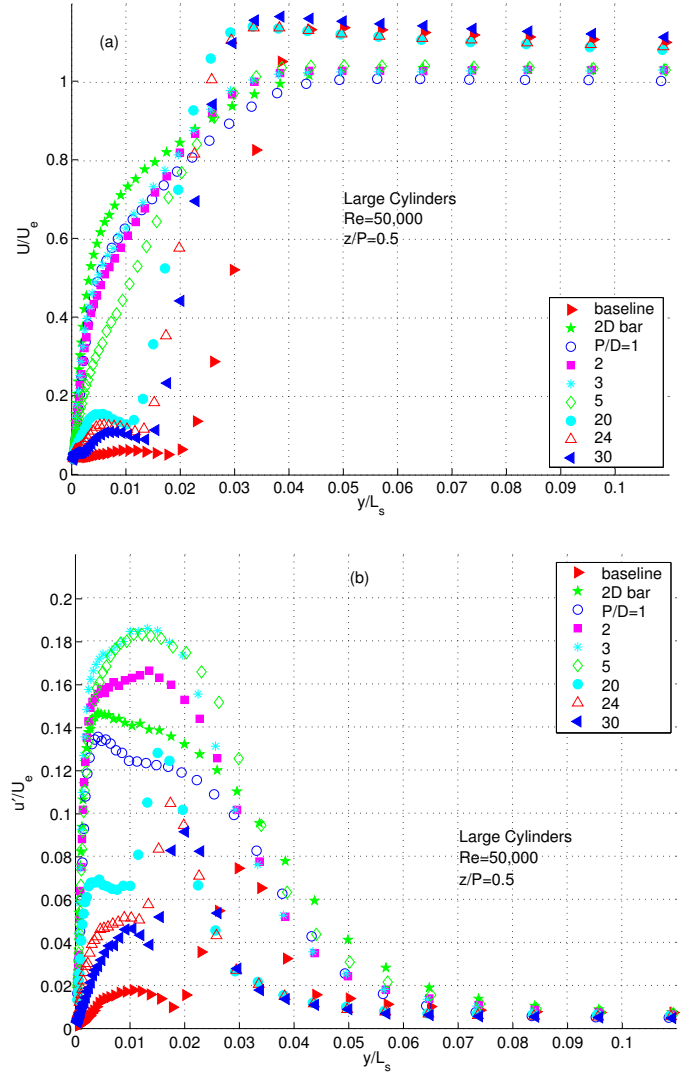


Fig. 9 Trailing edge velocity profiles, large cylinders, $Re=50,000$, $z/P=0.5$, a) U/U_e , b) u'/U_e

all cases. The u' peaks are near the wall, as expected for attached turbulent boundary layers. The baseline case has the highest u' peak, indicating that it is the case with the least developed turbulence. The bar and cylinders move transition upstream, resulting in a more developed turbulent boundary layer by the trailing edge. Both the mean and u' profiles collapse for the cases with $P \geq 20D$. This suggests that the cylinders are far enough apart in these cases so that they act as if isolated from each other. Both the mean and u' profiles show that the boundary layer becomes thicker as the cylinder spacing is decreased. The $P=1D$ case has a second u' peak away from the wall that is not present in the two-dimensional bar case. The touching cylinders appear to generate more turbulence than the bar. Figure 13 shows the profiles at $z/P=0.5$. The profiles for the $P=24D$ and $30D$ cases are very similar to the baseline results, again suggesting that with large enough spacing the cylinders are effectively isolated from each other and cannot directly influence the flow across the entire span. As P is reduced, the boundary layer becomes thicker, and u' assumes a more turbulent like shape. Figure 14 shows the profiles at several spanwise positions for the $P=30D$ case. The cylinders appear to influence the boundary layer u' nearly uniformly from $z/P=0$ to

$z/P=20$. For $z/P > 27$, the cylinders have little influence and the profiles are very similar to the baseline case profiles. The spanwise extent of the cylinder influence spreads at a half angle of about 20 degrees for a strong effect on the boundary layer and about 30 degrees for some effect.

Figure 15 shows the shape factor at $s/L_s=0.94$ for the profiles of the $Re=300,000$ cases with the larger cylinders. The boundary layer is attached, so the shape factor is between 1.4 and 1.7 in all cases. Figure 16 shows the momentum thickness for these cases. The momentum thickness is related to losses in the boundary layer, and in cases with equal shape factor and exit flow angle, the momentum thickness is directly proportional to profile losses (Howell et al. [21]). In the $Re=50,000$ cases, the large variation in H (Fig. 11) precludes a comparison of losses based on θ , but with the smaller range of H at $Re=300,000$ (Fig. 15) the comparison is appropriate. Figure 16 shows that the cylinders cause a rise in momentum thickness above the baseline case value and that the effect increases as cylinder spacing is decreased. Since the separation bubble is small even in the baseline case, the cylinders and bars add an unnecessary disturbance and

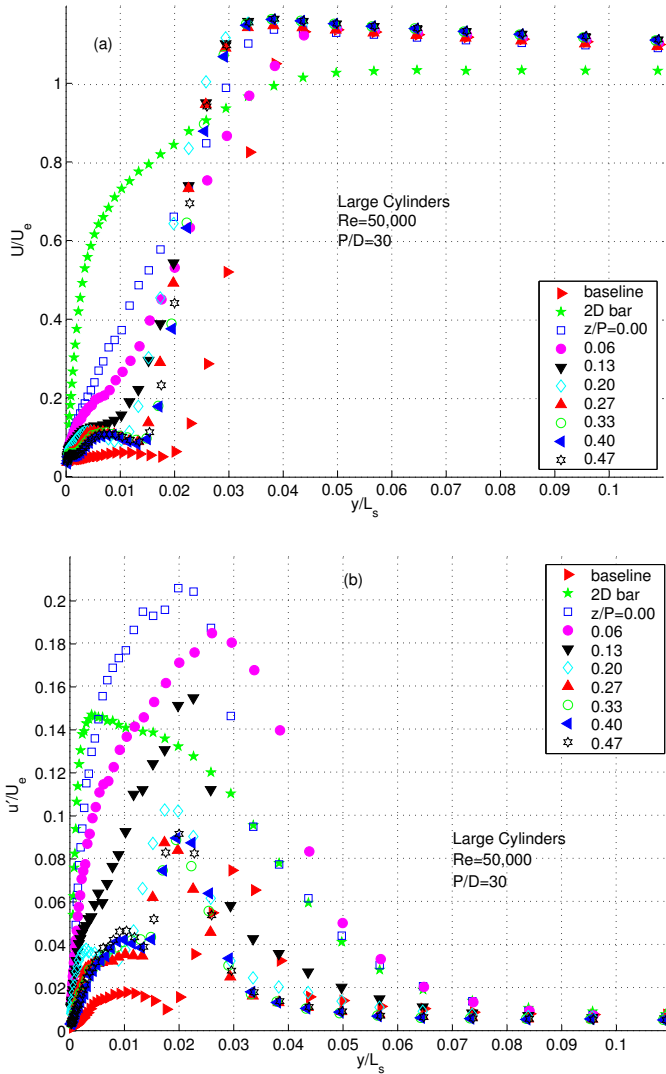


Fig. 10 Trailing edge velocity profiles, large cylinders, $Re=50,000$, $P/D=30$, a) U/U_e , b) u'/U_e

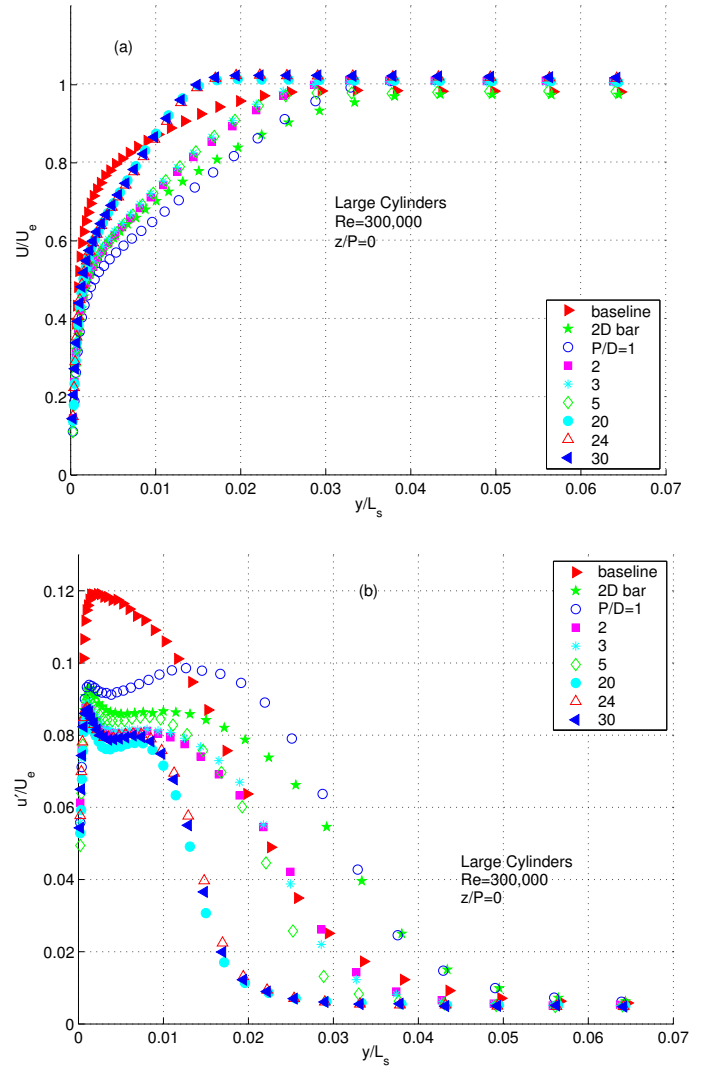


Fig. 12 Trailing edge velocity profiles, large cylinders, $Re=300,000$, $z/P=0$, a) U/U_e , b) u'/U_e

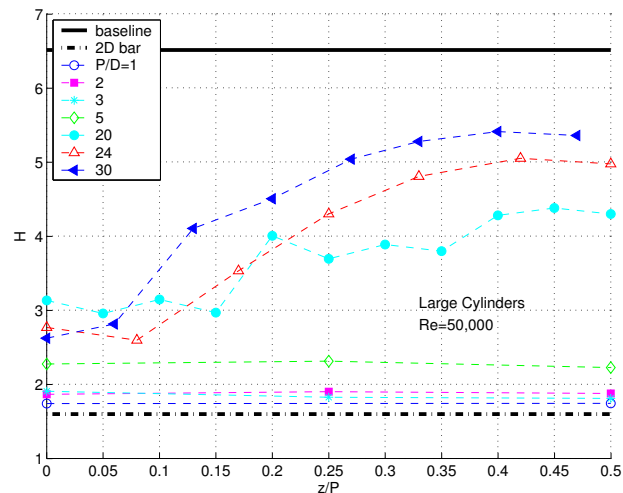


Fig. 11 Shape factor, H , at trailing edge, large cylinders, $Re=50,000$

increase losses. The more widely spaced cylinders cause less blockage and create less of a disturbance, therefore the losses are lower.

Velocity profiles for the $Re=50,000$ cases with the smaller bar and cylinders are shown in Fig. 17. Cylinder spacings up to $P=5D$ were considered. No variation was observed between the results from different spanwise locations, so only the results from $z/P=0$ are shown. The boundary layer did not reattach for cases with $P \geq 2D$, although the separation bubble was slightly thinner and there was a slight increase in the u' peak compared to the baseline case. With $P=1D$ the boundary layer appears to be on the verge of reattachment, and with the two-dimensional bar the boundary layer has just begun to reattach. The smaller cylinders are inadequate for control of the boundary layer at this Reynolds number, as previously indicated by the pressure profiles.

The effect of the smaller cylinders on the velocity profiles at $Re=300,000$ are shown in Fig. 18. No spanwise variation was observed, so only results from $z/P=0$ are shown. The mean profile for the $P/D=1$ case is noticeably different than those for the other cases, including the 2D bar case. As was noted above, the touching cylinders apparently generate more turbulence than the 2D bar, resulting in a thicker boundary layer. As was the case with the larger cylinders (Fig.

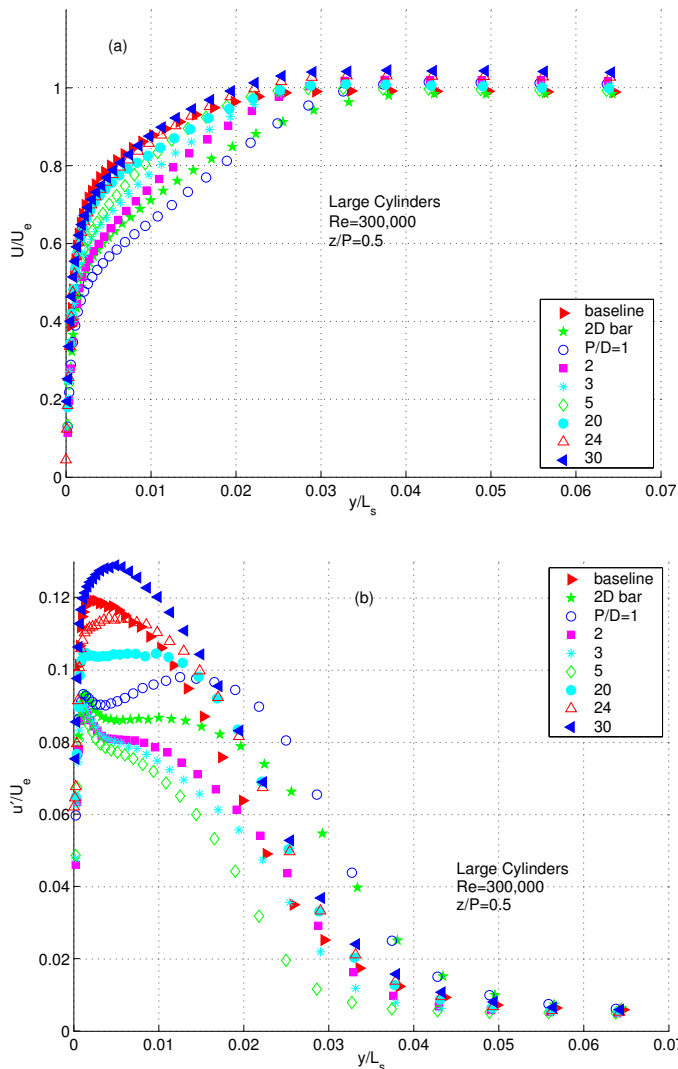


Fig. 13 Trailing edge velocity profiles, large cylinders, $Re=300,000$, $z/P=0.5$, a) U/U_e , b) u'/U_e

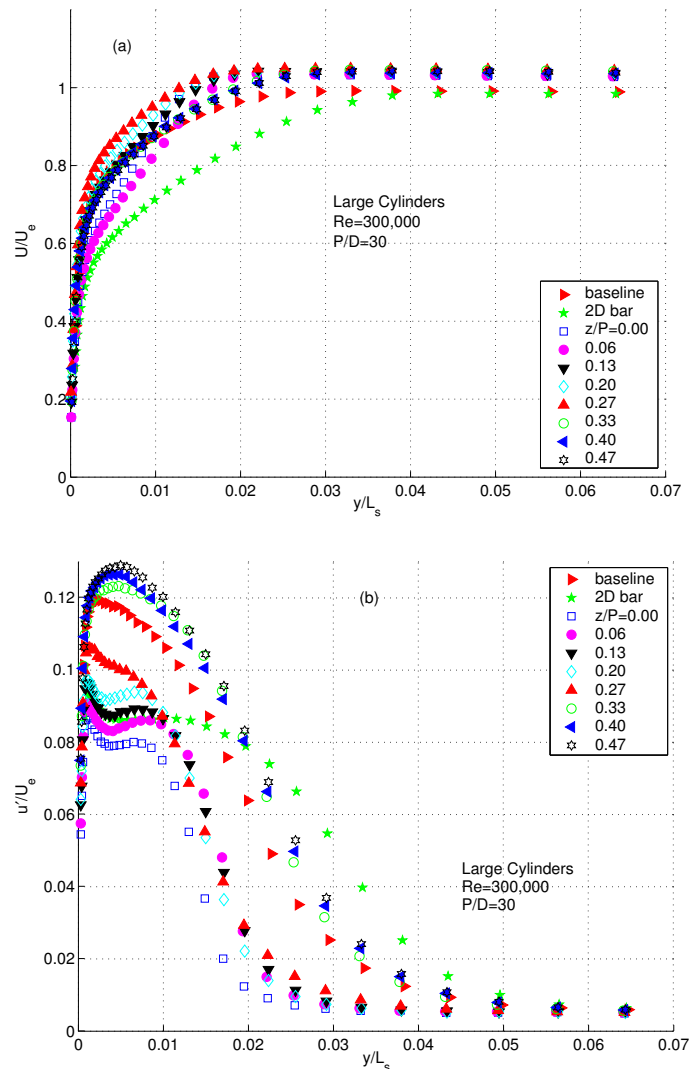


Fig. 14 Trailing edge velocity profiles, large cylinders, $Re=300,000$, $P/D=30$, a) U/U_e , b) u'/U_e

12), the smaller cylinders cause a drop in the u' peak from the baseline case value, indicating that the cases with cylinders are closer to fully developed turbulent behavior. Shape factors are shown in Fig. 19 as a function of spanwise position. There is little variation between cases, as expected since the separation bubble is small and the boundary layer has fully reattached in all cases. The momentum thickness is shown in Fig. 20. All of the cases with cylinders have higher momentum thickness than the baseline case. The case with $P=1D$ has the highest values, again indicating that the touching cylinders generate higher losses than the two-dimensional bars or more widely spaced cylinders.

DISCUSSION

The results presented above suggest that the half angle for the spreading of the disturbances from the cylinders is about 30 degrees. This is a rough estimate due to the finite spacing between pressure tap locations and the finite number of cylinder spacings investigated, but the half angle roughly agrees with the spreading angle for turbulent spots in an adverse pressure gradient, as given by D'Ovidio et al. [22]. This angle suggests that a cylinder spacing of between $P/D=5$ and

$P/D=10$ is necessary to insure flow control across the span. The velocity profiles showed good spanwise uniformity for $P/D<10$.

The optimal spacing for spanwise disturbances was investigated in an analytical study by Tumin and Ashpis [23]. They considered disturbances in both favorable and adverse pressure gradient flows, including the favorable pressure gradient found in the upstream region of the present test section. Although these results do not apply directly to the adverse pressure gradient region of the present study, they can be extrapolated to the present conditions. They suggest an optimal spacing for maximum disturbance growth in the $Re=50,000$ cases of $P/L_s \approx 0.03$. For the $Re=300,000$ cases, the optimal spacing would be $P/L_s \approx 0.012$. With the present cylinder diameter of 6 mm, these spacings correspond to $P/D=1$ and $P/D=0.4$ respectively, and could not be achieved unless the cylinders were touching. Consistent with this, the present results show that the disturbance created by the cylinders decreases as the spacing increases. To better test the Tumin and Ashpis [23] results, however, smaller diameter, separated cylinders with the recommended spacing should be considered.

The results at $Re=50,000$ show that the larger cylinders with the closest spacing are needed to effectively control separation. At

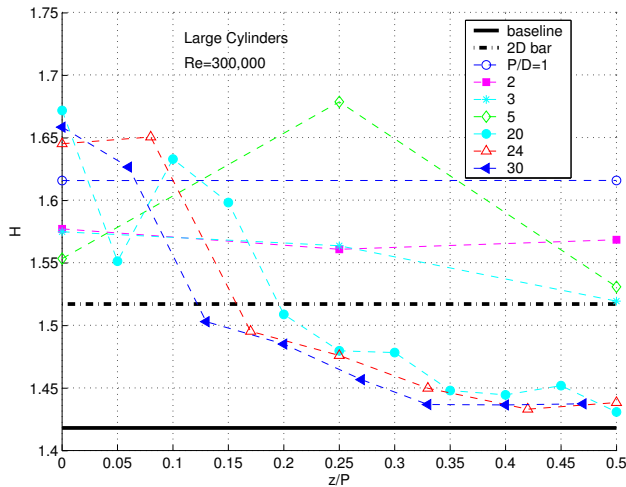


Fig. 15 Shape factor, H , at trailing edge, large cylinders, $Re=300,000$

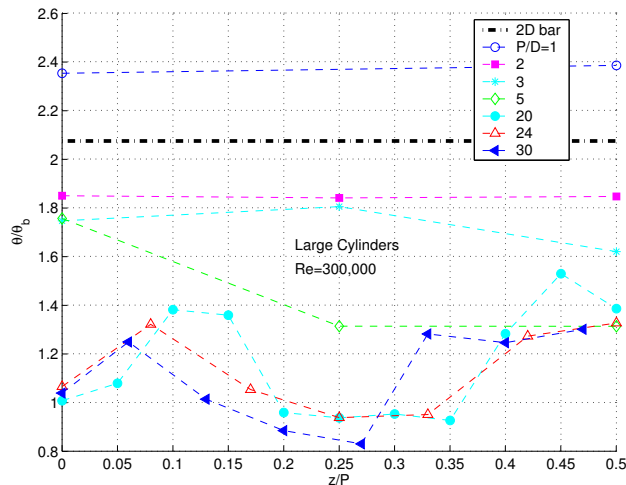


Fig. 16 Momentum thickness at trailing edge, large cylinders, $Re=300,000$

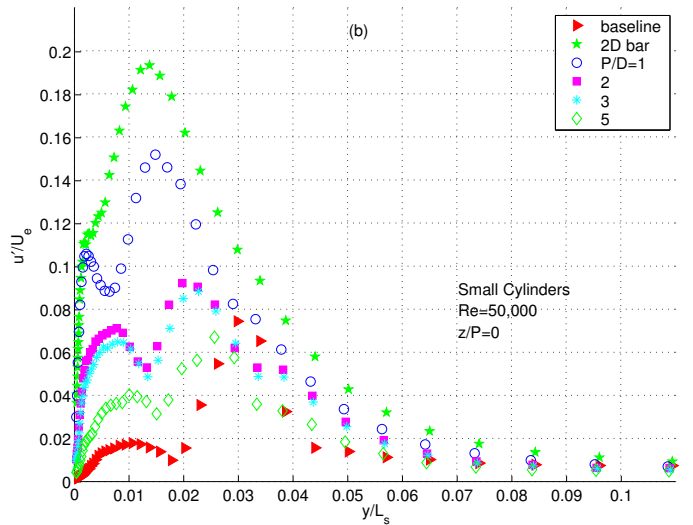
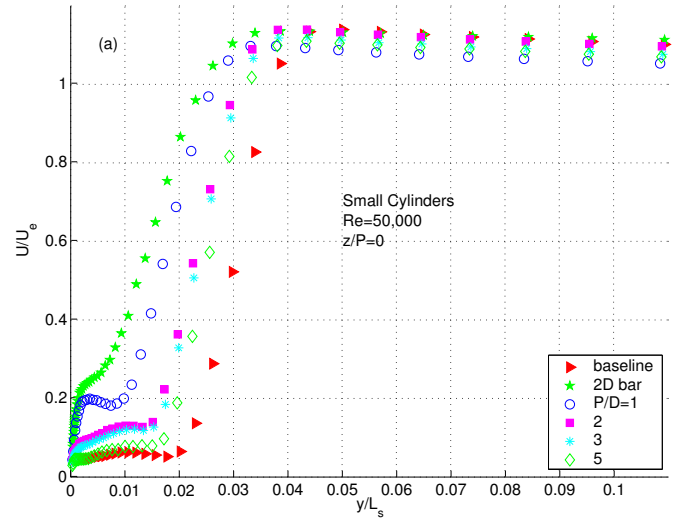


Fig. 17 Trailing edge velocity profiles, small cylinders, $Re=50,000$, $z/P=0$, a) U/U_e , b) u'/U_e

$Re=300,000$, the separation bubble is small in the baseline case, and cylinders or bars cause transition to move upstream, increasing losses. Hence, the thinnest, most widely spaced (which in the limit means non-existent) devices are optimal. The cylinders which are best at $Re=50,000$ cause significantly higher losses at $Re=300,000$. This is the same result found by Volino [15] using two-dimensional bars, and agrees with other findings in the literature, as noted above. So long as the cylinders are close enough to provide spanwise uniformity, it appears that varying the cylinder (or bar) thickness and varying the cylinder spacing are both effective for controlling the transition location and moving it to an optimal location for minimizing losses.

The present results can address the question of whether separated cylinders provide an advantage over a 2-dimensional bar. A case with a 2-dimensional bar that is capable of controlling separation while keeping losses to a minimum at a low Reynolds number should be compared to a case with cylinders that are thicker than this optimal bar but produce the same reattachment and low losses. Cases with these same geometries should then be compared at a high Reynolds number to see which results in lower high- Re losses. The thin bar in the

present study results in marginally reattached flow at $Re=50,000$. The larger cylinders result in spanwise uniform reattachment at $Re=50,000$ when $P/D=5$. The momentum thicknesses at $s/L_s=0.94$ for these two cases are within 8% of each other. At $Re=300,000$ the thin bar results in a momentum thickness 7% above the baseline case value, while the thick, $P/D=5$ cylinders result in a spanwise averaged momentum thickness that is 46% above the baseline value. Clearly the thin 2-dimensional bar is superior to the thicker cylinders. This comparison is not completely adequate, however, since the thin bar only causes marginal reattachment at $Re=50,000$, while the thick cylinders result in a somewhat more complete reattachment. Volino [15] also considered an intermediate bar with thickness twice that of the thin bar considered above. At $Re=50,000$ the intermediate bar induced complete reattachment with $H=1.8$ and $\theta/\theta_b=1.23$. These results are very close to those obtained with the large cylinders spaced at $P/D=3$. At $Re=300,000$ the intermediate bar resulted in $H=1.59$ and $\theta/\theta_b=1.29$. The thick, $P/D=3$ spaced cylinders resulted in an approximately equal shape factor, but $\theta/\theta_b=1.72$. With this better comparison, it is still clear that a thin bar is superior to larger cylinders.

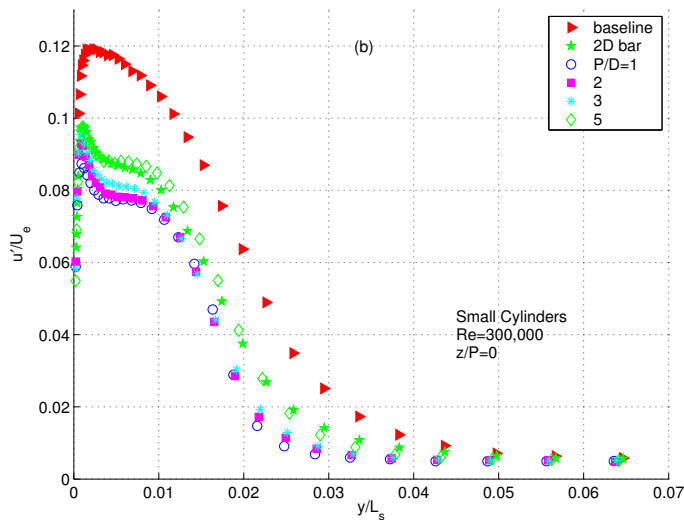
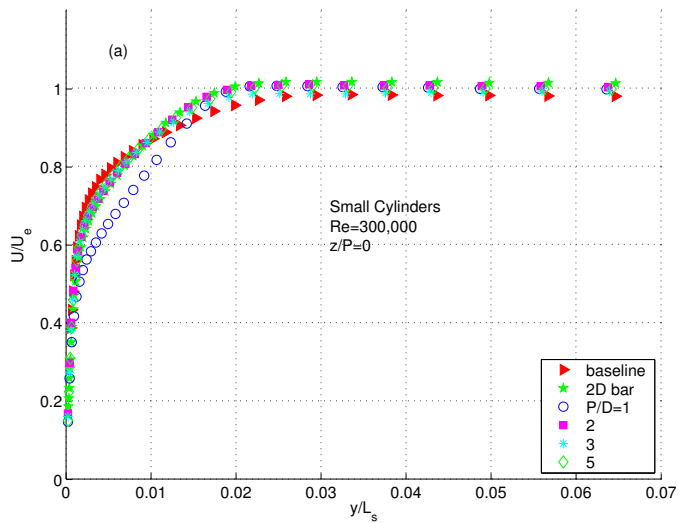


Fig. 18 Trailing edge velocity profiles, small cylinders, $Re=300,000$, $z/P=0$, a) U/U_e , b) u'/U_e

The present results support the conclusions of Sieverding [10] and Zhang and Hodson [17] who found that 2-dimensional bars or trips are as good or better than 3-dimensional devices for controlling separation. The present results cannot be considered absolutely conclusive, however, since only a single geometry was considered under a limited number of conditions. The number of possible geometries and spacings for three dimensional devices is infinite, so it will never be possible to prove conclusively through experiments that 2-dimensional devices are always better. Further study of devices such as the dimples considered by Lake et al. [12] would be useful. The effects of high freestream turbulence and unsteady wakes should also be considered. Perhaps thinner, smaller diameter cylinders with spacings closer to those extrapolated from Tumin and Ashpis [23] could provide better separation control with lower losses. This is merely speculation. What can be said is that the present results add to the evidence that simple 2-dimensional bars are preferable.

CONCLUSIONS

A row of small cylinders located at the suction peak on an LPT airfoil were effective for separation control. The reattachment of the

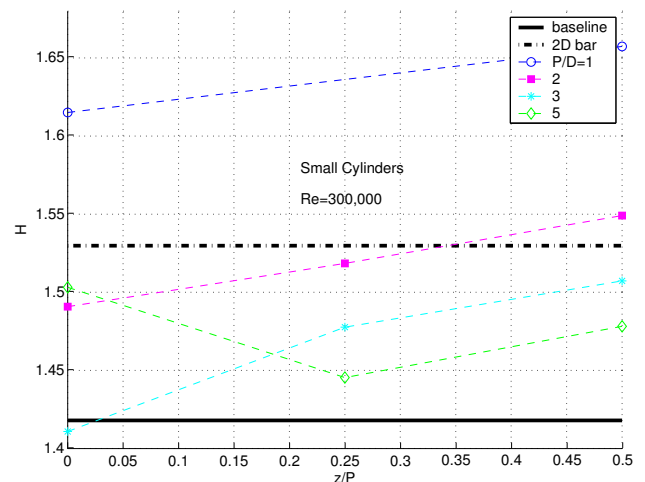


Fig. 19 Shape factor, H , at trailing edge, small cylinders, $Re=300,000$

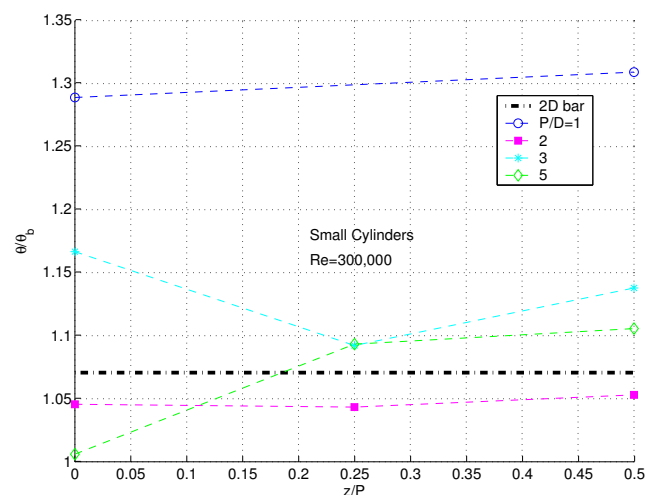


Fig. 20 Momentum thickness at trailing edge, small cylinders, $Re=300,000$

boundary layer moves upstream as the cylinder height is increased or the cylinder spacing is decreased. The half angle of the spreading of the disturbance created by the cylinders was of the order 30 degrees. This is roughly the same as the expected spreading angle for a turbulent spot under the same adverse pressure gradient conditions. Based on this angle, the maximum allowable spacing for spanwise uniform separation control can be determined. By varying the cylinder height and spacing, an optimal reattachment location can be achieved for minimum losses at a given Reynolds number. Cylinders optimized for low Reynolds numbers resulted in higher losses at high Reynolds numbers. The present results add to the evidence that 3-dimensional passive flow control devices are not as effective as 2-dimensional bars for minimizing losses over a range of Reynolds numbers.

ACKNOWLEDGEMENTS

This work was sponsored by the NASA Glenn Research Center. The grant monitor is Dr. David Ashpis. The first author received matching support from the Office of Naval Research as a postdoctoral fellow.

REFERENCES

- [1] Hourmouziadis, J., 1989, "Aerodynamic Design of Low Pressure Turbines," AGARD Lecture Series 167.
- [2] Mayle, R.E., 1991, "The Role of Laminar-Turbulent Transition in Gas Turbine Engines," *ASME Journal of Turbomachinery*, **113**, pp. 509-537.
- [3] Sharma, O.P., Ni, R.H., and Tanrikut, S., 1994, "Unsteady Flow in Turbines," AGARD Lecture Series 195, Paper No. 5.
- [4] Bons, J.P., Sondergaard, R., and Rivir, R.B., 2001, "Turbine Separation Control Using Pulsed Vortex Generator Jets," *ASME Journal of Turbomachinery*, **123**, pp. 198-206.
- [5] Volino, R.J., and Hultgren, L.S., 2001, "Measurements in Separated and Transitional Boundary Layers Under Low-Pressure Turbine Airfoil Conditions," *ASME Journal of Turbomachinery*, **123**, pp. 189-197.
- [6] Volino, R.J., 2002, "Separated Flow Transition Under Simulated Low-Pressure Turbine Airfoil Conditions: Part 1 – Mean Flow and Turbulence Statistics," *ASME Journal of Turbomachinery*, **124**, pp. 645-655.
- [7] Huang, J., Corke, T., and Thomas, F., 2003, "Plasma Actuators for Separation Control on Low Pressure Turbine Blades," AIAA Paper 2003-1027.
- [8] Hultgren, L.S., and Ashpis, D.E., 2003, "Demonstration of Separation Delay with Glow Discharge Plasma Actuators," AIAA Paper 2003-1025.
- [9] Volino, R.J., 2003, "Separation Control on Low-Pressure Turbine Airfoils Using Synthetic Vortex Generator Jets," *ASME Journal of Turbomachinery*, **125**, pp. 765-777.
- [10] Sieverding, C.H., Bagnera, C., Boege, A.C., Antòn, J.A.C., and Luère, V., 2004, "Investigation of the Effectiveness of Various Types of Boundary Layer Transition Elements of Low Reynolds Number Turbine Bladings," ASME Paper GT2004-54103.
- [11] Van Treuren, K.W., Simon, T., von Koller, M., Byerley, A.R., Baughn, J.W., and Rivir, R., 2002, "Measurements in a Turbine Cascade Flow Under Ultra Low Reynolds Number Conditions," *ASME Journal of Turbomachinery*, **124**, pp. 100-106.
- [12] Lake, J.P., King, P.I., and Rivir, R.B., 2000, "Low Reynolds Number Loss Reduction on Turbine Blades With Dimples and V-Grooves," AIAA Paper 00-738.
- [13] Murawski, C.G., and Vafai, K., 1999, "Effect of Variable Axial Chord on a Low-Pressure Turbine Blade," *Journal of Propulsion and Power*, **15**, pp. 667-674.
- [14] Byerley, A.R., Störmer, O., Baughn, J.W., Simon, T.W., VanTreuren, K.W., and List, J., 2002, "Using Gurney Flaps to Control Laminar Separation on Linear Cascade Blades," *ASME Journal of Turbomachinery*, **125**, pp. 114-120.
- [15] Volino, R.J., 2003, "Passive Flow Control on Low-Pressure Turbine Airfoils," *ASME Journal of Turbomachinery*, **125**, pp. 754-764.
- [16] Vera, M., Hodson, H.P., and Vazquez, R., 2004, "The Effects of a Trip Wire and Unsteadiness on a High Speed Highly Loaded Low-Pressure Turbine Blade," ASME Paper GT2004-53822.
- [17] Zhang, X.F., and Hodson, H., 2004, "The Combined Effects of Surface Trips and Unsteady Wakes on the Boundary Layer Development of an Ultra-High-Lift LP Turbine Blade," ASME Paper GT2004-53081.
- [18] Volino, R.J., and Bohl, D.G., 2003, "Separated Flow Transition Mechanisms and Prediction With High and Low Freestream Turbulence Under Low Pressure Turbine Conditions," ASME Paper GT2004-63360.
- [19] Volino, R.J., Schultz, M.P., and Pratt, C.M., 2001, "Conditional Sampling in a Transitional Boundary Layer Under High Free-Stream Turbulence Conditions," *ASME Journal of Fluids Engineering*, **125**, pp. 28-37.
- [20] Wills, J.A.B., 1962, "The Correction of Hot-Wire Readings for Proximity to a Solid Boundary," *Journal of Fluid Mechanics*, **12**, pp. 65-92.
- [21] Howell, R.J., Ramesh, O.N., Hodson, H.P., Harvey, N.W., and Schulte, V., 2001, "High Lift and Aft-Loaded Profiles for Low-Pressure Turbines," *ASME Journal of Turbomachinery*, **123**, pp. 181-188.
- [22] D'Ovidio, A., Harkins, J.A., and Gostelow, J.P., "Turbulent Spots in Strong Adverse Pressure Gradients: Part 2 – Spot Propagation and Spreading Rates," ASME Paper 2001-GT-0406.
- [23] Tumin, A., and Ashpis, D.E., 2003, "Optimal Disturbances in Boundary Layers Subject to Streamwise Pressure Gradients," *AIAA Journal*, **41**, pp. 2297-2300.

A Comprehensive CFD Study of Transitional Flows in Low-Pressure Turbines Under a Wide Range of Operating Conditions

Y. B. Suzen^{*}, P. G. Huang[†]

*University of Kentucky
Department of Mechanical Engineering
Lexington, Kentucky 40506-0503*

R. J. Volino[‡]

*United States Naval Academy
Department of Mechanical Engineering
Annapolis, Maryland 21402*

T. C. Corke[§], F. O. Thomas[¶], J. Huang[#]

*University of Notre Dame
Department of Aerospace and Mechanical Engineering
Notre Dame, Indiana 46556-56372*

J. P. Lake^{}**

*AFRL/PRSS
Edwards AFB, CA 93524*

P. I. King^{††}

*Air Force Institute of Technology
WPAFB, OH*

Abstract

A transport equation for the intermittency factor is employed to predict the transitional flows in low-pressure turbines. The intermittent behavior of the transitional flows is taken into account and incorporated into computations by modifying the eddy viscosity, μ_t , with the intermittency factor, γ . Turbulent quantities are predicted by using Menter's two-equation turbulence model (SST). The intermittency factor is obtained from a transport equation model which can produce both the experimentally observed streamwise variation of intermittency and a realistic profile in the cross stream direction.

The model had been previously validated against low-pressure turbine experiments with success. In this paper, the model is applied to predictions of three sets of recent low-pressure turbine experiments on PAK-B blade to further validate its predicting capabilities under various

flow conditions. Comparisons of computational results with experimental data are provided. Overall, good agreement between the experimental data and computational results is obtained. The new model has been shown to have the capability of accurately predicting transitional flows under a wide range of low-pressure turbine conditions.

Nomenclature

C_p	pressure coefficient, $2(P - P_\infty)/(\rho_\infty U_{in}^2)$
C_x	axial chord
FSTI	freestream turbulence intensity(%)
K_t	flow acceleration parameter, $(\nu/U^2)(dU/ds)$
k	turbulent kinetic energy
L_x	axial chord
N	non-dimensional spot breakdown rate parameter, $n\sigma\theta_t^3/\nu$
n	spot generation rate
P	static pressure
P_{total}	total pressure
Re	Reynolds number
Re_{st}	$(s_t - s_s)U_e/\nu$
Re_{θ_t}	$\theta_t U_e/\nu$
s	streamwise distance along suction surface

^{*}Senior Engineer Associate, Member AIAA.

[†]Professor, Senior Member AIAA.

[‡]Associate Professor.

[§]Professor.

[¶]Professor.

[#]Graduate Assistant.

^{**}Research Engineer, Member AIAA.

^{††}Associate Professor, Senior Member AIAA

Tu	turbulence intensity(%), u'/U
U	boundary layer streamwise velocity
U_e	local freestream velocity
U_{in}	inlet freestream velocity
u_τ	friction velocity
W	magnitude of vorticity
y_n	distance normal to the wall
y^+	$y_n u_\tau / \nu$
γ	intermittency factor
θ	momentum thickness
λ_θ	pressure gradient parameter, $(\theta^2 / \nu)(dU / ds)$
μ	molecular viscosity
μ_t	eddy viscosity
ν	μ / ρ
ν_t	μ_t / ρ
ρ	density
σ	spot propagation parameter

subscripts

e	freestream
s	onset of separation
t	onset of transition

1 Introduction

The process of transition from laminar to turbulent flow is a major unsolved problem in fluid dynamics and aerodynamics. One area where the transition process plays an important role and is even more complicated due to the diverse flow conditions encountered is the low-pressure turbine applications. Transitional flows in these applications are affected by several factors such as varying pressure gradients, wide range of Reynolds number and freestream turbulence variations, flow separation, and unsteady wake-boundary layer interactions. Accurate simulation and prediction of transitional flows under these diverse conditions is key to design of more efficient jet engines.

In low-pressure turbine applications, flow over the blades is mostly turbulent at the high Reynolds number conditions encountered at take off and the efficiency is at its design maximum. However, at lower Reynolds number conditions which correspond to high altitudes and cruise speeds the boundary layers on the airfoil surface have a tendency to remain laminar and hence the flow may separate on the suction surface of the turbine blades before it becomes turbulent. This laminar

separation causes unpredicted losses, substantial drops in efficiency, and increase in fuel consumption (Mayle, 1991; Rivir, 1996; Lake et al. 2000).

In order to calculate the losses and heat transfer on various components of gas turbine engines, and to be able to improve component efficiencies and reduce losses through better designs, accurate prediction of development of transitional boundary layers is essential (Mayle, 1991).

One approach proven to be successful for modeling transitional flows is to incorporate the concept of intermittency into computations. This can be done by multiplying the eddy viscosity obtained from a turbulence model, μ_t , used in the diffusive parts of the mean flow equations, by the intermittency factor, γ (Simon and Stephens, 1991). This method can be easily incorporated into any Reynolds Averaged Navier Stokes solver. In this approach, the intermittency factor, γ , can be obtained from an empirical relation such as the correlation of Dhawan and Narasimha (1958), or it can be obtained from a transport model.

Dhawan and Narasimha (1958) correlated the experimental data and proposed a generalized intermittency distribution function across flow transition. Gostelow et al. (1994) extended this correlation to flows with pressure gradients under the effects of a range of freestream turbulence intensities. Solomon et al. (1995), following the work of Chen and Thyson (1971), developed an improved method to predict transitional flows involving changes in pressure gradients. These empirical methods led to a development of transport equations for intermittency.

Steelant and Dick (1996) proposed a transport equation for intermittency, in which the source term of the equation is developed such that the γ distribution of Dhawan and Narasimha (1958) across the transition region can be reproduced. Steelant and Dick used their model, coupled with two sets of conditioned Navier-Stokes equations, to predict transitional flows with zero, favorable, and adverse pressure gradients. However, since their technique involved the solution of two sets of strongly coupled equations, the method is not compatible with existing CFD codes, in which only one set of Navier-Stokes equations is involved. Moreover, the model was designed to provide a realistic streamwise γ behavior but with no consideration of the variation of γ in the cross-stream direction.

Cho and Chung (1992) developed a $k-\varepsilon-\gamma$ turbulence model for free shear flows. Their turbulence model explicitly incorporates the intermittency effect into the conventional $k-\varepsilon$ model equations by introducing an additional transport equation for γ . They applied this model to compute a plane jet, a round jet, a plane far wake, and a plane mixing layer with good agreements. Although this method was not designed to reproduce flow transition it provided a realistic profile of γ in the cross-stream direction.

Suzen and Huang (1999) developed an intermittency transport equation combining the best properties of Steelant and Dick's model and Cho and Chung's model. The model reproduces the streamwise intermittency distribution of Dhawan and Narasimha (1958) and also produces a realistic variation of intermittency in the cross-stream direction. This model has been validated against T3-series experiments of Savill (1993a,1993b), low-pressure turbine experiments of Simon et al. (2000) and separated and transitional boundary layer experiments of Hultgren and Volino (2000) with success (Suzen and Huang, 1999, 2000a, 2000b; Suzen et al. 2000, 2001, 2002, 2003).

In this paper we concentrate on prediction of three recent low-pressure turbine experiments on the Pratt and Whitney's PAK-B blade under low Reynolds number conditions using the transport model for intermittency. Due to the fact that PAK-B blade is very sensitive to changes of flow conditions, it is an ideal test blade for validating the transition/turbulence models. The three sets of experiments considered are conducted by Lake et al. (1999, 2000), Corke et al. (2002), and Volino (2002) at three independent facilities. These experiments provide an extensive database for investigating transitional flows under low pressure turbine conditions and are employed as benchmark cases for further testing of the predicting capabilities of the current intermittency model. A summary of the experiments are given in the next section. In section 3, the intermittency transport model is presented and implementation of the model and the empirical correlations employed for the onset of transition are described. In Section 4, the predictions of the new intermittency model are compared against the experimental data. Conclusions are provided in Section 5.

2 Low-Pressure Turbine Experiments

In this paper, we concentrate on computation of three sets of low-pressure turbine experiments using the intermittency transport model. These experiments are conducted by Lake et al. (1999, 2000), Corke et al.

(2002), and Volino (2002). In these experiments Pratt and Whitney's PAK-B blade is used and the details of the blade are shown in Figure 1. Overall these experiments cover a Reynolds number range from 10,000 to 172,000 and the freestream turbulence intensity range from 0.08% to 4%. The cases and data used for comparison in this paper are summarized in Table 1. In the following sections details of these experimental efforts are given.

2.1 PAK-B Blade Cascade Experiments of Lake et al. (1999, 2000)

Lake et al. (1999, 2000) conducted experiments on the PAK-B blade in order to identify methods for reducing separation losses on low-pressure turbine blades under low Reynolds number conditions. In the experiments, they investigated flows at low Reynolds numbers of 43,000, 86,000, and 172,000 based on inlet velocity and axial chord and freestream turbulence intensities of 1% and 4%. These conditions are similar to those encountered at high altitude, low speed flight of reconnaissance unmanned aerial vehicles used by USAF.

In Lake's experiments, surface pressure coefficients, boundary layer velocity and turbulence profiles, total pressure loss data were obtained at FSTI=1% and FSTI=4%. The test set up shown in Figure 2 included eight blades with axial chord of 7 inches, and blade spacing of 6.2 inches. The blades were numbered 1 through 8 starting from the inside bend. Boundary layer measurements were taken on blade 5 and surface pressures were measured around blades 4 and 6. In this paper, the PAK-B blade experiments with Reynolds numbers of 43,000, 86,000, and 172,000 and freestream turbulence intensities of 1% and 4% are computed and comparison of pressure distributions between experiments and computations are performed.

2.2 PAK-B Blade Cascade Experiments of Corke et al. (2002)

Corke et al. (2002) conducted experiments on PAK-B blade cascade for a range of Reynolds numbers and turbulence intensities. The Reynolds numbers range from 10,000 to 100,000 based on inlet velocity and axial chord as listed in Table 1. In their experiments the blades had an axial chord length of 6.28 inches. The freestream turbulence intensity in the tunnel was measured as 0.08%. In order to increase the turbulence intensity, two grids with different mesh sizes were used. One of the grids had the mesh size of 2.54cm (denoted as Grid 0) and the other had 0.80cm (denoted as Grid 3). The decay of turbulence after the grids was measured using crosswire and they are shown in Figures 3 and 4 along

with the computed results for Grid 0 and Grid 3 respectively. The grids were movable in the tunnel so that the turbulence level of the flow that reaches the blades could be controlled by moving the grid that is, by increasing or decreasing the distance between the grid and the blade. Experiments were performed for Reynolds numbers 50,000, 75,000, and 100,000, with grids placed 30 inches away from the blade leading edge, corresponding to turbulence intensities of 2.85% and 1.6% at the leading edge for Grid 0 and Grid 3, respectively. For Re=100,000, Grid 0 is placed at 22 inches and 14 inches corresponding to turbulence intensities of 3.62% and 5.2%, respectively. Pressure coefficient data is available for all cases and detailed boundary layer measurements are available for Re=50,000, 75,000, and 100,000 with FSTI=0.08% and 2.85% cases. The cases and data used for comparisons in this paper are listed in Table 1.

2.3 PAK-B Experiments of Volino (2002)

Volino (2002) investigated the boundary layer separation, transition, and reattachment under low-pressure turbine airfoil conditions. The experiments included five different Reynolds numbers ranging between 10,291 and 123,492 and freestream turbulence intensities of 0.5% and 9%. The test section consisted of a single passage between two PAK-B blades as shown in Figure 5. The axial chord length of the blades was 6.05 inches. There are flaps located upstream of each blade to control the amount of bleed air allowed to escape from the passage. These flaps were adjusted by matching measured pressure distribution for a high Reynolds number with the inviscid pressure distribution on the blade. In addition to the upstream bleed flaps, a tailboard on the pressure side was used to set the pressure gradient. The compiled data include pressure surveys, mean and fluctuating velocity profiles, intermittency profiles, and turbulent shear stress profiles. It was observed that, the effect of high Reynolds number or high free stream turbulence level was to move transition upstream. Transition started in the shear layer over the separation bubble and led to rapid boundary layer reattachment. At the lowest Re case, transition did not take place before the trailing edge and the boundary layer did not reattach. The beginning of transition corresponded to the beginning of a significant rise in the turbulent shear stress. These experimental results provide detailed documentation of the boundary layer and extend the existing database to lower Reynolds numbers. The cases used for comparisons with computations in this paper are listed in Table 1 along with the type of data used for comparisons.

3 Intermittency Transport Model

In this section, the transport model for intermittency is presented. The model combines the transport equation models of Steelant and Dick (1996) and Cho and Chung (1992). Details of the development and implementation of the transport model are given in Suzen and Huang (1999, 2000a, 2000b), Suzen et al. (2000).

The model equation is given by:

$$\begin{aligned} \frac{\partial \rho \gamma}{\partial t} + \frac{\partial \rho u_j \gamma}{\partial x_j} = & (1-\gamma) \left[(1-F) 2C_0 \rho \sqrt{u_k u_k} f(s) f'(s) \right. \\ & \left. + F \left(\frac{C_1 \gamma}{k} \tau_{ij} \frac{\partial u_i}{\partial x_j} - C_2 \rho \frac{k^{3/2}}{\varepsilon} \frac{u_i}{(u_k u_k)^{1/2}} \frac{\partial u_i}{\partial x_j} \frac{\partial \gamma}{\partial x_j} \right) \right] \\ & + C_3 \rho \frac{k^2}{\varepsilon} \frac{\partial \gamma}{\partial x_j} \frac{\partial \gamma}{\partial x_j} \\ & + \frac{\partial}{\partial x_j} \left(((1-\gamma) \gamma \sigma_{\gamma} \mu + (1-\gamma) \sigma_{\gamma} \mu_i) \frac{\partial \gamma}{\partial x_j} \right) \end{aligned} \quad (1)$$

The distributed breakdown function, $f(s)$ has the form:

$$f(s) = \frac{as'^4 + bs'^3 + cs'^2 + ds' + e}{gs'^3 + h} \quad (2)$$

where $s' = s - s_t$, and s is the distance along the streamline coordinate, and s_t is the transition location.

The coefficients are;

$$\begin{aligned} a &= 50 \sqrt{\frac{n\sigma}{U}} \\ b &= -0.4906 \\ c &= 0.204 \left(\frac{n\sigma}{U} \right)^{-0.5} \\ d &= 0.0 \\ e &= 0.04444 \left(\frac{n\sigma}{U} \right)^{-1.5} \\ h &= 10e \\ g &= 50 \end{aligned} \quad (3)$$

The shear stresses are defined as:

$$\tau_{ij} = \mu_i \left[\frac{\partial u_i}{\partial x_j} + \frac{\partial u_j}{\partial x_i} - \frac{2}{3} \frac{\partial u_k}{\partial x_k} \delta_{ij} \right] - \frac{2}{3} \rho k \delta_{ij} \quad (4)$$

The blending function F is constructed using a nondimensional parameter, k/Wv where k is the turbulent kinetic energy and W is the magnitude of the vorticity. The blending function has the form:

$$F = \tanh^4 \left[\frac{k/Wv}{200(1-\gamma^{0.1})^{0.3}} \right] \quad (5)$$

The model constants used in Equation 1 are:

$$\sigma_{\mu} = \sigma_{\mu} = 1.0 \quad C_0 = 1.0 \quad C_1 = 1.6 \\ C_2 = 0.16 \quad C_3 = 0.15$$

The intermittency is incorporated into the computations simply by multiplying the eddy viscosity obtained from a turbulence model, μ_t , by the intermittency factor, γ . Simon and Stephens (1991) showed that by combining the two sets of conditioned Navier-Stokes equations and making the assumption that the Reynolds stresses in the nonturbulent part are negligible, the intermittency can be incorporated into the computations by using the eddy viscosity, μ_t^* which is obtained by multiplying the eddy viscosity from a turbulence model, μ_t , with the intermittency factor, γ . That is,

$$\mu_t^* = \gamma \mu_t \quad (6)$$

is used in the mean flow equations. It must be noted that γ does not appear in the generation term of the turbulent kinetic energy equations.

Computations of the experiments are performed using a recently developed multi-block Navier-Stokes solver, called GHOST. The code is developed at University of Kentucky, by George Huang, and is a pressure-based code based on SIMPLE algorithm with second order accuracy in both time and space. Advection terms are approximated by a QUICK scheme and central differencing is used for the viscous terms. The 'Rhie and Chow' momentum interpolation method (1983) is employed to avoid checkerboard oscillations usually associated with the non-staggered grid arrangement. This code is capable of handling complex geometries, moving, and overset grids and includes multiprocessor computation capability using MPI. Since multiple processors are used during the computations, it is more efficient to divide the computational domain into several smaller pieces with very fine grids and distribute the zones to processors with the consideration of load balancing. This code has been used extensively in a recent turbulence model validation effort (Hsu et al., 2003) and computations of unsteady wake/blade interaction (Suzen and Huang, 2003) conducted at University of Kentucky.

In using this intermittency approach, the turbulence model selected to obtain μ_t must produce fully turbulent features before transition location in order to allow the intermittency to have full control of the transitional behavior. Menter's (1994) SST model satisfies this requirement. It produces almost fully turbulent flow in the leading edge of the boundary layer and therefore it is

used as a baseline model to compute μ_t and other turbulent quantities in the computations (Suzen et al., 2000).

The value of $n\sigma$ used in evaluating the constants given by (3) is provided by the following correlation for zero pressure gradient flows (Suzen et al., 2000);

$$\hat{n}\sigma = (nv^2/U^3)\sigma = 1.8 \times 10^{-11} Tu^{7/4} \quad (7)$$

When flows are subject to pressure gradients, the following correlation is used:

$$\frac{\hat{n}\sigma}{(\hat{n}\sigma)_{ZPG}} = \begin{cases} M^{(1-\exp(0.75 \times 10^6 K_t Tu^{-0.7}))}, & K_t < 0 \\ 10^{-3227 K_t^{0.5985}}, & K_t > 0 \end{cases} \quad (8)$$

with M defined as:

$$M = (850 Tu^{-3} - 100 Tu^{-0.5} + 120)$$

where, $(\hat{n}\sigma)_{ZPG}$ is the value for flow at zero pressure gradient and can be obtained from equation (7) and $K_t = (v/U_t^2)(dU/dx)_t$ is the flow acceleration parameter. The favorable pressure gradient part of the above correlation (for $K_t > 0$) is from Steelant and Dick (1996). The portion of the correlation for adverse pressure gradient flows for $K_t < 0$, is formulated using the transition data of Gostelow et al. (1994) and Simon et al. (2000) (Suzen et al., 2000).

The current approach uses the intermittency transport model to obtain the intermittency distribution for the transitional flows, while the onset of transition is defined by correlations.

The onset of attached flow transition is determined by the following correlation in terms of turbulence intensity, Tu , and the acceleration parameter, K_t ,

$$Re_{\theta} = (120 + 150 Tu^{-2/3}) \coth[4(0.3 - K_t \times 10^5)] \quad (9)$$

where K_t was chosen as the maximum absolute value of that parameter in the downstream deceleration region (Suzen et al., 2000). This correlation maintains the good features of Abu-Ghannam and Shaw (1980) correlation in the adverse pressure gradient region and in addition it reflects the fact that the flow becomes less likely to have transition when subject to favorable pressure gradients by rapidly rising as K_t becomes positive.

In order to determine the onset of separated flow transition Re_{st} is expressed in terms of the turbulence intensity (Tu) and the momentum thickness Reynolds number at the point of separation (Re_{θ_s}) in the form (Suzen et al., 2001);

$$Re_{st} = 874 Re_{\theta_s}^{0.71} \exp[-0.4Tu] \quad (10)$$

This correlation provides a better representation of the experimental data than Davis et al. (1987) correlation and is used to predict onset of separated flow transition in the present computations.

4 Results and Discussion

4.1 Simulations of Experiments of Lake et al. (1999,2000)

The intermittency model is applied to predict the PAK-B blade experiments of Lake et al. (1999, 2000). In the computations, flows at Reynolds numbers of 43,000, 86,000, and 172,000 based on inlet velocity and axial chord with freestream intensities of 1% and 4% were investigated.

The computations are performed using the grid consisting of five zones shown in Figure 6. The four zones on which the blade grid is superposed each have 125x225 grid points and the O-type grid around the blade has 401x101 points with first y^+ less than 0.5.

The comparisons of computed and experimental pressure coefficient distributions are shown in Figures 7(a) through (f). In these figures, the experimental distributions correspond to the measurements made on test blades 4 and 6.

The computed results compare well with the experiments for high turbulence intensity, $FSTI=4\%$, cases shown in Figures 7(a), (c) and (e). However, for $FSTI=1\%$ cases shown in Figures 7(b), (d) and (f) the extent of the separation bubbles are under predicted in the computations. For example, for $Re=86,000$, $FSTI=1\%$, shown in Figure 7(d), the flow reattaches earlier in computations than it does in the experiment as can be observed from the difference in the pressure coefficient distributions between $x/L_x = 0.8$ to 0.85 . This discrepancy is more pronounced for the lowest Reynolds number case, $Re=43,000$ and $FSTI=1\%$ case.

The onset of separation locations, reattachment locations, and onset of transition locations on the suction surface are summarized in Table 2 for these cases along with the

corresponding values from experiments. In the experiments, the onset of transition locations and the reattachment locations are not reported.

The experimental onset of separation and reattachment points are extracted from the experimental pressure coefficient data. The onset of separation is taken to be the axial location where the plateau in the pressure coefficient distribution of the suction side begins and the reattachment point is taken to be the axial location after the sharp change in C_p following the plateau.

The onset of separation, reattachment, and onset of transition locations are plotted against Reynolds number in Figures 8(a) and (b) for $FSTI=4\%$ and 1% respectively. For the high turbulence intensity case, computation predicts onset of separation and reattachment slightly upstream of the experiment. For the low $FSTI$ case shown in Figure 8(b) separation zone is predicted smaller than the experiments. The onset of transition is predicted over the separated flow region in the shear layer. From comparison of these figures it is evident that with decreasing freestream turbulence intensity, the separation zone becomes larger, and for a given $FSTI$ condition separated flow region gets smaller with increasing Reynolds number.

4.2 Simulations of Experiments of Corke et al. (2002)

In this set of experiments, first the cases with no grid in tunnel corresponding to $FSTI=0.08\%$ are computed. In these computations, the same grid system used for the computations of experiments of Lake et al. (1999, 2000) shown in Figure 6 is used.

The comparisons of computed and the experimental pressure coefficients are shown in Figures 9(a) through (e) for $Re=100,000$, $75,000$, $50,000$, $25,000$, and $10,000$ based on inlet velocity and axial chord. The agreement between the experiments and computations is very good for all cases.

The onset of separation, transition, and reattachment locations are tabulated in Table 3 for all cases and plotted against Reynolds number in Figures 10(a), (b), and (c) for $FSTI=0.08\%$, 1.6% , and 2.85% respectively.

Computed velocity profiles at seven axial stations along the suction surface of the blade are compared to the experiments for $Re=100,000$, $75,000$, and $50,000$ in Figures 11, 12, and 13, respectively.

For $Re=100,000$ case, the computed velocity profiles compare very well with the experiment as shown in

Figures 11(a) through (g). At the first three measurement stations, flow is laminar and attached as shown in Figures 11(a), (b) and (c). Flow separation takes place at $x/C_x = 0.725$ and the separated flow region is visible in Figures 11(d) and (e) corresponding to axial locations of $x/C_x = 0.75$ and 0.80 . The flow transition and reattachment takes place around $x/C_x = 0.84$ in the computation. Reattachment location is earlier than the experiment which takes place at $x/C_x = 0.875$. In Figure 11(f) corresponding to axial station of $x/C_x = 0.85$ the computed flow field has already attached, although the experimental profile indicates a very small separation zone close to wall. At $x/C_x = 0.9$ shown the flow is completely attached as shown in Figure 11(g).

When Reynolds number is reduced to 75,000, the size of the separation bubble increases as can be observed from the comparison of the velocity profiles shown in Figures 12(a) through (g). At this Reynolds number the flow separates around $x/C_x \approx 0.72$ and reattaches around $x/C_x \approx 0.87$. The transition onset location is predicted at $x/C_x = 0.854$. The size of the separation bubble is larger than Re=100,000 case from comparison of Figures 12(d), (e), and (f) and 11(d), (e), and (f).

Next, the Reynolds number is reduced to 50,000 and the comparison of computed and experimental velocity profiles are shown in Figures 13(a) through (g). For this case the separation bubble is much larger from the previous cases and extends until $x/C_x \approx 0.975$ in the experiment and $x/C_x \approx 0.93$ in the computations as can be seen in Figures 13(d) through (g). Computations predicted the transition onset location at $x/C_x = 0.89$. In the computations, the onset of separation is predicted well in agreement with experiment, however, the reattachment point is earlier making the size of the separation bubble smaller when compared to experiment. This is evident from the comparison of velocity profiles at the last two stations shown in Figures 13(f) and (g).

The onset of separation and reattachment points for FSTI=0.08% cases are predicted upstream of the experiments as shown in Figure 10(a).

Next, the high FSTI cases are computed using the six zone multiblock grid system shown in Figure 14. The computational domain is extended upstream of the blade in order to specify the correct turbulence intensity at the inlet and to match the decay of turbulence that reaches the blade. The matched computed and experimental turbulence decays are shown in Figures 3 and 4 for Grid

0 and Grid 3 respectively. The cases considered have the grids placed 30 inches upstream of the blade, corresponding to turbulence intensities of 2.85% and 1.6% for Grid 0 and Grid 3, respectively.

The comparison of the computed and the experimental pressure coefficient distributions for Re=50,000, 75,000, and 100,000 for FSTI=2.85% cases are shown in Figure 15. The agreement is very good between computations and experiments.

Comparisons of computed velocity profiles with the experiments for Re=100,000 are given in Figures 16(a) through (g). In this case, the flow separates around $x/C_x \approx 0.74$ and reattaches at $x/C_x \approx 0.85$. The onset of transition is predicted at $x/C_x = 0.806$. The computed size and extent of the separation bubble is in well agreement with the experiment as tabulated in Table 3 and as can be seen in Figures 10(c), and 16(d), (e), and (f).

For the lower Reynolds number of 75,000, computed velocity profiles are compared with the experiments in Figures 17(a) through (g). The agreement between experiment and computation is well prior to the reattachment as shown in Figures 17(a) through (e). There is a discrepancy in the reattachment region. The flow separation takes place around $x/C_x \approx 0.73$ and reattaches at $x/C_x \approx 0.87$ according to the experiment whereas computation predicts reattachment earlier at around $x/C_x \approx 0.84$ with the onset of transition is predicted at $x/C_x = 0.816$. The difference in reattachment points is evident in the comparison of the computed and experimental velocity profiles shown in Figure 17(f). At this station the experimental profile indicates separated flow and the computed profile shows an already attached flow.

Next case considered has the same FSTI= 2.85% but with Reynolds number being reduced to 50,000. The comparison of velocity profiles are shown in Figures 18(a) through (g). The computations agree well with the experiment and the size and extent of the separation bubble are well predicted as can be seen from Figure 10(c). The onset of separation is around $x/C_x \approx 0.72$ and the flow reattaches around $x/C_x \approx 0.9$ with transition onset at $x/C_x = 0.837$.

In Figure 19 computed and experimental pressure coefficient distributions for Grid 3 case are compared for Re=50,000, 75,000, and 100,000. Again, very good agreement between computations and experiments are obtained. The onset of separation and reattachment

locations shown in Figure 10(b) compare well with the experiments.

Overall, Figures 10(a), (b), and (c) indicate that as FSTI increases, the separated flow region decreases, and at a given FSTI, increasing Reynolds number has the same effect on the separated flow region.

4.3 Simulations of PAK B Experiments of Volino (2002)

In computation of experiments of Volino (2002) the flow field is modeled with the 31 zone multiblock grid shown in Figure 20. The bleed flaps below the lower blade and above the upper blade are defined by fitting third order polynomials through the available points obtained from experimental setup and these curves are used as the flap shapes in generating the computational grid. Initial computations indicated that shape of the bleed flaps and the orientation of the tailboard behind the upper blade greatly affect the computed results especially the onset of separation and reattachment points on the lower blade's suction surface. In order to select the most accurate orientation for the tailboard and the shape of the bleed flaps, several test computations were performed for the case with $Re=41,162$ and $FSTI=0.5\%$ using different tailboard orientations and bleed flap shapes. In these computations the main goal was to match the experimental velocity profiles in the laminar flow part and to capture the correct onset point of separation. Once an acceptable geometry is obtained, the final bleed flap shapes and tailboard orientation is used for computation of all other Reynolds number cases.

Computed pressure coefficient distributions are compared to experiments in Figures 21(a) through (d) for $Re=82,324$, $41,162$, $20,581$, and $10,291$ and the separation onset, reattachment and transition onset information is summarized in Table 4. The C_p comparison for $Re=82,324$ shown in Figure 21(a) indicates that the computation predicts early reattachment of the flow and in the recovery region following reattachment pressure coefficient distribution is overpredicted.

The computed pressure coefficient distributions for the lower Reynolds number cases shown in Figures 21(c) and (d) compare well with experiments. For $Re=41,162$ case shown in Figure 21(b) the onset of separation and reattachment locations match the experiment as given in Table 4, however, in the recovery region pressure coefficient distribution is overpredicted.

Computed velocity profiles are compared to experiment at 11 stations along the suction surface of the blade in

Figures 22(a) through (k) for $Re=82,324$ and $FSTI=0.5\%$. The results compare well with the experiment up to $x/C_x = 0.732$ shown in Figures 22(a) through (g). After this station flow separation takes place. Separation onset and reattachment are slightly earlier in the computations compared to experiment as given in Table 4. This can be also observed from the velocity profiles at stations $x/C_x = 0.798$ to 0.912 shown in Figures 22(h) through (j). Overall computations compare well with the experimental measurements.

Next Reynolds number is reduced to $41,162$ and the computed and experimental velocity profiles are compared in Figures 23(a) through (k). The computed profiles agree well with experiments except at $x/C_x = 0.912$ shown in Figure 23(j). At this station the computation indicates a smaller separated flow region close to reattachment in contrast to the experiment. However, the flow reattaches around $x/C_x = 0.95$ both in computation and experiment and in the next measurement station the agreement is well.

The next case considered has Reynolds number of $20,581$. Computed velocity profiles are shown along with the experimental data at 11 axial stations in Figures 24(a) through (k).

In this case flow separates around $x/C_x \approx 0.76$ and does not reattach in experiment, however computations indicated reattachment at $x/C_x \approx 0.98$. This discrepancy is evident from the comparison of velocity profiles at the last two measurement stations shown in Figures 24(j) and (k). The computation indicates a smaller separated region in these stations and finally reattaches very close to the trailing edge. Onset of transition was predicted at $x/C_x = 0.978$.

Final case in this set of experiments is the one with $Re=10,291$. The computed velocity profiles are compare very well with the experimental data as shown in Figures 25(a) through (k). In this case the flow separates around $x/C_x \approx 0.76$ and does not reattach. The flow is completely laminar, transition was not predicted on the blade.

5 Concluding Remarks

A transport equation for the intermittency factor is employed to predict three sets of recent low-pressure turbine experiments on PAK-B blade. The intermittent behavior of the transitional flows is taken into account by modifying the eddy viscosity with the intermittency factor. Comparisons of the computed and experimental data are made and overall good agreement with the

experimental data is obtained. The predicting capabilities of the current intermittency approach and the intermittency transport model in prediction of transitional flows under a wide range of low-pressure turbine conditions is demonstrated.

Acknowledgements

This work is supported by NASA Glenn Research Center under grant NCC3-590 and followed by grant NCC3-1040. The project is part of the Low Pressure Turbine Flow Physics program of NASA-Glenn. We like to thank Dr. David Ashpis for his coordination of the LPT effort.

References

- Abu-Ghannam, B.J. and Shaw, R., 1980, "Natural Transition of Boundary Layers-The Effects of Turbulence, Pressure Gradient, and Flow History," *Journal of Mechanical Engineering Science*, Vol. 22, Vol. 5, pp. 213-228.
- Chen, K. K. and Thyson, N. A., 1971, "Extension of Emmons' Spot Theory to Flows on Blunt Bodies," *AIAA Journal*, Vol. 9, No. 5, pp. 821-825.
- Cho, J.R. and Chung, M.K., 1992, "A $k-\varepsilon-\gamma$ Equation Turbulence Model," *Journal of Fluid Mechanics*, Vol. 237, pp. 301-322.
- Corke, T.C., Thomas, F.O., Huang, J., 2002, Private communications.
- Davis, R.L., Carter, J.E., and Reshotko, E., 1987, "Analysis of Transitional Separation Bubbles on Infinite Swept Wings," *AIAA Journal*, Vol. 25, No. 3, pp. 421-428.
- Dhawan, S. and Narasimha, R., 1958, "Some Properties of Boundary Layer During the Transition from Laminar to Turbulent Flow Motion," *Journal of Fluid Mechanics*, Vol. 3, pp. 418-436.
- Gostelow, J.P., Blunden, A.R., and Walker, G.J., 1994, "Effects of Free-Stream Turbulence and Adverse Pressure Gradients on Boundary Layer Transition," *ASME Journal of Turbomachinery*, Vol. 116, pp. 392-404.
- Hsu, M. C., Vogiatzis, K. and Huang, P. G. 2003, "Validation and Implementation of Advanced Turbulence Models in Swirling and Separated Flows", AIAA 2003-0766, 41st AIAA Aerospace Science Meeting & Exhibit, 6-9 Jan, 2003, Reno, NV.
- Huang, P.G. and Coakley, T.J., 1992, "An Implicit Navier-Stokes Code for Turbulent Flow Modeling," AIAA Paper AIAA-92-0547.
- Hultgren, L.S. and Volino, R.J., 2000, "Separated and Transitional Boundary Layers Under Low-Pressure Turbine Airfoil Conditions," NASA TM in preparation.
- Lake, J.P., King, P.I., Rivir, R.B., 1999, "Reduction of Separation Losses on a Turbine Blade with Low Reynolds Number," AIAA Paper AIAA-99-0242, Reno, NV.
- Lake, J.P., King, P.I., Rivir, R.B., 2000, "Low Reynolds Number Loss Reduction on Turbine Blades with Dimples and V-Grooves," AIAA-00-0738, Reno, NV.
- Mayle, R.E., 1991, "The Role of Laminar-Turbulent Transition in Gas Turbine Engines," *Journal of Turbomachinery*, Vol. 113, pp. 509-537.
- Menter, F. R., 1994, "Two-Equation Eddy-Viscosity Turbulence Models for Engineering Applications," *AIAA Journal*, Vol. 32, No. 8, pp. 1598-1605.
- Rhie, C. M. and Chow, W. L. 1983, "Numerical study of the turbulent flow past an airfoil with trailing edge separation," *AIAA Journal* Vol.21, pp.1525-1532.
- Rivir, R.B., 1996, "Transition on Turbine Blades and Cascades at Low Reynolds Numbers," AIAA-96-2079.
- Savill, A.M., 1993a, "Some Recent Progress in The Turbulence Modeling of By-pass Transition," *Near-Wall Turbulent Flows*, R.M.C. So, C.G. Speziale and B.E. Launder, eds., Elsevier Science Publishers B.V., pp. 829-848.
- Savill, A.M., 1993b, "Further Progress in The Turbulence Modeling of By-pass Transition," *Engineering Turbulence Modeling and Experiments 2*, W. Rodi and F. Martelli, eds., Elsevier Science Publishers B. V., pp. 583-592.
- Simon, F.F. and Stephens, C.A., 1991, "Modeling of the Heat Transfer in Bypass Transitional Boundary-Layer Flows," NASA Technical Paper 3170.
- Simon, T.W., Qiu, S., Yuan, K., 2000, "Measurements in a Transitional Boundary Layer Under Low-Pressure Turbine Airfoil Conditions," NASA-CR-2000-209957.
- Solomon, W.J., Walker, G.J., and Gostelow, J.P., 1995, "Transition Length Prediction for Flows with Rapidly Changing Pressure Gradients," ASME Paper ASME-95-GT-241, International Gas Turbine and Aeroengine Congress & Exposition, Houston, Texas, June 5-8.
- Steelant, J. and Dick, E., 1996, "Modelling of Bypass Transition with Conditioned Navier-Stokes Equations Coupled to an Intermittency Transport Equation," *International Journal for Numerical Methods in Fluids*, Vol. 23, pp. 193-220.
- Suzen, Y.B., and Huang, P.G., 1999, "Modelling of Flow Transition Using an Intermittency Transport Equation," NASA Contractor Report, NASA-CR-1999-209313.
- Suzen, Y.B., and Huang, P.G., 2000a, "Modeling of Flow Transition Using an Intermittency Transport Equation," AIAA-2000-0287, 38th AIAA Aerospace Sciences Meeting & Exhibit, Reno, NV.

Suzen, Y.B., and Huang, P.G., 2000b, "Modeling of Flow Transition Using an Intermittency Transport Equation," *Journal of Fluids Engineering*, Vol. 122, pp. 273-284.

Suzen, Y.B., and Huang, P.G., 2003, "Numerical Simulation of Wake Passing on Turbine Cascades," AIAA-2003-1256, , 41st AIAA Aerospace Science Meeting & Exhibit, 6-9 Jan, 2003, Reno, NV.

Suzen, Y.B., Xiong, G., Huang, P.G., 2000, "Predictions of Transitional Flows in Low-Pressure Turbines Using an Intermittency Transport Equation," AIAA-2000-2654, Fluids 2000, Denver, CO.

Suzen, Y.B., and Huang, P.G., Hultgren, L.S., Ashpis, D.E., 2001, "Predictions of Separated and Transitional Boundary Layers Under Low-Pressure Turbine Airfoil Conditions Using an Intermittency Transport Equation," AIAA-2001-0446, 39th AIAA Aerospace Sciences Meeting & Exhibit, Reno, NV.

Suzen, Y.B., and Huang, P.G., Hultgren, L.S., Ashpis, D.E., 2003, "Predictions of Separated and Transitional Boundary Layers Under Low-Pressure Turbine Airfoil Conditions Using an Intermittency Transport Equation," *ASME Journal of Turbomachinery*, accepted for publishing.

Suzen, Y.B., Xiong, G., Huang, P.G., 2002, "Predictions of Transitional Flows in Low-Pressure Turbines Using an Intermittency Transport Equation," *AIAA Journal*, Vol. 40, No 2, pp. 254-266.

Volino, R.J., 2002, "Separated Flow Transition Under Simulated Low-Pressure Turbine Airfoil Conditions: Part 1-Mean Flow and Turbulence Statistics," ASME-GT-30236, ASME TURBO EXPO 2002, Amsterdam, The Netherlands.

Source	Test Section	C_x (inch)	Re ($U_{in} C_x / \nu$)	FSTI (%)	Data used for Comparison
Lake et.al (1999, 2000)	P&W PAK-B cascade	7.0	43,000	1 & 4	C_p distribution
			86,000	1 & 4	C_p distribution
			172,000	1 & 4	C_p distribution
Corke et al. (2002)	P&W PAK-B cascade	6.28	10,000	0.08	C_p distribution
			25,000	0.08	C_p distribution
			50,000	0.08, 1.6, 2.85	C_p distribution, velocity profiles*
			75,000	0.08, 1.6, 2.85	C_p distribution, velocity profiles*
			100,000	0.08, 1.6, 2.85	C_p distribution, velocity profiles*
Volino (2002)	P&W PAK-B single passage	6.05	10,291	0.5	C_p distribution, velocity profiles
			20,581	0.5	C_p distribution, velocity profiles
			41,162	0.5	C_p distribution, velocity profiles
			82,324	0.5	C_p distribution, velocity profiles

* Velocity profiles are available for FSTI=0.08% and 2.85% from experiments.

Table 1. Details of the experiments used for comparison with computations.

Re ($U_{in}C_x/\nu$)	FSTI (%)	x_s/C_x (Computation)	x_s/C_x (Experiment)	x_t/C_x (Computation)	x_t/C_x (Experiment)	x_{tr}/C_x (Computation)
172,000	4	0.732	0.74	0.83	0.84	0.806
86,000	4	0.725	0.74	0.86	0.88	0.832
43,000	4	0.718	0.73	0.93	0.93	0.881
172,000	1	0.728	0.72	0.82	0.84	0.808
86,000	1	0.722	0.72	0.87	0.90	0.849
43,000	1	0.711	0.62	0.95	0.99	0.896

Table 2: Separation, reattachment, and transition locations for cases of Lake et al. (1999, 2000).

Re ($U_{in}C_x/\nu$)	FSTI (%)	x_s/C_x (Computation)	x_s/C_x (Experiment)	x_t/C_x (Computation)	x_t/C_x (Experiment)	x_{tr}/C_x (Computation)
10,000	0.08	0.661	0.725	---	---	---
25,000	0.08	0.656	0.725	0.980	---	0.936
50,000	0.08	0.714	0.725	0.925	0.975	0.890
75,000	0.08	0.718	0.725	0.860	0.870	0.854
100,000	0.08	0.725	0.725	0.840	0.875	0.840
50,000	1.6	0.722	0.728	0.900	0.900	0.854
75,000	1.6	0.728	0.730	0.867	0.875	0.834
100,000	1.6	0.732	0.730	0.860	0.877	0.821
50,000	2.85	0.728	0.722	0.887	0.900	0.837
75,000	2.85	0.732	0.729	0.840	0.870	0.816
100,000	2.85	0.735	0.734	0.842	0.850	0.806

Table 3: Separation, reattachment, and transition locations for cases of Corke et al. (2002).

Re ($U_{in}C_x/\nu$)	FSTI (%)	x_s/C_x (Computation)	x_s/C_x (Experiment)	x_t/C_x (Computation)	x_t/C_x (Experiment)	x_{tr}/C_x (Computation)
10,291	0.5	0.760	0.750	---	---	---
20,581	0.5	0.765	0.760	0.980	---	0.978
41,162	0.5	0.760	0.770	0.950	0.950	0.840
82,324	0.5	0.757	0.767	0.890	0.900	0.857

Table 4: Separation, reattachment, and transition locations for cases of Volino (2002).

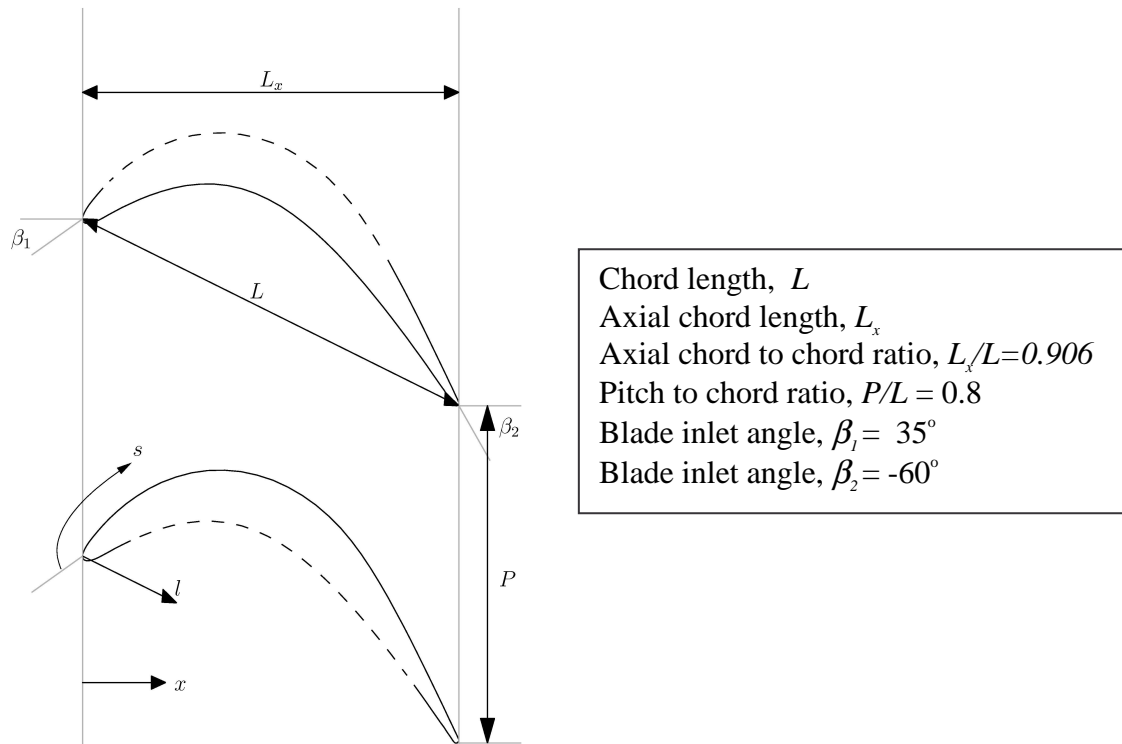


Figure 1: P&W PAK-B blade cascade details.

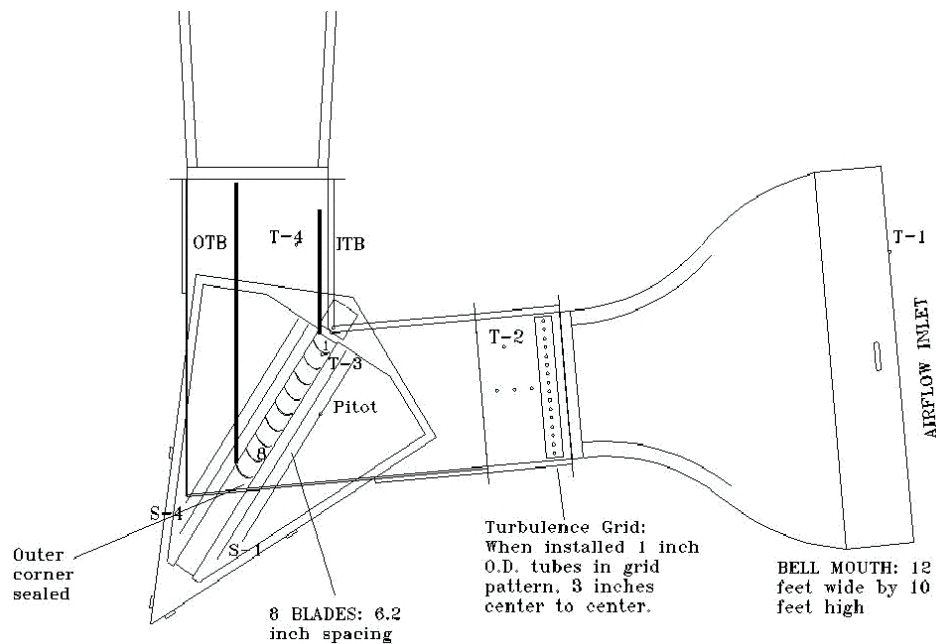


Figure 2: Experimental set up for used by Lake et al. (1999, 2000).

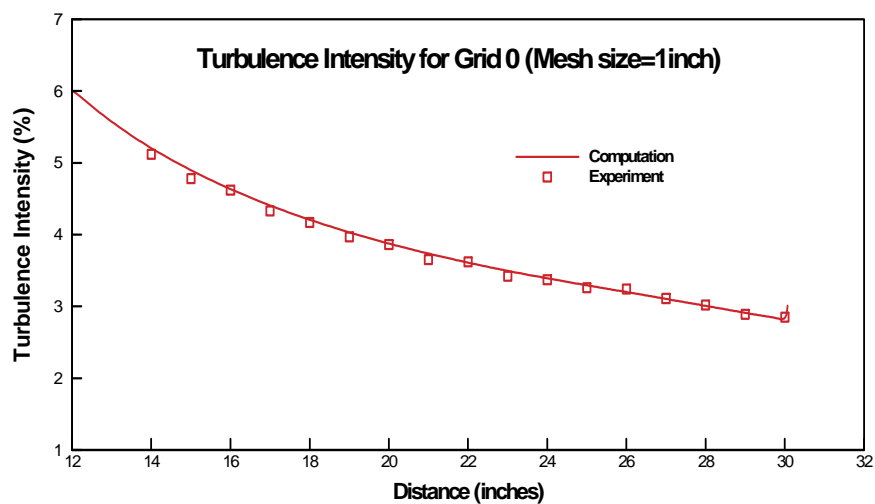


Figure 3: Comparison of computed and experimental decay of turbulence for experiments of Corke et al. (2002), with Grid 0.

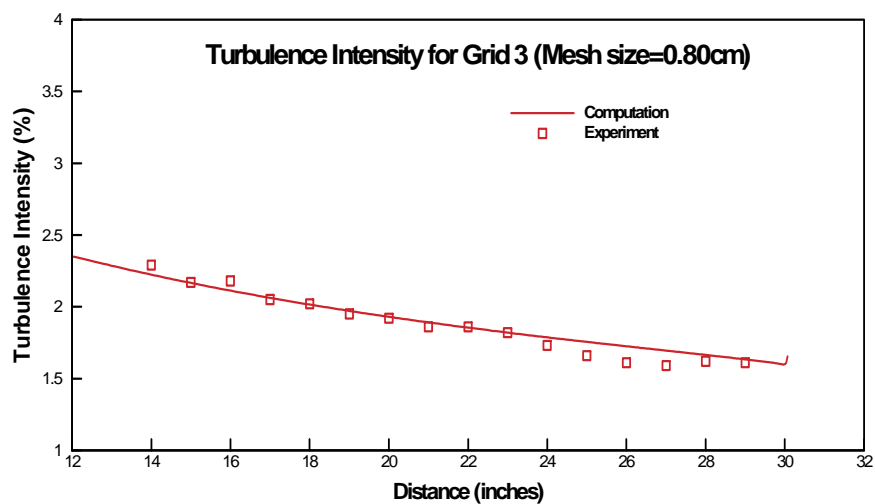


Figure 4: Comparison of computed and experimental decay of turbulence experiments of Corke et al. (2002), for Grid 3.

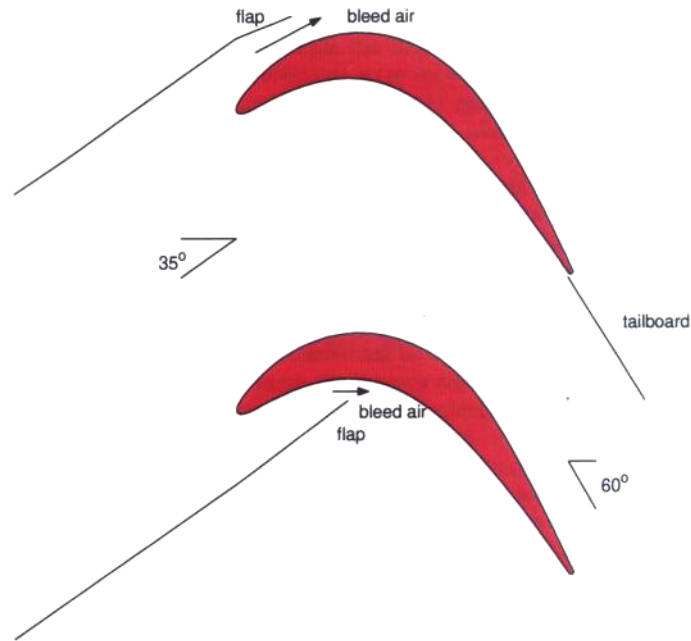


Figure 5: Schematic of the test section for experiments of Volino(2002).

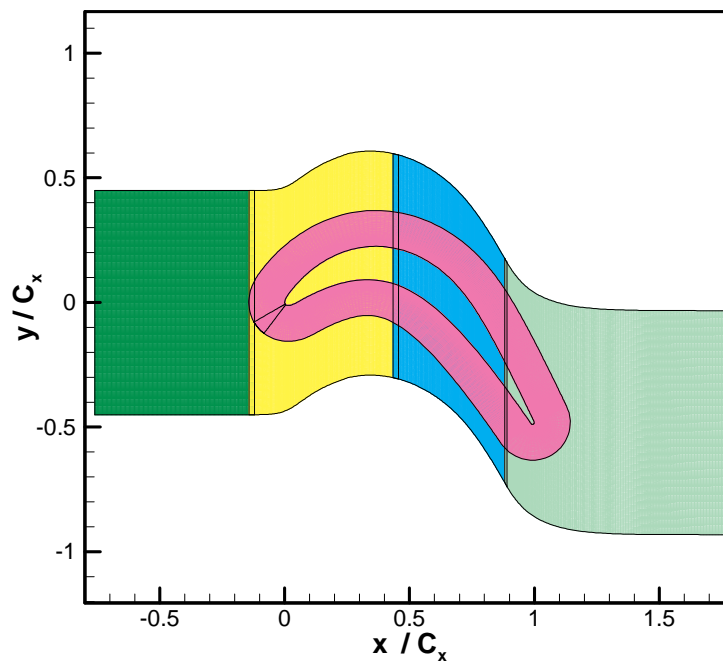


Figure 6: Multiblock grid used for computations of experiments of Lake et al. (1999, 2000) and FSTI=0.08% experiments of Corke et al. (2002) .

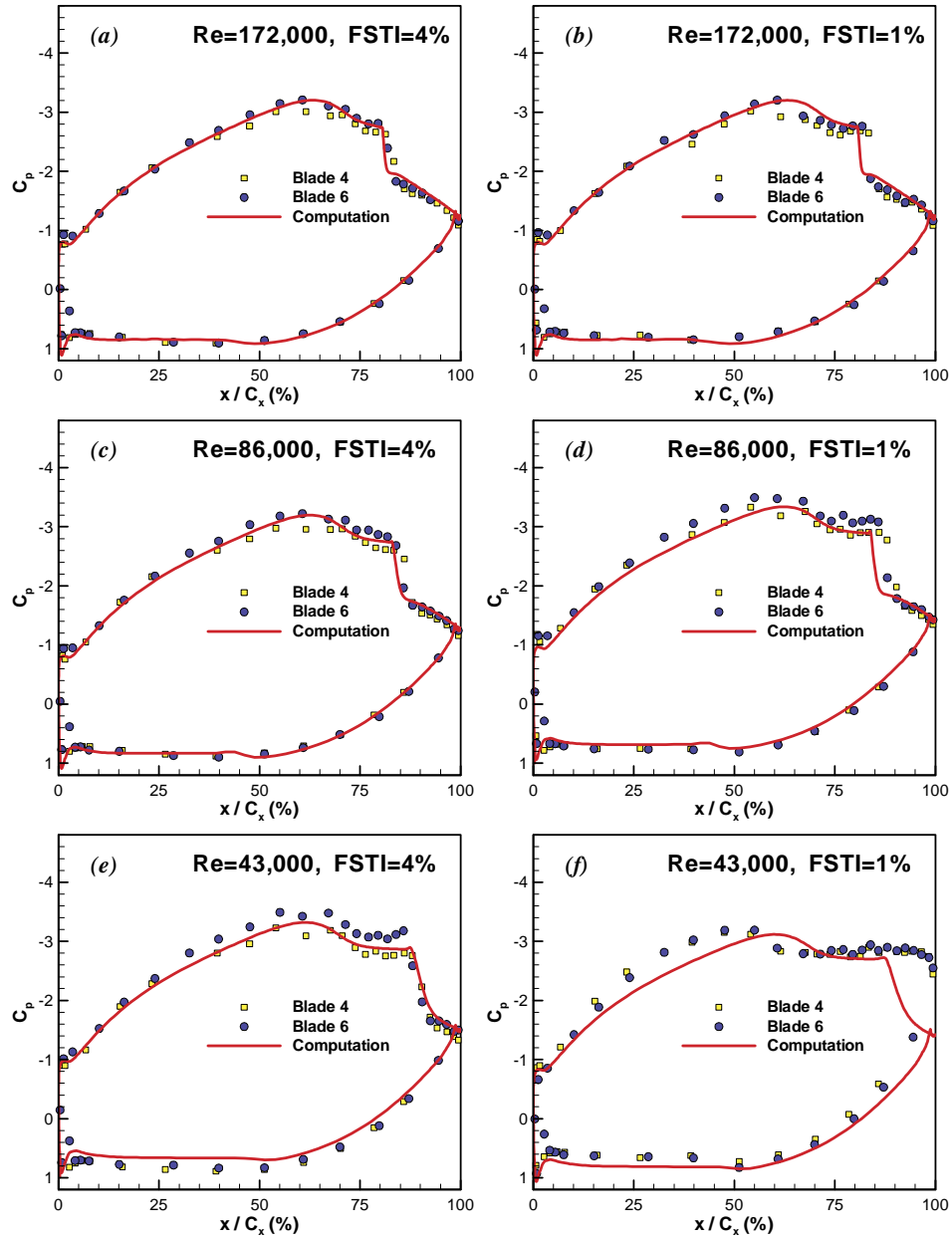


Figure 7: Comparison of computed pressure coefficient with experiments of Lake et al. (1999, 2000).

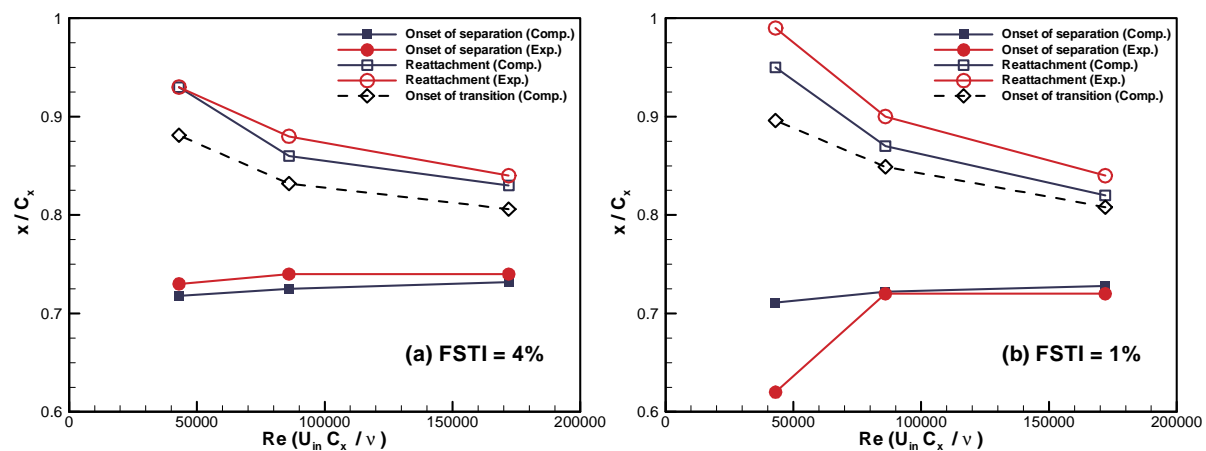


Figure 8: Comparison of separation, reattachment and transition locations for experiments of Lake et al. (1999, 2000).

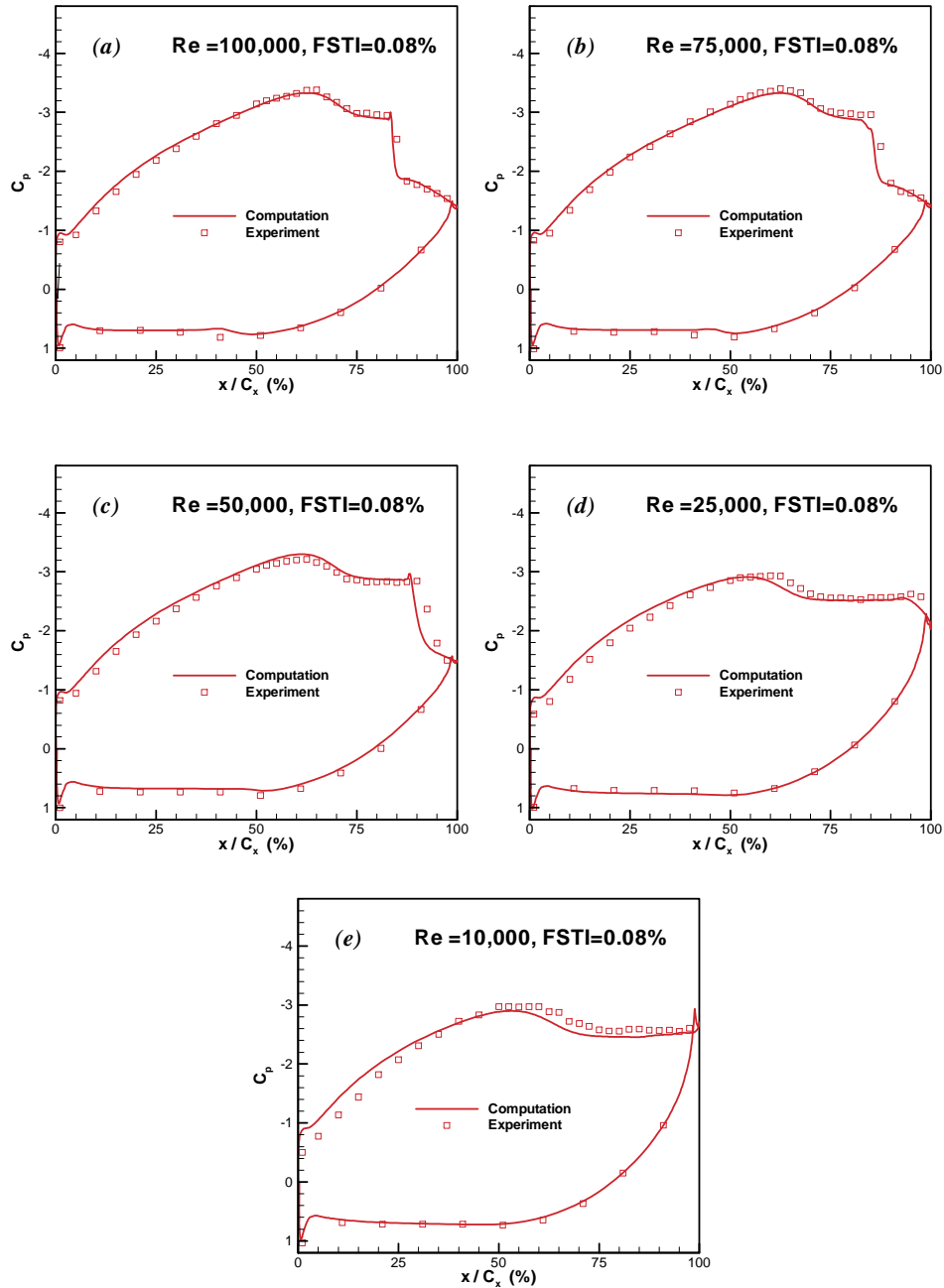


Figure 9: Comparison of computed pressure coefficients with experiments of Corke et al. (2002) for FSTI=0.08% cases.

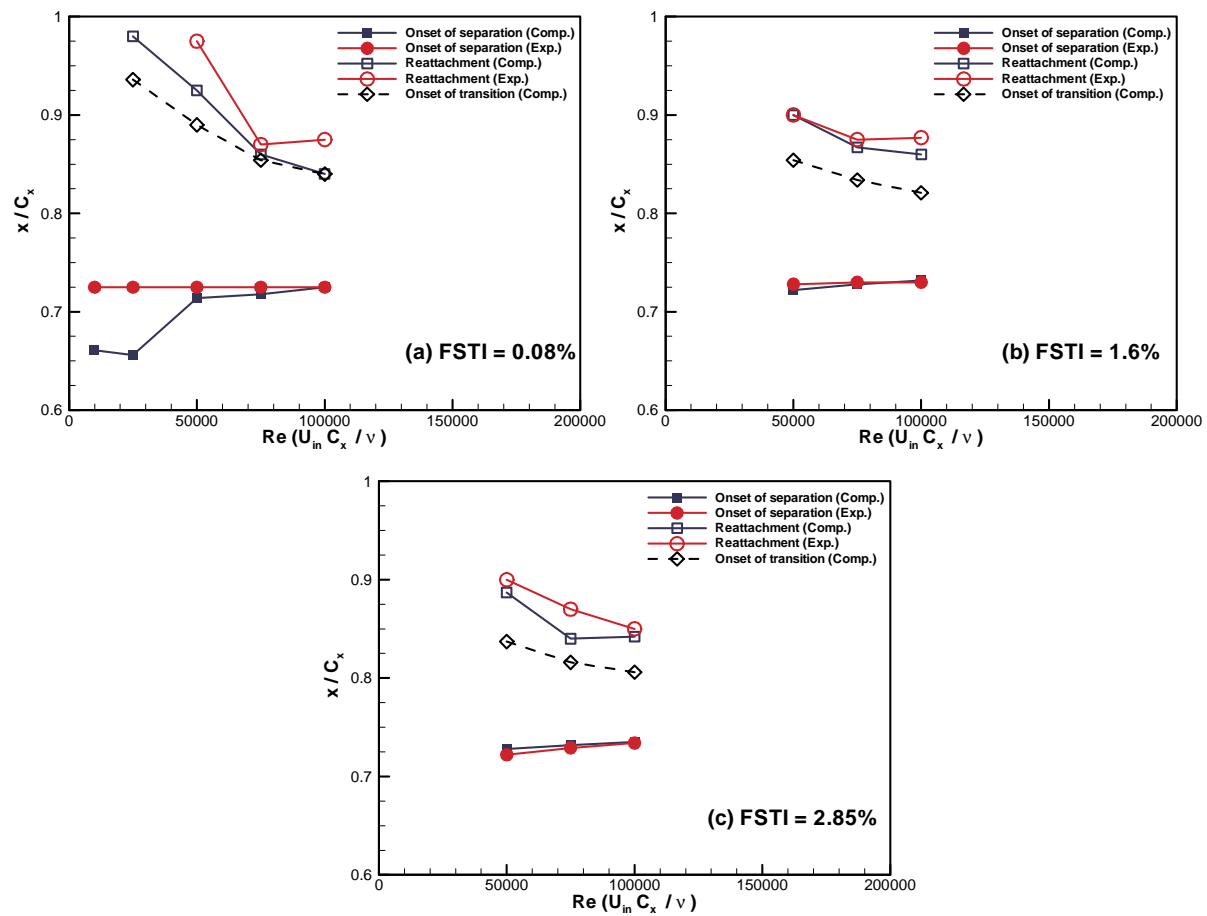


Figure 10: Comparison of separation, reattachment and transition locations for experiments of Corke et al. (2002).

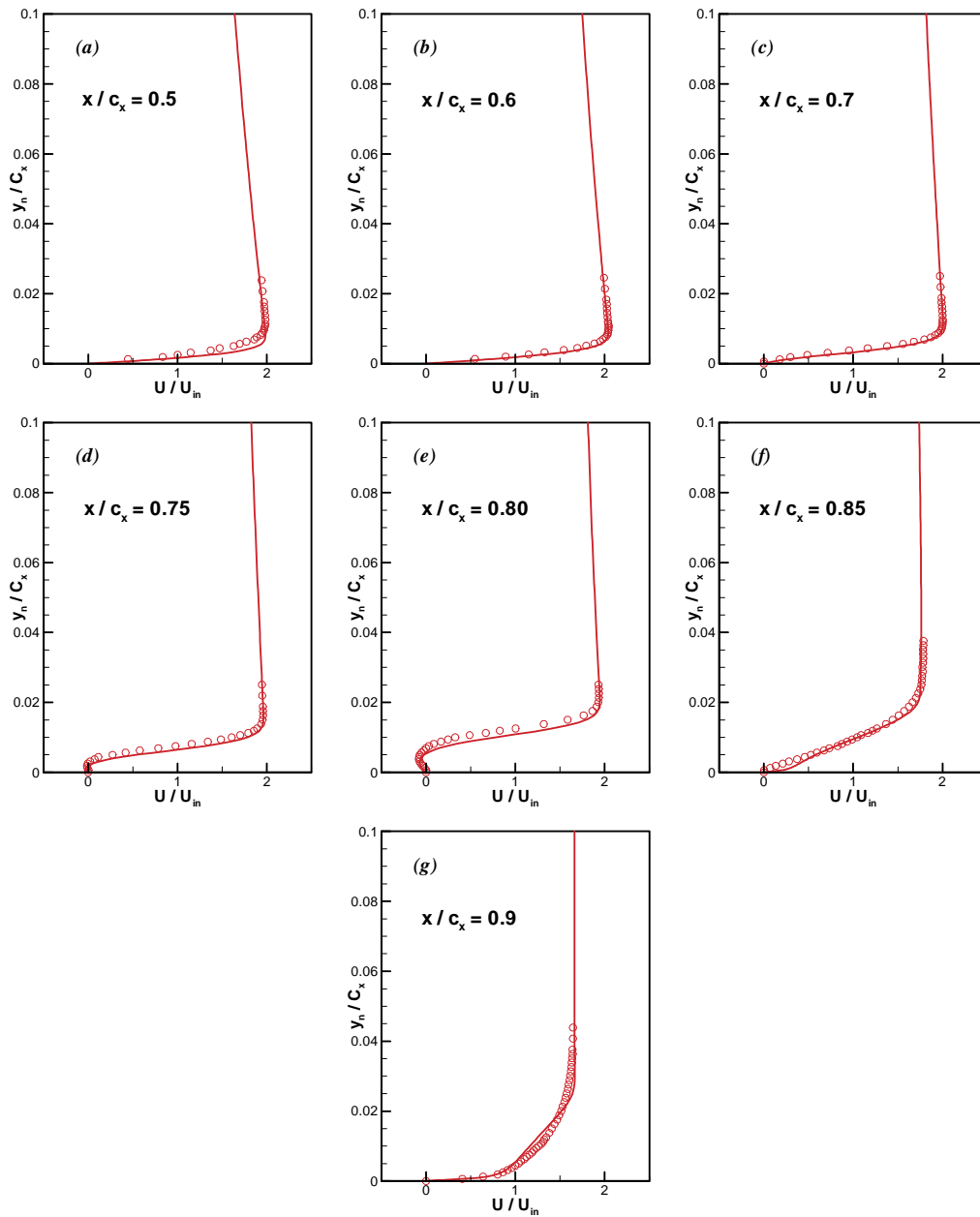


Figure 11: Comparison of computed velocity profiles with experiments of Corke et al. (2002), Re=100,000, FSTI=0.08% case.

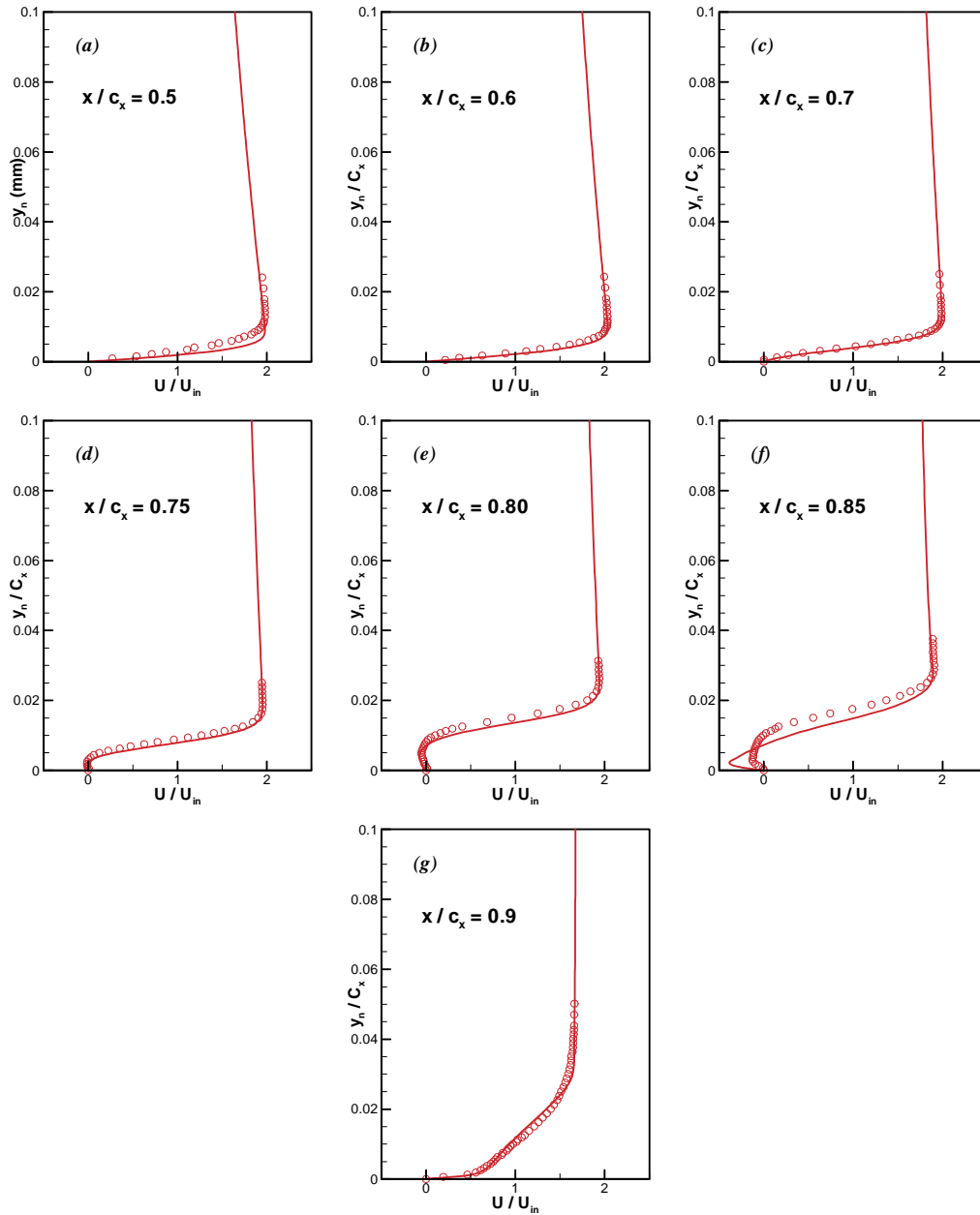


Figure 12: Comparison of computed velocity profiles with experiments of Corke et al. (2002), $Re=75,000$, $FSTI=0.08\%$ case.

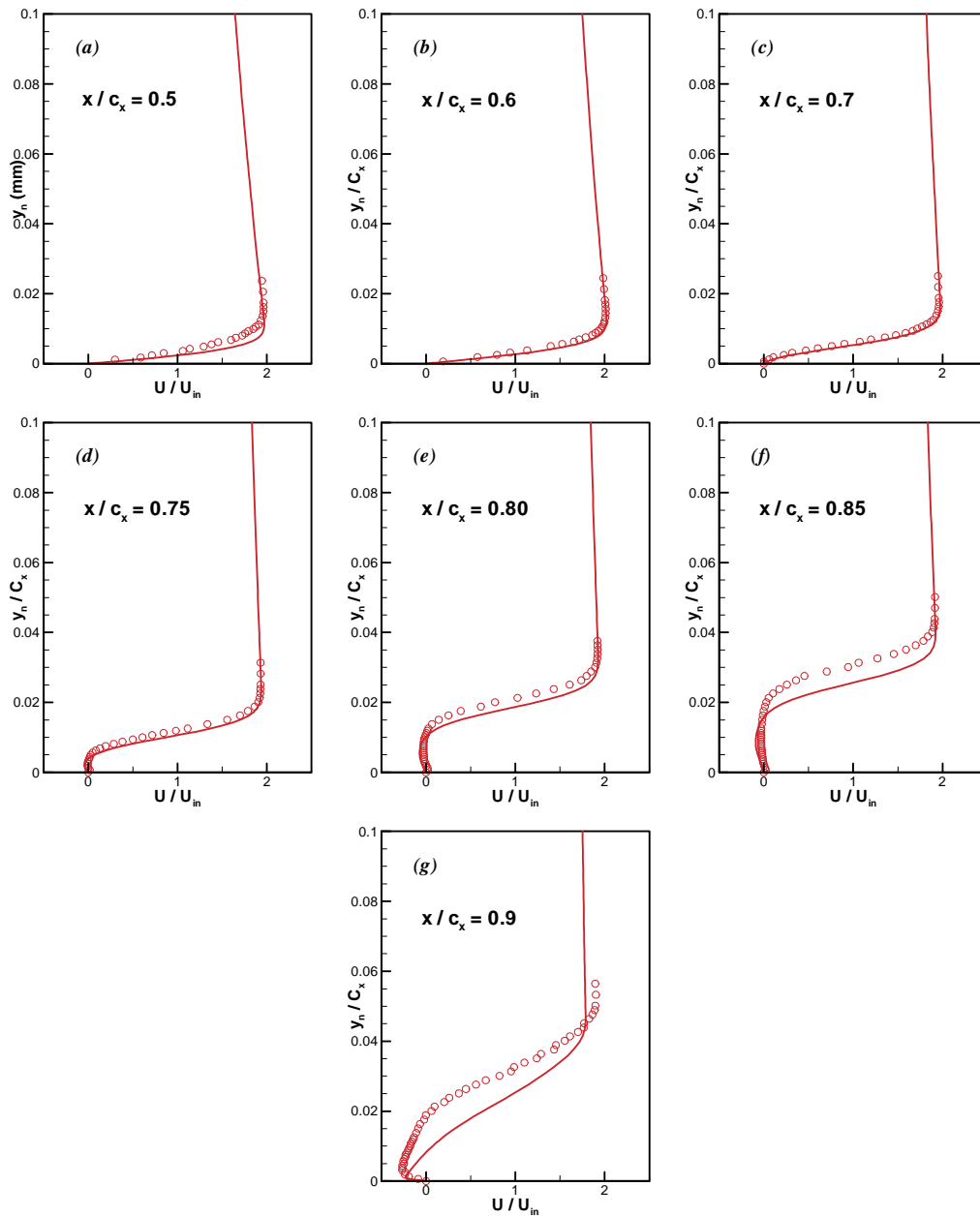


Figure 13: Comparison of computed velocity profiles with experiments of Corke et al. (2002), $Re=50,000$, $FSTI=0.08\%$ case.

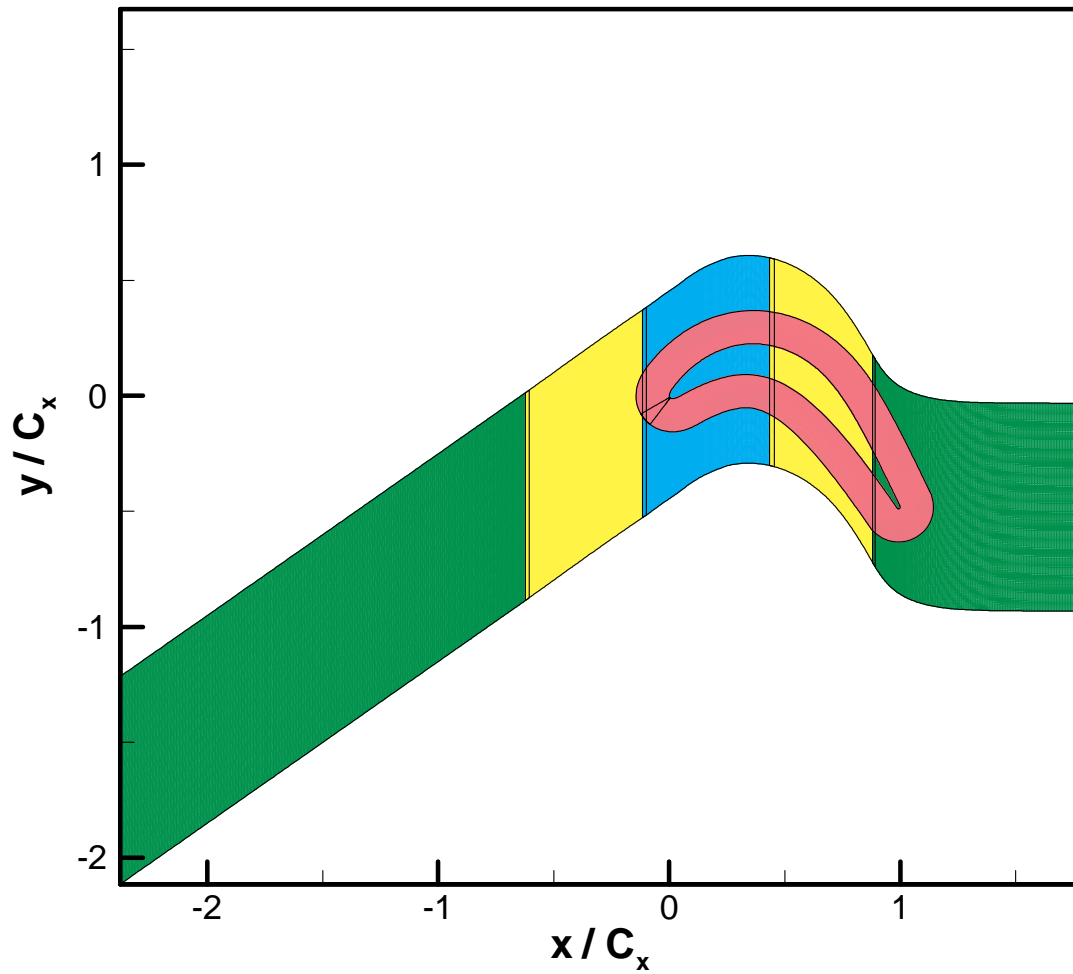


Figure 14: Grid used for computation of experiments of Corke et al. (2002) with FSTI=1.6% and 2.85%.

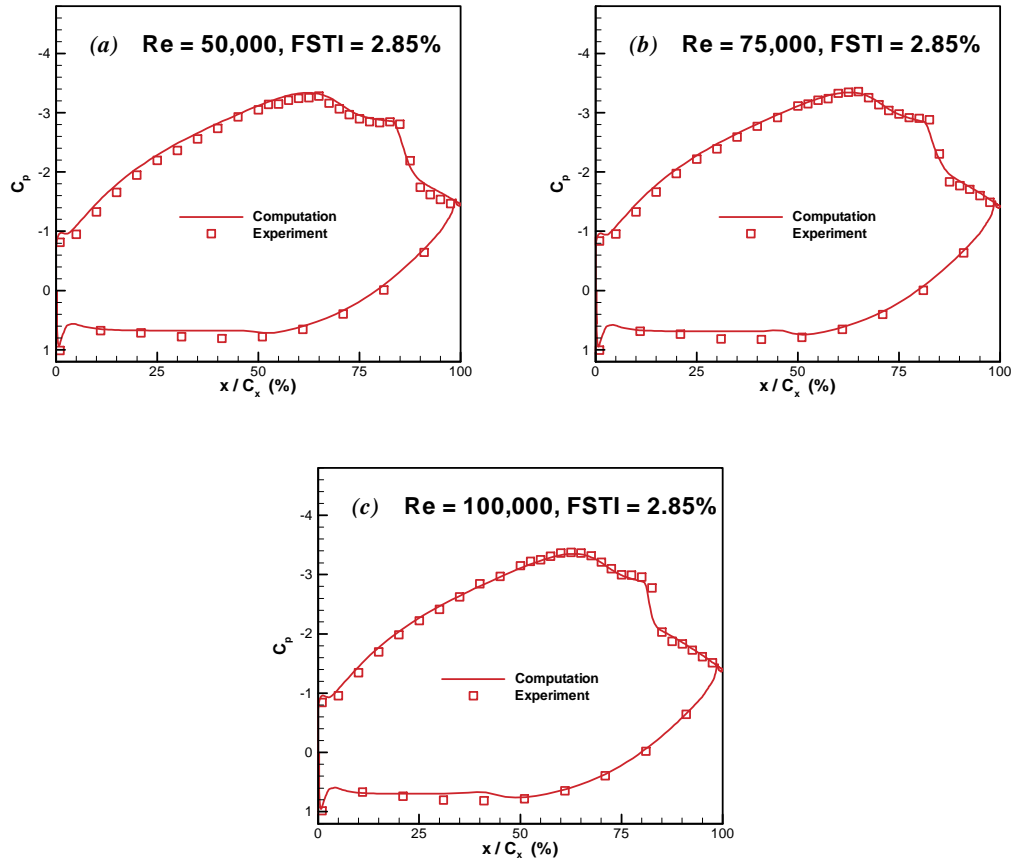


Figure 15: Comparison of computed pressure coefficients with experiments of Corke et al. (2002) for $FSTI=2.85\%$ cases.

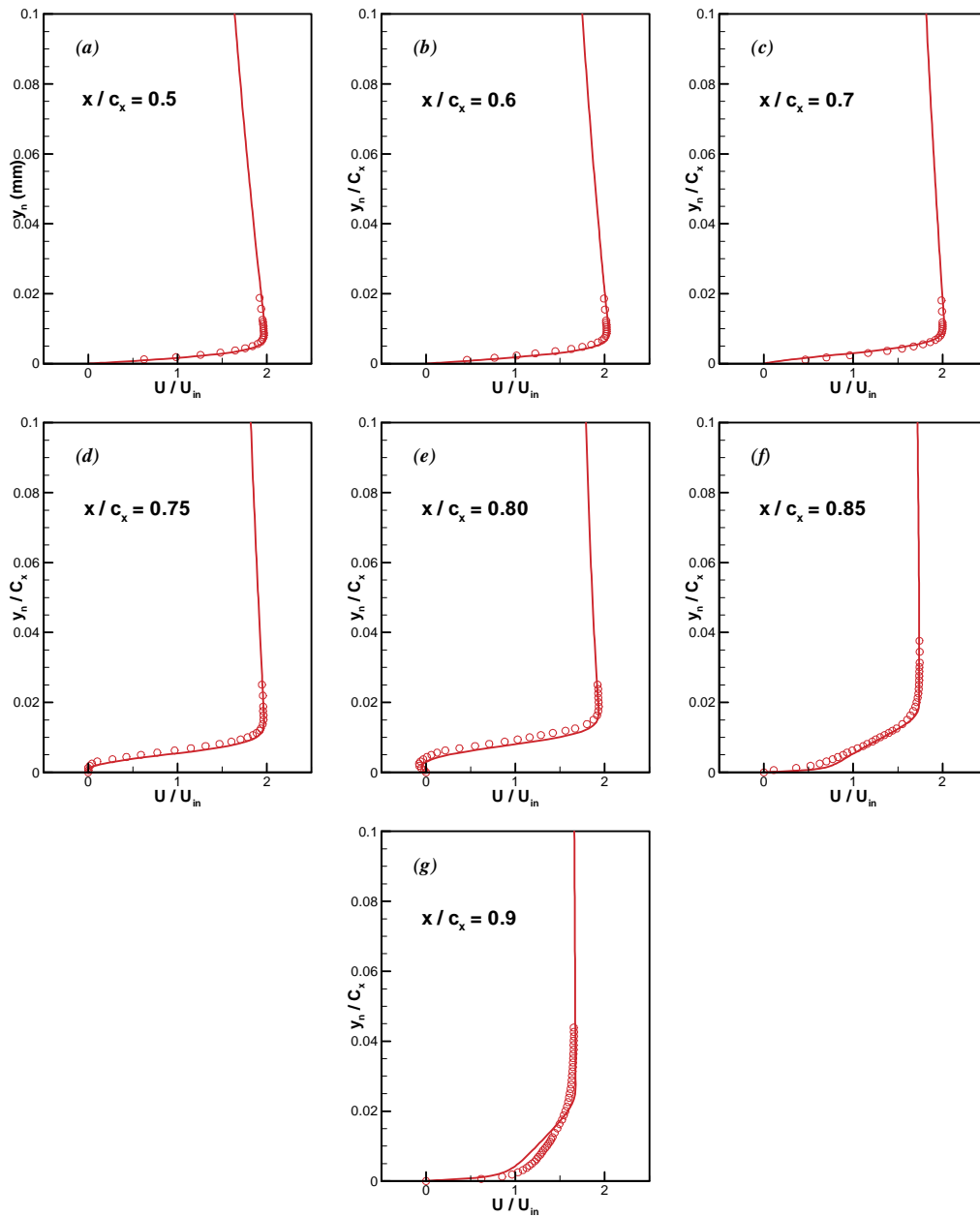


Figure 16: Comparison of computed velocity profiles with experiments of Corke et al. (2002), $Re=100,000$, $FSTI=2.85\%$ case.

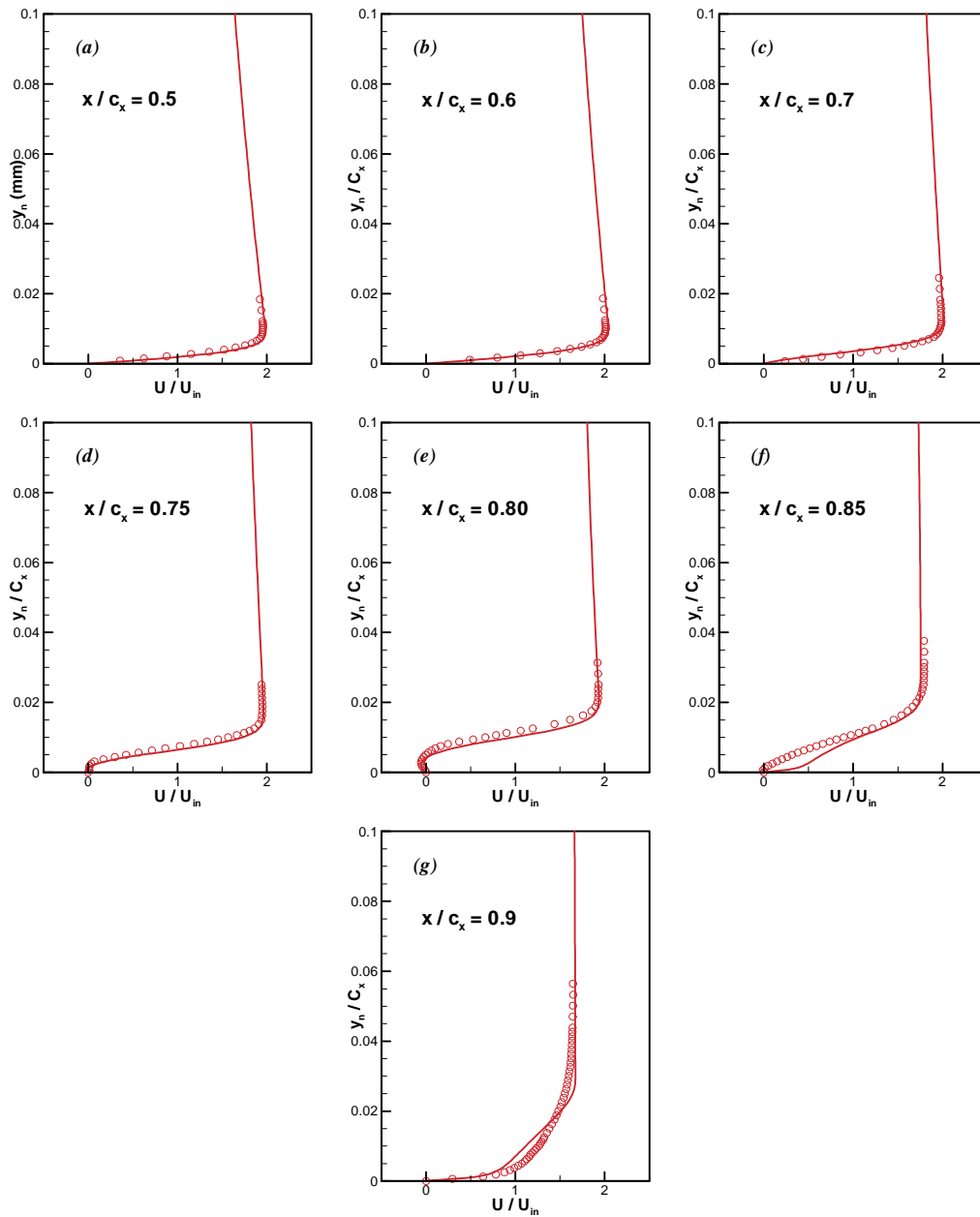


Figure 17: Comparison of computed velocity profiles with experiments of Corke et al. (2002), $Re=75,000$, $FSTI=2.85\%$ case.

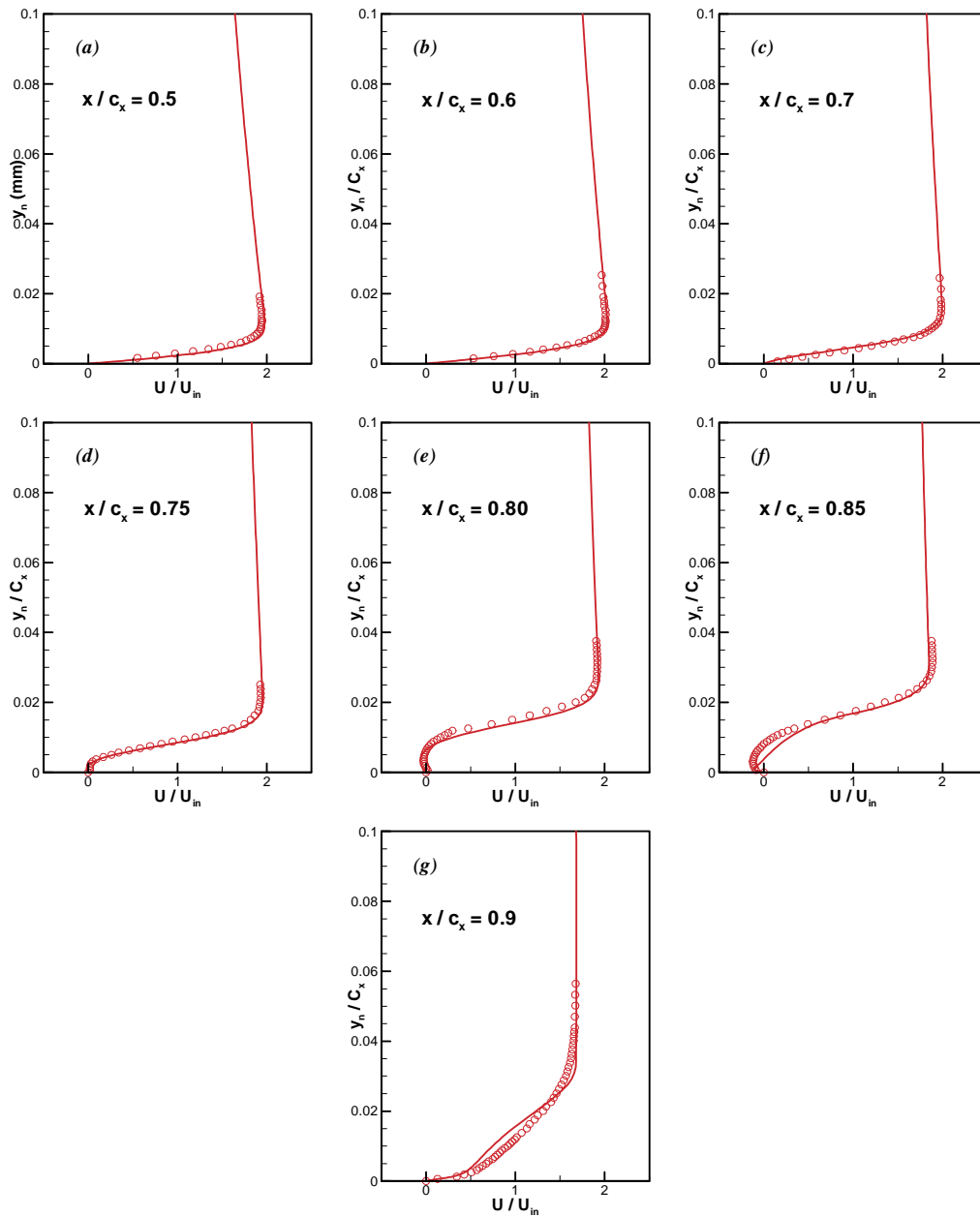


Figure 18: Comparison of computed velocity profiles with experiments of Corke et al. (2002), $Re=50,000$, $FSTI=2.85\%$ case.

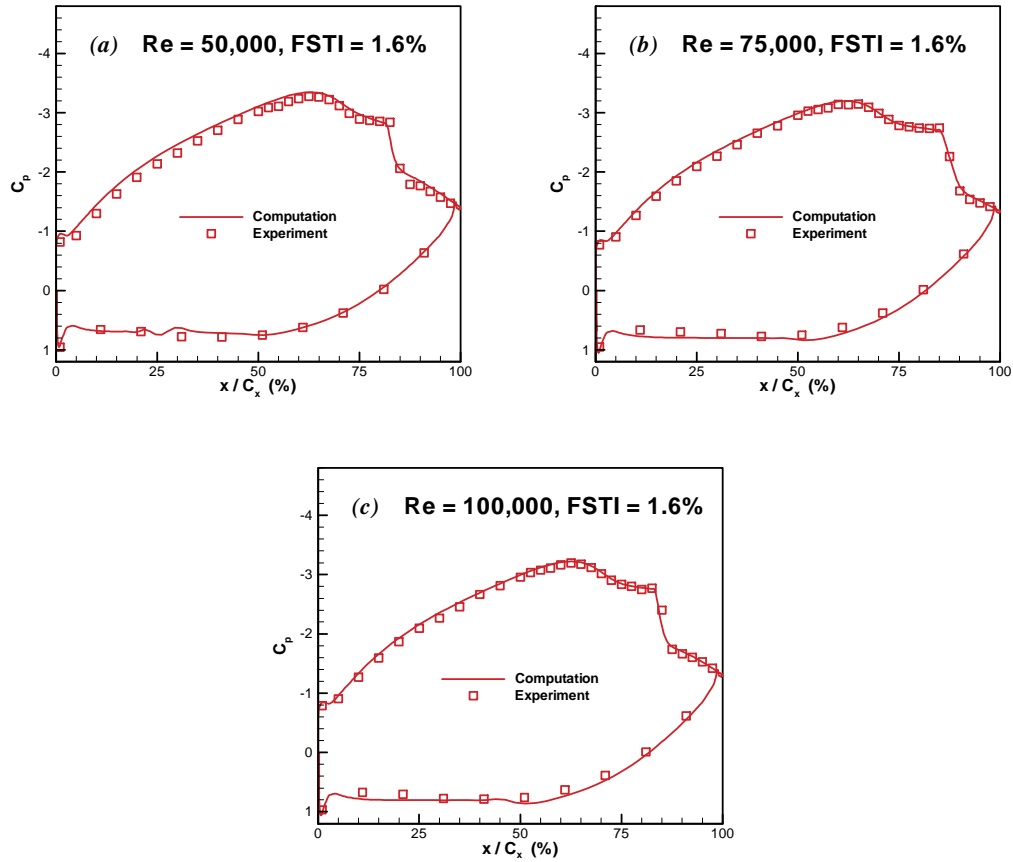


Figure 19: Comparison of computed pressure coefficients with experiments of Corke et al. (2002) for $FSTI=1.6\%$ cases.

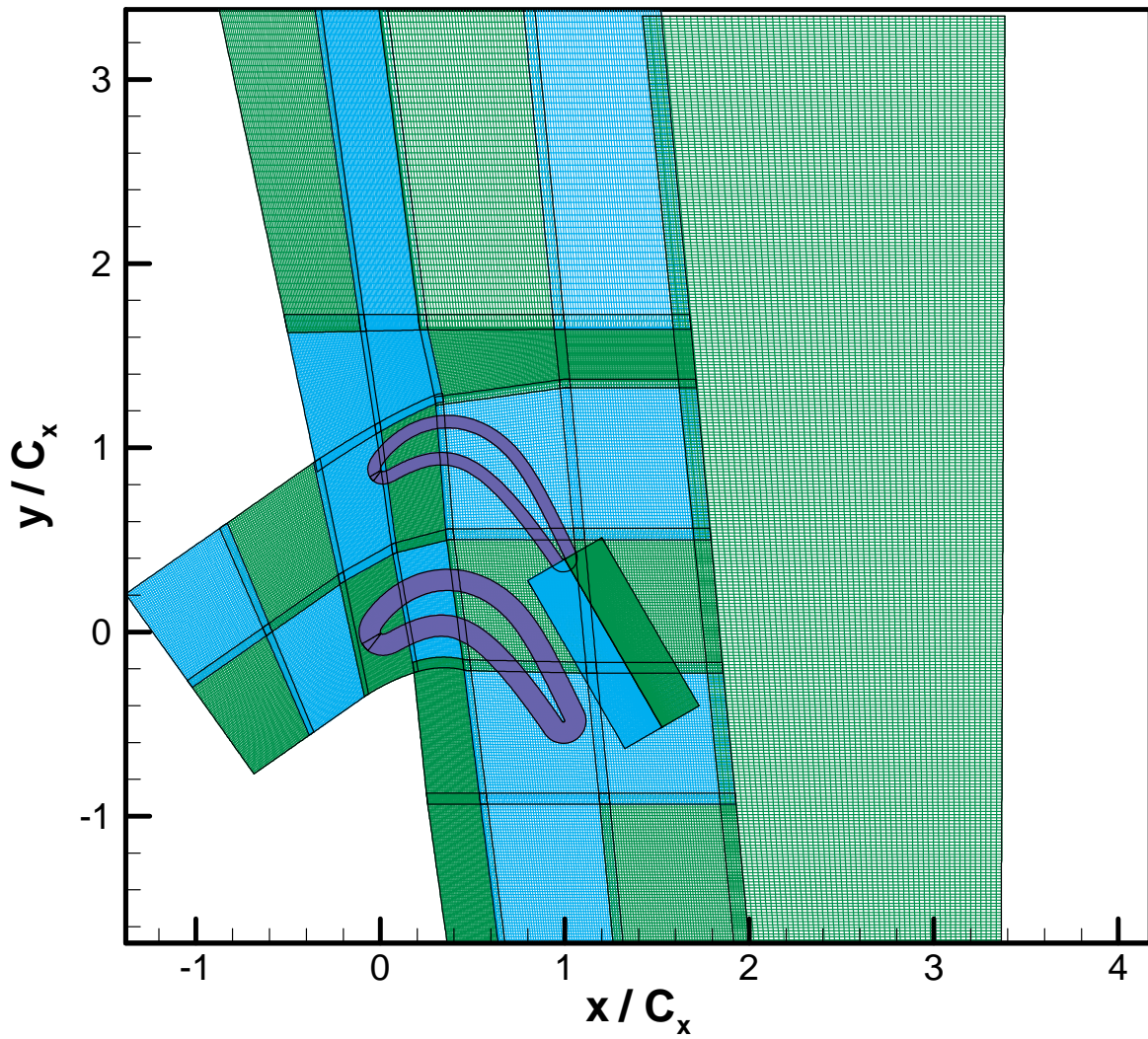


Figure 20: 31 zone multi-block grid used for computation of experiments of Volino (2002).

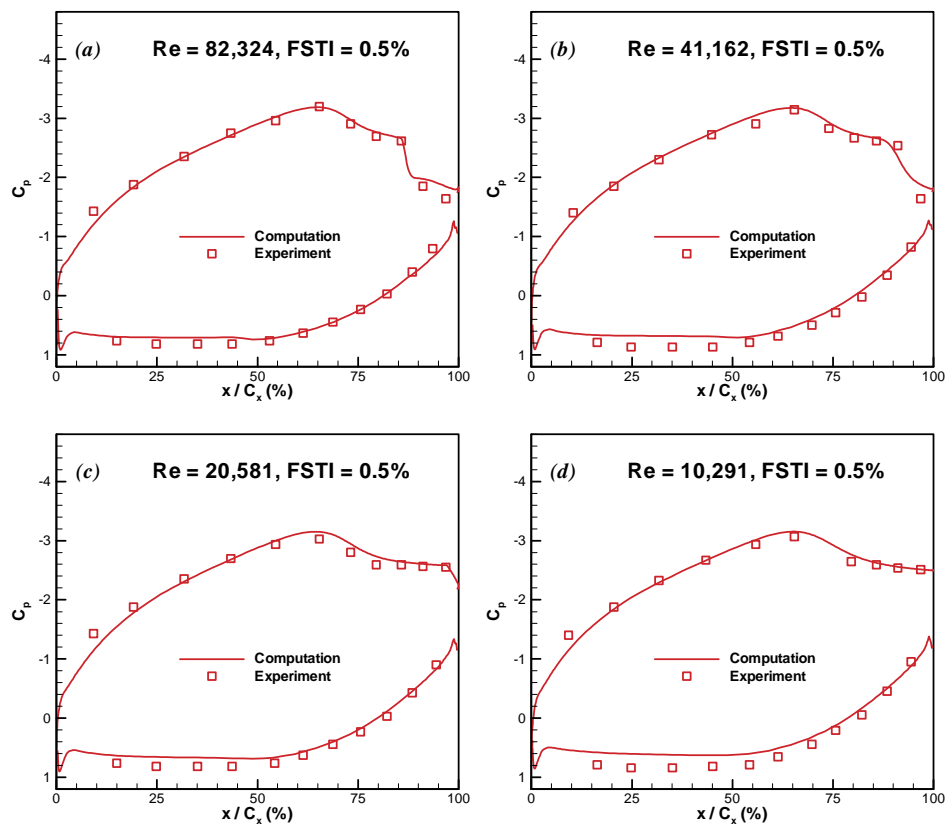


Figure 21: Comparison of computed pressure coefficient distributions with experiments of Volino (2002), FSTI=0.5%.

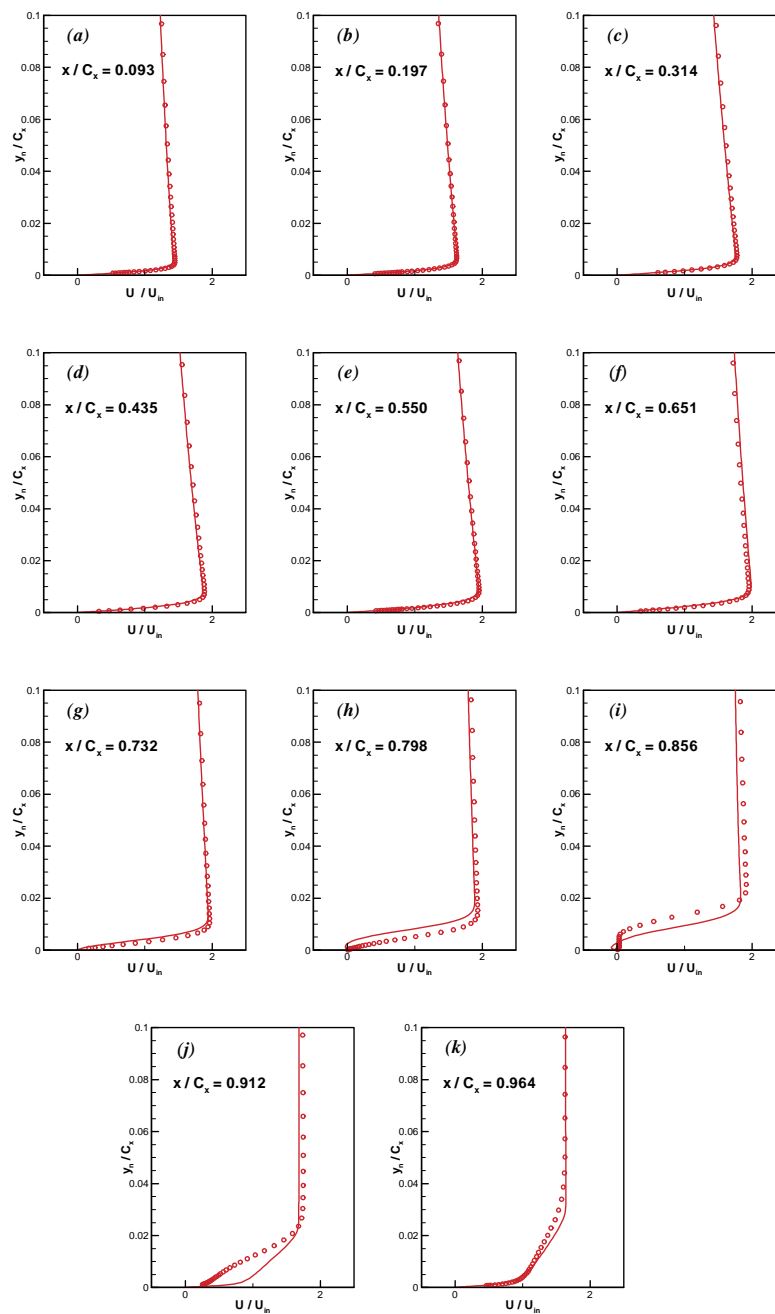


Figure 22: Comparison of computed velocity profiles with experiments of Volino (2002), $Re=82,324$, $FSTI=0.5\%$.

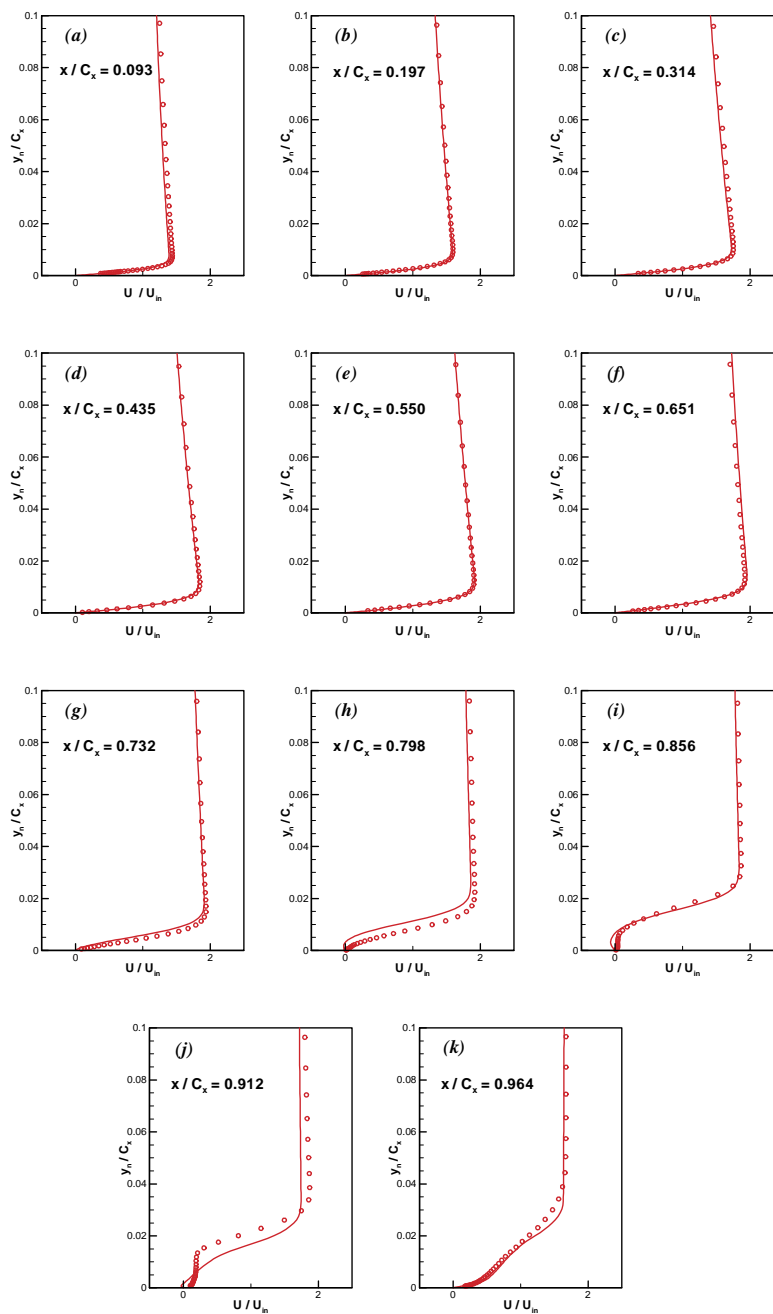


Figure 23: Comparison of computed velocity profiles with experiments of Volino (2002), $Re=41,162$, $FSTI=0.5\%$.

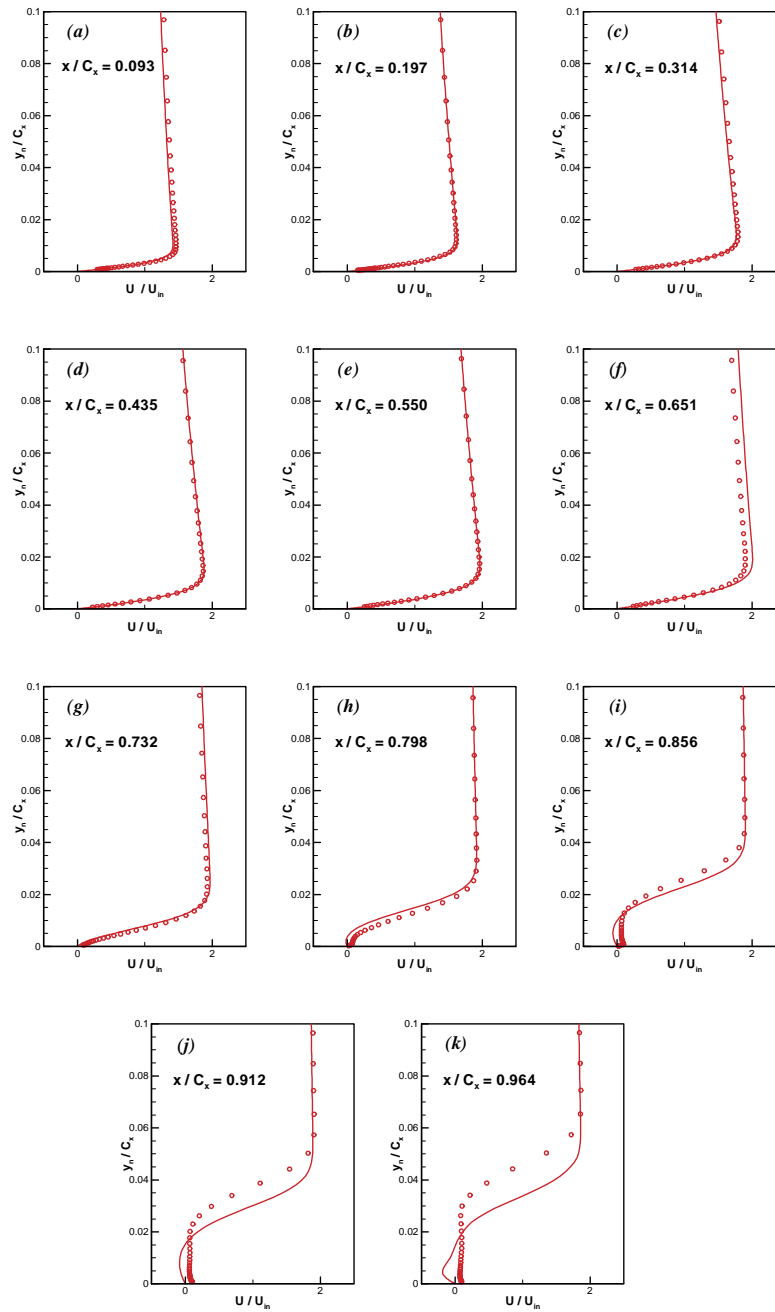


Figure 24: Comparison of computed velocity profiles with experiments of Volino (2002), $Re=20,581$, $FSTI=0.5\%$.

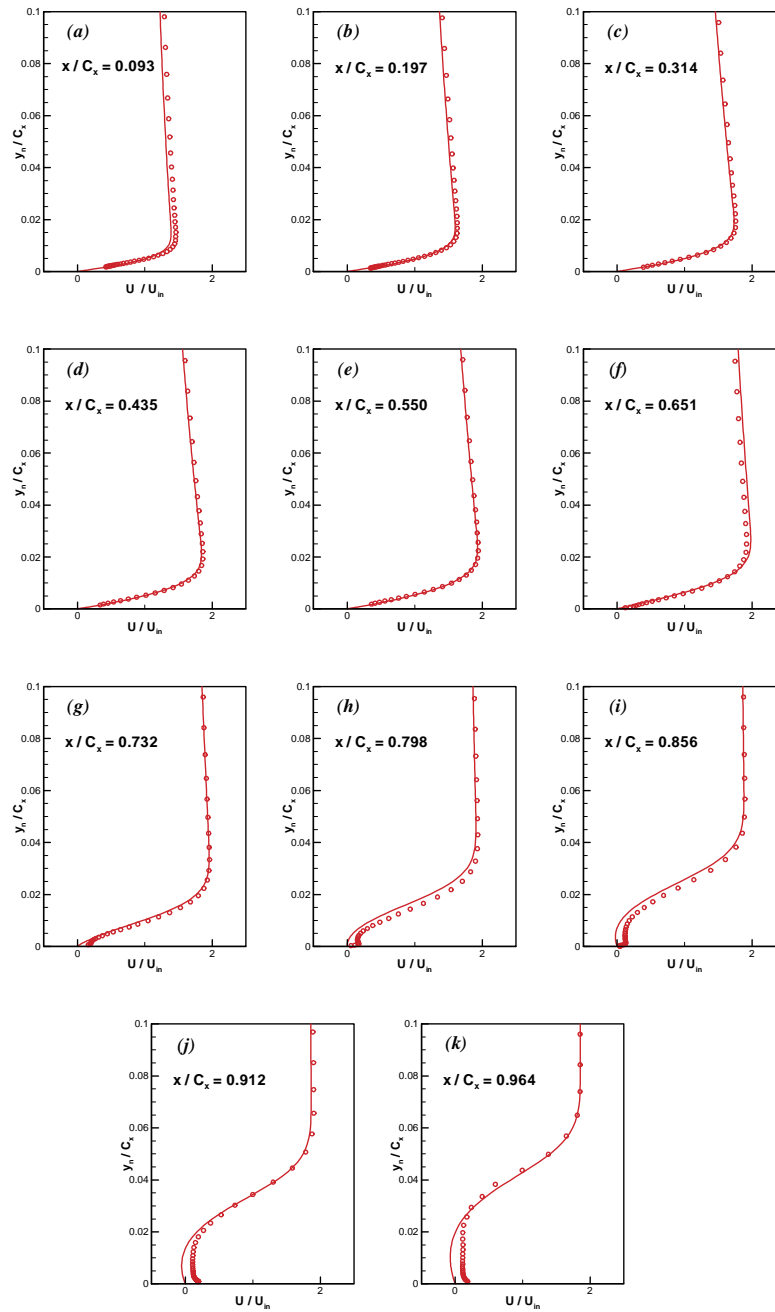


Figure 25: Comparison of computed velocity profiles with experiments of Volino (2002), $Re=10,291$, $FSTI=0.5\%$.

STRUCTURE OF OSCILLATING VORTEX GENERATOR JETS

Ralph J. Volino and Douglas G. Bohl

Department of Mechanical Engineering

United States Naval Academy

Annapolis, Maryland 21402-5042, USA

volino@usna.edu

ABSTRACT

The suction side boundary layer of an airfoil passage was studied experimentally. The pressure gradient along the airfoil was typical of a low pressure turbine environment, and the Reynolds number, based on suction surface length and exit velocity, was 25,000. A row of oscillating vortex generator jets (VGJs), located at the pressure minimum on the suction side was used for flow control. The jets had no net mass flow and a dimensionless oscillation frequency, F^+ , of 0.65. Velocity profiles were acquired with single and cross sensor hot-wire probes at multiple streamwise and spanwise positions downstream of the VGJs. Time averaged results showed that with the VGJs active, the boundary remained attached and essentially laminar, and was spanwise uniform. Without the VGJs the boundary layer separated and did not reattach. Phase averaged results showed that instantaneously the boundary layer was very non-uniform across the span. The outpulse of the jets generated turbulence and produced streamwise vortices, which brought high speed fluid into the near wall region and helped to keep the boundary layer attached. The vortices persisted to the trailing edge. A calmed region followed the jet pulsing events, and the calmed flow was characterized by a thin, spanwise uniform boundary layer that was resistant to separation. Phase averaged mean velocity, Reynolds stresses, and integral quantities are presented to illustrate the structure of the unsteady boundary layer.

INTRODUCTION

Vortex generator jets (VGJs) are used to control or prevent boundary layer separation. The jets, as described by Johnston and Nishi (1990), exit a surface from “small, skewed, and pitched holes” to create streamwise vortices similar to those created by solid vortex generators. Any jet will produce some turbulence, and the turbulent mixing will tend to bring high momentum fluid into the near wall region and inhibit separation. Streamwise vortices bring additional high momentum fluid into the near wall region. The most effective VGJs enter the boundary layer at a relatively shallow pitch angle relative to the wall and a high skew angle relative to the main flow. Compton and Johnston (1992) showed that the co-rotating vortices produced by VGJs are stronger and more effective for separation control than the counter-rotating vortices which form downstream of a normal jet.

The present use of VGJs is motivated by the need to control separation on the suction side of some low-pressure turbine (LPT) airfoils in aircraft engines. Airfoils are designed so that separation does not occur under takeoff conditions, where Reynolds numbers are relatively high. At altitude, however, the ambient density is lower, resulting in lower Re and separation problems. Passive devices such as solid vortex generators can be used to control separation, but they can increase aerodynamic losses at high Re . VGJs could be turned on only when needed, providing separation control at low Re with no harmful effects at high Re .

Most studies of VGJs have considered jets with steady flow (e.g. Johnston and Nishi, 1990 and Compton and Johnson, 1992), but a few have also considered pulsed jets. McManus et al. (1994) found that pulsed VGJs were more effective than steady jets in turbulent boundary layers. Bons et al. (2002) used pulsed jets to suppress separation in a laminar boundary layer under simulated LPT conditions. They used spanwise rows of VGJs on the suction surface of an airfoil, and found that a row near the suction surface pressure minimum was most effective. Reynolds numbers as low as 60,000 (based on suction surface length, L_s , and exit velocity, U_e) were considered. Bons et al. (2002) found that the pulsed jets were fully effective even when the dimensionless pulsing frequency, F^+ , was as low as 0.1, where F^+ is a ratio of the transit time for flow between the VGJ hole and the trailing edge to the time interval between pulses. Ensemble averaged velocity profiles showed a long relaxation or “calmed” period following each jet pulse. During this calm period the boundary layer remained attached long after the turbulence generated by the pulse had moved downstream. Calmed regions have been observed following turbulent spots in transitional boundary layers (e.g. Gostelow et al., 1997). The mean velocity profiles in the calmed region gradually relax from a turbulent shape to a laminar (and in some cases separated) profile shape. The calmed boundary layer is very resistant to separation, much like a turbulent boundary layer, but it is very laminar-like in terms of its fluctuation levels and low losses. The pulsed jets were more effective than steady jets, even with pulsed jet duty cycles as low as 1%. This was believed to indicate that the starting vortex formed at the beginning of each pulse was responsible for most of the flow control with pulsed jets.

Volino (2003) considered oscillating jets with no net mass flow under conditions similar to those of Bons et al. (2002), but at a lower Reynolds number of 25,000. In uncontrolled flow, the laminar boundary layer separated and did not reattach. With the jets operating at a pulsing frequency $F^+=0.65$, the separation was effectively eliminated. The jets produced turbulent and calmed regions which kept the boundary layer attached. The leading and trailing edge celerities of the turbulent and calmed regions matched those expected for a turbulent spot. Following the calmed region, the boundary layer did separate, but the separation bubble was only present for a small fraction of the jet pulsing cycle, and it remained very small and thin. In fact, the boundary layer remained thin, laminar and attached along the entire airfoil over most of the cycle.

While pulsed and oscillating VGJs have been shown effective in a few studies, information about their structure is limited. Bons et al. (2002) and Volino (2003) provide data only at a single spanwise position. Johari and Rixon (2003) studied a single pulsed VGJ in a zero pressure gradient turbulent boundary layer using particle image velocimetry. They provide documentation of the location, vorticity and circulation of the streamwise vortices induced by the VGJ. More information is needed in cases with adverse pressure gradients, laminar flow and multiple VGJs. Also, quantities such as turbulence statistics and boundary layer integral quantities should be documented at multiple spanwise locations. It is not clear at present whether the turbulent and calmed flow produced by the VGJs is sufficient to prevent separation or whether the streamwise vortices are necessary. If the turbulence alone is sufficient, then simpler normal jets might suffice. The persistence or dissipation of the vortices in the streamwise direction is also unclear. The spanwise uniformity of the flow should be studied, as it is not certain that the vortices suppress separation across the entire span. The present study addresses these issues.

EXPERIMENTS

The experimental facility and measurements are described in detail by Volino (2003). Briefly, air enters a low speed wind tunnel through blowers and passes through a honeycomb, screens, settling chambers, and a contraction before entering the test section. At the exit of the contraction, the mean velocity is uniform to within 1%. The freestream unsteadiness is $0.5\% \pm 0.05\%$. Most of this is streamwise unsteadiness at frequencies below 20 Hz. The actual freestream turbulence intensity (as indicated by the cross-stream and spanwise components) is about 0.2%.

The test section follows the contraction and consists of the passage between two airfoils, as shown in Fig. 1. A large span to chord ratio of 4.3 insures nominally two-dimensional flow at the midspan of the airfoils. Just upstream of each airfoil are bleed flaps, which allow air to escape from the passage. The flaps, the inlet flow angle, and a tailboard on the pressure side of the passage are adjusted so that the leading edge flows and pressure gradient along the airfoils match those in a multi-airfoil cascade representation of a typical LPT.

The oscillating VGJs were produced from a plenum which extended along the span at about mid-chord within the suction side airfoil, as shown in Fig. 2. A loudspeaker was sealed to the wide end of a funnel, and the funnel was inserted into the plenum at one end of the airfoil. The speaker was powered by an audio amplifier, which was in turn driven with a sine wave by a function generator. Holes for the VGJs were drilled through the suction surface into the plenum in a spanwise line at the pressure minimum, $s/L_s=0.514$, where s is the distance from the leading edge along the suction surface and $L_s=229$

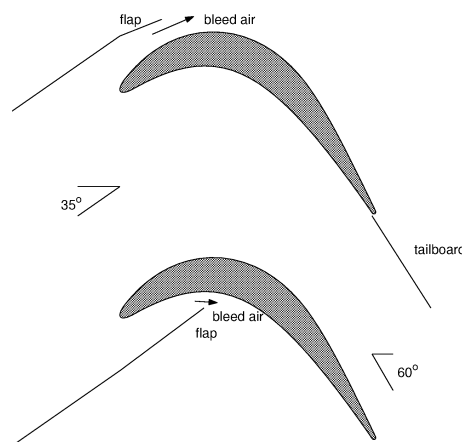


Fig. 1 Schematic of the test section

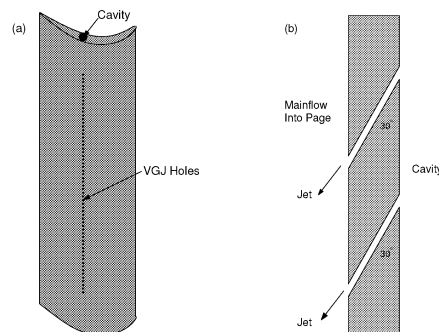


Fig. 2 Drawing of suction side airfoil with cavity and VGJs: (a) full airfoil, (b) cross section of VGJ holes

mm. The hole diameter is $0.0035L_s$ and the spacing, P , is $0.037L_s$. The holes were drilled at a 90 degree skew angle with respect to the main flow and a 30 degree pitch with respect to the surface. The function generator and amplifier were set to produce jets with maximum velocity 5 times the local freestream velocity and dimensionless frequency $F^+=0.65$. Just upstream of the jets, the momentum thickness Reynolds number $Re_\theta=62$, and the boundary layer thickness was 1.1 mm ($0.0048L_s$). The $Re=U_e L_s/\nu$ was 25,000.

Measurements consisted of velocity profiles acquired using hot-wire anemometry at five streamwise locations between the VGJ holes and the trailing edge. At each streamwise location, profiles were acquired at five spanwise positions. As in Volino (2003), a single-sensor probe was traversed from the wall to the freestream, providing streamwise velocity data, from which boundary layer thicknesses and local skin friction coefficients, c_f , were computed (based on sublayer velocities). At the same streamwise and spanwise locations, a cross-wire probe was traversed from $y=1\text{mm}$ from the wall to the freestream. At each measurement point, data were acquired for 26 s at a 20 kHz sampling rate. Details are available in Volino (2003).

Both time and phase averaged results are presented below. The velocity data were phase averaged at 24 evenly spaced increments around the jet pulsing cycle. At each increment, data were averaged over $1/180^{\text{th}}$ of the cycle. For each 26 second data trace, this results in roughly 3000 data points to average for each ensemble. Uncertainties are 3% in the mean velocity, 10% in the momentum thickness, 8% in the shape factor and skin friction coefficient, and 10% in the Reynolds stresses. Further details are available in Volino (2003).

RESULTS

Figure 3 provides an example of the time averaged mean streamwise velocity, U , and time averaged turbulence statistics from the stations at $s/L_s=0.78$. Profiles are shown for the 5 spanwise measurement locations, with $z/P=0$ directly downstream of a VGJ hole, and $z/P=1$ directly downstream of the adjacent hole. All velocities and turbulence quantities in the figures are normalized using U_e . There is some spanwise variation in the rms u' profiles, although all have the same general double-peak shape. The U/U_e profile is essentially uniform across the span. The mean streamwise velocity profiles show that the boundary layer is attached, so the flow control is effective everywhere between the jets. Figure 4 shows the time averaged shape factor, $H=\delta^*/\theta$, and Re_θ at all locations. Again, there is little variation across the span. The shape factor rises at first, indicating a tendency toward separation, but it remains between 2 and 2.6, indicating an attached laminar boundary layer. As the time averaged flow is essentially spanwise uniform, further details can be obtained from the time averaged results presented in Volino (2003) for a single spanwise position.

Although the time averaged results are spanwise uniform, instantaneously there is considerable non-uniformity when the jet disturbance passes. The time average is simply dominated by the period between disturbances, which is uniform. The remainder of the present paper focuses on phase averaged results. Figure 5 shows contour plots of the mean streamwise velocity in the y - z plane at streamwise locations $s/L_s=0.61$ (Figs. 3a,b) and 0.94 (Figs. 3c,d). The data shown at $0 < z/P < 1$ are repeated at $1 < z/P < 2$ and $2 < z/P < 3$ to illustrate the periodic nature across the span. Plots are shown for the period between jet disturbances (Figs. 3a,c) and while the disturbance is present (Figs. 3b,d). In the figure captions, t is the time from the start of the cycle (roughly when the outflow begins at the VGJ hole) and T is the cycle period. Between disturbances the boundary layer is spanwise uniform and thin. The streamwise boundary layer growth can also be observed. In the presence of the disturbance there is a clear variation across the span, and it persists to the trailing edge. Figure 6 shows the data from Fig. 5 as velocity profiles. Comparison of Figs. 6b and 6d shows that the spanwise variation is clearly stronger at the upstream station.

Figure 7 shows the jet induced change in the mean wall-normal velocity, ΔV . That is, the mean V fields corresponding to the planes and phases of Figs. 5a and 5c were subtracted from the mean V fields corresponding to Figs. 5b and 5d respectively. Upwash ($\Delta V > 0$) and downwash ($\Delta V < 0$) regions are clear. The upwash corresponds to the region of low streamwise velocity in Fig. 5, as low speed fluid is pulled away from the wall. The downwash corresponds to the region of high streamwise velocity, where higher speed fluid is brought closer to the wall. The vortices and their associated mixing persist to the trailing edge.

The behavior of the boundary layer over the course of a jet pulsing cycle is shown in Fig. 8, which shows contours of the rms fluctuating streamwise velocity u' in a plane at $s/L_s=0.78$. Results are shown for evenly spaced phases over part of a full jet pulsing cycle. In the phase shown in Fig. 8a, the boundary layer is between disturbances, and u' is essentially zero. In Fig. 8b, the disturbance is just beginning to arrive, and u' levels start to increase at $y/P \approx 1$. The variation across the span is clear. At the next phase shown (Fig. 8c), the magnitude of u' has increased, with a peak still at $y/P \approx 1$ and a second peak near the wall. The double peaks agree with the time averaged profiles of Fig. 3b. The next three phases of Fig. 8 (Figs. 8d-f) show u' decreasing in the outer part of the boundary layer and remaining high near the wall. In the remaining three phases

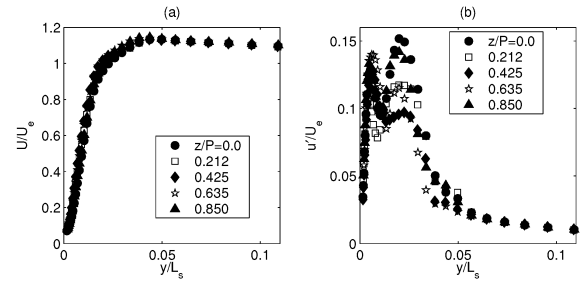


Fig. 3 Time averaged U/U_e and rms u'/U_e at $s/L_s=0.78$

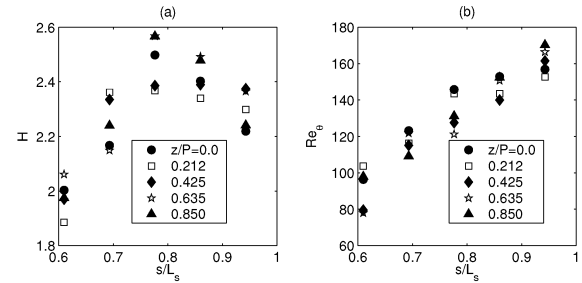


Fig. 4 Time averaged a) H and b) Re_θ

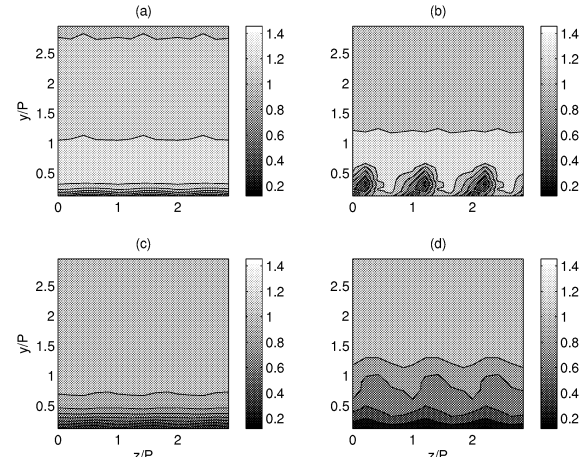


Fig. 5 Phase averaged U/U_e at a) $t/T=0.04$, $s/L_s=0.61$; b) $t/T=0.54$, $s/L_s=0.61$; c) $t/T=0.71$, $s/L_s=0.94$; d) $t/T=0.08$, $s/L_s=0.94$

(Figs. 8g-i), the u' level drops back to the undisturbed value near zero. For the rest of the cycle (not shown) the u' level remains low, as in Fig. 8a. The behavior shown in Fig. 8 is typical of all streamwise locations. The disturbance first appears near the edge of the undisturbed boundary layer and then moves into the near wall region. The disturbance level then begins to drop, first in the outer part of the boundary layer and then near the wall. For a significant part of the cycle the boundary layer is undisturbed. The fraction of the time that the boundary layer is disturbed increases in the streamwise direction. This occurs, as shown in more detail for a single spanwise position in Volino (2003), because the leading edge of the disturbance travels faster than the trailing edge.

Figure 9 shows the Reynolds shear stress, $u'v'$ at the same location and phases as in Fig. 8. The disturbance has not arrived yet in Fig. 9a, and $u'v'$ is essentially zero everywhere. By the third phase shown (Fig. 9c), negative valued peaks appear at $y/P \approx 1$ and very near the wall. The negative sign is

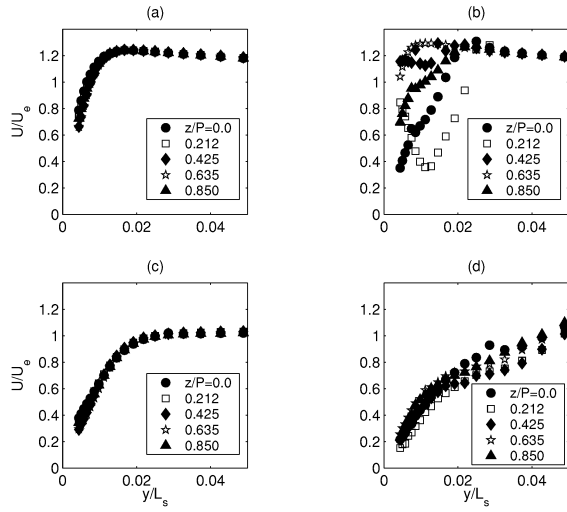


Fig. 6 Phase averaged U/U_e profiles at a) $t/T=0.04$, $s/L_s=0.61$; b) $t/T=0.54$, $s/L_s=0.61$; c) $t/T=0.71$, $s/L_s=0.94$; d) $t/T=0.08$, $s/L_s=0.94$

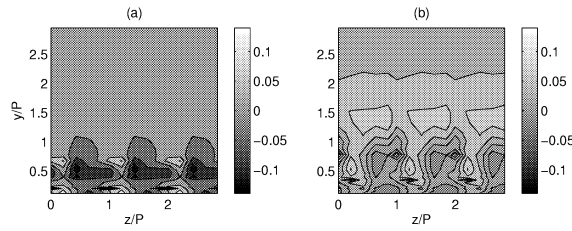


Fig. 7 Phase averaged $\Delta V/U_e$ at a) $t/T=0.54$, $s/L_s=0.61$; b) $t/T=0.08$, $s/L_s=0.94$

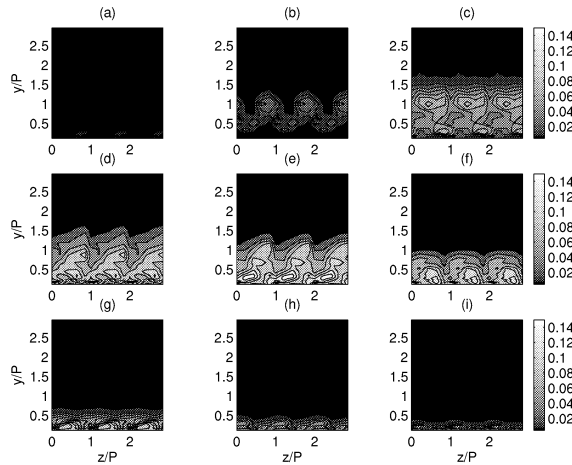


Fig. 8 Phase averaged u'/U_e at $s/L_s=0.78$, $t/T=$ a) 0.50, b) 0.58, c) 0.67, d) 0.75, e) 0.83, f) 0.92, g) 0.0, h) 0.08, i) 0.16

expected for $u'v'$ and the locations agree with the peak locations in u' shown in Fig. 8c. There is also a small positive peak at $y/P \approx 0.5$, centered between the negative peaks. The data from Fig. 9c are shown as profiles in Fig. 10 for a better quantitative comparison. The positive peak is clear at $z/P=0.212$, and the two negative peaks are largest at $z/P=0$ and $z/P=0.425$. Negative $u'v'$ is typical of most boundary layers since the mean streamwise velocity generally increases with distance from the wall. If turbulence causes slow fluid to

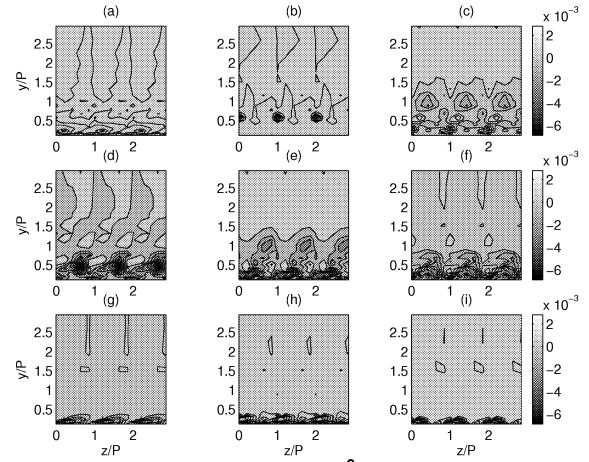


Fig. 9 Phase averaged $u'v'/U_e^2$ at $s/L_s=0.78$, $t/T=$ a) 0.50, b) 0.58, c) 0.67, d) 0.75, e) 0.83, f) 0.92, g) 0.0, h) 0.08, i) 0.16

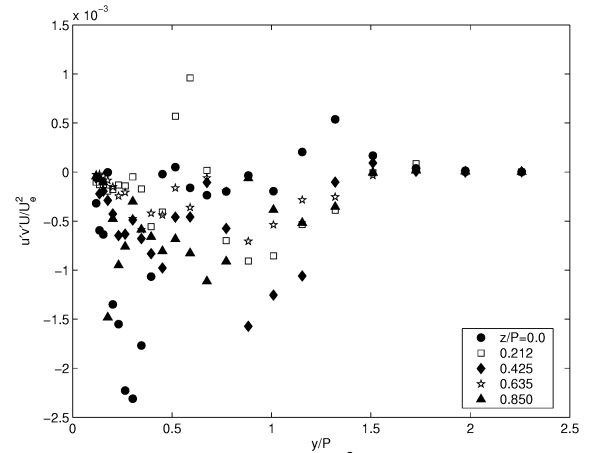


Fig. 10 Phase averaged $u'v'/U_e^2$ profiles at $s/L_s=0.78$, $t/T=0.67$

move away from the wall, v' will be positive and u' will be negative, resulting in negative $u'v'$. If higher speed fluid moves toward the wall, the result is again negative $u'v'$. In the present case, however, the streamwise vortices created by the VGJs cause instantaneously negative local streamwise velocity gradients, as shown in Fig. 6b. This causes the local positive $u'v'$ in Fig. 9c. In Fig. 9d, the negative $u'v'$ reaches its highest magnitude. In Figs. 9e-g, the $u'v'$ magnitude gradually decreases, and at the last two phases shown (Figs. 9h-i), $u'v'$ is near zero. The nonzero $u'v'$ caused by the VGJs is indicative of the turbulent mixing which helps to keep the boundary layer attached. The near zero $u'v'$ for most of the jet pulsing cycle is indicative of a laminar boundary layer, and helps explain the laminar like time averaged velocity profiles of Fig. 3a. Comparing Figs. 8g-i and Figs. 9g-i, $u'v'$ returns to zero before u' . Volino (2003) also saw this faster return of $u'v'$ to zero and noted that the calmed region following the disturbance is characterized by some velocity fluctuations in u' , but very little momentum transport.

For a different perspective on the boundary layer behavior, Fig. 11 shows the phase averaged u' results in an s - z plane at $y=2$ mm ($y/L_s=0.0087$, $y/P=0.23$). Three phases of the cycle are shown, and the convection of the disturbance along the surface and its three-dimensional nature are clear. In Fig. 11a, one disturbance is just leaving the trailing edge, while the next

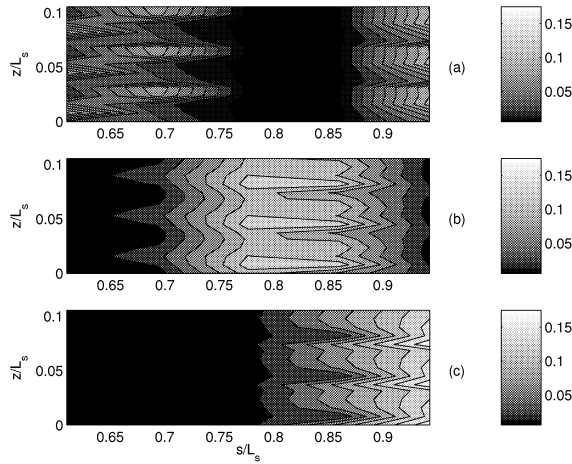


Fig. 11 Phase averaged u'/U_e at $y/L_s=0.0087$ and a) $t/T=0.54$; b) $t/T=0.88$; c) $t/T=0.21$

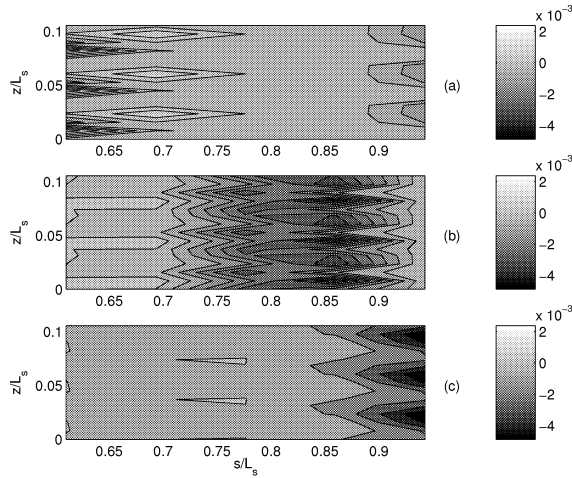


Fig. 12 Phase averaged $u'v'/U_e$ at $y/L_s=0.0087$ and a) $t/T=0.54$; b) $t/T=0.88$; c) $t/T=0.21$

disturbance is present at lower s/L_s . The second disturbance is then seen moving across the surface in Figs. 11b-c. Note that u' is near zero over for much of the cycle at all locations, indicating a laminar boundary layer. Figure 12 shows the Reynolds shear stress at the same locations and phases as in Fig. 11. Qualitatively, Figs. 11 and 12 are very similar. In Fig. 12a, regions of positive $u'v'$ are visible at $s/L_s=0.7$, as were also noted in Figs. 9c and 10. In other areas, $u'v'$ is negative. Over much of the cycle, the boundary layer is laminar and $u'v'$ is near zero.

Integral quantities were computed from the phase averaged streamwise velocity profiles. Figure 13 shows the local Re_θ at the same phases shown in Figs. 11 and 12. The VGJ disturbance causes a local thickening of the boundary layer, but in the absence of the disturbance θ is very low, even near the trailing edge. Figure 14 shows the shape factor, $H=\delta^*/\theta$, at the same phases. When the boundary layer is laminar and attached, H is between about 2 and 2.5. When it becomes turbulent, the value drops. If the boundary layer approaches separation, the shape factor increases significantly while the momentum thickness remains nearly constant. The result is a high shape factor. Comparing Figs. 11-14, H is highest between the VGJ disturbances. When the disturbance arrives at a location, H begins to drop, and it reaches its lowest value in the calmed period immediately after the disturbance has

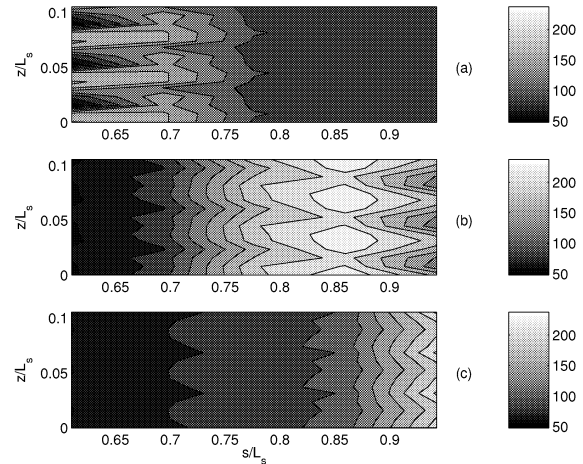


Fig. 13 Phase averaged Re_θ at $y/L_s=0.0087$ and a) $t/T=0.54$; b) $t/T=0.88$; c) $t/T=0.21$

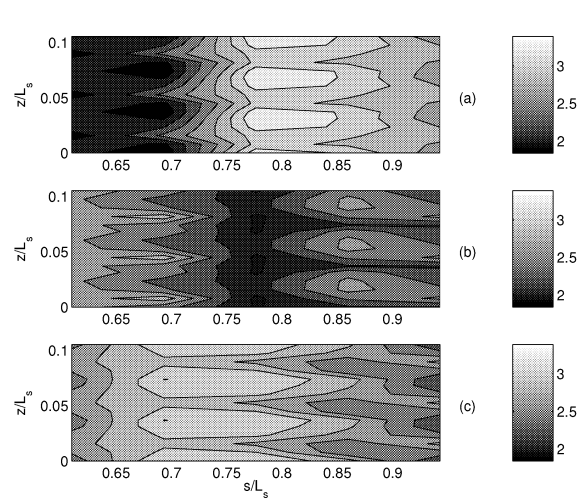


Fig. 14 Phase averaged shape factor, H , at $y/L_s=0.0087$ and a) $t/T=0.54$; b) $t/T=0.88$; c) $t/T=0.21$

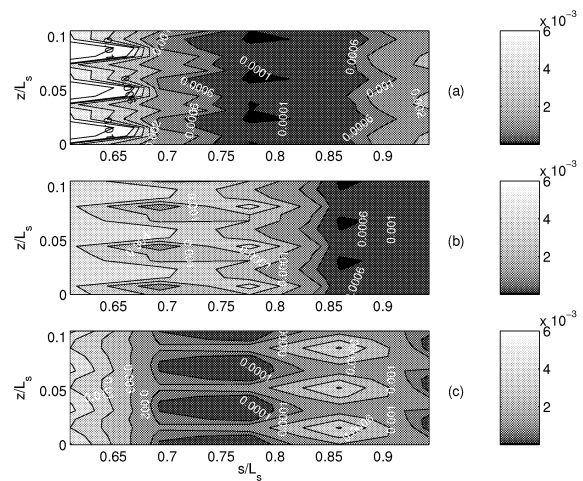


Fig. 15 Phase averaged c_r at $y/L_s=0.0087$ and a) $t/T=0.54$; b) $t/T=0.88$; c) $t/T=0.21$

past. Hence, the disturbance keeps the boundary layer attached, and the effect persists into the calmed period. Following the calmed period, the boundary layer begins to relax toward its uncontrolled, separated state. Figure 15 shows the local skin friction coefficient at the same phases as Figs. 11-14. The black regions indicate $c_f=0$ and separated flow. When the jets begin their outward pulse, they induce high speed fluid into the near wall region, resulting in very high skin friction just downstream of the jet holes, as shown by the white regions in Fig. 15a. Between the turbulent regions the skin friction is very low, and the boundary layer momentarily separates at locations between $s/L_s=0.7$ and 0.9 . The regions of zero or very low c_f in Fig. 15 are consistent with the regions of high H in Figs. 14. Figure 15b shows the boundary layer is separated at $s/L_s=0.86$, and Figs. 11b and 12b show that the VGJ disturbance is above this low c_f location. Fig. 13b shows that Re_θ is high at this location, while Fig. 14b shows that H is relatively high. The disturbance has arrived and begun to affect the outer part of the boundary layer, but it has not affected the near wall region yet, so the boundary layer remains separated. Slightly upstream at $s/L_s=0.78$ and the phase of Fig. 15b, the skin friction is high, the shape factor is low and the disturbance has just past. This is the calmed region following the disturbance, where the boundary layer has fully reattached.

CONCLUSIONS

The response of a boundary layer to a row of VGJs has been shown. The time averaged flow is spanwise uniform, but instantaneously the boundary layer is very three-dimensional. Streamwise vortices bring high speed fluid into the near wall region, suppressing separation. Evidence of the vortices persists to the trailing edge. The disturbance induced by the jets produces turbulence, but the boundary layer is thin and laminar between disturbances. The boundary layer separates at some locations, but the separation bubble remains thin and is only present for a small fraction of the VGJ cycle.

ACKNOWLEDGEMENTS

This work was sponsored by the NASA Glenn Research Center. The grant monitor was David Ashpis. Additional matching support was provided by the Office of Naval Research to the second author as a Naval Academy postdoctoral fellow.

REFERENCES

- Bons, J.P., Sondergaard, R., and Rivir, R.B., 2002, "The Fluid Dynamics of LPT Blade Separation Control Using Pulsed Jets," *ASME J. Turbomachinery*, Vol. 124, pp. 77-85.
- Compton, D.A., and Johnston, J.P., 1992, "Streamwise Vortex Production by Pitched and Skewed Jets in a Turbulent Boundary Layer," *AIAA J.*, Vol. 30, pp. 640-647.
- Gostelow, J.P., Walker, G.J., Solomon, W.J., Hong, G., and Melwani, N., 1997, "Investigation of the Calmed Region Behind a Turbulent Spot," *ASME J. Turbomachinery*, Vol. 119, pp. 802-809.
- Johnston, J.P., and Nishi, M., 1990, "Vortex Generator Jets. Means for Flow Separation Control," *AIAA J.*, Vol. 28, pp. 989-994.
- Johari, H., and Rixon, G.S., 2003, "Effects of Pulsing on a Vortex Generator Jet," *AIAA J.*, Vol. 41, pp. 2309-2315.
- McManus, K., Legner, H., and Davis, S., 1994, "Pulsed Vortex Generator Jets for Active Control of Flow Separation," *AIAA Paper 94-2218*.
- Volino, R.J., 2003, "Separation Control on Low-Pressure Turbine Airfoils Using Synthetic Vortex Generator Jets," *ASME J. Turbomachinery*, Vol. 125, pp. 765-777.

Abstract of presentation at the 55th Annual Meeting of the Division of Fluid Dynamics of the American Physical Society, Dallas, TX, 2002

Separation Control Using Synthetic Vortex Generator Jets

Ralph Volino (U.S. Naval Academy)

Boundary layer separation is a problem on some low-pressure turbine airfoils in aircraft engines. Airfoils are typically designed for optimal performance at takeoff, where maximum power is needed. When the aircraft climbs, however, the lower pressure at altitude (and lower Re) can result in separation from the suction side of the airfoils. Flow control would be desirable to minimize separation at low Re , without sacrificing performance at high Re . In the present experiments, synthetic vortex generator jets are used for flow control. This is the first known application of synthetic vortex generator jets. At low Reynolds numbers, without flow control, a large separation bubble is present. With the jets, the bubble is eliminated. The time averaged boundary layer appears laminar and attached. Ensemble averaged data shows that during each jet pulsing cycle, a turbulent patch moves down the airfoil, followed by a calmed period of attached laminar flow. Losses are lower than for a case in which reattachment was forced with a passive boundary layer trip. Smoke visualization as well as animations of ensemble averaged hot-wire data from boundary layer profiles will be presented.

Abstract of presentation at the 56th Annual meeting of the Division of Fluid Dynamics of the American Physical Society, East Rutherford, NJ, 2003

Separated Flow Transition Mechanism with Passive Flow Control under Low Pressure Turbine Conditions

Ralph J. Volino, Douglas G. Bohl (U. S. Naval Academy)

Boundary layer separation and transition have been studied experimentally on the suction side of a simulated low pressure turbine passage. Rectangular ribs were used as passive flow control devices to induce transition and promote reattachment. Thin ribs promote reattachment after a small separation bubble, resulting in lower aerodynamic losses. The ribs appear to have no immediate effect on the mean or rms streamwise velocity profiles, but do impart a very small disturbance in the boundary layer. The boundary layer separates, as in the unmodified flow, but undergoes transition and reattachment upstream of the location in the unmodified flow. Measurements of the wall normal velocity show the regular growth of small disturbances in the pre-transitional flow in cases with and without ribs. The transition mechanism appears similar in all cases. Ribs and elevated freestream turbulence increase the magnitude of the initial disturbance, leading to an earlier attainment of a disturbance large enough to initiate transition. These observations lead to a new correlation for transition onset location which accounts for rib height, freestream turbulence level, and Reynolds number

Abstract of presentation at the 57th Annual Meeting of the Division of Fluid Dynamics of the American Physical Society, Seattle, WA, 2004

Three-Dimensional Flow Structure Resulting from Oscillating Vortex Generator Jets

Ralph Volino, Douglas Bohl (U.S. Naval Academy)

A row of oscillating vortex generator jets is used in an experimental study to control boundary layer separation from an airfoil. Without flow control a large, burst separation bubble is present at low Reynolds numbers. With the jets active, the separation is eliminated. Ensemble averaged data (relative to the jet pulsing) show a turbulent patch moving down the surface after each outward jet pulse, followed by an extended calmed period characterized by a thin, attached laminar boundary layer. In the present study, profiles of streamwise and wall normal velocity have been measured at multiple spanwise locations between adjacent jets. The structure of the streamwise vortices is clear, with upwash and downwash regions. Ensemble averaged Reynolds shear and normal stresses, wall skin friction, mean velocity and integral quantities have been documented. Animations of the data show the generation of the vortices and their progression downstream, followed by periods of laminar, spanwise-uniform flow. The action of the vortices in bringing high speed fluid into the near wall region to achieve the separation control is illustrated

NOTE: The following pages were excerpted from Minnowbrook IV—2003 Workshop on Transition and Unsteady Aspects of Turbomachinery Flows, J.E. LaGraff and D.E. Ashpis, Editors, NASA/TM—2004-212913, August 2004, pp. 78–97.

ACTIVE AND PASSIVE FLOW CONTROL ON LOW PRESSURE TURBINE AIRFOILS

Ralph J. Volino
United States Naval Academy
Annapolis, Maryland 21402

Modern low-pressure turbine airfoils are subject to increasingly stronger pressure gradients as designers impose higher loading to improve efficiency and lower cost by reducing the number of airfoils in an engine. If the adverse pressure gradient on the suction side becomes strong enough, the boundary layer will separate. Separation bubbles, particularly those which fail to reattach, can result in a significant degradation of engine efficiency. The problem is particularly relevant in aircraft engines. Airfoils optimized to produce maximum power under takeoff conditions may still experience separation at cruise conditions, due to the thinner air and lower Reynolds numbers at altitude. An efficiency drop of 2% may occur between takeoff and cruise in large commercial transport engines, and the difference could be larger in smaller engines operating at higher altitudes. Needed is a means of controlling separation at low Re , without sacrificing the gains achieved at high Re .

In the present study, passive and active flow control are applied to the suction surface boundary layer on an LP turbine airfoil. Experiments are conducted in a single passage cascade simulator. Reynolds numbers (based on exit velocity and suction surface length) from 25,000 to 300,000 are considered under both high (8% inlet) and low (0.5%) free-stream turbulence (FSTI) conditions. In the passive control experiments, thin rectangular bars are applied to the airfoil near the suction surface velocity peak. Bars that are sufficiently large immediately trip the boundary layer to turbulent and prevent separation. Smaller bars initially appear to have little or no effect, and the boundary layer separates. Some distance downstream, however, small disturbances induced by the bars induce transition in the shear layer over the separation bubble, causing reattachment to move upstream relative to its location in the unmodified flow. The cases with the shortened separation bubbles appear to have lower losses than those with the larger trips. Bars which produce optimal results at low Re , however, invariably cause higher losses at the highest Re , suggesting the possible benefit of active flow control.

Active control is achieved using synthetic (oscillating, i.e. no net mass flow) vortex generator jets. An airfoil was constructed with a central cavity and a spanwise row of small holes extending from the cavity to the suction surface. The cavity is pulsed with a loudspeaker, causing jets to enter the boundary layer at a compound angle relative to the blade surface and the main flow. A single case has been documented to date with $Re=25,000$ and low FSTI. The separation bubble is completely eliminated, as shown through smoke visualization and animations of phase locked quantitative data. Ensemble averaged data (relative to the jet pulsing) show a turbulent patch moving down the blade after each outward jet pulse, followed by an extended "calmed" period characterized by a thin, attached laminar boundary layer. Losses appear substantially lower than with passive control.

Passive and Active Flow Control on Low Pressure Turbine Airfoils

Ralph J. Volino

Department of Mechanical Engineering

United States Naval Academy

Annapolis, Maryland

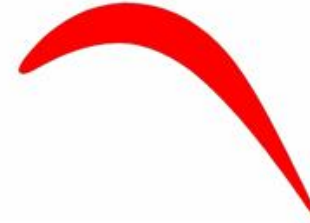


**Minnowbrook IV
August 18, 2003**

**Sponsor:
NASA Glenn Research Center**



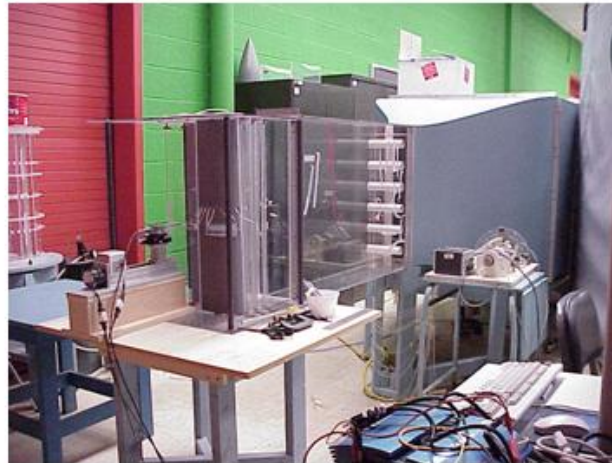
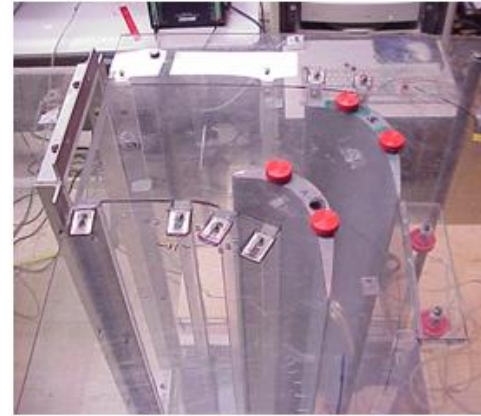
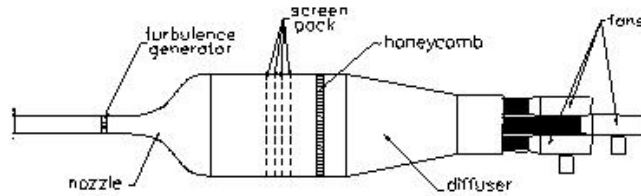
Introduction



Boundary layer separation is a problem on some LPT airfoils at low Re

- **Airfoils designed for takeoff**
 - Maximize thrust to weight ratio
 - Highly loaded airfoils
 - Strong pressure gradients
- **Separation affects performance at cruise**
- **2% or more drop in efficiency**
- **Want to minimize problem without sacrificing performance in other areas**

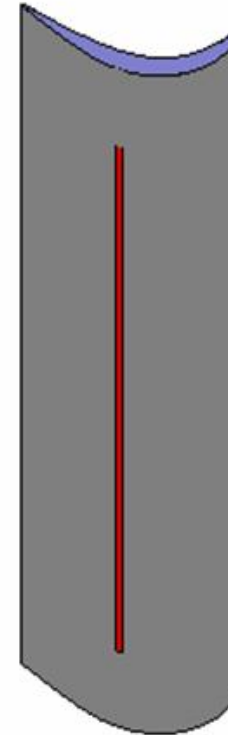
Experimental Facility



- Low speed wind tunnel
- $Re = U_e L_x / \nu$ from 25,000 (cruise) to 300,000 (takeoff)
- High (8.5%) and Low (0.5%) inlet Free-Stream Turbulence
- Single passage cascade simulator

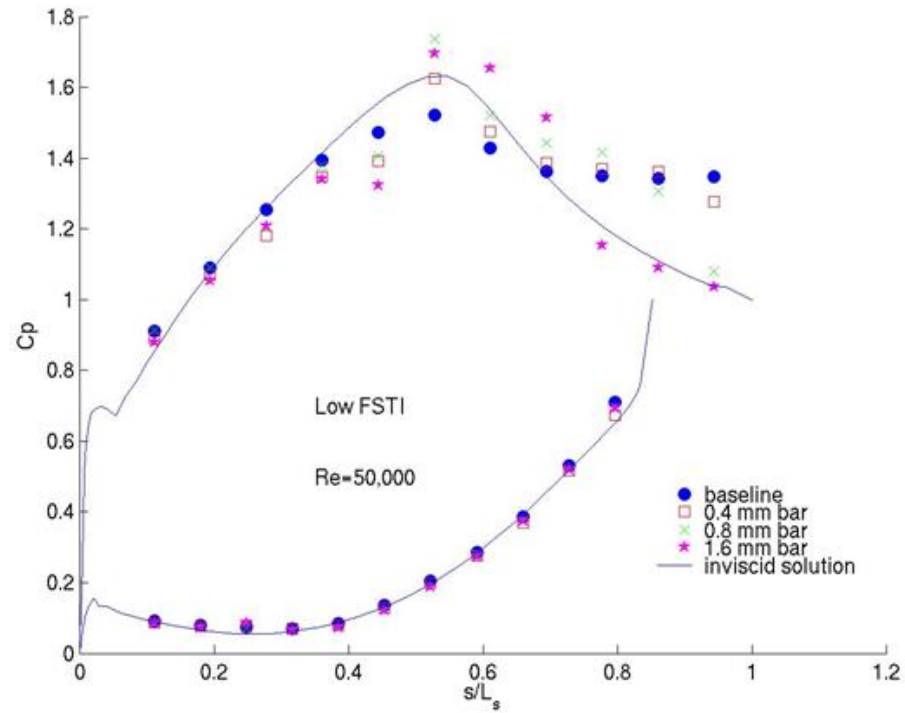
Passive Flow Control

- Rectangular bars (ribs)
 - Leading edge position, width not critical
 - Trailing edge position important
 - Located at suction surface velocity peak
 - 6 mm wide (suction surface length = 229 mm)
 - 4 heights: 0 (baseline), 0.4 mm, 0.8 mm, 1.6 mm
 - Compares to local $\delta_{99,5}$ between 1 and 4 mm depending on Reynolds number
- Single hot-wire, X-wire and pressure profiles for 40 conditions (5 Re, 2 TI, 4 heights)
- Data at 5 stations downstream of bar



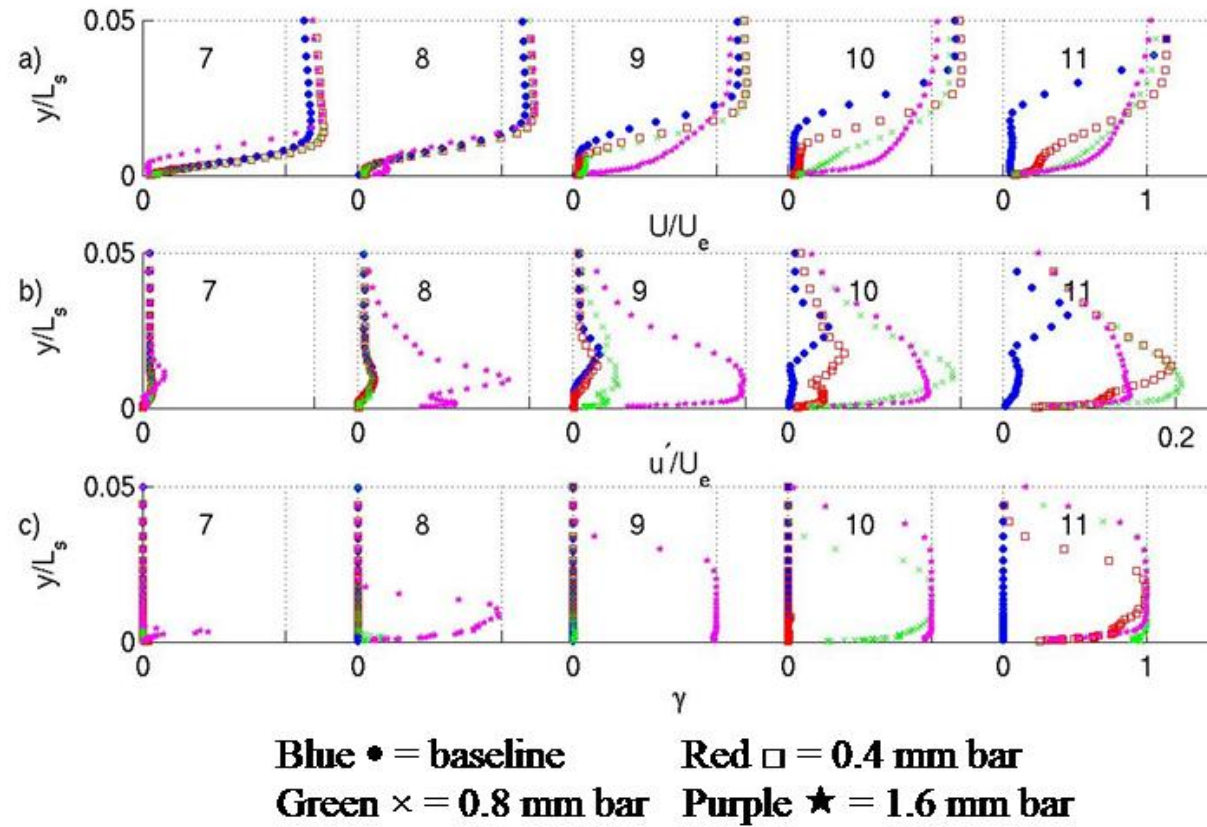
Results – Pressure Profiles

s =distance along surface
 L_s =suction surface length
 $C_p = \frac{2(P_T - P)}{\rho U_e^2}$



Low FSTI, Re=50,000

Low FSTI, $Re=50,000$



Shape Factor and Momentum Thickness

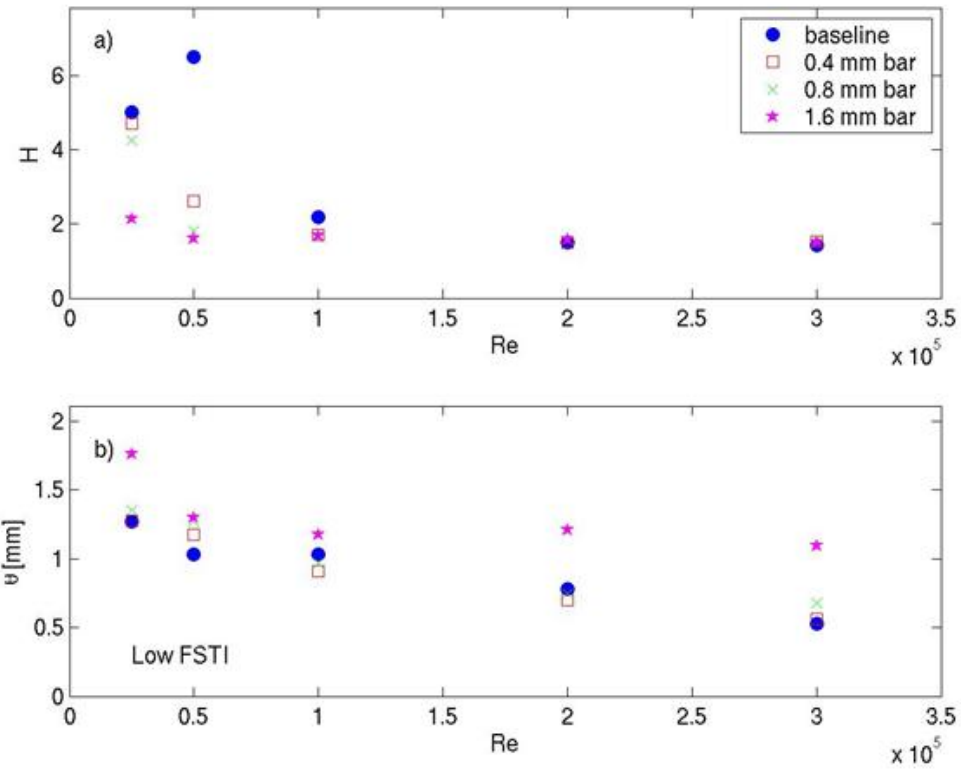
$$H = \delta^* / \theta$$

H at turbulent
value of 1.6
indicates
reattachment

St. 11
(near trailing edge)
Low FSTI

$$\theta$$

When attached,
momentum
thickness
proportional
to losses



Transition Mechanism

- **Transition mechanism appears similar to baseline, but shifted upstream with bars**
- **High and low FSTI cases have similar mechanism**
 - Same peak frequencies in spectra
 - Small disturbances from bars as important as FSTI level
 - Not a pure free stream induced bypass transition
- **Large bars have immediately detectable effect**
 - Bar blockage results in losses
- **Small bars add small disturbances to flow**
 - Initial detectable effect on the flow is minimal
 - Disturbances eventually grows to detectable level and promote transition
- **Optimal bar height allows small separation bubble**
 - Not big enough to trip boundary layer
 - Big enough to keep bubble small
 - Want reattachment near $s/L_s=0.74$ for conditions of present study
 - Optimal height depends on the Reynolds number
 - Correlation developed

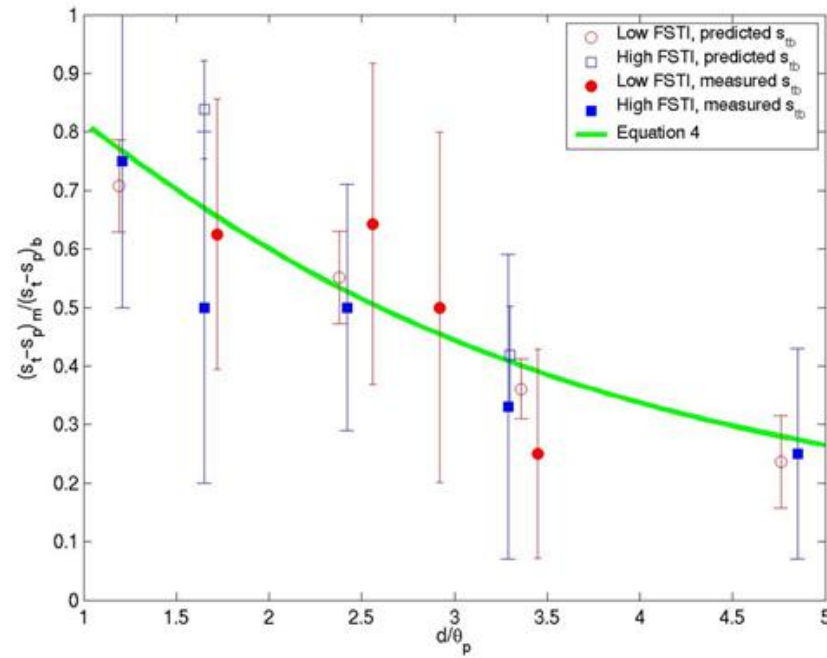
Optimal Bar Height

- Correlation of reattachment location to bar height

Ratio of distance from suction peak to transition start, $(s_t - s_p)$, in baseline, b , and modified, m , flow cases depends on bar height, d , and momentum thickness at suction peak, θ_p .

All variables except d are known or predictable. s_{tm} can be set to desired location.

Solve for d which will produce desired reattachment location in modified flow.



$$\text{Eq. 4: } (s_t - s_p)_m / (s_t - s_p)_b = (1 + 0.23(d/\theta_p)^{1.56})^{-1}$$

v' Boundary Layer Spectra

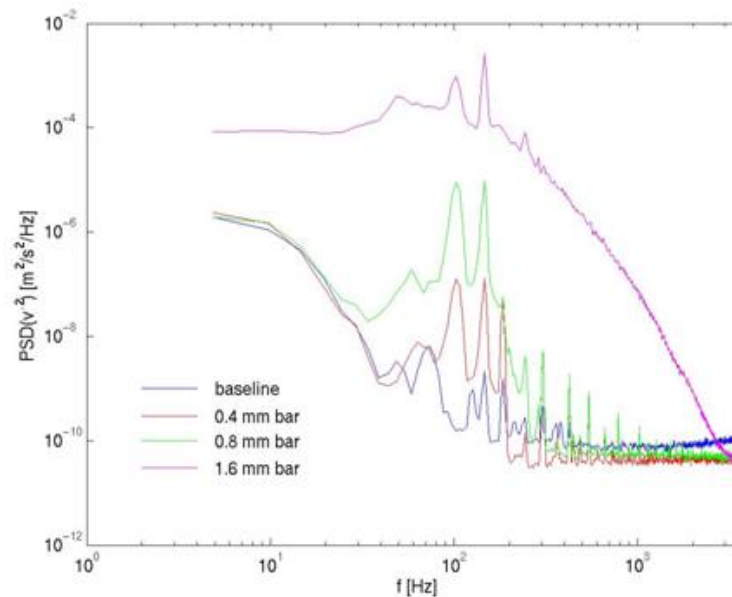
- Spectra show small disturbances induced by bars

Disturbances induced by bars were not immediately detectable in mean U or u' profiles.

While still very small, they are visible in the v' spectra.

Larger bars induce larger disturbances (note log scale).

Disturbances grow until large enough to induce transition.



Low FSTI, $Re=50,000$, Station 8

Growth of Disturbances

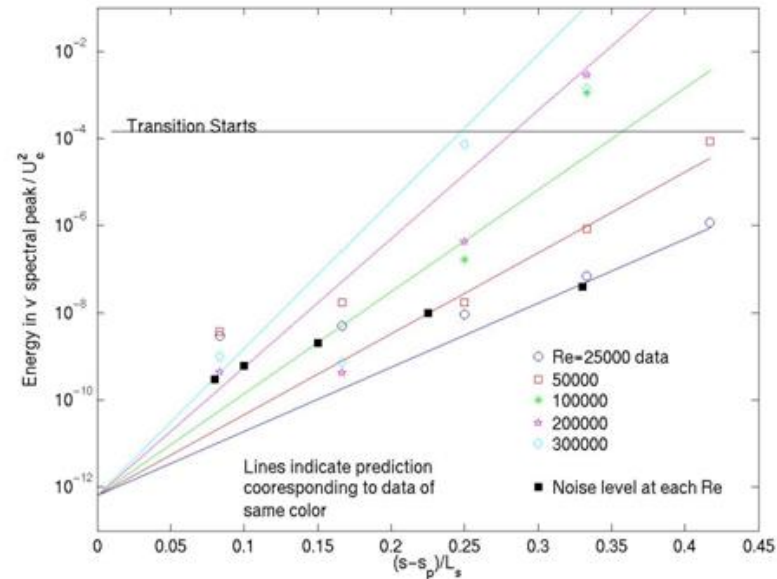
Energy in v' spectral peak plotted vs streamwise distance from suction peak.

Boundary layer becomes unstable when pressure gradient becomes adverse. Disturbances assumed to start growing at suction peak.

Values rise from a lower “noise” level up to a level high enough to induce transition.

Initial size of disturbance (intercept) appears to depend on FSTI and bar height.

Growth rate (slope) appears to depend on Re .

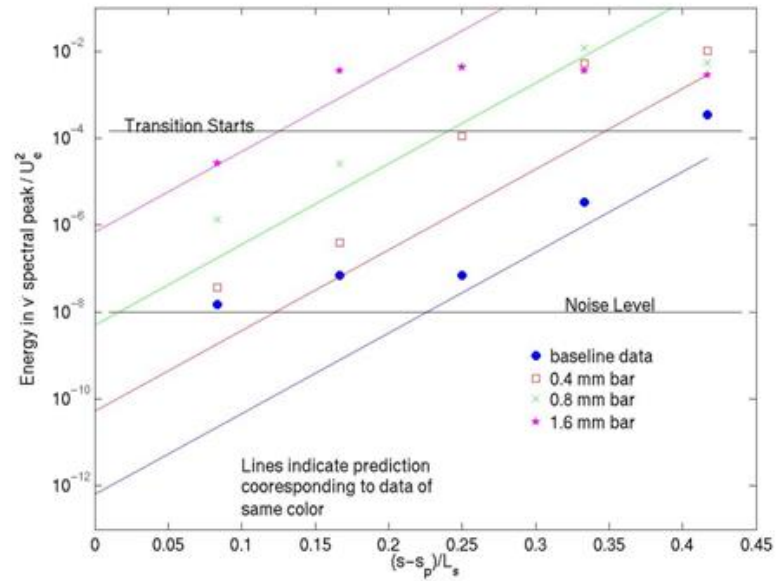


Low FSTI, Baseline Cases

Growth of Disturbances

All cases at same Re appear to have approximately the same slope.

Initial disturbance size increases with bar height.



Low FSTI, Re=50,000 Cases

Correlation of Observations

$$Re_{pt} = 2.42 \frac{(6.37 - \log(FSTI^2))}{1 + 0.23 \left(\frac{d}{\theta_p} \right)^{1.56}} Re^{2/3}$$

$$\frac{(s_t - s_p)}{L_s} = 1.98 \frac{(6.37 - \log(FSTI^2))}{1 + 0.23 \left(\frac{d}{\theta_p} \right)^{1.56}} Re^{-1/3}$$

$$Re_{pt} = 8.42 \frac{(6.37 - \log(FSTI^2))}{1 + 0.23 \left(\frac{d}{\theta_p} \right)^{1.56}} Re_{\theta_p}^{4/3}$$

Notes:

FSTI in % based on
local v_w' at suction peak

p=suction peak
t=transition start

$$Re_{pt} = U_{ap}(s_t - s_p)^{1/2}$$

These three equations
are equivalent for the
present cases. Because
the third equation uses a
local Re_{θ_p} value, it may
be more generally
applicable.

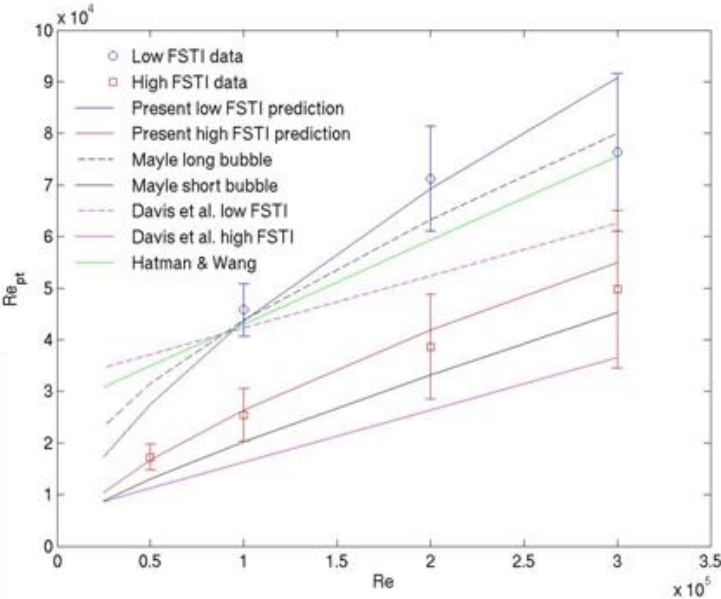
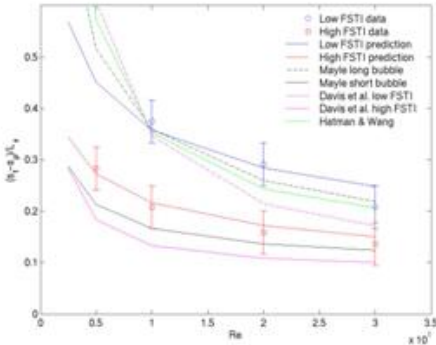
Comparison of Correlation to Data

Agreement is reasonable.

Correlations from literature also shown for comparison

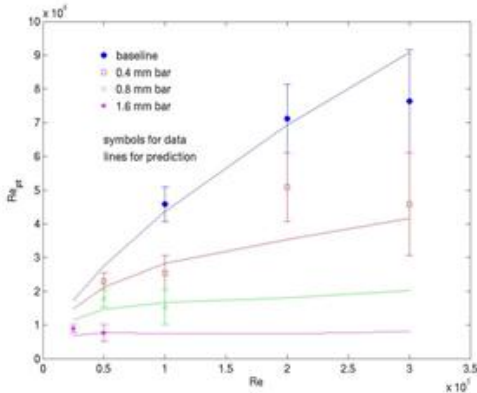
New correlation includes both Re and FSTI dependence.
Other correlations include only one of these effects.

Preliminary comparisons to other experimental cases in literature appear promising.

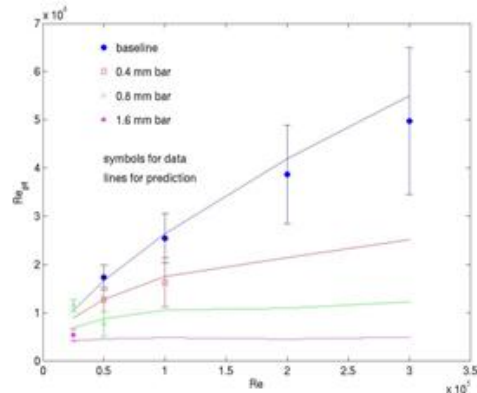
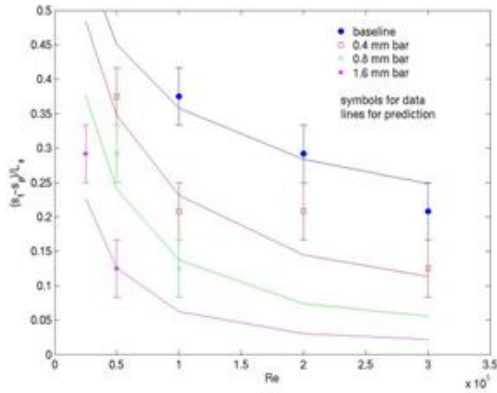


Baseline Cases

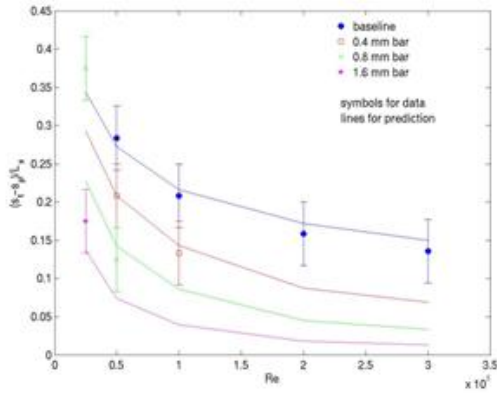
Comparison of Correlation to Data



**Low
FSTI**

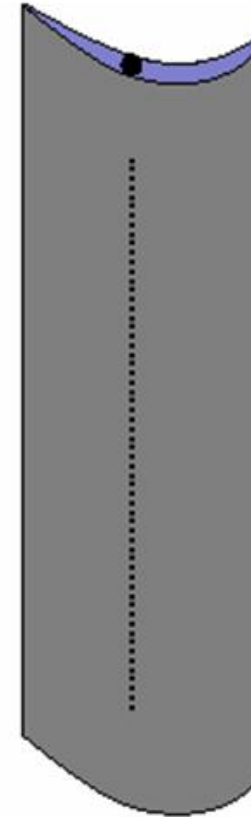


**High
FSTI**

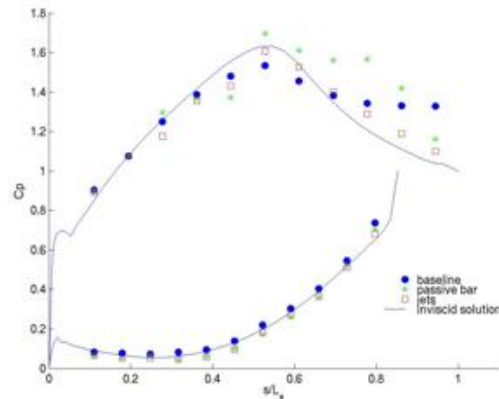


Active Flow Control with Synthetic (Oscillating) Vortex Generator Jets

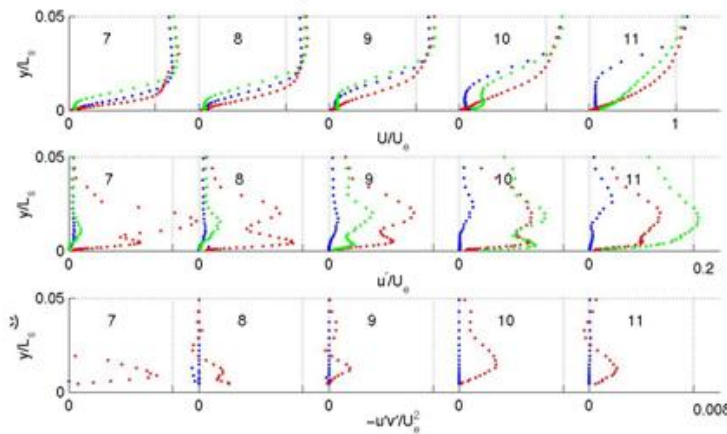
- Provide more flexibility than passive control
- Driven by loudspeaker through central cavity in airfoil
 - Single jet condition tested, not necessarily optimal
 - 10 Hz sine wave, $F^+ = 0.65$, maximum $V_{jet}/U_\infty = 5$
- Geometry copied from Bons et al.
 - Single row of jets
 - 0.8 mm diameter holes
 - 10:1 pitch /diameter ratio
 - 90° angle to flow
 - 30° angle to surface
- Located at suction surface velocity peak
- Low FSTI, $Re = 25,000$ case studied in detail
 - Most challenging case for flow control



Pressure and Velocity Profiles

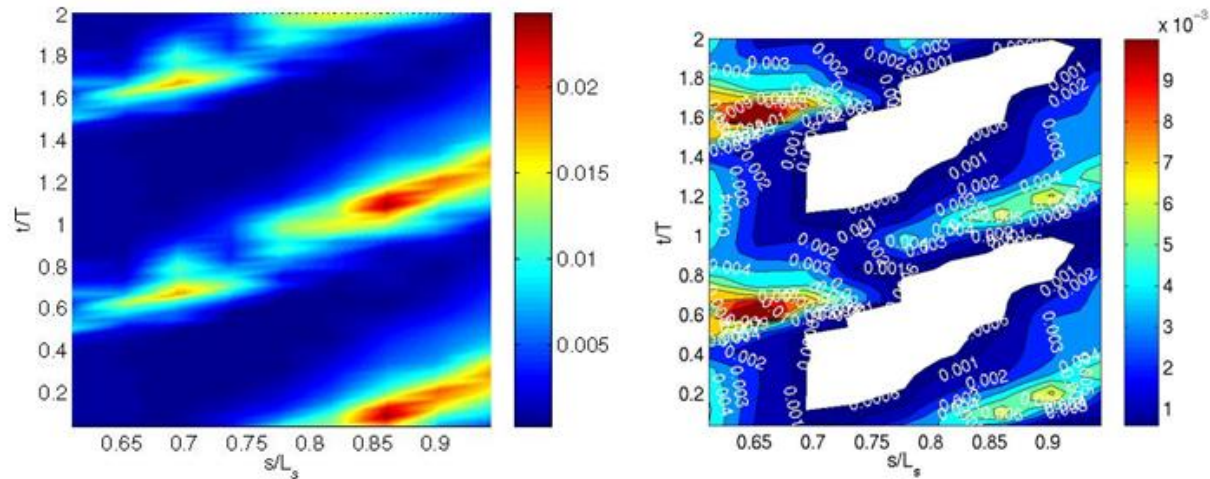


Pressure and mean velocity profiles show separation bubble is effectively eliminated



Mean velocity profiles appear laminar at all locations. Losses, as indicated by momentum thickness, are 20% lower than in cases with passive bar

Time Space Plots



Near wall u'/U_e

Skin Friction, C_f

- Jet produce turbulent events with celerities matching a turbulent spot
- Laminar flow between jet events
- C_f plot shows turbulent flow, separated flow under very thin separation bubble, and calmed region

Conclusions

- **Passive and active flow control demonstrated effective**
 - Passive holds advantage of simplicity
 - Active potentially more flexible and effective
- **Newest passive control results may shed light on separated flow transition mechanism**
- **Work continues**
 - Currently studying 3-D passive devices
 - Dimples next
 - More work with jets anticipated

REPORT DOCUMENTATION PAGE			Form Approved OMB No. 0704-0188		
<p>The public reporting burden for this collection of information is estimated to average 1 hour per response, including the time for reviewing instructions, searching existing data sources, gathering and maintaining the data needed, and completing and reviewing the collection of information. Send comments regarding this burden estimate or any other aspect of this collection of information, including suggestions for reducing this burden, to Department of Defense, Washington Headquarters Services, Directorate for Information Operations and Reports (0704-0188), 1215 Jefferson Davis Highway, Suite 1204, Arlington, VA 22202-4302. Respondents should be aware that notwithstanding any other provision of law, no person shall be subject to any penalty for failing to comply with a collection of information if it does not display a currently valid OMB control number.</p> <p>PLEASE DO NOT RETURN YOUR FORM TO THE ABOVE ADDRESS.</p>					
1. REPORT DATE (DD-MM-YYYY) 01-09-2012		2. REPORT TYPE Final Contractor Report		3. DATES COVERED (From - To) March 2000 to March 2005	
4. TITLE AND SUBTITLE Experimental Studies of Low-Pressure Turbine Flows and Flow Control Final Report		5a. CONTRACT NUMBER C-31011-K			
		5b. GRANT NUMBER			
		5c. PROGRAM ELEMENT NUMBER			
6. AUTHOR(S) Volino, Ralph, J.		5d. PROJECT NUMBER			
		5e. TASK NUMBER			
		5f. WORK UNIT NUMBER WBS 561581.02.08.03.21.13.02			
7. PERFORMING ORGANIZATION NAME(S) AND ADDRESS(ES) United States Naval Academy Anapolis, Maryland 21402		8. PERFORMING ORGANIZATION REPORT NUMBER E-18233			
9. SPONSORING/MONITORING AGENCY NAME(S) AND ADDRESS(ES) National Aeronautics and Space Administration Washington, DC 20546-0001		10. SPONSORING/MONITOR'S ACRONYM(S) NASA			
		11. SPONSORING/MONITORING REPORT NUMBER NASA/CR-2012-217656			
12. DISTRIBUTION/AVAILABILITY STATEMENT Unclassified-Unlimited Subject Categories: 02, 05, 07, and 34 Available electronically at http://www.sti.nasa.gov This publication is available from the NASA Center for AeroSpace Information, 443-757-5802					
<p align="center">Notice for Copyrighted Information</p> <p>This manuscript has been authored by an employee of the United States Naval Academy under a NASA Interagency Agreement No. C-31011-K with the National Aeronautics and Space Administration. The United States Government has a nonexclusive, irrevocable, worldwide license to prepare derivative works, publish or reproduce this manuscript, and allow others to do so, for United States Government purposes. Any publisher accepting this manuscript for publication acknowledges that the United States Government retains such a license in any published form of this manuscript. All other rights are retained by the copyright owner. Attachments are reprinted by permission.</p>					
13. SUPPLEMENTARY NOTES This report contains a supplemental CD-ROM containing processed data in ASCII format of streamwise pressure profiles and velocity profiles, along with the full text PDF file of this report. The CD-ROM can be obtained from the Center for AeroSpace Information (CASI) Web site at http://www.sti.nasa.gov Grant technical monitor, David E. Ashpis, Aeropropulsion Division, Glenn Research Center, organization code RTTO, ashpis@nasa.gov					
14. ABSTRACT This report summarizes research performed in support of the NASA Glenn Research Center (GRC) Low-Pressure Turbine (LPT) Flow Physics Program. The work was performed experimentally at the U.S. Naval Academy faculties. The geometry corresponded to "Pak B" LPT airfoil. The test section simulated LPT flow in a passage. Three experimental studies were performed: (a) Boundary layer measurements for ten baseline cases under high and low freestream turbulence conditions at five Reynolds numbers of 25,000, 50,000, 100,000, 200,000, and 300,000, based on passage exit velocity and suction surface wetted length; (b) Passive flow control studies with three thicknesses of two-dimensional bars, and two heights of three-dimensional circular cylinders with different spanwise separations, at same flow conditions as the 10 baseline cases; (c) Active flow control with oscillating synthetic (zero net mass flow) vortex generator jets, for one case with low freestream turbulence and a low Reynolds number of 25,000. The Passive flow control was successful at controlling the separation problem at low Reynolds numbers, with varying degrees of success from case to case and varying levels of impact at higher Reynolds numbers. The active flow control successfully eliminated the large separation problem for the low Reynolds number case. Very detailed data was acquired using hot-wire anemometry, including single and two velocity components, integral boundary layer quantities, turbulence statistics and spectra, turbulent shear stresses and their spectra, and intermittency, documenting transition, separation and reattachment. Models were constructed to correlate the results. The report includes a summary of the work performed and reprints of the publications describing the various studies.					
15. SUBJECT TERMS Gas turbines; Turbomachinery; Turbine; Low-pressure turbine; Turbulence; Flow control; Synthetic jets; Wakes; Separation; Vortex generated jets; Boundary layer; Tripps					
16. SECURITY CLASSIFICATION OF:			17. LIMITATION OF ABSTRACT	18. NUMBER OF PAGES 212	19a. NAME OF RESPONSIBLE PERSON STI Help Desk (email: help@sti.nasa.gov)
a. REPORT U	b. ABSTRACT U	c. THIS PAGE U			19b. TELEPHONE NUMBER (include area code) 443-757-5802

